



Manufacturing Constraints and Multi-Phase Shape and Topology Optimization via a Level-Set Method

Georgios Michailidis

► To cite this version:

Georgios Michailidis. Manufacturing Constraints and Multi-Phase Shape and Topology Optimization via a Level-Set Method. Optimization and Control [math.OC]. Ecole Polytechnique X, 2014. English. NNT : . pastel-00937306

HAL Id: pastel-00937306

<https://pastel.hal.science/pastel-00937306>

Submitted on 28 Jan 2014

HAL is a multi-disciplinary open access archive for the deposit and dissemination of scientific research documents, whether they are published or not. The documents may come from teaching and research institutions in France or abroad, or from public or private research centers.

L'archive ouverte pluridisciplinaire **HAL**, est destinée au dépôt et à la diffusion de documents scientifiques de niveau recherche, publiés ou non, émanant des établissements d'enseignement et de recherche français ou étrangers, des laboratoires publics ou privés.



Thesis submitted to obtain the title of

Doctor of École Polytechnique

Speciality: APPLIED MATHEMATICS

**Manufacturing Constraints and Multi-Phase Shape and
Topology Optimization via a Level-Set Method**

by

Georgios MICHAILIDIS

under the supervision of

Grégoire ALLAIRE

defended publicly on 27 January 2014 in front of the jury composed of

Marc ALBERTELLI	Technocentre Renault	Industrial advisor
Grégoire ALLAIRE	École Polytechnique	Thesis advisor
Nicolas CHARALAMBAKIS	Aristotle University of Thessaloniki	Thesis co-advisor
Pierre DUYSINX	Université de Liège	Reviewer
François JOUVE	Université Paris Diderot (Paris 7)	Thesis co-advisor
Mohamed MASMOUDI	Université Toulouse III - Paul Sabatier	Reviewer
Olivier PANTZ	École Polytechnique	Examiner

Prepared at
Centre de Mathématiques Appliquées,
École Polytechnique, Palaiseau, France.

To my parents Ioannis and Elli and to my brother Dimitrios,
who have always supported my choices.

In the memory of Fotini Kafetzi.

Acknowledgements

During the last decades, the number of Phd students has increased dramatically. The Lord of Academics and Protector of Phd Students meets great difficulties in coping with their continuous, consistent and varying demands. Therefore, in order to ease his work through uniformity, he has searched for somebody that meets all the requirements of a lucky student and asked him to write down a pray, which will be established in the future as "the pray of Phd students". This lucky guy is me and here is the pray:

Lord of Academics and Protector of Phd Students,

let my Phd conditions and collaborators resemble those of Georgios Michailidis - but please make the school be downtown!

Let my Phd advisor have the knowledge, personality and ability to supervise of Grégoire Allaire. To inspire me never to give up, to enter disciplines that are completely unknown to me without fear, just with the courage that I will finally make it. To trust me in projects of importance for himself and to respect my own personality and necessity to live a happy life.

Next to him, please place a co-advisor like François Jouve, willing to answer my silly questions for hours, reply to my emails on weekends and holidays and being always direct and honest with me.

If I get lost in my academic journey, please send me a mentor like Nicolas Charalambakis. And give me the patience and discipline to follow his advice, no matter if they seem strange sometimes, because he will care for me like a father for his son.

If you decide to send me an industrial project, put me in a team like the DREAM-team of Renault. Define someone like Marc Albertelli to be my advisor, psychologist, friend, etc. and surround me with people like Pierre, Paul, Fred, Pascal, ChriChri, Laurent and Yves that know how to combine work with joy.

And if it is your will that I suffer coding in a commercial software, then give me collaborators like Damien Lachouette and Thomas Abballe, patient to answer for years to my informatic questions, most of them at the level of elementary school, solve my bugs, having an outstanding understanding of my Phd-induced stress and willing to ease tremendously my work and life... without any obvious reason!

And if it is written in my destiny to participate in a big project, let it be like RODIN, to enjoy the discussions and disputs of Philippe versus all, but also to listen to his useful remarks.

Let me experience, at least once in my life, the moment that somebody like Yves Bréchet has something I have written on his table and says "I have read what you have written and I think it is interesting!", because this will encourage me through my whole life. Since you know that I am a very strange person, please take care that my close collaborators be like Raphael, Guillaume and Natasha, because then I will enjoy collaborating.

Put me in a laboratory like CMAP and set people like Kamel Hamdache and Nassera to play the role of my father and mother abroad. Let all my administrative problems be solved by CMAP secretaries and, of course, General Sylvain! For my difficult days - you know there will be a lot of them! - I will need people like Gabriel, Harsha, Matteo, Gwenael, Laetitia, Jean, Aymeric, Anna, Mamadou, Nicole, LiMa, Alex, Khalid and Xavier to speak with or take a beer - or two!

And if I need somebody to be all-in-one, advisor, collaborator, psychologist and friend, please make a replicate of Charles Dapogny! Place me in the same project with him, in order to understand and accept my limited skills, but also to stay motivated for work for fear of humiliation.

When I visit other laboratories, arrange things so that I meet people like François Murat and Pascal Frey, living to help young people and showing to others how a Professor in academics should be.

But also my Lord, don't forget of my personal life. Let my family support my dreams and believe in me as much as Georgios' family did. Give me friends like Koumparakos, Papadopoulos and Kafes to change my mood just by looking at them via Skype - please give also life to Skype employees! And give me some more time to spend with friends like Katerina, Monsef, George, Thanos, Sol, Antonis, Popi, etc.

And at the photo finish, let my thesis reporters be as kind as Pierre Duysinx and Mohamed Masmoudi were with Georgios, accepting to spend some of their precious vacation time to revise his manuscript.

Amen.

Manufacturing Constraints and Multi-Phase Shape and Topology Optimization via a Level-Set Method

Abstract

The main contribution of this thesis is the implementation of manufacturing constraints in shape and topology optimization. Fabrication limitations related to the casting process are formulated as mathematical constraints and introduced in the optimization algorithm. In addition, based on the same theoretical and modelization tools, we propose a novel formulation for multi-phase optimization problems, which can be extended to the optimization of structures with functionally-graded properties. A key ingredient for the mathematical formulation of most problems throughout our work is the notion of the signed distance function to a domain.

This work is divided into three parts. The first part is bibliographical and contains the necessary background material for the understanding of the thesis' main core. It includes the first two chapters. Chapter 1 provides a synopsis of shape and topology optimization methods and emphasizes the combination of shape sensitivity analysis and the level-set method for tracking a shape's boundary. In Chapter 2 we give a short description of the casting process, from which all our manufacturing constraints derive. We explain how industrial designers account for these limitations and propose a strategy to incorporate them in shape and topology optimization algorithms.

The second part is about the mathematical formulation of manufacturing constraints. It starts with Chapter 3, where the control of thickness is discussed. Based on the signed distance function, we formulate three constraints to ensure a maximum and minimum feature size, as well as a minimal distance between structural members. Then, in Chapter 4, we propose ways to handle molding direction constraints and combine them with thickness constraints. Finally, a thermal constraint coming from the solidification of cast parts is treated in Chapter 5 using several thermal models.

Multi-phase optimization is discussed in the third part. The general problem of shape and topology optimization using multiple phases is presented in detail in Chapter 6. A "smoothed-interface" approach, based again on the signed distance function, is proposed to avoid numerical difficulties related to classical "sharp-interface" problems and a shape derivative is calculated. An extension of this novel formulation to general types of material properties' gradation is shown in the Appendix A.

Keywords

Shape and topology optimization, level-set method, manufacturing constraints, casting constraints, thickness control, signed distance function, molding constraint, thermal constraints, multi-phase optimization.

Contraintes de Fabrication et Optimisation Multiphasiques de Forme et de Topologie avec la Méthode des Lignes de Niveaux

Résumé

La principale contribution de cette thèse est la mise en oeuvre des contraintes de fabrication dans l'optimisation géométrique et topologique de formes. Les limitations de fabrication relatives au procédé de fonderie sont formulées comme des contraintes mathématiques et sont introduites dans l'algorithme d'optimisation. En outre, en utilisant les mêmes outils théoriques et de modélisation, nous proposons une nouvelle formulation pour des problèmes d'optimisation à plusieurs phases, qui peut être étendue à l'optimisation des structures avec des propriétés fonctionnellement graduées. Un ingrédient clé pour la formulation mathématique de la plupart des problèmes tout au long de notre travail est la notion de fonction de distance signée d'un domaine.

Ce travail est divisé en trois parties. La première partie est bibliographique et contient le matériel de base nécessaire à la compréhension du noyau principal de la thèse. Il comprend les deux premiers chapitres. Le Chapitre 1 présente une synthèse des méthodes pour l'optimisation de formes et de la topologie et souligne la combinaison de l'analyse de sensibilité de la forme et la méthode des lignes de niveaux pour la description de la frontière de la forme. Dans le Chapitre 2 nous donnons une brève description du procédé de moulage, à partir de laquelle toutes nos contraintes de fabrication sont déduites. Nous expliquons comment les designers industriels tiennent compte de ces limitations et proposons une stratégie visant à les incorporer dans les algorithmes de l'optimisation de formes.

La deuxième partie est consacrée à la formulation mathématique des contraintes de fabrication. Il commence par le Chapitre 3, où le contrôle de l'épaisseur est discuté. Basé sur la fonction distance signée, on formule trois contraintes afin d'assurer une taille d'épaisseur maximale et minimale, ainsi qu'une distance minimale entre les membres de la structure. Puis, au Chapitre 4 nous proposons des façons de gérer les contraintes de la direction de démoulage et de les combiner ensuite avec des contraintes d'épaisseur. Finalement, une contrainte thermique provenant de la solidification des pièces coulées est traitée dans le Chapitre 5 utilisant plusieurs modèles thermiques.

L'optimisation multiphasique est discutée dans la troisième partie. Le problème général de l'optimisation de formes utilisant plusieurs phases est présentée en détail dans le Chapitre 6. Une approche des interfaces "lissées", encore une fois basée sur la fonction de distance signée, est proposée pour éviter les difficultés numériques liées aux problèmes classiques d'une interface "nette" et une dérivée de forme est calculée. Une extension de cette nouvelle formulation à l'optimisation de matériaux aux propriétés graduées est montrée dans l'Annexe A.

Mots-clés

Optimisation géométrique et topologique de formes, méthode des lignes de niveaux, contraintes de fabrication, contraintes de coulée, contrôle de l'épaisseur, fonction de distance signée, contrainte de démoulage, contraintes thermiques, optimisation à plusieurs phases.

Contents

Introduction	15
I Background material	27
1 Introduction to shape and topology optimization	29
1.1 Structural optimization	29
1.2 Shape optimization	30
1.2.1 Ill-posedness of shape optimization problems and remedies	30
1.2.2 Main categories of shape optimization	31
1.3 Shape and topology optimization via a level-set method	33
1.3.1 Shape sensitivity analysis	33
1.3.2 Level-set method	39
1.3.3 Coupling shape sensitivity with a level-set description	42
1.3.4 Extension and regularization of the velocity field	43
2 Casting constraints: physical description and classification	49
2.1 Introduction	49
2.2 Casting process	50
2.2.1 General description	50
2.2.2 Casting defects	50
2.3 Testing castability	51
2.3.1 Moldability	51
2.3.2 Feedability	53
2.3.3 Fillability	54
2.4 Conclusions	54
II Manufacturing constraints	57
3 Thickness control in structural optimization	59
3.1 Introduction	59
3.2 Formulation of thickness constraints	60
3.2.1 Maximum thickness	61
3.2.2 Minimum thickness	61
3.2.3 Minimum members' distance	62
3.2.4 Penalty functionals	63
3.3 Shape differentiability of the signed distance function	63
3.3.1 An application of the coarea formula to integral functions of the signed distance function	65
3.4 Shape derivative of penalty functionals	67
3.5 Augmented Lagrangian method and descent direction	69
3.6 Numerical implementation	70
3.6.1 Construction of d_Ω	70
3.6.2 Maximum thickness	72
3.6.3 Minimum thickness and minimum members' distance	72
3.7 Numerical examples	73

3.7.1	Maximum thickness	73
3.7.2	Minimum Thickness	93
3.7.3	Combination of thickness constraints	120
3.8	Other formulations of the thickness constraints	123
3.8.1	Maximum Thickness	123
3.8.2	Minimum Thickness	128
4	Molding direction constraints in structural optimization	133
4.1	Introduction	133
4.2	Formulation of the molding direction constraint	134
4.2.1	Molding direction condition on design velocity	134
4.2.2	Generalised molding constraint	135
4.2.3	Uniform cross-section surface constraint	135
4.3	Shape derivative	136
4.3.1	Molding direction condition on design velocity	136
4.3.2	Generalised molding constraint	137
4.3.3	Uniform cross-section surface constraint	139
4.4	Numerical examples	139
4.4.1	Molding direction	140
4.4.2	Uniform cross-section	146
5	Thermal constraints in structural optimization	149
5.1	Introduction	149
5.2	Formulation of the thermal constraint	150
5.3	Heat equation models and shape derivatives	150
5.3.1	Poisson equation	151
5.3.2	Linear transient heat equation	152
5.3.3	Eigenvalue approximation	155
5.3.4	Linear transient heat equation with piecewise discontinuous conductivity	158
5.3.5	Linear transient heat equation with piecewise discontinuous conductivity and heat flux across the moving boundary	164
5.3.6	Non-linear transient heat equation with phase-change	169
5.3.7	Numerical results	171
III	Multi-phase optimization	177
6	Multi-phase structural optimization	179
6.1	Introduction	180
6.2	Sharp-interface formulation in a fixed mesh framework	181
6.2.1	Description of the problem	181
6.2.2	Shape-sensitivity analysis of the sharp-interface problem	182
6.3	Shape derivative in the smoothed-interface context	186
6.3.1	Description of the problem	186
6.3.2	Shape derivative of the compliance in the multi-materials setting	187
6.3.3	Approximate formulas for the shape derivative	188
6.3.4	Convergence of the smoothed-interface shape optimization problem to the sharp-interface problem	189
6.4	Discussion and comparison with previous formulae in the literature	191
6.5	Extension to more than 2 materials	192
6.6	Numerical results	194
6.6.1	Level-set representation	194
6.6.2	Two materials in the sharp interface context	194
6.6.3	Two materials in the smoothed-interface context	195
6.6.4	Four materials in the smoothed interface context	200
6.6.5	Multi-functional optimization example	214
6.7	Material design using inverse homogenization	217
6.7.1	Setting of the problem	217
6.7.2	Calculation of the homogenized properties	218

<i>CONTENTS</i>	13
6.7.3 Shape derivative	220
6.7.4 Numerical results	221
Conclusions and future work	229
Appendices	231
A Material interface effects on the topology optimization of multi-phase structures	233

Introduction

This Thesis has been launched in the framework of the RODIN (Robust structural Optimization for Design in INdustry) project. RODIN has been motivated by the observation of many engineers and industrial designers that, although shape and topology optimization techniques can be a valuable tool for accelerating the design cycle and improving the final structure, existing shape and topology optimization software present several limitations and do not provide them with satisfying enough solutions.

The majority of commercial topology optimization softwares use density-based methods. A density field $\theta(x) \in [0, 1]$ is defined in the design domain and the original topology optimization problem is traded for a problem of optimal distribution of the material density. Despite the conceptual and mathematical convenience of such an approach, some new problems may appear. A first inconvenience is that, although the notion of a varying density makes sense for a composite structure, it has no meaning for a classical continuous medium, for which the value of the density is either 0 or 1 (we shall refer to such structures as 0 – 1 shapes). The majority of density-based methods use some penalization scheme for the material properties, which favors the formation of 0 – 1 shapes, at least for rigidity maximization in linearized elasticity. For example, the well-known SIMP (Solid Isotropic Material with Penalization) method, uses the scheme $A_{ijkl}(\rho) = \theta^p A_{ijkl}$, where A_{ijkl} is the elasticity tensor of the full material ($\theta = 1$) and p is a penalization power (usually $p = 3$). This scheme makes material with intermediate density values too expensive, since its volume depends linearly in θ . However, in more complex mechanical frameworks, the impact of such penalization schemes is not always evident and it is possible that the optimal solution contains large areas with intermediate values of the density field (see Figure 1). Then, the engineers need to interfere and extract a 0 – 1 shape using their mechanical intuition. This "interpretation" step can be non-trivial and results in non-optimal structures, especially in case of a complex mechanical framework, where intuition is limited.

Another limitation is related to the restricted range of applications that the existing softwares can treat efficiently. A first cause is that the use of a density field changes the formulation of the mechanical problem at play. The mechanical properties depend on the values of the density field in a more or less heuristic way. Although this dependence seems to work well for simple problems, e.g. compliance minimization in linearized elasticity, modifications need to be done for more complex problems, such as dynamics or stress-based criteria. Moreover, the density description makes impossible to treat efficiently problems where the precise position of the boundary plays an important role, e.g. thermal problems with heat exchange along an optimizable boundary.

In addition to the above mentioned confinements, it seems that existing softwares have not managed to

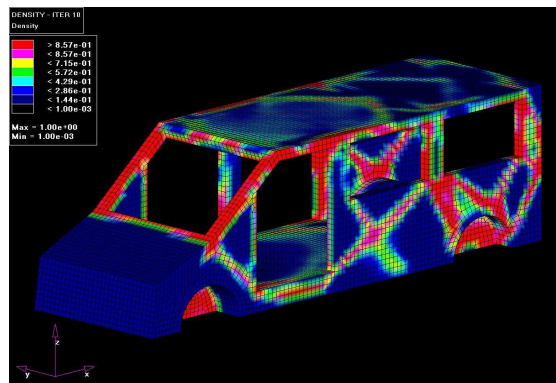


Figure 1: Optimized density distribution of a minivan's structural part, obtained with the commercial software OptiStruct of Altair Engineering (figure extracted from <http://www.vm.co.nz/examples.html>).

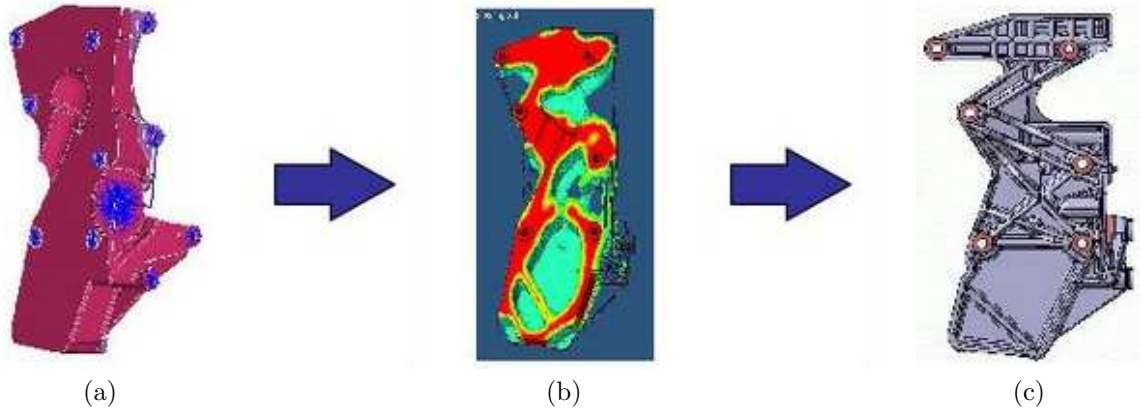


Figure 2: Optimization of an engine bracket; (a): design domain; (b) topology optimization result; (c) final design.

incorporate or combine efficiently manufacturing constraints in topology optimization. Although several ideas have appeared in the literature concerning the handling of some specific manufacturing constraints of geometric nature in a density framework, the results provided by commercial softwares are most of the times not manufacturable. In Figure 2, we see the basic steps for the design of an engine bracket, based on topology optimization. In the optimized result, we can observe the existence of some thin features in the lower part and some thick parts in the upper part. The final result requires then a postprocessing step, which can change significantly the shape and also cause a complete loss of its optimal characteristics.

We believe that there are two main reasons for this limitation. First, some of the proposed methods are very sensitive to the optimization parameters and thus are not suitable for a black box optimization software. Second, most of the methods are based on the notion of filters which relate the densities of different points using some scheme. Thus, when several constraints need to be combined, it is not clear how different filters interact and if a general filter that accounts for all constraints can be formulated.

Several industrial (Renault, EADS-IW, ESI-Group, SNECMA, etc...) and academic (Ecole Polytechnique, University Pierre et Marie Curie (Paris 6), University Denis Diderot (Paris 7), INRIA Bordeaux) partners participate in the RODIN project for the creation of a novel shape and topology optimization software, the goals of which are

- to eliminate the "interpretation" step, which is inherent in density-based methods, i.e. provide optimization results that are directly exploitable or need minimal manipulations,
- to expand the range of applications and improve the efficiency of shape and topology optimization in existing domains (stress-based criteria, etc...),
- to treat efficiently manufacturing constraints.

Based on the first two specifications, the combination of shape sensitivity analysis and a level-set description of the shape has been chosen as optimization method. Without entering into many details, the level-set method is a way of implicitly describing the boundary of a shape Ω , enclosed in a large computational domain D , via an auxiliary function ψ , such that (see Figure 3)

$$\begin{cases} \psi(x) = 0 & \leftrightarrow x \in \partial\Omega \cap D, \\ \psi(x) < 0 & \leftrightarrow x \in \Omega, \\ \psi(x) > 0 & \leftrightarrow x \in (D \setminus \bar{\Omega}). \end{cases}$$

The level-set description of the shape is well-known to be very efficient for topology optimization due to the ease at which topological changes occur, while keeping at the same time a "clear" 0 – 1 description of the shape. It is possible to mesh the level-set function on a fixed grid once during the optimization, or to adjust the mesh on the zero level-set at each iteration of the algorithm, after the work of C. Dapogny during his Phd thesis, also in the framework of the RODIN project (see Figure 4). In the first case, minimal changes are required in the formulation of the mechanical problem. The "void" part $D \setminus \Omega$ is represented by a weak "ersatz" material, whose material properties can be adjusted such that it has negligible mechanical contribution. In the second case, the mechanical problem is treated as such.

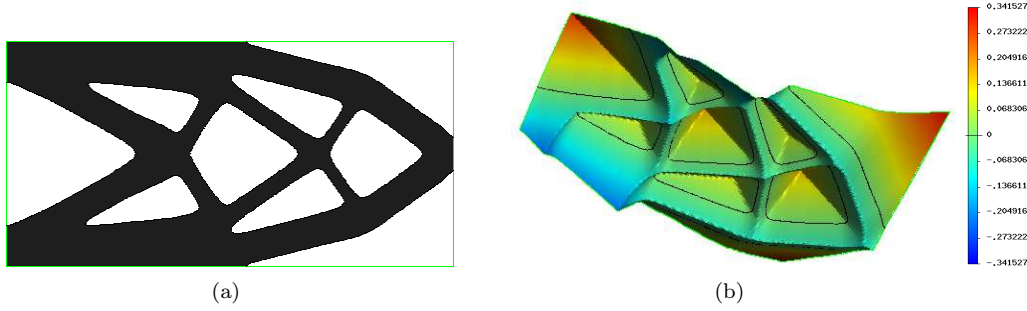


Figure 3: (a): Optimized shape Ω (in black), enclosed in a square working domain D ; (b): level-set representation of the shape.

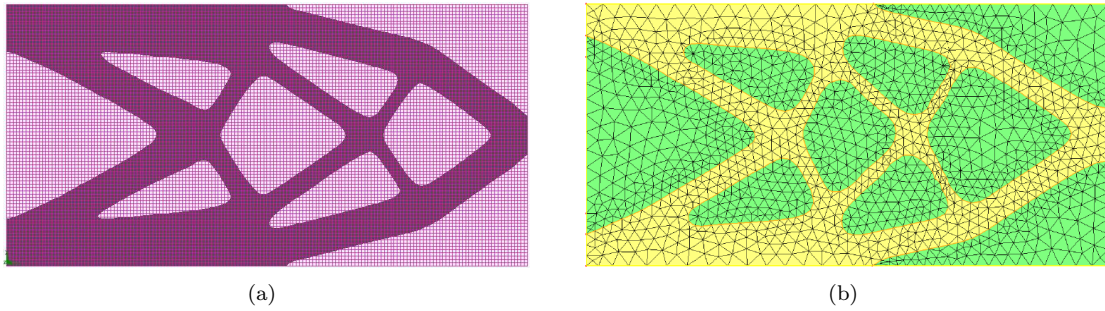


Figure 4: (a): Optimized structure using a fixed mesh for the level-set function; (b): optimized structure using an adapted mesh (figure extracted from [44]).

The main topic of this work is the implementation of manufacturing constraints in shape and topology optimization, using a level-set description of the shape. The reason why we highlight the "level-set description" is that the majority of the formulations herein are based on the assumption that a geometric description of the shape exists and that all geometric information for the shape are derived from the level-set description. However, some of them may also be used with slight modifications in the framework of other shape and topology optimization methods.

On top of manufacturing constraints, we also worked on multi-phase optimization. For this topic, our motivation came from discussions with researchers from the SIMAP laboratory at Joseph Fourier University in Grenoble who are interested in the impact of diffused interfaces on the optimal shapes. The formulations of multi-phase problems that previously existed in the literature were making a smooth approximation of sharp-interface problems but were plagued with an erroneous formula for the shape gradient, used in numerical algorithms. We worked in collaboration with C. Dapogny and G. Delgado and presented a thorough analysis of multi-phase problems in shape and topology optimization. An application of our work was a collaboration with the SIMAP laboratory about the effects of interface properties on the optimal shape.

The thesis is divided into three parts, which contain six chapters and one appendix. We present now a brief outline of each part separately. Technical details and bibliographical references on the corresponding topics are included in each chapter separately and are omitted in this introduction.

Part I: Background material

The first part contains Chapter 1 and 2 and provides the necessary background material for the analysis in the sequel. In Chapter 1, we recall the basic ingredients of shape and topology optimization and we insist more on the shape sensitivity analysis and the level-set method. In Chapter 2, we give a short description of the casting process, categorize the manufacturing constraints of interest and explain the strategy to follow in order to include them in shape and topology optimization.

Chapter 1: Introduction to shape and topology optimization

The first chapter starts with the basic elements about shape and topology optimization. The theoretical problem of non-existence, without additional constraints, of an optimal domain Ω that minimizes a shape-dependent cost functional $J(\Omega)$ is explained and techniques to circumvent it are discussed. The differences between the main categories of shape optimization, i.e. parametric, geometric and topology optimization, are explained. Then, we focus more on topology optimization, which addresses the problem of shape optimization in all generality. Among well-known methods for topology optimization, such as the homogenization method, the topological sensitivity method and the Soft Kill Option, we focus more on the SIMP method, since it is the method of choice for the majority of commercial softwares and there exists a great amount of literature on the topics of our interest, compared to other topology optimization methods.

In the sequel, we present the basic ingredients of our method of choice for shape and topology optimization, which combines a shape sensitivity analysis to obtain a descent direction and a level-set method for the shape description in order for topological changes to occur naturally during shape advection. We use Hadamard's method for shape variation, in which an initial domain Ω is perturbed by a smooth enough vector field θ to get a new domain $\Omega_\theta = (\text{Id} + \theta)\Omega$. This description allows to obtain a notion of shape derivative $J'(\Omega)(\theta)$ and to extract a notion of shape gradient for the iterative minimization of a functional J . The differences and the connection between Eulerian and Lagrangian shape derivatives of shape-dependent functions are explained and formulas for the shape derivative of volume and surface integrals are recalled. The background material on the shape sensitivity method closes with an example about how to find the shape derivative expression of a general type functional

$$J(\Omega, u(\Omega)) = \int_{\Omega} j(x, u(\Omega, x))dx + \int_{\partial\Omega} l(s, u(\Omega, s))ds,$$

where u is the solution to a linearized elasticity system, using the method of Céa.

The second basic element of our topology optimization method, i.e. the level-set method for the description of the shape, is then described. All shapes are assumed to be included in a big computational domain D and are represented implicitly via the zero level-set of a scalar function ψ , defined as:

$$\begin{cases} \psi(x) = 0 & \leftrightarrow x \in \partial\Omega \cap D, \\ \psi(x) < 0 & \leftrightarrow x \in \Omega, \\ \psi(x) > 0 & \leftrightarrow x \in (D \setminus \overline{\Omega}). \end{cases}$$

The advection of the shape Ω under a velocity field θ is then described via the advection of the level-set function through the transport equation:

$$\frac{\partial\psi}{\partial t}(t, x) + \theta(t, x(t)) \cdot \nabla\psi(t, x) = 0, \quad \forall t, \forall x(t) \in \partial\Omega(t),$$

which, for the case $\theta(t, x) = V(t, x) \frac{\nabla\psi(t, x)}{|\nabla\psi(t, x)|}$, which is of interest for shape optimization, writes again as:

$$\frac{\partial\psi}{\partial t}(t, x) + V(t, x)|\nabla\psi(t, x)| = 0, \quad \forall t, \forall x \in D.$$

Finally, the coupling of shape sensitivity with a level-set description is explained. The shape gradient is interpreted as an advection velocity for the level-set function and an iterative algorithm is built for the numerical minimization of the cost function. Two basic steps for this coupling are explained, the "ersatz material" approach for representing the void part $D \setminus \Omega$ and the extension and regularization of the velocity field in order to accelerate the convergence speed.

Chapter 2: Casting constraints: physical description and classification

In the second chapter, we provide a physical description of casting constraints, which are the manufacturing constraints of our interest, explain how industrial designers usually account for them and propose a general framework under which they can be introduced in shape and topology optimization.

The molding system, i.e. the number, the position and the direction of removal of the molds, plays a crucial role on the final design of a cast part. Furthermore, among the variety of possible casting defects,

the design engineer needs to take into consideration the shrinkage porosity and the pouring metal defects, which are closely linked to the shape of the structure. We propose to test castability through ensuring the following three properties of the cast part:

- moldability, i.e. the ability to construct and remove the molds after solidification of the cast part,
- feedability, i.e. the ability to construct a feeding system in order to drive the shrinkage porosity due to solidification into the risers, at an acceptable cost,
- fillability, i.e. the ability to fill the molds with liquid metal, avoiding premature solidification and the use of high additional pressure.

Some of the above properties are of purely geometric nature, while others derive from the physics of casting. In this last case, the complete casting system is needed for the analysis, which we believe is not practical for topology optimization, since the shape changes during the optimization. For this reason, equivalent geometric criteria are usually set by the designers in place of the mechanical ones, or the actual mechanical problems are simplified by omitting the complete casting system and setting approximative boundary conditions.

The three above requirements impose several specifications that the design needs to comply with. More specifically, moldability induces constraints on the:

- molding direction
- minimum members' distance
- maximum curvature.

Feedability can be treated either geometrically, by imposing a:

- maximum thickness feature,

or mechanically, by setting a:

- maximum solidification time,

working with a simplified casting model.

Finally, fillability is very difficult to be treated mechanically and thus, we follow a geometric approach by imposing a:

- minimum thickness feature.

Part II: Manufacturing constraints

The second part is devoted to manufacturing constraints and covers Chapter 3, 4 and 5. Thickness control is discussed in Chapter 3. Chapter 4 is more linked to cast parts and we propose therein methods to treat constraints on the molding direction. Chapter 5 refers in general to thermal problems, but we concentrate more on a thermal constraint derived from the cooling process during casting. We have coded almost all developments of this part (with a slight exception in Chapter 5), in the commercial software SYSTUS of ESI-Group.

Chapter 3: Thickness control in structural optimization

In the third chapter we deal with thickness control. A priori, the level-set description provides no geometric information about the thickness of the structure. In addition to this, it is not clear how a notion of thickness can be defined for continuous structures.

We tackle both problems using the signed distance function to the domain Ω , defined as

$$d_{\Omega}(x) = \begin{cases} -d(x, \partial\Omega) & \text{if } x \in \Omega, \\ 0 & \text{if } x \in \partial\Omega, \\ d(x, \partial\Omega) & \text{if } x \in \overline{^c\Omega}, \end{cases}$$

where $d(\cdot, \partial\Omega)$ is the usual Euclidean distance. We highlight the difference between d_Ω and ψ , the level-set function used for the advection of the shape.

First, we formulate three pointwise constraints for the maximum and minimum thickness feature and for the minimum distance between the shape's members. We have based the maximum thickness constraint on the idea that no point should be the center of a ball of radius $d_{max}/2$, fully covered with material. For the minimum thickness and the minimum members' distance constraints, we have adopted a different concept, based on the idea of offset sets. For the minimum thickness, starting from a point on the boundary of the domain, we move in the opposite direction of the normal vector and check if we get out of the shape up to a distance d_{min} . We do the same for the members' distance, in the opposite direction. Their mathematical formulation, using the signed distance function, read:

$$\begin{aligned} \text{Maximum Thickness :} & \quad d_\Omega(x) \geq -d_{max}/2 \quad \forall x \in \Omega, \\ \text{Minimum Thickness :} & \quad d_\Omega(x - d_{off}n(x)) \leq 0 \quad \forall x \in \partial\Omega, \forall d_{off} \in [0, d_{min}], \\ \text{Minimum Members' Distance :} & \quad d_\Omega(x + d_{off}n(x)) \geq 0 \quad \forall x \in \partial\Omega, \forall d_{off} \in [0, d_{min}]. \end{aligned}$$

Then, in order to avoid the complexity of treating a large number of constraints, we propose to formulate global averaged constraints using simple quadratic penalty functionals:

$$\begin{aligned} \text{Maximum Thickness :} & \quad P_{MaxT}(\Omega) = \int_\Omega \left[(d_\Omega(x) + d_{max}/2)^- \right]^2 dx = 0, \\ \text{Minimum Thickness :} & \quad P_{MinT}(\Omega) = \int_{\partial\Omega} \int_0^{d_{min}} \left[(d_\Omega(s - \xi n(s)))^+ \right]^2 d\xi ds = 0, \\ \text{Minimum Members' Distance :} & \quad P_{MMD}(\Omega) = \int_{\partial\Omega} \int_0^{d_{min}} \left[(d_\Omega(s + \xi n(s)))^- \right]^2 d\xi ds = 0, \end{aligned}$$

where: $(f)^+ = \max(f, 0)$ and $(f)^- = \min(f, 0)$.

The shape derivatives of the above functionals are computed, using information about the shape differentiation of the signed distance function and a co-area formula.

We propose an alternative formulation for the maximum thickness functional, as well as some modifications on the computation of its shape derivative, in order to avoid distortions at the crossing of features and close to the boundary of the working domain, which are inherent in the formulation of the constraint. We test the above formulations with several 2d and 3d examples on volume minimization under a compliance constraint, using a simple augmented Lagrangian algorithm (see Figure 5).

Finally, we discuss on some well-known formulations of thickness control in the framework of the SIMP method, explain the differences with our formulations and propose constraints following a similar concept in the framework of classical shape optimization, wherever possible.

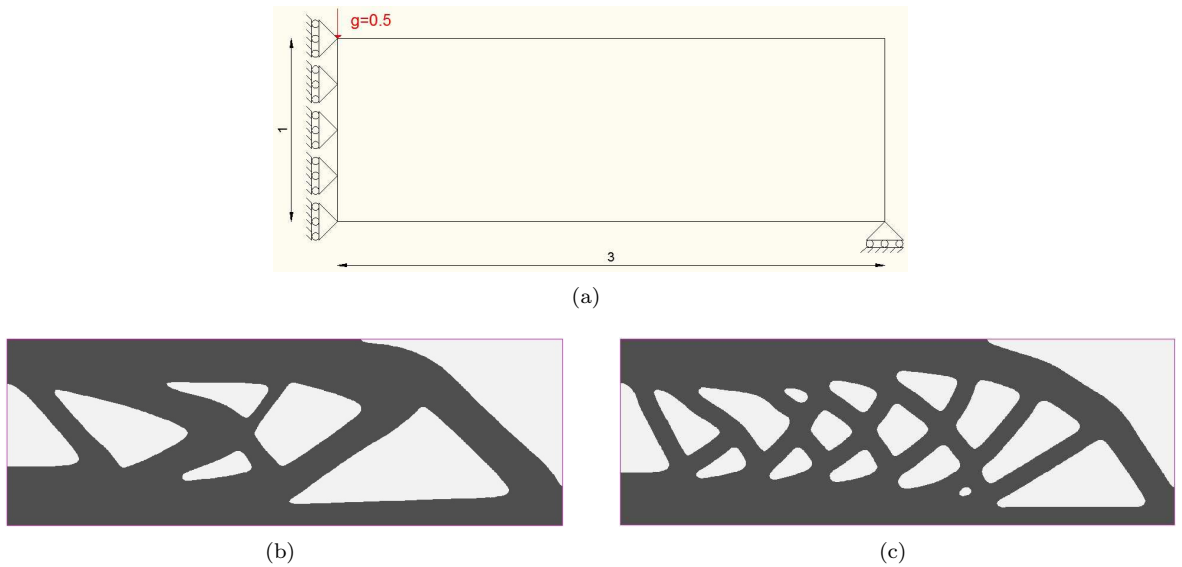


Figure 5: (a): boundary conditions for a 2d MBB beam; (b): optimized shape without thickness constraints; (c) optimized shape with maximum and minimum thickness constraints.

Chapter 4: Molding direction constraints in structural optimization

The fourth chapter refers to the molding direction constraint, which is particular of cast parts. The molding system is supposed to be fixed and the optimized shape must not contradict with the removal of the molds.

We present first the idea of Xia et al. on this topic, which consists of starting with a feasible shape and allow each part to move only parallel to its corresponding parting direction. This strategy ensures that the shape will remain always feasible and is very efficient when it is not combined with thickness constraints. We explain that the limitation of the shape to increase in size orthogonally to its parting direction excludes the possibility of combining this strategy with a constraint on the minimum thickness feature.

Therefore, we formulate some generalized molding direction constraints, using information from the unit normal vector or the signed distance function. A first formulation reads:

$$d_i \cdot n(x) \geq 0, \quad \forall x \in \Gamma_i,$$

where d_i is the parting direction of the boundary part $\Gamma_i \subset \partial\Omega$. The shape derivation of the normal vector is quite complicated, as we show later in this chapter and thus, we propose also the following formulation using the signed distance function:

$$d_\Omega(x + \xi d_i) \geq 0 \quad \forall x \in \Gamma_i, \forall \xi \in [0, \text{diam}(D)],$$

where we denote $\text{diam}(D) = \sup_{x,y} \{\text{dist}(x,y), x,y \in D\}$ the diameter of the fixed domain D . In case the area of possible contact between two molds is not a priori defined, the constraint is slightly modified and reads

$$d_\Omega(x + \xi \text{sign}(n \cdot d)d) \geq 0 \quad \forall x \in \partial\Omega, \forall \xi \in [0, \text{diam}(D)],$$

where d is the parting direction of the molds. The above pointwise constraints are formulated again as global averaged constraints and their shape derivative is computed.

Finally, we propose ways to impose a uniform cross-section constraint. One of them consists simply in starting with a shape with a uniform cross-section and consider vector fields that are constant along its normal direction. Another idea is to start again with a shape that respects the constraint and impose the constraint numerically via an anisotropic regularization.

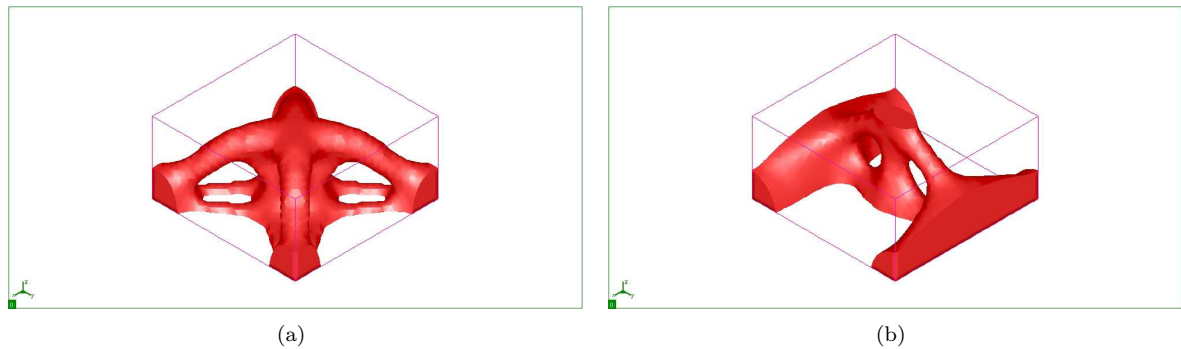


Figure 6: Optimized shape (a): without molding direction constraint; (b): with molding direction constraint ($d = (1, 0, 0)$).

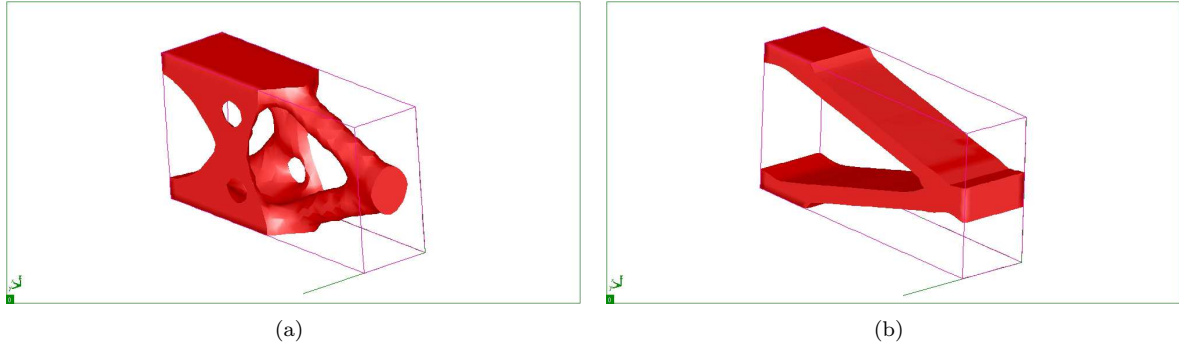


Figure 7: Optimized shape (a): without uniform cross-section; (b): with uniform cross-section.

Chapter 5: Thermal constraints in structural optimization

The fifth chapter is devoted to the only manufacturing constraint of mechanical nature in this work, i.e. the constraint on the maximum solidification time. For a cast part that starts solidifying ideally from a uniform initial temperature, we need to ensure that it solidifies at most at time t_f , i.e. the temperature T must be everywhere under the corresponding solidus temperature of the metal T_s . The mathematical formulation of the constraint reads:

$$T(x, t_f) \leq T_s, \quad \forall x \in \Omega.$$

The thermal model that describes the solidification process is a non-linear transient heat equation with phase change. We believe that the application of the constraint since the beginning of the optimization algorithm using this model is too costly in memory and time. Moreover, the calculation of the shape derivative is not straightforward, since there is a discontinuity of the temperature field on the interface between the cast part and the mold. For the above reasons, we have proposed to use much simpler models as a first step. However, we expect that even these models will give satisfying results, since in all of them the large volumes of material tend to reduce.

We propose to test the following thermal models of increasing difficulty and computational cost:

- Poisson equation with Dirichlet boundary conditions.
- Linear transient heat equation with Dirichlet boundary conditions.
- Approximation of the previous model via the first term of its Fourier series (eigenvalue approximation).
- Linear transient heat equation with piecewise constant conductivity.
- Linear transient heat equation with heat flux across the moving boundary.
- Non-linear transient heat equation with heat flux across the moving boundary and phase-change.

For all of them, we present the formulation of the problem and we compute the shape derivative of a global averaged constraint. We present 2d numerical results using the first three models. The temperature limit needs to be adjusted for each case in order for the results to be comparable in a certain sense. For this reason, we consider an one-dimensional model of the casting system for a cast part of size d_{max} and we set the temperature limit equal to the maximum value of the temperature after time t_f .

Part III: Multi-phase optimization

Finally, Part III is about multi-phase optimization and includes Chapter 6 and the Appendix. In Chapter 6, we discuss the general problem of multi-phase optimization. "Sharp-interface" and "smoothed-interface" models are presented in detail and the difference with the previous literature on the topic is explained. The Appendix contains an article that we submitted in the journal SMO (Structural and

Multi-disciplinary Optimization) about the interface-effects on the optimized shape, which is a result of our collaboration with the SIMAP laboratory of Joseph Fourier University in Grenoble. All numerical results for multi-phase optimization with a "diffuse" interface have been done using a 2d code written in Scilab, while for the case of a "sharp-interface" a 2d code in FreeFem++ was used.

Chapter 6: Multi-phase structural optimization

The final chapter of this work is about multi-phase optimization. It starts with the problem of optimal distribution of two materials with Hooke's tensor A_0 and A_1 , occupying two subdomains Ω^0 and Ω^1 of the working domain D .

First, we study the classical "sharp-interface" model, in which the global Hooke's tensor is assumed to be discontinuous on the interface between the materials and is given as

$$A = \chi_{\Omega^0} A_0 + (1 - \chi_{\Omega^0}) A_1,$$

χ_{Ω^0} being the characteristic function of the domain Ω^0 . We compute the shape derivative for the compliance of the structure and explain the difficulties in the numerical approximation of its terms when a fixed mesh is used. We propose instead to differentiate the discretized problem, which provides a consistent approximation.

Then, we consider a "smoothed-interface" model, where the material properties are interpolated between the two phases in an area of width 2ε around their intermediate interface, defined as the zero level-set of a level-set function ψ . A smooth interpolation function $h_\varepsilon(d_{\Omega^0})$ is used, which depends on the signed distance function to the domain Ω^0 . In this chapter, $h_\varepsilon(d_{\Omega^0})$ is chosen to be a smooth approximation of the Heaviside function and we prove that this problem converges to the "sharp-interface" problem when the interpolation width tends to zero.

Our main contribution in this "smoothed-interface" formulation is the correct computation of the shape derivative. For the case of the compliance:

$$J(\Omega^0) = \int_D A e(u) : e(u) dx$$

it reads

$$J'(\Omega^0)(\theta) = - \int_{\Gamma} \theta(x) \cdot n(x) (f_0(x) + f_1(x)) dx,$$

where Γ is the optimizable boundary, n is the outer unit normal to Ω^0 and f_0, f_1 are scalar functions defined by

$$f_0(x) = \int_{\text{ray}_{\Gamma}(x) \cap \Omega^0} h'_\varepsilon(d_{\Omega^0}(z)) (A_1 - A_0) e(u)(z) : e(p)(z) \prod_{i=1}^{N-1} (1 + d_{\Omega^0}(z) \kappa_i(x)) dz,$$

$$f_1(x) = \int_{\text{ray}_{\Gamma}(x) \cap \Omega^1} h'_\varepsilon(d_{\Omega^0}(z)) (A_1 - A_0) e(u)(z) : e(p)(z) \prod_{i=1}^{N-1} (1 + d_{\Omega^0}(z) \kappa_i(x)) dz,$$

where z denotes a point in the ray emerging from $x \in \Gamma$, i.e. the line connecting $x \in \Gamma$ with its corresponding point on the skeleton of the shape.

We emphasize the differences with previous publications on the topic and propose simplified formulas. We show how the method is extended for more than two phases and test this formulation in compliance minimization, multi-functional optimization for the design of rigid and thermally isolating structures and materials design using inverse homogenization.

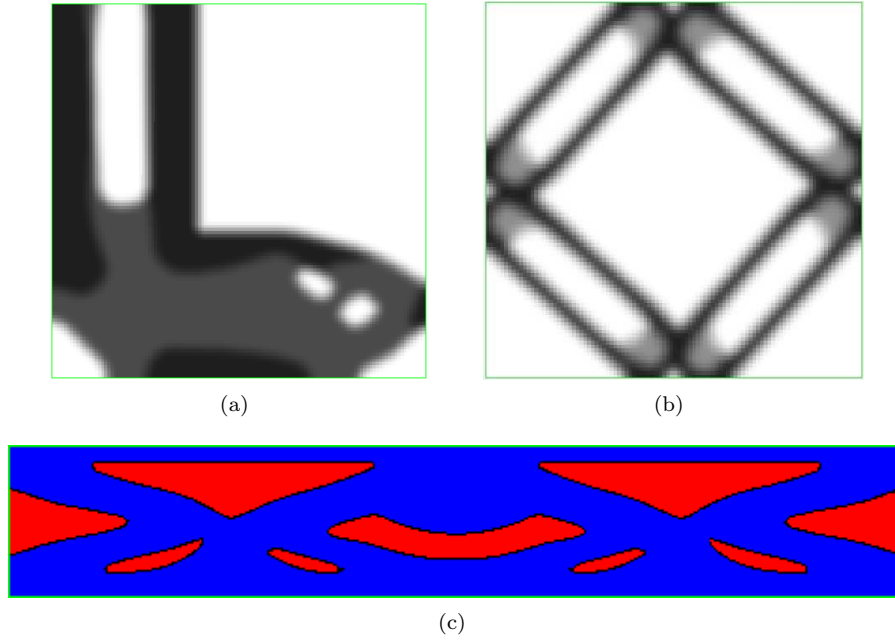


Figure 8: Optimized shape of (a): L-shaped structure for compliance minimization; (b): unit-cell of periodic medium with target thermoelastic coefficients; (c): multi-functional structure for structural rigidity and thermal isolation.

Appendix A: Material interface effects on the topology optimization of multi-phase structures

The Appendix is the exact reproduction of a submitted article, which is a result of our collaboration with a team from the SIMAP laboratory of Joseph Fourier University in Grenoble.

This work can be regarded as an extension of the applications of the "smoothed-interface" formulation in Chapter 6, in the sense that it accounts for general types of the interpolation function $h_\varepsilon(d_{\Omega^0})$. Motivated by physical observations, we study the effect in the optimal shape of non-monotonic interpolation of the material properties around the interface of the two phases. Previous formulas in the literature cannot be used even for the approximative study of such cases, since it is the integration along the "rays" that allow to take into consideration the specific gradation profile.

We view this study as a first step towards the shape and topology optimization of functionally-graded structures of general type.

Part of our work on multi-phase optimization, presented mainly in Chapter 6 and partly in Chapter 3, has been accepted for publication under the title:

G. Allaire, C. Dapogny, G. Delgado, and G. Michailidis. *Mutli-phase structural optimization via a level-set method*. (to appear in ESAIM: Control, Optimisation and Calculus of Variations), 2013.

We have also submitted for publication our work on material interface effects, in collaboration with the SIMAP laboratory, which is presented as such in the Appendix, with the title:

N. Vermaak, G. Michailidis, G. Parry, R. Estevez, Y. Brechet, and G. Allaire. *Material interface effects on the topology optimization of multi-phase thermoelastic structures using a level set method*. (submitted in SMO: Structural and Multi-disciplinary Optimization), 2013.

Based on the material of chapters 3 and 4, we prepare to submit the following two preprints:

G. Allaire, F. Jouve, and G. Michailidis. *Thickness constraints in structural optimization via a level-set method*. (In preparation), 2013.

G. Allaire, F. Jouve, and G. Michailidis. *Molding direction constraints in structural optimization via a level-set method*. (In preparation), 2013.

Finally, two conference proceedings, based on this work, can be found on the web:

G. Allaire, F. Jouve, and G. Michailidis. *Casting constraints in structural optimization via a level-set method*. 10th World Congress on Structural and Multidisciplinary Optimization, Orlando, Florida, USA, 2013.

G. Allaire, F. Jouve, and G. Michailidis. *Structural and multi-functional optimization using multiple phases and a level-set method*. SEECM III, 3rd South-East European Conference on Computational Mechanics, Kos Island, Greece, 2013.

Part I

Background material

Chapter 1

Introduction to shape and topology optimization

Contents

1.1	Structural optimization	29
1.2	Shape optimization	30
1.2.1	Ill-posedness of shape optimization problems and remedies	30
1.2.2	Main categories of shape optimization	31
1.3	Shape and topology optimization via a level-set method	33
1.3.1	Shape sensitivity analysis	33
1.3.2	Level-set method	39
1.3.3	Coupling shape sensitivity with a level-set description	42
1.3.4	Extension and regularization of the velocity field	43

1.1 Structural optimization

The word "structure", from a mechanical point of view, is defined by J.E. Gordon [60] as "any assemblage of materials which is intended to sustain loads". Hence, the function of a structure is to transfer a load from the place where it is applied to another one, with safety. Its "optimization" is concerned with improving as much as possible some characteristics related to its mechanical behaviour.

The design cycle of a structure has changed significantly in the last decades. At a first step, an initial concept is proposed and evaluated with respect to criteria of different nature (mechanical, aesthetical, economical, etc...). Then, either the design is accepted, or changed to be improved. In the past, this improvement task was mostly based on the experience and knowledge of engineers. Moreover, in complicated problems where mechanical intuition is very limited (dynamics, non-linear problems, etc...), it is still common practice to use guidelines of design, which are extracted after a long period of trial and error efforts. This design loop could end after a significant number of iterations, resulting in a high design cost and, in all probability, in a structure that could be further improved.

The extreme progress in the computational field during the last decades, endowed engineers with the capability of introducing mathematical optimization methods and algorithms, that existed long before, into the design process. It made possible to use automatic optimization methods for criteria that could be mathematically formulated. This is exactly the kind of optimization of interest in this work. By "Structural Optimization" here, we should understand the application of methods of mathematical design optimization on mechanical structures. Furthermore, among the several fields of structural mechanics, we will deal here only with solid mechanics. This is the reason why the words "structure" and "shape" will be interchanged in this text.

Various types of structural optimization problems have appeared in the literature. Optimization of the material properties [25], [26], [117], [125], minimization of the stress concentration [11], [52], [53], [78], optimal choice among a set of cross-sections of members composing a structure [80], [110], etc... A first categorization of the above mentioned problems can be done according to what the optimization parameters represent. In this work we focus on problems of Shape Optimization, i.e. problems where the optimization variables define the shape of the structure.

1.2 Shape optimization

Shape Optimization examples have appeared very long time ago (see [44] for a short historical review). The extreme progress in computing capabilities during the last decades made possible to apply such techniques in real-life problems of structural mechanics. Since then, there has been an increasing number of publications on the topic [3], [4], [28], [71], [113], [96], [102], [132].

A general mathematical formulation of a Shape Optimization problem reads

$$\inf_{\Omega \in \mathcal{U}_{ad}} J(\Omega), \quad (1.1)$$

where Ω is the domain occupied by the structure, J is the objective function to be minimized and \mathcal{U}_{ad} is a set of admissible shapes to which Ω shall belong.

1.2.1 Ill-posedness of shape optimization problems and remedies

Non existence of optimal solutions

It is well-known that problem (1.1) lacks an optimal solution for a great variety of problems when the topology of the shape is not further constrained [4], [39], [71], [130]. Let us explain this artifact using an example from [4].

Suppose that we are given a membrane occupying the domain $D = (0, 1)^2$ and with a unitary uniform loading applied at its left and right boundary (see Figure 1.1). The membrane is filled with two isotropic elastic materials, with elastic coefficients $\alpha \gg \beta$. The coefficient β is set to a very small value ($\beta \ll 1$) such that it represents void. Assuming that the strong phase α occupies the domain $\Omega \subset D$ and using its characteristic function χ_Ω , such that

$$\chi_\Omega(x) = \begin{cases} 1 & \text{if } x \in \Omega, \\ 0 & \text{if } x \notin \Omega, \end{cases} \quad (1.2)$$

the elastic coefficient α_χ for the whole domain D is written

$$\alpha_\chi = \alpha\chi + \beta(1 - \chi)$$

and the displacement u_χ solves the state equation

$$\begin{cases} -\operatorname{div}(\alpha_\chi \nabla u_\chi) &= 0 & \text{in } D, \\ \alpha_\chi \nabla u_\chi \cdot n &= e_1 \cdot n & \text{on } \partial D. \end{cases} \quad (1.3)$$

Problem (1.1) can be written again as

$$\inf_{\chi \in \mathcal{U}_{ad}} J(\chi). \quad (1.4)$$

We look for the shape of the membrane that maximizes its rigidity, using a specific volume V_α of the

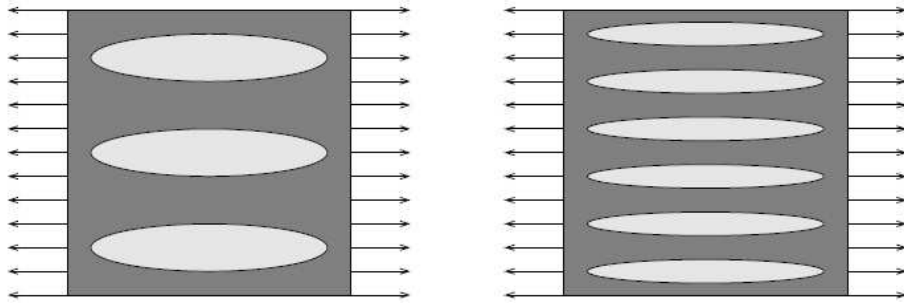


Figure 1.1: Membrane having the same volume, but different number of holes. The shape on the right is more rigid than that on the left (figure extracted from [4]).

rigid material. Mathematically the optimization problem reads

$$\inf_{\chi \in \mathcal{U}_{ad}} J(\chi) = \int_{\partial D} (e_1 \cdot n) u_\chi ds, \quad (1.5)$$

where the admissible set \mathcal{U}_{ad} is defined as

$$\mathcal{U}_{ad} = \left\{ \chi \in L^\infty(D; \{0, 1\}) \text{ such that } \frac{1}{|D|} \int_D \chi dx = V_\alpha \right\}.$$

Proposition 1.2.1. *There is no minimum point or optimal solution for problem (1.5) in the set \mathcal{U}_{ad} .*

The proof of Proposition 1.2.1 is omitted here and we address the interested reader to [4] for a detailed presentation. An intuitive explanation of the above result is that the rigidity of the structure could be always further improved by creating smaller and smaller inclusions of weak phase aligned with the direction of the force. Since the admissible set \mathcal{U}_{ad} imposes no constraint on the size or smoothness of the holes, this process could be continued without any limit.

In fact, the sequence of such shapes does not converge to a classical shape, described by a characteristic function, but instead to a composite material, a mixture of materials 1 and 2 with densities $\theta = \frac{V_\alpha}{|D|}$ and $1 - \theta$. This case, i.e. the optimality of composite materials, is common in topology optimization problems. Moreover, this result is of enormous numerical importance, since it explains and justifies the mesh-dependency of the optimized shapes, i.e. the appearance of more and more holes in the optimized shape as the mesh is refined.

Techniques to avoid non-existence

A quite natural idea in order to avoid this problem of non-existence is to enlarge the set of admissible shapes by including "homogenized" structures in \mathcal{U}_{ad} [3], [142], [100]. In this way the characteristic function χ is replaced by a density field θ which varies continuously in the interval $[0, 1]$. The elastic properties of each phase are replaced by the homogenized properties of the composite material created by their mixture. Once the properties of the homogenized elasticity tensor A^* have been optimized, problem (1.4) is replaced by the **relaxed** or **homogenized** problem

$$\inf_{\theta \in \mathcal{U}_{ad}^*} J(\theta), \quad (1.6)$$

where

$$\mathcal{U}_{ad}^* = \left\{ \theta \in L^\infty(D; [0, 1]) \text{ such that } \int_D \theta dx = V_\alpha \right\}.$$

This problem admits a solution that can be proved to correspond to the limit of a sequence of shapes of problem (1.4).

Another category of methods is based on the concept of further constraining the set of admissible shapes \mathcal{U}_{ad} in order to avoid extreme oscillations of its boundary or to impose limitations on its topology. In [21], Ambrosio et al. proposed to modify problem (1.1) and consider instead the optimization problem

$$\inf_{\Omega \in \mathcal{U}_{ad}} J(\Omega) + \ell_P P(\Omega), \quad (1.7)$$

where $\ell_P > 0$ is a fixed scalar parameter and $P(\Omega)$ is the perimeter of the domain Ω . In [99], [130], Murat et al. proved the existence of local optima for problem (1.1), for a large variety of objective functions, assuming that the admissible shapes are uniformly Lipschitz (see also [39]). Several other approaches have been proposed and we address the interested reader to [4] and [71] for a more detailed presentation.

1.2.2 Main categories of shape optimization

A further subdivision of Shape Optimization problems can be done depending on the choice of geometric representation. Traditionally, three main categories are recognized: parametric, geometric (or shape) and topology optimization.

Parametric optimization

In parametric optimization the shape is described a priori using a limited number of parameters. Such control variables can be for example the thickness distribution of the structure [24], [4], [42], the size of structural members [122] or the size of bars in a truss [28], [42]. Many approaches have also been presented, in which the boundary of the structure is parametrized using polynomials, such as Bézier curves, splines or NURBS (see [42] and the references therein). This type of optimization is widely used in industrial applications, but offers a limited possibility of shape variations.

Geometric (or Shape) optimization

In geometric (or shape) optimization the optimization parameter is the boundary of the structure itself. It is not a priori limited by decomposing it into a set of curves (splines, NURBS, etc...), but it is considered as such. It can be numerically represented using, for example, a finite element mesh [18], [4], [91]. The domain here has much more freedom to vary, but not to change topology.

Topology optimization

Topology optimization is a remedy to Shape Optimization's limitation concerning the preservation of the initial topology. Here the problem is posed a priori with minimum restrictions, as a problem of finding the best possible shape that solves problem (1.1). Unless it exists some reason to use a parametrization of the shape or to keep a specific topology, this category of shape optimization is the most interesting and allows to explore a larger set of shapes, increasing the possibility to obtain better optimal solutions. Several methods of topology optimization exist in literature, which differ in the way topological changes occur.

The first efforts to create optimal topologies in structural optimization used the homogenization method (see section 1.2.1) [3], [17], [27]. A typical solution of an homogenized problem results in an optimal shape like the one on the left of Figure(1.2). As expected, the notion of a "shape" is lost, i.e. there is no clear boundary of the domain. This is a significant drawback of the homogenization method for topology optimization in case one wants to design and fabricate a classical shape. Of course, one can always try to interpret the final density distribution, assuming that low densities correspond to holes and densities close to 1 correspond to the real structure and design a shape that serves as an initialization for a problem of Geometric Optimization. However, this is not always a trivial task.

Another idea, in order to get back into a classical shape, consists in penalizing intermediate densities by using a fictitious interpolation scheme for the material properties, which has the tendency to produce 0 – 1 shapes (see Figure(1.2)). The most well-known between these methods, the SIMP (Solid Isotropic Material with Penalization) method [28], [164], uses the scheme $A_{ijkl}(\theta) = \theta^p A_{ijkl}$, where A_{ijkl} is the elasticity tensor of the full material ($\theta = 1$) and p is the penalization power, used to create classical shapes (usually $p = 3$ is used). Other schemes, like the RAMP [134] or combinations of penalization techniques with Heaviside projection functions [63] have also appeared. All these methods can be seen at last as a trial to combine Geometric and Topology Optimization in order to change the topology and get a clear enough geometric representation of the shape at the same time.

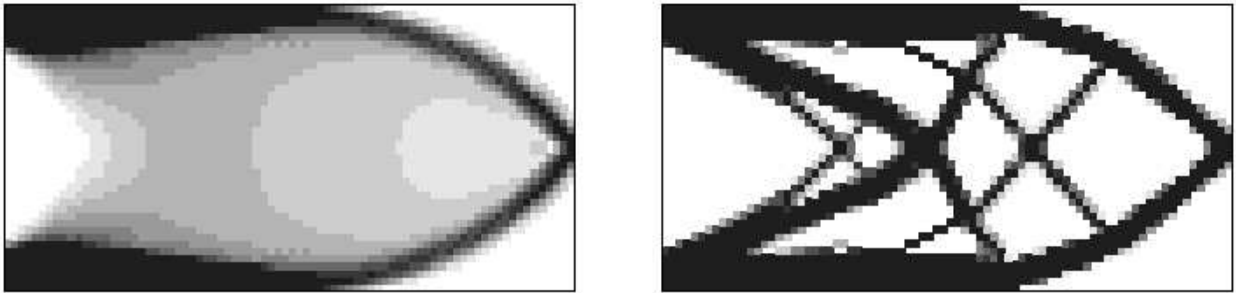


Figure 1.2: Left: density distribution of a composite optimal shape; right: penalized optimal shape (figure extracted from [3]).

Evolutionary algorithms have also been among the first methods to be applied for topology optimization. One of the most well-known method in this category is the Soft Kill Option (SKO) [91], [23]. Heuristic criteria, inspired by natural processes, like the addition of material in areas where a stress criterion is violated and the removal of bulk in areas that are under-stressed are applied. Such methods are very easy to be implemented, since they avoid the use of mathematical information about changing the shape. However, they carry all drawbacks of heuristic methods, like slow convergence, tendency to fall in local minima, very far from global ones and, of course, no guarantee that the heuristic criterion in use can minimize the objective function at play.

Instead of using heuristic criteria for removing material, one can use some notion of topological sensitivity [102], [131], [58], which tests the sensibility of the objective function with respect to the creation of infinitesimal holes in the design domain.

Another way to achieve this mixing of Geometric and Topology Optimization is to use tools of Geometric Optimization for the calculation of an advection velocity to change the shape and combine it with a method of geometric representation of the shape that allows topological changes to occur in a natural way. Such a method is the combination of shape sensitivity analysis with the level-set method [14], [155], [9], which is presented in detail in section 1.3. Similar ideas have appeared in [43] using an explicit mesh representation of the domain instead of a level-set method and in [162], [141], [167] using the phase-field method.

1.3 Shape and topology optimization via a level-set method

Since the first publications on "Shape and Topology Optimization via a Level-Set Method" [13], [14], [107], [121], [155], there has been a burst of publications on the topic. The method has proved its effectiveness and robustness in structural optimization for a great variety of problems. Its great advantages compared to the homogenization method and its variant, like the SIMP method, is the "clear" and smooth description of the shape's boundary and its independence of the mechanical framework at play. In this Section we describe the basic elements of the method, namely the shape sensitivity analysis and the level-set method, as well as their coupling in order to create a shape and topology optimization method.

1.3.1 Shape sensitivity analysis

Introduction

In Shape Optimization we are interested in changing iteratively the shape of the structure so as to reduce as much as possible the value of the objective function. The size of a typical shape optimization problem is usually prohibitive for discrete or zero-order methods [128], thus we shall prefer to use gradient-based continuous optimization algorithms. In order to calculate a notion of gradient, some kind of "calculus of variations" shall be applied. The first step towards this direction is the mathematical representation of the shape. We have seen in section 1.2 that a first choice is to use the characteristic function of the domain. However, this choice does not allow us to perform variations since the space of characteristic functions is not a linear space (a linear combination of characteristic functions is not necessarily a characteristic function). Thus, we have to resort to other techniques.

Definitions and results

For the calculation of a notion of "shape derivative" we shall use the analysis of Murat and Simon [130], which is based on Hadamard's variation method. Similar approaches have also been presented in [132] and [71].

Starting from a smooth reference domain Ω_0 , we will suppose that all admissible shapes Ω are obtained by applying a smooth vector field θ such that

$$\Omega = \{x + \theta(x) \text{ such that } x \in \Omega_0\}.$$

In other words, every admissible shape Ω will now be represented by a vector field $\theta : \mathbb{R}^N \rightarrow \mathbb{R}^N$ ($N = 2$ or 3) and we will write $\Omega = (\text{Id} + \theta)(\Omega_0)$ (see Figure(1.3)). The space of admissible shapes obtained by such a deformation of the domain Ω_0 will be denoted $\mathbb{C}(\Omega_0)$, i.e.

$$\mathbb{C}(\Omega_0) = \{\Omega \text{ s.t. } \exists \theta \in W^{1,\infty}(\mathbb{R}^N; \mathbb{R}^N), \Omega = (\text{Id} + \theta)(\Omega_0)\}.$$

Since θ belongs to some functional space (e.g. $W^{1,\infty}(\mathbb{R}^N; \mathbb{R}^N)$ or $C^{1,\infty}(\mathbb{R}^N; \mathbb{R}^N)$), we are able henceforth to define a notion of derivation with respect to θ .

Remark 1.3.1. *The above way of shape representation implies that for θ small enough, all admissible shapes will have the same topology with the reference domain Ω_0 , since a change of topology is not possible via continuous transformations of the domain Ω_0 .*

We are now ready to define a notion of differentiability with respect to the domain.

Definition 1.3.2. *The functional $J : \Omega \rightarrow \mathbb{R}$ is said to be **shape differentiable** at Ω_0 if the application*

$$\theta \rightarrow J((\text{Id} + \theta)(\Omega_0))$$

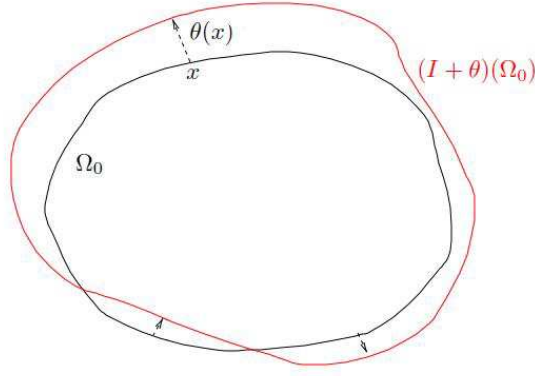


Figure 1.3: Variations of a shape using Hadamard's method.

is Fréchet differentiable at 0 in the Banach space $W^{1,\infty}(\mathbb{R}^N; \mathbb{R}^N)$. Then, the following asymptotic expansion holds in the vicinity of 0:

$$J((Id + \theta)(\Omega)) = J(\Omega) + J'(\Omega)(\theta) + o(\theta) \quad \text{with} \quad \lim_{\theta \rightarrow 0} \frac{|o(\theta)|}{\|\theta\|} = 0, \quad (1.8)$$

where $J'(\Omega)$ is a continuous linear form on $W^{1,\infty}(\mathbb{R}^N; \mathbb{R}^N)$.

Remark 1.3.3. A weaker notion of differentiability, that is also convenient for our purposes, is that of the **directional derivative** of a functional $J : \Omega \rightarrow \mathbb{R}$ at Ω in the direction $\theta \in W^{1,\infty}(\mathbb{R}^d; \mathbb{R}^d)$ which is defined as the limit in \mathbb{R} (if it exists)

$$J'(\Omega)(\theta) = \lim_{\delta \rightarrow 0} \frac{J((Id + \delta\theta)(\Omega)) - J(\Omega)}{\delta}.$$

Remark 1.3.4. Although we have defined the shape derivative using the space $W^{1,\infty}(\mathbb{R}^d; \mathbb{R}^d)$, some of our problems will require higher regularity. This fact poses no theoretical problem and for reasons of simplicity, we shall use the term "shape derivative" independently of the type of derivation or the functional space considered.

A classical result is derived from **Hadamard's structure theorem** and states that the shape derivative depends only on the normal component of θ on the boundary $\partial\Omega$ (the tangential component can be omitted).

Proposition 1.3.5. Let Ω_0 be a smooth bounded open set of \mathbb{R}^N and J a differentiable function at Ω_0 . If $\theta_1, \theta_2 \in W^{1,\infty}(\mathbb{R}^N; \mathbb{R}^N)$ are such that $\theta_2 - \theta_1 \in C^1(\mathbb{R}^N; \mathbb{R}^N)$ and $\theta_1 \cdot n = \theta_2 \cdot n$ on $\partial\Omega_0$, then the derivative $J'(\Omega_0)$ verifies

$$J'(\Omega_0)(\theta_1) = J'(\Omega_0)(\theta_2).$$

Proof. See [4]. □

We will give now some classical examples of shape derivatives of integrals, whose integrand does not depend on the domain Ω .

Proposition 1.3.6. Let Ω_0 be a smooth bounded open set of \mathbb{R}^N . If $f \in W^{1,1}(\mathbb{R}^N)$ and $J : \mathcal{C}(\Omega_0) \rightarrow \mathbb{R}$ is defined by

$$J(\Omega) = \int_{\Omega} f(x) dx,$$

then J is differentiable at Ω_0 and

$$J'(\Omega_0)(\theta) = \int_{\Omega_0} \operatorname{div}(\theta(x)f(x)) dx = \int_{\partial\Omega_0} \theta(s) \cdot n(s) f(s) ds,$$

for all $\theta \in W^{1,\infty}(\mathbb{R}^N; \mathbb{R}^N)$.

Proof. The principal idea to prove the shape differentiability of an integral is to use some theorem of change of variables in order to pass to a calculation on the reference domain Ω_0 . In our case we get

$$J(\Omega) = J((\text{Id} + \theta)(\Omega_0)) = \int_{(\text{Id} + \theta)(\Omega_0)} f(x) dx = \int_{\Omega_0} f \circ (\text{Id} + \theta) |det(I + \nabla \theta)| dx,$$

where $I = \nabla \text{Id}$ is the identity matrix. Substituting to the above expression the identities

$$det(I + \nabla \theta) = 1 + \text{div} \theta + o(\theta) \quad \text{with} \quad \lim_{\theta \rightarrow 0} \frac{\|o(\theta)\|_{L^\infty(\mathbb{R}^N)}}{\|\theta\|_{W^{1,\infty}(\mathbb{R}^N; \mathbb{R}^N)}} = 0$$

and

$$f \circ (\text{Id} + \theta)(x) = f(x) + \nabla f(x) \cdot \theta(x) + o(\theta) \quad \text{with} \quad \lim_{\theta \rightarrow 0} \frac{\|o(\theta)\|_{L^\infty(\mathbb{R}^N)}}{\|\theta\|_{W^{1,\infty}(\mathbb{R}^N; \mathbb{R}^N)}} = 0,$$

yields the desired result. \square

Proposition 1.3.7. *Let Ω_0 be a smooth bounded open set of \mathbb{R}^N . If $f \in W^{2,1}(\mathbb{R}^N)$ and $J : \mathcal{C}(\Omega_0) \rightarrow \mathbb{R}$ is defined by*

$$J(\Omega) = \int_{\partial\Omega} f(s) ds,$$

then J is differentiable at Ω_0 and $\forall \theta \in C^1(\mathbb{R}^N; \mathbb{R}^N)$ we have

$$J'(\Omega_0)(\theta) = \int_{\partial\Omega_0} (\nabla f \cdot \theta + f(\text{div} \theta - \nabla \theta n \cdot n)) ds = \int_{\partial\Omega_0} \theta \cdot n \left(\frac{\partial f}{\partial n} + Hf \right) ds,$$

where $H = \text{div} n$ is the mean curvature of $\partial\Omega_0$.

Proof. Using a change of variables theorem as previously, we get

$$\begin{aligned} J(\Omega) &= J((\text{Id} + \theta)(\Omega_0)) = \int_{\partial(\text{Id} + \theta)(\Omega_0)} f(s) ds \\ &= \int_{\partial\Omega_0} f \circ (\text{Id} + \theta) |det(I + \nabla \theta)| \left| \left((I + \nabla \theta)^{-1} \right)^T n \right|_{\mathbb{R}^N} ds. \end{aligned}$$

Substituting the identities

$$\left((I + \nabla \theta)^{-1} \right)^T n = n - (\nabla \theta)^T n + o(\theta) \quad \text{with} \quad \lim_{\theta \rightarrow 0} \frac{\|o(\theta)\|_{L^\infty(\partial\Omega_0 \mathbb{R}^N)}}{\|\theta\|_{C^1(\mathbb{R}^N; \mathbb{R}^N)}} = 0$$

and

$$\left\| \left((I + \nabla \theta)^{-1} \right)^T n \right\|_{\mathbb{R}^N} = 1 - (\nabla \theta)^T n \cdot n + o(\theta) \quad \text{with} \quad \lim_{\theta \rightarrow 0} \frac{\|o(\theta)\|_{L^\infty(\partial\Omega_0 \mathbb{R}^N)}}{\|\theta\|_{C^1(\mathbb{R}^N; \mathbb{R}^N)}} = 0$$

we get that

$$J'(\Omega_0)(\theta) = \int_{\partial\Omega_0} (\nabla f \cdot \theta + f(\text{div} \theta - \nabla \theta n \cdot n)) ds.$$

After an integration by parts at the boundary $\partial\Omega$ (see Lemma 6.25 in [4]), we result in

$$J'(\Omega_0)(\theta) = \int_{\partial\Omega_0} \theta \cdot n \left(\frac{\partial f}{\partial n} + Hf \right) ds.$$

\square

Shape derivative of a function that depends on the domain

In the previous section we have defined the notion of "shape derivative" of functionals and have presented some classical results of shape derivatives of integrals, when the integrands are independent of the domain Ω . In this section we will discuss the shape derivation of functions that depend on Ω and will extend the results about shape derivation of integrals to the general case of shape dependent integrands.

Suppose $u(\Omega, x)$ is a function defined $\forall x \in \Omega$ and which depends also on Ω . Such a case appears, for example, when $u(\Omega, x)$ is the solution of a PDE defined in Ω . Like in mechanics, we shall define two types of shape derivatives, an **Eulerian** and a **Lagrangian** one.

The **Eulerian** derivative has a local sense and shows the rate of change of u at a fixed point x . Thus, for a point x that belongs both to the reference domain Ω_0 and to the transported domain $\Omega = (\text{Id} + \theta)(\Omega_0)$, we can write the asymptotic expansion with respect to θ at the point x

$$u((\text{Id} + \theta)(\Omega_0), x) = u(\Omega_0, x) + U(\theta, x) + o(\theta), \quad \text{with} \quad \lim_{\theta \rightarrow 0} \frac{|o(\theta)|}{\|\theta\|} = 0, \quad (1.9)$$

where $U(\theta, x)$ is the Eulerian shape derivative of the function $u(\Omega, x)$.

Although the above expansion has a sense for points $x \in \Omega_0$, it is not obvious that the same occurs for a point $x \in \partial\Omega_0$, since it is not sure that such a point will belong to the boundary or to the interior of the new domain $\partial\Omega = \partial(\text{Id} + \theta)(\Omega_0)$.

This problem does not appear when the **Lagrangian** derivative is used, which is a measure of the rate of change of u at a point x that moves with the domain. Since $\theta(x)$ has been defined so that $(\text{Id} + \theta)$ is a bijection, the point $x \in \Omega_0$ corresponds to the point $x_\theta = x + \theta(x) \in \Omega$. Since the functions $u(\Omega_\theta, x_\theta) = u((\text{Id} + \theta)(\Omega_0)) \circ (\text{Id} + \theta) = u((\text{Id} + \theta)(\Omega_0), x + \theta(x))$ and $u(\Omega_0, x)$ are both defined on the same domain Ω_0 , we can write down the asymptotic expansion

$$u((\text{Id} + \theta)(\Omega_0), x + \theta(x)) = u(\Omega_0, x) + Y(\theta, x) + o(\theta), \quad \text{with} \quad \lim_{\theta \rightarrow 0} \frac{|o(\theta)|}{\|\theta\|} = 0, \quad (1.10)$$

where $Y(\theta, x)$ is the Lagrangian shape derivative of the function $u(\Omega, x)$.

Then, once the Lagrangian derivative has been calculated, the Eulerian derivative is found by a simple chain rule as

$$Y(\theta, x) = U(\theta, x) + \theta(x) \cdot \nabla u(\Omega_0, x).$$

We can extend now the results of Propositions 1.3.6 and 1.3.7 to the general case of integrands that are shape dependent.

Proposition 1.3.8. *Let Ω_0 be a smooth bounded open set of \mathbb{R}^N and $u(\Omega)$ be a function from $\mathbb{C}(\Omega_0)$ to $L^1(\mathbb{R}^N)$. We define its **transported function** from $C^1(\mathbb{R}^N; \mathbb{R}^N)$ to $L^1(\mathbb{R}^N)$*

$$u(\Omega_\theta, x_\theta) = u((\text{Id} + \theta)(\Omega_0)) \circ (\text{Id} + \theta),$$

which we suppose to be derivable at 0 with Lagrangian derivative Y . Then, the functional $J_1 : \mathbb{C}(\Omega_0) \rightarrow \mathbb{R}$ defined as

$$J_1 = \int_{\Omega} u(\Omega) dx$$

is differentiable at Ω_0 and $\forall \theta \in C^1(\mathbb{R}^N; \mathbb{R}^N)$ we have

$$J_1'(\Omega_0)(\theta) = \int_{\Omega_0} (u(\Omega_0) \text{div} \theta + Y(\theta)) dx = \int_{\Omega_0} (\text{div}(u(\Omega_0) \theta) + U(\theta)) dx.$$

Moreover, if $u(\Omega_\theta, x_\theta)$ is derivable at 0 as a function from $C^1(\mathbb{R}^N; \mathbb{R}^N)$ to $L^1(\partial\Omega_0)$, then the functional $J_2 : \mathbb{C}(\Omega_0) \rightarrow \mathbb{R}$ defined as

$$J_2 = \int_{\partial\Omega} u(\Omega) ds$$

is differentiable at Ω_0 and $\forall \theta \in C^1(\mathbb{R}^N; \mathbb{R}^N)$ we take

$$J_2'(\Omega_0)(\theta) = \int_{\partial\Omega_0} (u(\Omega_0)(\text{div} \theta - \nabla \theta n \cdot n) + Y(\theta)) ds = \int_{\Omega_0} \left(\theta \cdot n \left(\frac{\partial u(\Omega_0)}{\partial n} + H u(\Omega_0) \right) + U(\theta) \right) ds.$$

In all of the results of this section about shape derivatives we have supposed that the function $u(\Omega, x)$ at play is shape differentiable. Proving rigorously this assumption is not always an easy task, although much work has been done in this direction for well-known PDEs. The general picture of such a proof is the following:

- The PDE is written once for the transported function $u(\Omega_\theta, x_\theta)$ and for the original function $u(\Omega, x)$.
- Subtracting the two equations, a new PDE appears with the Lagrangian derivative $Y(\theta, x)$ as unknown function.
- Proof of the existence and uniqueness of the solution of this PDE and that the error estimate for the remainder is $o(\theta)$.

Instead of this rigorous proof, another much simpler method is usually used, introduced by C  a [35]. This method is formal, in the sense that we assume enough smoothness of the shape for all necessary operations and also we assume the shape differentiability of all the functions at play. In this work, we use C  a's method for shape derivation.

Shape derivation using C  a's method

The method of C  a is a very useful tool for finding the expression of the shape derivative of a functional $J(\Omega, u(\Omega))$ that depends on the shape Ω , but also on the solution $u(\Omega)$ of a PDE, since it avoids the direct calculation of the shape derivative of $u(\Omega)$. It amounts to regard the PDE as a constraint of the optimization problem that the variable u needs to satisfy. Let us explain the method in detail using an example.

Suppose that we want to calculate the shape gradient for a functional of the type

$$J(\Omega, u(\Omega)) = \int_{\Omega} j(x, u(\Omega, x)) dx + \int_{\partial\Omega} l(s, u(\Omega, s)) ds, \quad (1.11)$$

where $u \in H^1(\Omega)^N$ is the displacement of the structure, the unique solution of the linearized elasticity system

$$\begin{cases} -\operatorname{div}(Ae(u)) &= f & \text{in } \Omega, \\ u &= 0 & \text{on } \Gamma_D, \\ (Ae(u))n &= g & \text{on } \Gamma_N, \\ (Ae(u))n &= 0 & \text{on } \Gamma. \end{cases} \quad (1.12)$$

The shape's boundary is decomposed into three parts such that $\partial\Omega = \Gamma_D \cup \Gamma_N \cup \Gamma$. The structure is fixed on Γ_D and is subjected to volume forces $f \in L^2(\Omega)^N$ and to surface loads $g \in H^1(\Omega)^N$ on Γ_N . The strain tensor is denoted $e(u)$ and is equal to the symmetrized gradient of u .

Proposition 1.3.9. *The shape derivative of (1.11) reads*

$$\begin{aligned} J'(\Omega, u(\Omega))(\theta) = & + \int_{\partial\Omega} \theta \cdot n (j(u) + Ae(u) \cdot e(p) - f \cdot p) ds + \int_{\partial\Omega} \theta \cdot n \left(\frac{\partial l(u)}{\partial n} + Hl(u) \right) ds \\ & - \int_{\Gamma_N} \theta \cdot n \left(\frac{\partial(g \cdot p)}{\partial n} + H(g \cdot p) \right) \\ & - \int_{\Gamma_D} \theta \cdot n \left(\frac{\partial(u \cdot Ae(p)n + p \cdot Ae(u)n)}{\partial n} + H(u \cdot Ae(p)n + p \cdot Ae(u)n) \right) ds, \end{aligned}$$

where u is the unique solution of (1.12) and p is the unique solution of the adjoint state

$$\begin{cases} -\operatorname{div}(Ae(p)) &= -j'(u) & \text{in } \Omega, \\ p &= 0 & \text{on } \Gamma_D, \\ (Ae(p))n &= -l'(u) & \text{on } \Gamma_N \cup \Gamma. \end{cases} \quad (1.13)$$

Proof. Instead of deriving directly the functional $J(\Omega, u(\Omega))$ and trying to calculate the Eulerian or Lagrangian derivative of $u(\Omega)$, we formulate the Lagrangian function

$$\begin{aligned} \mathcal{L}(\Omega, v, q, \mu) = & + \int_{\Omega} j(v) dx + \int_{\partial\Omega} l(v) ds + \int_{\Omega} (-\operatorname{div}(Ae(v)) - f) \cdot q dx \\ & + \int_{\Gamma_N} (Ae(v)n - g) \cdot q ds + \int_{\Gamma} Ae(v)n \cdot q ds + \int_{\Gamma_D} v \cdot \mu ds, \end{aligned} \quad (1.14)$$

where $v, q, \mu \in H^1(\mathbb{R}^N)^N$ do not depend on the domain Ω . As we will see in the sequel, the shape derivative of the objective functional J at Ω will be derived by fixing the domain Ω and taking the optimality conditions for the Lagrangian function \mathcal{L} .

Setting the partial derivative of \mathcal{L} with respect to q in the direction of a test function $\phi \in H^1(\mathbb{R}^N; \mathbb{R}^N)$ at the optimal point (Ω, u, p, μ^*) equal to zero, we get

$$\begin{aligned} \frac{\partial \mathcal{L}}{\partial q}(\Omega, u, p, \mu^*)(\phi) = & + \int_{\Omega} (-\operatorname{div}(Ae(u)) - f) \cdot \phi dx + \int_{\Gamma_N} (Ae(u)n - g) \cdot \phi ds \\ & + \int_{\Gamma} Ae(u)n \cdot \phi ds = 0. \end{aligned}$$

Taking ϕ with compact support in Ω gives

$$-\operatorname{div}(Ae(u)) = f \quad \text{in } \Omega. \quad (1.15)$$

Varying the trace of ϕ on Γ_N and on Γ gives

$$Ae(u)n = g \quad \text{on } \Gamma_N \quad (1.16)$$

and

$$Ae(u)n = 0 \quad \text{on } \Gamma. \quad (1.17)$$

In the same way, setting the partial derivative of \mathcal{L} with respect to μ in the direction ϕ equal to zero

$$\frac{\partial \mathcal{L}}{\partial \mu}(\Omega, u, p, \mu^*)(\phi) = + \int_{\Gamma_D} u \cdot \phi ds = 0$$

results in

$$u = 0 \quad \text{on } \Gamma_D. \quad (1.18)$$

Equations (1.15), (1.16), (1.17) and (1.18) show that the function u is in fact the unique solution of the state equation (1.12).

We write again the function \mathcal{L} , after an integration by parts, in the form

$$\begin{aligned} \mathcal{L}(\Omega, v, q, \mu) = & + \int_{\Omega} j(v) dx + \int_{\partial\Omega} l(v) ds + \int_{\Omega} (Ae(v) \cdot e(q) - f \cdot q) dx \\ & - \int_{\Gamma_N} g \cdot q ds - \int_{\Gamma_D} Ae(v)n \cdot q ds + \int_{\Gamma_D} v \cdot \mu ds. \end{aligned}$$

The partial derivative of \mathcal{L} with respect to v , at the optimal point, in the direction $\phi \in H^1(\mathbb{R}^N; \mathbb{R}^N)$ gives

$$\begin{aligned} \frac{\partial \mathcal{L}}{\partial v}(\Omega, u, p, \mu^*)(\phi) = & + \int_{\Omega} j'(u) \cdot \phi dx + \int_{\partial\Omega} l'(u) \cdot \phi ds + \int_{\Omega} Ae(p) \cdot e(\phi) dx \\ & - \int_{\Gamma_D} Ae(\phi)n \cdot p ds + \int_{\Gamma_D} \phi \cdot \mu^* ds. \end{aligned}$$

Setting this derivative equal to zero and taking ϕ with compact support in Ω yields

$$-\operatorname{div}(Ae(p)) = -j'(u) \quad \text{in } \Omega. \quad (1.19)$$

Varying the trace of ϕ on Γ_N, Γ yields

$$Ae(p)n = -l'(u) \quad \text{on } \Gamma_N \cup \Gamma. \quad (1.20)$$

Varying the trace of ϕ on Γ_D with $Ae(\phi)n = 0$ yields

$$\mu^* = -Ae(p)n - l'(u) \quad \text{on } \Gamma_D. \quad (1.21)$$

Varying the normal stress $Ae(\phi)n$ on Γ_D with $\phi = 0$ on Γ_D yields

$$p = 0 \quad \text{on } \Gamma_D. \quad (1.22)$$

Therefore, p is the unique solution in Ω of the adjoint equation (1.13).

Finally, the shape derivative of the functional J at Ω will be equal to the shape derivative of the Lagrangian function \mathcal{L} at the optimal point (Ω, u, p, μ^*) , i.e.

$$\frac{\partial \mathcal{L}}{\partial \Omega}(\Omega, u, p, \mu^*)(\theta) = J'(\Omega)(\theta). \quad (1.23)$$

To prove this, take first any $q \in H^1(\mathbb{R}^N)$ and see that

$$\mathcal{L}(\Omega, u(\Omega), q) = J(\Omega),$$

where u is the solution of the state equation. Then, taking the shape derivative of both members and using the rule of composite derivatives yields

$$J'(\Omega)(\theta) = \frac{\partial \mathcal{L}}{\partial \Omega}(\Omega, u(\Omega), q, \mu)(\theta) + \left\langle \frac{\partial \mathcal{L}}{\partial v}(\Omega, u(\Omega), q, \mu), u'(\Omega)(\theta) \right\rangle.$$

If $q = p(\Omega)$, the solution of the adjoint state, and $\mu = \mu^*$, the last term disappears and relation (1.23) is revealed.

The shape derivative of \mathcal{L} is much easier to calculate, since it has been constructed such that the functions v, q and μ are independent of Ω . Thus, only the results of propositions 1.3.6 and 1.3.7 need to be applied. A simple calculation yields

$$\begin{aligned} \frac{\partial \mathcal{L}}{\partial \Omega}(\Omega, u, p, \mu^*)(\theta) = & + \int_{\partial \Omega} \theta \cdot n (j(u) + Ae(u) \cdot e(p) - f \cdot p) ds + \int_{\partial \Omega} \theta \cdot n \left(\frac{\partial l(u)}{\partial n} + Hl(u) \right) ds \\ & - \int_{\Gamma_N} \theta \cdot n \left(\frac{\partial (g \cdot p)}{\partial n} + H(g \cdot p) \right) \\ & - \int_{\Gamma_D} \theta \cdot n \left(\frac{\partial (u \cdot Ae(p)n + p \cdot Ae(u)n)}{\partial n} + H(u \cdot Ae(p)n + p \cdot Ae(u)n) \right) ds. \end{aligned}$$

□

For example, in the case of compliance minimization $j(u) = f \cdot u$ in Ω and $l(u) = g \cdot u$ on Γ_N , we easily see that $p = -u$, i.e. the problem is self-adjoint. If we further assume that $\theta = 0$ on $\Gamma_D \cup \Gamma_N$, then the shape derivative of J reads

$$J'(\Omega)(\theta) = \int_{\Gamma} \theta \cdot n (2f \cdot u - Ae(u) : e(u)) ds.$$

Steepest descent

Once we have found the shape derivative of the functional $J(\Omega)$ in the general form

$$J'(\Omega)(\theta) = \int_{\partial \Omega} \theta(s) \cdot n(s) j(s) ds,$$

a descent direction, corresponding to a notion of gradient descent, is revealed under the choice

$$\theta(s) = -tj(s)n(s), \tag{1.24}$$

for a small positive step $t > 0$. Although formula 1.24 makes sense only on the boundary $\partial \Omega$, it can be extended to the entire domain Ω (see section 1.3.4).

Substituting $\theta(s)$ in the shape derivative expression and back to the asymptotic expansion formula (1.8), we can formally write for $J(\Omega_t) = J((\text{Id} + t\theta)(\Omega))$

$$J(\Omega_t) = J(\Omega) - t \int_{\partial \Omega} j(s)^2 ds + o(t^2) \leq J(\Omega),$$

which guarantees a descent direction.

1.3.2 Level-set method

General description

The level-set method, developed by S. Osher and J. Sethian [106], is a technique for tracking interfaces which are implicitly defined via the zero level-set of an auxiliary function. Since its appearance, it has been applied in a great variety of fields (fluid mechanics, image processing, computer graphics, meshing, etc...). Beyond the simplicity of the geometric description of an interface, its great benefit lies in the ease under which topological changes occur. Let us give an example to explain this point.

Suppose we are given two circles that evolve in time and finally merge at some part. If we choose to describe this movement by parametrizing their boundaries, then we need to construct two initial parametrizations, update them at each time step, identify the exact time at which the topological change occurs, construct a new parametrization for the newly created domain and so on. Of course, it is easy to understand that such a process is both theoretically and numerically very difficult.

Instead of this, we can choose to use an one-dimension higher function, a so-called level-set function, and reveal the boundaries of the shapes as its zero level-set. At the upper part of Figure 1.4, we see a three-dimensional function, and several level-sets depicted in black colour. Its zero level-set corresponds to the lines separating the blue from the red region and represents two circles. At the lower part of the figure, we see that the function has changed and its zero level-set has evolved so that it now represents a domain with different topology, i.e. the circles have merged. This topological change has occurred in a very natural way, by performing simple operations on the level-set function.

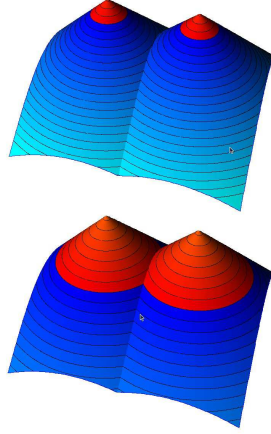


Figure 1.4: Level-set representation of two circles that finally merge.

More specifically, we choose all admissible shapes Ω to be subsets of a bounded working domain $D \subset \mathbb{R}^N$ (see Figure 1.5). Then, the boundary of Ω is defined by means of a level set function ψ such that

$$\begin{cases} \psi(x) = 0 & \leftrightarrow x \in \partial\Omega \cap D, \\ \psi(x) < 0 & \leftrightarrow x \in \Omega, \\ \psi(x) > 0 & \leftrightarrow x \in (D \setminus \overline{\Omega}). \end{cases}$$

For a domain $\Omega(t)$ that evolves in the time interval $t = [0, T]$ under a velocity field $\theta(t, x)$, we define a

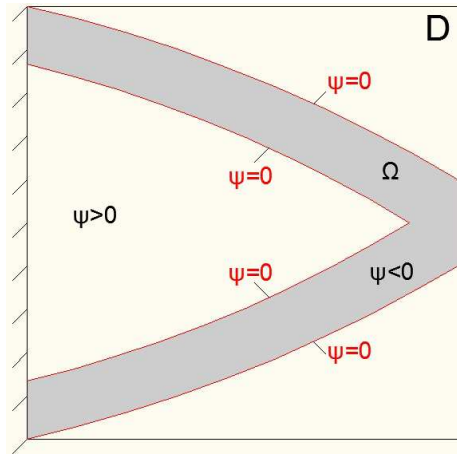


Figure 1.5: Level-set representation of a structure (in grey).

time-dependent level-set function $\psi(t, x(t))$, such that the boundary of the domain, $\partial\Omega(t)$, is given by the set of points $x(t)$ satisfying

$$\psi(t, x(t)) = 0, \quad \forall t \in [0, T].$$

A simple derivation in time yields

$$\frac{\partial \psi}{\partial t}(t, x) + \dot{x}(t) \cdot \nabla \psi(t, x) = 0, \quad \forall t, \forall x \in \partial\Omega(t), \quad (1.25)$$

which is a PDE that describes the advection of the boundary under a velocity field $\dot{x}(t)$. Each point $x(t) \in \partial\Omega(t)$ satisfies a Lagrangian type ODE

$$\dot{x}(t) = \theta(t, x(t)). \quad (1.26)$$

Substituting (1.26) in (1.25), we get

$$\frac{\partial \psi}{\partial t}(t, x) + \theta(t, x(t)) \cdot \nabla \psi(t, x) = 0, \quad \forall t, \forall x(t) \in \partial\Omega(t), \quad (1.27)$$

which can be extended in the whole computational domain D , since the same reasoning is valid for any value c of the level-set $\psi(t, x(t)) = c$. If only the normal component of the velocity field is of interest, like in shape optimization, the advection velocity can be written as $\theta(t, x) = V(t, x)n(t, x)$, $V(t, x)$ being a scalar field. The unit normal vector can be defined and extended at the same time in the whole domain D by means of the level-set function ψ (which is assumed to be smooth enough) as

$$n(x) = \frac{\nabla \psi(x)}{|\nabla \psi(x)|} \quad \text{a.e. in } D. \quad (1.28)$$

Then, equation (1.27) takes the form of the Hamilton-Jacobi equation

$$\frac{\partial \psi}{\partial t}(t, x) + V(t, x)|\nabla \psi(t, x)| = 0, \quad \forall t, \forall x \in D. \quad (1.29)$$

The method used to solve equation (1.29) depends on the discretization of the level-set function. The most common choice is to mesh the domain D once and for all using a structured grid and utilize finite difference schemes to approximate the differential operators. This is the method we have followed in this work. A robust, explicit, second-order scheme developed by S. Osher and J. Sethian [106] and presented in detail in section 5.1 of [120] has been used to solve (1.29) under a CFL condition for the time step.

Another choice is to use an unstructured mesh and possibly also adjust it so that the zero level-set is explicitly discretized [45]. This method is much more complex from a point of view of numerical implementation, however it presents at the same time many benefits compared to the classical one, especially in problems where the knowledge of the exact position of the boundary plays an important role. For such a method, other schemes have been developed, based mainly on the method of characteristics (see [135]). We adress the interested reader to [45, 46] and to the references therein for more information about the level-set method using unstructured meshes.

Signed-distance function

Until now we have refered in general to a level-set function, without giving any specific information about it. In fact, there is an infinity of level-set functions that can be used for the description of the shape. A priori, the only criterion that it should fulfill is to have sufficient regularity at a region around the boundary. The reason is that several geometric features that are necessary to be calculated during the advection or the optimization algorithm, such as unit normal vector to the exterior of the boundary (1.28) or the mean curvature (H), which is defined as

$$H(x) = \operatorname{div} n = \nabla \cdot \left(\frac{\nabla \psi(x)}{|\nabla \psi(x)|} \right),$$

are computed directly via the level-set function using differential operators. These operators are approximated using e.g. finite difference schemes on a fixed mesh. The accuracy of the approximations depends on the smoothness of the function ψ at the stencil of the schemes.

It is well-known [105, 120] that, during evolution, the level-set function can become too steep or flat, even if it starts from a smooth initialization. A way to guarantee its smoothness is to reinitialize it periodically as the **signed distance function** to the domain Ω . The signed distance function to Ω is the function $\mathbb{R}^N \ni x \mapsto d_\Omega(x)$ defined by :

$$d_\Omega(x) = \begin{cases} -d(x, \partial\Omega) & \text{if } x \in \Omega, \\ 0 & \text{if } x \in \partial\Omega, \\ d(x, \partial\Omega) & \text{if } x \in {}^c\Omega, \end{cases}$$

where $d(\cdot, \partial\Omega)$ is the usual Euclidean distance.

Several methods have been proposed for the numerical construction of the signed distance function (Fast-Marching method, Fast-Sweeping method, Hamilton-Jacobi equations, etc...). We adress the interested reader to [105], [120] for a detailed presentation on structured grids and to [46] and to the references therein for unstructured meshes. In this work, we mainly compute it by solving a PDE, as proposed in [105]. Since d_Ω satisfies the Eikonal equation

$$|\nabla d_\Omega| = 1 \quad \text{a.e. in } \Omega, \quad (1.30)$$

starting from an initial level-set function $\psi_0(x)$, d_Ω can be obtained as the stationary solution of the following PDE

$$\begin{cases} \frac{\partial \psi}{\partial t} + \text{sgn}(\psi_0)(|\nabla \psi| - 1) = 0 & \forall t > 0, x \in \mathbb{R}^N, \\ \psi(t=0, x) = \psi_0(x) & \forall x \in \mathbb{R}^N, \end{cases} \quad (1.31)$$

using the same numerical scheme as for the advection equation (1.29).

1.3.3 Coupling shape sensitivity with a level-set description

In Section 1.3.1 we have calculated a shape derivative and extracted a vector field that indicates how to change the shape in a way that reduces some cost functional and in Section 1.3.2 we have presented the basic elements of the level-set method for the description of an interface that evolves in time under a velocity field

$$\theta(x) = V(x)n(x). \quad (1.32)$$

What remains is to combine these two notions by taking an advection field proportional to the shape gradient and construct a method that is able to optimize at the same time the shape and the topology of the structure. It amounts simply to interpret the shape gradient calculated via shape sensitivity analysis as an advection velocity for a level-set function that describes the shape.

Ersatz material

Using the so-called "ersatz material" approach, we extend the state equations to the whole domain D . To do this, we fill the holes $D \setminus \Omega$ by a weak phase that mimicks the void, but at the same time avoids the singularity of the rigidity matrix. More precisely, we define an elasticity tensor $A^*(x)$ which is a mixture of A in Ω and of the weak material mimicking holes in $D \setminus \Omega$

$$A^*(x) = \rho(x)A \quad \text{with} \quad \rho = \begin{cases} 1 & \text{in } \Omega, \\ \varepsilon \ll 1 & \text{in } D \setminus \Omega, \end{cases} \quad (1.33)$$

where $\varepsilon \approx 10^{-3}$. Decomposing the boundary ∂D of the working domain in three parts

$$\partial D = \partial D_D \cup \partial D_N \cup \partial D_0,$$

such that $\Gamma_D \subset \partial D_D$ and $\Gamma_N \subset \partial D_N$, the displacement u is finally computed as the solution of

$$\begin{cases} -\text{div}(A^* e(u)) = f & \text{in } D, \\ u = 0 & \text{on } \partial D_D, \\ \begin{cases} (A^* e(u))n = g \\ (A^* e(u))n = 0 \end{cases} & \text{on } \partial D_N, \\ & \text{on } \partial D_0. \end{cases} \quad (1.34)$$

Optimization algorithm

The information given from the shape gradient is local, i.e. it refers to a neighbourhood around the current shape Ω . Therefore, an iterative algorithm needs to be constructed so as to minimize progressively the cost functional. Using a simple steepest descent algorithm, which guarantees the decrease of the objective function at each time step, the optimization algorithm has the following structure:

- Start with an initial guess shape Ω_0 , described by a level-set function ψ_0 .
- Iterate until convergence, for $k \geq 0$:
 1. Solve the state and adjoint equations for the domain Ω_k to obtain u_k and p_k .

2. Compute the shape gradient for the current domain Ω_k , which has the form

$$J'(\Omega_k)(\theta_k) = \int_{\partial\Omega_k} (\theta_k \cdot n) j_k ds.$$

3. Choose $\theta_k = -j_k n$ as an advection velocity and solve the Hamilton-Jacobi equation

$$\frac{\partial \psi_k}{\partial t}(t, x) + j_k(x) |\nabla \psi_k(t, x)| = 0, \quad \forall t \in [0, T_k], \quad \forall x \in D,$$

in order to get a new level-set function ψ_{k+1} , representing the domain Ω_{k+1} . The total advection time T_k is chosen so that $J(\Omega_{k+1}) < J(\Omega_k)$.

Several convergence criteria can be adopted, which usually test the decrease in the objective function and the total advection time, i.e. the algorithm terminates when $|J(\Omega_{k+1}) - J(\Omega_k)| < \varepsilon_k$ and $T_k < T_{lim}$, where ε_k and T_{lim} are user defined scalar parameters. Since their choice is not a priori obvious, it is common practise to set a computational cost criterion in terms of total number of iterations.

1.3.4 Extension and regularization of the velocity field

Although equation (1.29) for the advection of the level-set function is solved in the whole domain D , shape sensitivity analysis provides us with a shape gradient defined only on the boundary of the domain $\partial\Omega$. Since the boundary is not explicitly discretized in our case, we can assume that the normal velocity V is defined for the nodes of the elements that are crossed by the zero level-set. Then, one possibility is to consider $V = 0, \forall x \in D \setminus \partial\Omega$. Such a choice would slow down the algorithm. The reason is that for each finite element calculation, which is the most costly part of the algorithm, we want to perform several transport steps for the advection equation (1.29). If the velocity is extended by 0 at a small distance away from the boundary, the shape will stop there and the total movement will be too small, probably resulting in a great number of iterations until convergence.

A remedy to this inconvenience is to extend the velocity field in all the domain. At the same time, it would be numerically beneficial to smooth a bit the shape gradient, but in a way that guarantees the descent nature of the new advection velocity. One way to combine these two requirements is the following: Initially, the shape derivative has the form

$$J'(\Omega)(\theta) = \int_{\partial\Omega} \theta(s) \cdot n(s) j(s) ds, \quad (1.35)$$

or, for an advection velocity of the type $\theta(s) = w(s)n(s)$,

$$J'(\Omega)(wn) = \int_{\partial\Omega} w(s) j(s) ds. \quad (1.36)$$

Instead of choosing $w(s) = -j(s)$, we can solve the variational formulation for $Q \in H^1(D)$

$$\int_D (\alpha^2 \nabla Q \cdot \nabla W + QW) dx = J'(\Omega)(Wn) \quad \text{for any } W \in H^1(D), \quad (1.37)$$

where $\alpha > 0$ is a positive scalar (of the order of the mesh size) to control the regularization width and take $w = -Q$. Doing so, we see that

$$J'(\Omega)(wn) = - \int_D (\alpha^2 |\nabla Q|^2 + Q^2) dx,$$

which guarantees again a descent direction for J .

Discussion on topological changes

The careful reader shall have identified a conflict in the aforementioned about the coupling of the shape sensitivity analysis and the level-set method. Hadamard's method for shape variations supposes that the topology of the shape remains the same, while the level-set method lets such changes occur in a natural way.

In fact, this theoretical conflict does not pose a problem in our method. We can always choose to move at a step so small that the topology does not change, but we are not interested to do so! If a feature of

the structure tends to disappear, there is no need to hinder it, else we shall not use the level-set method for the description of the shape. When a topological change occurs, the shape derivative is not valid any more and it is possible that our algorithm cannot further decrease the objective function. One can choose to use at this point the notion of topological derivative (see section 1.2.2). However, this kind of derivation is more complicated and more limited compared to the shape derivative and we have preferred not to use it in this work.

We shall try to avoid this problem by allowing some small increase of the objective function for some number of iterations, in which we expect topological changes to occur. In addition, when a topological change occurs, e.g. when a bar breaks, it is possible that the objective function will increase, since the features do not disappear at once but it takes some iterations for the algorithm to adjust the shape to the new topology. However, we can hope that after this small increase, the algorithm will arrive at a better optimum and thus it is a good strategy to allow for it. In this sense, an iteration will be accepted if $J(\Omega_{n+1}) < (1 + \eta_{tol})J(\Omega_n)$, where $\eta_{tol} > 0$ is set to a small value (≈ 0.05) for some iterations and to 0 afterwards.

Examples

Let us finish this introductory part with two benchmark examples on compliance minimization in linearized elasticity, coded in the finite element software SYSTUS of ESI-Group.

We search to minimize a weighted sum of the work of the external forces and the volume of the structure, i.e.

$$J(\Omega) = \int_{\Gamma_N} g \cdot u ds + \ell_V \int_{\Omega} dx,$$

where u is the solution of (1.34) and $\ell_V > 0$ is a fixed Lagrange multiplier for the weight. The shape derivative of $J(\Omega)$ reads

$$J'(\Omega)(\theta) = \int_{\partial\Omega} \theta(s) \cdot n(s) (\ell_V - Ae(u)e(u)) ds.$$

The first example is a two-dimensional 2×1 cantilever, clamped on its left side and with a unitary vertical force applied on the middle of its right side (see Figure 1.6). The results for $\ell_V = 100$ are shown in Figure 1.7 and 1.8. The second example is a three-dimensional $2 \times 1 \times 1$ cantilever, clamped on its left side and

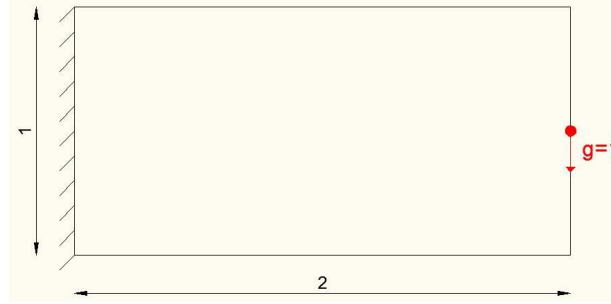


Figure 1.6: Boundary conditions for a two-dimensional cantilever.

with a unitary force applied on the middle of its right side (see Figure(1.9)). The results for $\ell_V = 200$ are shown in Figure 1.10 and 1.11.

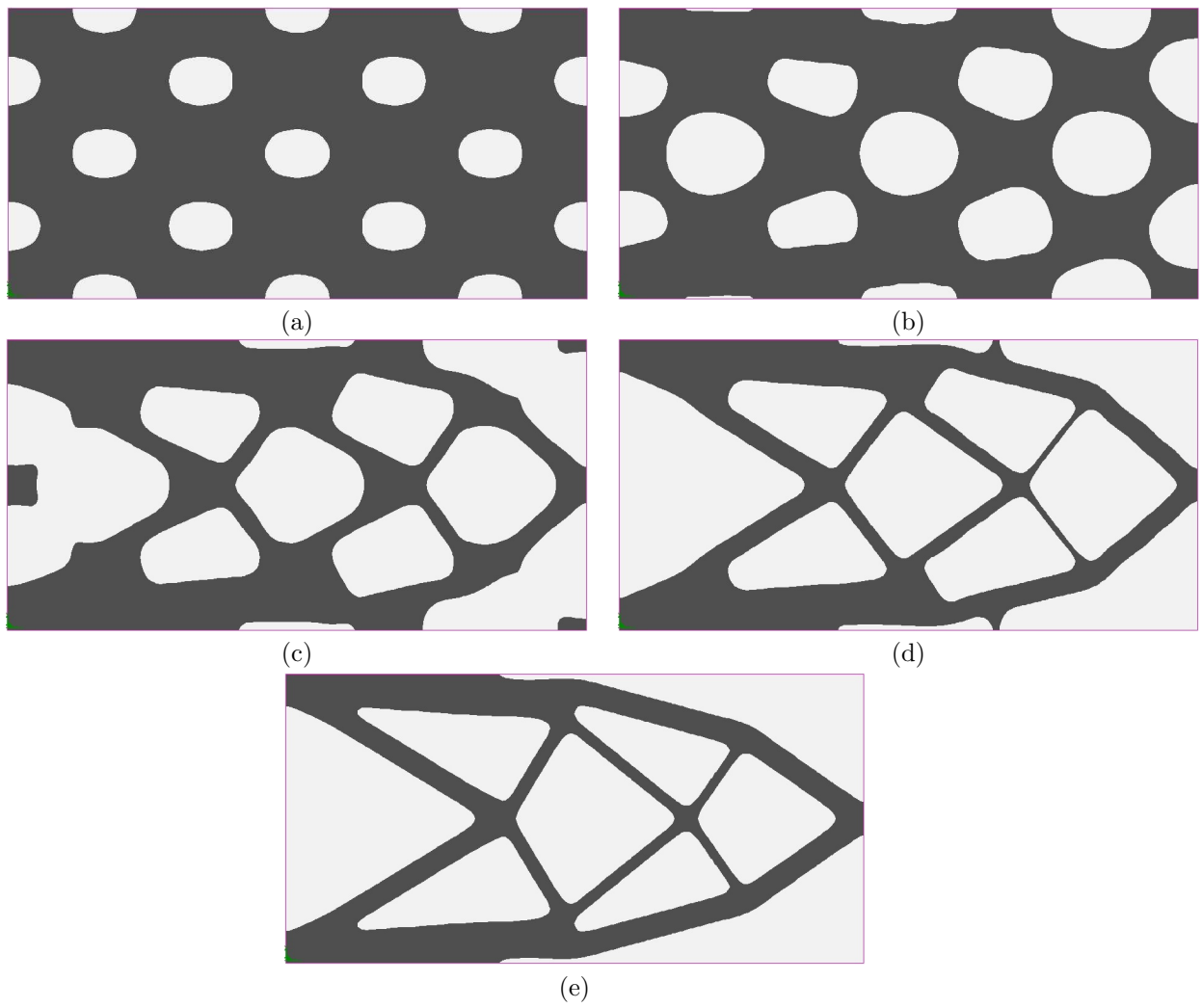


Figure 1.7: (a): Initialization; (b)-(d): iterations 3, 6, 15; (e): optimized shape; (f): convergence diagram.

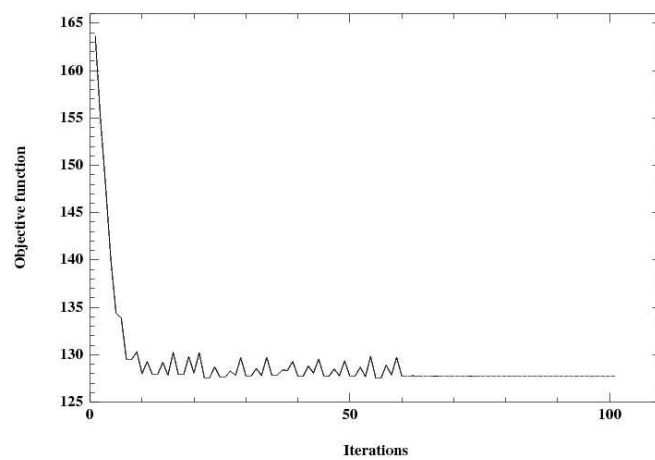


Figure 1.8: Convergence diagram for the results of Figure 1.7.

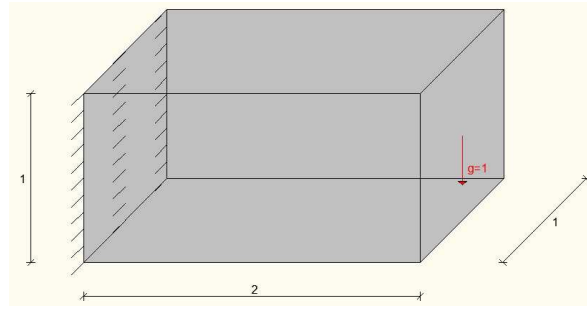


Figure 1.9: Boundary conditions for a three-dimensional cantilever.

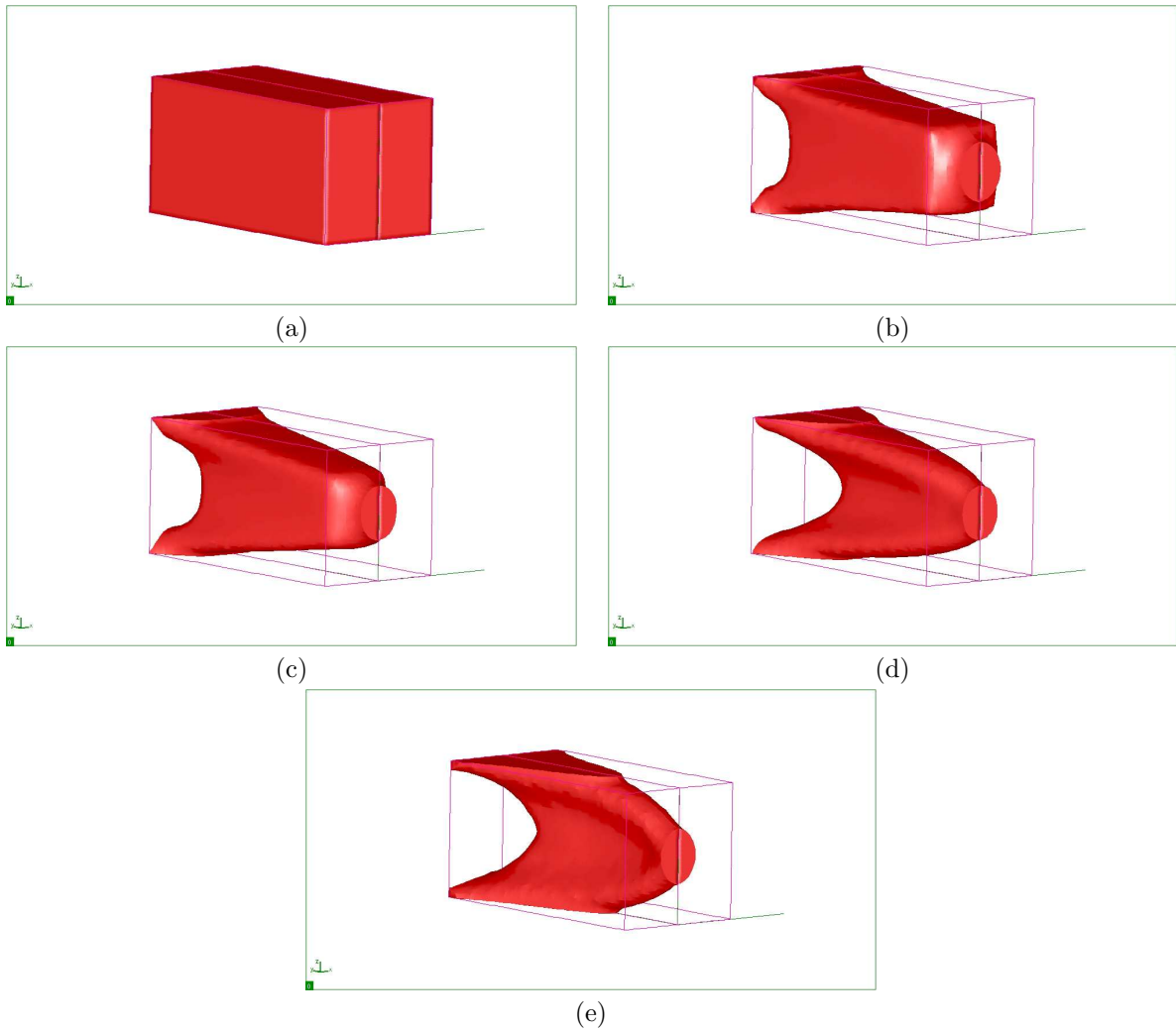


Figure 1.10: (a): Initialization; (b)-(d): iterations 5, 10, 30; (e): optimized shape.

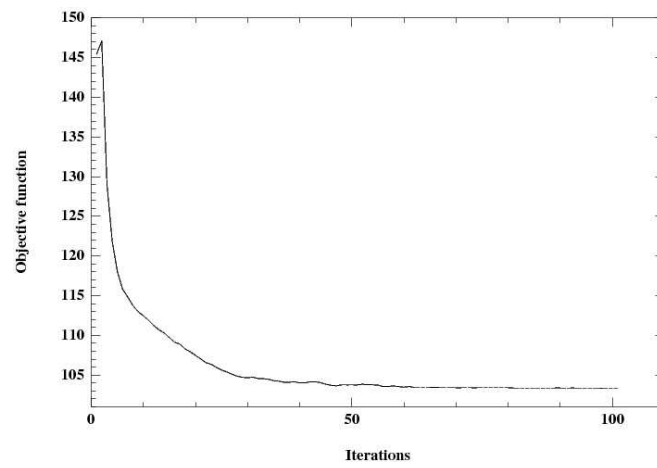


Figure 1.11: Convergence diagram for the results of Figure 1.10.

Chapter 2

Casting constraints: physical description and classification

Contents

2.1	Introduction	49
2.2	Casting process	50
2.2.1	General description	50
2.2.2	Casting defects	50
2.3	Testing castability	51
2.3.1	Moldability	51
2.3.2	Feedability	53
2.3.3	Fillability	54
2.4	Conclusions	54

2.1 Introduction

Every design that is intended to be realized is subjected to manufacturing constraints. They can refer to limitations of completely different nature, such as the total production cost, the available precision of the tooling machinery, or constraints that are related to some specific fabrication method. The restrictions that they impose on the shape can be significant, sometimes playing the major role in the concept of the design.

Shape and topology optimization methods are well-known to produce complex optimized shapes. The great advances that have occurred during the last decades in techniques of additive manufacturing such as 3D printing, laser stereo-lithography, electron beam melting, etc... [65], [73], [87], [111], have made possible to realize such designs. Although these methods pose, in general, very few limitations on the structural design, they are not yet suitable for parts of mass production, mainly due to the high production cost and time. For structures produced with traditional manufacturing methods, engineers usually try at a second step to interpret optimization results and change the shape in a way that turns it into manufacturable. However, the necessary modifications are, in full generality, not done in an optimal way, resulting in a shape that is not in fact optimal. In addition, the changes can be so dramatic that the structure loses completely its optimal characteristics and turns the result of shape and topology optimization practically useless.

Another choice instead of manually and heuristically interfering in the shape, is to incorporate manufacturing constraints in the optimization algorithm. Although the complexity of the problem and algorithm can increase significantly, as well as the probability to fall in an early local minimum, an optimized shape that respects at least the main manufacturing constraints will be much more helpful for the industrial designers. Moreover, as we will see later in this work, introducing manufacturing constraints in the optimization algorithm can totally change the loading path in the structure. Therefore, this choice is not just about automatizing in some way the heuristic steps followed by engineers to ensure manufacturability.

In this work, we are mainly interested in treating constraints imposed on cast parts, i.e. structures that are intended to be constructed via the casting process. However, we shall see that the major casting

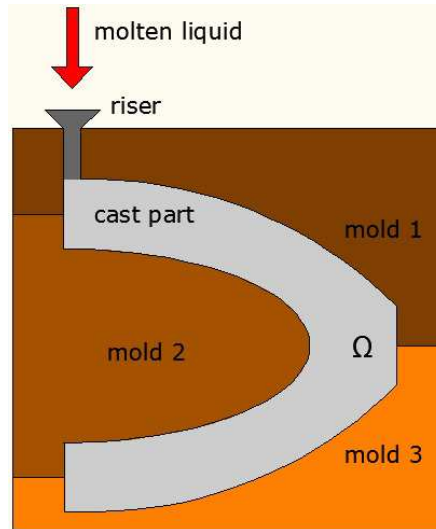


Figure 2.1: Simplified representation of a casting system.

constraints are very general and also appear in a great variety of other manufacturing methods. In the rest of this Chapter, we give a short description of the casting process and the major casting defects. Then, we describe how castability is checked in industry and how engineers usually proceed when it is not ensured. Finally, we explain our strategy on how shape and topology optimization should account for castability. The mathematical treatment of these constraints will be considered later in chapters 3, 4 and 5.

2.2 Casting process

2.2.1 General description

A great number of structures in industry are constructed via casting. A simplified casting system is shown in Figure 2.1. Molds are used to create a cavity with the shape of the structure to be constructed. A path is also created to lead the molten liquid to the cavity and a riser, a reservoir of molten liquid, provides the structure with the additional liquid needed due to contraction during solidification. After solidification, the molds are removed and the riser is cut to obtain the cast part. A complete presentation of the casting process can be found in [33], [116] and [133].

Several types of casting exist, depending on the type of the mold (sand, metal, wax, etc...), the application of additional pressure or the sole action of gravity during the flow of the liquid metal, etc... In this work, we are mostly interested for parts that are massively produced and whose molds need to remain functional for a large number of castings. Despite the fact that each type of casting can introduce its particular type of defects in the cast part, the major casting defects seem to be common for all categories and we shall not focus on a specific casting type.

2.2.2 Casting defects

We call **casting defects** the imperfections of the finally constructed structure compared to the intended design, that are due to the casting process. They can originate from anything that participates in the casting: the metal, the mold, the shape of the cast part, the caster, etc... The main categories of casting defects are the following:

- shrinkage defects,
- pouring metal defects,
- gas porosity,
- metallurgical defects,
- mold material defects.

Among the above categories, **shrinkage defects** and **pouring metal defects** are closely linked to the shape of the structure and thus they are of interest in our work.

Shrinkage defects

Shrinkage porosity can appear due to contraction of the liquid metal during the solidification. As the structure solidifies from the exterior to the interior, it contracts due to the lower density of the liquid compared to the solid state. Material is draught from neighboring points and thus no material remains for the last points to solidify (hot spots) [144]. The porosity that appears at these regions is called shrinkage porosity and it is the main category of defaults due to solidification of cast parts. Shrinkage porosity should be avoided, since it can have a great negative impact on the mechanical behavior of the cast part.

Pouring metal defects

This category includes defects that appear when some part of the mold is not filled properly. Possible reasons can be the lack of sufficient fluidity of the liquid or the existence of too thin features in the mold, where the metal solidifies before the mold has been filled and the filling process is thus interrupted, resulting in a complete failure of the casting.

2.3 Testing castability

Castability of a structure is usually verified by checking three properties of the cast part:

- **moldability,**
- **feedability** and
- **fillability.**

In this section, we give a short description of the above properties and explain the specifications that they impose on the design.

2.3.1 Moldability

Moldability refers to the ability to construct a mold with certain geometric requirements and to remove it after the cooling process has ended. It mainly imposes the following three specifications on the design of the structure:

- **Molding direction.**
- **Minimum members' distance.**
- **Maximum curvature.**

The above requirements are presented in more detail in the sequel.

Molding direction

As we have mentioned earlier, we focus on casting methods where the molds are used for a large number of pieces and thus need to be removed and reutilized. For mass production parts, the assembly and removal of the molds is done automatically using suitable machinery.

The molding direction specification simply states that the shape of the cast part must not contradict with the design of the molding system. Let us give an example of the above mentioned. Suppose that for an optimization problem like the one described in Section 1.3.4 we result in the optimized shape Ω , shown in Figure 2.2. In Figure 2.3 we see that depending on the molding system considered, this shape can be moldable or not. In the right image of Figure 2.3, some parts of the shape oppose to the removal of the molds in their corresponding **parting direction**, i.e. the direction along which the mold is removed.

The construction of the molding system is usually based on the intuition of the caster. Changes on the number and on the position of the molds can turn a non-moldable shape into a moldable one. The design of the whole molding system is very difficult (if possible) to be formulated mathematically and be subjected to continuous optimization. To our knowledge, the only work in this direction in the framework of shape and topology optimization has been presented in [160], where the simultaneous optimization of

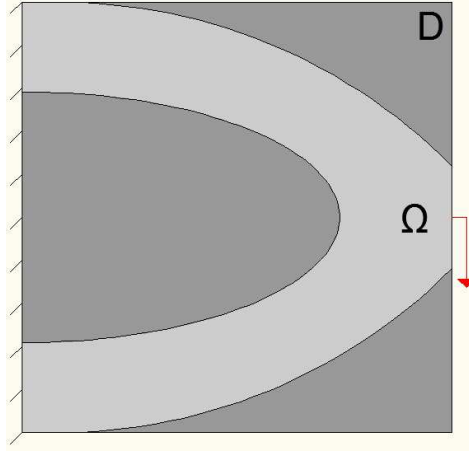
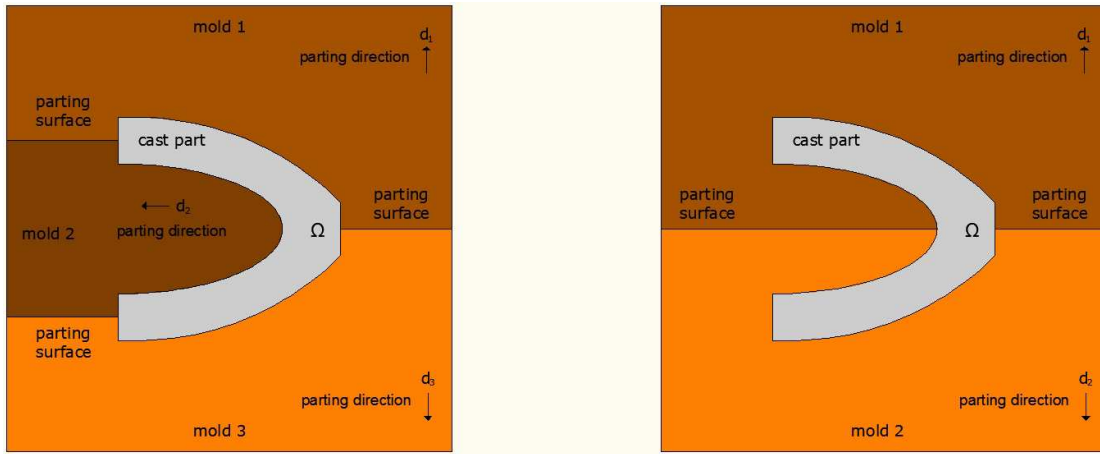
Figure 2.2: Optimized shape of a cast part (Ω).

Figure 2.3: Left: moldable shape; right: non-moldable shape.

the cast part and the parting direction is considered. In our work, the molding system is considered to be set a priori.

The only thing that we may allow to vary is the so-called **parting surface**, the surface on which different molds come in contact [159]. The parting surface between two molds can be predefined or it can be constructed after the optimization using suitable methods [1, 56]. In most of the industrial applications, planar parting surfaces are preferred because of reasons of cost and simplicity [159].

Minimum members' distance

This constraint imposes a minimum size between the features of the cast part, which is equivalent with setting a minimum size on the features of the mold. One reason for this specification comes from the tooling machinery which limits the shapes of realizable molds. Also, thin members of the molds could result in low precision of the final cast part, due to the deformation of these flexible parts under a high temperature field. Finally, this is an implicit way of accounting for the fatigue desirment of the molds, which need to remain functional for a large number of castings, in order to reduce the overall financial cost.

Maximum curvature

This specification is purely geometric and expresses the inability of constructing too curvy molds.

2.3.2 Feedability

In order to avoid shrinkage porosity formed during the solidification process, the caster needs to design a feeding system that drives "hot spots" outside of the structure. The risers (also called feeders) are reservoirs of metal and provide the cast part with the necessary amount of liquid metal so that solidification ends inside the riser. They are usually placed in the most massive parts of the shape. The classical approach is to design them through calculations of volume and surface area of various areas of the casting (modulus method). Volume represents the capacity to store heat and the surface area represents the capacity to transfer the heat to the surrounding by convection. A high modulus (M =modulus) value means high capacity to store heat (volume) compared to the heat loss by convection (surface area). For this reason, the modulus of the riser should be higher compared to the casting. In [33] it is suggested that $M_f = 1.2M_c$, where M_f is the modulus of the feeder and M_c is the modulus of the cast part.

This process is described in Figure 2.4, where the solidification and the solid fraction in a bar with different feeding systems is depicted. In the upper row, no feeders are placed. Solidification starts from the exterior to the interior and, at the end, shrinkage porosity is observed at the region to solidify last. Placing feeders in appropriate positions of the shape changes the direction of solidification and drives shrinkage porosity towards the risers. The size of the feeders is then increased until the shrinkage defect is completely moved to the feeders. Increasing the total volume of feeders leads to a corresponding augmentation of the casting cost. Feedability is concerned with the design of a feeding system, able to drive the shrinkage porosity due to solidification to the risers, at an acceptable cost.

However, where the casting is thin and plate-like the above strategy may not work. This is because the feeder does not only have to stay live while the casting is solidifying, but it must supply enough liquid metal to satisfy the shrinkage contraction within the casting. In the conventional method of gating design, the casting is split into number of hot zone areas depending on the hot spots identified from 2D sectional drawings of the casting. To these areas individual risers having higher modulus are attached. Other solutions include the use of feeder insulation or the use of exothermic materials. Insulating feeders extend the solidification time, promote directional solidification and reduce the total mass of feeders. In exothermic materials, an exothermic reaction is initiated when molten metal meets the feeder, heating the metal and extending solidification time still further. Such a choice is very much dependent on the experience and skill of the casting engineer. It can be that some regions are inaccessible for providing adequate risers because of process limitations (e.g. regions of high curvature). Then, the caster can decide to apply other tricks, like introducing copper chills to speed up solidification in these areas.

In contrast to the molding system, the feeding system is rarely set a priori, since it heavily depends on the shape of the cast part. Therefore, a natural question that arises is: "What should one change if the shape is not feedable with respect to a specific feeding system? Change the shape or the feeding system?". In fact, there is no global answer to this question. The decision is case dependent. It is possible that by conceiving another feeding system, or by applying slight changes to the existing one, the shape turns into feedable. It is also possible that one is interested to keep a standard and cheap feeding system and is willing to adjust the shape to it [51].

A common practice to decide if a shape shall be considered acceptable or not is to use an indication factor for the maximum riser to be used. This is done by simulating the solidification process of the cast part without including the feeding system and finding the final solidification time t_f . The higher the value of t_f , the greater the volume of the riser to be used. Therefore, the solidification time t_f provides a good indication of the riser's volume and shall be constrained.

Another way is to use a geometric reasoning, instead of a mechanical one. The higher the distance of a point to the boundary of the shape, the longer it takes to solidify. As a result, using their experience, casters are able to approximate the maximum allowed thickness of a feedable cast part. A structure that respects this thickness constraint is considered feedable in a first step and a feeding system is tried to be designed.

Concluding, feedability imposes one of the following two specifications:

- a **maximum solidification time**, or
- a **maximum thickness feature**.

Remark 2.3.1. In [144], [145] Tavakoli et al. have presented some approaches for the optimal design of risers for a fixed cast part, using the SIMP method for shape and topology optimization. One may wonder if the idea of optimal design of the casting system could be applied in our case. For example, a criterion of feedability could be the feasibility of an optimized casting system. First of all, although the formulation

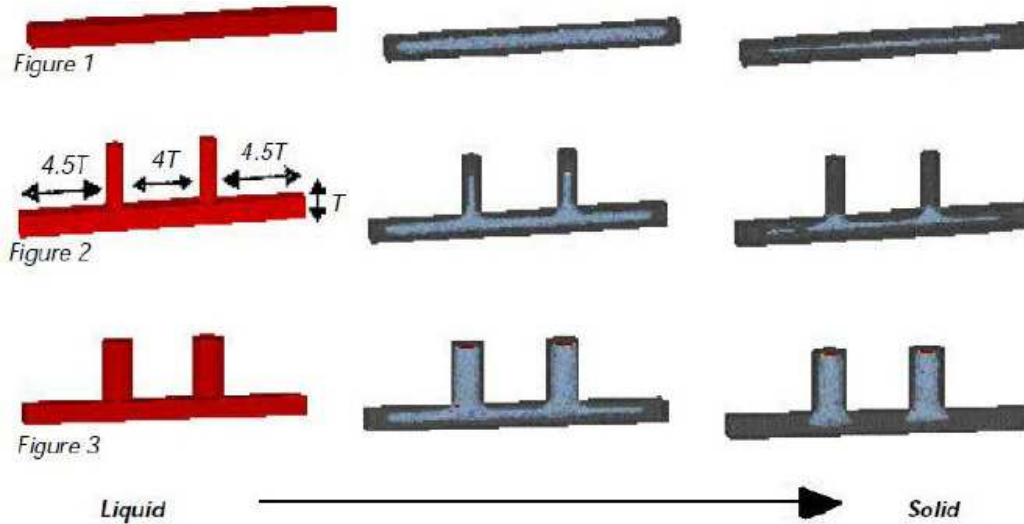


Figure 2.4: Solidification process and solid fraction for different feeding systems (figure extracted from www.esi-group.com).

of the problem in [144], [145] is interesting, it is much simplified compared to the real problem of casting in modern industries. An optimized casting system for the problem posed in [144, 145] could be very far from what a caster would consider as optimal and a cast part could be unreasonably rejected. Moreover, this would give no indication about how the shape should change, since a change in the shape could result in a totally different optimized feeding system. For these reasons, we have chosen criteria that are related to the shape and totally independent of any feeding system.

2.3.3 Fillability

Fillability ensures that the flow of liquid metal is efficiently performed and the mold is properly filled. Many problems can arise during the filling process of the mold. One of the most important is the appearance of precocious solidification, i.e. the interruption of the liquid flow due to the fast solidification of a thin part. This case appears in Figure 2.5, where the casting of a cast part under different feeding systems is depicted. For the second system, the flow is interrupted. Other problems can appear due to turbulence during the flow, the entrapment of air due to the bad design of the gating system (see Figure 2.6), etc...

Once again, solutions to the above mentioned can be given by changing the casting system, the cast part, or even using other techniques like augmentation of the fluidity of the metal, or additional pressure ("high pressure die casting"). The most important problems during the filling process are created due to narrow features of the shape. Trying to tackle the problem from a mechanical point of view is not easy at all, since the equations that govern the filling process are too complicated and a mechanical criterion of fillability is not at all clear. Instead, as in the case of feedability, it seems more reasonable to use an indicator factor of geometric nature in order to characterize (at least in a first step) the shape as acceptable or not with respect to the filling process.

Therefore, we consider that fillability imposes a specification of

- a minimum thickness feature.

2.4 Conclusions

In this Section, we resume our logic about how Shape and Topology Optimization should account for castability of a shape. We believe that the optimization of the general casting system (molding and feeding system) is not a purely continuous problem but involves discrete variables and in case it is formulated as such, it is usually very far from real applications. For this reason, the molding system is considered to be set a priori and the criteria for feedability and fillability are related just to the shape, i.e. no feeding system is considered. Especially for the feedability criterion, two different, although closely

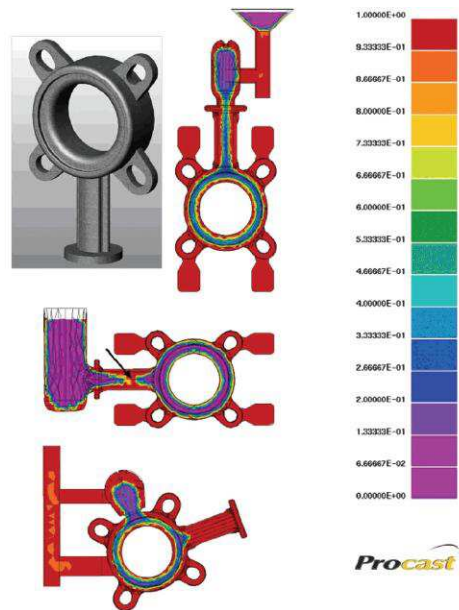


Figure 2.5: Testing a riser operation at different system constructions. An arrow indicates interruption in the possibility of feeding by a riser (figure extracted from [74]).

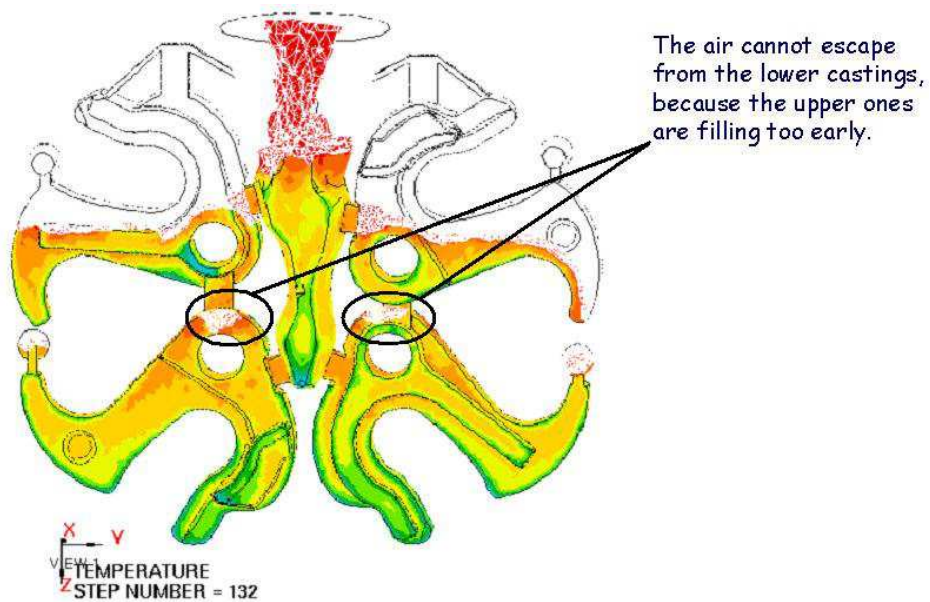


Figure 2.6: Problem in the gating system (figure extracted from [123]).

related, approaches are tested. A mechanical one and a geometric one. The first derives more from the real mechanical problem of casting, while the second tries to interpret the problem in terms of geometry specifications. For the fillability criterion only a geometric approach is tested, since there the mechanical problem is too difficult and the definition of a criterion is not clear.

More specifically, the maximum and minimum thickness feature specifications and the minimum members' distance are regarded in general as thickness constraints and are discussed in Chapter 3. Constraints on the molding direction are presented in Chapter 4. Finally, in Chapter 5 we present our approach for the maximum solidification time specification. The maximum curvature constraint has not been addressed in this work and is suggested for future work, although we shall see that imposing constraints on the minimum thickness and members' distance, implicitly sets limitations on the value of the curvature.

Part II

Manufacturing constraints

Chapter 3

Thickness control in structural optimization

Contents

3.1	Introduction	59
3.2	Formulation of thickness constraints	60
3.2.1	Maximum thickness	61
3.2.2	Minimum thickness	61
3.2.3	Minimum members' distance	62
3.2.4	Penalty functionals	63
3.3	Shape differentiability of the signed distance function	63
3.3.1	An application of the coarea formula to integral functions of the signed distance function	65
3.4	Shape derivative of penalty functionals	67
3.5	Augmented Lagrangian method and descent direction	69
3.6	Numerical implementation	70
3.6.1	Construction of d_Ω	70
3.6.2	Maximum thickness	72
3.6.3	Minimum thickness and minimum members' distance	72
3.7	Numerical examples	73
3.7.1	Maximum thickness	73
3.7.2	Minimum Thickness	93
3.7.3	Combination of thickness constraints	120
3.8	Other formulations of the thickness constraints	123
3.8.1	Maximum Thickness	123
3.8.2	Minimum Thickness	128

The purpose of this chapter is to propose a novel method for handling geometric constraints related to a notion of local thickness, in the context of structural optimization via a level-set method. The local thickness is calculated using the signed distance function to the shape. We implement this method in two and three space dimensions for a model of linear elasticity. We consider various formulations of the constrained optimization problem and compute a shape derivative to advect the shape from one iteration of the process to the next one. We discuss different ways to handle the constraints. In good agreements with well-known observations linked to gradient based shape optimization, the resulting optimized shape is strongly dependent on the initial guess and on the way the constraints are enforced.

3.1 Introduction

Numerical experience shows that shape and topology optimization very frequently results in shapes containing thin or thick members, or features that are too closely spaced. For different application-dependent reasons, such situations may be undesirable. For example, in Chapter 2 we have explained

that for structures made by casting, thick members should be avoided because of cooling constraints, while thin members are difficult to fill with liquid metal. Thin members or too closeby members may also violate the precision limitations in the tooling machinery.

Beyond manufacturing reasons, imposing a minimum member size can play a significant role in robust design or mesh independency of the optimal result. It can also be seen as an implicit way to avoid buckling, without treating explicitly the mechanical constraint. In the same way, limiting the maximum allowed thickness of the structure can be seen as an implicit way to increase the structural redundancy, since the loading path can change and the energy can be redistributed in more members, increasing its robustness, especially in case of loads under uncertainties [61]. There are many other mechanical reasons for introducing thickness constraints (e.g. limitations by physics in optimal fluid filter design [61]), not to mention those motivations outside of mechanics, such as aesthetics.

In the framework of the homogenization or SIMP method [28] for topology optimization, there is a relatively small body of literature devoted to this issue although many works discussed the notions of filtering or mesh independence [30]. Petersson and Sigmund [112] used a slope constraint for the elements' densities in order to impose a minimum length scale. In [115], Poulsen introduced the so-called "MOLE method", in which he examined the monotonicity of the density function along different diagonals of a circle centered at each grid point. Despite its limitations, mentioned in the paper, the MOLE method can also be applied in the void part, to avoid small holes in the structure. In [63], Guest et al. proposed to control the minimum length scale by combining projection functions with nodal design variables, defining the density of each node as a weighted sum of the densities of nodes lying at a distance up to the minimum length scale. In [61], Guest formulated a constraint of maximum length scale using the volume of balls of diameter equal to this length, centered at each element. The idea of projection functions was also used by Sigmund in [127], where a formulation for robust design was proposed to treat manufacturing constraints.

There are even fewer papers studying thickness control in the framework of the level-set method [106] for shape and topology optimization [13, 14, 107, 121, 157]. In [40], Cheng et al. favored the formation of specific geometric features in the structure and in [38, 89] they added an energy functional in the objective function, which privileges a family of shapes with strip-like features. The results obtained in these papers show significant differences compared to the ones obtained without adding any geometric constraint. The addition of an energy functional seems to give satisfying results for the alleviation of hinges in compliant mechanisms [89]. One of the difficulties in these works is to define the thickness (or other geometric quantities) of a structure in a precise and efficient way, especially since its geometry or shape is implicitly defined by the zero level-set of an auxiliary function.

In this work we propose a novel method for handling three major manufacturing constraints of geometric nature using the level-set method for structural optimization. Each one of them relies on a definition of the structure's thickness based on the signed distance function to the shape's boundary. First, we control the maximum local thickness of the shape. To define and compute a notion of maximum local thickness, we use the signed distance function to the shape. We make extensive use of the notion of the "skeleton" of the shape [77, 97]. Then, we control the minimum thickness as well as the distance between the members of the shape, using again the signed distance function and offset sets of the boundary [2, 76]. For the numerical optimization, we implement a simple augmented Lagrangian method to handle the constraints. We show several numerical results in two and three space dimensions and discuss different ways to impose the constraints.

3.2 Formulation of thickness constraints

The notion of thickness in structural mechanics can be understood in different ways. For example, in a truss composed of beams with circular cross-section, it can be claimed that the thickness of a beam is equal to the diameter of the cross-section. Same intuitive definitions can be given for a variety of structures in which the specific type of members used, give a satisfying enough description of the shape's thickness. However, for general continuous structures, things become more complicated and one usually uses a definition that corresponds to the specific problem caused by the thickness violation. The reader should also note that when we desire to treat simultaneously more than one constraint, e.g. minimum and maximum thickness, then we can work with two different definitions for the thickness at the same time.

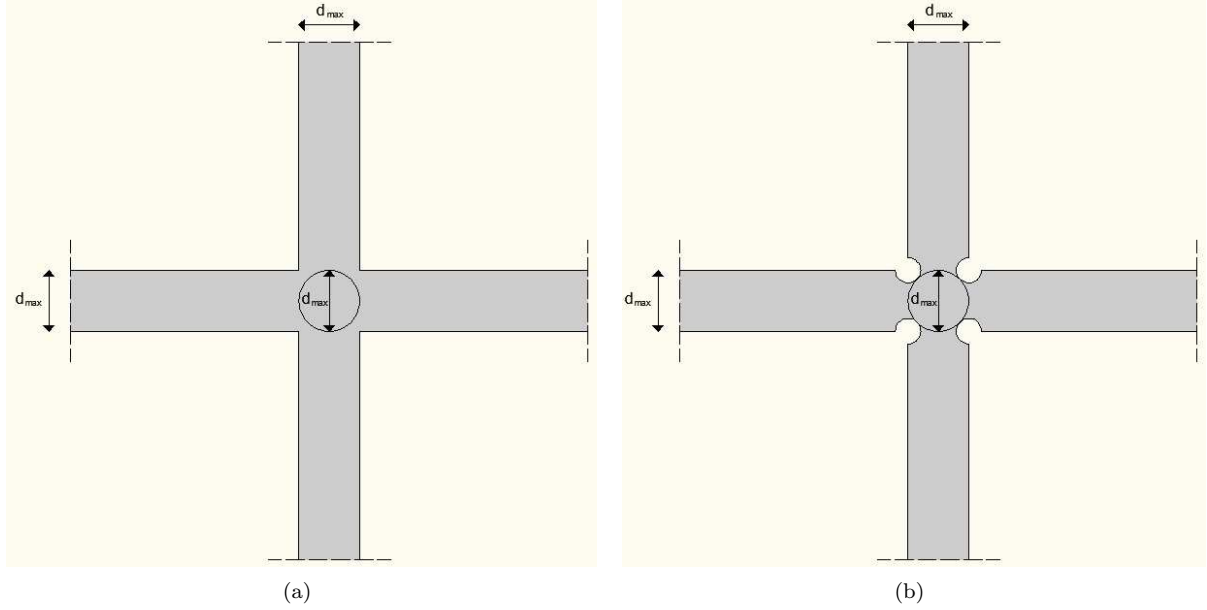


Figure 3.1: (a): bars violating the thickness constraint (3.2), (b): bars respecting the thickness constraint (3.2).

3.2.1 Maximum thickness

A maximum thickness constraint of size d_{max} could be interpreted such that there is no point in the shape, which is a center of a disk of diameter d_{max} fully covered by material. The above definition motivates the use of the signed distance function to the shape. Recalling that the signed distance function to the domain Ω is the function $\mathbb{R}^N \ni x \mapsto d_\Omega(x)$ defined by :

$$d_\Omega(x) = \begin{cases} -d(x, \partial\Omega) & \text{if } x \in \Omega, \\ 0 & \text{if } x \in \partial\Omega, \\ d(x, \partial\Omega) & \text{if } x \in \mathbb{R}^N \setminus \Omega, \end{cases} \quad (3.1)$$

where $d(\cdot, \partial\Omega)$ is the usual Euclidean distance, the formulation of the constraint reads

$$d_\Omega(x) \geq -d_{max}/2 \quad \forall x \in \Omega. \quad (3.2)$$

A possible drawback of the above definition is the appearance of distortions at the regions of crossing between bars. In Figure 3.1(a), we see two bars of uniform thickness d_{max} crossing. Although intuitively one would say that a maximum thickness constraint of value d_{max} is respected, we can see that there is a region around the center of the joint, where constraint (3.2) is violated. One possible solution, satisfying constraint (3.2) is given in Figure 3.1(b). However, such distortions of the shape close to the position of joints are not usually preferable for engineers, both for mechanical and manufacturing reasons. In section 3.7, we propose some modifications to avoid such distortions.

3.2.2 Minimum thickness

We now want to enforce a minimum thickness constraint of value $d_{min} > 0$. The formulation of this constraint is not so straightforward as the previous one, since it is not evident how the values of the signed distance function are related to a notion of minimum thickness. However, another definition based on offset sets [2, 76] gives an intuitive view of a minimum thickness constraint. Denoting with d_{off} a positive number, the set $\partial\Omega_{d_{off}} = \{x - d_{off}n(x) : x \in \partial\Omega\}$ is the offset set of $\partial\Omega$ in the direction $-n(x)$ at a distance d_{off} (see Figure 3.2).

A formulation of the constraint which guarantees that any offset set in the direction $-n(x)$ up to a distance d_{min} stays in the shape Ω is the following:

$$d_\Omega(x - d_{off}n(x)) \leq 0 \quad \forall x \in \partial\Omega, \forall d_{off} \in [0, d_{min}]. \quad (3.3)$$

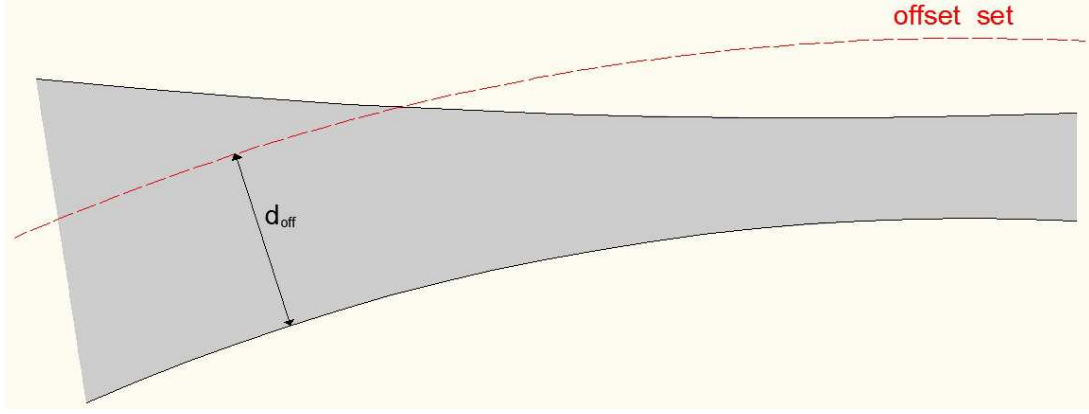


Figure 3.2: Offset set of the lower part of the boundary (shape in grey).

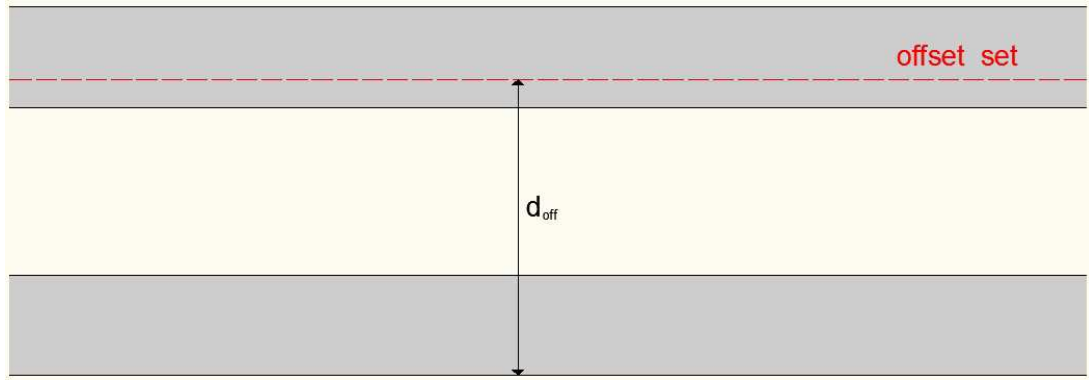


Figure 3.3: Inability to detect very thin members with a single offset set (shape in grey).

Remark 3.2.1. In order for the constraint (3.3) to be well-defined, it is necessary that it exists $\varepsilon_0 > 0$ such that $\forall d_{\text{off}} < \varepsilon_0$, $\partial\Omega_{d_{\text{off}}} \subset \Omega$. This is true if the boundary is $C^{1,1}$ (or more) (see [49], Lemma 3.3.2), since it guarantees the existence of a tubular neighborhood of thickness $\varepsilon > 0$ of the boundary, in which d_Ω is smooth.

We say that a shape satisfying constraint (3.3) has everywhere thickness greater or equal to d_{\min} . We emphasize that the inequality (3.3) must be valid for the whole interval $[0, d_{\min}]$ of offset parameters. A single offset set at the desired distance d_{\min} cannot possibly detect the case of members that are very thin and that are also very close to each other. This case can be obviously recognized in Figure 3.3. This figure shows two members of the structure Ω in grey color. The offset set just for one value d_{off} can fall entirely in the structure without detecting the void between the two parts. In this case the algorithm does not understand the violation of the constraint.

3.2.3 Minimum members' distance

This constraint looks exactly the same as the minimum thickness one, however it is now imposed on the complementary of the shape. We just need to invert the direction of offsetting and the constraint reads

$$d_\Omega(x + d_{\text{off}}n(x)) \geq 0 \quad \forall x \in \partial\Omega, \forall d_{\text{off}} \in [0, d_{\min}]. \quad (3.4)$$

If a shape satisfies this constraint, we say that its members have everywhere a distance greater or equal to d_{\min} .

Remark 3.2.2. We have formulated three constraints of geometric nature, related with a notion of local thickness of the shape. Although we have been motivated from the mechanics of casting and its limitations, the formulations remain purely geometric and the reader could easily find other interpretations of these constraints, away from cast parts. This means that these constraints can be introduced in any framework, even for structures that are intended to be constructed in a completely different way.

3.2.4 Penalty functionals

Constraints (3.2), (3.3) and (3.4) are pointwise, i.e. they are defined at each point of the domain Ω or of its boundary $\partial\Omega$. They are infinite in number and thus they cannot be treated numerically as such.

Discretizing the level-set function in the computational domain D , we obtain directly some kind of parametrization of the domain Ω by means of the values of the level-set function ψ . Furthermore, in case that the mesh is adapted to the zero level-set (see [9],[158]), the finite set of mesh nodes satisfying $\psi = 0$ can be assumed to compose its boundary $\partial\Omega$. If a fixed, structured grid is used, then a simple idea is to assume that the boundary $\partial\Omega$ is given by all grid nodes which belong to elements crossed by the zero level-set. In any case, we can then assume that constraints (3.2), (3.3) and (3.4) are posed at the corresponding discretization nodes. However, this can result in a significant number of constraints, which is very difficult to be tackled by optimization algorithms.

For this reason, it seems more natural to formulate global averaged constraints. A simple choice of a smooth global constraint is to use the *quadratic penalty function*. This function takes the following form for the three previous constraints:

$$\begin{aligned} \text{Maximum Thickness : } P_{MaxT}(\Omega) &= \int_{\Omega} \left[(d_{\Omega}(x) + d_{max}/2)^- \right]^2 dx, \\ \text{Minimum Thickness : } P_{MinT}(\Omega) &= \int_{\partial\Omega} \int_0^{d_{min}} \left[(d_{\Omega}(s - \xi n(s)))^+ \right]^2 d\xi ds, \\ \text{Minimum Members' Distance : } P_{MMD}(\Omega) &= \int_{\partial\Omega} \int_0^{d_{min}} \left[(d_{\Omega}(s + \xi n(s)))^- \right]^2 d\xi ds, \end{aligned}$$

where we have denoted: $(f)^+ = \max(f, 0)$ and $(f)^- = \min(f, 0)$.

Then, a pointwise constraint is satisfied once its corresponding penalty functional equals to zero. For example, for the maximum thickness functional P_{MaxT} :

$$P_{MaxT}(\Omega) = 0 \Rightarrow (d_{\Omega}(x) + d_{max}/2)^- = 0 \quad \text{in } \Omega \Rightarrow d_{\Omega}(x) \geq -d_{max}/2 \quad \text{in } \Omega.$$

3.3 Shape differentiability of the signed distance function

This section has been extracted from [8], where the signed distance function was used for the formulation of multi-phase problems. Its purpose is to recall some results on the signed distance function and to explore its shape differentiability which holds in a non-classical and subtle sense (see below for details). For a Lipschitz bounded domain $\Omega \subset D$ we consider shape variations in the sense of Hadamard as in section 1.3.1. Let us start by collecting some definitions (see Figure 3.4 for a geometric illustration).

Definition 3.3.1. Let $\Omega \subset \mathbb{R}^N$ be a Lipschitz bounded open set.

- For any $x \in \mathbb{R}^N$, $\Pi_{\partial\Omega}(x) := \{y_0 \in \partial\Omega \text{ such that } |x - y_0| = \inf_{y \in \partial\Omega} |x - y|\}$ is the set of projections of x on $\partial\Omega$. It is a closed subset of $\partial\Omega$. When $\Pi_{\partial\Omega}(x)$ reduces to a single point, it is called the projection $p_{\partial\Omega}(x)$ of x onto $\partial\Omega$.
- $\Sigma := \{x \in \mathbb{R}^N \text{ such that } (d_{\Omega})^2 \text{ is not differentiable at } x\}$ is the skeleton of $\partial\Omega$ (or Ω by a small abuse in terminology).
- For any $x \in \partial\Omega$, $\text{ray}_{\partial\Omega}(x) := \{y \in \mathbb{R}^N \text{ such that } d_{\Omega} \text{ is differentiable at } y \text{ and } p_{\partial\Omega}(y) = x\}$ is the ray emerging from x . Equivalently, $\text{ray}_{\partial\Omega}(x) = p_{\partial\Omega}^{-1}(x)$.

We now recall some classical results (see [49], Chapter 7, theorems 3.1, 3.3 and [20]).

Lemma 3.3.2. Let $\Omega \subset \mathbb{R}^N$ be a Lipschitz bounded open set.

- A point $x \notin \partial\Omega$ has a unique projection $p_{\partial\Omega}(x)$ on $\partial\Omega$ if and only if $x \notin \Sigma$. In such a case, it satisfies $d(x, \partial\Omega) = |x - p_{\partial\Omega}(x)|$ and the gradient of d_{Ω} at x reads

$$\nabla d_{\Omega}(x) = \frac{x - p_{\partial\Omega}(x)}{d_{\Omega}(x)}.$$

- As a consequence of Rademacher's theorem ([55], section 3.1.2), Σ has zero Lebesgue measure in \mathbb{R}^N . Furthermore, when Ω is C^2 , $\bar{\Sigma}$ has zero Lebesgue measure too [90].

- For any $x \in \mathbb{R}^N$, $p \in \Pi_{\partial\Omega}(x)$, $\alpha \in [0, 1]$, denoting $x_\alpha := p + \alpha(x - p)$ the points of the ray of x lying between p and x , we have $d_\Omega(x_\alpha) = \alpha d_\Omega(x)$ and $\Pi_{\partial\Omega}(x_\alpha) \subset \Pi_{\partial\Omega}(x)$.
- If Ω is of class \mathcal{C}^k , for $k \geq 2$, then d_Ω is \mathcal{C}^k too in a tubular neighborhood of $\partial\Omega$. In that case, d_Ω is differentiable at every point $x \in \partial\Omega$, and $\nabla d_\Omega(x) = n(x)$, the unit normal vector to Ω .

Unfortunately, the signed distance function is not, strictly speaking, shape differentiable in the sense of Definition 1.3.2. One reason is the lack of smoothness of the gradient of d_Ω at the skeleton Σ . However, its pointwise values $d_\Omega(x)$ are shape differentiable for $x \in D \setminus \Sigma$. This is the purpose of the next result which can be found in [48] (without much details however ; see [44] for detailed and complete proofs).

Proposition 3.3.3. *Assume $\Omega \subset D$ is an open set of class \mathcal{C}^1 , and fix a point $x \notin \Sigma$. Then $\theta \mapsto d_{(Id+\theta)\Omega}(x)$ is Gâteaux-differentiable at $\theta = 0$, as an application from $W^{1,\infty}(D, \mathbb{R}^N)$ into \mathbb{R} , and its derivative is*

$$d'_\Omega(\theta)(x) = -\theta(p_{\partial\Omega}(x)) \cdot n(p_{\partial\Omega}(x)).$$

Remark 3.3.4. *Actually, a more general result than that of Proposition 3.3.3 holds. Indeed, retaining the hypothesis that Ω is of class \mathcal{C}^1 , for any point $x \in \mathbb{R}^N$, and denoting, for a real parameter $t > 0$,*

$$\Omega_{t\theta} = (I + t\theta)\Omega,$$

the application $t \mapsto d_{\Omega_{t\theta}}(x)$ is right-differentiable at $t = 0^+$, and

- *if $x \in \Omega$, $\frac{d}{dt}(d_{\Omega_{t\theta}}(x))|_{t=0^+} = - \inf_{y \in \Pi_{\partial\Omega}(x)} \theta(y) \cdot n(y)$.*
- *if $x \in {}^c\bar{\Omega}$, $\frac{d}{dt}(d_{\Omega_{t\theta}}(x))|_{t=0^+} = - \sup_{y \in \Pi_{\partial\Omega}(x)} \theta(y) \cdot n(y)$.*

Of course, these formulae agree with the previous result since $\Pi_{\partial\Omega}(x) = \{p_{\partial\Omega}(x)\}$ if $x \notin \Sigma$.

Note also that a similar analysis could be performed when Ω is only assumed to be Lipschitz. However, the results are then more tedious to write, since the normal vector field n is not defined everywhere on $\partial\Omega$ (which is an indicator of specific geometric phenomena, see [44]).

Remark 3.3.5. *The signed distance function can also be seen as a solution of the following Hamilton-Jacobi equation*

$$\begin{cases} |\nabla d_\Omega(x)| = 1 & \text{in } D, \\ d_\Omega(x) = 0 & \text{on } \partial\Omega. \end{cases}$$

The behavior of the variations of d_Ω with respect to the domain can be retrieved by a formal computation. Indeed, assuming that d_Ω is shape differentiable, a formal computation yields that the directional shape derivative $d'_\Omega(\theta)$ satisfies

$$\begin{cases} \nabla d_\Omega(x) \cdot \nabla d'_\Omega(\theta)(x) = 0 & \text{in } D, \\ d'_\Omega(\theta)(x) = -\theta(x) \cdot n(x) & \text{on } \partial\Omega. \end{cases} \quad (3.5)$$

Equation (3.5) provides us with some important information for the analysis in the sequel. Its first part means that $d'_\Omega(\theta)(x)$ is constant along $\text{ray}_{\partial\Omega}(x)$, while the second part gives an explicit value of the derivative for the points on $\partial\Omega$.

Corollary 3.3.6. *Let Ω be a bounded domain of class \mathcal{C}^1 and $m(x, s) : \mathbb{R}_x^N \times \mathbb{R}_s \rightarrow \mathbb{R}$ a function of class \mathcal{C}^1 . Define the functional $J(\Omega)$ as*

$$J(\Omega) = \int_D m(x, d_\Omega(x)) dx. \quad (3.6)$$

The application $\theta \mapsto J((Id + \theta)\Omega)$, from $W^{1,\infty}(D, \mathbb{R}^N)$ into \mathbb{R} , is Gâteaux-differentiable at $\theta = 0$ and its derivative reads

$$J'(\Omega)(\theta) = - \int_D \frac{\partial m}{\partial s}(x, d_\Omega(x)) \theta(p_{\partial\Omega}(x)) \cdot n(p_{\partial\Omega}(x)) dx. \quad (3.7)$$

The shape derivative (3.7) satisfies Hadamard's structure theorem (see section 1.3.1) since it depends only on the values of $\theta \cdot n$ on the boundary of $\partial\Omega$. However (3.7) is not a surface integral on $\partial\Omega$ as usual. Therefore the task of the next subsection is to transform (3.7) into a surface integral by using the notion of *rays* (see Definition 3.3.1), along which d_Ω and $p_{\partial\Omega}$ take very simple forms, altogether with the coarea formula.

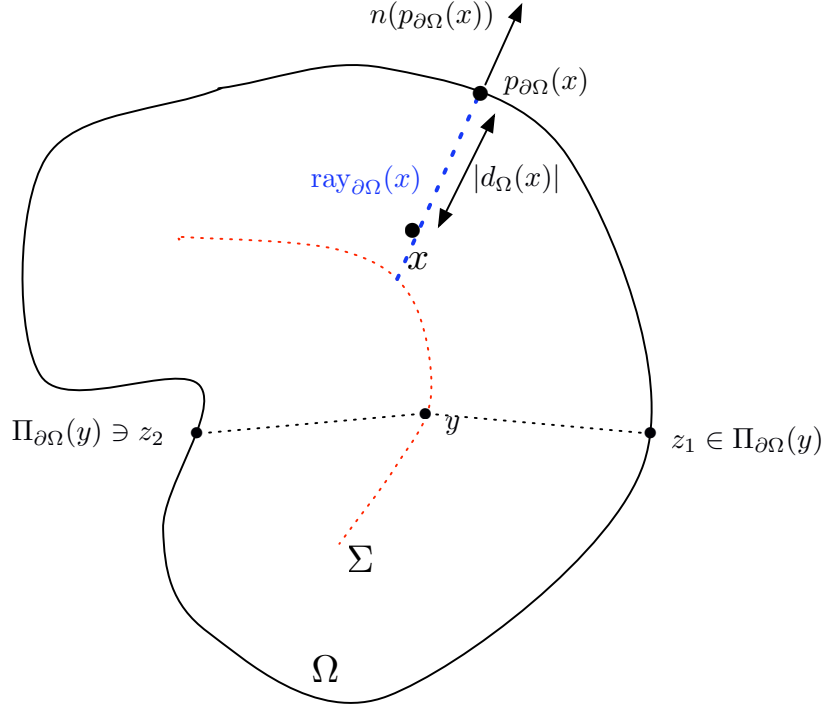


Figure 3.4: For a point x lying outside the skeleton Σ of Ω , unique projection point $p_{\partial\Omega}(x)$ and line segment $\text{ray}_{\partial\Omega}(x)$. For a point $y \in \Sigma$, at least two points z_1, z_2 belong to the set of projections $\Pi_{\partial\Omega}(y)$.

3.3.1 An application of the coarea formula to integral functions of the signed distance function

The purpose of this section is to derive a Fubini-like formula for integrals of the form (3.7) and transform them in surface integrals. To this end, we use the following coarea formula [36].

Proposition 3.3.7. *Let X, Y be two smooth Riemannian manifolds of respective dimension $m \geq n$, and $f : X \rightarrow Y$ a surjective map of class C^1 , whose differential $\nabla f(x) : T_x X \rightarrow T_{f(x)} Y$ is surjective for almost every $x \in X$. Let φ an integrable function over X . Then:*

$$\int_X \varphi(x) dx = \int_Y \left(\int_{z \in f^{-1}(y)} \varphi(z) \frac{1}{\text{Jac}(f)(z)} dz \right) dy$$

where $\text{Jac}(f)(z)$ is the the Jacobian of the function f .

Remark 3.3.8. *If $m \geq n$, and $f : \mathbb{R}^m \rightarrow \mathbb{R}^n$ is a differentiable function at a point $x \in \mathbb{R}^m$, the Jacobian $\text{Jac}(f)(x)$ of f at x is defined as*

$$\text{Jac}(f)(x) := \sqrt{\det(\nabla f(x) \nabla f(x)^T)}.$$

The definition of the Jacobian is similar when f is a map between two Riemannian manifolds X and Y , once the tangent planes $T_x X, T_{f(x)} Y$ have been identified to \mathbb{R}^m and \mathbb{R}^n respectively (see [36], exercise III.11). In any case, the Jacobian is positive $\text{Jac}(f)(x) > 0$ if and only if $\nabla f(x)$ is of maximum rank, or equivalently $\nabla f(x)$ is surjective from \mathbb{R}^m to \mathbb{R}^n .

We apply this formula in our context to $X = \Omega$, $Y = \partial\Omega$ and $f = p_{\partial\Omega}$. To apply Proposition 3.3.7 we need the differentiability of $p_{\partial\Omega}$ which will be deduced from the following classical result on the second-order differentiability of the signed distance function [34].

Lemma 3.3.9. *Assume Ω is of class C^2 . For $i = 1, \dots, d-1$, denote by κ_i the principal curvatures of $\partial\Omega$ and e_i its associated directions (see Figure 3.5). For every $x \in D$, and every $y \in \Pi_{\partial\Omega}(x)$, we have*

$$-\kappa_i(y) d_{\Omega}(x) \leq 1, \quad 1 \leq i \leq d-1. \quad (3.8)$$

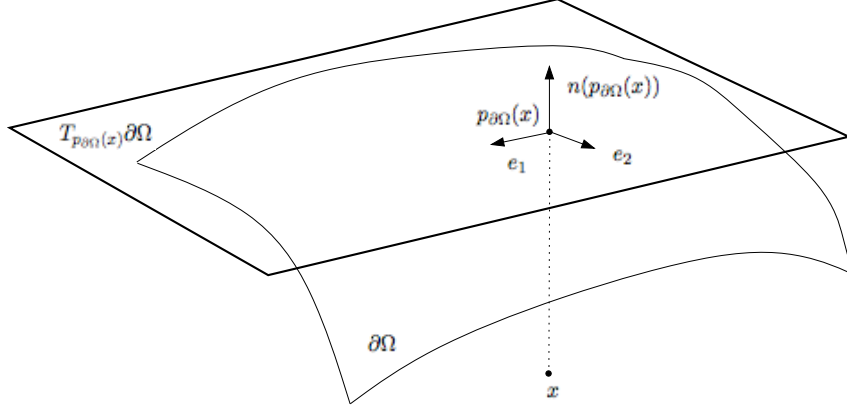


Figure 3.5: Principal directions, normal vector at the projection point of $x \in \mathbb{R}^N$.

Define Γ the singular set of Ω , namely the set of points $x \notin \Sigma$ such that, for some i , one of the inequality (3.8) is actually an equality. Then, $\bar{\Sigma} = \Sigma \cup \Gamma$ and $\bar{\Sigma}$ has zero Lebesgue measure. If $x \notin \bar{\Sigma}$, then all inequalities (3.8) are strict and d_Ω is twice differentiable at x . Its Hessian reads

$$\mathcal{H}d_\Omega(x) = \sum_{i=1}^{N-1} \frac{\kappa_i(p_{\partial\Omega}(x))}{1 + \kappa_i(p_{\partial\Omega}(x))d_\Omega(x)} e_i(p_{\partial\Omega}(x)) \otimes e_i(p_{\partial\Omega}(x)).$$

Lemma 3.3.10. *Let $x \in D \setminus \bar{\Sigma}$. The projection map $p_{\partial\Omega}$ is differentiable at x and, in the orthonormal basis $\{e_1, \dots, e_{N-1}, n\}(p_{\partial\Omega}(x))$ of \mathbb{R}^N (see Figure 3.5), its gradient is a $d \times d$ diagonal matrix*

$$\nabla p_{\partial\Omega}(x) = \begin{pmatrix} 1 - \frac{d_\Omega(x)\kappa_1}{1+d_\Omega(x)\kappa_1} & 0 & \dots & 0 \\ 0 & \ddots & \ddots & \vdots \\ \vdots & \ddots & 1 - \frac{d_\Omega(x)\kappa_{d-1}}{1+d_\Omega(x)\kappa_{d-1}} & 0 \\ 0 & \dots & 0 & 0 \end{pmatrix}, \quad (3.9)$$

where the principal curvatures κ_i are evaluated at $p_{\partial\Omega}(x)$.

Proof. The proof starts from the characterization of the projection map when $x \in D \setminus \Sigma$ (see Lemma 3.3.2)

$$p_{\partial\Omega}(x) = x - d_\Omega(x) \nabla d_\Omega(x).$$

This last equality can then be differentiated once more for $x \in D \setminus \bar{\Sigma}$

$$\nabla p_{\partial\Omega}(x) = Id - \nabla d_\Omega(x) \nabla d_\Omega(x)^T - d_\Omega(x) \mathcal{H}d_\Omega(x). \quad (3.10)$$

Since $\nabla d_\Omega(x) = n(p_{\partial\Omega}(x))$, a simple calculation ends the proof. \square

We now come to the main result of this section.

Corollary 3.3.11. *Let $\Omega \subset D$ be a \mathcal{C}^2 bounded domain, and let φ an integrable function over D . Then,*

$$\int_D \varphi(x) dx = \int_{\partial\Omega} \left(\int_{\text{ray}_{\partial\Omega}(y) \cap D} \varphi(z) \prod_{i=1}^{N-1} (1 + d_\Omega(z) \kappa_i(y)) dz \right) dy, \quad (3.11)$$

where z denotes a point in the ray emerging from $y \in \partial\Omega$ and dz is the line integration along that ray.

Proof. Since $\bar{\Sigma}$ is of zero Lebesgue measure, we have

$$\int_D \varphi(x) dx = \int_{D \setminus \bar{\Sigma}} \varphi(x) dx.$$

Applying Lemmas 3.3.9 and 3.3.10, $p_{\partial\Omega}$ is a surjective and differentiable map from $D \setminus \bar{\Sigma}$ into $\partial\Omega$, with a positive finite Jacobian for any $x \in D \setminus \bar{\Sigma}$

$$\text{Jac}(p_{\partial\Omega})(x) = \frac{1}{\prod_{i=1}^{N-1} (1 + d_\Omega(x) \kappa_i(p_{\partial\Omega}(x)))}.$$

Proposition 3.3.7 then yields the desired result. \square

3.4 Shape derivative of penalty functionals

In this section we compute the shape derivative of the penalty functional defined in section 3.2.4.

Maximum Thickness

Consider the quadratic penalty function

$$P_{MaxT}(\Omega) = \int_{\Omega} \left[(d_{\Omega}(x) + d_{max}/2)^- \right]^2 dx. \quad (3.12)$$

Lemma 3.4.1. *The shape derivative of (3.12) reads*

$$P'_{MaxT}(\Omega)(\theta) = \int_{\partial\Omega} -\theta(x) \cdot n(x) \int_{\text{ray}_{\partial\Omega}(x) \cap \Omega} 2(d_{\Omega}(z) + d_{max}/2)^- \prod_{i=1}^{N-1} (1 + d_{\Omega}(z)\kappa_i(x)) dz dx, \quad (3.13)$$

where $\kappa_i(x)$ are the principal curvatures at the point $x \in \partial\Omega$.

Proof. Applying Corollary 3.3.6 in (3.12), its shape derivative reads

$$P'_{MaxT}(\Omega)(\theta) = \int_{\Omega} 2d'_{\Omega}(\theta)(x) (d_{\Omega}(x) + d_{max}/2)^- dx. \quad (3.14)$$

Using the co-area formula (3.11), the shape derivative (3.14) takes the following form

$$P'_{MaxT}(\Omega)(\theta) = \int_{\partial\Omega} \int_{\text{ray}_{\partial\Omega}(x) \cap \Omega} 2d'_{\Omega}(\theta)(z) (d_{\Omega}(z) + d_{max}/2)^- \prod_{i=1}^{N-1} (1 + d_{\Omega}(z)\kappa_i(x)) dz dx.$$

Since $d'_{\Omega}(\theta)$ is constant along the ray emerging from x , it can be moved out of the second integral:

$$P'_{MaxT}(\Omega)(\theta) = \int_{\partial\Omega} d'_{\Omega}(\theta)(x) \int_{\text{ray}_{\partial\Omega}(x) \cap \Omega} 2(d_{\Omega}(z) + d_{max}/2)^- \prod_{i=1}^{N-1} (1 + d_{\Omega}(z)\kappa_i(x)) dz dx,$$

and since its expression on the boundary is known (see equation (3.5)), we finally end up with

$$P'_{MaxT}(\Omega)(\theta) = \int_{\partial\Omega} -\theta(x) \cdot n(x) \int_{\text{ray}_{\partial\Omega}(x) \cap \Omega} 2(d_{\Omega}(z) + d_{max}/2)^- \prod_{i=1}^{N-1} (1 + d_{\Omega}(z)\kappa_i(x)) dz dx,$$

which completes the proof. \square

Other functionals based on different formulations are computed in a similar way.

Minimum Thickness and Minimum Members' Distance

Consider now the quadratic penalty function

$$P_{MinT}(\Omega) = \int_{\partial\Omega} \int_0^{d_{min}} \left[(d_{\Omega}(x - \xi n(x)))^+ \right]^2 d\xi dx.$$

To make the text more compact, we change the notation according to Figure 3.6. We denote $x_m = x - \xi n(x)$ the offset point, from a point $x \in \partial\Omega$, at a distance ξ in the direction opposite to the normal vector, and $x_{m|\Omega}$ the projection of x_m onto the boundary. We can now rewrite the quadratic penalty function in more compact notation as

$$P_{MinT}(\Omega) = \int_{\partial\Omega} \int_0^{d_{min}} \left[(d_{\Omega}(x_m))^+ \right]^2 d\xi dx. \quad (3.15)$$

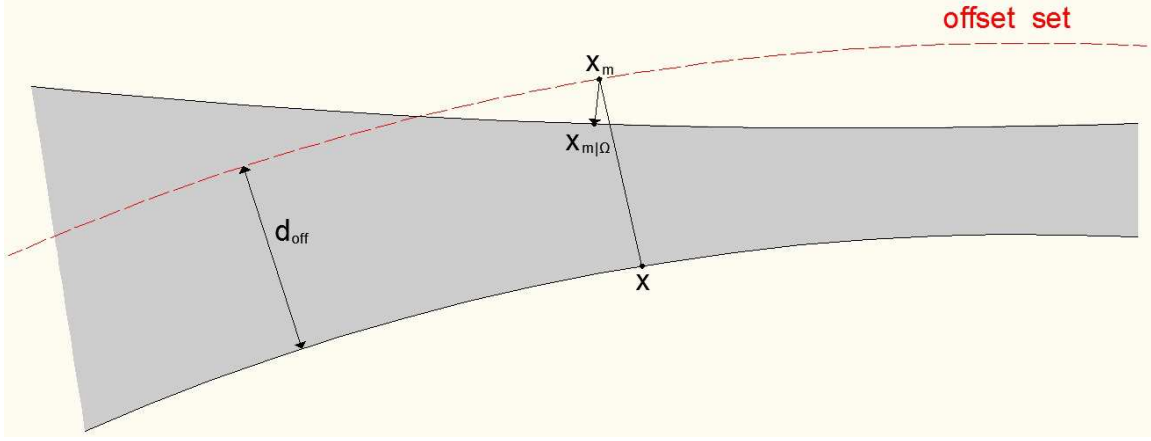


Figure 3.6: Offset point and projection onto the boundary.

Lemma 3.4.2. *The shape derivative of (3.15) reads*

$$\begin{aligned}
 P'_{MinT}(\Omega)(\theta) = & \int_{\partial\Omega} \int_0^{d_{min}} \theta(x) \cdot n(x) \left[H(x) \left((d_{\Omega}(x_m))^+ \right)^2 + 2 \left(d_{\Omega}(x_m)^+ \right) \nabla d_{\Omega}(x_m) \cdot \nabla d_{\Omega}(x) \right] d\xi dx \\
 & - \int_{\partial\Omega} \int_0^{d_{min}} \theta(x_{m|\Omega}) \cdot n(x_{m|\Omega}) 2 \left(d_{\Omega}(x_m)^+ \right) d\xi dx,
 \end{aligned} \quad (3.16)$$

where $H(x)$ denotes the mean curvature at the point $x \in \partial\Omega$.

Proof. Using Proposition 1.3.8 for the shape derivative of surface integrals with shape-dependent integrands, the shape derivative of (3.15) reads

$$\begin{aligned}
 P'_{MinT}(\Omega)(\theta) = & \int_{\partial\Omega} \int_0^{d_{min}} \theta(x) \cdot n(x) \left[H(x) \left((d_{\Omega}(x_m))^+ \right)^2 + \frac{\partial}{\partial n} \left(\left((d_{\Omega}(x_m))^+ \right)^2 \right) \right] d\xi dx \\
 & - \int_{\partial\Omega} \int_0^{d_{min}} \frac{\partial}{\partial \Omega} \left(\left((d_{\Omega}(x_m))^+ \right)^2 \right) (\theta) d\xi dx = \\
 & \int_{\partial\Omega} \int_0^{d_{min}} \theta(x) \cdot n(x) \left[H(x) \left((d_{\Omega}(x_m))^+ \right)^2 + 2 \left((d_{\Omega}(x_m))^+ \right) \nabla d_{\Omega}(x_m) \cdot n(x) \right] d\xi dx \\
 & - \int_{\partial\Omega} \int_0^{d_{min}} 2 \left(d_{\Omega}(x_m)^+ \right) d'_{\Omega}(x_m)(\theta) d\xi dx.
 \end{aligned} \quad (3.17)$$

From equation (3.5), we know that the shape derivative of the signed distance function at the offset point x_m will be equal to that of its projection point on the boundary $x_{m|\Omega}$, for which we can use an explicit formula

$$d'_{\Omega}(x_m)(\theta) = d'_{\Omega}(x_{m|\Omega})(\theta) = -\theta(x_{m|\Omega}) \cdot n(x_{m|\Omega}). \quad (3.18)$$

Using the fact that

$$n(x) = \frac{\nabla d_{\Omega}(x)}{|\nabla d_{\Omega}(x)|} = \nabla d_{\Omega}(x), \quad \forall x \in \partial\Omega$$

and substituting equation (3.18) in (3.17) yields the desired result. \square

The same exactly analysis holds for the quadratic penalty function used in the Minimum Members' Distance.

Remark 3.4.3. In Figure 3.6 we see for a point $x \in \partial\Omega$ its offset point in the direction $-n(x)$ at a distance $d_{off}(x_m)$ and the projection point of x_m on the boundary ($x_{m|\Omega}$). We shall observe that if $x_m \in \text{ray}_{\partial\Omega} \cap \Omega$, i.e. if x_m lies on the ray connecting the point x with its corresponding point on the skeleton of the shape, then $x \equiv x_{m|\Omega}$.

3.5 Augmented Lagrangian method and descent direction

Several efficient optimization algorithms have been applied in topology optimization, e.g. MMA [138], MFD [169], etc... For most of them, one needs to set the optimization parameters of the problem. As we have mentioned in section 3.2.4, several choices exist when a level-set description of the shape is used. In this work, we have preferred to avoid the use of optimization parameters and consider instead the whole shape as the optimization variable. We apply a simple augmented Lagrangian method to impose the geometric constraints. According to the approach described in [101], for a problem with m equality constraints of the form

$$P_i(\Omega) = 0 \quad (i = 1, \dots, m),$$

an augmented Lagrangian function is constructed as

$$L(\Omega, \ell, \mu) = J(\Omega) - \sum_{i=1}^m \ell_i P_i(\Omega) + \sum_{i=1}^m \frac{\mu_i}{2} P_i^2(\Omega), \quad (3.19)$$

where $J(\Omega)$ is the cost function, $\ell = (\ell_i)_{i=1, \dots, m}$ and $\mu = (\mu_i)_{i=1, \dots, m}$ are Lagrange multipliers and penalty parameters used to enforce the constraints at convergence. The Lagrange multipliers are updated at each iteration n according to the relation $\ell_i^{n+1} = \ell_i^n - \mu_i P_i(\Omega_n)$ (see [101] for more details). We also increase the penalty parameters every 5 iterations. A similar approach is followed for the case of inequality constraints (see [101]).

The shape derivative of the augmented Lagrangian function (3.19) reads:

$$L'(\Omega, \ell, \mu)(\theta) = J'(\Omega)(\theta) - \sum_{i=1}^m \ell_i P'_i(\Omega)(\theta) + \sum_{i=1}^m \mu_i P_i(\Omega) P'_i(\Omega)(\theta).$$

For example, for the optimization problem

$$\begin{aligned} \min_{\Omega \in \mathcal{U}_{ad}} \quad & J(\Omega) = \int_{\Omega} f \cdot u \, dx + \int_{\Gamma_N} g \cdot u \, ds, \\ \text{s.t.} \quad & P_1(\Omega) = \int_{\Omega} dx - \alpha_V |D| = 0, \quad (0 < \alpha_V < 1), \\ & P_2(\Omega) = P_{MaxT}(\Omega) = \int_{\Omega} \left[(d_{\Omega}(x) + d_{max}/2)^- \right]^2 dx = 0, \end{aligned} \quad (3.20)$$

where u is the solution of (1.12), we construct the augmented Lagrangian function

$$L(\Omega, \ell, \mu) = \int_{\Omega} f \cdot u \, dx + \int_{\Gamma_N} g \cdot u \, ds - \sum_{i=1}^2 \ell_i P_i(\Omega)(\theta) + \sum_{i=1}^2 \frac{\mu_i}{2} P_i^2(\Omega), \quad (3.21)$$

which can now be regarded as the new objective function to minimize.

The method of C ea can be used for the calculation of its shape derivative, which finally reads

$$L'(\Omega, \ell, \mu)(\theta) = \int_{\Gamma} \theta(x) \cdot n(x) (-Ae(u) e(u)) \, dx - \sum_{i=1}^2 \ell_i P'_i(\Omega)(\theta) + \sum_{i=1}^2 \mu_i P_i(\Omega) P'_i(\Omega)(\theta),$$

where Γ is the optimizable part of the boundary,

$$P'_1(\Omega)(\theta) = \int_{\Gamma} \theta(x) \cdot n(x) \, dx$$

and

$$P'_2(\Omega)(\theta) = - \int_{\Gamma} \theta(x) \cdot n(x) \left(\int_{\text{ray}_{\partial\Omega}(x) \cap \Omega} 2(d_{\Omega}(z) + d_{max}/2)^- \prod_{i=1}^{N-1} (1 - z\kappa_i(x)) \, dz \right) dx.$$

Denoting

$$g(x) = \int_{\text{ray}_{\partial\Omega}(x) \cap \Omega} 2(d_{\Omega}(z) + d_{max}/2)^- \prod_{i=1}^{N-1} (1 - z\kappa_i(x)) \, dz,$$

a descent direction is revealed as

$$\theta(x) = -n(x) (-Ae(u) : e(u) - \ell_1 + \mu_1 P_1(\Omega) + \ell_2 g(x) - \mu_2 P_2(\Omega) g(x)).$$

In the cases of Minimum Thickness and Minimum Members' Distance, things are a bit more complicated. The reason lies in the second integral of the shape derivative in (3.16):

$$\int_{\partial\Omega} \int_0^{d_{min}} \theta(x_{m|\Omega}) \cdot n(x_{m|\Omega}) 2 \left(d_\Omega(x_m)^+ \right) d\xi dx.$$

The vector field θ may be evaluated at a point $x_{m|\Omega} \neq x$ (see Figure 3.6) and a descent direction is not anymore obvious. However, the formula for $J'(\Omega)(\theta)$ still remains a linear form in θ . Using Riesz's representation theorem we can identify this linear form under another scalar product, e.g. H^1 , as we explain below. In this way, we manage to obtain a descent direction, while at the same time we regularize our velocity field [14, 47].

We now explain on an example how to use formula (3.16) for deducing a descent direction. To simplify a bit things, we use the fact that only the normal component of the velocity field θ is of interest, in good agreement with Hadamard's structure theorem (see section 1.3.1). Thus, we can write $\theta(x) = w(x)n(x)$, where $w(x)$ is a smooth enough scalar field and $n(x)$ is the unit normal vector field, suitably extended to the whole computational domain D . Then, for the optimization problem

$$\begin{aligned} \min_{\Omega \in \mathcal{U}_{ad}} \quad & J(\Omega) = \int_{\Omega} f \cdot u \, dx + \int_{\Gamma_N} g \cdot u \, ds, \\ \text{s.t.} \quad & P_1(\Omega) = \int_{\Omega} dx - \alpha_V |D| = 0, \quad (0 < \alpha_V < 1), \\ & P_2(\Omega) = P_{MinT}(\Omega) = \int_{\partial\Omega} \int_0^{d_{min}} \left[(d_\Omega(x_m))^+ \right]^2 d\xi dx, \end{aligned} \quad (3.22)$$

the shape derivative of the augmented Lagrangian function (3.21) reads

$$L'(\Omega, \ell, \mu)(wn) = \int_{\Gamma} w(x) (-Ae(u) : e(u) - \ell_1 + \mu_1 P_1(\Omega)) \, dx - \ell_2 P_2'(\Omega)(wn) + \mu_2 P_2(\Omega) P_2'(\Omega)(wn),$$

where

$$\begin{aligned} P_2'(\Omega)(wn) = & \int_{\Gamma} \int_0^{d_{min}} w(x) \left[H \left((d_\Omega(x_m))^+ \right)^2 + 2 (d_\Omega(x_m))^+ \nabla d_\Omega(x_m) \cdot \nabla d_\Omega(x) \right] d\xi dx \\ & - \int_{\Gamma} \int_0^{d_{min}} w(x_{m|\Omega}) 2 (d_\Omega(x_m))^+ d\xi dx. \end{aligned}$$

Solving instead the equation

$$\int_D (\alpha_{reg}^2 \nabla Q \cdot \nabla v + Qv) \, dx = L'(\Omega, \ell, \mu)(vn) \quad \forall v \in H^1(D), \quad (3.23)$$

where $\alpha_{reg} > 0$ is a positive scalar (of the order of the mesh size) to control the regularization width and choosing $w = -Q$, we find

$$L'(\Omega, \ell, \mu)(wn) = - \int_D (\alpha_{reg}^2 |\nabla Q|^2 + Q^2) \, dx \leq 0,$$

which guarantees again a descent direction for L .

3.6 Numerical implementation

In this section, we highlight some of the difficulties one may face when trying to implement the above methods and the solutions we have chosen for our numerical examples.

3.6.1 Construction of d_Ω

We shall highlight the fact that the level-set function ψ , used for the description and advection of the shape, even if it is reinitialized to be a signed distance function, does not necessarily contain the correct information for the thickness of the structure. The signed distance function d_Ω , that we use for the formulation of the constraints, refers to the actual shape. In order to construct this function, we take the initial one, set $\psi = 0$ at the points of the shape intersecting with the boundary of the working domain D (see Figure 3.7) and reinitialize this new level-set function. In Figure 3.8 we show the difference between the signed distance function constructed from the level-set function used for the advection of the shape and the one used for the penalty functional. The values of the level-set function not being zero at $\Omega \cap \partial D$ in the first one, we get completely wrong results for the thickness at these areas.

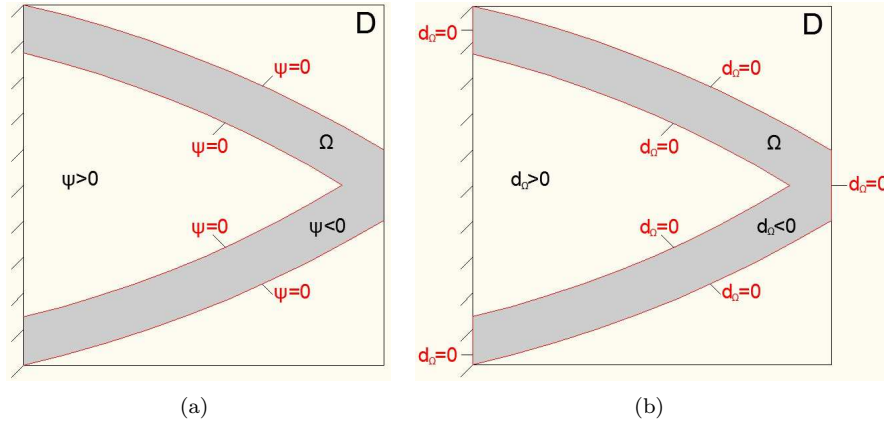


Figure 3.7: (a): level-set function ψ used for the advection of the shape; (b): signed distance function d_Ω .

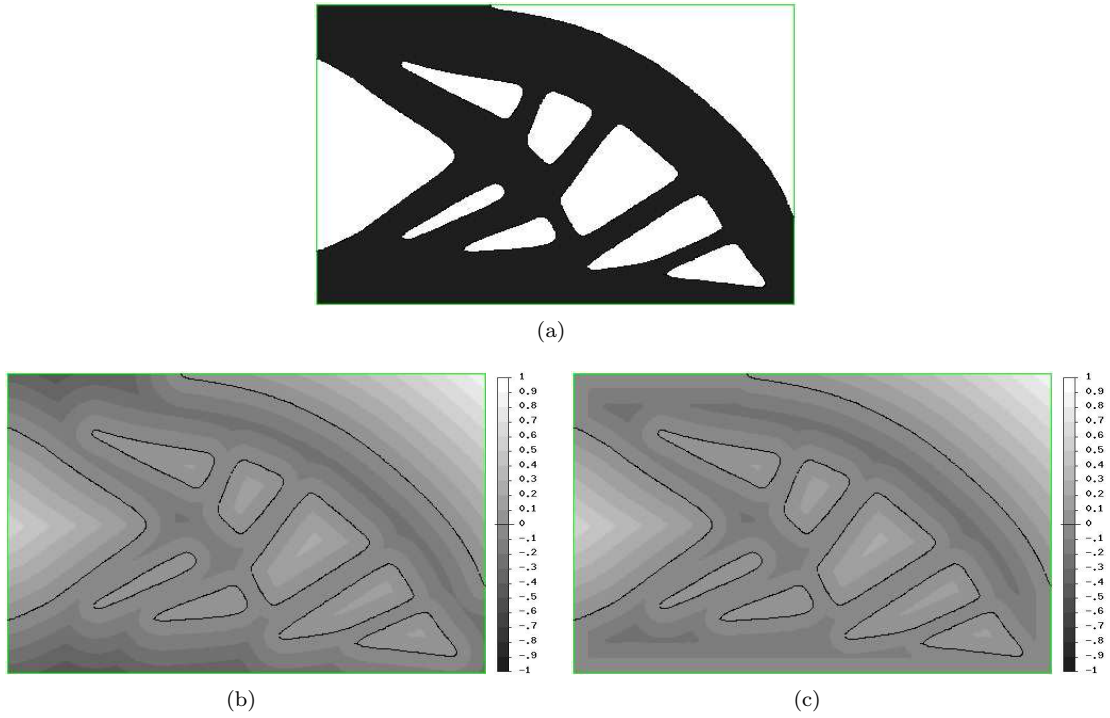
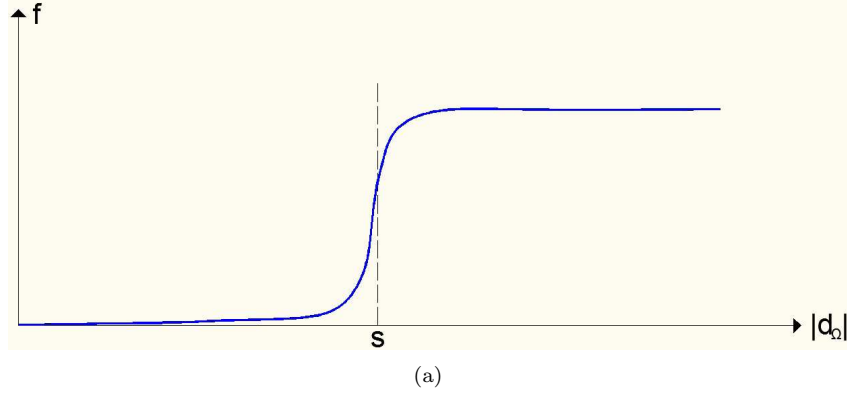


Figure 3.8: (a): shape in black (Ω); (b): iso-contours of the level-set function ψ for the advection of the shape; (c): iso-contours of d_Ω .

Figure 3.9: Graph of the regularization function $f(d_\Omega(x))$.

3.6.2 Maximum thickness

1. A first difficulty in the calculation of the shape derivative for the maximum thickness functional $P_{MaxT}(\Omega)$ comes from the identification of the skeleton. As we can see in equation (3.13), for every point on the boundary of the shape we need to travel along its emerging ray up to the skeleton. First, we consider as points of the boundary the nodes of the elements of the mesh that are cut by the zero level-set. Then, we start moving from each of these points in the direction opposite to the normal and we check the monotonicity of the signed distance function. Once the monotonicity changes, we say that we have detected its corresponding point on the skeleton.
2. In section 3.2.1, the pointwise constraint (3.2) has been replaced by the global penalty functional (3.12), so that the pointwise constraint is satisfied everywhere when $P(\Omega) = 0$. Although this formulation is very convenient in order to explain all theoretical aspects regarding the shape differentiation, it is not that effective from a numerical point of view. It would be preferable, if possible, to maintain the constraint in an inequality form, while keeping a global formulation at the same time. Moreover, the penalty functional (3.12) is "strict", in the sense that it is prone to create artifacts like the one depicted in Figure 3.1 for joints at bars crossing. Thus we would like to loosen somehow the constraint in order to get more regular shapes. The formulation that we have used for our numerical examples is

$$P_{MaxT}(d_\Omega) = \left(\frac{\int_\Omega f(d_\Omega(x)) d_\Omega(x)^2 dx}{\int_\Omega f(d_\Omega(x)) dx} \right)^{\frac{1}{2}} \leq d_{max}/2, \quad (3.24)$$

where

$$f(d_\Omega(x)) = 0.5 \left(1 + \tanh \left(\frac{|d_\Omega(x)| - (d_{max}/2)}{\alpha_f(d_{max}/2)} \right) \right),$$

$\alpha_f > 0$ being a parameter that controls the regularization of the constraint. When $\alpha_f \rightarrow 0$ then $f(d_\Omega) \rightarrow H(|d_\Omega| - (d_{max}/2))$, the Heaviside function at point $(d_{max}/2)$ (see Figure 3.9).

3. From Lemma 3.3.9 we see that the term $\prod_{i=1}^{N-1} (1 + d_\Omega(z) \kappa_i(x))$ in the shape derivative is always positive. Since the calculation of the curvature is not so accurate, especially when a fixed mesh is used, this term can be omitted without changing the descent nature of the shape derivative, since the term

$$(d_\Omega(\cdot) + d_{max}/2)^-$$

in the integrand is also of constant sign. Moreover, neglecting this term will have no influence for "straight" boundaries, where $k_i(x) \equiv 0$, while the shape derivative will be overestimated if $k_i(x) \geq 0$ and underestimated if $k_i(x) \leq 0$, helping to avoid distortions at these regions.

3.6.3 Minimum thickness and minimum members' distance

1. At this point let us emphasize that, by using the penalty functionals $P_{MinT}(\Omega)$ and $P_{MMD}(\Omega)$, it is the values of the signed distance function that we penalize and not the actual thickness of a

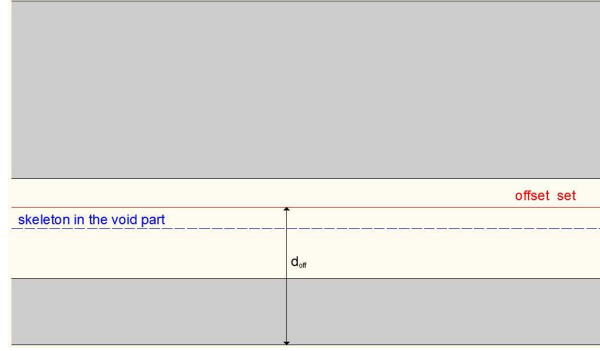


Figure 3.10: Crossing of the skeleton formed in the void part.

member, the latter being defined as the distance from a point $x \in \partial\Omega$ up to the next point on $\partial\Omega$ along the ray starting from x and in the direction of $-n(x)$. Since the constraint is by essence non local, this means that the derivative at a point will depend on the values of $d_\Omega(x)$ along the offset set. As a consequence, one can observe a significant difference in the velocity between points of equal thickness.

Another strange effect is the movement of points that do not violate the constraint! For instance, Figure 3.10 displays an offset set crossing the skeleton formed between two bars. In this case, one part of the shape derivative is set on the projection of the offset set on the boundary and thus the second bar is also affected due to the thickness violation of the first bar.

One possible choice to reduce the importance of the above observations is to apply a continuation method and increase progressively the offset distance up to the value d_{min} (we have not implemented this strategy in this work).

2. Another difficulty appears when some part of the offset set lies outside the working domain D , i.e. when we need to impose boundary conditions for $d_\Omega(x)$. Suppose that we start from a point $x \in \partial\Omega$ and start moving in the direction $-n(x)$ up to the offset set (see Figure 3.11). Once we cross the boundary of the working domain ∂D , we need to account for the boundary conditions of d_Ω . In case we have symmetry conditions, we just have to change the sign of some component of the normal vector and to continue moving in the new direction, i.e. the boundary acts like a mirror. Else, if the whole shape is included in the working domain D , one possibility is to consider that it is surrounded by void. If we wanted to use the actual values of $d_\Omega(x)$, then we would need to have a zone of non-optimizable weak material of thickness at least d_{min} around the domain D . A simplification, in order to avoid technical difficulties, is to use instead the Euclidean distance between the offset point x_m and the point where the line crosses ∂D , denoted x_D . Then, we approximate the value of $d_\Omega(x_m)$ by

$$d_\Omega(x_m) = d_\Omega(x_D) + \text{dist}(x_m, x_D),$$

where $\text{dist}(\cdot, \cdot)$ stands for the usual euclidean distance between two points, which is also our method of choice hereafter.

3.7 Numerical examples

All the examples of this chapter have been coded in the finite element software SYSTUS of ESI-Group [140]. A cartesian mesh has been used both for solving the elasticity system and as a support for the level-set function describing the shape. For the elasticity analysis, we have used Q1 finite elements. The Young modulus of the elastic material E is normalized to 1 and the Poisson ratio ν is set to 0.3. The "ersatz material" is considered to have the same Poisson ratio, while its Young modulus is set to 10^{-3} .

3.7.1 Maximum thickness

2d arch

The first example is a two-dimensional arch-like structure, clamped at its lower left and right corners and with a unitary force applied at the middle of its lower part (see Figure 3.12). Due to symmetry, only half

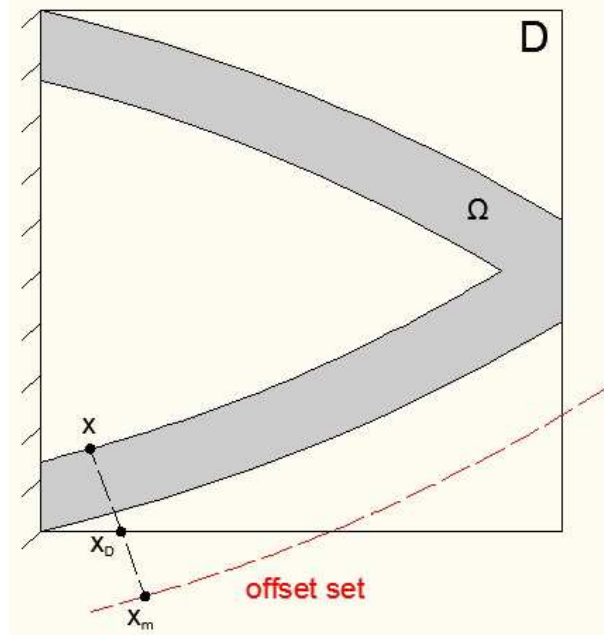


Figure 3.11: Offset set crossing the boundary of the working domain ∂D .

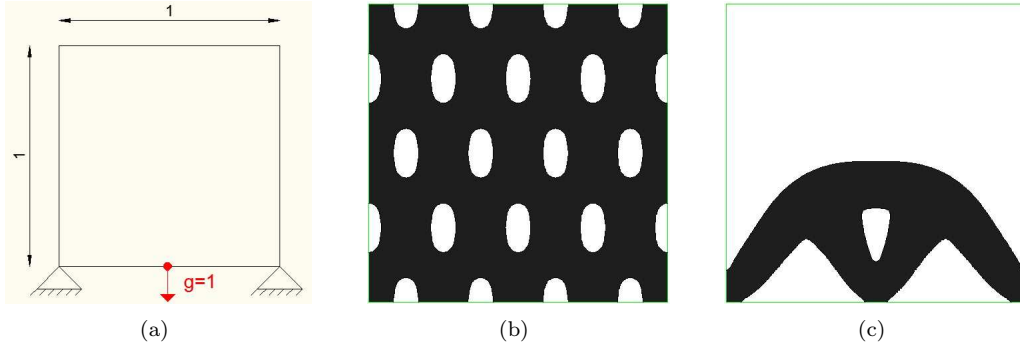


Figure 3.12: (a): Boundary conditions; (b): initialization; (c): optimized shape for the optimization problem (3.25), for the 2d arch.

of the domain is used and it is discretized by 80×160 elements. As a first step we solve the optimization problem

$$\begin{aligned} \min_{\Omega \in \mathcal{U}_{ad}} \quad & \int_{\Omega} dx \\ \text{s.t.} \quad & \int_{\partial\Omega} g \cdot u ds \leq g_{max}^1, \end{aligned} \quad (3.25)$$

where u is the solution of (1.34) and $g_{max}^1 = 5$. The initialization and the optimized shape are shown in Figure 3.12.

We suppose now that this optimized shape violates a constraint of maximum thickness. A first idea to treat this problem is to impose the constraint in a second step, i.e. after that the shape has been optimized without imposing any thickness restriction. Then, the optimized structure of Figure 3.12 serves as an initial guess for the optimization problem

$$\begin{aligned} \min_{\Omega \in \mathcal{U}_{ad}} \quad & \int_{\Omega} dx \\ \text{s.t.} \quad & \int_{\partial\Omega} g \cdot u ds \leq g_{max}^1, \\ & P_{MaxT}(\Omega) \leq g_{max}^2, \end{aligned} \quad (3.26)$$

where $g_{max}^1 = 5$, $g_{max}^2 = d_{max}/2$ and $P_{MaxT}(\Omega)$ is given by (3.24). In Figure 3.13 we can see the thickness violation $((|d_{\Omega}(x) - d_{max}/2|)^-)$ in the initial shape, the function $f(d_{\Omega}(x))$ and the shape gradient due to

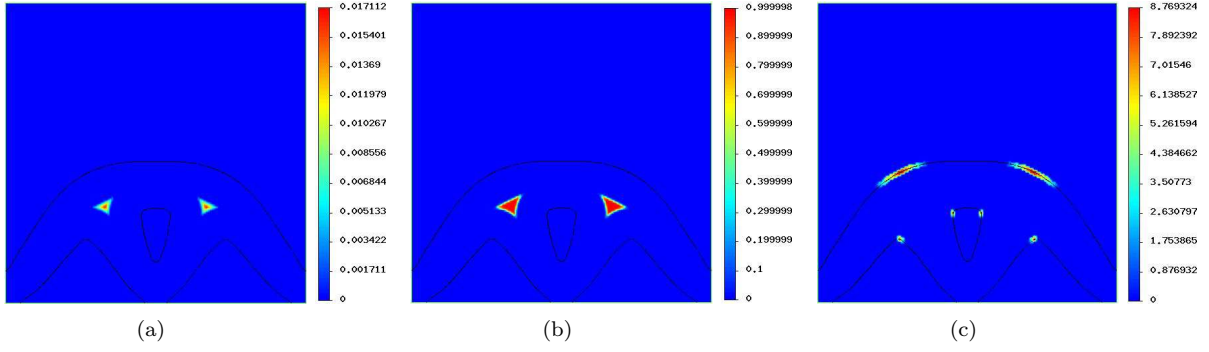


Figure 3.13: 2d arch; (a): $|(d_\Omega(x) - d_{max}/2)|$; (b): $f(d_\Omega(x))$; (c): shape gradient of $P_{MaxT}(\Omega)$, for the initial shape of problem (3.26) and $d_{max} = 0.2$.

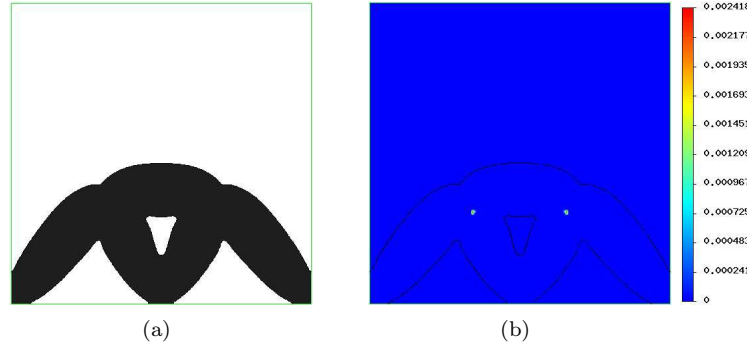


Figure 3.14: 2d arch; (a): optimized shape; (b): $|(d_\Omega(x) - d_{max}/2)|$, for the problem (3.26) and $d_{max} = 0.2$.

the maximum thickness constraint for $d_{max} = 0.2$. The optimized shape and the final thickness violation are depicted in Figure 3.14. We shall be satisfied with a thickness violation of the order of the mesh size, since this is the order of accuracy for the computation of the signed distance function. One can observe that the optimized shape contains some significantly curved regions, which serve to tackle the thickness constraint, while the size of regions that are far from violating the constraint has been augmented in order to satisfy the compliance constraint. The volume of the optimized shape has augmented from 0.1354 to 0.1384.

The idea of imposing the maximum thickness constraint in a second step is quite natural, however it presents several drawbacks. First of all, especially in 2d, the initially optimized shape usually has a much simpler topology compared to its initialization. Therefore, the algorithm will try to satisfy the constraint under much less freedom, as far as the formation of the topology is concerned, compared to the case when the constraint is applied since the beginning of the optimization process. Besides, it is highly possible that starting from a shape with reduced topology, a solution to the problem (3.26) does not exist, or at least the optimization algorithm does not find a feasible solution. This is the case, for example, when problem (3.26) is solved for $d_{max} = 0.16$ and the previous strategy is followed.

Therefore, it seems natural to apply the maximum thickness constraint since the beginning and hope that starting with a complicated enough topology, the algorithm will arrive at finding a feasible shape. Starting with the initialization of Figure 3.12, we show in Figure 3.15 the results for such a case. We can see in fact that the final topology is more complicated. The existence of many holes at the time the thickness constraint is applied, endows the algorithm with more flexibility in finding a feasible shape.

Although the optimized shape of Figure 3.15 is feasible, one could argue that distortions still appear close to joints. We emphasize that such distortions are natural when shape optimization is applied for reducing the thickness of continuous structures (see section 3.2). However, it could be interesting to test if they can be avoided (up to some extent) by using some easy heuristics. In order to test two such proposals, we have considered two bars of size 0.2, which cross each other at their middle. Contrary to the situation depicted in Figure 3.1, the intersection of the bars with the design domain is considered to belong to the boundary of the shape $\partial\Omega$. The reason for this choice, is that we expect distortions to

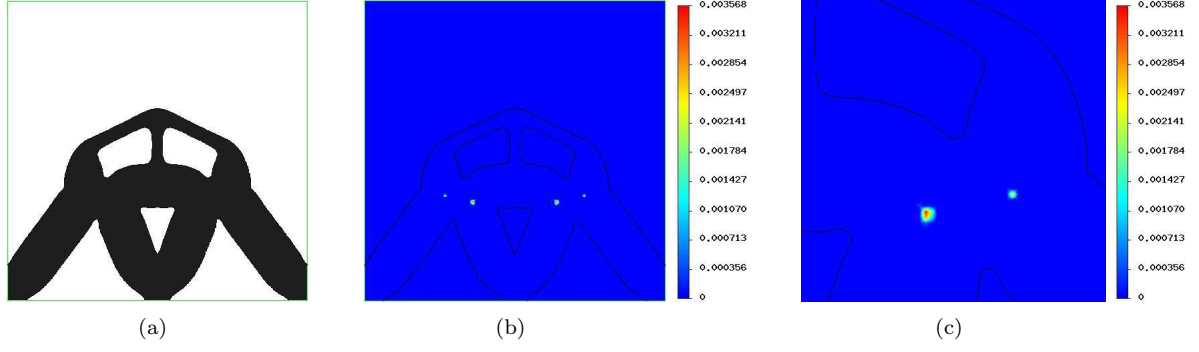


Figure 3.15: 2d arch; (a): optimized shape; (b): $|d_\Omega(x) - d_{max}/2|$; (c): zoom close to the thickness violation area, for the problem (3.26) and $d_{max} = 0.16$.

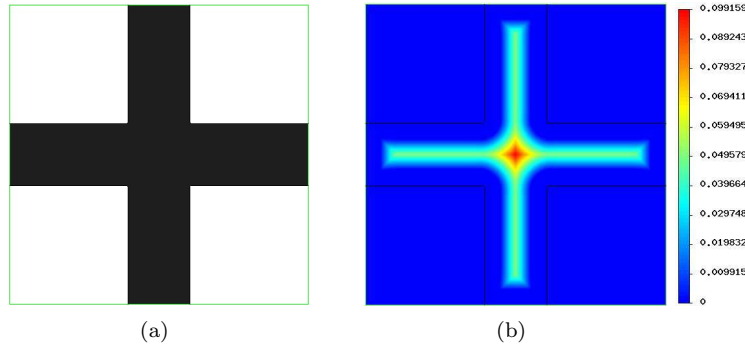


Figure 3.16: (a): initialization; (b): $|d_\Omega(x) - d_{max}/2|$, for $d_{max} = 0.10$.

appear close to regions of joints and close to parts that lie near to the boundary of the design domain. The initial thickness violation for $d_{max} = 0.10$ is shown in Figure 3.16. The penalty functional (3.12) is considered as objective function. The optimized shape and the initial shape gradient are shown in Figure 3.17. Another important observation is that, even when we neglect the Jacobian term in the expression (3.13), the shape gradient at the corners is much higher than in the nearby regions, since its ray travels up to the center of the joint. In case we had included the Jacobian term, the shape gradient in the flat regions would have been unchanged, since the curvature there is almost zero, but its value close to the curved corners would have been even higher.

A first idea would be to truncate the shape gradient deriving from the maximum thickness constraint for regions of high curvature. If $V_{P_{max}T}$ denotes this shape gradient, then we need to consider instead

$$V_{P_{max}T}^* = \begin{cases} V_{P_{max}T}, & \text{if } |k(x)| \leq k_{max}, \\ 0, & \text{if } |k(x)| > k_{max}, \end{cases}$$

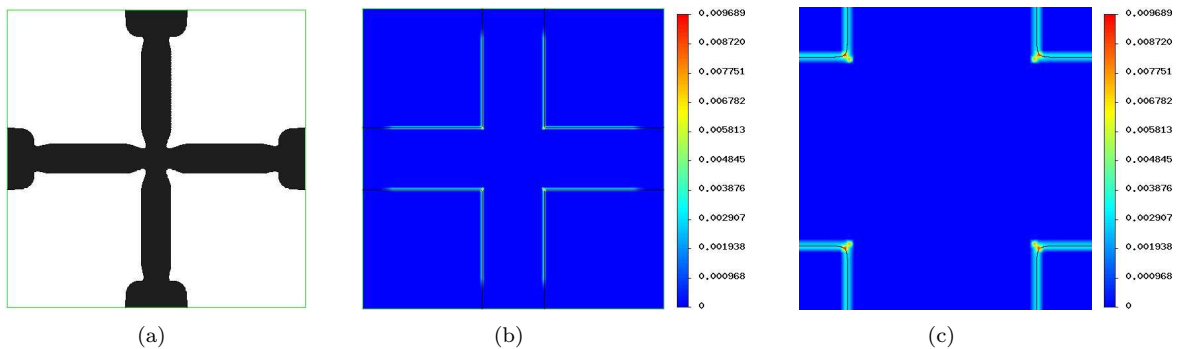


Figure 3.17: (a): optimized shape; (b): shape gradient; (c): zoom around the joint, for $d_{max} = 0.10$.

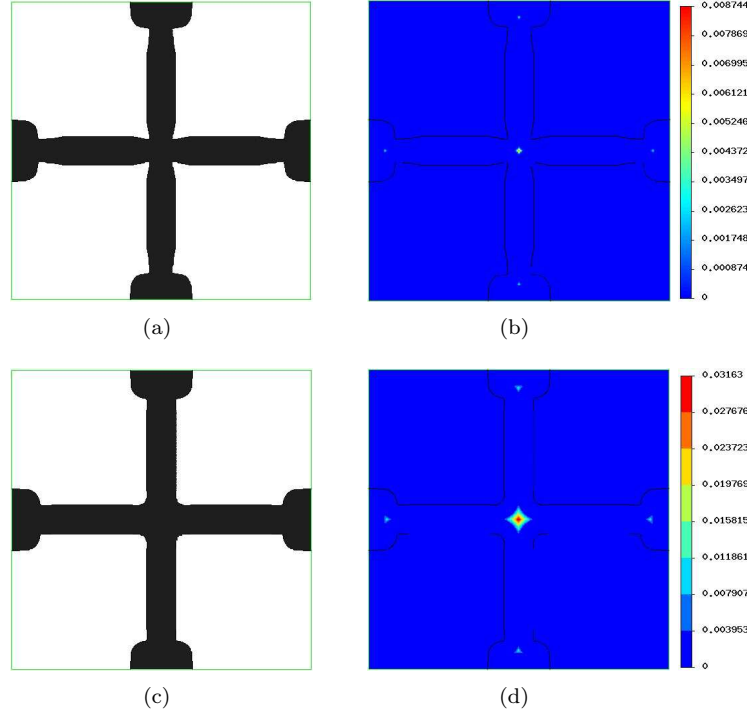


Figure 3.18: (a): optimized shape; (b): $|(d_\Omega(x) - d_{max}/2)^-|$, for $k_{max} = 100$; (c): optimized shape; (d): $|(d_\Omega(x) - d_{max}/2)^-|$, for $k_{max} = 20$.

where k stands for the mean curvature in 2d and the maximum principal curvature in 3d. In Figure 3.18 we show the results obtained with this method, using two different values for k_{max} . As k_{max} reduces, larger areas are constrained to move and the optimized shape is expected to be smoother. However, it is highly probable that the area where the constraint is not satisfied will increase. Our numerical experience has shown that it is very unlikely to control efficiently these areas and one can result with shapes containing thick parts.

Volumetric approach

We now present another heuristic method that gives very promising numerical results. Starting from the shape derivative (3.14), we would like to substitute $d'_\Omega(\theta)(x)$ with an explicit expression defined in the whole domain Ω . However, such an expression exists only for the points on the boundary $\partial\Omega$ (see equation (3.5)). At a first step, we extend the expression of $d'_\Omega(\theta)(x)$ on $\partial\Omega$ to the whole domain Ω , i.e. we consider the approximation $d'_\Omega(\theta)(x) \approx -\theta(x) \cdot n(x) = -w(x), \forall x \in \Omega$, where an extension of the vector field θ and the exterior normal n to the whole domain has been assumed. Then, the approximation of the shape derivative of $P_{MaxT}(\Omega)$ reads

$$P'_{MaxT}(\Omega)(\theta) \approx - \int_{\Omega} 2w(x) (d_\Omega(x) + d_{max}/2)^- dx. \quad (3.27)$$

Formula (3.27) does not verify the Hadamard structure theorem (see section 1.3.1), since the choice

$$w(x) = +2 (d_\Omega(x) + d_{max}/2)^-, \quad \forall x \in \Omega,$$

gives a zero velocity for the points $x \in \partial\Omega$. However, this approximation of the shape derivative could be put as a right-hand side in the regularization equation (1.37), which would define another velocity with non-zero values on $\partial\Omega$. The regularization parameter α_{reg} should be adjusted accordingly, so that the values of the new velocity field are not too small on $\partial\Omega$. For our numerical examples, we have set

$$\alpha_{reg} = \left(2 \frac{\max_{\Omega} |d_\Omega(x)|}{\Delta x} \right) (\Delta x)^2,$$

for this type of regularization, where Δx is the uniform mesh size.

Let us try to explain intuitively this heuristic choice. The term $2 (d_\Omega(x) + d_{max}/2)^-$ is non-zero only

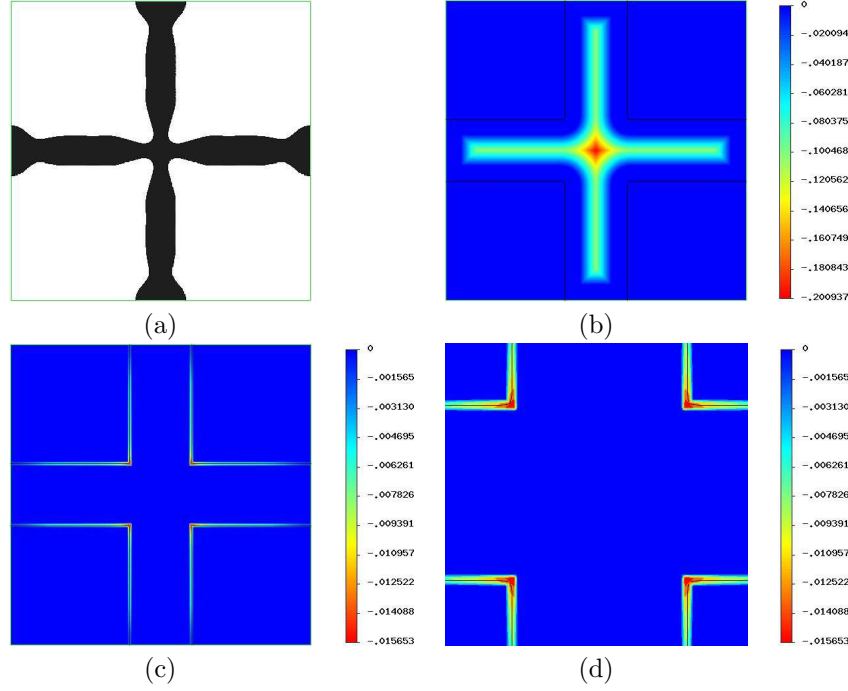


Figure 3.19: (a): optimized shape; (b): $2(d_{\Omega}(x) + d_{max}/2)^-$ before regularization; (c): values on $\partial\Omega$ after regularization; (d): zoom close to the joint, for $d_{max} = 0.10$.

at regions violating the thickness constraint. Using the mathematically correct coarea transformation, this term influences significantly the highly curved parts. When the above approximation is used, the curvature information is not used. Instead what matters is the distance of the boundary to the area of thickness violation.

What is also important is that the direction of the velocity field will not change at any point, i.e. the final velocity field will always tend to reduce the thickness everywhere and thus it is a descent direction. In Figure 3.19 we plot the results obtained with this method. Our numerical experience shows that this last method performs better than the rest presented in this chapter. We will call it the "volumetric" formula to distinguish it from the rigorous "coarea" formula. The "volumetric" formula has been used for most of the results below, unless otherwise specified.

In figures 3.20 and 3.21 we show the results of problem (3.26) for $g_{max}^1 = 5$ and for different values of $g_{max}^2 = d_{max}/2$. Although we expect in general that the volume of the optimal shape increases when the maximum thickness threshold decreases, this is not always true since plenty of local minima may exist. We also observe that when d_{max} is set to 0.12, the optimized shape contains curved members. As we have mentioned before, this situation could possibly be avoided by starting with a more complicated topology. In Figure 3.22 we see the optimized shapes for $d_{max} = 0.12$, starting from initializations with more holes. Of course, one could expect that starting from more complicated topologies, it could be possible to obtain optimal shapes that respect the thickness constraint without actually imposing that constraint. This can occasionally happen, but there is no guarantee in general. In Figure 3.23 we plot the results for the examples of Figure 3.22 without imposing a thickness constraint.

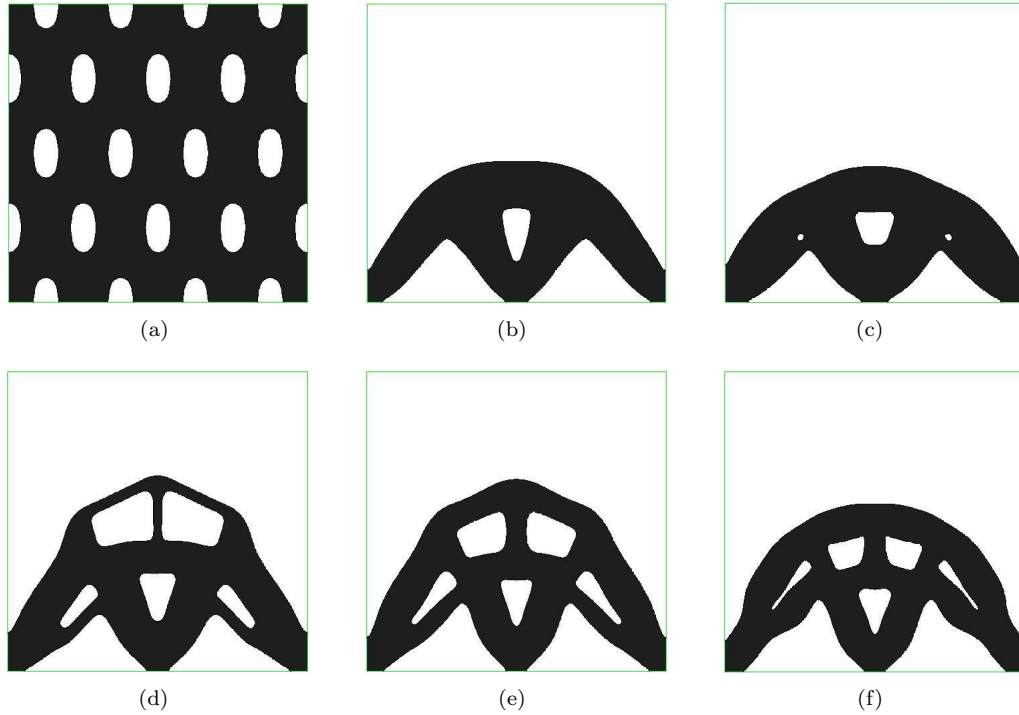


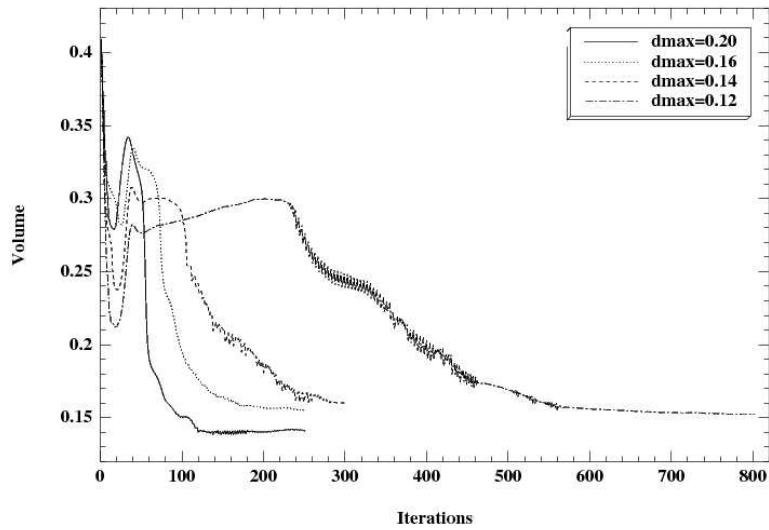
Figure 3.20: 2d arch; (a): initialization; optimized shapes (b): without thickness restriction; (c): for $d_{max} = 0.20$; (d): for $d_{max} = 0.16$; (e): for $d_{max} = 0.14$; (f): for $d_{max} = 0.12$, for the optimization problem (3.26).

Discussion on topological changes

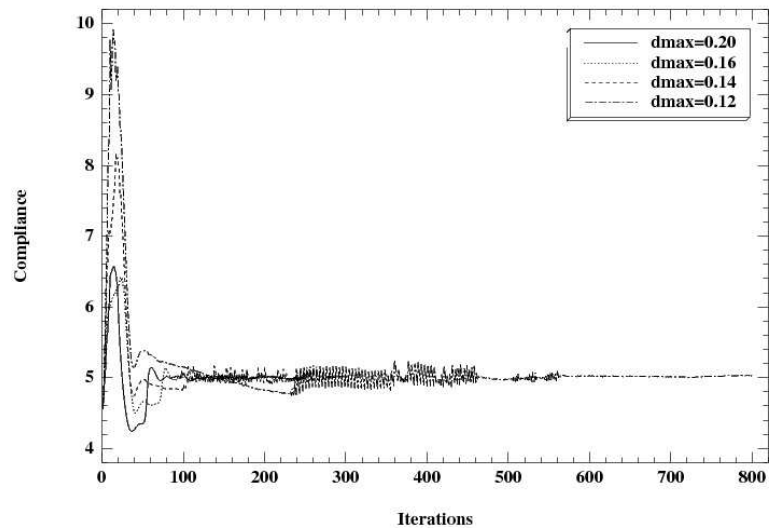
The optimized shape of Figure 3.22(b) urges to discuss a very important topic, with severe numerical implications for our method. We can see in this shape the existence of very small holes, the absence of which would result in a severe violation of the thickness constraint. The question that comes naturally in mind, is whether a solution of problem (3.26) could be obtained by perforating the optimized shape without the thickness constraint with infinitesimally small holes. This perforation would have an infinitesimal impact on the compliance and it would satisfy the maximum thickness constraint, in the way it has been mathematically formulated. However, from an engineering point of view, this would not be a satisfying solution both because the size of the holes would violate some tooling limitations and also because the "modulo" ratio used in casting (see Chapter 2) would remain unchanged. If one wants to avoid such tiny holes, one should impose at the same time a constraint on their size. Else, it is inevitable that such holes can appear in the optimized shape, since they are preferable for solving the problem (3.26).

There are two mechanisms for the appearance of such holes. The first one, which is the most usual, is the reduction in size of an existing hole. The second one is more tricky and consists in splitting an existing hole into two holes. This is the case for the shape in Figure 3.22(b). In Figure 3.24 we show how these holes were progressively created. At iteration 208 the top left and right holes have already got elongated in order to tackle the thickness constraint. Since this elongation is not sufficient, the edge needs to progress more towards the thick part of the structure, while a bit farther the boundary of the hole is more affected by the compliance and tends to close. At iteration 209 hole has started splitting in two and at iteration 210 we can clearly distinguish the appearance of the second hole. The great problem caused by the formation of such tiny holes is the impact of their disparition on the values of d_Ω and consequently those of $P_{MaxT}(\Omega)$. An infinitesimal change in the topology of the shape, e.g. the creation or disparition of a small hole, can change dramatically their values. This is because the signed distance function is topologically not derivable. Let us give an example in order to better understand this problem.

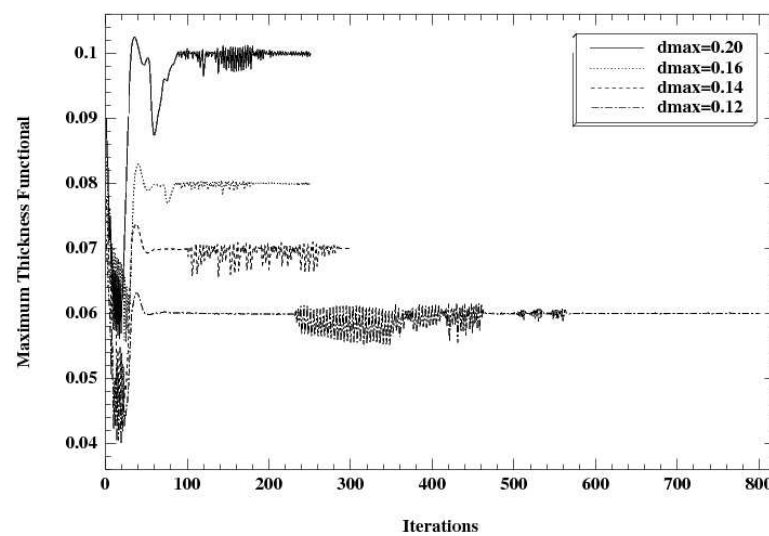
Consider two bars that cross each other, like in Figure 3.1, with a small hole in the middle of the joint. The bars have a uniform thickness of 0.2. Setting a constraint of maximum thickness with $d_{max} = 0.2$, we can see the great difference caused by the existence of a small hole in figures 3.25 and 3.26. The existence of the hole reduces significantly the values of d_Ω and as a result no violation of the thickness appears. On the contrary, the elimination of the hole changes dramatically the values of d_Ω and a region around



(a)



(b)



(c)

Figure 3.21: Convergence diagrams for (a): the volume; (b): the compliance; (c): the maximum thickness functional, for the results of Figure 3.20.

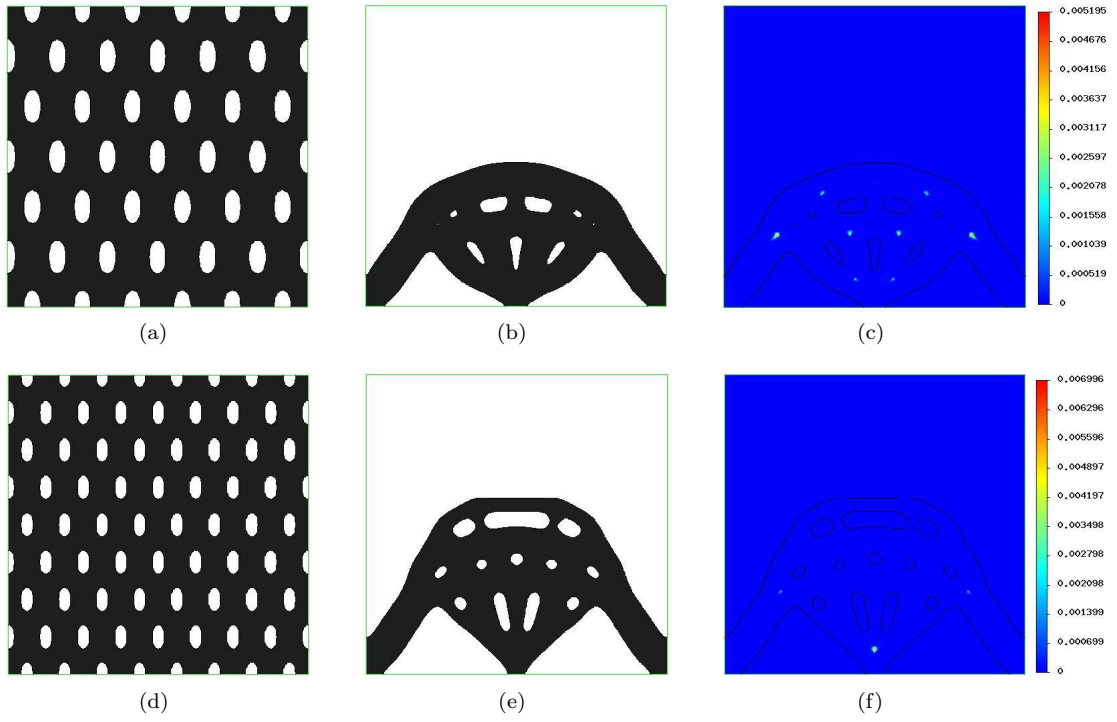


Figure 3.22: 2d arch; (a),(d): initialization; (b),(e): optimized shape for the optimization problem (3.26) and $d_{max} = 0.12$; (c),(f): $|(d_{\Omega}(x) - d_{max}/2)^-|$.

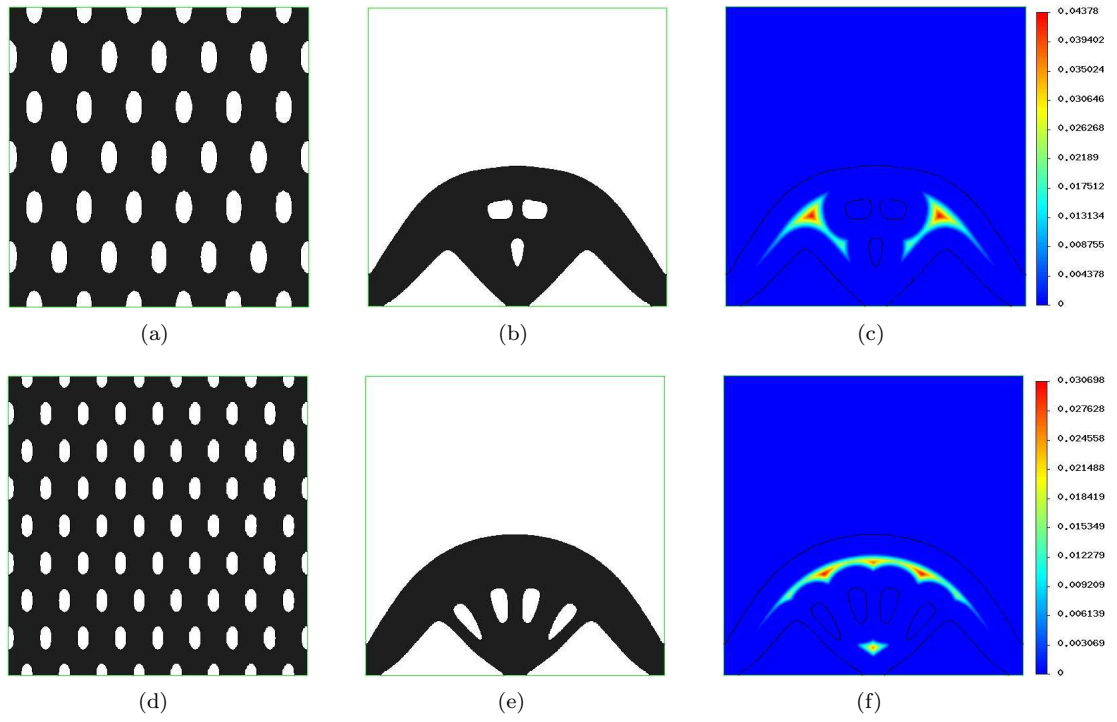


Figure 3.23: 2d arch; (a),(d): initialization; (b),(e): optimized shape for the optimization problem (3.25); (c),(f): $|(d_{\Omega}(x) - d_{max}/2)^-|$.

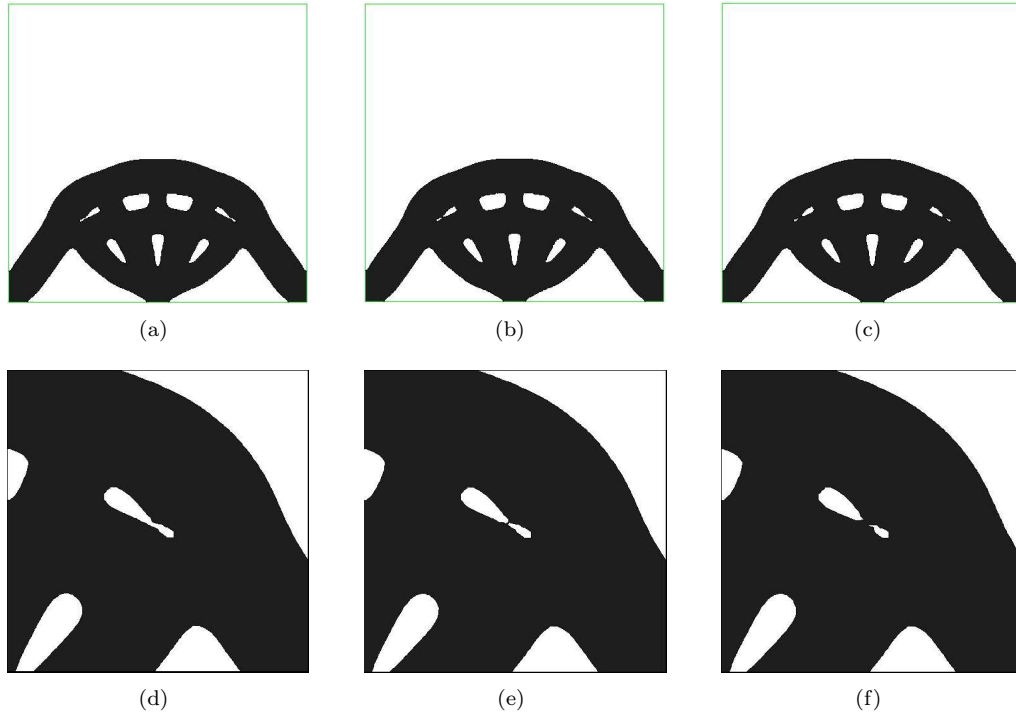


Figure 3.24: Iteration (a): 208; (b): 209; (c): 210, zoom close to the hole at iteration (d): 208; (e): 209; (f): 210.

the center of the joint appears, where the thickness constraint is violated. Finally, we discuss how this fact influences the optimization algorithm. Using an augmented Lagrangian algorithm and accepting every iteration, hoping to converge at last, seems to give satisfying results for the majority of cases. The reason is that even if some small holes disappear, the shape will continue changing until the thickness violation is hopefully treated. However, if d_{max} is set to a very low value compared to the size of the working domain, it is possible that the formation and disparition of holes under the mechanism described in Figure 3.24 does not terminate and thus the algorithm does not converge.

Another idea is to use an MFD (Method of Feasible Directions) algorithm (see [169]). The benefit is that the shape will remain always feasible. Thus, there is not really a problem of existence of a feasible solution for a certain topology, since we are sure that there is at least one such topology. However, using such a method makes it difficult to escape from the previously described situation of disparition of tiny holes. Consider once more the case of figures 3.25 and 3.26. Once the hole disappears, the shape is no more feasible and thus not accepted. But, on the other hand, calculating another descent direction that focuses more on the thickness constraint is unlikely to change the situation, since it is not evident from the shape derivative which part creates this problem.

One heuristic remedy could be the following. If a shape Ω is feasible for the maximum thickness constraint at iteration k (Ω^k) and unfeasible at iteration $k + 1$ (Ω^{k+1}), then:

1. Find the region of Ω^{k+1} where the violation appears.
2. Test if the values of d_Ω have rapidly changed at this region from iteration k to $k + 1$.
3. If so, check if there was some part of $\partial\Omega$ at this region which has disappeared from iteration k to $k + 1$.
4. Reject iteration $k + 1$, set the additional constraints $w(x) = \theta(x) \cdot n(x) > 0$ for all nodes belonging to this region and go back computing a descent direction with this additional requirement.

2d cantilever

The next example is a 3.2×2 cantilever, clamped at its left boundary and with a unitary force applied at its lower-right corner (see Figure 3.27) and discretized using 160×100 elements. In Figure 3.28 we plot the initial and the optimized shapes for problem (3.25) and $g_{max}^1 = 40$. In Figure 3.29 we plot the

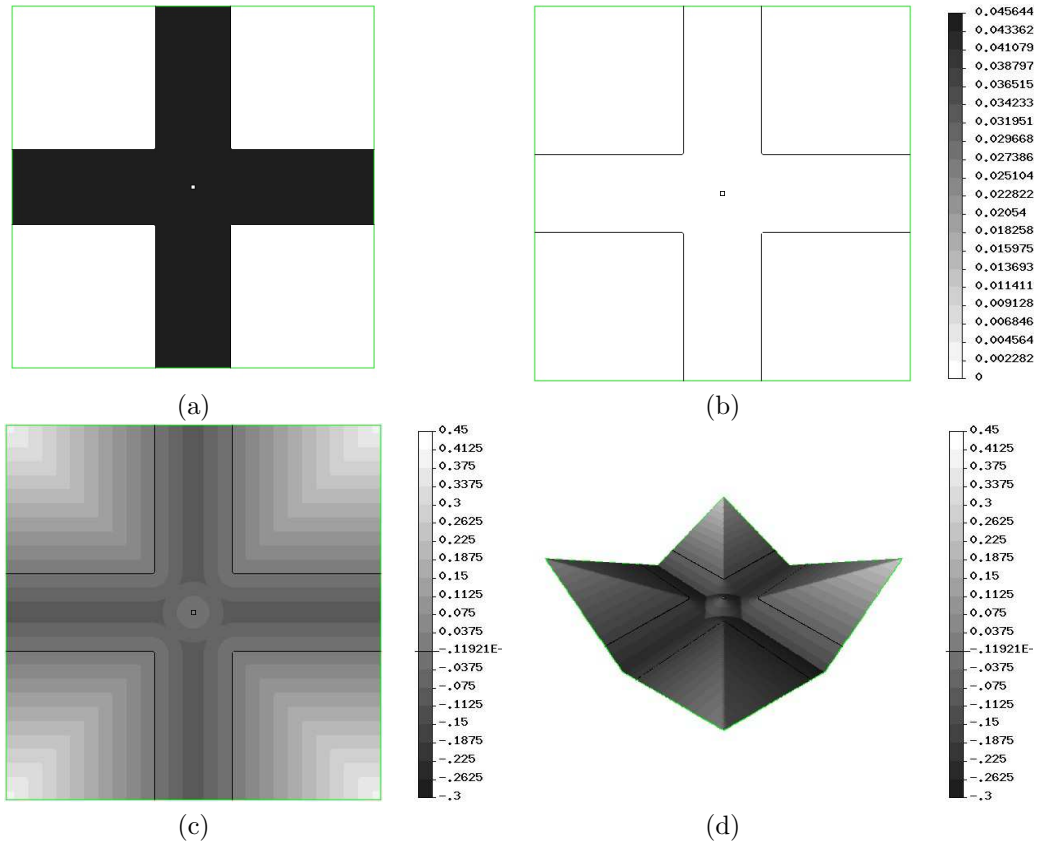


Figure 3.25: Joint with a hole in the middle (a): shape in black (Ω); (b): thickness violation; (c): 2d plot of d_Ω ; (d): 3d plot of d_Ω .

Table 3.1: Optimized 2d cantilever.

	Volume	Compliance	$P_{MaxT}(\Omega)$
Without thickness restriction	3.794	39.99	-
$d_{max} = 0.50$	3.783	39.97	0.250
$d_{max} = 0.40$	3.931	39.84	0.200
$d_{max} = 0.35$	4.204	39.95	0.176

optimized shapes and the violation of the thickness constraint for problem (3.26) and for different values of d_{max} . The same initialization as in Figure 3.28(a) has been used for all of the cases. The convergence diagrams and the final results are shown in Figure 3.30 and Table 3.1.

2d MBB beam

The last two-dimensional example for this type of constraint is the benchmark MBB beam. The dimensions of the enclosing box D are 6×1 and a unitary vertical load is applied at the middle of its top edge (see Figure 3.31). Due to symmetry, half of the domain is considered and is discretized by 240×80 elements. The initial and the optimized shapes for problem (3.25) and $g_{max}^1 = 40$ are shown at Figure 3.32. Using the same initialization, the optimized shapes and the violation of the thickness constraint for problem (3.26) and for different values of d_{max} are plotted in Figure 3.33. The convergence diagrams are shown in Figure 3.34 and the final results in Table 3.2.

3d cantilever

Our first 3d example is a $3.2 \times 2 \times 2$ cantilever, clamped at its left boundary and with a unit force applied at the middle of its lower-right side (see Figure 3.35). Due to symmetry, half of the domain is considered and is discretized using $20 \times 64 \times 40$ elements. The initial and optimized shapes for problem (3.25) and

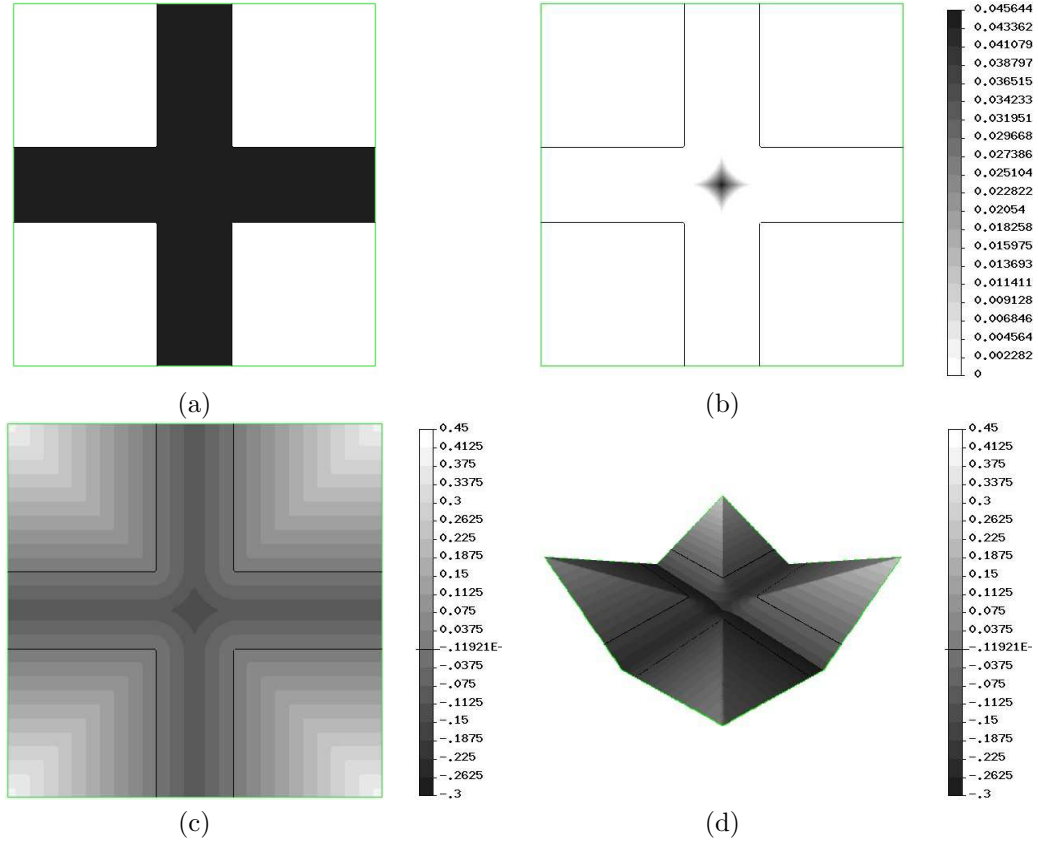


Figure 3.26: Joint without a hole in the middle (a): shape in black (Ω); (b): thickness violation; (c): 2d plot of d_Ω ; (d): 3d plot of d_Ω .

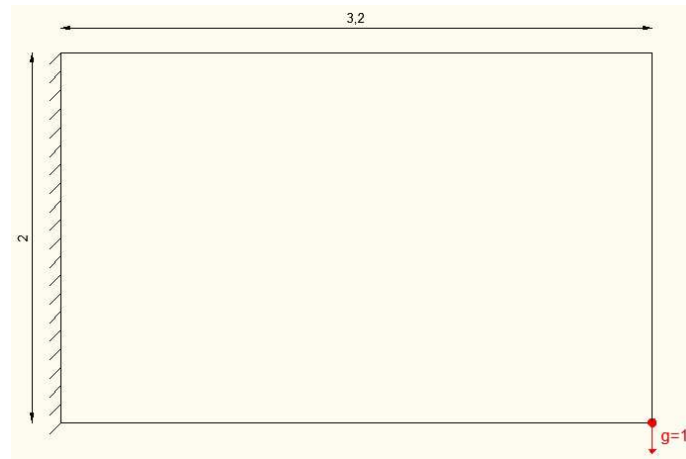


Figure 3.27: Boundary conditions for a 2d cantilever.

Table 3.2: Optimized 2d MBB beam.

	Volume	Compliance	$P_{MaxT}(\Omega)$
Without thickness restriction	1.881	39.99	-
$d_{max} = 0.30$	1.845	40.05	0.149
$d_{max} = 0.25$	1.900	39.89	0.125
$d_{max} = 0.20$	2.155	39.73	0.102

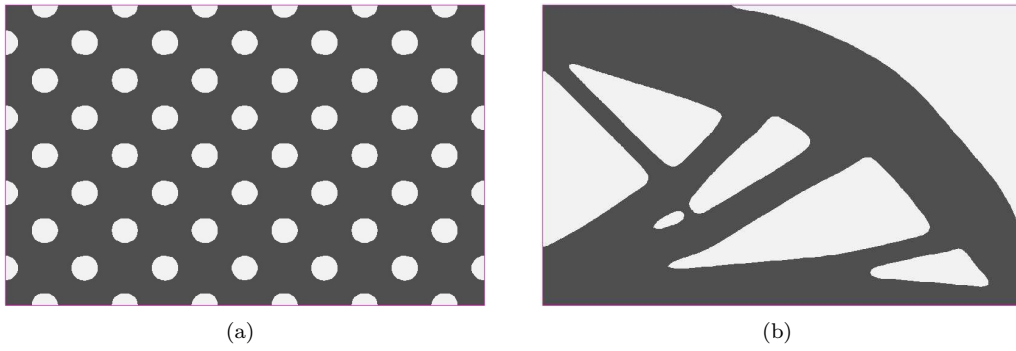


Figure 3.28: (a): Initialization; (b): optimized shape, for problem (3.25) and $g_{max}^1 = 40$, for the 2d cantilever.

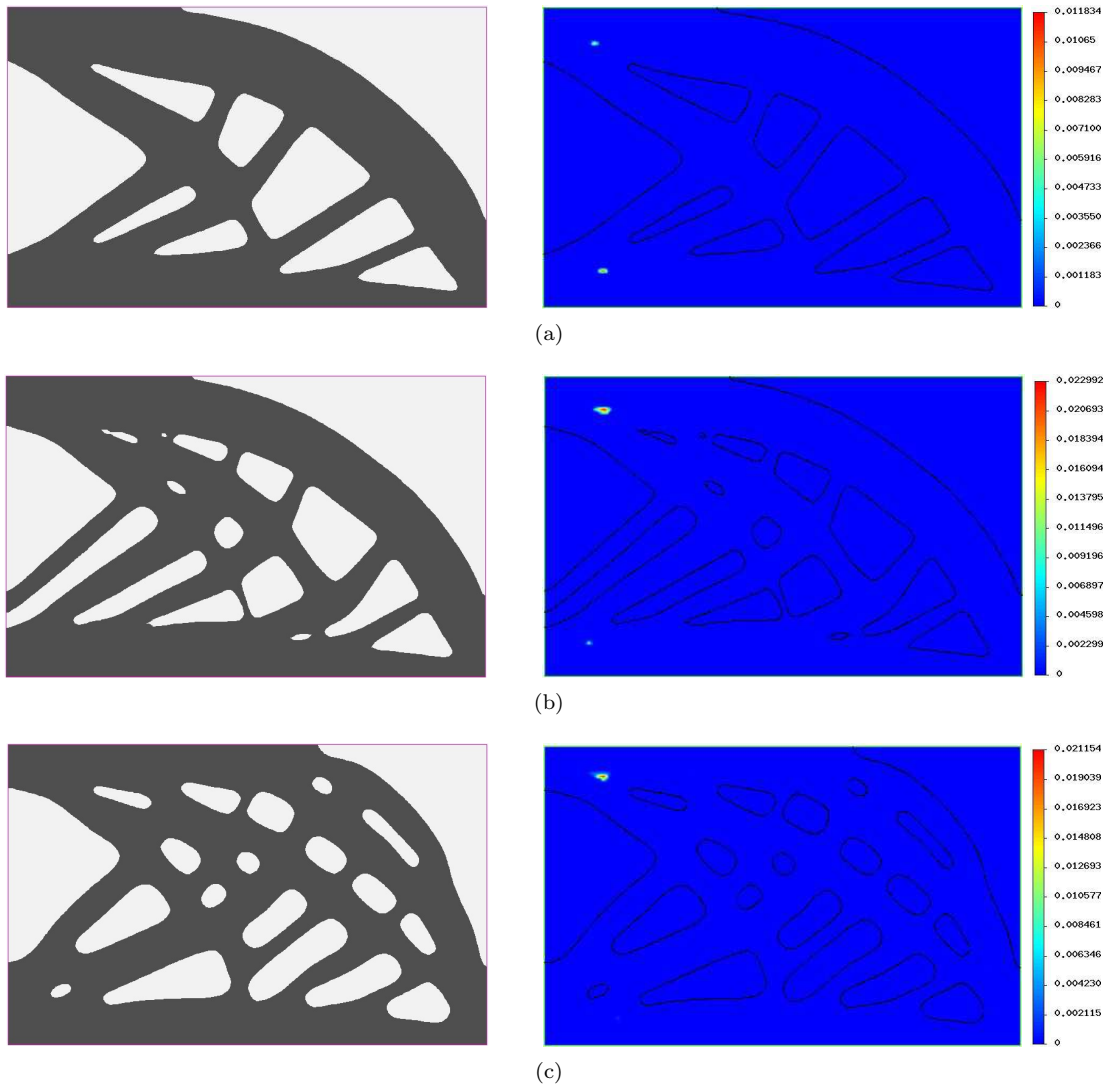
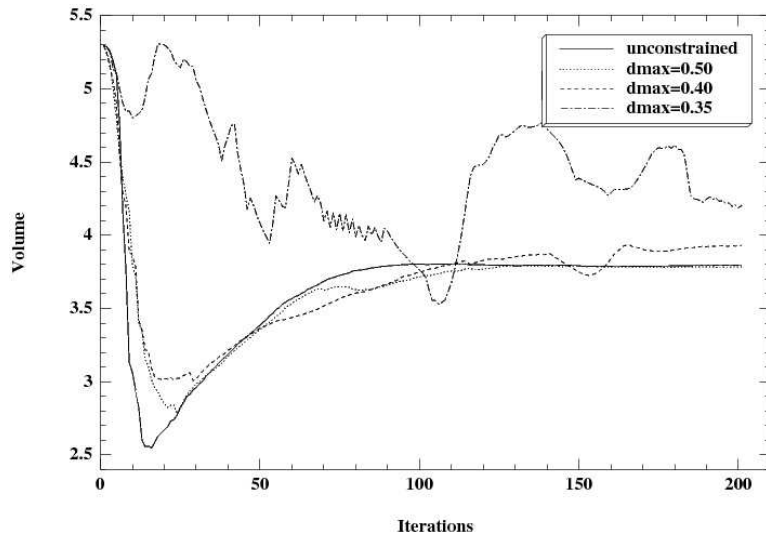
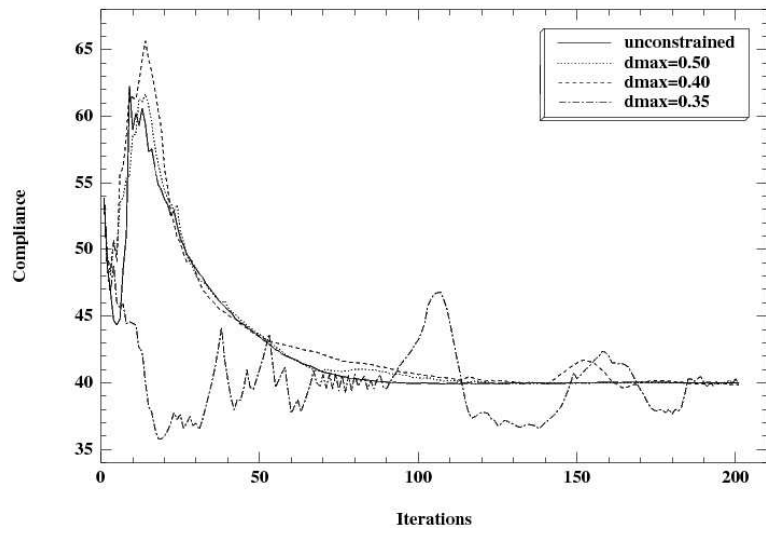


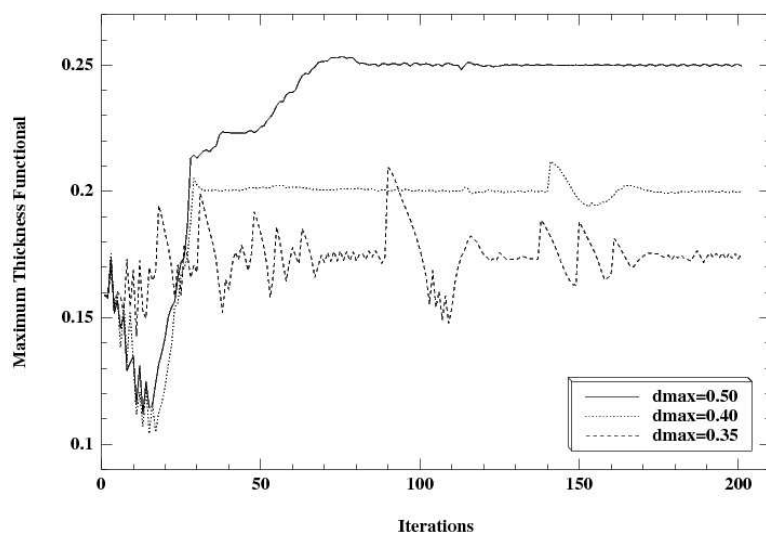
Figure 3.29: Optimized shapes for problem (3.26) and thickness violation ($|(d_{\Omega}(x) - d_{max}/2)^-|$) for (a): $d_{max} = 0.50$; (b): $d_{max} = 0.40$; (c): $d_{max} = 0.35$, for the 2d cantilever.



(a)



(b)



(c)

Figure 3.30: Convergence diagrams for the (a): volume; (b): compliance; (c): maximum thickness functional, for the results of figures 3.28 and 3.29.

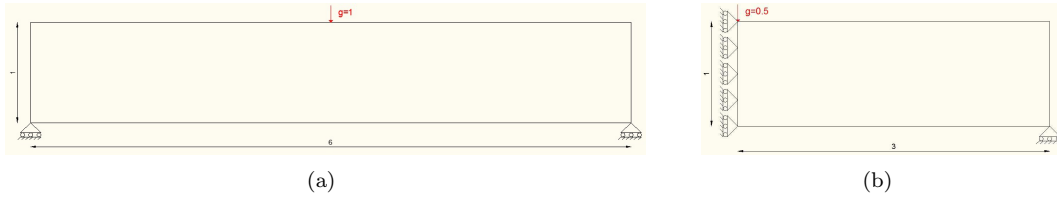


Figure 3.31: Boundary conditions for a 2d MBB beam; (a): full-domain; (b): half-domain.

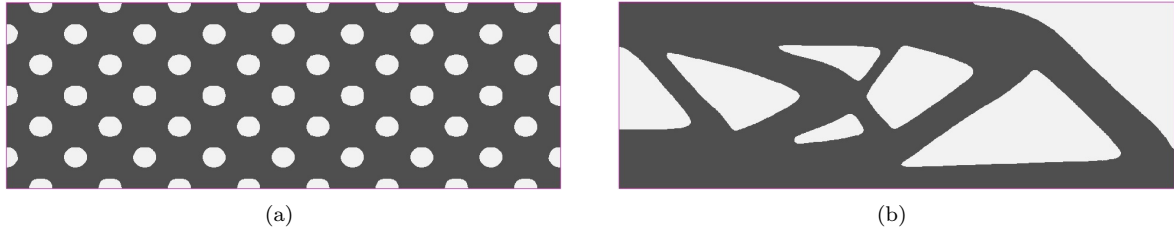


Figure 3.32: (a): Initialization; (b): optimized shape, for problem (3.25) and $g_{max}^1 = 40$, for the 2d MBB beam.

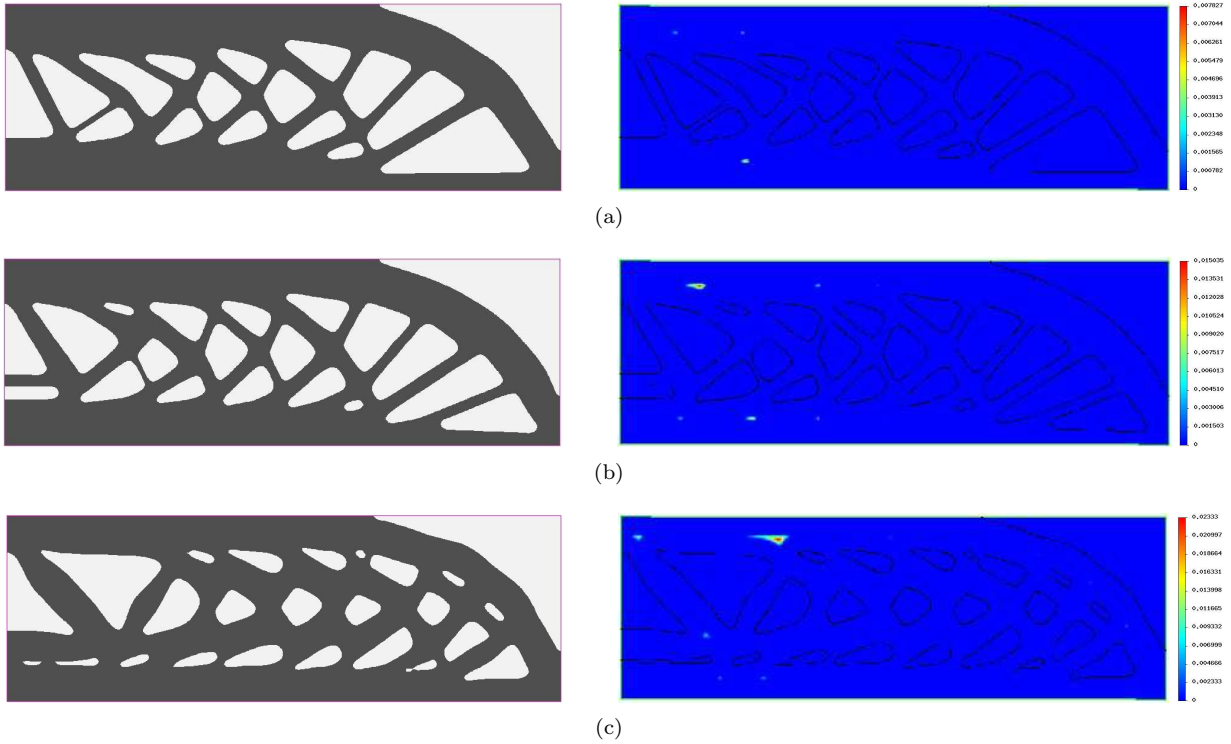
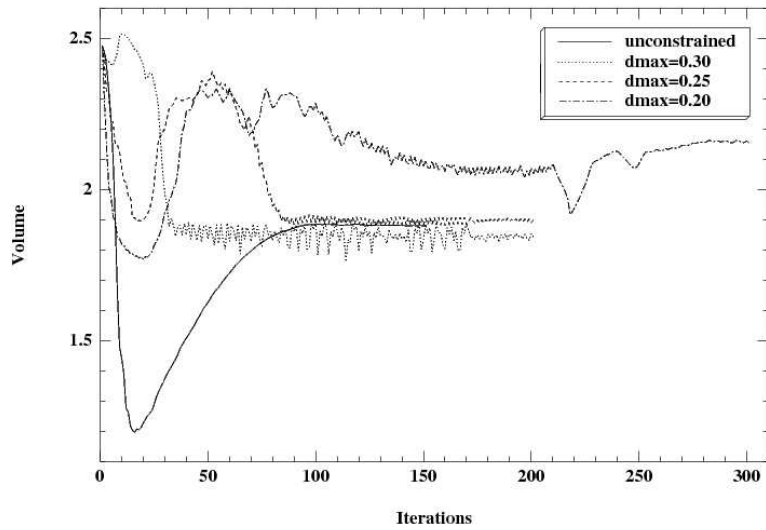
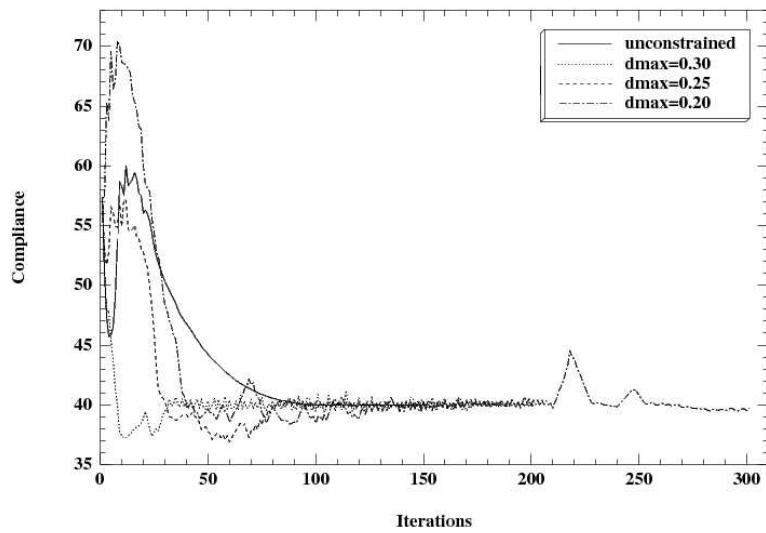


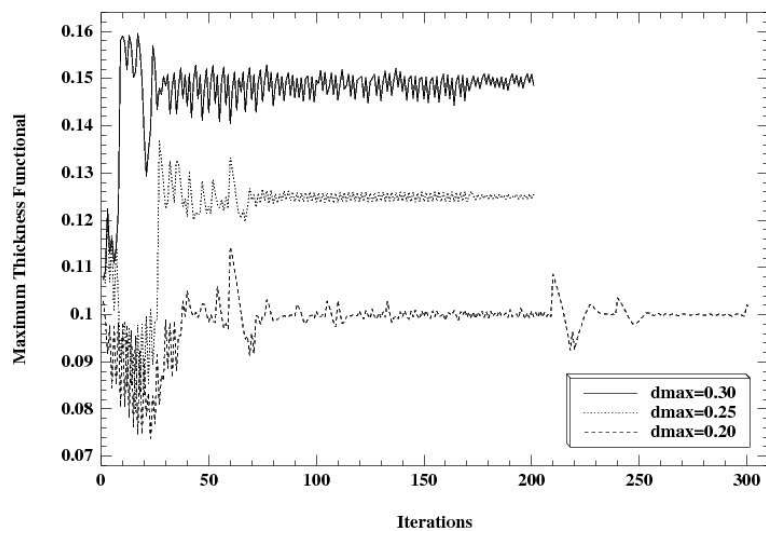
Figure 3.33: Optimized shapes for problem (3.26) and thickness violation $(|(d_{\Omega}(x) - d_{max}/2)^-|)$ for (a): $d_{max} = 0.30$; (b): $d_{max} = 0.25$; (c): $d_{max} = 0.20$, for the 2d MBB beam.



(a)



(b)



(c)

Figure 3.34: Convergence diagrams for the (a): volume; (b): compliance; (c): maximum thickness functional, for the results of figures 3.32 and 3.33.

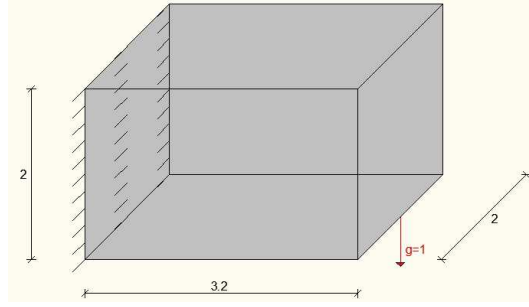
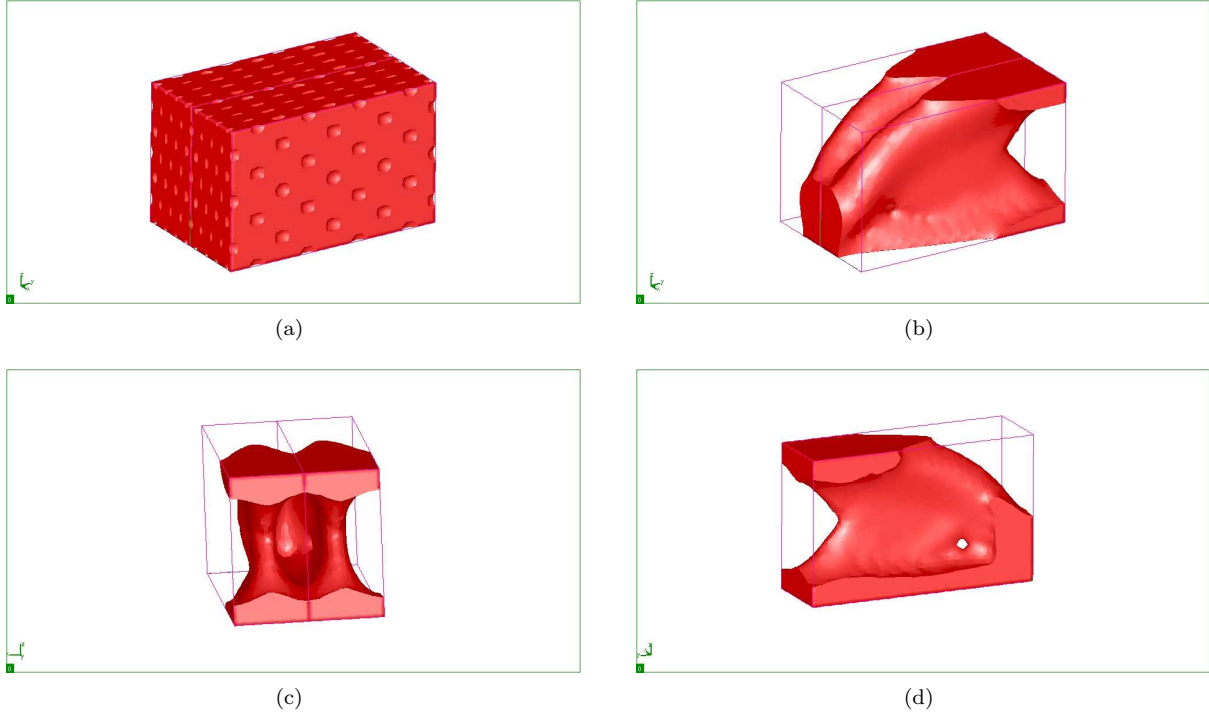


Figure 3.35: Boundary conditions for a 3d cantilever.

Figure 3.36: (a): Initialization; optimized shape's (b): front view; (c): back view; (d) half-domain, for problem (3.25) and $g_{max}^1 = 53$, for the 3d cantilever.

$g_{max}^1 = 53$ are shown in Figure 3.36. Adding the maximum thickness constraint with $d_{max} = 0.40$ and $d_{max} = 0.35$ to the previous problem, results in the optimized shapes of figures 3.37 and 3.38. The convergence diagrams are shown in Figure 3.39 and the final results in Table 3.3.

3d MBB beam

The second 3d example is a $6 \times 1 \times 1$ MBB beam, shown in Figure 3.40. Since the structure is doubly symmetric, only one quarter of the bounding box is considered for the analysis and is discretized by $60 \times 20 \times 40$ elements. The initialization and the optimized shape for problem (3.25) and $g_{max}^1 = 12$ are shown in Figure 3.41. The optimized shapes for $g_{max}^1 = 12$ and $d_{max} = 0.60$ and $d_{max} = 0.50$ are plotted in figures 3.42 and 3.43 correspondingly. The convergence diagrams are shown in Figure 3.44 and the final results in Table 3.4.

3d box

The last example for the maximum thickness constraint is a three dimensional $2 \times 2 \times 1$ box-like structure, clamped at its four lower corners and with a unit load applied at the middle of its lower edge (see Figure 3.45). Here again, one quarter of the structure is used for the analysis and is discretized by $30 \times 30 \times 30$ elements. The initialization and the optimized shape for problem (3.25) and $g_{max}^1 = 32$ are shown in

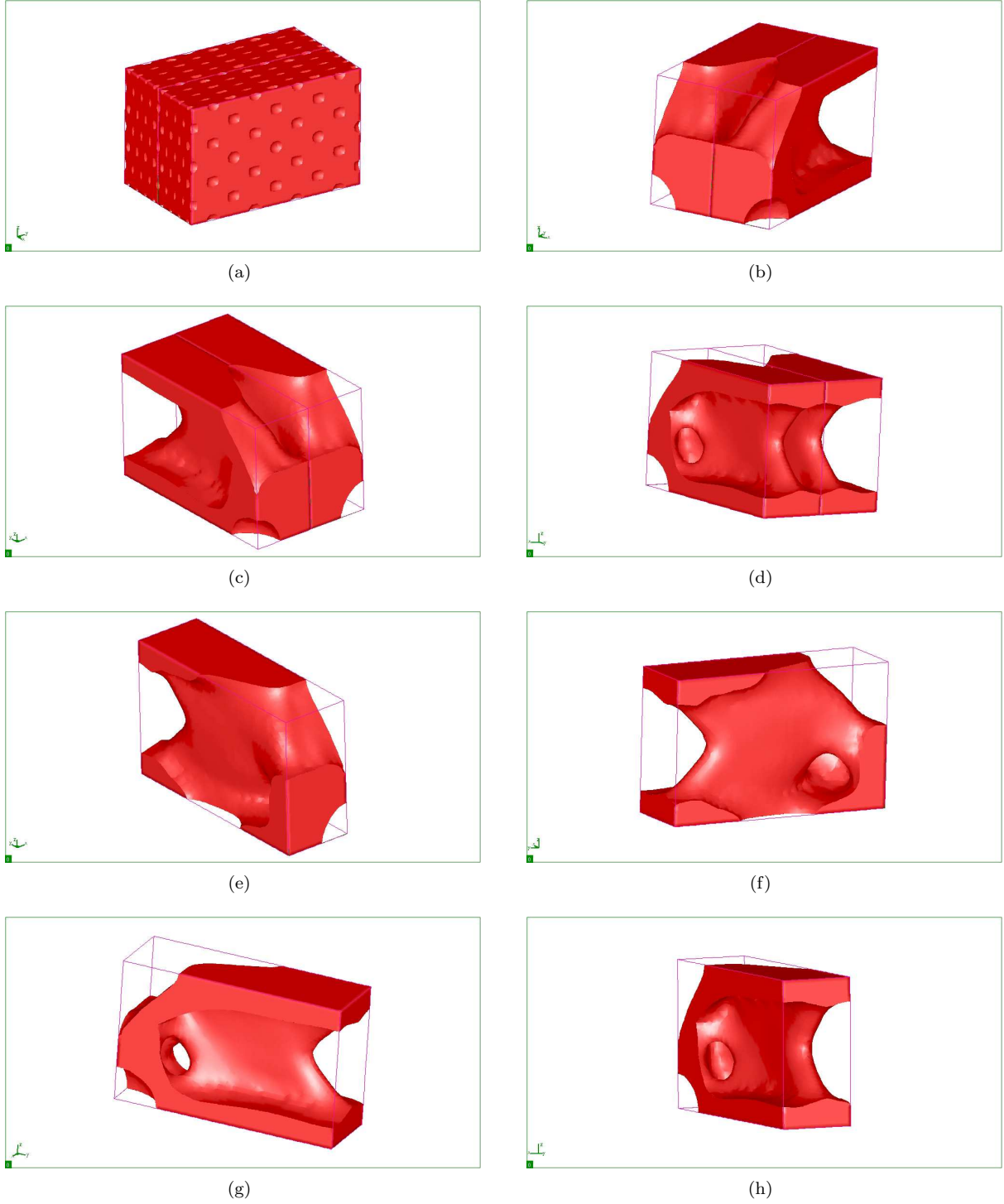


Figure 3.37: (a): Initialization; (b)-(h): different views of the optimized shape for problem (3.26), $g_{max}^1 = 53$ and $d_{max} = 0.40$, for the 3d cantilever.

Table 3.3: Optimized 3d cantilever.

	Volume	Compliance	$P_{MaxT}(\Omega)$
Without thickness restriction	2.676	53.00	-
$d_{max} = 0.40$	3.062	53.02	0.200
$d_{max} = 0.35$	3.055	53.08	0.175

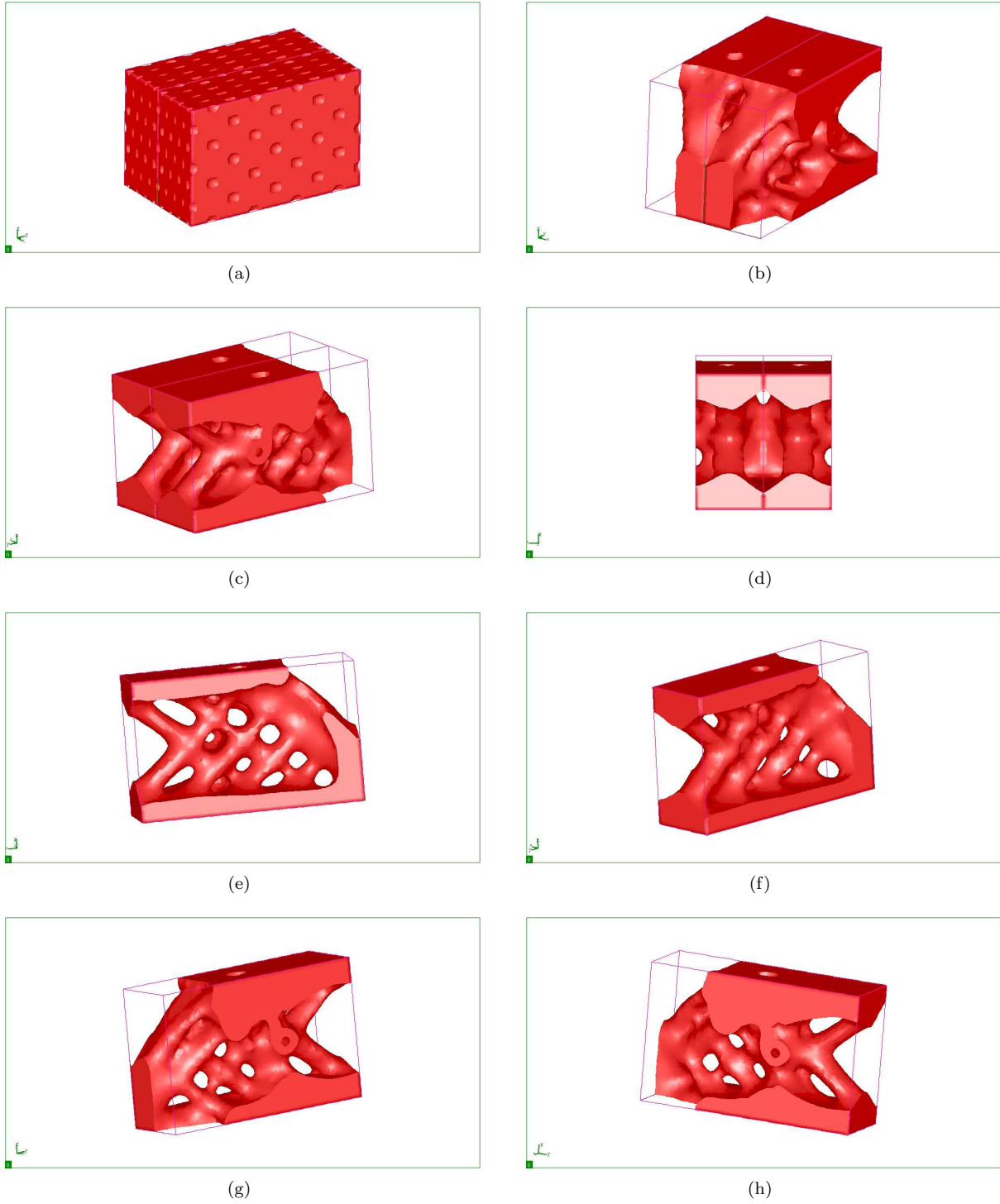
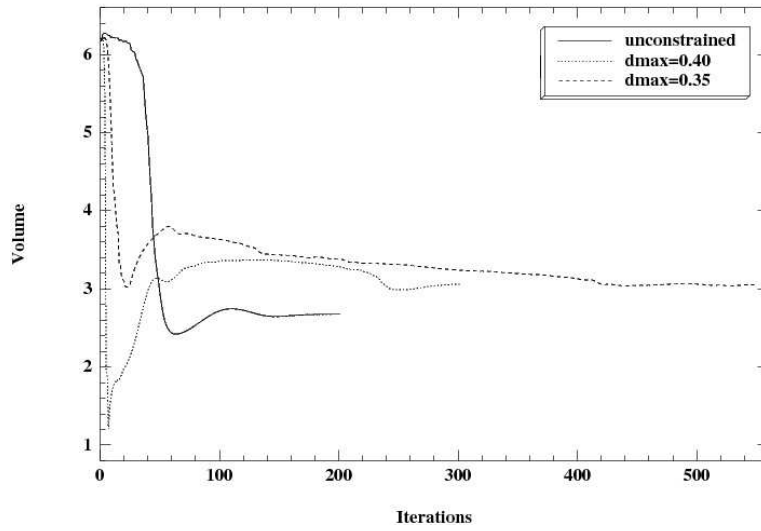


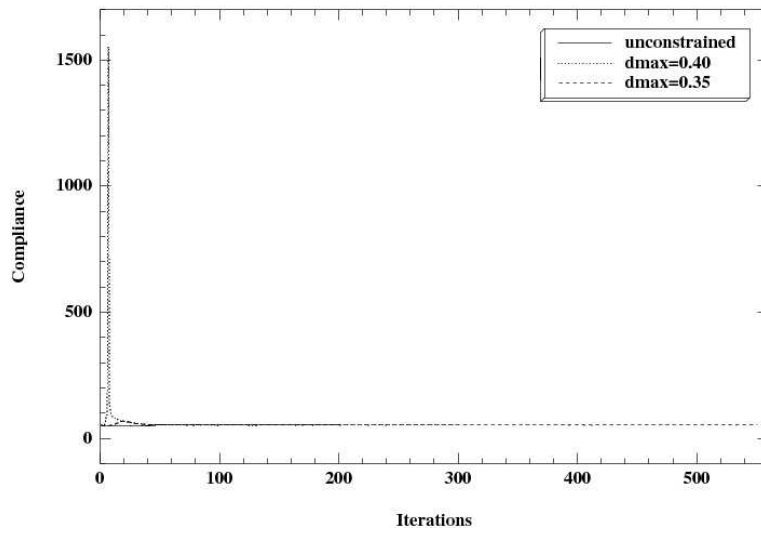
Figure 3.38: (a): Initialization; (b)-(h): different views of the optimized shape for problem (3.26), $g_{max}^1 = 53$ and $d_{max} = 0.35$, for the 3d cantilever.

Table 3.4: Optimized 3d MBB beam.

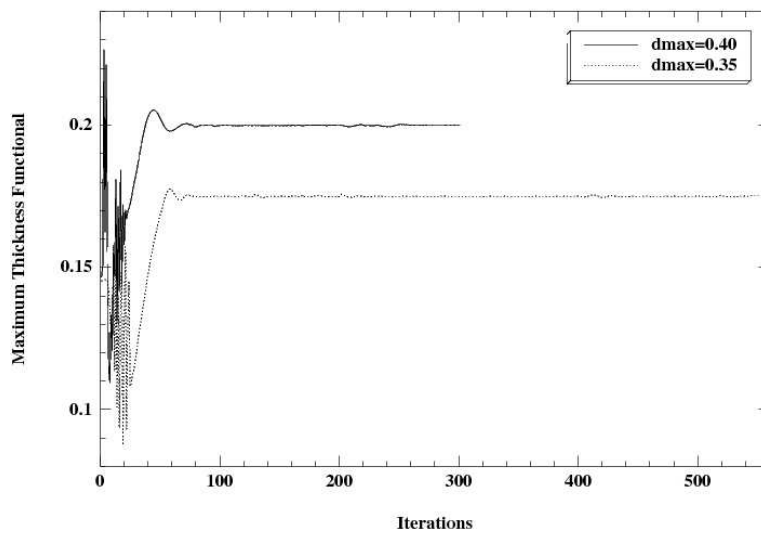
	Volume	Compliance	$P_{MaxT}(\Omega)$
Without thickness restriction	2.997	12.50	-
$d_{max} = 0.60$	3.119	12.51	0.300
$d_{max} = 0.50$	3.429	12.44	0.250



(a)



(b)



(c)

Figure 3.39: Convergence diagrams for the (a): volume; (b): compliance; (c): maximum thickness functional, for the results of figures 3.36, 3.37 and 3.38.

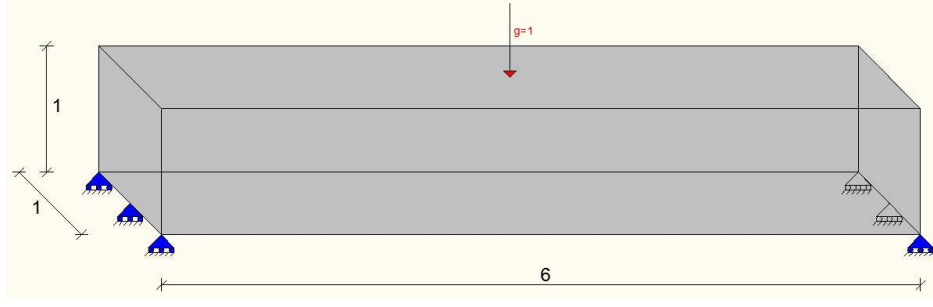


Figure 3.40: Boundary conditions for a 3d MBB beam.

Table 3.5: Optimized 3d box.

	Volume	Compliance	$P_{MaxT}(\Omega)$
Without thickness restriction	0.303	31.97	-
$d_{max} = 0.60$	0.281	32.00	0.234
$d_{max} = 0.40$	0.326	32.00	0.200

Figure 3.46. The optimized shapes for $g_{max}^1 = 32$ and $d_{max} = 0.60$ and $d_{max} = 0.40$ are plotted in figures 3.47 and 3.48 correspondingly. The final results are shown in Table 3.5. We see that the optimized shape for $d_{max} = 0.60$ is more rigid than the one obtained without a thickness constraint and thus it is clear that the shape of Figure 3.46 corresponds to a local minimum.

3.7.2 Minimum Thickness

2d cantilever

Similar to what we did with the maximum thickness constraint, we will test several formulations and strategies for the minimum thickness constraint. Our model test case is chosen to be the two-dimensional cantilever of Figure 3.27. Starting with the initialization of Figure 3.28(a) and solving problem (3.25) for $g_{max}^1 = 60$, we get the optimized shape of Figure 3.49. We suppose now that we want to avoid thin features that appear in this shape. We define a minimum thickness size d_{min} and solve the optimization problem

$$\begin{aligned}
 & \min_{\Omega \in \mathcal{U}_{ad}} \int_{\Omega} dx \\
 & \text{s.t.} \quad \int_{\partial\Omega} g \cdot u ds \leq g_{max}^1, \\
 & P_{MinT}(\Omega) = \int_{\partial\Omega} \int_0^{d_{min}} \left[(d_{\Omega}(s - \xi n(s)))^+ \right]^2 d\xi ds = 0.
 \end{aligned} \tag{3.28}$$

Once more, we need to choose whether the thickness constraint will be applied since the beginning, or in a second step, after an optimized shape for problem (3.25) has been obtained. Contrary to the maximum thickness case, it seems more natural to choose the second strategy for this constraint. The reason is that the penalty functional $P_{MinT}(\Omega)$ in (3.28) will cause, in general, a trend to increase the thickness of thin features. Thus, the disappearance of less useful parts of the structure will be hindered and we shall expect the existence of parts in the optimized shape with negligible mechanical importance. This is the case in the optimized shape of Figure 3.50, where the minimum thickness constraint has been applied since the beginning of the optimization algorithm. Evidently, the upper-right bar of the shape has negligible mechanical contribution, but it cannot be removed because of the minimum thickness constraint.

Using the shape of Figure 3.49(a) as an initial guess for problem (3.28), the optimized shapes for different values of d_{min} are shown in Figure 3.51. As we could have expected, for relatively small values of d_{min} , the algorithm augments the size of thin members and, usually, reduces a bit the size of features whose thickness exceeds this value. In such cases, the shape does not change significantly and the final topology is the same with the initialization. However, when the value of d_{min} is such that several parts of the structure are penalized, then we can expect topological changes to occur. Initially, the size of the bars increases and then, since the compliance constraint is no more active, it is easier for the shape to change. Members can merge, which is usually beneficial for the minimum thickness constraint. We can

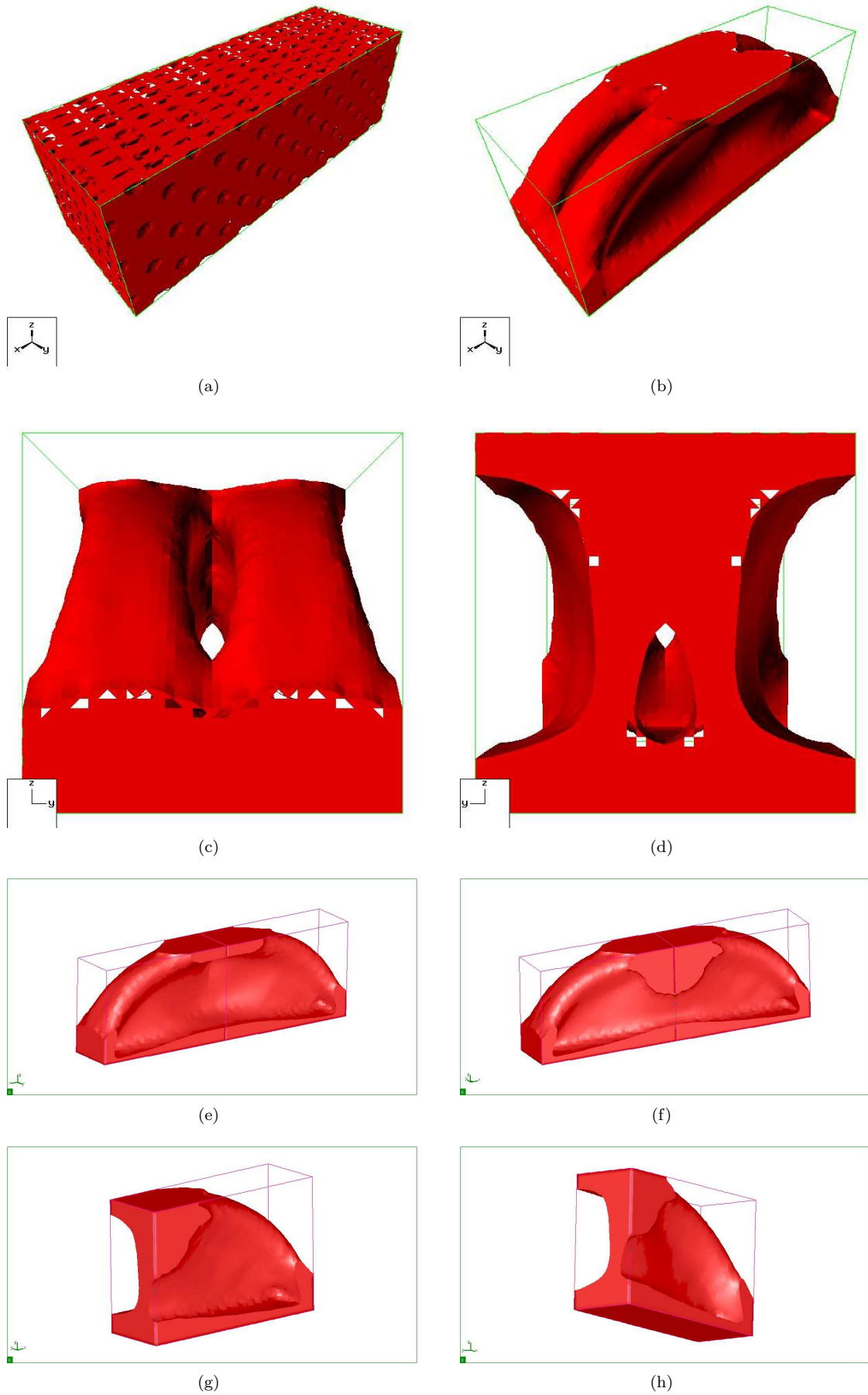


Figure 3.41: (a): Initialization; (b)-(h): different views of the optimized shape for problem (3.25) and $g_{max}^1 = 12$, for a 3d MBB beam.

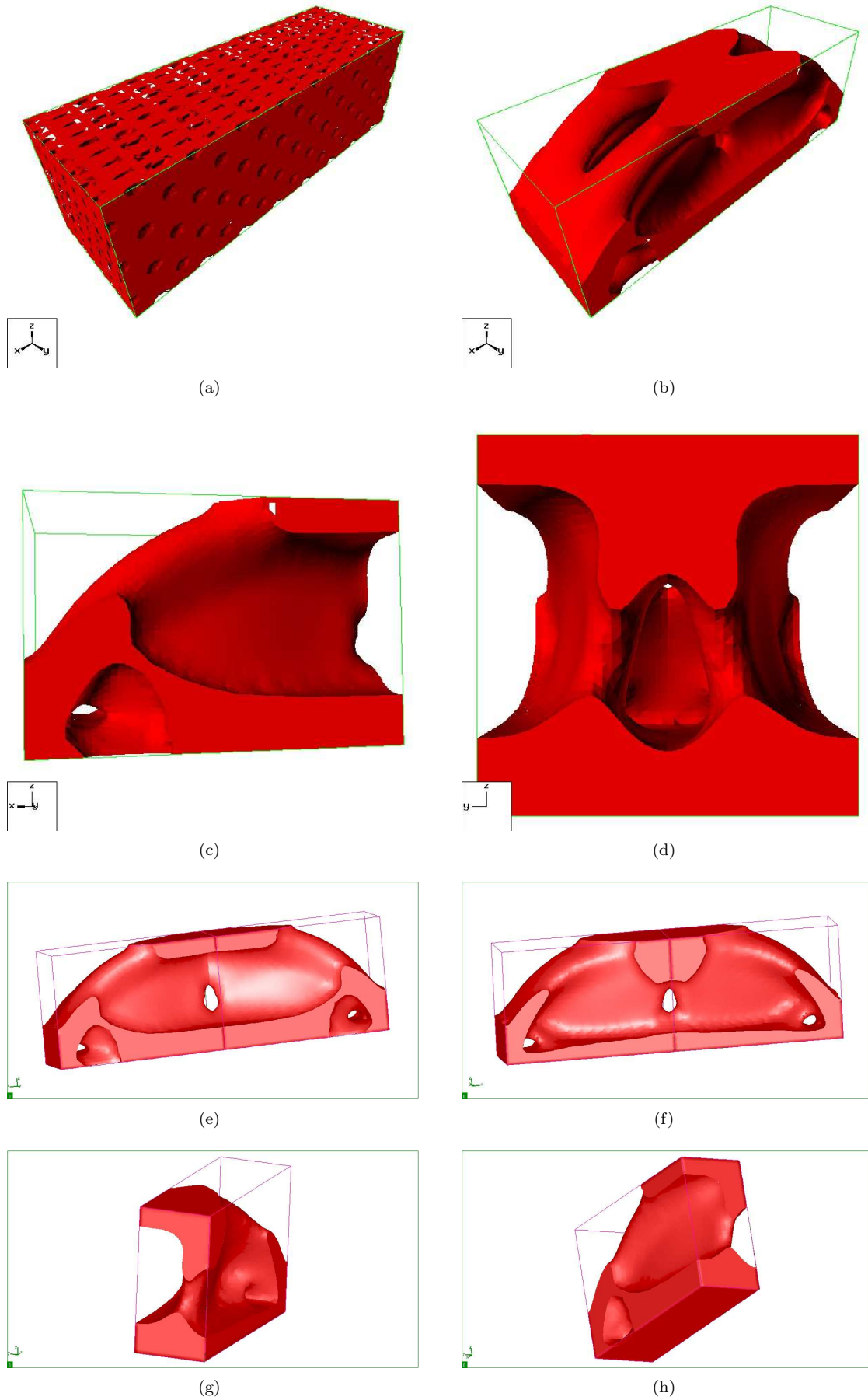


Figure 3.42: (a): Initialization; (b)-(h): different views of the optimized shape for problem (3.26), $g_{max}^1 = 12$ and $d_{max} = 0.60$, for a 3d MBB beam.

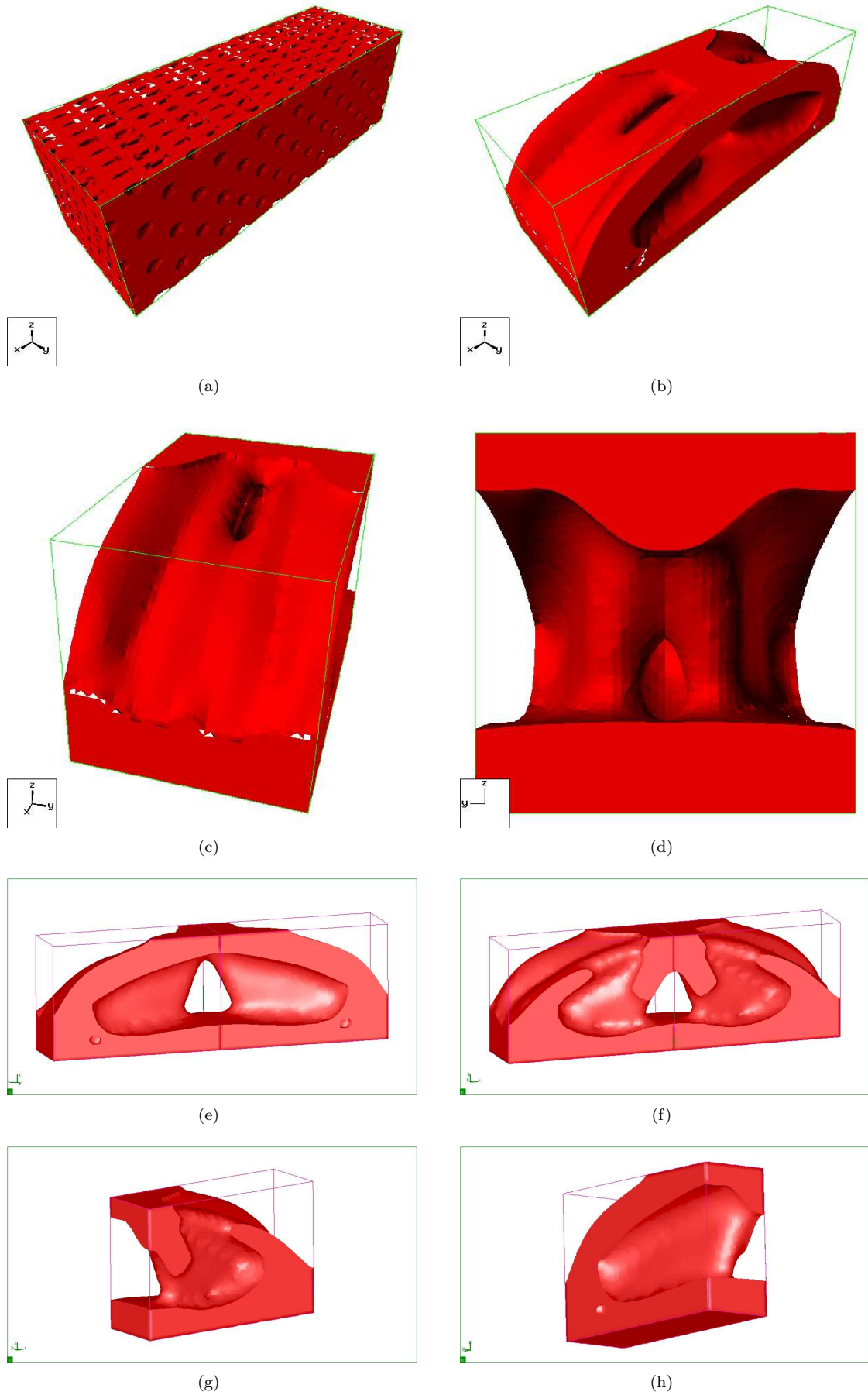
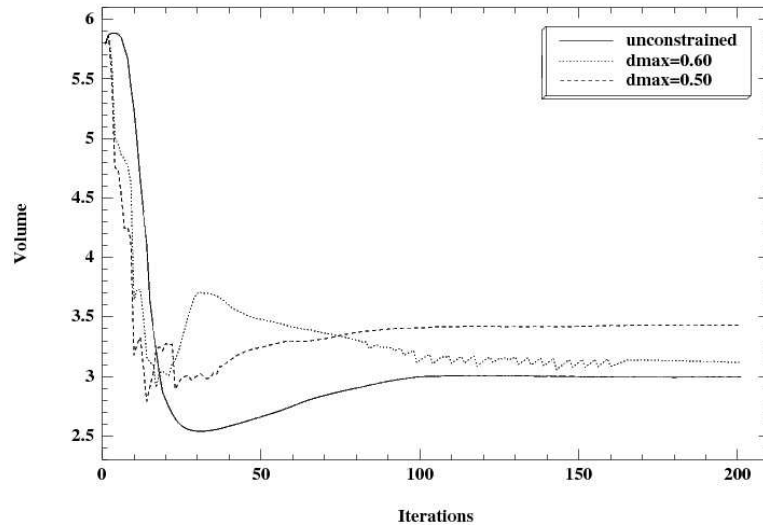
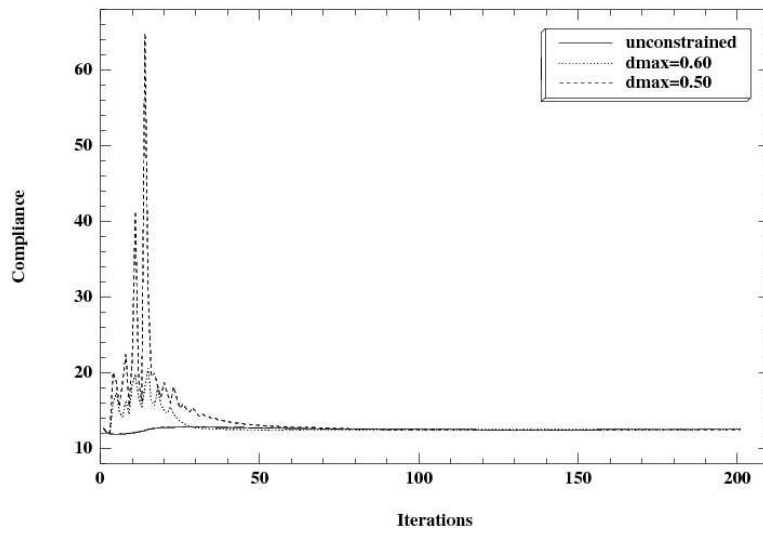


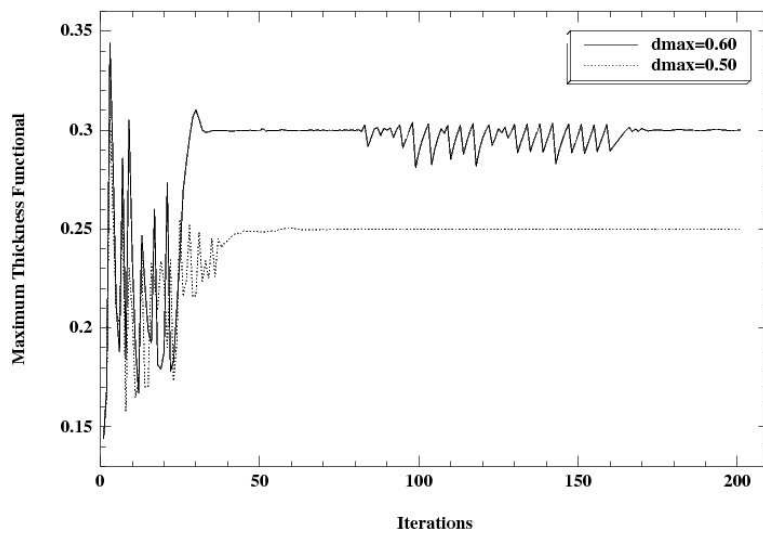
Figure 3.43: (a): Initialization; (b)-(h): different views of the optimized shape for problem (3.26), $g_{max}^1 = 12$ and $d_{max} = 0.50$, for a 3d MBB beam.



(a)



(b)



(c)

Figure 3.44: Convergence diagrams for the (a): volume; (b): compliance; (c): maximum thickness functional, for the results of figures 3.41, 3.42 and 3.43.

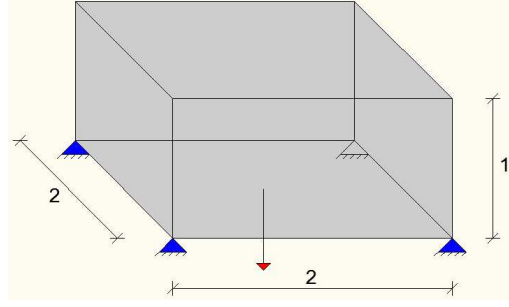


Figure 3.45: Boundary conditions for a 3d box.

see this process in Figure 3.52, where several intermediate iterations are depicted before arriving to the optimized shape of Figure 3.51(d).

Remark 3.7.1. *One may wonder why the upper-right bar of the shape in Figure 3.50 does not disappear. This happens because we have chosen not to set $\psi = 0$ for the nodes of the shape that belong also to the boundary of the working domain (see Figure 3.7). There are several reasons for this choice. First, we have observed numerically that it can lead to the appearance of spurious holes in the structure. Then, it is possible that the algorithm converges much slower, because the new optimizable boundary contains areas with high velocity and thus the CFL condition for the advection of the level-set function becomes too strict. Practically, it is possible that we observe very slight changes of the shape, which is totally due to the stability condition for the Hamilton-Jacobi equation.*

Many ideas can be proposed about how to avoid such artifacts, but the good strategy to follow remains always case-dependent. Now, we would like to show the above described with an example. Suppose that we start with the optimized shape of Figure 3.50 and we decide to set

$$\psi(x) = 0 \quad \forall x \in \partial\Omega \cap \partial D,$$

i.e. we consider as optimizable all the boundary of the shape Ω . Then, with a small abuse in theory since we have neglected some terms in the shape derivative that should have been included (see Proposition 1.3.9), the algorithm "sticks" in the shape of Figure 3.53(a). However, the upper-right bar has changed and the previous problem for the minimum thickness constraint shall no more appear. Starting from this shape and coming back to the initial choice for ψ (see Figure 3.7(a)), we can solve again problem (3.28). In Figure 3.53 we can see that the shape can now change radically and converge to an optimized shape that is intuitively acceptable. However, since we expect to start from a shape very far from an optimum, the optimization may need a lot of iterations to converge.

Energy functionals for the minimum thickness

Although the minimum thickness constraint (3.3) and its corresponding penalty functional $P_{MinT}(\Omega)$ are mathematically well-defined, the numerical calculation of the shape derivative (3.16) is not trivial. Among other things, in order for the calculation to be sufficiently accurate, the mesh shall not be too coarse.

Instead of formulating a constraint, it is interesting to see if we can manage to control the thickness of the structure in such a way that thin features are avoided by adding to the objective function some energy functional. As we have foresaid, this approach has also been followed in [38], [40], [89]. However, instead of favoring specific patterns and shapes, we shall better base the formulation of this energy functional on the values of the signed distance function. In addition, it would be preferable that the functional has no impact on features where the thickness exceeds the desired limit.

A first proposal of such a functional is the following:

$$E_1(\Omega) = - \int_{\Omega} d_{\Omega}(x)^2 [(d_{\Omega}(x) + d_{min}/2)^+]^2 dx. \quad (3.29)$$

Let us study the behaviour of functional $E_1(\Omega)$ with an example. Consider the semi-infinite bar of Figure 3.54, which has a uniform thickness of value 0.2. We want to solve the optimization problem

$$\min_{\Omega} E_1(\Omega), \quad (3.30)$$

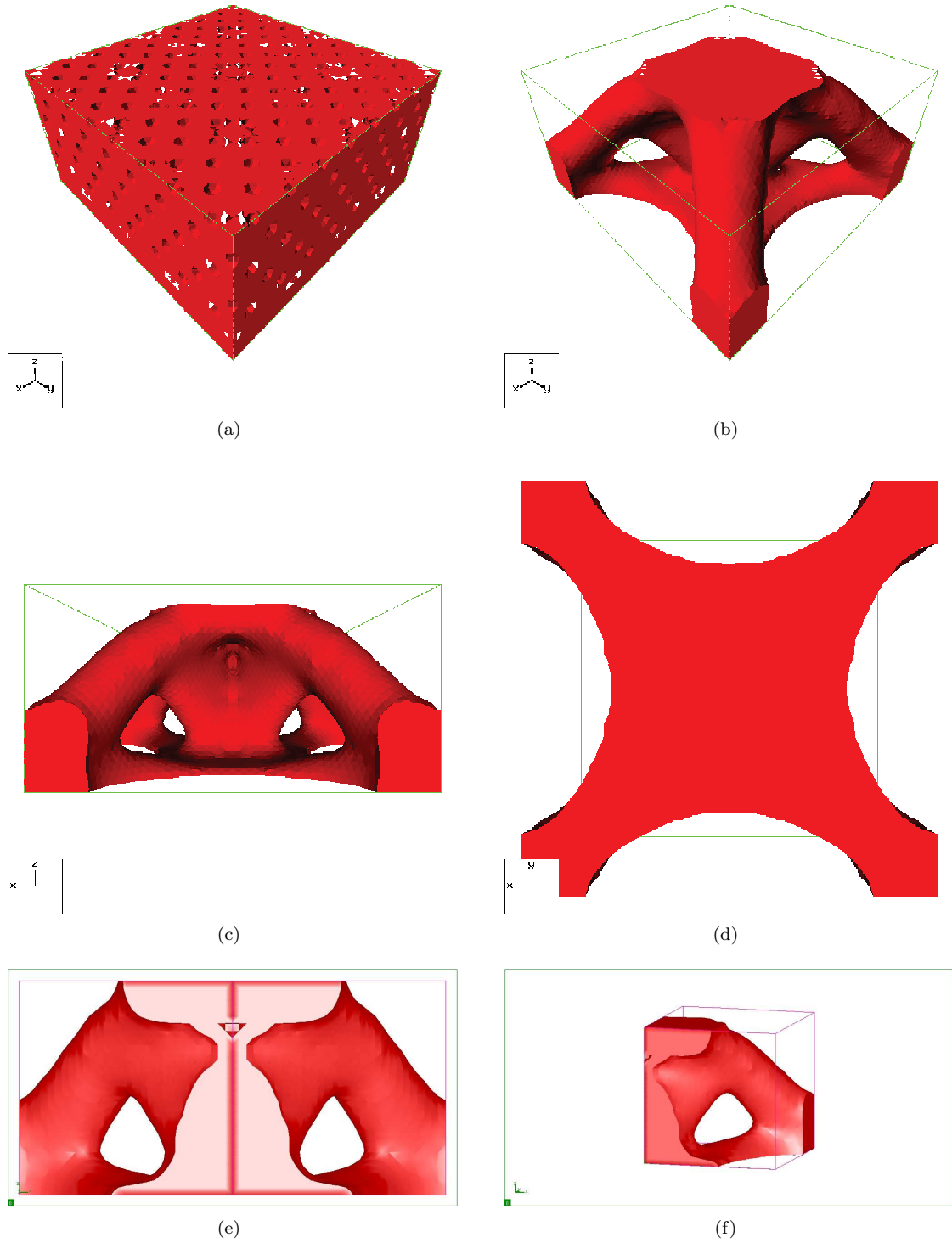


Figure 3.46: (a): Initialization; (b)-(e): different views of the optimized shape for problem (3.25) and $g_{max}^1 = 32$, for a 3d box.

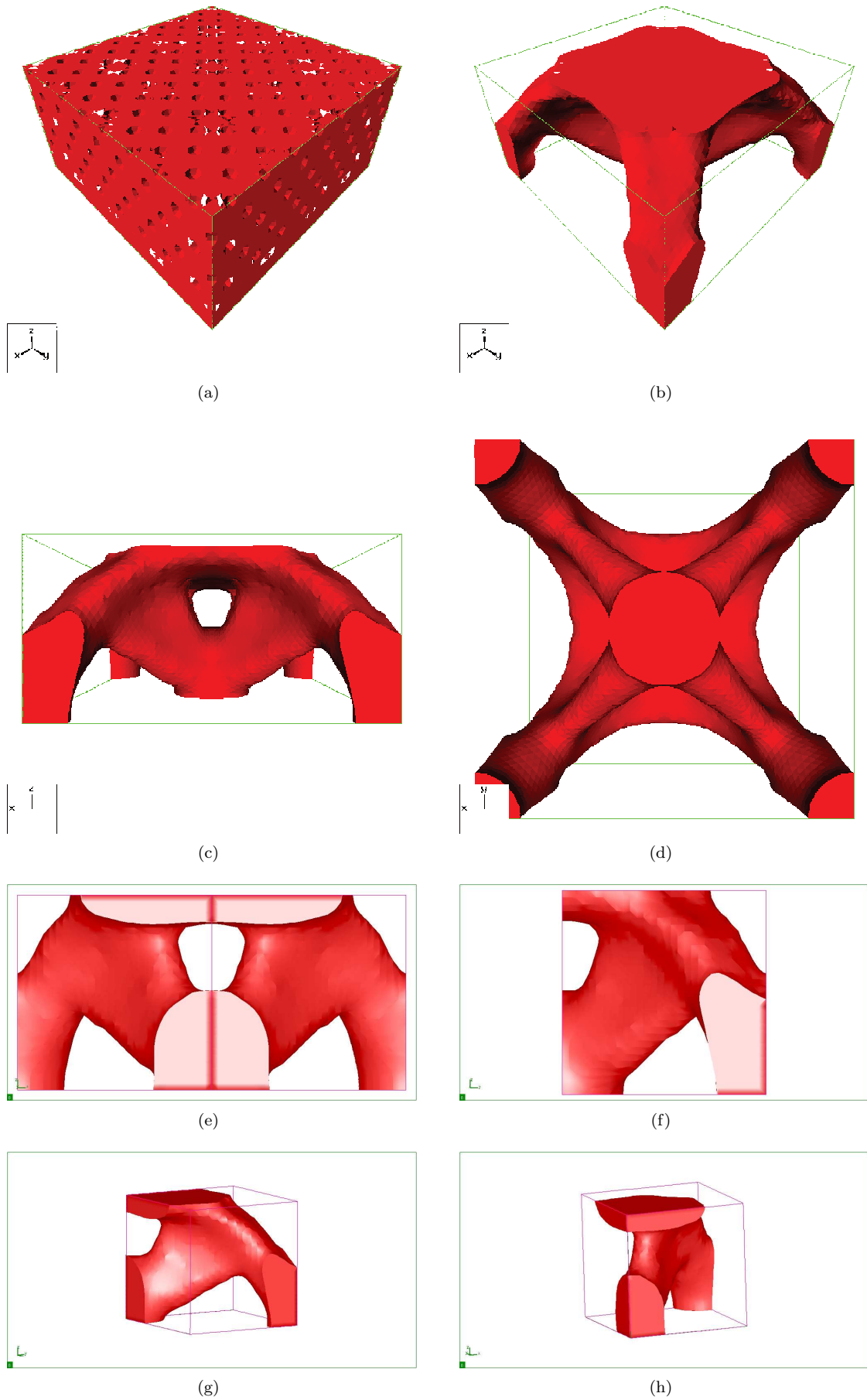


Figure 3.47: (a): Initialization; (b)-(h): different views of the optimized shape for problem (3.26), $g_{max}^1 = 32$ and $d_{max} = 0.60$, for a 3d box.

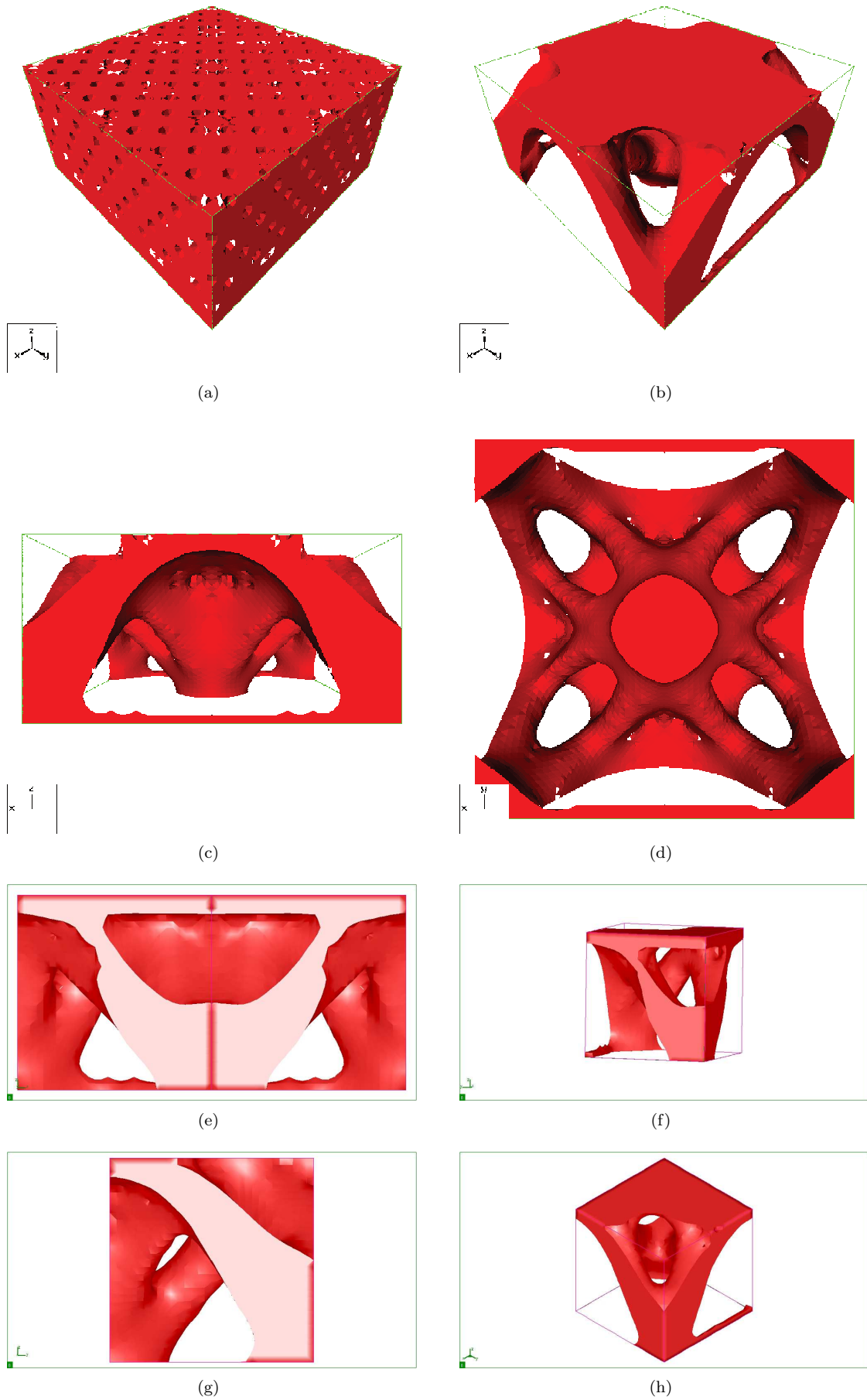


Figure 3.48: (a): Initialization; (b)-(h): different views of the optimized shape for problem (3.26), $g_{max}^1 = 32$ and $d_{max} = 0.40$, for a 3d box.

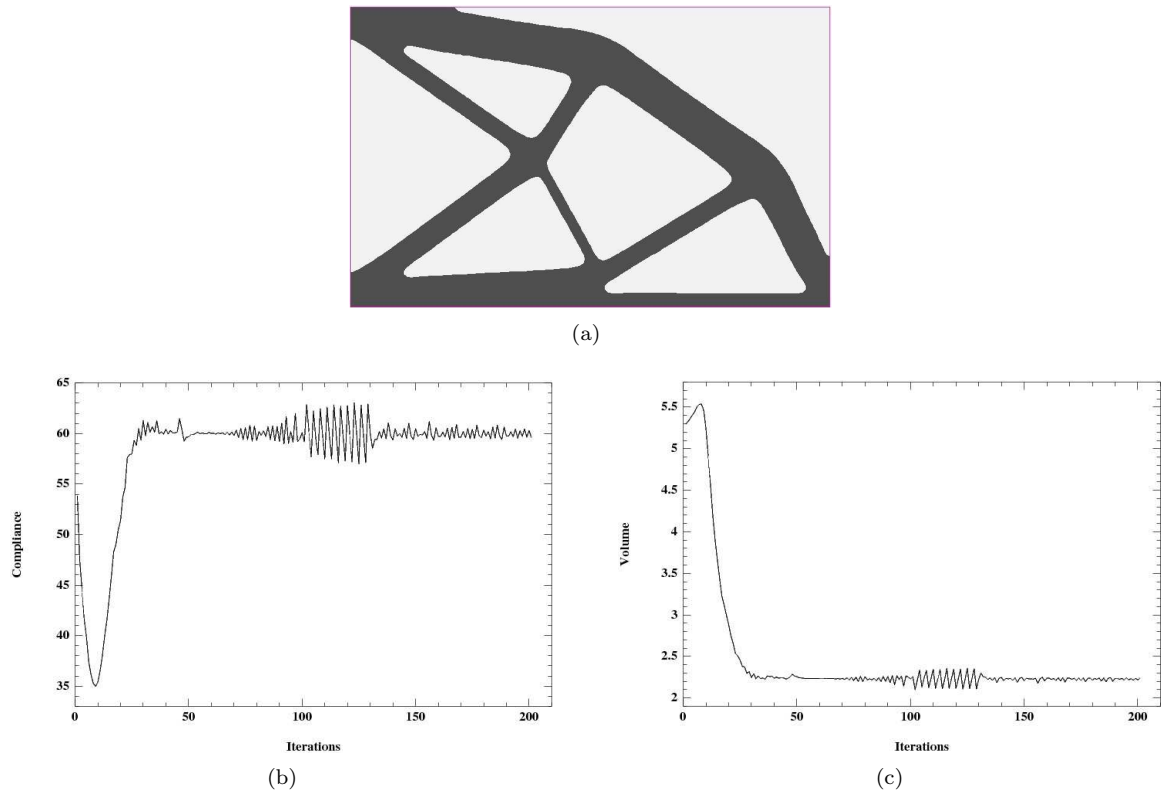


Figure 3.49: (a): Optimized shape for problem (3.25) and $g_{max}^1 = 60$; convergence diagrams for (b): the compliance and (c): the volume, for the 2d cantilever.

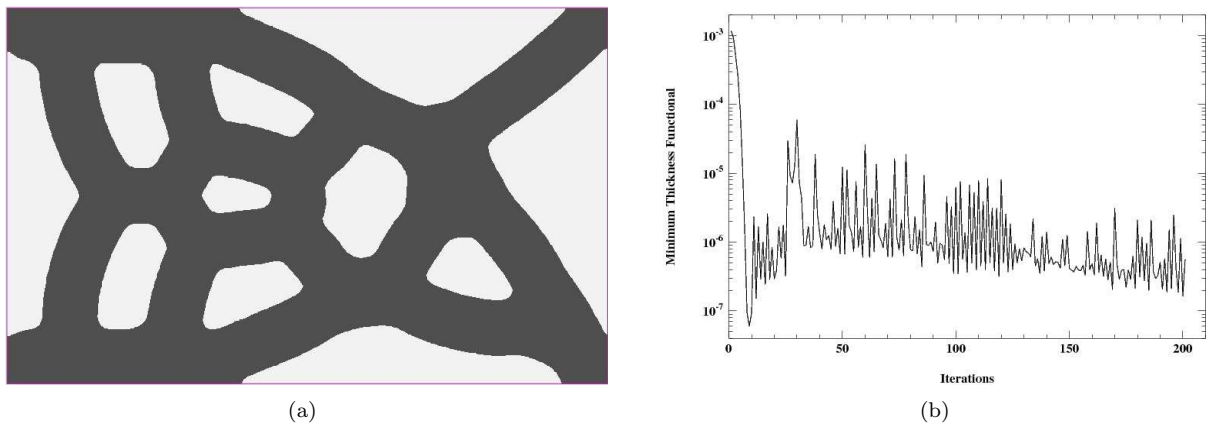


Figure 3.50: (a): Optimized shape for problem (3.28), $g_{max}^1 = 60$ and $d_{min} = 30$ and (b): minimum thickness functional (in logarithmic scale), for the 2d cantilever.

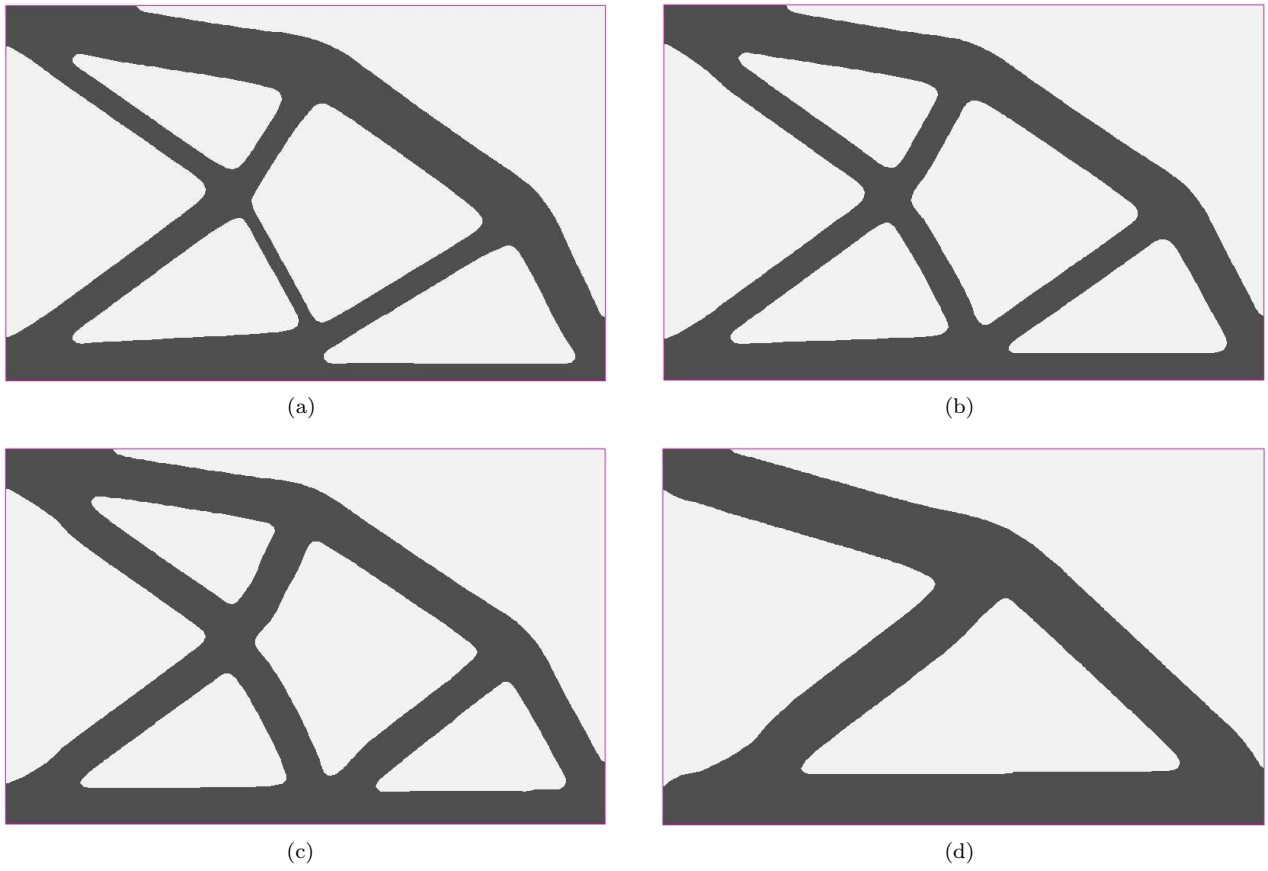


Figure 3.51: Optimized shapes (a): without thickness constraint; (b): for $d_{min} = 0.15$; (c): for $d_{min} = 0.20$ and (d): for $d_{min} = 0.30$, for the 2d cantilever.

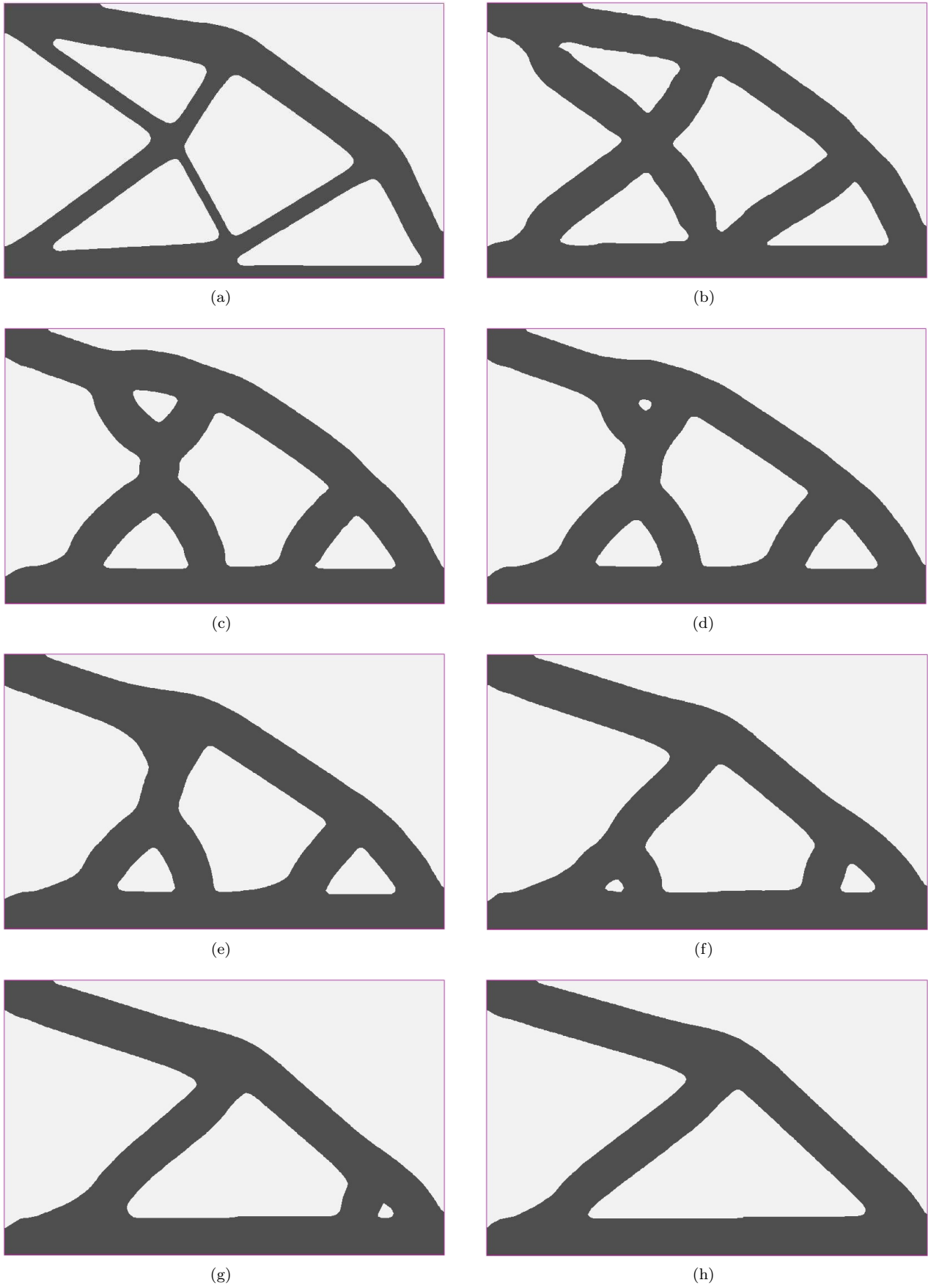
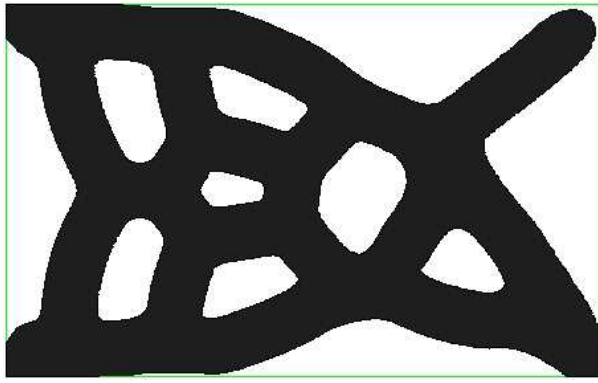
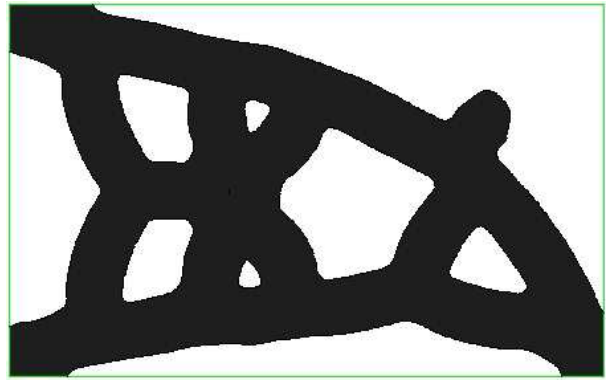


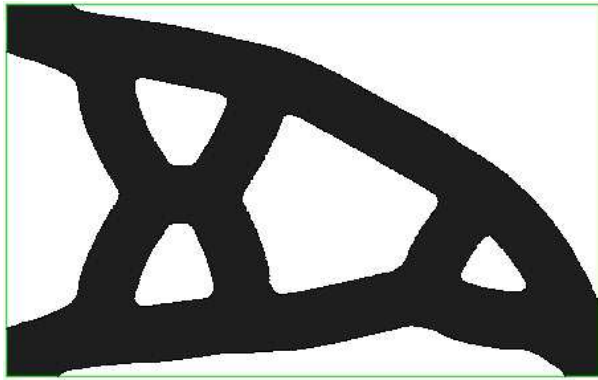
Figure 3.52: (a): Initialization; iteration; (b): 30; (c): 100; (d): 130; (e): 150; (f): 250; (g): 300; (h): optimized shape, for $d_{min} = 0.30$, for the 2d cantilever.



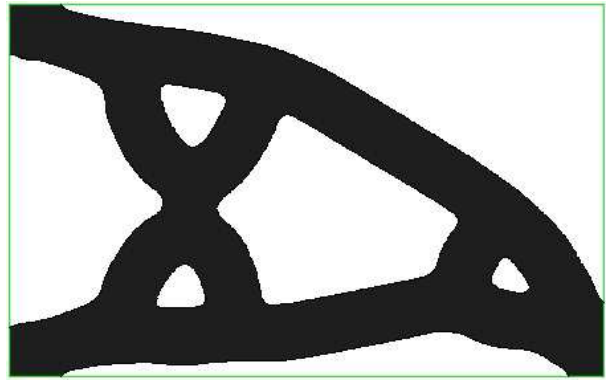
(a)



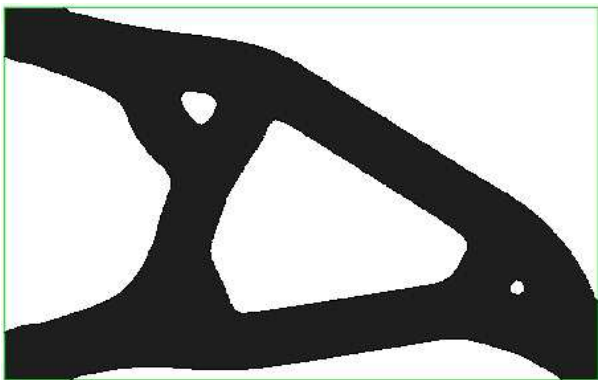
(b)



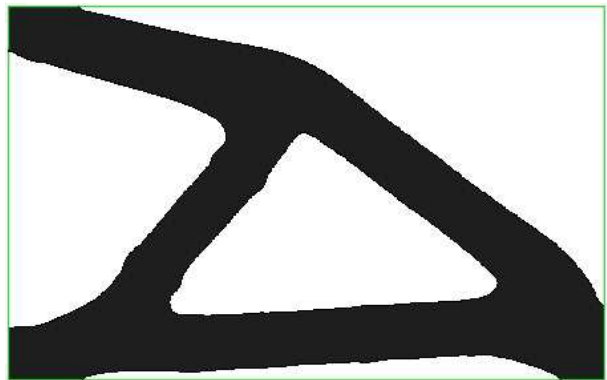
(c)



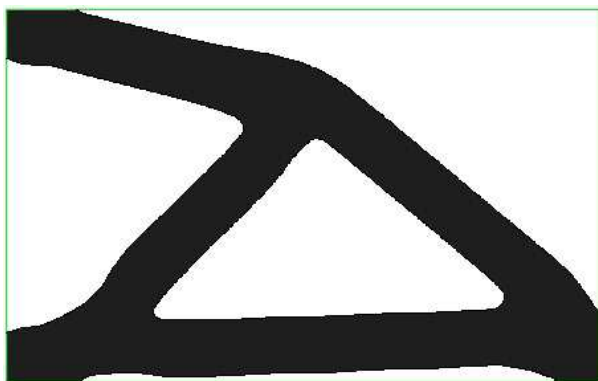
(d)



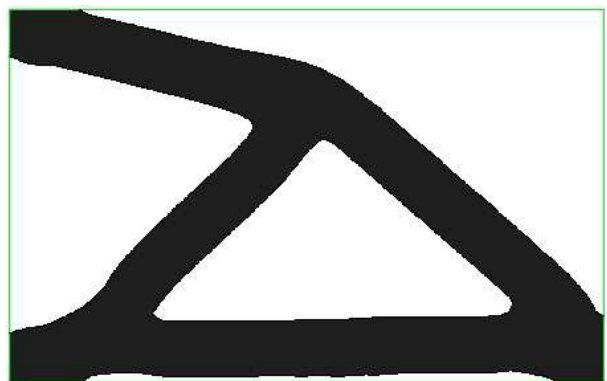
(e)



(f)



(g)



(h)

Figure 3.53: (a)-(h): Iterations 1,100,200,300,400,500,600,700 for the problem (3.28), for the 2d cantilever.

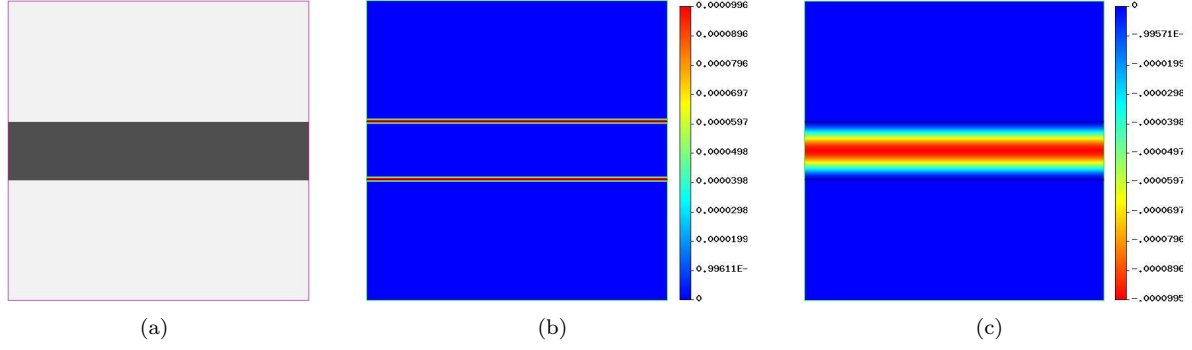


Figure 3.54: (a): Initialization; (b) shape gradient; (c): energy density.

with $d_{min} = 0.4$. The shape derivative of the energy functional reads

$$\begin{aligned}
 E'_1(\theta) &= - \int_{\partial\Omega} \theta(s) \cdot n(s) \left[d_\Omega(s)^2 \left((d_\Omega(s) + d_{min}/2)^+ \right)^2 \right] ds \\
 &\quad - \int_{\Omega} d'_\Omega(\theta) \left[2d_\Omega(x) \left((d_\Omega(x) + d_{min}/2)^+ \right)^2 + 2d_\Omega(x)^2 (d_\Omega(x) + d_{min}/2)^+ \right] dx \\
 &= \int_{\partial\Omega} \theta(x) \cdot n(x) \int_{\text{ray}_{\partial\Omega}(x) \cap \Omega} C(d_\Omega(z)) \prod_{i=1}^{N-1} (1 + d_\Omega(z) \kappa_i(x)) dz dx,
 \end{aligned} \tag{3.31}$$

where

$$C(d_\Omega(z)) = \left[2d_\Omega(z) \left((d_\Omega(z) + d_{min}/2)^+ \right)^2 + 2d_\Omega(z)^2 (d_\Omega(z) + d_{min}/2)^+ \right], \tag{3.32}$$

from which a descent direction is readily revealed as

$$\theta(x) = -n(x) \int_{\text{ray}_{\partial\Omega}(x) \cap \Omega} C(d_\Omega(z)) \prod_{i=1}^{N-1} (1 + d_\Omega(z) \kappa_i(x)) dz, \quad \forall x \in \partial\Omega.$$

It is easy to see that $\theta(x) \cdot n(x) \geq 0$. In Figure 3.55 we show the optimized shape for problem (3.30), which is nothing but a bar of thickness d_{min} . As soon as the bar takes the desired value of thickness, the shape derivative of the energy functional is zero, since a further increase of its size would have no impact on the value of $E_1(\Omega)$.

Let us examine now how this functional behaves when topological changes occur. Consider the two semi-infinite bars of Figure 3.56(a), which are of uniform thickness 0.1. The distance between them is also 0.1 and the optimization problem (3.30) is solved for $d_{min} = 0.5$ and $d_{min} = 0.25$. In both cases, we should expect the bars to increase in size and merge, which should be beneficial for a minimum thickness constraint. However, merging the two bars can cause an increase in the value of functional (3.29), when the shape before merging is close to optimal. In this case, which is shown in Figure 3.56(b) for $d_{min} = 0.25$, its value almost increases by two, same as the decrease of its perimeter. For $d_{min} = 0.50$, the functional is far from obtaining its minimum value before merging. After the two bars have joined into one, the values of the signed distance function change discontinuously and the functional $E_1(\Omega)$ gets further reduced.

Bars are very likely to try to merge during shape and topology optimization under a minimum thickness constraint, as it is shown in Figure 3.52, and thus a proposed energy functional needs to account effectively for such changes. Inspired from the equivalence of the increase in $E_1(\Omega)$ with the decrease in the total perimeter for the simple example of Figure 3.56, we propose the energy functional

$$E_2(\Omega) = \frac{- \int_{\Omega} d_\Omega(x)^2 \left[(d_\Omega(x) + d_{min}/2)^+ \right]^2 dx}{\left(\int_{\partial\Omega} ds \right)^2} \tag{3.33}$$

and we perform the same test as previously. The results are shown in Figure 3.57.

The previous functionals tend, in general, to augment the size of thin bars. Using them since the beginning of the optimization algorithm is likely to result in problems such as those of Figure 3.50, where

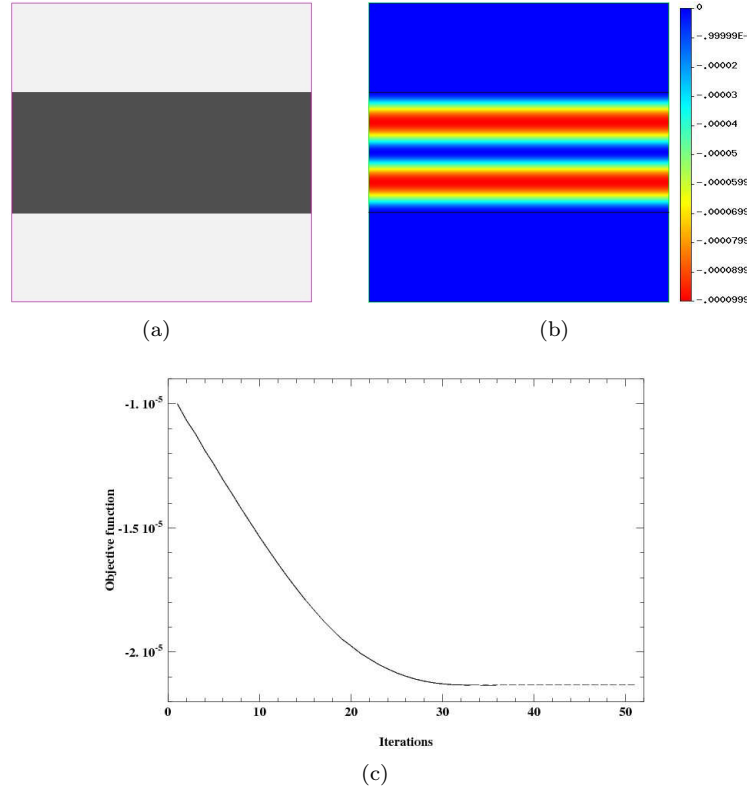


Figure 3.55: (a): Optimized shape for problem (3.30) and $d_{min} = 0.4$; (b) energy density; (c): convergence diagram.

members cannot progressively disappear due to the thickness constraint. However, it seems tempting to try formulate a functional that treats features differently according to their thickness. We can define, for example, a critical value d_{cr} for the thickness, such that when the thickness of a bar is less than d_{cr} , it will tend to reduce in size and in case it lies between d_{cr} and d_{min} , it will increase up to the value of d_{min} (see Figure 3.58). One such functional reads

$$E_3(\Omega) = \int_{\Omega} [d_{\Omega}(x)^2((d_{\Omega}(x) + d_{cr}/2)^+)^2 - ((d_{\Omega}(x) + d_{cr}/2)^-)^2((d_{\Omega}(x) + d_{min}/2)^+)^2] dx. \quad (3.34)$$

In Figure 3.59 we show a numerical test using once more two semi-infinite bars of thickness 0.1 and 0.3. Functional (3.34) is set as objective function and is minimized for $d_{min} = 0.4$ and $d_{cr} = 0.2$. As expected, the thin bar in the upper part disappears, while the lower bar increases in thickness up to the size d_{min} .

We return now to the general setting of structural optimization and examine the behaviour of the proposed energy functionals when applied to the optimized shape of Figure 3.49. Instead of problem (3.28), where a minimum thickness constraint is formulated, a weighted sum of the volume and the thickness functional is considered and the new problem reads

$$\begin{aligned} \min_{\Omega \in \mathcal{U}_{ad}} \quad & \int_{\Omega} dx + \ell_E E_i(\Omega) \\ \text{s.t.} \quad & \int_{\partial\Omega} g \cdot u ds \leq g_{max}^1, \end{aligned} \quad (3.35)$$

where $i = 1, 2, \text{ or } 3$, depending on the energy functional at play and ℓ_E is the weight coefficient for the thickness functional. A satisfying scaling between the volume and the thickness constraint is achieved by choosing $\ell_E = V(\Omega^0)/E_i(\Omega^0)$. Initializing the shape as in Figure 3.60(a) and solving problem (3.35) for $E_1(\Omega)$ and $d_{min} = 0.15$, we result in the shape of Figure 3.60(b). We can see that the addition of the energy functional has caused distortions close to the boundary of the working domain. Such distortions have not appeared in the semi-infinite bars previously, since the intersection of the shape with the working domain is not considered to be part of the structure's boundary and thus d_{Ω} is equivalent with reinitializing the level-set function ψ used for the advection of the shape. In fact, using ψ instead

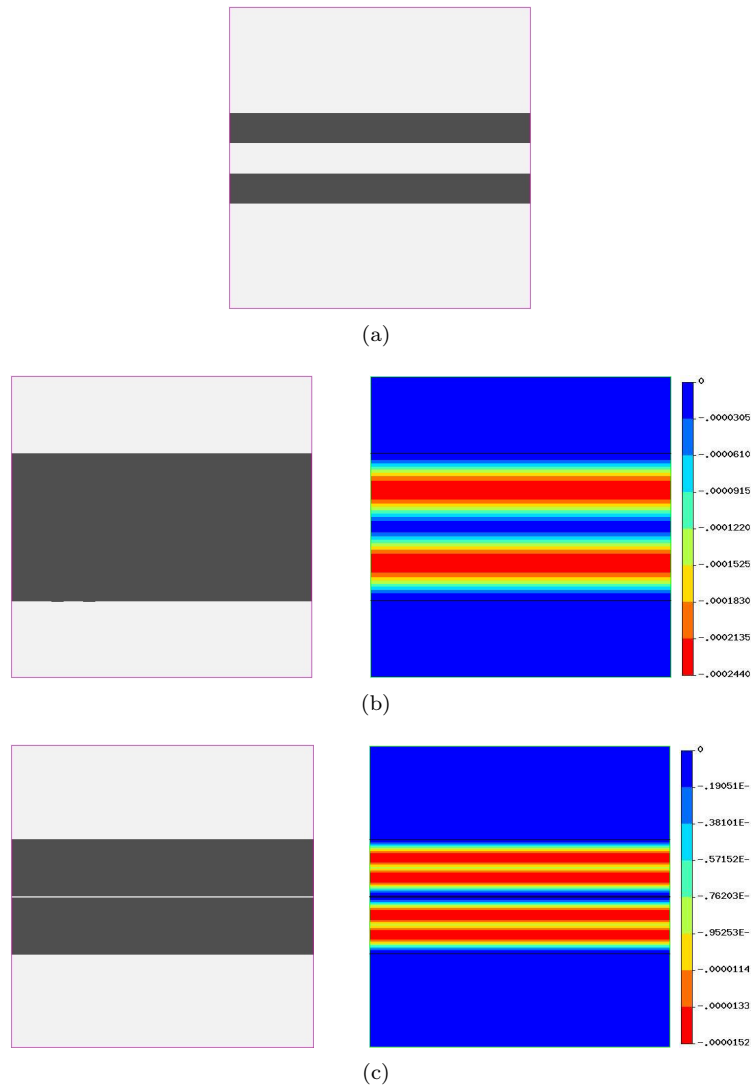


Figure 3.56: (a): Initialization; optimized shape for problem (3.30) and energy density for (b): $d_{min} = 0.50$; (c): $d_{min} = 0.25$.

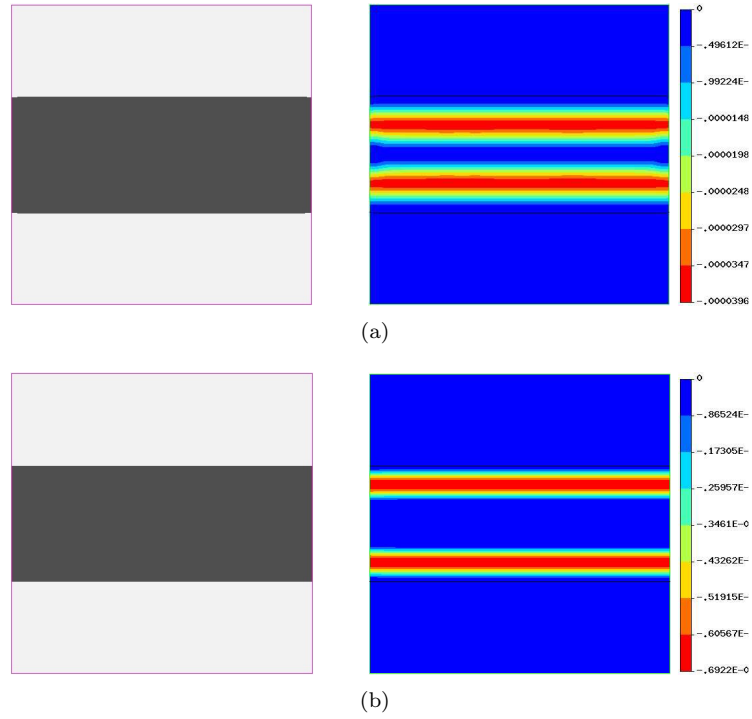


Figure 3.57: Optimized shape and energy density for (a) $d_{min} = 0.50$; (b): $d_{min} = 0.25$, using the energy functional (3.33).

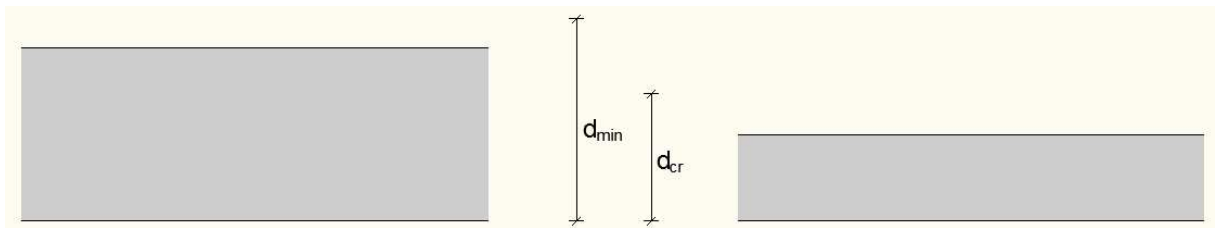


Figure 3.58: The bar on the left will increase in size, while the bar on the right will disappear when the energy functional (3.34) is minimized.

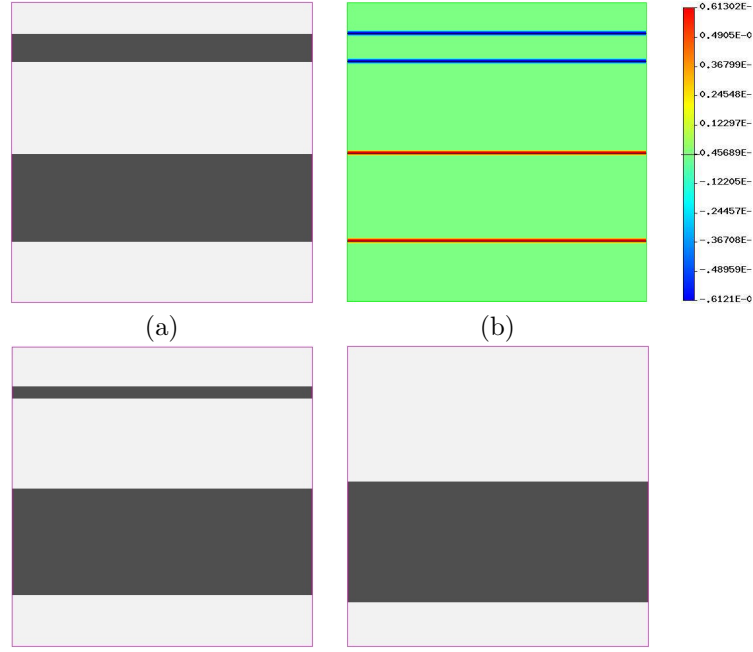


Figure 3.59: (a): Initialization; (b): initial shape gradient; (c): iteration 10; (d): optimized shape, using the energy functional (3.34), $d_{min} = 0.4$ and $d_{cr} = 0.2$.

of d_Ω , we can see in Figure 3.60(c) that the previous distortions disappear. However, one can observe that the lower-right bar has not increased in size. The reason is that using ψ instead of d_Ω , the "rays" emerging from the boundary that touch the boundary of the working domain do not detect a point on the skeleton of the shape. An intuitive modification that works well in numerical practise, is to consider that in case a "ray" passes to the exterior of the working domain, the skeleton lies at half the distance from the point on $\partial\Omega$ to ∂D . Applying this modification, we get the optimized shape of Figure 3.60(d). In all of the examples concerning the use of the energy functionals E_1, E_2, E_3 , these two choices, i.e. the use of the reinitialized function ψ and the modification in the detection of the skeleton have been used. The results for problem (3.35) for different values of d_{min} using functionals (3.29) and (3.33) are respectively shown in figures 3.61 and 3.62. Using an augmented Lagrangian algorithm without checking the decrease of the objective function at each step avoids the previously described problem of topological changes for $E_1(\Omega)$. The optimized shapes look quite similar, but for the case $d_{min} = 0.30$, the addition of the perimeter term in E_2 seems to affect the curvature of the bars. Also, we mention that for the same thickness limit, both the final topologies using E_1 and E_2 differ from the one in Figure 3.51(d), which was obtained by the explicit thickness constraint. Adding functionals E_1 or E_2 since the beginning of the optimization algorithm requires some more attention. The choice of the weight coefficient ℓ_E plays a major role in the efficiency of the algorithm. If we adopt the same scaling as before, it is highly possible that very slight changes in the initial topology will occur. This is shown in Figure 3.63. Instead we can choose to start with a smaller value of ℓ_E and increase it during the optimization. For the results of Figure 3.64 the weight multiplier is initialized as $\ell_E = 0.3V(\Omega^0)/E_1(\Omega^0)$ and is multiplied by 1.5 every 20 iterations. This update process is stopped after 100 steps. In figures 3.64(e),(f) we can see that the algorithm has not been able to remove completely a strange feature that exists in the shape. This is clearly an artifact of the premature dominance of the thickness functional. However, as we see in the same figure, this feature augments in size under the effect of the thickness functional, since it has not yet obtain the minimum thickness size, turns and merges with another bar under the effect of the compliance and finally disappears. Using a multiplier of 1.2 instead of 1.5 and keeping updating ℓ_E to the end of the optimization algorithm leads to a smoother penalization, as we can see in Figure 3.65. Contrary to the use of E_1 and E_2 , the use of E_3 in a second step does not seem to be a robust choice. The reason is that the optimized shape without the thickness penalization is very likely to contain thin features, which however can play a significant role for its mechanical behaviour. If these members have a thickness lower than the value of d_{cr} , the algorithm will probably eliminate them, which can cause significant instabilities during the optimization. Of course, the case when d_{cr} has a very low value is not of great interest, since then the functional has a samelike behaviour like E_1 (as $d_{cr} \rightarrow 0$, $E_3 \rightarrow E_1$).

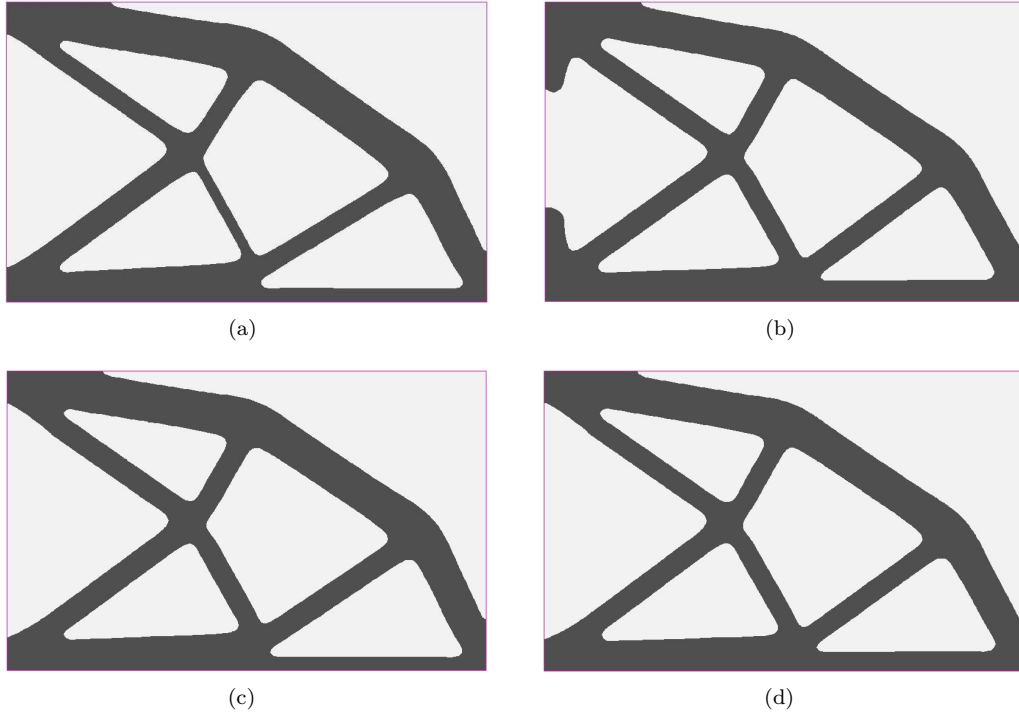


Figure 3.60: Optimized shape for problem (3.35) using the energy functional (3.29) and $d_{min} = 0.15$ (a): without thickness constraint; using (b): d_{Ω} ; (c): ψ ; (d): ψ and modifying the skeleton detection , for the 2d cantilever.

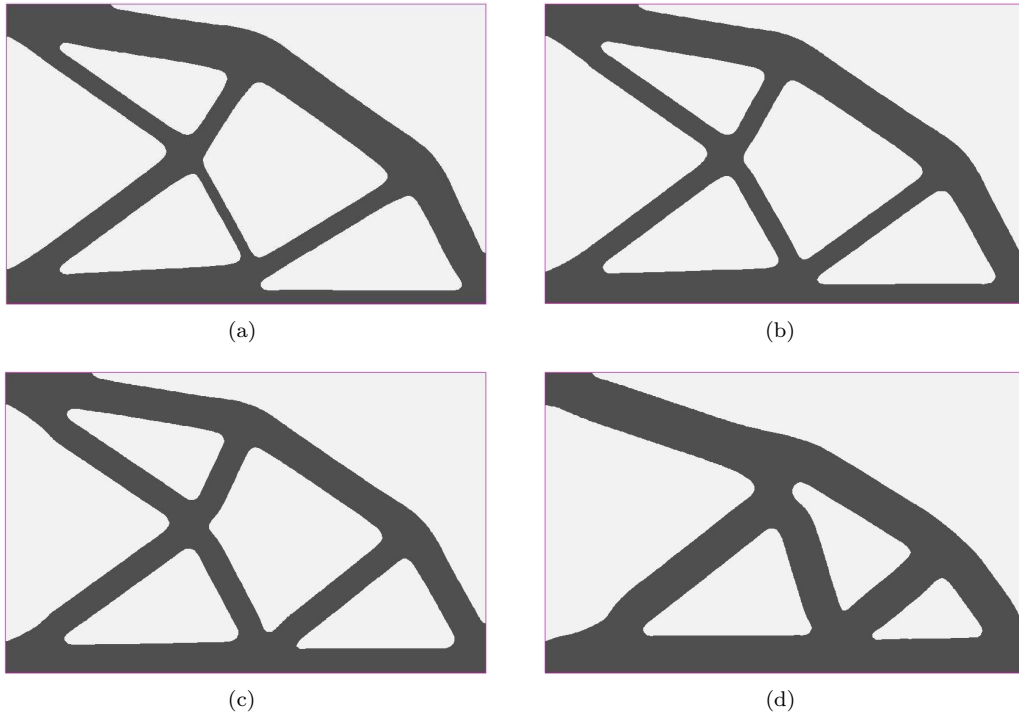


Figure 3.61: (a): Initialization; optimized shapes for (b): $d_{min} = 0.15$; (c): $d_{min} = 0.20$; (d): $d_{min} = 0.30$, for problem (3.35) using $E_1(\Omega)$, for the 2d cantilever.

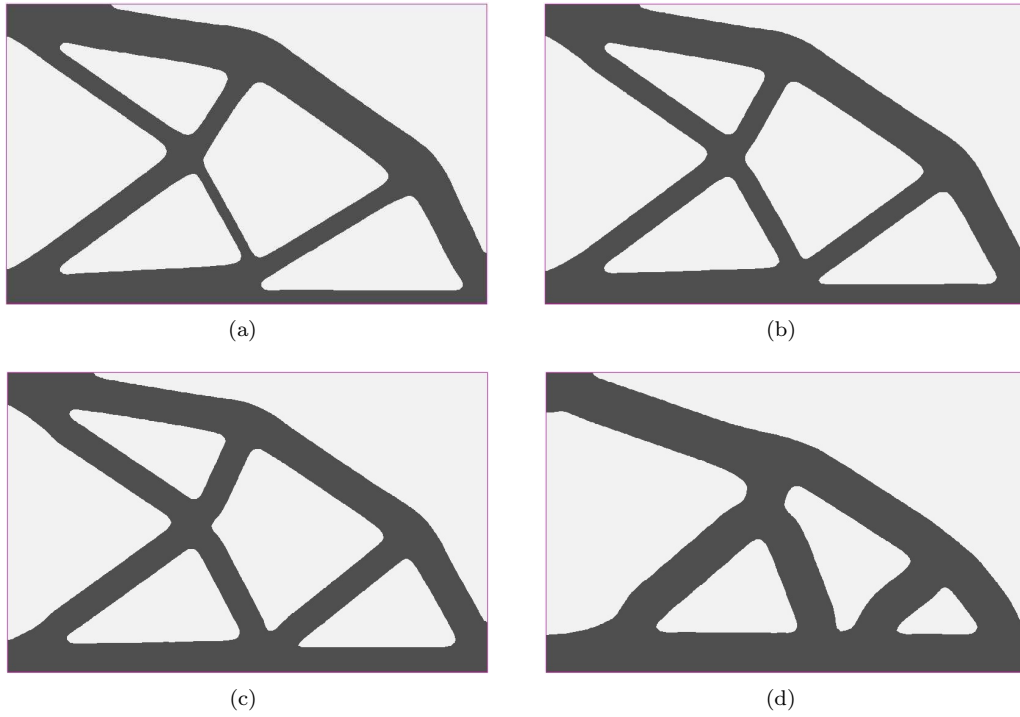


Figure 3.62: (a): Initialization; optimized shapes for (b): $d_{min} = 0.15$; (c): $d_{min} = 0.20$; (d): $d_{min} = 0.30$, for problem (3.35) using $E_2(\Omega)$, for the 2d cantilever.

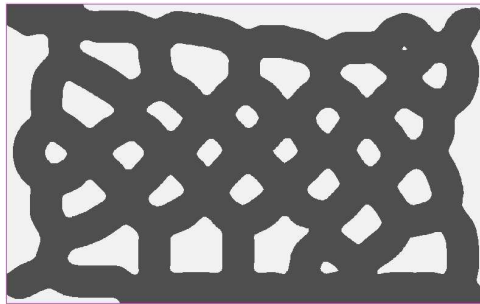


Figure 3.63: Optimized shape for problem (3.35) and $d_{min} = 0.30$, using E_1 and $\ell_E = V(\Omega^0)/E_1(\Omega^0)$, for the 2d cantilever.

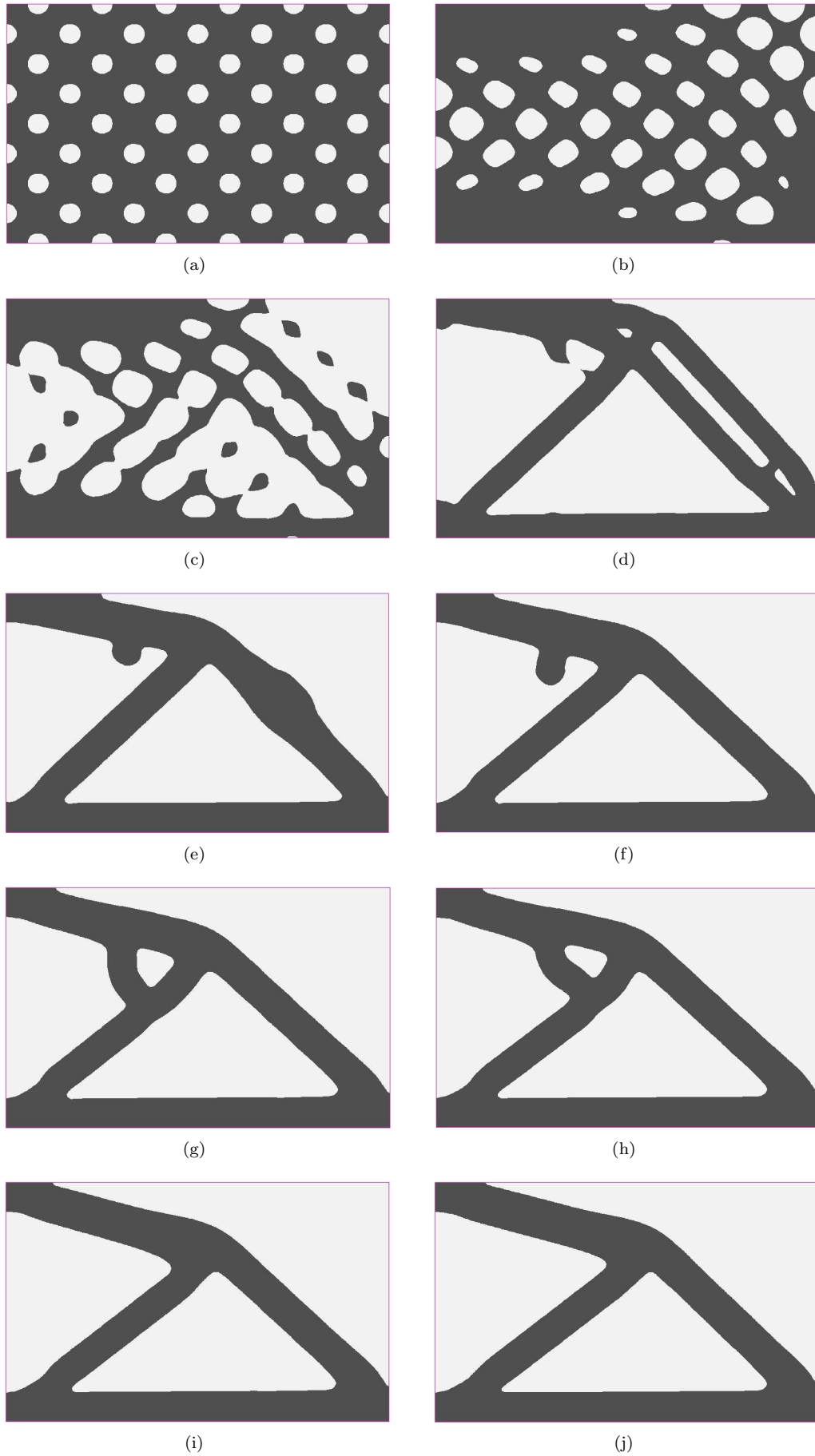


Figure 3.64: (a): Initialization; (b)-(i): iterations 15, 25, 50, 100, 150, 200, 250, 350; (j): optimized shape after 400 iterations for problem (3.35), using $E_1(\Omega)$ and $d_{min} = 0.30$, for the 2d cantilever.

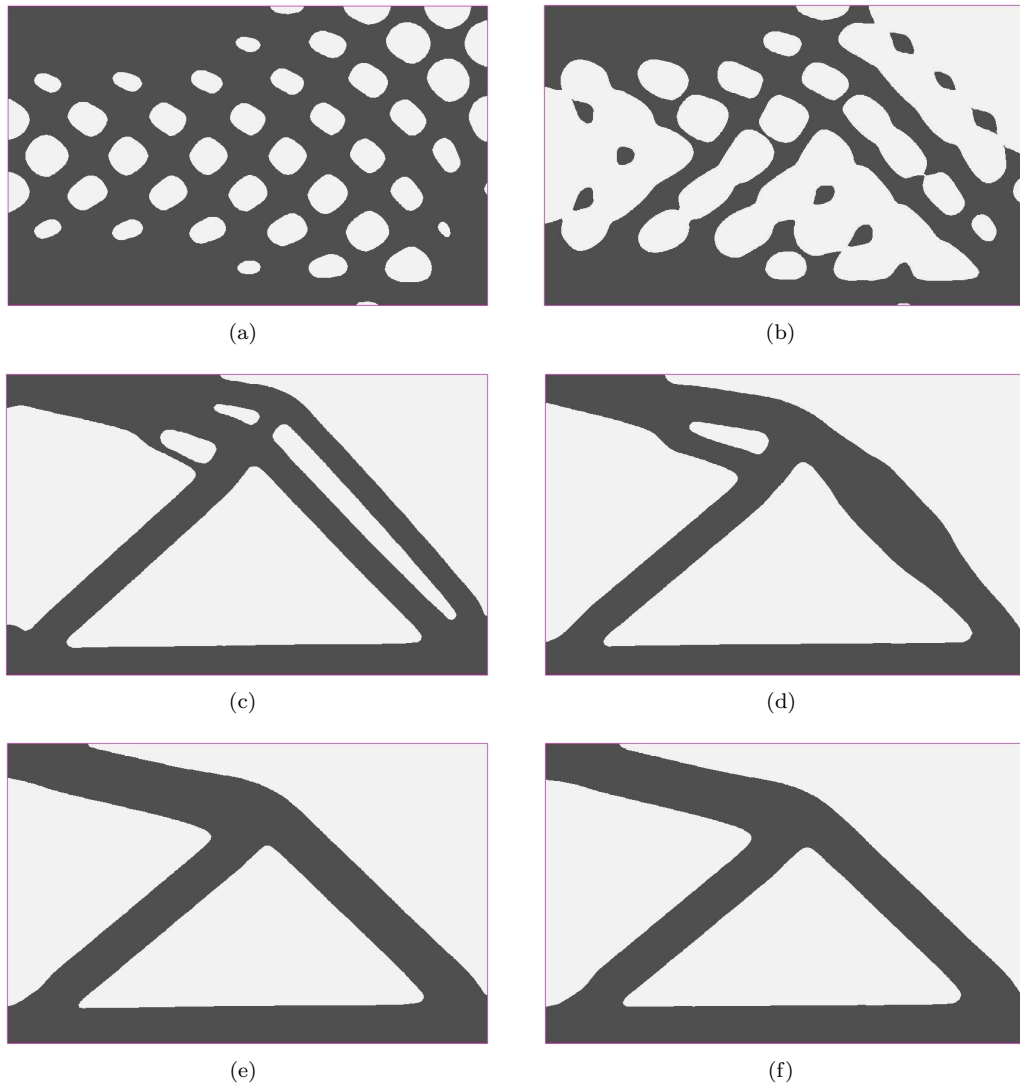


Figure 3.65: (a)-(e): Iterations 15, 25, 50, 100, 150; (f): optimized shape after 200 iterations for problem (3.35), using $E_1(\Omega)$ and $d_{min} = 0.30$, for the 2d cantilever.

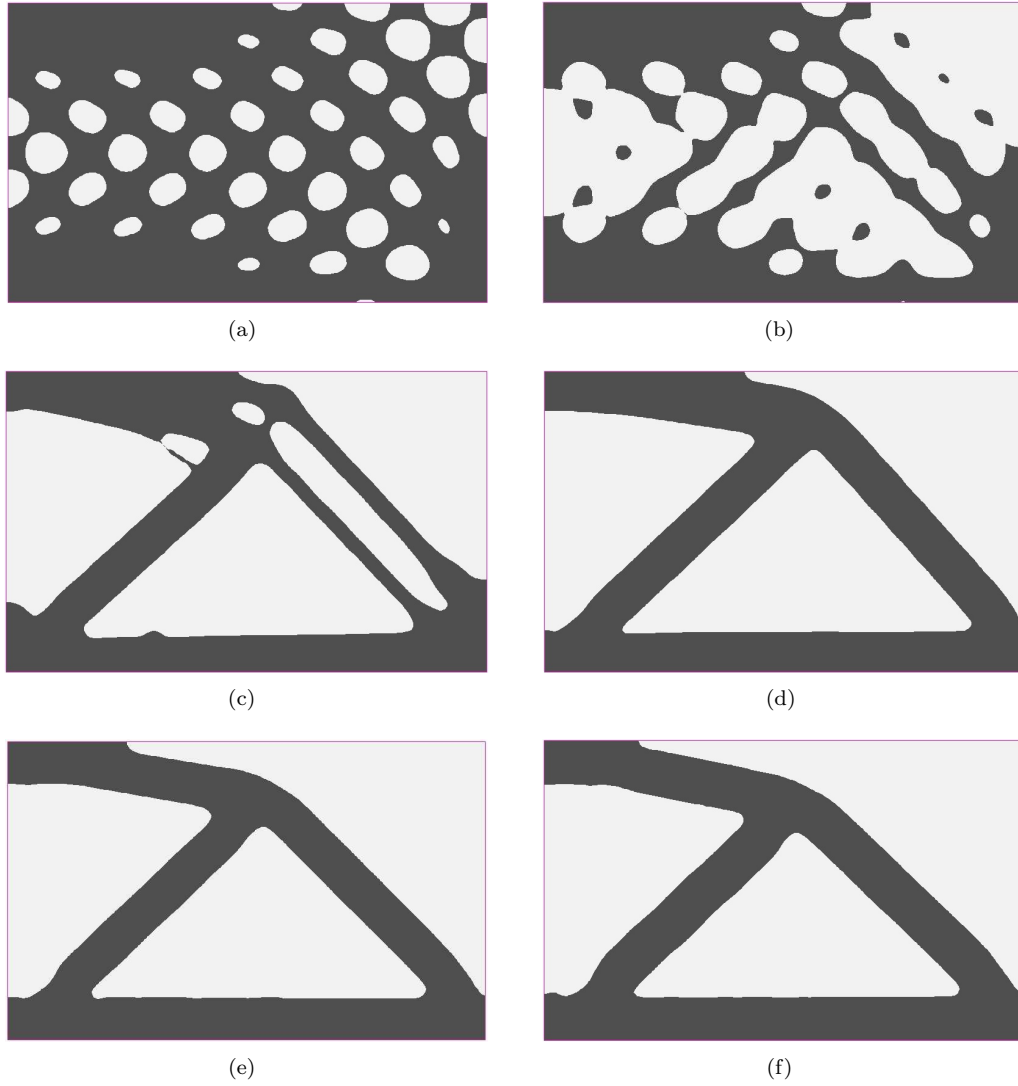


Figure 3.66: (a)-(e): Iterations 15, 25, 50, 100, 150; (f): optimized shape after 200 iterations for problem (3.35), using $E_3(\Omega)$ and $d_{min} = 0.30$, for the 2d cantilever.

Therefore, we prefer to add E_3 since the very beginning. As previously, the choice of ℓ_E plays also an important role in the optimization process. For the results of Figure 3.66 we have set $d_{min} = 0.30$, $d_{cr} = 0.15$, ℓ_E is initialized as $\ell_E = 0.3V(\Omega^0)/E_3(\Omega^0)$ and is multiplied by 1.5 every 20 iterations until the end of the optimization algorithm.

2d MBB beam

We consider again the MBB beam of Figure 3.31. Problem (3.25) is solved for $g_{max}^1 = 50$ and Figure 3.67 displays the initialization and the optimized shape for the half-domain. Initializing problem (3.28) with the shape of Figure 3.67(b), the optimized shapes for different values of d_{min} are plotted in Figure 3.68. Solving problem (3.35) for $d_{min} = 0.2$, $g_{max}^1 = 50$ for the energy functional E_1 and starting from the initial non-optimized shape, we take a different optimal solution, shown in Figure 3.69.

2d displacement inverter

The last example of this section concerns the design of a two-dimensional displacement inverter mechanism. The displacement of the upper-left and lower-left corner are fixed and we apply a unitary horizontal force at the middle (see Figure 3.70). We search to minimize the horizontal displacement u_h at the middle

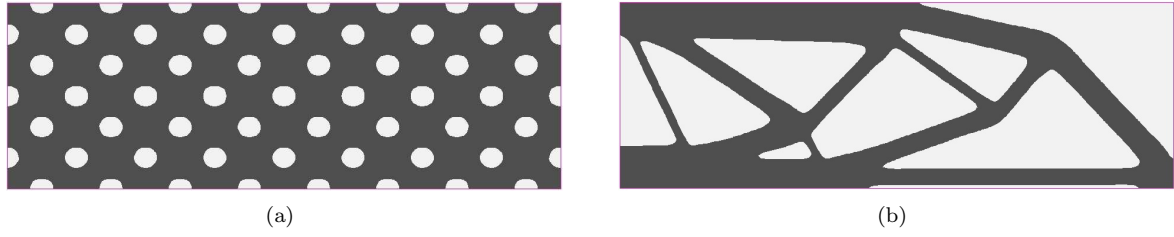


Figure 3.67: (a): Initialization; (b): optimized shape, for problem (3.25) and $g_{max}^1 = 50$, for the 2d MBB beam.

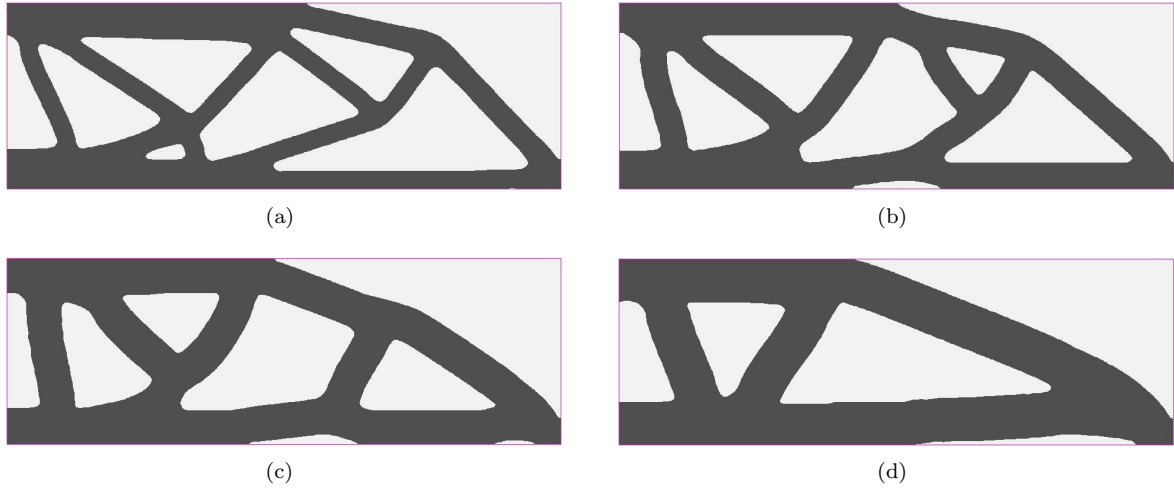


Figure 3.68: Optimized shapes for problem (3.28), $g_{max}^1 = 50$ and (a): $d_{min} = 0.10$; (b): $d_{min} = 0.15$; (c): $d_{min} = 0.20$; (d): $d_{min} = 0.25$, for the 2d MBB beam.

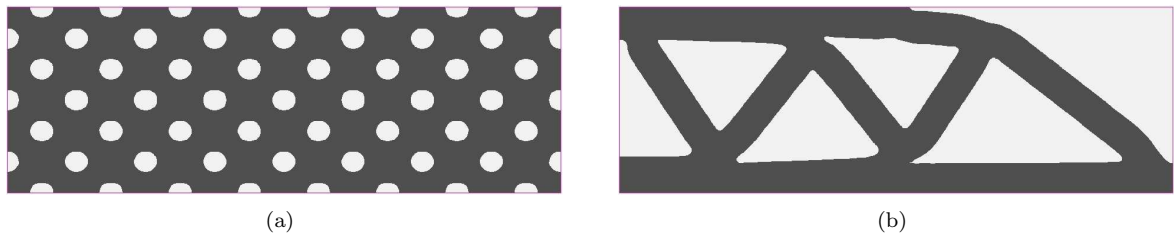


Figure 3.69: (a): Initialization and (b): optimized shape for problem (3.35), $d_{min} = 0.20$ and $g_{max}^1 = 50$, using E_1 , for the 2d MBB beam.

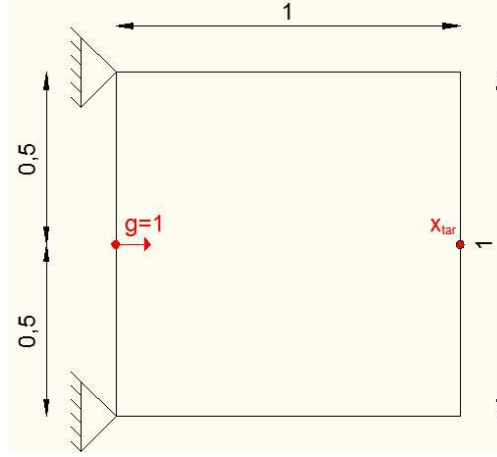


Figure 3.70: Boundary conditions for the displacement inverter mechanism.

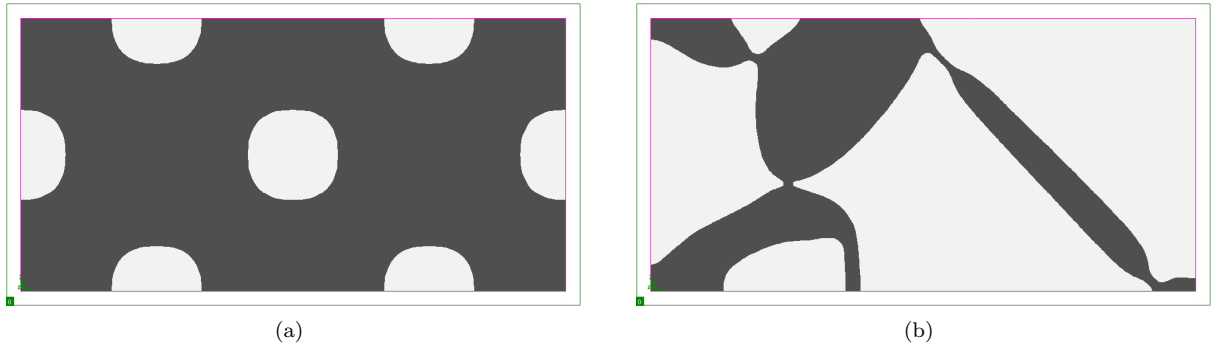


Figure 3.71: (a): Initialization and (b): optimized shape, without thickness limitations, for the displacement inverter mechanism.

point of its right side, denoted x_{tar} . The optimization problem reads

$$\begin{aligned} \min_{\Omega \in \mathcal{U}_{ad}} \quad & u_h(x_{tar}) \\ \text{s.t.} \quad & \int_{\Omega} dx \leq V_{max}. \end{aligned} \quad (3.36)$$

Due to symmetry, only the upper half-domain is used for the analysis. In all results here, V_{max} is set to $0.30|D|$. An initialization and its corresponding optimized shape are shown in Figure 3.71. As expected, we observe some very thin parts that act like hinges.

Usually the scale of interest for such structures is so small, that the geometric uncertainty on the actually manufactured shape may have a significant impact. Consequently, designs containing thin features shall be avoided for such structures. One way to achieve this goal is to impose a minimum thickness constraint and solve the problem

$$\begin{aligned} \min_{\Omega \in \mathcal{U}_{ad}} \quad & u_h(x_{tar}) \\ \text{s.t.} \quad & \int_{\Omega} dx \leq V_{max}, \\ & P_{MinT}(\Omega) = \int_{\partial\Omega} \int_0^{d_{min}} \left[(d_{\Omega}(x - \xi n(x)))^+ \right]^2 d\xi dx = 0. \end{aligned} \quad (3.37)$$

The optimized shapes and their deformed configurations for different values of d_{min} are shown in Figure 3.72. In Table 3.6, we display the final displacement for each case. As expected, increasing the minimum thickness limit d_{min} leads to a less compliant structure and consequently to a greater displacement value. For $d_{min} = 0.08$, we see that the displacement of the optimized shape has become positive, i.e. the structure no longer acts as a displacement inverter.

One may wonder if it is possible to formulate a minimum thickness constraint in the form of (3.2) instead of using the notion of offset sets. In order to formulate such a constraint, we need to decide

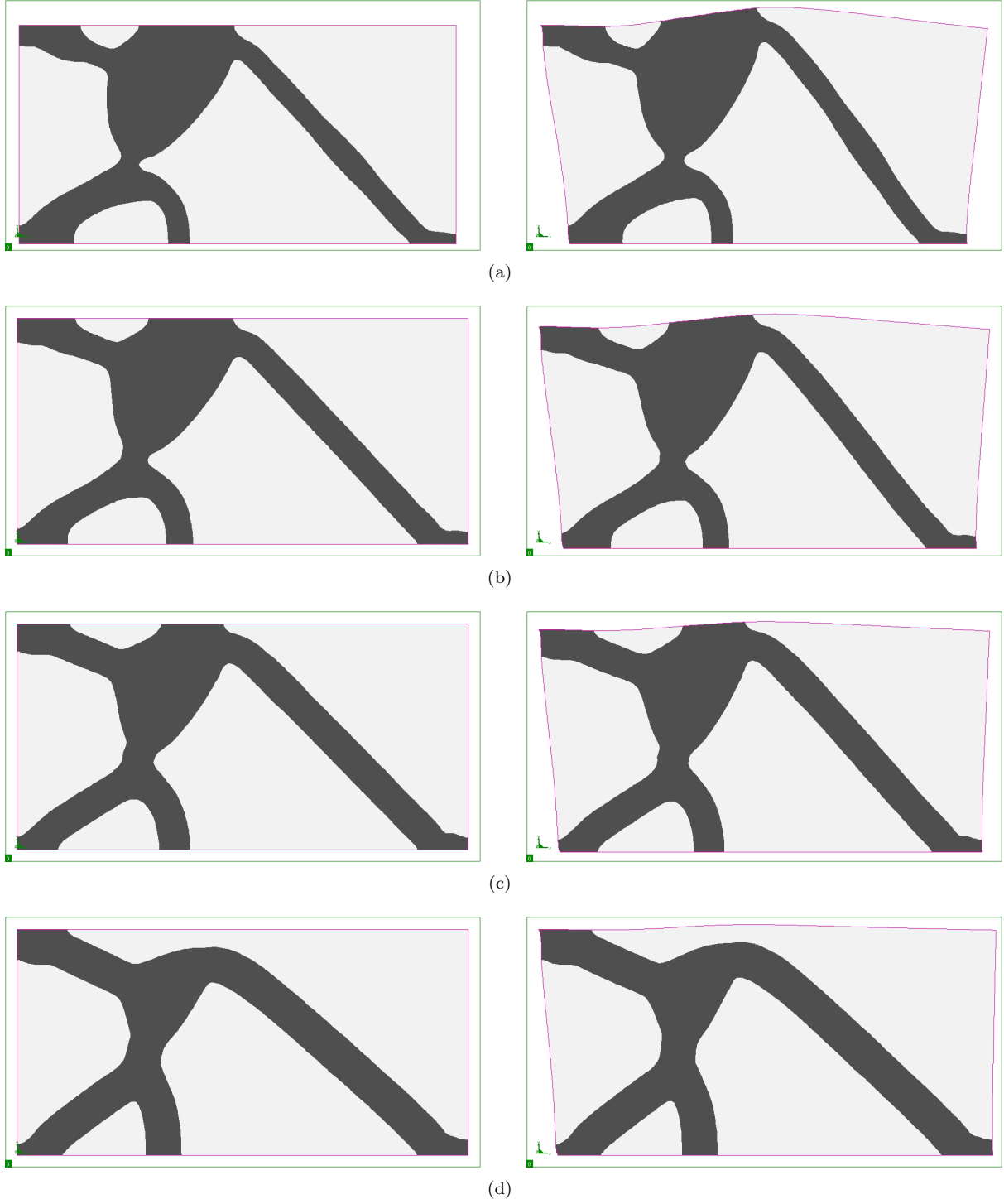


Figure 3.72: Optimized shapes and deformed configurations for (a): $d_{min} = 0.05$; (b): $d_{min} = 0.06$; (c): $d_{min} = 0.07$; (d): $d_{min} = 0.08$, for the displacement inverter mechanism.

Table 3.6: 2d displacement inverter.

	Without thickness restriction	$d_{min} = 0.05$	$d_{min} = 0.06$	$d_{min} = 0.07$	$d_{min} = 0.08$
$u_h(x_{tar})$	-47.56	-12.34	-5.53	-0.45	3.89

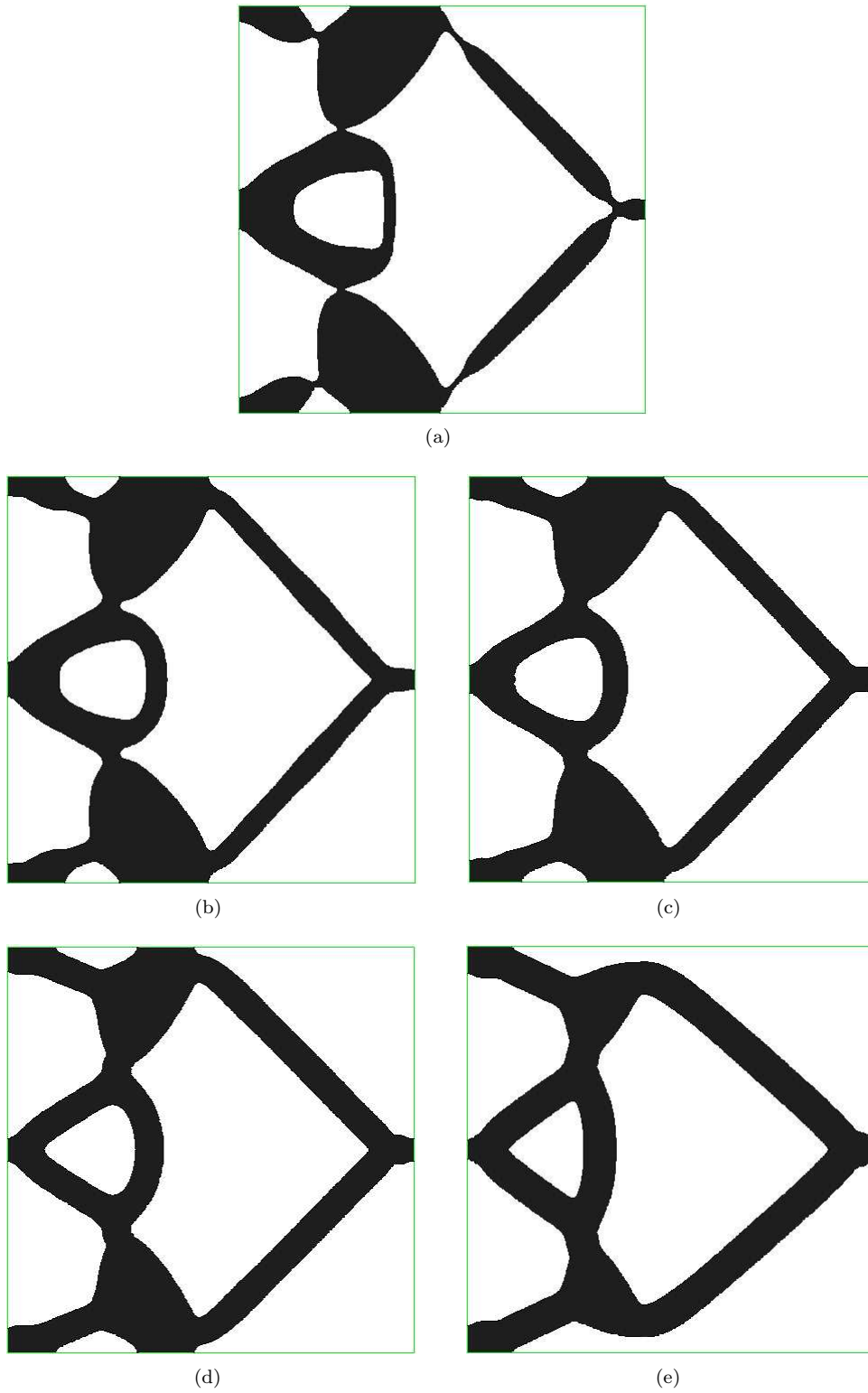


Figure 3.73: Full optimized shapes (a): without thickness constraint; for (b): $d_{min} = 0.05$; (c): $d_{min} = 0.06$; (d): $d_{min} = 0.07$; (e): $d_{min} = 0.08$, for the displacement inverter mechanism.

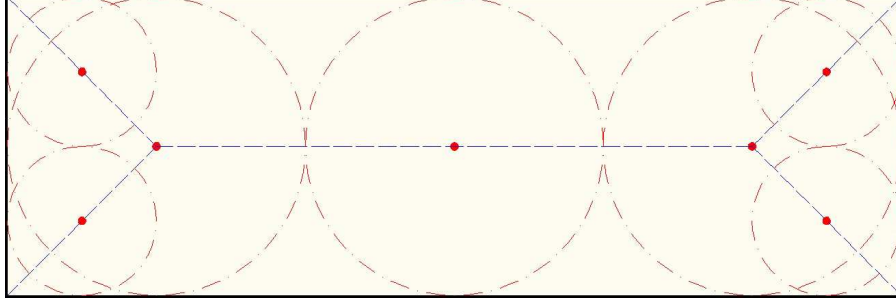


Figure 3.74: Skeleton of a rectangle (in blue) and maximal disks (in red).

which points to check. A first answer would be to test the signed distance function at the points that belong to the skeleton. Although it is true that if a minimum thickness limit is violated then there will be points on the skeleton whose value of d_Ω will be under this limit, the inverse is not always true. Consider, for example, the shape of a rectangle in Figure 3.74. Its skeleton is depicted in blue colour. The signed distance function at the parts of the skeleton which are oriented in a direction ± 45 degrees takes small values, although the thickness of the rectangle defined using offset sets is not that small. On the contrary, the values of d_Ω on the horizontal part of the skeleton correspond to what one would expect as half-thickness of the bar. Without being precise, we shall name "inconvenient" those parts of the skeleton, where the value of the signed distance function does not provide us with correct information about the minimum thickness at this area. We shall also call "interesting" the skeleton's parts where $|d_\Omega|$ takes values close to the half of the thickness, when the last is defined using the notion of offset sets.

We remind that every point on the skeleton is equidistant to two or more points on the boundary $\partial\Omega$, which means that the rays emerging from these boundary points cross at the same point on the skeleton. One can observe that these "inconvenient" parts of the skeleton seem to be formed by rays crossing almost perpendicularly, while at the "interesting" part rays are almost parallel. This observation drives us to the following numerical method to eliminate some "inconvenient" parts. First, we introduce the numerical function

$$k(d_\Omega) = 0.5 - 0.5 \frac{\nabla^b d_\Omega \cdot \nabla^f d_\Omega}{|\nabla^b d_\Omega| |\nabla^f d_\Omega|}, \quad (3.38)$$

where ∇^b and ∇^f mean that the gradient is evaluated using respectively backward and forward finite differences. The function $k(d_\Omega)$ takes values from 0 to 1, depending on the angle at which the isocontours of d_Ω cross at the skeleton. At the "inconvenient" parts we expect $k(d_\Omega)$ to take values close to 0.5. Using a threshold value k_{min} we can construct a cut-off function as

$$k_\Sigma(d_\Omega) = \max(\text{sign}(k(d_\Omega) - k_{min}), 0). \quad (3.39)$$

An example is shown in Figure 3.75. In the upper part we can see a shape in black color and a plot of the function $k_\Sigma(d_\Omega)$ for $k_{min} = 0.6$. Below we plot in 3d its signed distance function d_Ω . It turns out that, using a threshold greater than 0.5 helps to avoid the "inconvenient" parts of the skeleton, which can be identified in the plot of d_Ω as the ridges formed by isocontours crossing almost perpendicularly. Finally, we can formulate a minimum thickness penalty functional as

$$P_{MinT}(\Omega) = \int_\Omega k_\Sigma(d_\Omega) \left[(d_\Omega(x) + d_{min}/2, 0)^+ \right]^2 dx. \quad (3.40)$$

The shape derivation of (3.40) is not evident at all. In fact, (3.40) penalizes values of d_Ω at some part of the skeleton. As we have seen at Remark 3.3.4, the expression of $d'_\Omega(\theta)$ is not straightforward for these points, but depends on the choice of θ . Furthermore, it is even less evident how and if one could differentiate the function $k_\Sigma(d_\Omega)$. Ignoring the dependence of $k_\Sigma(d_\Omega)$ on the shape Ω , we have tried some numerical tests using formulation (3.40). Our numerical experience shows that, in all generality, such a formulation is not efficient, since the skeleton -both its "interesting" and "inconvenient" parts- and thus $k_\Sigma(d_\Omega)$ are discontinuous with respect to perturbations of the shape.

3.7.3 Combination of thickness constraints

There is no theoretical difficulty in combining the previously presented thickness constraints. Of course, adding more constraints in the optimization algorithm increases its complexity, as well as the possibility

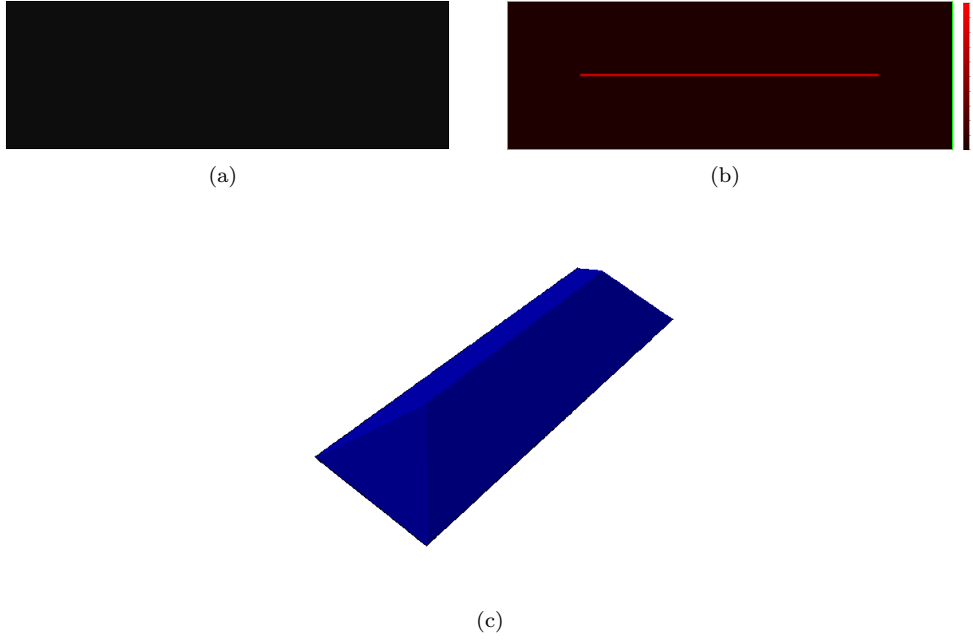


Figure 3.75: (a): Shape (in black); (b): $k_\Sigma(d_\Omega)$ for $k_{min} = 0.6$; (c): d_Ω .

that it does not manage to find a feasible shape, either because of reasons of non existence, or because the necessary topological changes are not likely to take place.

Maximum thickness and minimum distance between members

In Figure 3.29 we have shown the optimized shapes for the two dimensional cantilever of Figure 3.27, when a maximum thickness constraint is applied. For $d_{max} = 0.40$, we can observe the existence of small holes and closely spaced parts in the shape that we would like now to avoid. Starting from the shape of Figure 3.29(b), we add a constraint on the minimum distance between members to problem (3.26). The new optimization problem reads

$$\begin{aligned}
 \min_{\Omega} \quad & \int_{\Omega} dx \\
 \text{s.t.} \quad & \int_{\partial\Omega} g \cdot u ds \leq g_{max}^1, \\
 P_1(\Omega) = P_{MaxT}(\Omega) = & \left(\frac{\int_{\Omega} f(d_\Omega(x)) d_\Omega(x)^2 dx}{\int_{\Omega} f(d_\Omega(x)) dx} \right)^{\frac{1}{2}} \leq g_{max}^2, \\
 P_2(\Omega) = P_{MMD}(\Omega) = & \int_{\partial\Omega} \int_0^{d_{min}} \left[(d_\Omega(s + \xi n(s)))^+ \right]^2 d\xi ds = 0,
 \end{aligned} \tag{3.41}$$

where $g_{max}^1 = 40$, $d_{max} = 0.40$ and d_{min} accounts for the minimum feature size. The results for $d_{min} = 0.05$ and $d_{min} = 0.10$ are presented in Figure 3.76.

Maximum and minimum thickness

We consider once more the MBB beam example of Figure 3.31. In Figure 3.33 we have shown the optimized shapes when a maximum thickness constraint is added to the original problem. We can see, for example for $d_{max} = 0.30$, the apparition of thin features in the shape that we would like now to avoid. Starting from the shape of Figure 3.33(a), we also add a minimum thickness constraint to problem (3.26).

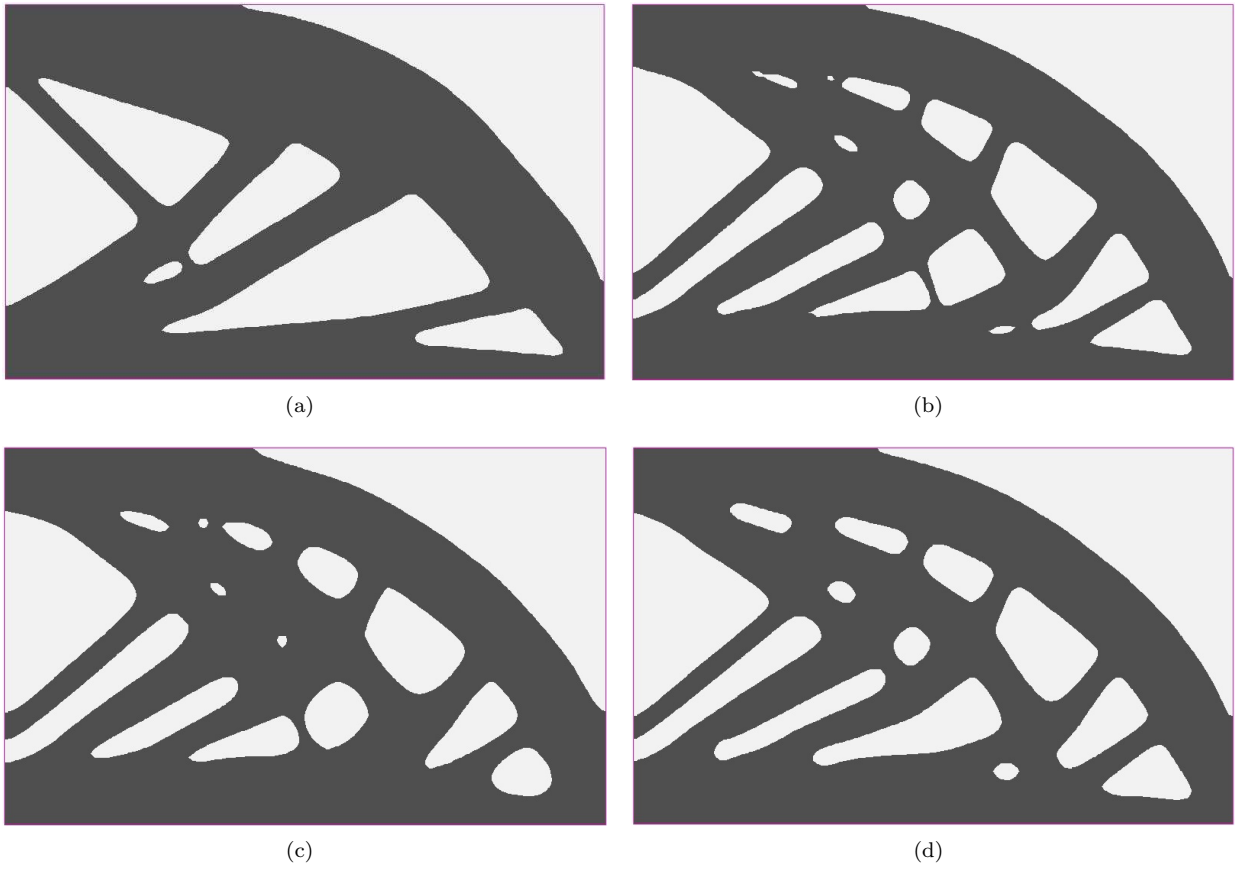


Figure 3.76: Optimized shapes for (a): $g_{max}^1 = 40$; (b): $g_{max}^1 = 40$ and $d_{max} = 0.40$; (c): $g_{max}^1 = 40$, $d_{max} = 0.40$ and $d_{min} = 0.05$; (d): $g_{max}^1 = 40$, $d_{max} = 0.40$ and $d_{min} = 0.10$, for the 2d cantilever.

The new optimization problem reads

$$\begin{aligned}
& \min_{\Omega} \int_{\Omega} dx \\
& \text{s.t.} \quad \int_{\partial\Omega} g \cdot u ds \leq g_{max}^1, \\
& P_1(\Omega) = P_{MaxT}(\Omega) = \left(\frac{\int_{\Omega} f(d_{\Omega}(x)) d_{\Omega}(x)^2 dx}{\int_{\Omega} f(d_{\Omega}(x)) dx} \right)^{\frac{1}{2}} \leq g_{max}^2, \\
& P_2(\Omega) = P_{MinT}(\Omega) = \int_{\partial\Omega} \int_0^{d_{min}} \left[(d_{\Omega}(x - \xi n(x)))^+ \right]^2 d\xi dx = 0,
\end{aligned} \tag{3.42}$$

where $g_{max}^1 = 40$, $d_{max} = 0.30$ and d_{min} accounts for the minimum feature size. The results for $d_{min} = 0.10$ and $d_{min} = 0.15$ are presented in Figure 3.77.

3.8 Other formulations of the thickness constraints

Inspired from the formulations used to control a notion of thickness in [61],[63] by J. Guest et al., in the framework of the SIMP method (see section 1.3), we try in this section to study if considerations using the same logic can be applied in the framework of the level-set method for shape and topology optimization.

3.8.1 Maximum Thickness

Formulation of the constraint

The initial concept of the maximum thickness constraint formulated in [61] is the following: defining at each point $x \in \Omega$ its closed ball of radius $r = d_{max}/2$ as

$$B(x, r) = \{y \in \Omega, \text{ s.t. } |x - y| \leq r\},$$

the pointwise constraint reads

$$\int_{B(x, r) \cap D} \rho(y) dy < V_{B(x, r) \cap D}, \tag{3.43}$$

where $\rho(y)$ is the density at the point $y \in \Omega$ and $V_{B(x, r) \cap D}$ is the volume of the intersection of the ball $B(x, r)$ with the working domain D . The interpretation of the above constraint in the framework of a "classical" shape description would be

$$\int_{B(x, r) \cap D} \chi_{\Omega}(y) dy < V_{B(x, r) \cap D}, \tag{3.44}$$

where χ_{Ω} is the characteristic function of the domain Ω .

Then, J. Guest proposes to use another formulation instead of (3.43), that takes under consideration the volume of the void part in $B(x, r)$. The final constraint, again in a "classical" description, reads

$$\int_{B(x, r) \cap D} (1 - \chi_{\Omega}(y)) dy \geq V_{min}, \tag{3.45}$$

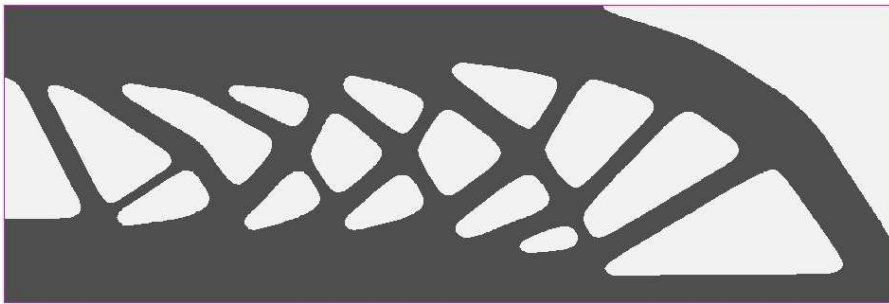
where $V_{min} > 0$ is the minimum required volume of void part in $B(x, r)$. One proposal is to use $V_{min} = \alpha_{void} V_{B(x, r) \cap D}$, where $\alpha_{void} \approx 5\%$ is a small scalar parameter that defines the minimum demanded percentage of void in the ball of a point.

Comparison with the formulation based on d_{Ω}

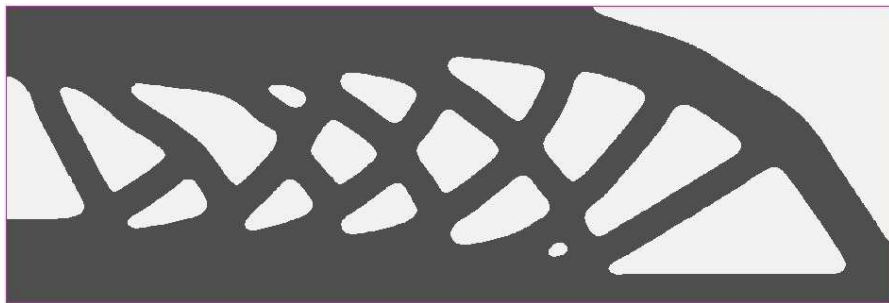
We begin with the general formulation (3.44) and compare it with our formulation (3.2) based on the signed distance function. When inequality (3.2) is satisfied, there exists no point whose distance to the boundary is greater than $d_{max}/2$ and thus there is no point which is the center of a ball of radius greater than $d_{max}/2$, fully contained in the shape. Inequality (3.44) is strict, i.e. the allowed inscribed circle must be of radius less than $d_{max}/2$. Satisfying inequality (3.44) means that no inscribed circle of radius greater



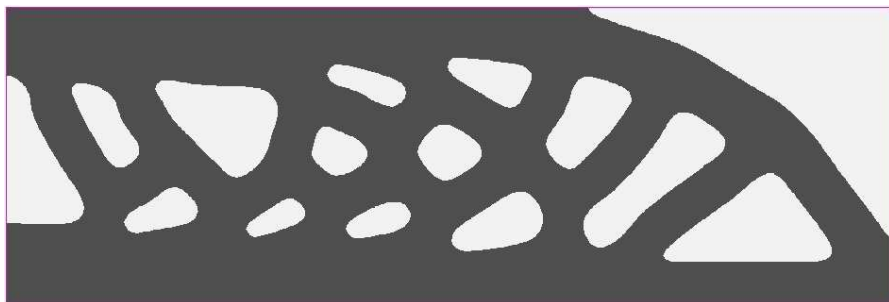
(a)



(b)



(c)



(d)

Figure 3.77: Optimized shapes for (a): $g_{max}^1 = 40$; (b): $g_{max}^1 = 40$ and $d_{max} = 0.30$; (c): $g_{max}^1 = 40$, $d_{max} = 0.30$ and $d_{min} = 0.10$; (d): $g_{max}^1 = 40$, $d_{max} = 0.30$ and $d_{min} = 0.15$, for the 2d MBB beam.

or equal to $d_{max}/2$ exists and thus no point is at a distance greater than $d_{max}/2$ from the boundary, so inequality (3.2) is also satisfied. Thus, the two formulations are very similar.

Let us pass now to the final constraint (3.45). From our point of view, this formulation is just a relaxation of (3.44), which is numerically easier to implement. The reason is that inequality (3.44) is in fact equivalent to

$$\int_{B(x,r) \cap D} \chi(y) dy \neq V_{B(x,r) \cap D}, \quad (3.46)$$

since the right-hand side is an upper bound of the left-hand side. Numerically, such a strict inequality constraint is not easy to handle.

A drawback of formulation (3.45) is that the maximum allowed thickness is reduced from its initial value d_{max} , depending on the choice of the parameter α_{void} in V_{min} . However, implementing constraint (3.45) in a shape optimization framework could help alleviating the problem of small balls surrounded by a large bulk of material, but for small values of α_{void} we shall expect it to be still somehow unstable, since small balls could easily disappear and would need to be regenerated either using a topological derivative or via the inherent mechanism described in Figure 3.24.

The cost of calculation increases with mesh refinement for all the three methods we have presented for the maximum thickness. The "coarea" formula requires to travel slower up to the skeleton, for reasons of precision, the size of the linear system in the "volumetric" formula increases, while for this last method the number of nodes in the ball of each point augments, which makes the calculations more costly. In general, we shall expect that the "coarea" formula is the least influenced by a mesh refinement. Increasing the maximum allowed thickness (d_{max}) can also increase significantly the cost of the method presented in this section and slightly the one of the "coarea" method, while the "volumetric" method is not affected at all.

Shape differentiation

In order to ease the presentation, let us rewrite the pointwise constraint (3.45) in the general form

$$g(\Omega, x) \leq g_{max}(x), \quad \forall x \in \Omega, \quad (3.47)$$

where $g(\Omega, x) = \int_{B_{eff}(x,r)} \chi_{\Omega}(y) dy$, $g_{max}(x) = \int_{B_{eff}(x,r)} dy - V_{min}$, $B_{eff}(x, r) = B(x, r) \cap D$.

As previously, we shall use a global constraint of the same type as (3.24). However, the formulation will be slightly different since the right-hand side of inequality (3.47) depends on the space variable x . This dependence is due to the change of the "effective ball" $B_{eff}(x, r)$ as we approach the boundary of the working domain D . Finally, the global constraint reads

$$P_{MaxT}(\Omega) = \left(\frac{\int_{\Omega} f(g) g(\Omega, x)^2 dx}{\int_{\Omega} f(g) g_{max}(x)^2 dx} \right) \leq 1. \quad (3.48)$$

Lemma 3.8.1. *The shape derivative of $P_{MaxT}(\Omega)$ in (3.48) reads*

$$P'_{MaxT}(\Omega)(\theta) = \int_{\partial\Omega} \theta(s) \cdot n(s) V(s) ds,$$

where

$$V(s) = + \frac{1}{(C_2(\Omega, x))^2} \left[C_2(\Omega, x) \left(f(g) g(\Omega, s)^2 + \int_{\Omega} C_3(\Omega, x) \chi_{B_{eff}(x,r)}(s) dx \right) \right] \\ - \frac{1}{(C_2(\Omega, x))^2} \left[C_1(\Omega, x) \left(f(g) g_{max}(s)^2 + \int_{\Omega} \frac{\partial f(g)}{\partial g} g_{max}(x)^2 \chi_{B_{eff}(x,r)}(s) dx \right) \right],$$

$$C_1(\Omega, x) = \int_{\Omega} f(g) g(\Omega, x)^2 dx,$$

$$C_2(\Omega, x) = \int_{\Omega} f(g) g_{max}(x)^2 dx$$

and

$$C_3(\Omega, x) = \left(\frac{\partial f(g)}{\partial g} g(\Omega, x)^2 + f(g) p g(\Omega, x) \right).$$

Proof. $P_{MaxT}(\Omega)$ is written again as

$$P_{MaxT}(\Omega) = \frac{C_1(\Omega, x)}{C_2(\Omega, x)}. \quad (3.49)$$

Differentiating 3.49 and using Proposition 1.3.8, we get

$$\begin{aligned} P'_{MaxT}(\Omega)(\theta) &= \frac{1}{(C_2(\Omega, x))^2} (C_2(\Omega, x)C'_1(\Omega, x)(\theta) - C_1(\Omega, x)C'_2(\Omega, x)(\theta)) \\ &= \frac{1}{(C_2(\Omega, x))^2} \left(C_2(\Omega, x) \left(\int_{\partial\Omega} \theta(s) \cdot n(s) f(g) g(\Omega, s)^2 ds \right) \right. \\ &\quad + \frac{1}{(C_2(\Omega, x))^2} \left(\int_{\Omega} C_3(\Omega, x) g'(\Omega, x)(\theta) dx \right) \\ &\quad - \frac{1}{(C_2(\Omega, x))^2} \left(C_1(\Omega, x) \left(\int_{\partial\Omega} \theta(s) \cdot n(s) f(g) g_{max}(s)^2 ds \right) \right) \\ &\quad \left. - \frac{1}{(C_2(\Omega, x))^2} \left(C_1(\Omega, x) \left(\int_{\Omega} \frac{\partial f(g)}{\partial g} g'(\Omega, x)(\theta) g_{max}(x)^2 dx \right) \right) \right). \end{aligned} \quad (3.50)$$

The function $g(\Omega, x)$ can be written again as

$$g(\Omega, x) = \int_{\Omega} \chi_{B_{eff}(x, r)}(y) dy,$$

where $\chi_{B_{eff}(x, r)}$ is the characteristic function of the ball of radius r centered at point x , defined as

$$\chi_{B_{eff}(x, r)}(y) = \begin{cases} 1, & \text{if } y \in B_{eff}(x, r), \\ 0, & \text{else.} \end{cases}$$

The shape derivative of $g(\Omega, x)$ is formally calculated as

$$g'(\Omega, x)(\theta) = \int_{\partial\Omega} \theta(s) \cdot n(s) \chi_{B_{eff}(x, r)}(s) ds.$$

In order to write $P'_{MaxT}(\Omega)(\theta)$ in the form given by Hadamard's structure theorem, we use that

$$\begin{aligned} &\int_{\Omega} j(x) g'(\Omega, x)(\theta) dx \\ &= \int_{\Omega} j(x) \int_{\partial\Omega} \theta(s) \cdot n(s) \chi_{B_{eff}(x, r)}(s) ds dx \\ &= \int_{\partial\Omega} \theta(s) \cdot n(s) \int_{\Omega} j(x) \chi_{B_{eff}(x, r)}(s) dx ds, \end{aligned} \quad (3.51)$$

for a general function $j(x)$. Using (3.51) in (3.50) we arrive at the desired result. \square

Numerical results

2d cantilever

In order to test this method and compare with the previously obtained results, we consider here again the 2d cantilever of the previous section. The same initialization is used and problem (3.26) is solved for $g_{max}^1 = 40$, $d_{max} = 0.40$ and for different values of the void percentage " α_{void} ". In Figure 3.78, we see how the constraint limit $g_{max}(x)$ is modified close to the boundary according to the volume of the effective ball $B_{eff}(x, r)$. The optimized shapes and the thickness violation for different values of the void percentage are shown in Figure 3.79. As expected, the optimization algorithm is very sensitive for $\alpha_{void} = 0.01$ and we witness again the repetitious formation and disparition of tiny holes, as described in Figure 3.24. For $\alpha_{void} = 0.10$ and $\alpha_{void} = 0.05$ there is no violation of the thickness limit at the optimized shape. However, this is somehow expected, since an increase in the void percentage causes a decrease in the maximum thickness limit. For $\alpha_{void} = 0.01$, the thickness constraint is not satisfied at convergence, the shape has become oscillatory and thickness violation appears. The final volume for the three cases is shown in Table 3.7. We can see that the shape previously obtained via the "volumetric" formula is the lightest of all.

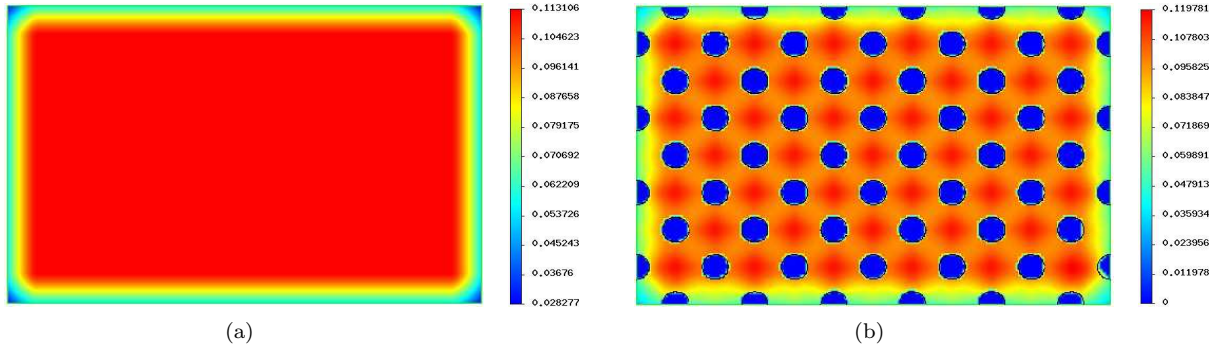


Figure 3.78: (a): $g_{max}(x)$; (b): $g(\Omega_0, x)$ for $d_{max} = 0.40$ and $\alpha_{void} = 0.1$.

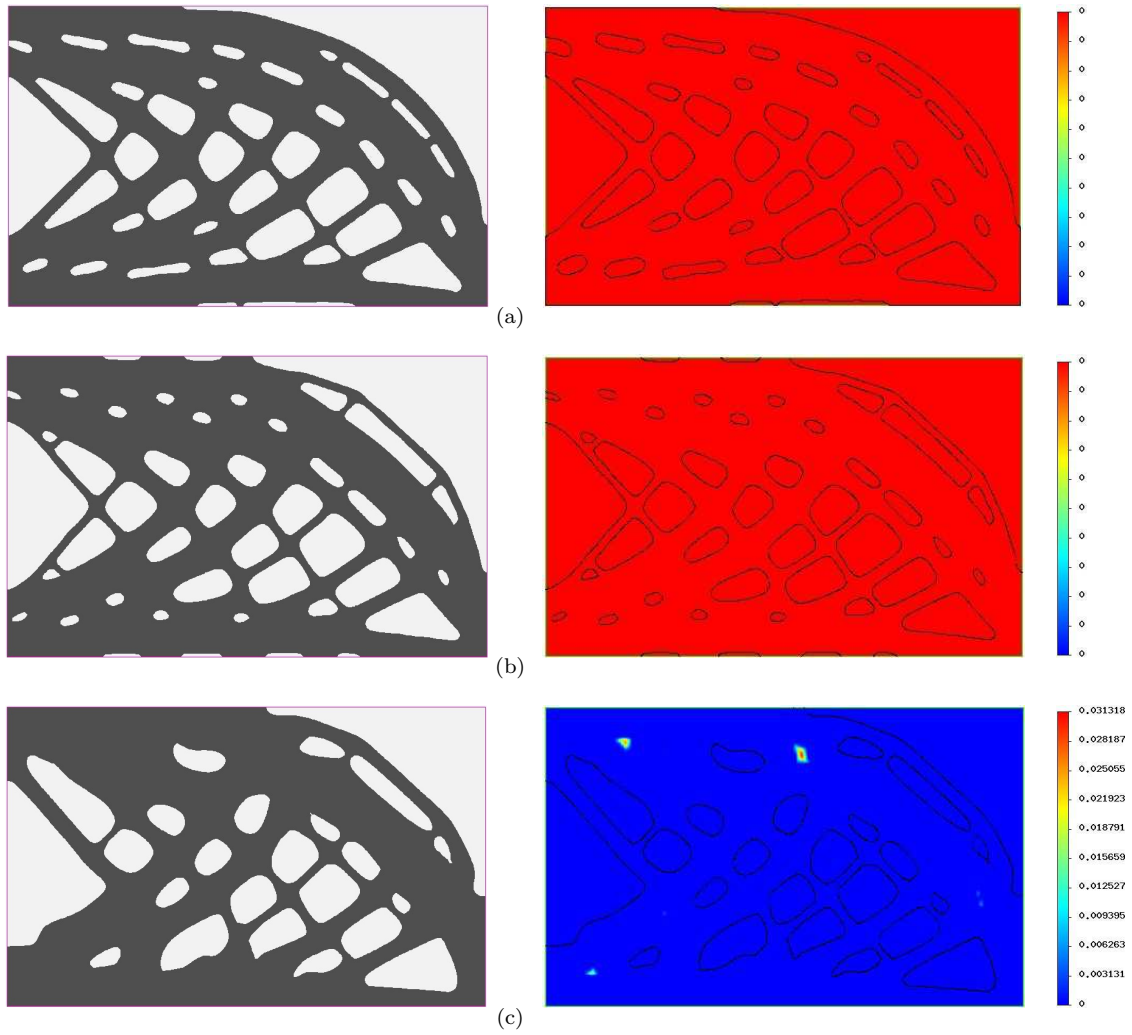


Figure 3.79: Optimized shapes and thickness violation ($|(d_{\Omega}(x) - d_{max}/2)^-|$) for (a): $\alpha_{void} = 0.10$; (b): $\alpha_{void} = 0.05$; (c): $\alpha_{void} = 0.01$, for the 2d cantilever.

Table 3.7: Volume comparison for the results of figures 3.79 and 3.29)(b).

	Volume
"volumetric" formula	3.931
$\alpha_{void} = 0.10$	4.030
$\alpha_{void} = 0.05$	4.067
$\alpha_{void} = 0.01$	4.135

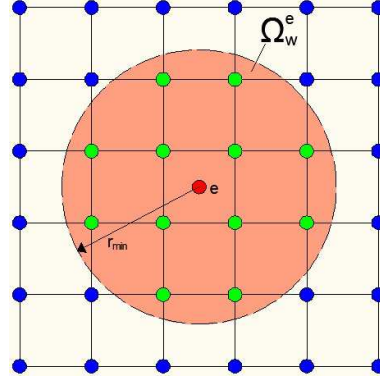


Figure 3.80: Influence area of an element "e".

3.8.2 Minimum Thickness

Design and physical variables

In [63], Guest et al. proposed a new idea to tackle the minimum thickness specification. Instead of formulating a constraint they integrated the constraint in the optimization variables. As a first step, the distinction between "design" and "physical" variables is done. Design variables are in fact the optimization variables and they determine the physical variables, on which the material properties depend. The physical variables are chosen as usual to be the densities of the elements of the mesh. For the interpolation scheme, the SIMP method can be chosen.

We describe now the connection of the physical with the design variables. For every element "e" of the mesh we define a domain of influence denoted Ω_w^e , which is simply its ball of radius $r_{min} = d_{min}/2$ centered at the center of the element (see Figure 3.80). At each node "j" of the mesh, design variables ρ_j are defined. The values of ρ_j in the influence area of each element determine the value of its physical density ρ^e . This is done in two steps. First, a weighted average of the design variables, also called "nodal volume fraction", is calculated in Ω_w^e as

$$\mu^e = \frac{\sum_{j \in S_e} \rho_j w(|x_j - \bar{x}^e|)}{\sum_{j \in S_e} w(|x_j - \bar{x}^e|)}, \quad (3.52)$$

where S_e is the set of nodes belonging to Ω_w^e (the nodes in green color for the element "e" in Figure 3.80) and w is a weighting function that depends on the distance between the position of node j (x_j) and the center of the element e (\bar{x}^e). Then, the element density is calculated as a Heaviside function such that

$$\rho^e = \begin{cases} 1 & \text{if } \mu^e(\rho_n) > \rho_n^{min}, \\ \rho_{min}^e & \text{if } \mu^e(\rho_n) = \rho_n^{min}, \end{cases} \quad (3.53)$$

where ρ_n^{min} and ρ_{min}^e are the minimum allowed densities for the nodal and the elemental variables, in order to avoid singularity of the stiffness matrix. In numerical practice, a regularized version of (3.53) is used.

Comments on the concept of the method

It is easy to see that the formation of features respecting some notion of minimum thickness is inherent in the above formulation. A great benefit of the method is its simplicity and that the above scheme can be applied at any step of the optimization algorithm without creating significant problems to the evolution of the shape. For example, small "islands" that are created during the optimization are easily eliminated.

Of course, we should expect that the algorithm would be very sensitive to the regularization parameters and to local minima. In [62] Guest et al. proposed some modifications in the method of moving asymptotes (MMA) in order to circumvent some of the above inconveniences.

One more significant comment about this method has to do with the notion of minimum thickness itself. It is not clear at all that an optimized structure using the above strategy for the minimum thickness specification would be accepted by a designer. Most of the examples for compliance minimization in [63] and [62] provide the designer with a clear idea of how the optimized shape should look like. In Figure 3.81 we show some optimized shapes for inverter mechanisms obtained in [62] for different values of the

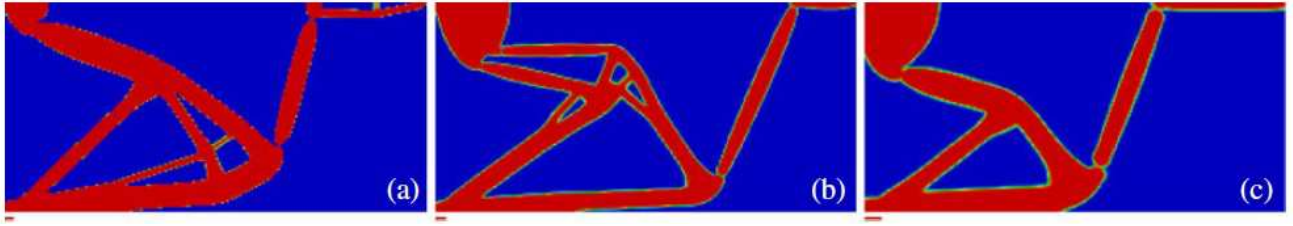


Figure 3.81: Inverter mechanisms obtained in [62].

minimum allowed feature size. A red line below each figure represents the size of this feature. Although the feature size seems to be well respected for bars, the same thing is not true for the regions around the joints that endow the mechanism with high flexibility, or at least the optimization result is not very satisfying from an intuition point of view. If we observe carefully these areas, we can see that intermediate material has been placed, which of course is beneficial for the displacement criterion. We shall emphasize that this is not just a question of post-processing, since respecting a strict criterion, like the one described in section 3.2.2, could result in a much more rigid structure and the optimization algorithm would possibly try to change the way flexibility is created.

Finally, we would like to discuss around the core idea of the method, that is, the distinction between design and physical variables and the way they are related. At first glance, the fact that no additional constraint is imposed on the optimization problem is a significant benefit of the method. However, things remain relatively simple when no other geometric constraint is set on the shape. If several geometric specifications are simultaneously set, especially of conflicting nature, it is not very clear how the relation between the design and the physical variables shall be defined and if such a definition would be efficient for an optimization algorithm. Instead, formulating one constraint for each geometric problem simply adds an extra difficulty to the optimization algorithm, but at least has no impact on the general optimization method.

Interpretation of the method using a "classical" shape description

In this Section we try to adapt the main concept of the method, the distinction between design and physical variables, in the framework of classical shape optimization. Since our optimization variable is the shape itself, we speak about a "design shape" and a "physical shape". We will try to optimize the design shape in order to minimize functionals that dependent on the physical shape, which is the real shape.

Denoting the design shape as Ω_{des} , one way to define the physical shape Ω_{phys} is to consider

$$\Omega_{phys} = \Omega_{des} \cup \Omega_{offset}^{d_{min}}, \quad (3.54)$$

where

$$\Omega_{offset}^{d_{min}} = \{x \text{ such that } d_{\Omega_{des}}(x) \leq d_{min}/2\}, \quad (3.55)$$

is the set of points lying up to a distance $d_{min}/2$ from the boundary $\partial\Omega_{des}$ (see Figure 3.82). A level-set function $\psi_{phys}(x)$ corresponding to the physical shape can be easily constructed in two ways. Either by creating $d_{\Omega_{des}}$, the signed distance function to the design shape, and setting

$$\psi_{phys}(x) = d_{\Omega_{des}}(x) - d_{min}/2, \quad (3.56)$$

or by advecting the level-set function ψ_{des} that describes the design domain up to a distance $d_{min}/2$.

The general type of a shape optimization problem under a minimum thickness constraint now reads

$$\min_{\Omega_{des}} J(\Omega_{phys}), \quad (3.57)$$

where the constraint does not appear explicitly, but has been incorporated into the relation (3.54) connecting the physical and the design shape.

Computation of a descent direction

What remains is the calculation of a descent direction for the functional $J(\Omega_{phys})$. This is not straightforward, since the advection velocity is now defined on the boundary of the design domain Ω_{des} . In other words, we need to find how the domain Ω_{des} shall change so as to decrease a functional defined on Ω_{phys} .

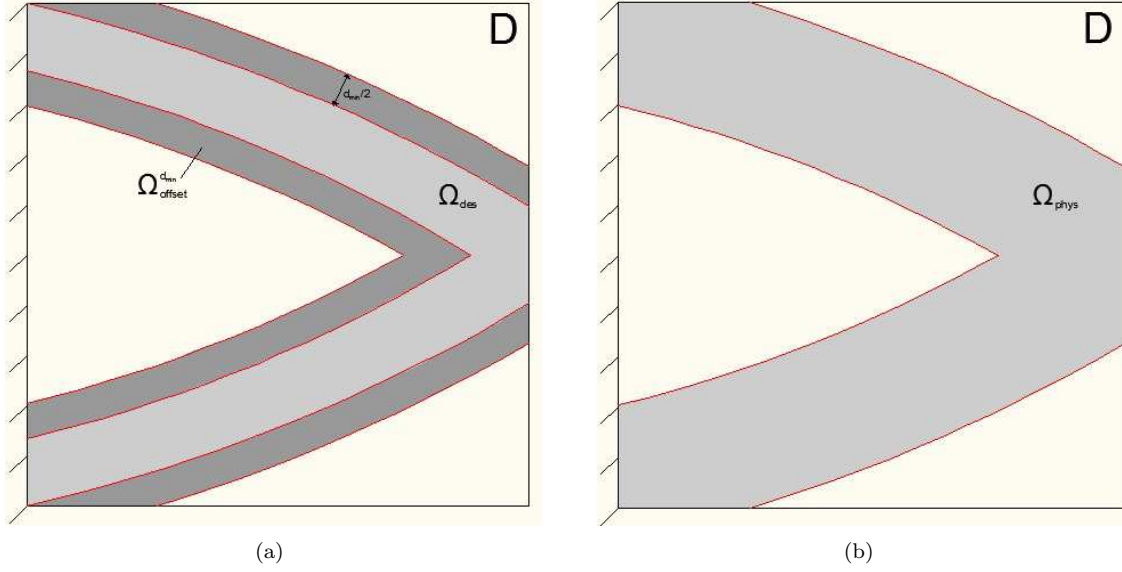


Figure 3.82: (a): Design (Ω_{des}) and offset shape ($\Omega_{offset}^{d_{min}}$); (b): physical shape (Ω_{phys}).

Chen et al. have tried to answer to the above question in [37], where the optimization of the shape under some uncertainty of the boundary's position is studied. The functional to be minimized depends on the values of $J(\Omega)$ on the perturbed domains. Supposing that the perturbed domain Ω_{per} is taken by applying a diffeomorphism $F = \text{Id} + \theta^*$ to the current shape Ω , such that every point $x \in \Omega$ is mapped to the point $X = F(x)$, $X \in \Omega_{per}$, the authors claimed that a descent direction can be obtained by

$$v(x) = V(X), \quad (3.58)$$

where v is the velocity on the unperturbed domain Ω and $V(X)$ is the velocity on the perturbed domain Ω_{per} . Unfortunately, the analysis in [37] is not correct, as we will show in the sequel, and thus relation (3.58) does not necessarily guarantee a descent direction.

Let us explain where the mistake in [37] lies and calculate a shape derivative for $J(\Omega_{phys})$. Using a standard change of variables, for a smooth enough function f , we can pass from an integral on the physical domain Ω_{phys} to an integral on the design domain Ω_{des}

$$J(\Omega_{phys}) = J((\text{Id} + \theta^*)(\Omega_{des})) = \int_{(\text{Id} + \theta^*)(\Omega_{des})} f(x) dx = \int_{\Omega_{des}} f \circ (\text{Id} + \theta^*)(x) |\det(I + \nabla \theta^*)| dx.$$

At this point we shall not forget that the diffeomorphism θ^* is shape dependent, that is

$$\theta^* = (d_{min}/2)n(x),$$

where $n(x)$ is the exterior normal vector to $\partial\Omega_{des}$. For the shape derivative of the functional J , Proposition 1.3.8 needs to be used, i.e. the Eulerian derivative of the integrand will also appear. This part is omitted in [37] in the equation (26). The shape derivative reads

$$\begin{aligned} J'(\Omega_{phys})(\theta_{des}) &= J'(\Omega_{des}, \theta^*)(\theta_{des}) = \\ &= \int_{\partial\Omega_{des}} (\theta_{des}(s) \cdot n(s)) f \circ (\text{Id} + \theta^*)(s) |\det(I + \nabla \theta^*)| ds \\ &+ \int_{\Omega_{des}} \frac{\partial (f \circ (\text{Id} + \theta^*)(x) |\det(I + \nabla \theta^*)|)}{\partial \Omega_{des}} (\theta_{des}) dx, \end{aligned} \quad (3.59)$$

where θ_{des} is a vector field defined on the boundary of Ω_{des} . In [37] the second term of the right-hand side did not appear in the calculation and the authors claimed that the choice

$$\theta_{des}(s) = -f \circ (\text{Id} + \theta^*)(s) n(s) = -f \circ (s + (d_{min}/2)n(s)) n(s),$$

which is equivalent to the relation (3.58), guarantees a descent direction for J . Let us now continue the calculation of the shape derivative (3.59). Using Lemma 3.3.9 we can write

$$\begin{aligned} \det(I + \nabla \theta^*) &= \det(I + (d_{\min}/2)\nabla n) = \det(I + (d_{\min}/2)\mathcal{H}d_{\Omega_{des}}) = \prod_{i=1}^{N-1} \left(1 + (d_{\min}/2) \frac{\kappa_i}{1 + d_{\Omega_{des}} \kappa_i} \right) \\ \Rightarrow \det(I + \nabla \theta^*) &= \prod_{i=1}^{N-1} \left(\frac{1 + (d_{\Omega_{des}} + d_{\min}/2)\kappa_i}{1 + d_{\Omega_{des}} \kappa_i} \right). \end{aligned}$$

This term is always positive, since

$$\kappa_i \geq 0 \quad \Rightarrow \quad 1 + (d_{\Omega_{des}} + d_{\min}/2)\kappa_i \geq 1 + d_{\Omega_{des}} \kappa_i > 0,$$

because of Lemma 3.3.9 and

$$\kappa_i < 0 \quad \Rightarrow \quad 1 + (d_{\Omega_{des}} + d_{\min}/2)\kappa_i \geq 1 + d_{\min}/2\kappa_i > 0,$$

because $d_{\min}/2 < \text{reach}(\Omega_{des})$ (see [44] for the definition of the "reach" of a set), in order for $(\text{Id} + \theta^*)$ to be a diffeomorphism. Thus (3.59) becomes

$$\begin{aligned} J'(\Omega_{des}, \theta^*)(\theta_{des}) &= \\ &\int_{\partial\Omega_{des}} (\theta_{des}(s) \cdot n(s)) f \circ (\text{Id} + (d_{\min}/2)n)(s) \prod_{i=1}^{N-1} (1 + (d_{\min}/2)\kappa_i) ds \\ &+ \int_{\Omega_{des}} \frac{\partial \left(f \circ (\text{Id} + (d_{\min}/2)n)(x) \prod_{i=1}^{N-1} \left(1 + (d_{\min}/2) \frac{\kappa_i}{1 + d_{\Omega_{des}} \kappa_i} \right) \right)}{\partial \Omega_{des}} (\theta_{des}) dx = \\ &\int_{\partial\Omega_{des}} (\theta_{des}(s) \cdot n(s)) f \circ (\text{Id} + (d_{\min}/2)n)(s) \prod_{i=1}^{N-1} (1 + (d_{\min}/2)\kappa_i) ds \\ &+ \int_{\Omega_{des}} (d_{\min}/2) \frac{\partial f}{\partial X}(X) \frac{\partial n}{\partial \Omega_{des}}(\theta_{des}) \prod_{i=1}^{N-1} \left(1 + (d_{\min}/2) \frac{\kappa_i}{1 + d_{\Omega_{des}} \kappa_i} \right) \\ &+ f \circ (\text{Id} + (d_{\min}/2)n)(x) \frac{\partial \prod_{i=1}^{N-1} \left(1 + (d_{\min}/2) \frac{\kappa_i}{1 + d_{\Omega_{des}} \kappa_i} \right)}{\partial \Omega_{des}} (\theta_{des}) \end{aligned} \tag{3.60}$$

The computation of the shape derivative of the exterior normal is numerically quite difficult, as we will see in the next Chapter, while the one of the principal curvatures shall be even more difficult to be found. Of course, the hypothesis that the design and the physical shapes are related by a diffeomorphism is not always true, unless d_{\min} is small enough and Ω_{des} is smooth enough. In case it is not, the above analysis is not mathematically valid.

Chapter 4

Molding direction constraints in structural optimization

Contents

4.1	Introduction	133
4.2	Formulation of the molding direction constraint	134
4.2.1	Molding direction condition on design velocity	134
4.2.2	Generalised molding constraint	135
4.2.3	Uniform cross-section surface constraint	135
4.3	Shape derivative	136
4.3.1	Molding direction condition on design velocity	136
4.3.2	Generalised molding constraint	137
4.3.3	Uniform cross-section surface constraint	139
4.4	Numerical examples	139
4.4.1	Molding direction	140
4.4.2	Uniform cross-section	146

In this Chapter we propose some methods and strategies for imposing molding direction constraints in shape and topology optimization using a level-set description of the shape. We combine existing proposals in the literature with novel formulations that generalize the previous ones and can be effectively combined with thickness constraints. We show several examples of compliance minimization in linearized elasticity with such constraints.

4.1 Introduction

As we have mentioned in Chapter 2, one of the essential specifications for the design of cast parts is the molding direction. The shape of the structure should not hinder the molds' removal in their corresponding parting direction. For reasons of simplicity and economy, the casting system is usually predefined, while the possible parting surface, i.e. the surface where two molds come in touch, can be either fixed a priori or can be easily reconstructed in a second step. Same as for the thickness constraints, we shall not hope that shape and topology optimization results naturally in a feasible shape for a specific casting system, unless some molding direction constraint is introduced in the optimization algorithm.

Depending on the shape and topology optimization method in use, different proposals have appeared to handle molding direction constraints. In the framework of the SIMP method (see Chapter 1), Zhou et al. [165] implemented a penalization scheme that favors higher densities at specific parts of the structure, according to the casting design, which reduces the possibility of obtaining complicated topologies. Leiva et al. [82, 83] have chosen to incorporate directly the growth direction in the parametrization of the problem, while methods of topology control, such as connectivity and growth direction control, have been applied for the Soft Kill Option [66]. A complete review of these methods and a comparison of results using topology optimization with and without manufacturing constraints can be found in [67, 68]. In the framework of the level-set method, the first works on the topic -to our knowledge- are those of Xia et al. [159, 160]. In [159], Xia et al. proposed a molding direction condition on the design velocity, i.e. a

modification of the descent direction that ensures the feasibility of the shape at each iteration, provided that the initial shape is also feasible. In this work, the casting system is also a priori defined. In [160], Xia et al. have added the optimization of the parting direction in the optimization problem. The same choice for the design velocity is done. Although the method allows those topological changes that do not come in conflict with the removal of the molds, it is mentioned in [159] that the shape cannot expand orthogonally to the parting direction. This is a great disadvantage in case one wants to impose thickness constraints. Finally, in the framework of the phase-field method, Yamada et al. have presented in [162] a special type of molding direction constraint, called "uniform cross-section surface constraint", according to which the structure has a constant cross-section along some direction. This is a sufficient but not necessary condition for satisfying the molding direction specification.

In this chapter, we present a general method to handle the molding direction constraint in the framework of the level-set method for shape and topology optimization. A pointwise constraint is formulated using the signed distance function and a penalty functional is then constructed to turn the constraint into a global one. This method is independent of the initialization and can be combined with thickness constraints, since there is no limitation in the advection of the shape's boundary. In order to reduce the computational cost and simplify the optimization process, a strategy that combines the previous idea of Xia et al. with this new formulation is proposed. Finally, the "uniform cross-section surface constraint" is discussed and a simple method is proposed to enforce it. We show several numerical results for compliance minimization in linearized elasticity with such constraints.

4.2 Formulation of the molding direction constraint

4.2.1 Molding direction condition on design velocity

A molding direction condition on the design velocity was proposed by Xia et al. in [159], which is inspired by Fu et al. [56]. According to the authors, if a shape is feasible with respect to the molding direction specification for its corresponding casting system, then the boundary of the structure $\partial\Omega$ can be divided into m disjoint parts Γ_i , $i = \{1, \dots, m\}$, such that $\Gamma_i \cap \Gamma_j = \emptyset$, $j = \{1, \dots, m\}$, $\bigcup_{i=1}^m \Gamma_i = \partial\Omega$ and Γ_i can be parted in the direction d_i . Thus, a molding direction condition for this shape is

$$d_i \cdot n(x) \geq 0, \quad \forall x \in \Gamma_i. \quad (4.1)$$

The shape on the left in Figure 4.2.1 satisfies the condition (4.1), while the shape on the right does not. In fact, as it is mentioned in [159], undercuts (slots that hint the removal on the mold in its parting direction) and interior voids are not allowed.

Based on the the molding condition (4.1), Xia et al. proposed the following method : starting from a

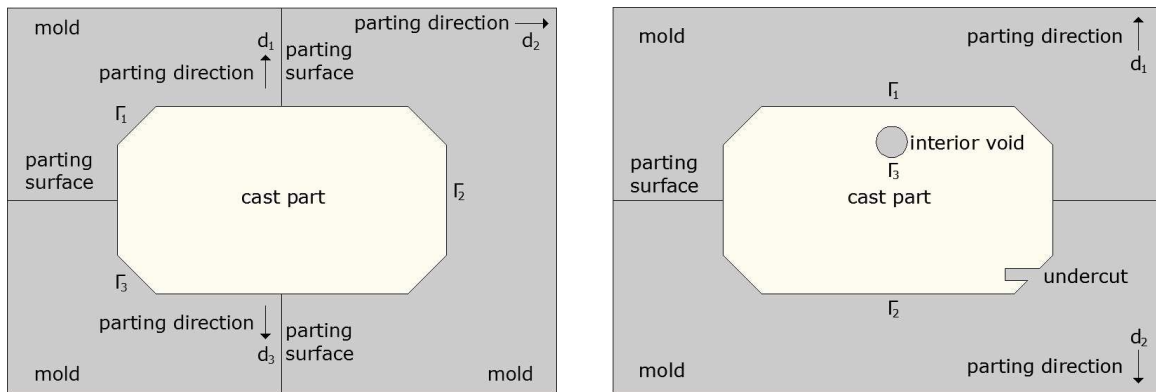


Figure 4.1: Left: moldable shape; right: non-moldable shape.

shape that satisfies the constraint (4.1), consider an advection velocity of the form

$$\theta_i(x) = \lambda(x)d_i, \quad \forall x \in \Gamma_i. \quad (4.2)$$

In this way, the shape remains always moldable, since no undercut can be created during the advection of the shape with this type of velocity and no interior void can be nucleated. The topological changes that can occur using this advection velocity cannot turn the shape from moldable to non-moldable [159].

This method, despite its simplicity and effectiveness, presents two major drawbacks. First, that the shape should always satisfy the molding constraint, which limits enormously the choices of initial guess shapes. We think that this limitation is not really crucial, since the method is flexible enough, especially in 3d, and complicated topologies can be created from very trivial initializations. Second, and more important from our point of view, is the limitation introduced by the type of advection velocity in the movement of the shape. As it is stated in [159], there is no component of the advection velocity normal to the parting direction. Therefore, the shape can shrink by extinction of some part, but it cannot expand normal to its corresponding parting direction. Thus, in case that a minimum thickness constraint is applied in a second step [12], the structure will be able to move only parallel to its parting directions and in all probability the constraint will not be respected. Therefore, it is necessary to formulate a general molding constraint, free of the above limitations.

4.2.2 Generalised molding constraint

A first idea for a generalised way to treat the molding direction constraint consists simply in regarding (4.1) as a constraint in our optimization problem. The main difficulty under this choice is related to the computation of its shape derivative, as we will see in the sequel.

A second idea is to use the signed distance function to the boundary of the domain to derive all necessary information, as we have done in Chapter 3. Denoting Ω the actual shape and D the design domain, a generalized molding direction constraint can be formulated as:

$$d_{\Omega}(x + \xi d_i) \geq 0 \quad \forall x \in \Gamma_i, \forall \xi \in [0, \text{dist}(x, \partial D)], \quad (4.3)$$

or equivalently

$$d_{\Omega}(x + \xi d_i) \geq 0 \quad \forall x \in \Gamma_i, \forall \xi \in [0, \text{diam}(D)], \quad (4.4)$$

where we denote $\text{diam}(D) = \sup_{x,y} \{\text{dist}(x, y), x, y \in D\}$ the diameter of the fixed domain D . We prefer to use formulation (4.4) instead of (4.3), in order to avoid the dependence of the term $\text{dist}(x, \partial D)$ on the shape Ω .

Intuitively, this formulation says that, starting from a point on the boundary, which will be casted in the direction d_i and travelling along this direction, we should not meet again some part of the structure (see Figure 4.2). In case that the parting surface is not defined a priori, but is revealed at a second step after the design has been completed and for a system of two molds (see Figure 2.3, right image), the constraint (4.4) becomes:

$$d_{\Omega}(x + \xi \text{sign}(n \cdot d)d) \geq 0 \quad \forall x \in \partial\Omega, \forall \xi \in [0, \text{diam}(D)]. \quad (4.5)$$

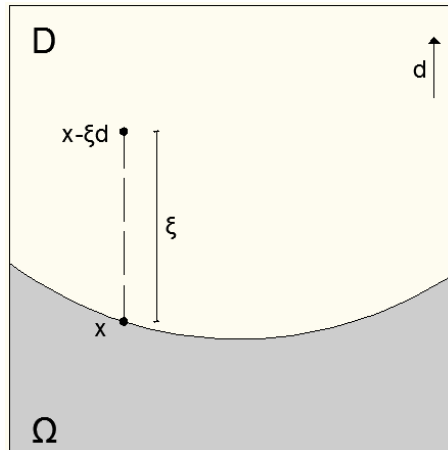


Figure 4.2: Checking castability along the parting direction d at the point $x \in \partial\Omega$.

4.2.3 Uniform cross-section surface constraint

Another useful constraint for cast parts is the so-called "uniform cross-section surface constraint" [162], since it simplifies a lot the shape of the desired molds. To our knowledge, Yamada et al. [162] were

the first to study this type of constraint in shape and topology optimization using a combination of a phase-field and a level-set method. The constraint states that the cast part should have a uniform constant thickness along some direction d . An example of a uniform thickness cantilever of thickness h is given in Figure 4.3. The boundary conditions may not be uniform along this direction and therefore the problem cannot be reduced to a 2d problem. We can formulate this type of constraint at least in two

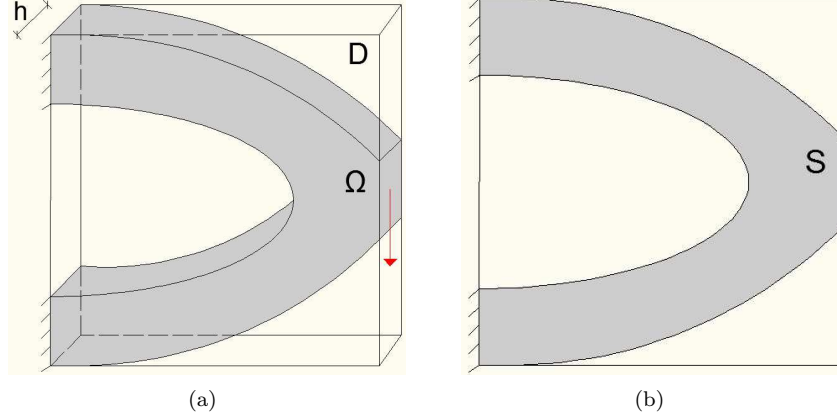


Figure 4.3: (a): uniform cross-section cantilever of thickness h ; (b): cross-section S .

ways. The first formulation states that there should be no non-zero component of the exterior normal to the boundary along this direction d :

$$d \cdot n(x) = 0, \quad \forall x \in \partial\Omega \setminus \partial D. \quad (4.6)$$

A second way to enforce the constraint is to limit the admissible advection fields θ . Starting from an initial guess shape that has a uniform thickness along the desired direction d and constraining the advection fields to be constant along this direction, the thickness along d will not change. In fact, this is the easiest way to follow, since we don't need to impose a mathematical constraint and the calculation of the velocity field is reduced to a 2d problem, as we will see in the next section.

Satisfying this type of constraint, we also assure the feasibility of the shape for casting along the direction d , i.e. this constraint is a sufficient but not a necessary condition.

4.3 Shape derivative

4.3.1 Molding direction condition on design velocity

Xia et al. proposed in [159] a modification of the advection velocity according to (4.2), that guarantees a descent direction. Starting from the general form of the shape derivative for a functional $J(\Omega)$

$$J'(\Omega)(\theta) = \int_{\partial\Omega} \theta(s) \cdot n(s) V(s) ds = \sum_{i=1}^m \int_{\Gamma_i} \theta_i(s) \cdot n(s) V_i(s) ds$$

and considering admissible advection fields of the type (4.2), we get

$$J'(\Omega)(\theta) = \sum_{i=1}^m \int_{\Gamma_i} \lambda_i(s) d_i \cdot n(s) V_i(s) ds,$$

and choosing

$$\lambda_i(s) = -V_i(s) d_i \cdot n(s), \quad \forall i = 1, \dots, m$$

for each part Γ_i of the boundary $\partial\Omega$, the shape derivative becomes

$$J'(\Omega)(\theta) = - \sum_{i=1}^m \int_{\Gamma_i} (d_i \cdot n(s))^2 (V_i(s))^2 ds \leq 0,$$

which shows that the chosen advection velocity

$$\theta_i(s) = -V_i(s) (d_i \cdot n(s)) d_i(s), \quad \forall i = 1, \dots, m$$

is indeed a descent direction.

4.3.2 Generalised molding constraint

We start with the derivation of constraint (4.1). One advantage of this constraint is that it is of local nature, i.e. it contains information only for points on the boundary without searching along rays emerging from them. On the other hand, it contains the exterior normal vector, whose derivation is more complicated than the one of the signed distance function. In a first step, a global penalty functional can be formulated as

$$P_{GMC}(\Omega) = \int_{\partial\Omega} [(d \cdot n(s))^-]^2 ds. \quad (4.7)$$

Proposition 4.3.1. *The shape derivative of (4.7) reads*

$$P'_{GMC}(\Omega)(\theta) = \int_{\partial\Omega} w(s) [+ 2d \cdot \nabla_s (d \cdot n(s))^- - H(s) [(d \cdot n(s))^-]^2] ds, \quad (4.8)$$

where H is the mean curvature and $w = \theta \cdot n$.

Proof. Using Proposition 1.3.8 of Chapter 1, the shape derivative of (4.7) reads

$$\begin{aligned} P'_{GMC}(\Omega)(\theta) &= \int_{\partial\Omega} \theta(s) \cdot n(s) [H(s) [(d \cdot n(s))^-]^2 + \frac{\partial([(d \cdot n(s))^-]^2)}{\partial n}] ds + \int_{\partial\Omega} \frac{\partial([(d \cdot n(s))^-]^2)}{\partial \Omega}(\theta) ds = \\ &= \int_{\partial\Omega} \theta(s) \cdot n(s) [H(s) [(d \cdot n(s))^-]^2 + 2(d \cdot n(s))^- \frac{\partial(d \cdot n(s))}{\partial n}] ds \\ &+ \int_{\partial\Omega} 2(d \cdot n(s))^- d \cdot n'(s)(\theta) ds = \\ &= \int_{\partial\Omega} \theta(s) \cdot n(s) [H(s) [(d \cdot n(s))^-]^2 + 2(d \cdot n(s))^- d \cdot ((\nabla n)n)] ds \\ &+ \int_{\partial\Omega} 2(d \cdot n(s))^- d \cdot n'(s)(\theta) ds \end{aligned} \quad (4.9)$$

Making the assumption that the boundary of the shape is of C^1 regularity, we can make an extension of the unit normal in a tubular area around the boundary by $n(x) = \nabla d_\Omega(x)$. Now, the unit normal satisfies the equation $|n(x)|^2 = 1$ from which differentiating both sides, we obtain $(\nabla n)n = 0$. Thus, equation (4.9) reduces to

$$P'_{GMC}(\Omega)(\theta) = \int_{\partial\Omega} \theta(s) \cdot n(s) H(s) [(d \cdot n(s))^-]^2 ds + \int_{\partial\Omega} 2(d \cdot n(s))^- d \cdot n'(s)(\theta) ds. \quad (4.10)$$

What remains is the calculation of the shape derivative of the unit normal to the boundary. From Lemma 4.8 in [99], we have that the transported of the unit normal $n(\Omega, x)$ is

$$\begin{aligned} n((Id + \theta)(\Omega), x + \theta(x)) &= \frac{((I + \nabla\theta)^{-1})^T n}{|((I + \nabla\theta)^{-1})^T n|} = \\ &= \frac{n - (\nabla\theta)^T n + o(\theta)}{1 - (\nabla\theta)^T n \cdot n + o(\theta)} = (n - (\nabla\theta)^T n + o(\theta))(1 + (\nabla\theta)^T n \cdot n + o(\theta)) \\ &= n(\Omega, x) - (\nabla\theta)^T n + ((\nabla\theta)^T n \cdot n)n + o(\theta), \end{aligned} \quad (4.11)$$

and so the Lagrangian shape derivative of the unit normal is

$$Y(\theta, x) = -(\nabla\theta)^T n + ((\nabla\theta)^T n \cdot n)n. \quad (4.12)$$

Choosing a vector field $\theta(x)$ of the form $\theta(x) = w(x)n(x)$, we have that $(\nabla n)^T \theta = w(x)(\nabla n)^T n = 0$ and thus

$$\begin{aligned} Y(\theta, x) &= -(\nabla\theta)^T n - (\nabla n)^T \theta + ((\nabla\theta)^T n \cdot n)n + ((\nabla n)^T \theta \cdot n)n \\ &= -\nabla(\theta \cdot n) + [n \cdot \nabla(\theta \cdot n)]n \\ &= -\nabla_s(\theta \cdot n) \\ &= -\nabla_s(w(x)). \end{aligned} \quad (4.13)$$

The Eulerian shape derivative of the unit normal reads

$$n'(x)(\theta) = U(\theta, x) = Y(\theta, x) - \nabla n \theta(x) = Y(\theta, x) = -\nabla_s(w(x)). \quad (4.14)$$

The same result was found in [79], using similar variational principles. Using the above results, equation (4.10) becomes

$$P'_{GMC}(\Omega)(\theta) = \int_{\partial\Omega} w(s)H(s)[(d \cdot n(s))^-]^2 ds - \int_{\partial\Omega} 2(d \cdot n(s))^- d \cdot \nabla_s w(s) ds \quad (4.15)$$

and using the identity (see [79])

$$\int_{\partial\Omega} a \cdot \nabla_s(b) ds + \int_{\partial\Omega} \nabla_s \cdot (a)b ds = \int_{\partial\Omega} a \cdot n H(s)b ds,$$

where a is a vector field and b is a scalar field, we result in

$$\begin{aligned} P'_{GMC}(\Omega)(\theta) &= \int_{\partial\Omega} w(s) [+ \nabla_s \cdot (2(d \cdot n(s))^- d) - H(s)[(d \cdot n(s))^-]^2] ds \\ &= \int_{\partial\Omega} w(s) [+ 2d \cdot \nabla_s(d \cdot n(s))^- - H(s)[(d \cdot n(s))^-]^2] ds, \end{aligned} \quad (4.16)$$

which completes the proof. \square

Lemma 4.3.2. *The shape derivative (4.16) can be also written in the form*

$$P'_{GMC}(\Omega)(\theta) = \int_{\partial\Omega} w(s) \left[\sum_{i=1}^{N-1} \kappa_i(s) (d \cdot e_i(s))^2 (-\text{sign}((d \cdot n(s))^-)) - H(s)[(d \cdot n(s))^-]^2 \right] ds, \quad (4.17)$$

where κ_i are the principal curvatures of $\partial\Omega$ at point $s \in \partial\Omega$ and e_i the associated principal curvature directions ($i = 1, \dots, N-1$).

Proof. For a point $s \in \partial\Omega$ we can write $\nabla_s n(s)$ in the form (see [8]):

$$\nabla_s n(s) = \sum_{i=1}^{N-1} \kappa_i(s) e_i(s) \otimes e_i(s). \quad (4.18)$$

Substituting (4.18) in (4.16) yields the desired result. \square

Constraints (4.4) and (4.5) are pointwise constraints of the same type as the minimum thickness constraint in Chapter 3 and the same steps, described in detail in sections 3.4 and 3.5, need to be followed for their shape derivation and the final extraction of a descent direction. For the sake of completeness, let us mention once more the basic steps of this procedure.

For constraint (4.4) we formulate a penalty functional of the form

$$P_{GMC}(\Omega) = \sum_{i=1}^m \int_{\Gamma_i} \int_0^{\text{diam}(D)} \left[(d_\Omega(s + \xi d_i))^- \right]^2 d\xi ds,$$

while for constraint (4.5), it reads

$$P_{GMC}(\Omega) = \int_{\partial\Omega} \int_0^{\text{diam}(D)} \left[(d_\Omega(s + \xi \text{sign}(n(s) \cdot d)d))^- \right]^2 d\xi ds,$$

where we have denoted $(f)^- = \min(f, 0)$.

The two functionals are of the same type and can be written in compact notation (see Figure 3.6)

$$P_{GMC}(\Omega) = \int_{\partial\Omega} \int_0^{\text{diam}(D)} \left[(d(x_m))^- \right]^2 d\xi dx,$$

where x_m denotes an offset point of the boundary.

The derivation of the above integral has been explained in section 3.4 and it reads

$$\begin{aligned} P'_{GMC}(\Omega)(\theta) &= \int_{\partial\Omega} \int_0^{d_{\min}} \theta(x) \cdot n(x) \left[H \left((d_\Omega(x_m))^- \right)^2 + 2 \left((d_\Omega(x_m))^- \right) \nabla d_\Omega(x_m) \cdot \nabla d_\Omega(x) \right] d\xi dx \\ &\quad - \int_{\partial\Omega} \int_0^{d_{\min}} \theta(x_{m|\Omega}) \cdot n(x_{m|\Omega}) 2 (d_\Omega(x_m))^- d\xi dx. \end{aligned}$$

Remark 4.3.3. As we have mentioned in Section 3.5, a descent direction can be found in a second step, after identifying the linear form (shape derivative) with another scalar product. Solving the equation

$$\int_D (\alpha_{reg}^2 \nabla Q \cdot \nabla v + Qv) dx = P'(\Omega)(v) \quad \forall v \in H^1(D), \quad (4.19)$$

where $\alpha_{reg} > 0$ is a positive scalar (of the order of the mesh size) to control the regularization width and choosing $w = \theta \cdot n = -Q$, we find

$$P'_{GMC}(\Omega)(wn) = - \int_D (\alpha^2 |\nabla Q|^2 + Q^2) dx,$$

which guarantees a descent direction for P_{GMC} .

4.3.3 Uniform cross-section surface constraint

For the constraint (4.6), a quadratic penalty functional reads

$$P_{UCS}(\Omega) = \int_{\partial\Omega} (d \cdot n(s))^2 ds, \quad (4.20)$$

which highly ressembles to (4.7) and thus its shape derivation is omitted here.

Defining the advection velocity to be constant along some direction d of uniform thickness, gives us the idea of applying Fubini theorem for the shape derivative. Thus, starting from the general type of the shape derivative

$$J'(\Omega)(\theta) = \int_{\partial\Omega} V(s)\theta(s) \cdot n(s) ds,$$

where $\partial\Omega$ is the optimizable surface along the direction d , we can write (see Figure 4.3)

$$J'(\Omega)(\theta) = \int_{\partial S} \int_0^h V(\xi)\theta(s) \cdot n(s) d\xi ds = \int_{\partial S} \theta(s) \cdot n(s) \int_0^h V(\xi) d\xi ds,$$

where we denote ∂S the uniform cross-section optimizable boundary. Therefore, a descent direction is revealed under the choice

$$\begin{cases} \theta(s) = -n(s) \int_0^h V(\xi) d\xi & \forall s \text{ on } \partial S, \\ \nabla \theta(s) \cdot d = 0, \text{ i.e. } \theta \text{ is constant along the direction } d. \end{cases}$$

Another, even simpler way to treat this constraint is through the regularization of the velocity field via equation (4.19). Choosing α to be a tensor, instead of a positive scalar, we can smooth the advection field in an anisotropic way. Then, equation (4.19) is written again as

$$\int_D \left(\sum_{i=1}^N \alpha_i^2 \frac{\partial Q}{\partial e_i} \frac{\partial v}{\partial e_i} + Q_i v_i \right) dx = J'(\Omega)(v) \quad \forall v \in H^1(D), \quad (4.21)$$

where e_i , $i = 1, \dots, N$ is the canonical basis of \mathbb{R}^N and $\alpha = \sum_{i=1}^N \alpha_i e_i \otimes e_i$ is the regularization tensor. For example, if we want θ to be constant along the 2-axis, we can set $\alpha_2 \gg \alpha_i, i \neq 2$. Starting from a guess shape that respects the constraint and regularizing the advection field in the way just described, we can get a final optimized shape with a uniform cross-section.

4.4 Numerical examples

Same as in Chapter 3, we have coded all numerical examples herein in the finite element software SYSTUS of ESI-Group [140]. A quadrangular mesh has been used both for the solution of the elasticity system and for the level set function. For the elasticity analysis, Q1 finite elements have been used, the Young modulus E is normalized to 1 and the Poisson ratio ν is set to 0.3. The "ersatz material" is considered to have the same Poisson ratio, while its Young modulus is set to 10^{-3} .

4.4.1 Molding direction

3d box

The three-dimensional box-like structure of Figure 3.45 is used here to apply several molding direction constraints and compare the corresponding optimized shapes. The entire domain is used for the analysis and is discretized using $40 \times 40 \times 20$ $Q1$ elements. We change slightly the optimization problem compared to Chapter 3 and minimize the compliance under an equality constraint for the volume. The optimization problem reads

$$\begin{aligned} \min_{\Omega \in \mathcal{U}_{ad}} \quad & \int_{\partial\Omega} g \cdot u ds \\ \text{s.t.} \quad & \int_{\Omega} dx = a_V |D|, \end{aligned} \quad (4.22)$$

where u is the solution of (1.34) and $a_V \in [0, 1]$ determines the final volume of the structure as percentage of the volume of the working domain D . An augmented Lagrangian method is also used here to enforce the constraints, as in section 3.7.

At a first step, we impose no molding constraint and solve the optimization problem (4.22) for $a_V = 0.2$ using the arbitrary initialization of Figure 4.4(a). The optimized shape after 250 iterations is shown in Figure 4.4(b).

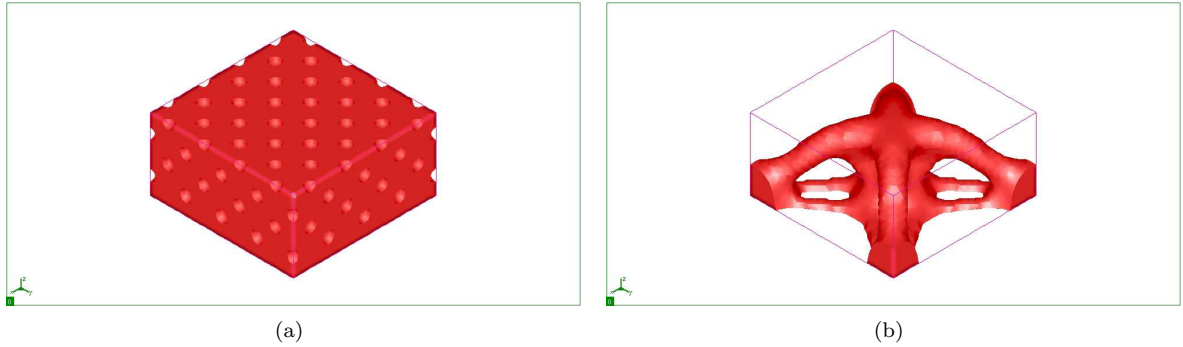


Figure 4.4: Initialization and optimized shape for the problem of Eq.(4.22) without a molding constraint.

Let us now solve the same optimization problem for a cast part that must comply with a predefined casting system. For example, if we want to use one mold in the design domain D , remove it in the direction $d = (0, 0, 1)$ and impose the plane $z = 0$ to be a possible parting surface, then obviously the shape in Figure 4.4(b) is no more feasible. Of course, we shall not hope that starting with a different, even much simpler initialization, we would result in a castable optimized shape.

As we have mentioned before, in the absence of thickness constraints, we believe that imposing a molding direction condition on the design velocity, as described in section 4.2.1 gives quite satisfying results. Starting with a full-domain initialization (see Figure 4.5(a)) and taking the initial level-set function equal to the signed distance function to the upper part of the domain, we choose an advection velocity of the type (4.2), where $d = (0, 0, 1)$, and result in the optimized shape of Figure 4.5(b).

More flexibility in shape variations is given if the casting direction is set as $d = (0, 0, 1)$ and no parting surface is imposed. In this case, the design domain D can contain two molds, one removed in the direction d and the second in the opposite direction $(-d)$. The same initialization as in Figure 4.5(a) can be chosen, but this would necessarily result in a system of one mold. Instead, it seems more efficient to take the initial level-set function equal to the signed distance function both to the upper and lower part of the domain. The optimized shape is shown in Figure 4.7(b).

As expected, a completely different optimized shape is obtained if we change the casting direction. Separating the molds horizontally, in the direction $d = (1, 0, 0)$ and imposing no specific parting surface, results in the optimized shape of Figure 4.9. In both figures 4.7 and 4.9 we see that topological changes can take place by "pinching a thin wall" [14].

A constraint on the maximum local thickness can be combined with the molding condition on the design velocity without any difficulty a priori. The reason is that the maximum thickness constraint gradient will be of uniform sign, tending always to reduce the thickness (and the volume) of the shape. As we have mentioned in section 4.2.1, when an advection velocity of the type 4.2 is chosen, the shape can shrink, but not expand normal to the casting direction. Adding a maximum thickness constraint to

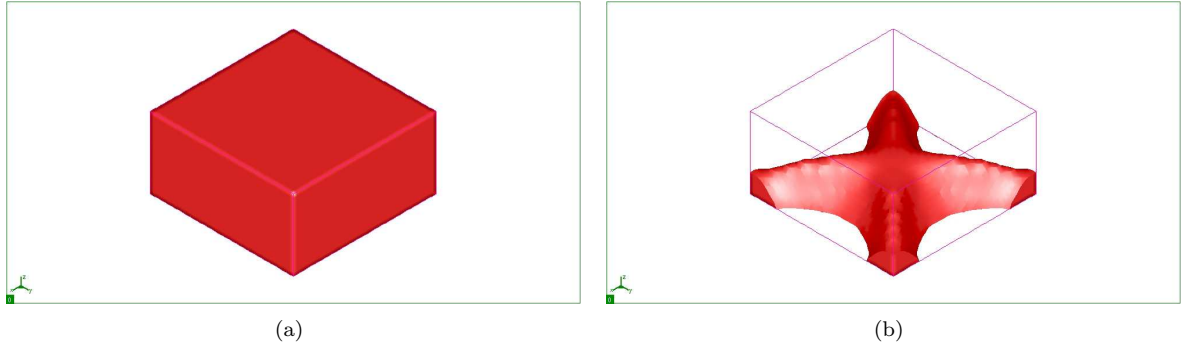


Figure 4.5: Initialization and optimized shape for the optimization problem (4.22), setting $d = (0, 0, 1)$ as casting direction, $z = 0$ as a possible parting surface and using the molding direction condition (4.2).

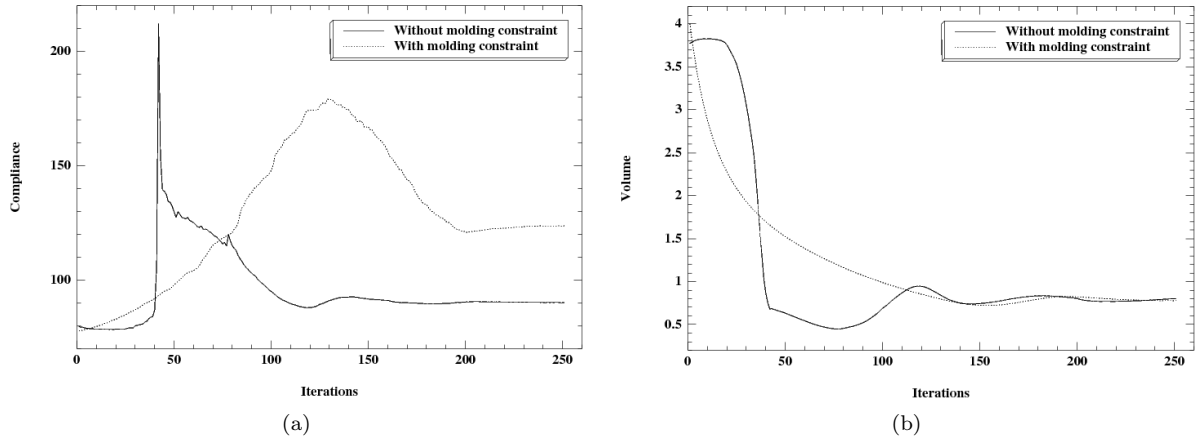


Figure 4.6: (a): compliance and (b): volume convergence diagrams for the results in figures 4.4(b) and 4.5(b).

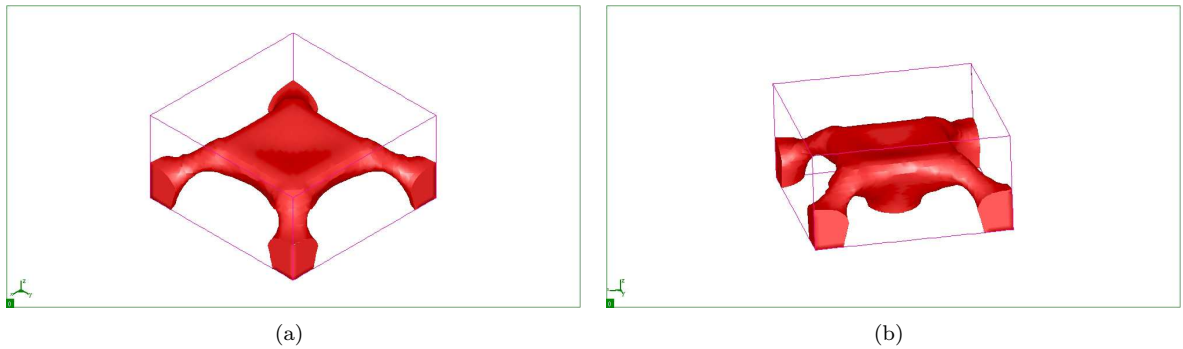


Figure 4.7: Plots of the optimized shape for the optimization problem (4.22), setting $d = (0, 0, 1)$ as casting direction, no a priori defined parting surface and using the molding direction condition (4.2).

the test case of Figure 4.5, where the shape is casted along the direction $d = (0, 0, 1)$ and the plane $z = 0$

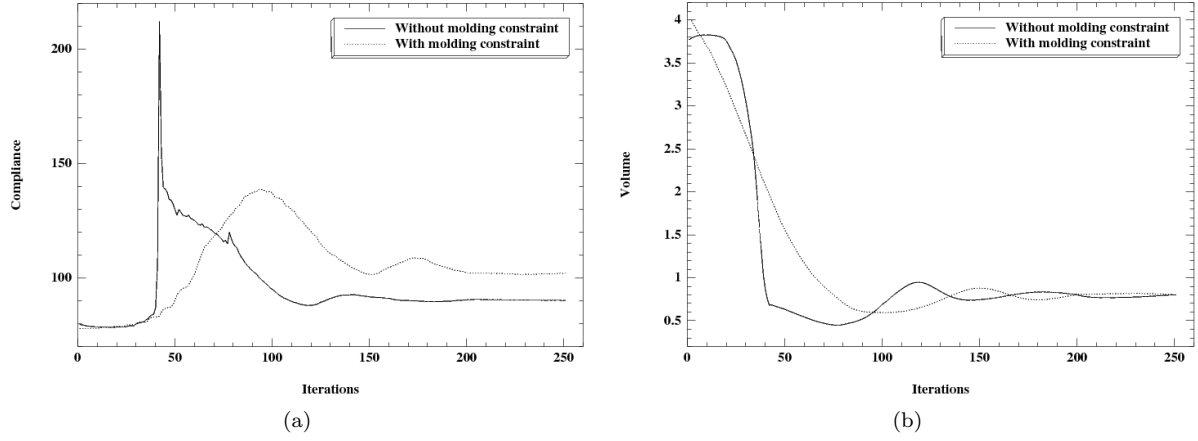


Figure 4.8: (a): compliance and (b): volume convergence diagrams for the results in figures 4.4(b) and 4.7.

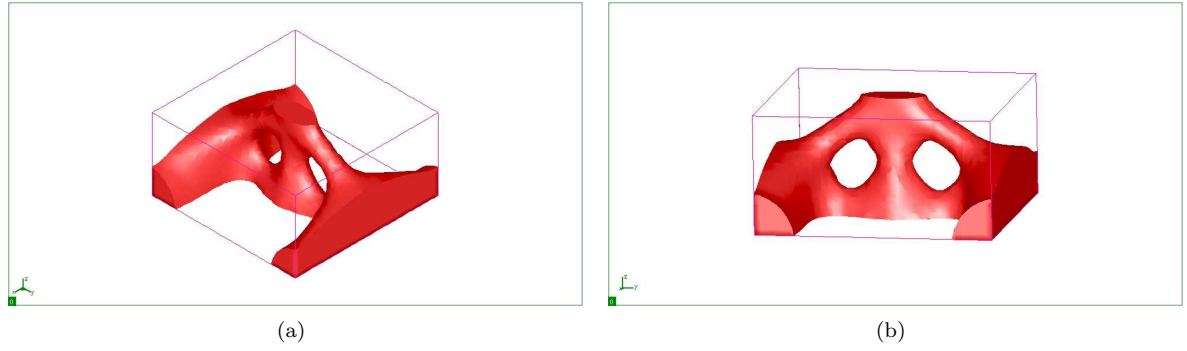


Figure 4.9: Plots of the optimized shape for the optimization problem (4.22), setting $d = (1, 0, 0)$ as casting direction, no a priori defined parting surface and using the molding direction condition (4.2).

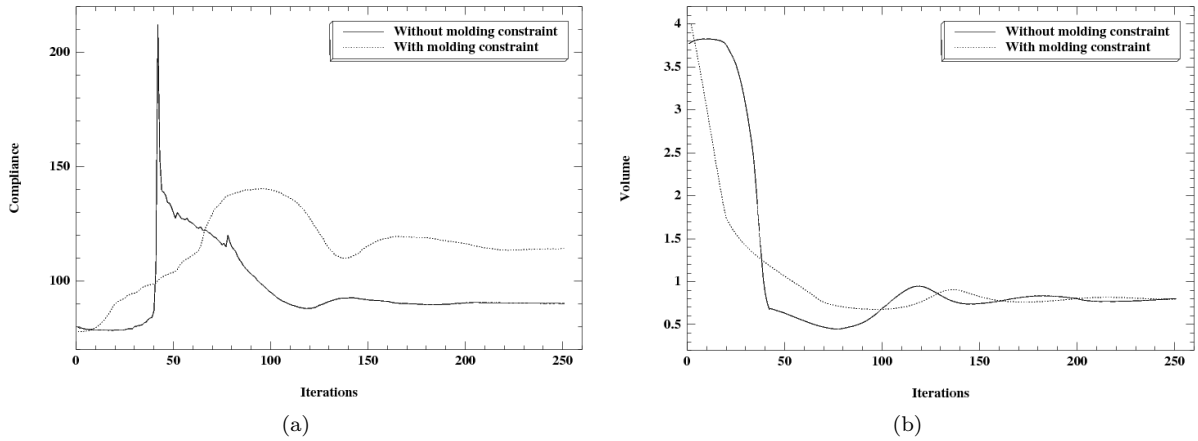


Figure 4.10: (a): compliance and (b): volume convergence diagrams for the results in figures 4.4(b) and 4.9.

is chosen as a possible parting surface, we solve the optimization problem

$$\begin{aligned}
 & \min_{\Omega \in \mathcal{U}_{ad}} \int_{\partial\Omega} g \cdot u \, ds \\
 & \text{s.t.} \quad \int_{\Omega} dx = a_V |D|, \\
 & P_{MaxT}(\Omega) = \left(\frac{\int_{\Omega} f(d_{\Omega}(x)) d_{\Omega}(x)^2 dx}{\int_{\Omega} f(d_{\Omega}(x)) dx} \right)^{\frac{1}{2}} \leq d_{max}/2,
 \end{aligned} \tag{4.23}$$

using the same initialization as in Figure 4.5(a). The optimized shape after 250 iterations and the convergence diagrams are shown in figures 4.11 and 4.12.

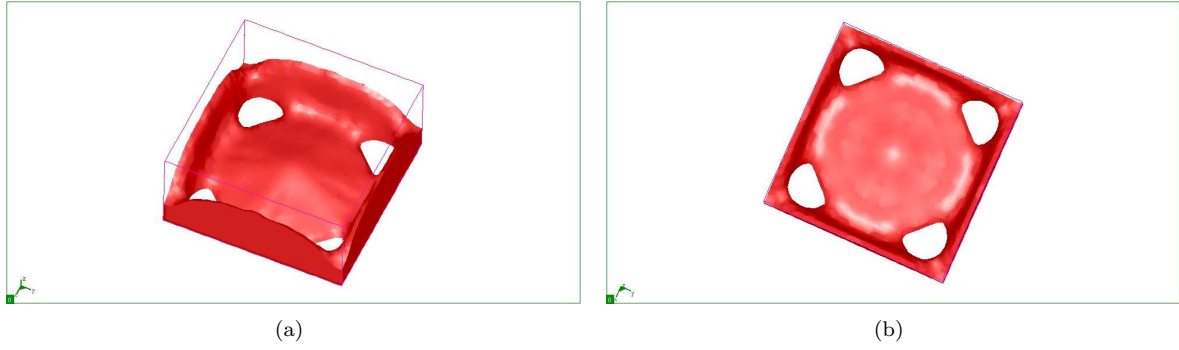


Figure 4.11: Optimized shape for the optimization problem (4.23), setting $d = (0, 0, 1)$ as casting direction, $z = 0$ as a possible parting surface and using the molding direction condition (4.2).

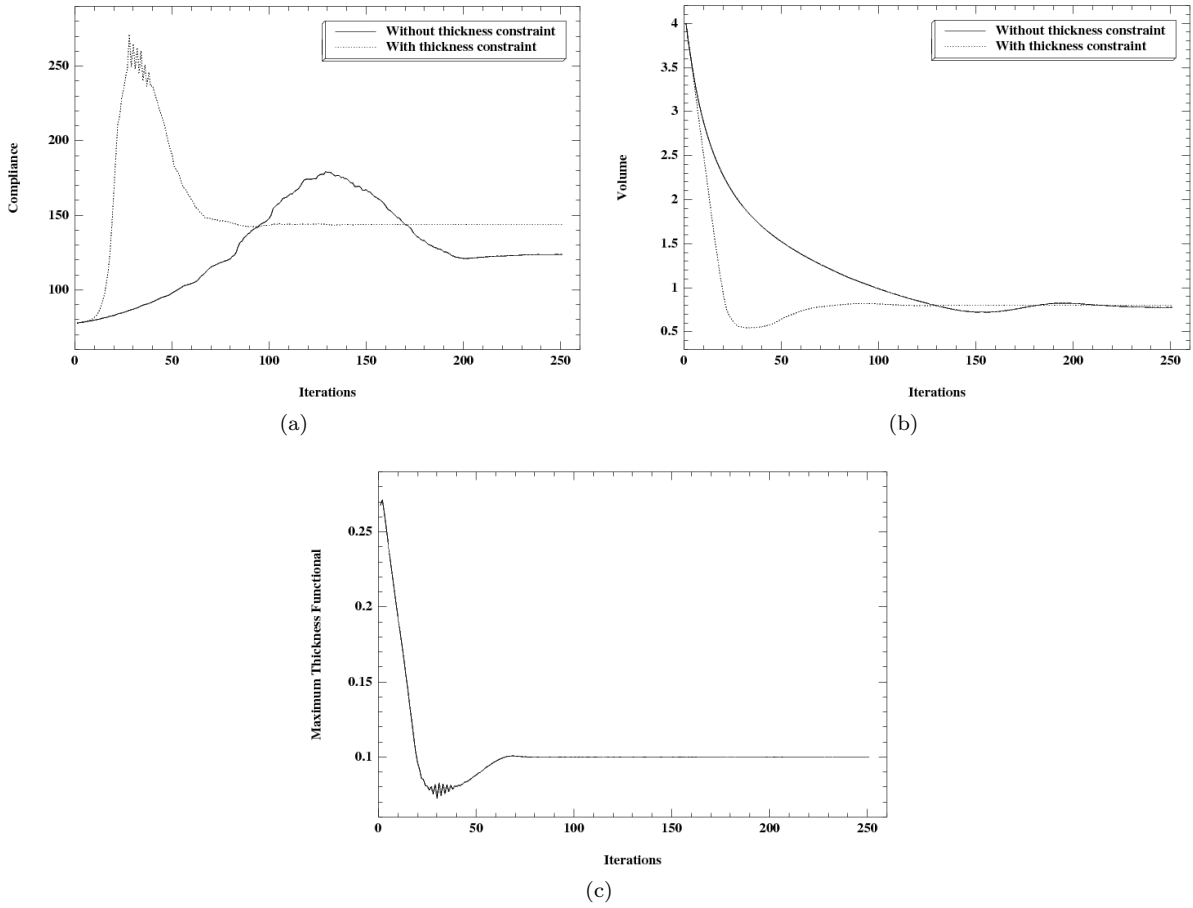


Figure 4.12: (a): compliance and (b): volume convergence diagrams for the results in figures 4.5(b) and 4.11; (c) convergence diagram for the maximum thickness functional $P_{MaxT}(\Omega)$ for the optimized shape in Figure 4.11.

Suppose now that we want to add a minimum thickness constraint with $d_{min} = 0.4$ in the shape of Figure 4.5(b). The molding condition (4.2) is no more a suitable method to follow (see section 4.2.1) and we shall instead combine a minimum thickness constraint with the generalised molding constraint (4.3).

The previously optimized shape is taken as an initial guess to solve the problem

$$\begin{aligned}
& \min_{\Omega \in \mathcal{U}_{ad}} \int_{\partial\Omega} g \cdot u ds \\
& \text{s.t.} \quad \int_{\Omega} dx = a_V |D|, \\
& P_1(\Omega) = P_{MinT}(\Omega) = \int_{\partial\Omega} \int_0^{d_{min}} \left[(d_{\Omega}(s - \xi n(s)))^+ \right]^2 d\xi ds = 0, \\
& P_2(\Omega) = P_{GMC}(\Omega) = \int_{\partial\Omega} \int_0^{diam(D)} \left[(d_{\Omega}(s + \xi d))^- \right]^2 d\xi ds = 0,
\end{aligned} \tag{4.24}$$

without any condition on the advection velocity. An optimized shape for the problem of Eq.(4.24) is shown in Figure 4.13(b). The convergence diagrams for the penalty functionals P_1 and P_2 are shown in Fig.4.14.

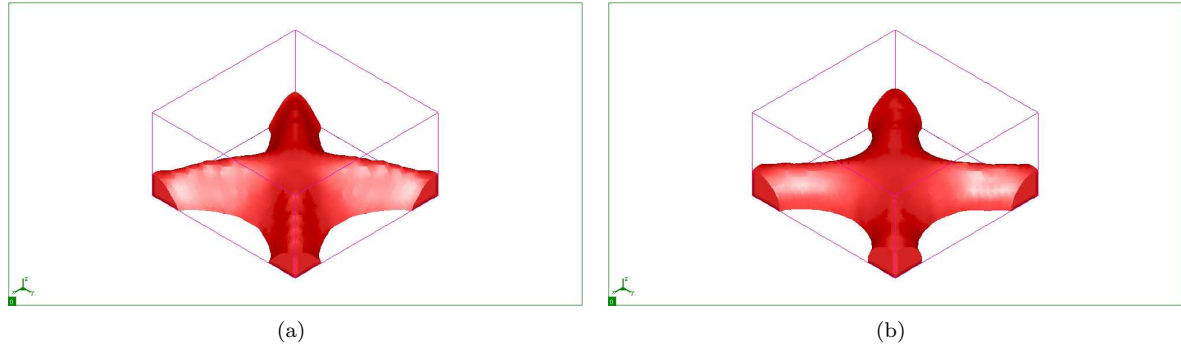


Figure 4.13: Optimized shapes under (a): a molding constraint and (b): a molding and minimum thickness constraint, with a predefined parting surface at $z = 0$.

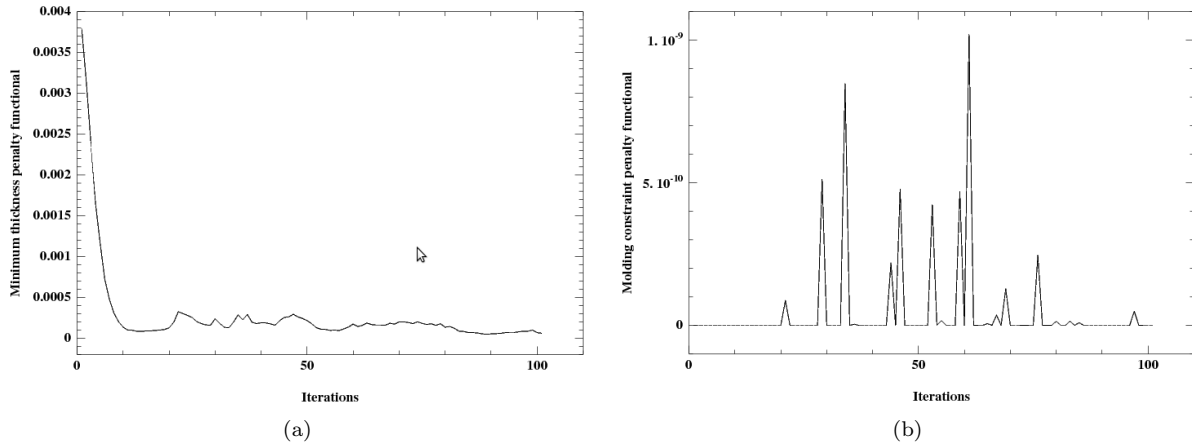


Figure 4.14: Convergence diagrams for the penalty functionals (a): P_1 and (b): P_2 .

When a minimum thickness constraint of $d_{min} = 0.3$ is applied to the shape of Figure 4.7(b), the optimization problem reads

$$\begin{aligned}
& \min_{\Omega \in \mathcal{U}_{ad}} \int_{\partial\Omega} g \cdot u ds \\
& \text{s.t.} \quad \int_{\Omega} dx = a_V |D|, \\
& P_1(\Omega) = P_{MinT}(\Omega) = \int_{\partial\Omega} \int_0^{d_{min}} \left[(d_{\Omega}(s - \xi n(s)))^+ \right]^2 d\xi ds = 0, \\
& P_2(\Omega) = P_{GMC}(\Omega) = \int_{\partial\Omega} \int_0^{diam(D)} \left[(d_{\Omega}(s + \xi \text{sign}(n \cdot d)))^- \right]^2 d\xi ds = 0
\end{aligned} \tag{4.25}$$

and we get the optimized shape of Figure 4.15. The convergence diagrams for the penalty functionals P_1 and P_2 are shown in Figure 4.16.

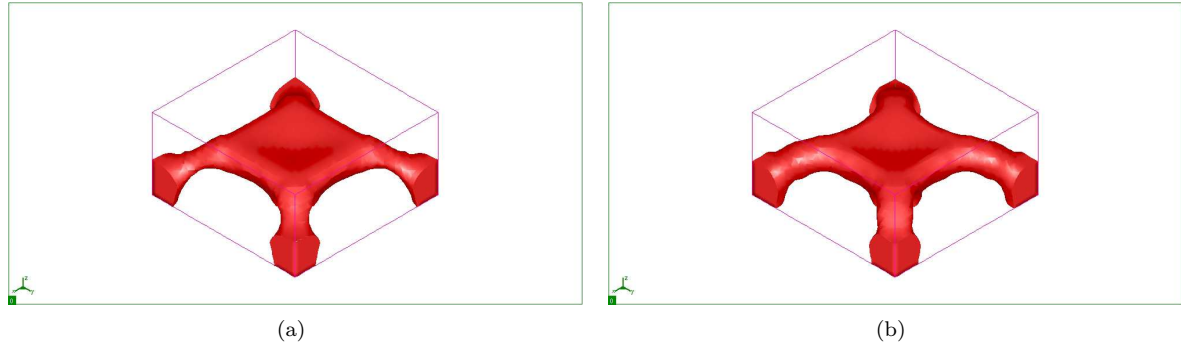


Figure 4.15: Optimized shapes under (a): a molding constraint and (b): a molding and minimum thickness constraint, without a predefined parting surface.

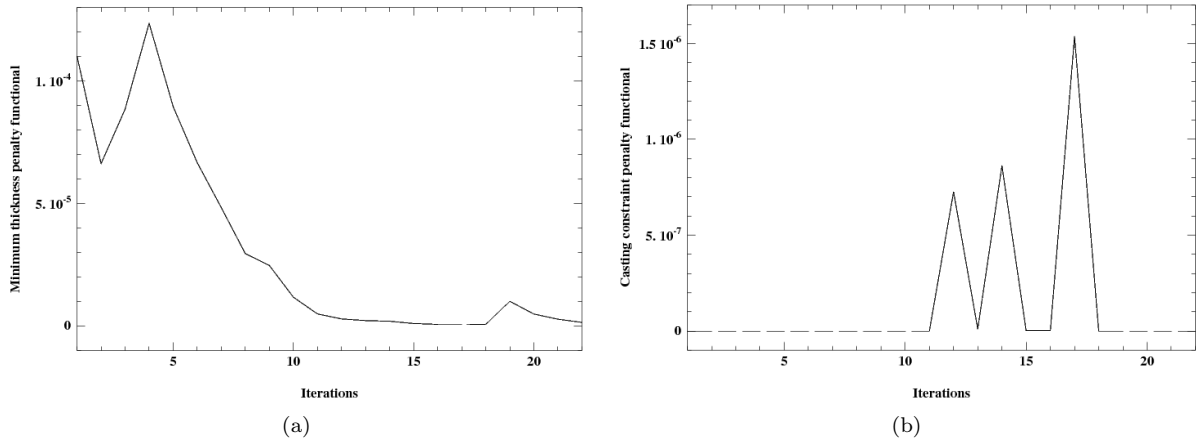


Figure 4.16: Convergence diagrams for the penalty functionals (a): P_1 and (b): P_2 .

Table 4.1: Compliance of the optimized structures.

	Compliance
Without molding constraint.	90.14
With casting direction $d = (0, 0, 1)$ and no parting surface.	102.07
With casting direction $d = (0, 0, 1)$, no parting surface and minimum thickness constraint.	105.87
With casting direction $d = (1, 0, 0)$ and no parting surface.	114.13
With casting direction $d = (0, 0, 1)$ and parting surface at $z = 0$.	123.68
With casting direction $d = (0, 0, 1)$, parting surface at $z = 0$ and minimum thickness constraint.	134.68
With casting direction $d = (0, 0, 1)$, parting surface at $z = 0$ and maximum thickness constraint.	143.65

4.4.2 Uniform cross-section

3d cantilever

The $2 \times 0.5 \times 1$ three dimensional cantilever of Figure 4.17, discretized by $40 \times 10 \times 20$ $Q1$ elements, is chosen as test case to apply the uniform cross-section surface constraint. It is clamped on one side and, at the middle of its opposite side, a unitary vertical load is applied. At a first step, problem (4.22) is

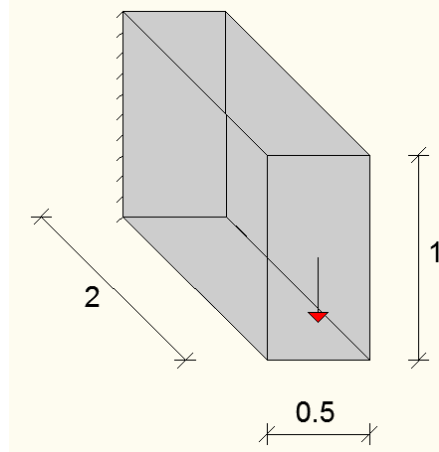


Figure 4.17: Boundary conditions for the "uniform cross-section" test case.

solved for $a_V = 0.25$ without imposing any further geometric constraint on the shape. Starting from the arbitrarily perforated shape of Figure 4.18(a), we obtain after 200 iterations the optimized shape of Figure 4.18(b). We ask now for an optimized shape with a uniform cross-section along the y -axis. Starting from

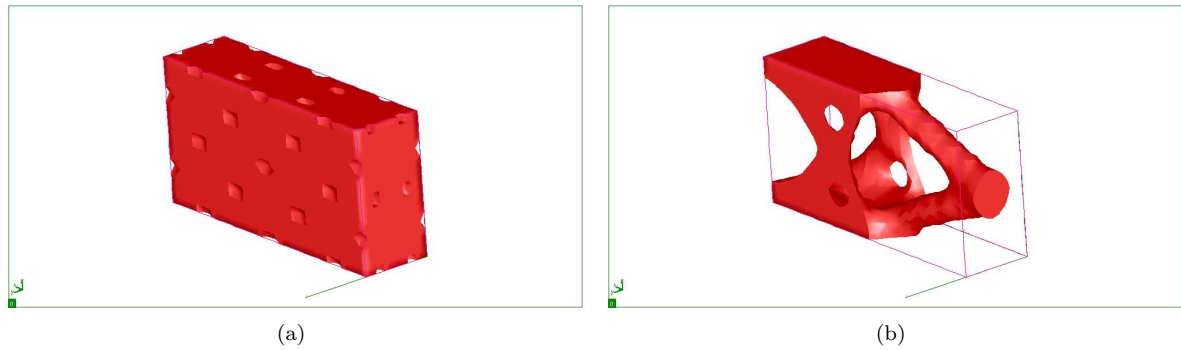


Figure 4.18: (a): Initialization and (b): optimized shape, without the "uniform cross-section" constraint.

the initial shape of Figure 4.19(a), which has five uniform holes along this direction, we regularize at each iteration the velocity field for the advection of the shape in an anisotropic way, setting a much higher regularization coefficient in the y -direction ($a_y \gg a_x, a_z$). In our example, $a_x = a_z = 2\Delta x$, Δx being the uniform mesh size, has been used to regularize the advection velocity in a small region around the shape boundary in the direction of the x - and z -axis, while $a_y = \sqrt{10}$ has been set to create a uniform velocity along this direction. The optimized shape is shown in Figure 4.19(b). The convergence diagrams for the compliance and the volume are shown in Figure 4.20.

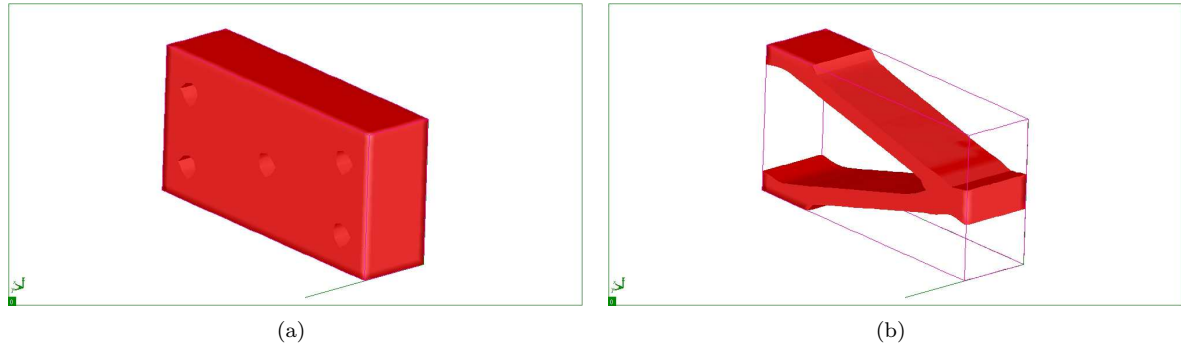


Figure 4.19: (a): Initialization and (b): optimized shape, with a "uniform cross-section" constraint.

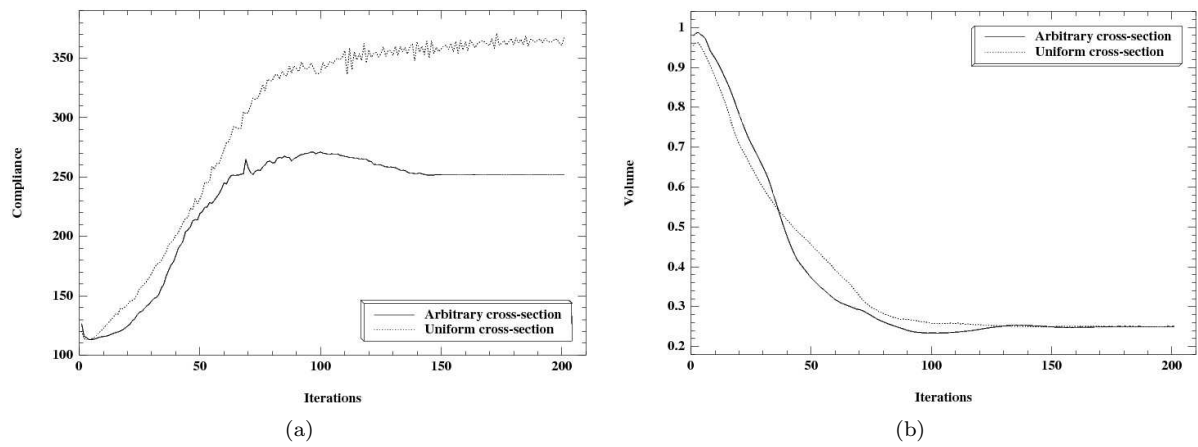


Figure 4.20: (a): Compliance and (b): volume convergence diagrams for the results of figures 4.18 and 4.19.

Chapter 5

Thermal constraints in structural optimization

Contents

5.1	Introduction	149
5.2	Formulation of the thermal constraint	150
5.3	Heat equation models and shape derivatives	150
5.3.1	Poisson equation	151
5.3.2	Linear transient heat equation	152
5.3.3	Eigenvalue approximation	155
5.3.4	Linear transient heat equation with piecewise discontinuous conductivity	158
5.3.5	Linear transient heat equation with piecewise discontinuous conductivity and heat flux across the moving boundary	164
5.3.6	Non-linear transient heat equation with phase-change	169
5.3.7	Numerical results	171

In this chapter we enforce the feedability of a cast part (see Chapter 2) via a specification of a maximum solidification time t_f . The cooling process in casting is simulated by solving a non-linear heat equation with phase change and an upper bound is set on the final temperature inside the cast part at time t_f . Since the optimization process using this equation is too costly, we study the possibility of using simpler thermal models, at least as a first step.

5.1 Introduction

In Chapter 2 we explained that feedability, i.e. the ability of designing a feeding system that drives the shrinkage porosity due to solidification to the risers at an acceptable cost, can be treated via either a geometrical or a mechanical approach. The geometrical approach has been presented in Chapter 3 and consists in imposing a maximum thickness limit. The mechanical approach, as a concept, lies closer to the actual problem. A simplified model of the cooling process is considered, in which the feeding system is omitted and replaced by appropriate boundary conditions. A thermal equation that simulates the cooling process is used and the structure is required to solidify up to a time limit t_f , which gives an indication for an acceptable total feeding cost.

Summarizing, the mechanical approach for feedability boils down to a thermal constraint. Beyond cast parts, thermal constraints can appear in very different frameworks, for example in structures that work under high temperatures for reasons of functionality and increased product durability [161] (diesel engines, steam turbines, etc...).

Several works on shape and topology optimization for thermal problems have appeared in literature. In the framework of purely shape optimization, several works have been presented for the optimization of the casting system [84], [98], [54], [148], [149]. In the framework of the SIMP method, Tavakoli et al. [144] have optimised the shape of a riser for a problem of heat conduction. Haslinger et al. [70] have implemented the homogenization method in order to minimize the deviation from a prescribed temperature field, again for problems of heat conduction. Li et al. [86] have used evolutionary optimization techniques to

minimize the mean flux for a Poisson-type problem. In the framework of the level-set method, Ha et al. [64] and Yamada [161] worked on the minimization of the thermal compliance, while Zhuang et al. [168] treated the case of multiple thermal loads. The case of discontinuous thermal coefficients was discussed by Allaire et al. [19] and Pantz [108] in the framework of inverse problems.

In this chapter, we study the problem of solidification of a cast part into a prescribed time interval. The optimization of the cast part is done with respect to its mechanical behaviour and the solidification problem is inserted as a thermal constraint that the structure needs to respect to insure manufacturability. In industrial practice, the temperature field is the solution to a non-linear transient heat equation with phase change. The use of this equation in the optimization algorithm is very costly in time and memory. Thus, we propose to use several simplified models as a first step. We show results in 2d for structural compliance minimization.

5.2 Formulation of the thermal constraint

The mathematical formulation of the thermal constraint, described above, is:

$$T(x, t_f) \leq T_s, \quad \forall x \in \Omega, \quad (5.1)$$

where T_s denotes the solidus temperature and $T(x, t)$ is the solution to a heat equation model that describes the solidification process. In other words, inequality (5.1) assures that the structure has solidified in the time interval $[0, t_f]$.

The same global constraint formulation as in (3.24) will be used here. It reads

$$P_{th}(T(x, t_f)) = \left(\frac{\int_{\Omega} f(T(x, t_f)) T(x, t_f)^2 dx}{\int_{\Omega} f(T(x, t_f)) dx} \right)^{\frac{1}{2}} \leq T_s, \quad (5.2)$$

where the regularization function $f(T(x, t_f))$ is given by

$$f(T(x, t_f)) = 0.5 \left(1 + \tanh \left(\frac{T(x, t_f) - T_s}{\alpha_f T_s} \right) \right),$$

$\alpha_f > 0$ being a parameter that controls the regularization of the constraint (see section 3.6).

5.3 Heat equation models and shape derivatives

As we have mentioned earlier, the partial differential equation that simulates the solidification process is a non-linear transient heat equation with phase change. The solution of such an equation, as well as the calculation of its shape derivative, is too costly (see section 5.3.6). Therefore, it seems reasonable to use some simplified model instead and, if necessary, let the actual equation for the last iterations of the optimization algorithm. In this section, we will present several candidate thermal models and compute their shape derivative.

Of course, for each thermal model in play, the value of T_s or t_f shall be adjusted accordingly in order for the results to be somehow comparable. When the non-linear transient heat equation model with phase change is used, T_s corresponds to the actual solidus temperature of the metal and t_f is set by the industrial engineers, usually based on experimental observations, so that thick members are avoided. Therefore, the choice of t_f is essentially linked to a notion of maximum thickness of the structure. Based on the same logic, we have chosen here to fix the maximum solidification time t_f and adjust the upper bound on the temperature T_s using the one-dimensional casting model of Figure 5.1. A bar of size d_{max} is considered, surrounded in both sides by molds of thickness $d_{max}/2$. Each thermal model is solved for this casting system and T_s is set to the maximum temperature in the cast part. In this way, we shall hope that if the temperature constraint is satisfied, the structure will not contain features of maximum thickness greater than d_{max} . A similar idea, for a fast solution of the solidification equation and identification of the location of hot spots, is described in [109], where a 1d-model of the equation is constructed, from a point $x \in \partial\Omega$ and along its "ray", up to the corresponding point on the seleton x_{sk} (see Figure 5.2).

Finally, in order to simplify the presentation, we will use the quadratic penalty functional

$$P_{th}(\Omega) = \int_{\Omega} [(T(x, t_f) - T_s)^+]^2 dx, \quad (5.3)$$

instead of (5.2) for the shape derivation part.

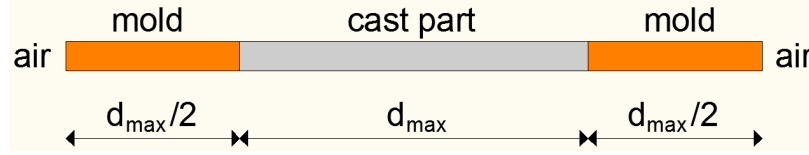
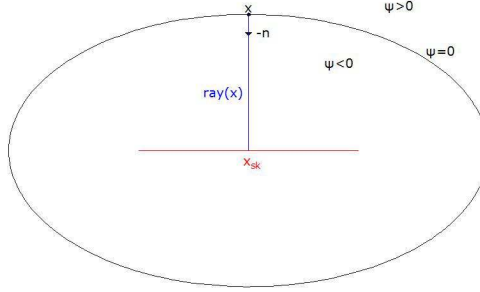


Figure 5.1: One-dimensional model of the casting system.

Figure 5.2: "Ray" connecting a point $x \in \partial\Omega$ to its corresponding point on the skeleton x_{sk} .

5.3.1 Poisson equation

In [144], Tavakoli et al. proposed to use a simple Poisson equation with Dirichlet boundary conditions in order to accelerate the optimization process. The authors have used the SIMP method and they minimized a macroscopic quality indicator function (the half of the thermal compliance). They have claimed that, since the location of the hot spots is independent of the heat equation under consideration, even a much simplified model should give correct information for the change of the shape.

In this case, the state equation has the following simple form

$$\begin{cases} -a\Delta T(x) &= f(x) & \text{in } \Omega, \\ T(x) &= 0 & \text{on } \partial\Omega, \end{cases} \quad (5.4)$$

where a denotes the thermal diffusivity of the material, and f is a volumetric term to account for the latent heat release due to phase change.

Proposition 5.3.1. *Let $T(x)$ be the unique solution of (5.4). Then, the shape derivative of (5.3) reads*

$$P'_{th}(\Omega)(\theta) = - \int_{\partial\Omega} \theta(s) \cdot n(s) \left[a \frac{\partial T}{\partial n}(s) \frac{\partial \zeta}{\partial n}(s) \right] ds, \quad (5.5)$$

where ζ is the unique solution of the adjoint problem

$$\begin{cases} -a\Delta \zeta(x) &= -2(T(x) - T_s)^+ & \text{in } \Omega, \\ \zeta(x) &= 0 & \text{on } \partial\Omega. \end{cases} \quad (5.6)$$

Proof. Following the method of C  a (see section 1.3.1), we formulate the Lagrangian function

$$\mathcal{L}(\Omega, \hat{T}, \hat{\zeta}, \hat{\mu}) = \int_{\Omega} [(\hat{T}(x) - T_s)^+]^2 dx + \int_{\Omega} (-a\Delta \hat{T}(x) - f(x)) \hat{\zeta}(x) dx + \int_{\partial\Omega} \hat{T}(x) \hat{\mu}(x) dx, \quad (5.7)$$

where $\hat{T}, \hat{\zeta}, \hat{\mu} \in H^1(\mathbb{R}^N)$ are scalar functions, independent of the domain Ω .

Setting the partial derivative of \mathcal{L} with respect to $\hat{\zeta}$ in the direction of a test function $\phi \in H^1(\mathbb{R}^N)$ at the optimal point $(\Omega, T^*, \zeta^*, \mu^*)$ equal to zero, we get

$$\frac{\partial \mathcal{L}}{\partial \hat{\zeta}}(\Omega, T^*, \zeta^*, \mu^*)(\phi) = \int_{\Omega} (-a\Delta T^*(x) - f(x)) \phi(x) dx = 0,$$

which implies

$$-a\Delta T^*(x) = f(x) \quad \text{in } \Omega. \quad (5.8)$$

The partial derivative of \mathcal{L} with respect to $\hat{\mu}$ in the direction of ϕ , at $(\Omega, T^*, \zeta^*, \mu^*)$, reads

$$\frac{\partial \mathcal{L}}{\partial \hat{\mu}}(\Omega, T^*, \zeta^*, \mu^*)(\phi) = \int_{\partial\Omega} T^*(s) \phi(s) ds = 0,$$

from which we derive

$$T^*(x) = 0 \quad \text{on } \partial\Omega. \quad (5.9)$$

Equations (5.8) and (5.9) imply that $T^*(x)$ is the unique solution of (5.4).

The partial derivative of \mathcal{L} with respect to \hat{T} in the direction of ϕ reads

$$\begin{aligned} & \frac{\partial \mathcal{L}}{\partial \hat{T}}(\Omega, T^*, \zeta^*, \mu^*)(\phi) \\ &= \int_{\Omega} 2(T^*(x) - T_s)^+ \phi(x) dx + \int_{\Omega} -a \Delta \phi(x) \zeta^*(x) dx + \int_{\partial\Omega} \phi(s) \mu^*(s) ds \\ &= \int_{\Omega} 2(T^*(x) - T_s)^+ \phi(x) dx + \int_{\Omega} a \nabla \zeta^*(x) \cdot \nabla \phi(x) dx - \int_{\partial\Omega} a \frac{\partial \phi}{\partial n}(s) \zeta^*(s) ds \\ &+ \int_{\partial\Omega} \phi(s) \mu^*(s) ds \\ &= \int_{\Omega} 2(T^*(x) - T_s)^+ \phi(x) dx - \int_{\Omega} a \Delta \zeta^*(x) \phi(x) dx + \int_{\partial\Omega} a \frac{\partial \zeta^*}{\partial n}(s) \phi(s) ds \\ &- \int_{\partial\Omega} a \frac{\partial \phi}{\partial n}(s) \zeta^*(s) ds + \int_{\partial\Omega} \phi(s) \mu^*(s) ds \\ &= \int_{\Omega} [-a \Delta \zeta^*(x) + 2(T^*(x) - T_s)^+] \phi(x) dx + \int_{\partial\Omega} (\mu^*(s) + a \frac{\partial \zeta^*}{\partial n}(s)) \phi(s) ds \\ &- \int_{\partial\Omega} a \frac{\partial \phi}{\partial n}(s) \zeta^*(s) ds. \end{aligned}$$

Taking ϕ with compact support in Ω yields

$$-a \Delta \zeta^*(x) = -2(T^*(x) - T_s)^+, \quad \text{in } \Omega. \quad (5.10)$$

Varying the normal flux $a \frac{\partial \phi}{\partial n}(x)$ on the boundary $\partial\Omega$, with $\phi(x) = 0$ in Ω reveals the boundary conditions for ζ^* :

$$\zeta^*(x) = 0, \quad \text{on } \partial\Omega. \quad (5.11)$$

Equations (5.10) and (5.11) show that ζ^* is the unique solution of (5.6).

Varying the trace of ϕ on $\partial\Omega$ with $a \frac{\partial \phi}{\partial n}(x) = 0$ on $\partial\Omega$ gives

$$\mu^*(x) = -a \frac{\partial \zeta^*}{\partial n}(x), \quad \text{on } \partial\Omega. \quad (5.12)$$

Finally, the shape derivative of 5.3 in the direction θ coincides with the shape derivative of \mathcal{L} at the optimal point $(\Omega, T^*, \zeta^*, \mu^*)$:

$$\begin{aligned} P'_{th}(\Omega)(\theta) &= \int_{\partial\Omega} \theta(s) \cdot n(s) [(T^*(s) - T_s)^+]^2 ds + \int_{\partial\Omega} \theta(s) \cdot n(s) (a \Delta T^*(s) - f(s)) \zeta^*(s) ds \\ &+ \int_{\partial\Omega} \theta(s) \cdot n(s) (H(s) T^*(s) \mu^*(s) + \frac{\partial}{\partial n}(T^*(s) \mu^*(s))) ds \\ &= + \int_{\partial\Omega} \theta(s) \cdot n(s) \left[\frac{\partial}{\partial n}(T^*(s)) \mu^*(s) \right] ds \\ &= - \int_{\partial\Omega} \theta(s) \cdot n(s) \left[a \frac{\partial T^*}{\partial n}(s) \frac{\partial \zeta^*}{\partial n}(s) \right] ds, \end{aligned} \quad (5.13)$$

which completes the proof. \square

5.3.2 Linear transient heat equation

A significant increase in the total computational cost takes place by taking under consideration the transient nature of the equation. Adding the time dependence of the temperature field to the previous equation and neglecting the latent heat release, the temperature field $T(x, t)$ is the solution in the space

$C^0([0, T]; L^2(\Omega)) \cap L^2((0, T); V)$ with $V := \{v \in H^1(\Omega); v = 0 \text{ on } \partial\Omega\}$, of the transient linear heat equation model

$$\begin{cases} \partial_t T(x, t) - a\Delta T(x, t) &= 0 & \text{in } \Omega \times (0, t_f), \\ T(x, t) &= 0 & \text{on } \partial\Omega \times (0, t_f), \\ T(x, 0) &= T_{in}(x) & \text{in } \Omega \times \{0\}, \end{cases} \quad (5.14)$$

where $T_{in}(x) = T_l$ is the liquidus temperature, i.e. the change of temperature during the filling of the cavity is ignored and the cast part is considered to start solidifying from a uniform temperature equal to the temperature of the molten liquid. The analysis for the shape derivative of this problem can be found in [19], but we present it also here for reasons of completeness.

Proposition 5.3.2. *Let $T(x, t)$ be the unique solution of (5.14). Then, the shape derivative of (5.3) reads*

$$P'_{th}(\Omega)(\theta) = - \int_{\partial\Omega} \int_0^{t_f} \theta(s) \cdot n(s) \left[a \frac{\partial}{\partial n}(T(s, t)) \frac{\partial}{\partial n}(\zeta(s, t)) \right] dt ds, \quad (5.15)$$

where $\zeta(x, t)$ is the solution of the adjoint problem

$$\begin{cases} -\partial_t \zeta((x, t) - a\Delta \zeta((x, t) &= 0 & \text{in } \Omega \times (0, t_f), \\ \zeta((x, t) &= 0 & \text{on } \partial\Omega \times (0, t_f), \\ \zeta((x, t_f) &= -2(T(x, t_f) - T_s)^+ & \text{in } \Omega \times \{t_f\}. \end{cases} \quad (5.16)$$

Proof. We formulate the Lagrangian function

$$\begin{aligned} \mathcal{L}(\Omega, \widehat{T}, \widehat{\zeta}, \widehat{\mu}, \widehat{\xi}) &= \int_{\Omega} \left[(\widehat{T}(x, t_f) - T_s)^+ \right]^2 dx \\ &\quad + \int_0^{t_f} \int_{\Omega} (\partial_t \widehat{T}(x, t) - a\Delta \widehat{T}(x, t) - f(x, t)) \widehat{\zeta}(x, t) dx dt \\ &\quad + \int_{\Omega} (\widehat{T}(x, 0) - T_{in}(x)) \widehat{\mu}(x) dx + \int_0^{t_f} \int_{\partial\Omega} \widehat{T}(s, t) \widehat{\xi}(s, t) ds dt, \end{aligned} \quad (5.17)$$

where $\widehat{T}, \widehat{\zeta}, \widehat{\xi} \in C^0([0, T]; L^2(\mathbb{R}^N)) \cap L^2((0, T); H^1(\mathbb{R}^N))$ and $\widehat{\mu} \in L^2(\mathbb{R}^N)$.

The partial derivative of \mathcal{L} with respect to $\widehat{\zeta}$ in the direction of a test function $\phi(x, t)$ at the optimal point $(T^*, \zeta^*, \mu^*, \xi^*)$ reads

$$\frac{\partial \mathcal{L}}{\partial \widehat{\zeta}}(\Omega, T^*, \zeta^*, \mu^*, \xi^*)(\phi) = \int_0^{t_f} \int_{\Omega} (\partial_t T^*(x, t) - a\Delta T^*(x, t) - f(x, t)) \phi(x, t) dx dt. \quad (5.18)$$

Setting (5.18) equal to zero, we get

$$\partial_t T^*(x, t) - a\Delta T^*(x, t) - f(x, t) = 0 \quad \text{in } \Omega \times (0, t_f). \quad (5.19)$$

Its derivative with respect to $\widehat{\mu}$ in the direction ϕ reads

$$\int_{\Omega} (T^*(x, 0) - T_{in}(x)) \phi(x) dx = 0,$$

which implies

$$T^*(x, 0) = T_{in}(x) \quad \text{in } \Omega \times \{0\}, \quad (5.20)$$

while the derivative of \mathcal{L} with respect to $\widehat{\xi}$ in the direction of ϕ

$$\int_0^{t_f} \int_{\partial\Omega} T^*(s, t) \phi(s, t) ds dt = 0,$$

gives the boundary conditions for T^*

$$T^*(x, t) = 0 \quad \text{in } \partial\Omega \times (0, t_f). \quad (5.21)$$

Equations (5.19), (5.20) and (5.21) imply that T^* is the unique solution of (5.14).

The partial derivative of \mathcal{L} with respect to \widehat{T} in the direction of a test function ϕ reads

$$\begin{aligned} \frac{\partial \mathcal{L}}{\partial \widehat{T}}(\Omega, T^*, \zeta^*, \mu^*, \xi^*) &= \int_{\Omega} 2(T^*(x, t_f) - T_s)^+ \phi(x, t_f) dx \\ &\quad + \int_0^{t_f} \int_{\Omega} (\partial_t \phi(x, t) - a\Delta \phi(x, t)) \zeta^*(x, t) dx dt \\ &\quad + \int_{\Omega} \phi(x, 0) \mu^*(x) dx + \int_0^{t_f} \int_{\partial\Omega} \phi(s, t) \xi^*(s, t) ds dt. \end{aligned} \quad (5.22)$$

The second integral of equation (5.22) can be further developed as

$$\begin{aligned}
& \int_0^{t_f} \int_{\Omega} (\partial_t \phi(x, t) - a \Delta \phi(x, t)) \zeta^*(x, t) dx dt \\
&= \left[\int_{\Omega} \phi(x, t) \zeta^*(x, t) dx \right]_0^{t_f} - \int_0^{t_f} \int_{\Omega} \phi(x, t) \partial_t \zeta^*(x, t) dx dt \\
&\quad - \int_0^{t_f} \int_{\partial\Omega} a \frac{\partial \phi}{\partial n}(s, t) \zeta^*(s, t) ds dt + \int_0^{t_f} \int_{\Omega} a \nabla \phi(x, t) \cdot \nabla \zeta^*(x, t) dx dt \\
&= \left[\int_{\Omega} \phi(x, t) \zeta^*(x, t) dx \right]_0^{t_f} - \int_0^{t_f} \int_{\Omega} \phi(x, t) \partial_t \zeta^*(x, t) dx dt - \int_0^{t_f} \int_{\partial\Omega} a \frac{\partial \phi}{\partial n}(s, t) \zeta^*(s, t) ds dt \\
&\quad + \int_0^{t_f} \int_{\partial\Omega} a \frac{\partial \zeta^*}{\partial n}(s, t) \phi(s, t) ds dt - \int_0^{t_f} \int_{\Omega} a \Delta \zeta^*(x, t) \phi(x, t) dx dt.
\end{aligned} \tag{5.23}$$

Substituting (5.23) in (5.22) and setting the last one equal to zero, we get

$$\begin{aligned}
\frac{\partial \mathcal{L}}{\partial T}(\Omega, T^*, \zeta^*, \mu^*, \xi^*) &= \int_{\Omega} 2(T^*(x, t_f) - T_s)^+ \phi(x, t_f) dx + \int_{\Omega} \phi(x, 0) \mu^*(x) dx \\
&\quad + \int_0^{t_f} \int_{\partial\Omega} \phi(s, t) \xi^*(s, t) ds dt + \left[\int_{\Omega} \phi(x, t) \zeta^*(x, t) dx \right]_0^{t_f} \\
&\quad - \int_0^{t_f} \int_{\Omega} \phi(x, t) \partial_t \zeta^*(x, t) dx dt - \int_0^{t_f} \int_{\partial\Omega} a \frac{\partial \phi}{\partial n}(s, t) \zeta^*(s, t) ds dt \\
&\quad + \int_0^{t_f} \int_{\partial\Omega} a \frac{\partial \zeta^*}{\partial n}(s, t) \phi(s, t) ds dt \\
&\quad - \int_0^{t_f} \int_{\Omega} a \Delta \zeta^*(x, t) \phi(x, t) dx dt = 0.
\end{aligned} \tag{5.24}$$

Taking ϕ with compact support in $\Omega \times (0, t_f)$, we derive

$$-\partial \zeta^*(x, t) - a \Delta \zeta^*(x, t) = 0 \quad \text{in } \Omega \times (0, t_f). \tag{5.25}$$

The, varying the normal flux of ϕ on the boundary and setting $\phi(x, t) = 0$ in $\partial\Omega \times [0, t_f]$, we derive

$$\zeta^*(x, t) = 0 \quad \text{on } \partial\Omega \times (0, t_f). \tag{5.26}$$

Varying ϕ on the boundary and setting its normal flux equal to zero ($a \frac{\partial \phi}{\partial n}(x, t) = 0$ on $\partial\Omega \times (0, t_f)$), the Lagrange multiplier ξ^* is revealed

$$\xi^*(x, t) = -a \frac{\partial \zeta^*}{\partial n}(x, t) \quad \text{on } \partial\Omega \times (0, t_f). \tag{5.27}$$

Varying $\phi(x, 0)$ and $\phi(x, t_f)$ in Ω , we derive

$$\mu^*(x) = \zeta^*(x, 0) \quad \text{in } \Omega, \tag{5.28}$$

and

$$\zeta^*(x, t_f) = -2(T^*(x, t_f) - T_s)^+ \quad \text{in } \Omega. \tag{5.29}$$

From equations (5.25), (5.26), (5.29), we deduce that ζ^* is the unique solution of the adjoint equation (5.16).

Finally, the shape derivative of the penalty functional (5.3) equals the shape derivative of the Lagrangian function \mathcal{L} at the optimal point. Thus:

$$\begin{aligned}
P'_{th}(\Omega)(\theta) &= \int_{\partial\Omega} \theta(s) \cdot n(s) [(T^*(s, t_f) - T_s)^+]^2 ds \\
&\quad + \int_0^{t_f} \int_{\partial\Omega} \theta(s) \cdot n(s) (\partial_t T^*(s, t) - a \Delta T^*(s, t) - f(s, t)) \zeta^*(s, t) ds dt \\
&\quad + \int_{\partial\Omega} \theta(s) \cdot n(s) (T^*(s, 0) - T_{in}(s)) \mu^*(s) ds \\
&\quad + \int_0^{t_f} \int_{\partial\Omega} \theta(s) \cdot n(s) \left[H(s) T^*(s, t) \zeta^*(s, t) + \frac{\partial}{\partial n} (T^*(s, t) \xi^*(s, t)) \right] ds dt \\
&= + \int_0^{t_f} \int_{\partial\Omega} \theta(s) \cdot n(s) \left[\frac{\partial}{\partial n} (T^*(s, t)) \zeta^*(s, t) \right] ds dt \\
&= - \int_0^{t_f} \int_{\partial\Omega} \theta(s) \cdot n(s) \left[a \frac{\partial}{\partial n} (T^*(s, t)) \frac{\partial}{\partial n} (\zeta^*(s, t)) \right] ds dt,
\end{aligned} \tag{5.30}$$

which completes the proof. \square

The adjoint equation (5.16) is backward in time and thus, for the calculation of the shape derivative (5.15), we need to save all solutions of the state and adjoint equation, which increases significantly the amount of memory needed compared to the previous Poisson model.

5.3.3 Eigenvalue approximation

Since the previous transient linear model is already a simplification of the solidification equation, a further simplification that reduces the computational cost, while keeping the time dependency of the temperature, is to consider the Fourier series of equation (5.14). From the spectral theorem (see [5]) we can write

$$T(x, t_f) = \sum_{i=1}^{\infty} e^{\lambda_i t_f} \beta_i T_i(x), \quad (5.31)$$

where $\beta_i = \frac{\int_{\Omega} T_{in}(x) T_i(x) dx}{\int_{\Omega} (T_i(x))^2 dx}$ and $(\lambda_i, T_i(x)) \in \mathbb{R}^- \times H_0^1(\Omega)$ (the eigenvalues λ_i are chosen to be negative)

solves the following eigenvalue problem:

$$\begin{cases} a\Delta T_i(x) &= \lambda_i T_i(x) & \text{in } \Omega, \\ T_i(x) &= 0 & \text{on } \partial\Omega. \end{cases} \quad (5.32)$$

Normalizing $T_i(x)$ to satisfy $\int_{\Omega} (T_i(x))^2 dx = 1$ and assuming that $t_f \rightarrow \infty$, i.e. that t_f is large enough so that the first eigenvalue dominates in (5.31), we deduce

$$T(x, t_f) \approx T^f(x) \equiv e^{\lambda_1 t_f} \beta_1 T_1(x) = e^{\lambda_1 t_f} \left(\int_{\Omega} T_{in}(x) T_1(x) dx \right) T_1(x). \quad (5.33)$$

Therefore, the state equation is now a simple eigenvalue problem

$$\begin{cases} a\Delta T_1(x) &= \lambda_1 T_1(x) & \text{in } \Omega, \\ T_1(x) &= 0 & \text{on } \partial\Omega. \end{cases} \quad (5.34)$$

Proposition 5.3.3. *Let $T^f(x)$ be given by (5.33), where (λ_1, T_1) solve the eigenvalue problem (5.34). Then, the shape derivative of (5.3) reads*

$$P'_{th}(\Omega)(\theta) = - \int_{\partial\Omega} \theta(s) \cdot n(s) \left[a \frac{\partial T_1}{\partial n}(s) \frac{\partial \zeta}{\partial n}(s) \right] ds, \quad (5.35)$$

where ζ is the solution of the adjoint system

$$\begin{cases} a\Delta \zeta(x) - \lambda_1 \zeta(x) &= -T_{in}(x) \int_{\Omega} 2(T^f(x) - T_s)^+ e^{\lambda_1 t_f} T_1(x) dx \\ &\quad + 2T_1(x) \int_{\Omega} 2(T^f(x) - T_s)^+ e^{\lambda_1 t_f} T_1(x) dx \int_{\Omega} T_{in}(x) T_1(x) dx \\ &\quad - 2(T^f(x) - T_s)^+ e^{\lambda_1 t_f} \int_{\Omega} T_{in}(x) T_1(x) dx, & \text{in } \Omega, \\ \zeta(x) &= 0, & \text{on } \partial\Omega. \end{cases} \quad (5.36)$$

Proof. We construct the Lagrangian function

$$\mathcal{L}(\Omega, \hat{T}, \hat{\zeta}, \hat{\mu}) = \int_{\Omega} \left[(e^{\hat{\lambda} t_f} \hat{\beta} \hat{T} - T_s)^+ \right]^2 dx + \int_{\Omega} (a\Delta \hat{T} - \hat{\lambda} \hat{T}) \hat{\zeta} dx + \int_{\partial\Omega} \hat{T} \hat{\mu} ds, \quad (5.37)$$

, where $\hat{T}, \hat{\zeta}, \hat{\mu} \in H^1(\mathbb{R}^N)$, $\hat{\lambda} = \frac{\int_{\Omega} a \nabla \hat{T} \cdot \nabla \hat{T} dx}{\int_{\Omega} \hat{T}^2 dx}$ and $\hat{\beta} = \frac{\int_{\Omega} T_{in}(x) \hat{T} dx}{\int_{\Omega} \hat{T}^2 dx}$.

Setting the partial derivative of \mathcal{L} with respect to $\hat{\zeta}$ in the direction of a test function ϕ , at the optimal point $(\Omega, T^*, \zeta^*, \mu^*)$, equal to zero, yields

$$\frac{\partial \mathcal{L}}{\partial \hat{\zeta}}(\Omega, T^*, \zeta^*, \mu^*)(\phi) = 0 \Rightarrow a\Delta T^* = \lambda^* T^* \quad \text{in } \Omega. \quad (5.38)$$

The derivative with respect to $\hat{\mu}$ gives the boundary consitions for μ^*

$$\frac{\partial \mathcal{L}}{\partial \hat{\mu}}(\Omega, T^*, \zeta^*, \mu^*)(\phi) = 0 \Rightarrow T^* = 0 \quad \text{on } \partial\Omega. \quad (5.39)$$

Equations (5.38) and (5.39) show that (λ^*, T^*) solves the eigenvalues problem (5.32). To simplify the exposition, we assume henceforth that T^* is normalized, such that

$$\int_{\Omega} (T^*(x))^2 dx = 1. \quad (5.40)$$

The partial derivative of \mathcal{L} with respect to \hat{T} in the direction ϕ reads

$$\begin{aligned} \frac{\partial \mathcal{L}}{\partial \hat{T}}(\Omega, T^*, \zeta^*, \mu^*)(\phi) &= \int_{\Omega} 2(e^{\lambda^* t_f} \beta^* T^* - T_s)^+ \frac{\partial(e^{\lambda^* t_f} \hat{\beta} \hat{T})}{\partial \hat{T}}(\phi) dx \\ &\quad + \int_{\Omega} (a \Delta \phi - \lambda^* \phi - \frac{\partial \hat{\lambda}}{\partial \hat{T}}(\phi)) \zeta^* dx + \int_{\partial\Omega} \phi \mu^* ds. \end{aligned} \quad (5.41)$$

After a simple calculation, we see that

$$\frac{\partial \hat{\lambda}}{\partial \hat{T}}(\Omega, T^*, \zeta^*, \mu^*)(\phi) = 0$$

and

$$\frac{\partial \hat{\beta}}{\partial \hat{T}}(\Omega, T^*, \zeta^*, \mu^*)(\phi) = \int_{\Omega} T_{in}(x) \phi(x) dx - 2 \int_{\Omega} T^*(x) \phi(x) dx \int_{\Omega} T_{in}(x) T^*(x) dx.$$

Replacing the above relations in (5.41) and using integration by parts, we get

$$\begin{aligned} \frac{\partial \mathcal{L}}{\partial \hat{T}}(\Omega, T^*, \zeta^*, \mu^*)(\phi) &= \int_{\Omega} 2(e^{\lambda^* t_f} \beta^* T^* - T_s)^+ e^{\lambda^* t_f} T^* dx \int_{\Omega} T_{in}(x) \phi(x) dx \\ &\quad - 2 \int_{\Omega} 2(e^{\lambda^* t_f} \beta^* T^* - T_s)^+ e^{\lambda^* t_f} T^* dx \int_{\Omega} T_{in}(x) T^*(x) dx \int_{\Omega} T^*(x) \phi(x) dx \\ &\quad + \int_{\Omega} 2(e^{\lambda^* t_f} \beta^* T^* - T_s)^+ e^{\lambda^* t_f} \beta^* \phi(x) dx \\ &\quad - \int_{\Omega} a \Delta \zeta^* \phi(x) dx + \int_{\partial\Omega} a \frac{\partial \zeta^*}{\partial n}(s) \phi(s) ds + \int_{\partial\Omega} a \frac{\partial \phi}{\partial n}(s) \zeta^*(s) ds \\ &\quad - \int_{\Omega} \lambda^* \zeta^*(x) \phi(x) dx + \int_{\partial\Omega} \mu^*(s) \phi(s) ds \end{aligned} \quad (5.42)$$

Taking ϕ with compact support in Ω , we take

$$\left\{ \begin{aligned} a \Delta \zeta^*(x) - \lambda^* \zeta^*(x) &= -T_{in}(x) \int_{\Omega} 2(e^{\lambda^* t_f} \beta^* T^* - T_s)^+ e^{\lambda^* t_f} T^*(x) dx \\ &\quad + 2T^*(x) \int_{\Omega} 2(e^{\lambda^* t_f} \beta^* T^* - T_s)^+ e^{\lambda^* t_f} T^*(x) dx \int_{\Omega} T_{in}(x) T^*(x) dx \\ &\quad - 2(e^{\lambda^* t_f} \beta^* T^* - T_s)^+ e^{\lambda^* t_f} \int_{\Omega} T_{in}(x) T^*(x) dx, \quad \text{in } \Omega. \end{aligned} \right. \quad (5.43)$$

Varying the normal flux of ϕ on the boundary $\partial\Omega$, while setting $\phi = 0$ on $\partial\Omega$, we reveal the boundary conditions for ζ^* :

$$\zeta^*(x) = 0 \quad \text{on } \partial\Omega. \quad (5.44)$$

From equations (5.43) and (5.44) we deduce that ζ^* is in fact the solution of the adjoint system (5.36). Finally, varying ϕ on the boundary, while setting its normal flux equal to zero, the optimal Lagrange multiplier μ^* is

$$\mu^*(s) = -a \frac{\partial \zeta^*}{\partial n}(s) \quad \forall s \in \partial\Omega. \quad (5.45)$$

The shape derivative of (5.3) at Ω is revealed as the shape derivative of \mathcal{L} at the optimal point $(\Omega, T^*, \zeta^*, \mu^*)$:

$$\begin{aligned}
P'_{th}(\Omega)(\theta) &= \int_{\partial\Omega} \theta(s) \cdot n(s) \left[(e^{\lambda^* t_f} \beta^* T^*(s) - T_s)^+ \right]^2 ds \\
&\quad + \int_{\partial\Omega} \theta(s) \cdot n(s) [(a \Delta T^*(s) - \lambda^* T^*(s)) \zeta^*(s)] ds \\
&\quad + \int_{\partial\Omega} \theta(s) \cdot n(s) \left[H(s) T^*(s) \mu^*(s) + \frac{\partial(T^* \mu^*)}{\partial n}(s) \right] ds \\
&= \int_{\partial\Omega} \theta(s) \cdot n(s) \left[\frac{\partial(T^*)}{\partial n}(s) \mu^*(s) \right] ds \\
&= - \int_{\partial\Omega} \theta(s) \cdot n(s) \left[a \frac{\partial(T^*)}{\partial n}(s) \frac{\partial(\zeta^*)}{\partial n}(s) \right] ds,
\end{aligned} \tag{5.46}$$

which completes the proof. \square

Remark 5.3.4. In order to compute the shape derivative (5.35), we have assumed that the functional (5.3) is shape differentiable. This is a classical result under the assumption that the first eigenvalue is simple [10, 118, 47, 122, 132]. The Theorem of Krein-Rutman [5] proves this assumption for the Laplacian equation (5.34) under the assumptions that Ω is an open, bounded, connected domain of C^1 regularity in \mathbb{R}^N .

Remark 5.3.5. The adjoint equation (5.36) admits a solution because of the following reason. First, note that the operator $A = a\Delta(\cdot) - \lambda_1(\cdot)$ on the left-hand side of (5.36) has a kernel of dimension 1, generated by T_1 . Therefore, the solution is unique, only up to the addition of a multiple of T_1 . Second, since A is a self-adjoint operator, the existence of a solution is guaranteed if the right-hand side belongs to the range of A . A formal computation (working as if A was a finite dimensional operator and ignoring any issue of closedness of unbounded operators) shows that

$$Im(A) = (Ker A^T)^\perp = (Ker A)^\perp. \tag{5.47}$$

Denoting $b(x)$ the right-hand side of equation (5.36) and

$$C(T^f(x)) = 2(T^f(x) - T_s)^+,$$

we have that

$$\begin{aligned}
\int_{\Omega} T_1(x) b(x) dx &= - \int_{\Omega} C(T^f(x)) e^{\lambda_1 t_f} T_1(x) dx \int_{\Omega} T_1(x) T_{in}(x) dx \\
&\quad + 2 \int_{\Omega} C(T^f(x)) e^{\lambda_1 t_f} T_1(x) dx \int_{\Omega} T_{in}(x) T_1(x) dx \int_{\Omega} (T_1(x))^2 dx \\
&\quad - \int_{\Omega} T_{in}(x) T_1(x) dx \int_{\Omega} C(T^f(x)) e^{\lambda_1 t_f} T_1(x) dx = 0
\end{aligned}$$

, which means that $T_1 \perp b$ and, because of (5.47), $b \in Im(A)$. In numerical practice, instead of equation (5.36), we solve the equation

$$\left\{ \begin{aligned} a \Delta \tilde{\zeta}(x) - \lambda_1 \tilde{\zeta}(x) + \varepsilon T_1 \otimes T_1 \tilde{\zeta} &= -T_{in}(x) \int_{\Omega} C(T^f(x)) e^{\lambda_1 t_f} T_1(x) dx \\ &\quad + 2T_1(x) \int_{\Omega} C(T^f(x)) e^{\lambda_1 t_f} T_1(x) dx \int_{\Omega} T_{in}(x) T_1(x) dx \\ &\quad - C(T^f(x)) e^{\lambda_1 t_f} \int_{\Omega} T_{in}(x) T_1(x) dx, \quad \text{in } \Omega, \\ \tilde{\zeta}(x) &= 0, \quad \text{on } \partial\Omega, \end{aligned} \right. \tag{5.48}$$

where we denote

$$T_1 \otimes T_1 \tilde{\zeta} = \left(\int_{\Omega} T_1 \tilde{\zeta} dx \right) T_1$$

and $\varepsilon > 0$ is a small positive parameter ($\varepsilon \ll 1$). Equation (5.48) has a unique solution. Then, the adjoint state is taken by

$$\zeta(x) = \tilde{\zeta}(x) - T_1 \otimes T_1 \tilde{\zeta},$$

in order to satisfy that $\zeta \perp T_1$.

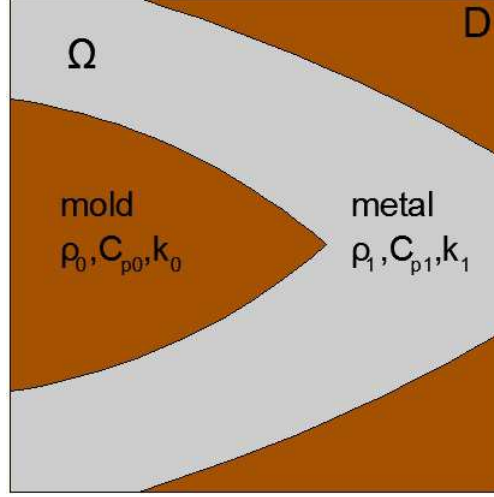


Figure 5.3: Simplified casting system.

5.3.4 Linear transient heat equation with piecewise discontinuous conductivity

Until now, the material properties of the mold have been neglected and homogeneous Dirichlet boundary conditions have been set, for reasons of simplicity. However, the material properties of the mold play a significant role in the cooling process and we need to test its effect on the optimal shape. At a first step, we consider the material properties to be piecewise constant in the working domain D and ignore their dependence on the temperature. The state equation becomes

$$\begin{cases} \rho(x)C_p(x)\partial_t T(x,t) - \nabla \cdot (k(x)\nabla T(x,t)) = 0 & \text{in } D \times (0, t_f), \\ k(x)\frac{\partial T(x,t)}{\partial n} - h(x)(T(x,t) - T_{air}) = 0 & \text{on } \partial D \times (0, t_f), \\ T(x, 0) = T_{in}(x) & \text{in } D \times \{0\}, \end{cases} \quad (5.49)$$

where

$$(\rho(x), C_p(x), k(x)) = \begin{cases} (\rho_1, C_{p1}, k_1) & \text{in } \Omega, \\ (\rho_0, C_{p0}, k_0) & \text{in } D \setminus \Omega, \end{cases}$$

ρ being the density of the material, C_p its thermal capacity, k its conductivity and

$$h(x) = \begin{cases} h_{c-a} & \text{in } \partial\Omega \cap \partial D, \\ h_{m-a} & \text{in } \partial D \setminus \partial\Omega, \end{cases}$$

a heat transfer coefficient that simulates the heat flux across the boundary of the domain D (see Figure 5.3).

Remark 5.3.6. As we have explained in Chapter 2, it is common practice in industrial applications to use an idealized and simplified casting system in order to check if the shape satisfies some design specifications. In such a model, the structure is usually surrounded by the mold and a heat transfer coefficient is used to account for the heat exchange between the mold and the environment. This is not the case in Figure 5.3 and equation (5.49), where a heat transfer coefficient has been used for the ideal interface between the metal and the air for reasons of simplicity in the numerical implementation. The choice of the value for this coefficient can have a great impact on the numerical results.

The discontinuity in the conductivity adds an extra difficulty in the calculation of the shape derivative, when equation (5.49) is used. The reason is the discontinuity of the normal derivative of $T(x, t)$ across the boundary $\partial\Omega$ (see [19, 108]). In order to calculate properly the shape derivative of the problem, we prefer to view the above equation as a transmission problem, where the temperature and the normal flux across the boundary $\partial\Omega$ are continuous (see Chapter 6 for a complete analysis and proposals in order to

avoid numerical difficulties). Then, equation (5.49) is equivalent to the coupled system

$$\left\{ \begin{array}{ll} \rho_1 C_{p1} \partial_t T_1(x, t) - k_1 \Delta T_1(x, t) &= 0 \quad \text{in } \Omega \times (0, t_f) \\ k_1 \frac{\partial T_1(x, t)}{\partial n} - h_{c-a}(T_1(x, t) - T_{air}) &= 0 \quad \text{on } (\partial\Omega \cap \partial D) \times (0, t_f) \\ T_1(x, 0) &= T_{in}(x) \quad \text{in } \Omega \times \{0\} \\ T_1(x, t) &= T_0(x, t) \quad \text{on } \partial\Omega \setminus (\partial\Omega \cap \partial D) \times (0, t_f) \\ k_1 \frac{\partial T_1(x, t)}{\partial n} - k_0 \frac{\partial T_0(x, t)}{\partial n} &= 0 \quad \text{on } \partial\Omega \setminus (\partial\Omega \cap \partial D) \times (0, t_f) \end{array} \right. \quad (5.50)$$

and

$$\left\{ \begin{array}{ll} \rho_0 C_{p0} \partial_t T_0(x, t) - k_0 \Delta T_0(x, t) &= 0 \quad \text{in } (D \setminus \Omega) \times (0, t_f) \\ k_0 \frac{\partial T_0(x, t)}{\partial n} - h_{m-a}(T_0(x, t) - T_{air}) &= 0 \quad \text{on } (\partial D \setminus \partial\Omega) \times (0, t_f) \\ T_0(x, 0) &= T_{in}(x) \quad \text{in } (D \setminus \Omega) \times \{0\} \\ T_0(x, t) &= T_1(x, t) \quad \text{on } \partial\Omega \setminus (\partial\Omega \cap \partial D) \times (0, t_f) \\ -k_0 \frac{\partial T_0(x, t)}{\partial n} + k_1 \frac{\partial T_1(x, t)}{\partial n} &= 0 \quad \text{on } \partial\Omega \setminus (\partial\Omega \cap \partial D) \times (0, t_f) \end{array} \right. \quad (5.51)$$

and the global temperature field is given as

$$T(x, t) = T_1(x, t)\chi_\Omega(x) + T_0(x, t)(1 - \chi_\Omega(x)), \quad (5.52)$$

where χ_Ω is the characteristic function of the domain Ω , defined in equation (1.2).

Proposition 5.3.7. *Let $T_1(x, t)$ and $T_0(x, t)$ be solutions of equations (5.50) and (5.51) respectively and $T(x, t)$ defined as in (5.52). Then, the shape derivative of (5.3) reads*

$$\begin{aligned} P'_{th}(\Omega)(\theta) = & \int_{\partial\Omega} \theta(s) \cdot n(s) ([T_1(x, t_f) - T_s]^+)^2 ds \\ & + \int_0^{t_f} \int_{\partial\Omega} \theta(s) \cdot n(s) (\rho_1 C_{p1} \partial_t T_1(s, t) \zeta_1(s, t) - \rho_0 C_{p0} \partial_t T_0(s, t) \zeta_0(s, t)) ds dt \\ & + \int_{\partial\Omega} \int_0^{t_f} \theta(s) \cdot n(s) [(k_1 - k_0) \frac{\partial T_1}{\partial \tau} \frac{\partial \zeta_1}{\partial \tau} - (\frac{1}{k_1} - \frac{1}{k_0}) (k_1 \frac{\partial T_1}{\partial n}) (k_1 \frac{\partial \zeta_1}{\partial n})] dt ds, \end{aligned} \quad (5.53)$$

where

$$\zeta(x, t) = \zeta_1(x, t)\chi_\Omega + \zeta_0(x, t)(1 - \chi_\Omega) \quad (5.54)$$

is the global adjoint state and ζ_1, ζ_0 are solutions to the following coupled pdes:

$$\left\{ \begin{array}{ll} -\rho_1 C_{p1} \partial_t \zeta_1(x, t) - k_1 \Delta \zeta_1(x, t) &= 0 \quad \text{in } \Omega \times (0, t_f) \\ k_1 \frac{\partial \zeta_1(x, t)}{\partial n} - h_{c-a}(\zeta_1(x, t)) &= 0 \quad \text{on } (\partial\Omega \cap \partial D) \times (0, t_f) \\ \zeta_1(x, t_f) &= \frac{-2(T_1(x, t_f) - T_s)^+}{\rho_1 C_{p1}} \quad \text{in } \Omega \times \{0\} \\ \zeta_1(x, t) &= \zeta_0(x, t) \quad \text{on } \partial\Omega \setminus (\partial\Omega \cap \partial D) \times (0, t_f) \\ k_1 \frac{\partial \zeta_1(x, t)}{\partial n} - k_0 \frac{\partial \zeta_0(x, t)}{\partial n} &= 0 \quad \text{on } \partial\Omega \setminus (\partial\Omega \cap \partial D) \times (0, t_f) \end{array} \right. \quad (5.55)$$

and

$$\left\{ \begin{array}{ll} -\rho_0 C_{p0} \partial_t \zeta_0(x, t) - k_0 \Delta \zeta_0(x, t) &= 0 \quad \text{in } (D \setminus \Omega) \times (0, t_f) \\ k_0 \frac{\partial \zeta_0(x, t)}{\partial n} - h_{m-a}(\zeta_0(x, t)) &= 0 \quad \text{on } (\partial D \setminus \partial\Omega) \times (0, t_f) \\ \zeta_0(x, t_f) &= 0 \quad \text{in } (D \setminus \Omega) \times \{0\} \\ \zeta_0(x, t) &= \zeta_1(x, t) \quad \text{on } \partial\Omega \setminus (\partial\Omega \cap \partial D) \times (0, t_f) \\ -k_0 \frac{\partial \zeta_0(x, t)}{\partial n} + k_1 \frac{\partial \zeta_1(x, t)}{\partial n} &= 0 \quad \text{on } \partial\Omega \setminus (\partial\Omega \cap \partial D) \times (0, t_f). \end{array} \right. \quad (5.56)$$

Proof. We formulate the Lagrangian function

$$\begin{aligned}
\mathcal{L}(\Omega, \widehat{T}_1, \widehat{T}_0, \widehat{\zeta}_1, \widehat{\zeta}_0, \widehat{\mu}_1, \widehat{\mu}_0, \widehat{\nu}, \widehat{\xi}, \widehat{q}_1, \widehat{q}_0) = & \\
& \int_{\Omega} \left[(\widehat{T}_1(x, t_f) - T_s)^+ \right]^2 dx \\
& + \int_0^{t_f} \int_{\Omega} (\rho_1 C_{p1} \partial_t \widehat{T}_1(x, t) - k_1 \Delta \widehat{T}_1(x, t)) \widehat{\zeta}_1(x, t) dx dt + \int_{\Omega} (\widehat{T}_1(x, 0) - T_{in}(x)) \widehat{\mu}_1(x) dx \\
& + \int_0^{t_f} \int_{\Omega} (\rho_0 C_{p0} \partial_t \widehat{T}_0(x, t) - k_0 \Delta \widehat{T}_0(x, t)) \widehat{\zeta}_0(x, t) dx dt + \int_{\Omega} (\widehat{T}_0(x, 0) - T_{in}(x)) \widehat{\mu}_0(x) dx \\
& + \int_0^{t_f} \int_{(\partial\Omega \setminus (\partial\Omega \cap \partial D))} (\widehat{T}_1(s, t) - \widehat{T}_0(s, t)) \widehat{\nu}(s, t) ds dt \\
& + \int_0^{t_f} \int_{(\partial\Omega \setminus (\partial\Omega \cap \partial D))} (k_1 \frac{\partial \widehat{T}_1}{\partial n} - k_0 \frac{\partial \widehat{T}_0}{\partial n}) \widehat{\xi}(s, t) ds dt \\
& + \int_0^{t_f} \int_{(\partial\Omega \cap \partial D)} (k_1 \frac{\partial \widehat{T}_1}{\partial n} - h_{c-a}(\widehat{T}_1 - T_{air})) \widehat{q}_1(s, t) ds dt \\
& + \int_0^{t_f} \int_{(\partial D \setminus \partial\Omega)} (k_0 \frac{\partial \widehat{T}_0}{\partial n} - h_{m-a}(\widehat{T}_0 - T_{air})) \widehat{q}_0(s, t) ds dt.
\end{aligned} \tag{5.57}$$

Fixing the domain Ω , the first order optimality conditions for \mathcal{L} at the optimal point

$$w^* \equiv (\Omega, T_1^*, T_0^*, \zeta_1^*, \zeta_0^*, \mu_1^*, \mu_0^*, \nu^*, \xi^*, q_1^*, q_0^*)$$

read

$$\frac{\partial \mathcal{L}}{\partial \widehat{\zeta}_1}(w^*)(\phi) = 0 \Rightarrow \rho_1 C_{p1} \partial_t T_1^*(x, t) - k_1 \Delta T_1^*(x, t) = 0 \quad \text{in } \Omega \times (0, t_f), \tag{5.58}$$

$$\frac{\partial \mathcal{L}}{\partial \widehat{\mu}_1}(w^*)(\phi) = 0 \Rightarrow T_1^*(x, 0) = T_{in}(x) \quad \text{in } \Omega \times \{0\}, \tag{5.59}$$

$$\frac{\partial \mathcal{L}}{\partial \widehat{\nu}}(w^*)(\phi) = 0 \Rightarrow T_1^*(x, t) = T_0^*(x, t) \quad \text{on } \partial\Omega \setminus (\partial\Omega \cap \partial D) \times (0, t_f), \tag{5.60}$$

$$\frac{\partial \mathcal{L}}{\partial \widehat{\xi}}(w^*)(\phi) = 0 \Rightarrow k_1 \frac{\partial T_1^*}{\partial n}(x, t) = k_0 \frac{\partial T_0^*}{\partial n}(x, t) \quad \text{on } \partial\Omega \setminus (\partial\Omega \cap \partial D) \times (0, t_f), \tag{5.61}$$

$$\frac{\partial \mathcal{L}}{\partial \widehat{q}_1}(w^*)(\phi) = 0 \Rightarrow k_1 \frac{\partial T_1^*}{\partial n}(x, t) = h_{c-a}(T_1^*(x, t) - T_{air}) \quad \text{on } (\partial\Omega \cap \partial D) \times (0, t_f), \tag{5.62}$$

$$\frac{\partial \mathcal{L}}{\partial \widehat{\zeta}_0}(w^*)(\phi) = 0 \Rightarrow \rho_0 C_{p0} \partial_t T_0^*(x, t) - k_0 \Delta T_0^*(x, t) = 0 \quad \text{in } (D \setminus \Omega) \times (0, t_f) \tag{5.63}$$

$$\frac{\partial \mathcal{L}}{\partial \widehat{\mu}_0}(w^*)(\phi) = 0 \Rightarrow T_0^*(x, 0) = T_{in}(x) \quad \text{in } D \setminus \Omega \times \{0\}, \tag{5.64}$$

$$\frac{\partial \mathcal{L}}{\partial \widehat{q}_0}(w^*)(\phi) = 0 \Rightarrow k_0 \frac{\partial T_0^*}{\partial n}(x, t) = h_{m-a}(T_0^*(x, t) - T_{air}) \quad \text{on } (\partial D \setminus \partial\Omega) \times (0, t_f). \tag{5.65}$$

From equations (5.58), (5.59), (5.60), (5.61), (5.62), we deduce that T_1^* solves equation (5.50), while equations (5.60), (5.61), (5.63), (5.64), (5.65) show that T_0^* solves equation (5.51).

The partial derivative of \mathcal{L} with respect to \widehat{T}_1 in the direction of a test function ϕ reads

$$\begin{aligned}
\frac{\partial \mathcal{L}}{\partial \widehat{T}_1}(w^*)(\phi) = & \int_{\Omega} 2(T_1^*(x, t_f) - T_s)^+ \phi(x, t_f) dx \\
& + \int_0^{t_f} \int_{\Omega} (\rho_1 C_{p1} \partial_t \phi(x, t) - k_1 \Delta \phi(x, t)) \zeta_1^*(x, t) dx dt + \int_{\Omega} \phi(x, 0) \mu_1^*(x) dx \\
& + \int_0^{t_f} \int_{(\partial\Omega \setminus (\partial\Omega \cap \partial D))} \phi(s, t) \nu^*(s, t) ds dt \\
& + \int_0^{t_f} \int_{(\partial\Omega \setminus (\partial\Omega \cap \partial D))} k_1 \frac{\partial \phi}{\partial n} \xi^*(s, t) ds dt \\
& + \int_0^{t_f} \int_{(\partial\Omega \cap \partial D)} (k_1 \frac{\partial \phi}{\partial n} - h_{c-a} \phi) q_1^*(s, t) ds dt.
\end{aligned} \tag{5.66}$$

Replacing in (5.66) the following equality

$$\begin{aligned}
& \int_0^{t_f} \int_{\Omega} (\rho_1 C_{p1} \partial_t \phi(x, t) - k_1 \Delta \phi(x, t)) \zeta_1^*(x, t) dx dt = \\
& \left[\int_{\Omega} \rho_1 C_{p1} \phi(x, t) \zeta_1^*(x, t) dx \right]_0^{t_f} - \int_0^{t_f} \int_{\Omega} \rho_1 C_{p1} \partial_t \zeta_1^*(x, t) \phi(x, t) dx dt \\
& - \int_0^{t_f} \int_{\partial \Omega} k_1 \frac{\partial \phi}{\partial n}(s, t) \zeta_1^*(s, t) ds dt + \int_0^{t_f} \int_{\Omega} k_1 \nabla \phi(x, t) \cdot \nabla \zeta_1^*(x, t) dx dt \\
& = \left[\int_{\Omega} \rho_1 C_{p1} \zeta_1^*(x, t) \phi(x, t) dx \right]_0^{t_f} - \int_0^{t_f} \int_{\Omega} \rho_1 C_{p1} \partial_t \zeta_1^*(x, t) \phi(x, t) dx dt \\
& - \int_0^{t_f} \int_{\partial \Omega} k_1 \frac{\partial \phi}{\partial n}(s, t) \zeta_1^*(s, t) ds dt + \int_0^{t_f} \int_{\partial \Omega} k_1 \frac{\partial \zeta_1^*}{\partial n}(s, t) \phi(s, t) ds dt \\
& - \int_0^{t_f} \int_{\Omega} k_1 \Delta \zeta_1^*(x, t) \phi(x, t) dx dt,
\end{aligned} \tag{5.67}$$

we get

$$\begin{aligned}
\frac{\partial \mathcal{L}}{\partial \hat{T}_1}(w^*)(\phi) = & \int_{\Omega} 2(T_1^*(x, t_f) - T_s)^+ \phi(x, t_f) dx + \int_{\Omega} \rho_1 C_{p1} \zeta_1^*(x, t_f) \phi(x, t_f) dx \\
& - \int_{\Omega} \rho_1 C_{p1} \zeta_1^*(x, 0) \phi(x, 0) dx - \int_0^{t_f} \int_{\Omega} \rho_1 C_{p1} \partial_t \zeta_1^*(x, t) \phi(x, t) dx dt \\
& - \int_0^{t_f} \int_{\Omega} k_1 \Delta \zeta_1^*(x, t) \phi(x, t) dx dt + \int_{\Omega} \phi(x, 0) \mu_1^*(x) dx \\
& - \int_0^{t_f} \int_{\partial \Omega} k_1 \frac{\partial \phi}{\partial n}(s, t) \zeta_1^*(s, t) ds dt + \int_0^{t_f} \int_{\partial \Omega} k_1 \frac{\partial \zeta_1^*}{\partial n}(s, t) \phi(s, t) ds dt \\
& + \int_0^{t_f} \int_{(\partial \Omega \setminus (\partial \Omega \cap \partial D))} \phi(s, t) \nu^*(s, t) ds dt + \int_0^{t_f} \int_{(\partial \Omega \setminus (\partial \Omega \cap \partial D))} k_1 \frac{\partial \phi}{\partial n} \xi^*(s, t) ds dt \\
& + \int_0^{t_f} \int_{(\partial \Omega \cap \partial D)} (k_1 \frac{\partial \phi}{\partial n} - h_{c-a} \phi) q_1^*(s, t) ds dt.
\end{aligned} \tag{5.68}$$

Taking ϕ with compact support in $\Omega \times (0, t_f)$, we get

$$- \rho_1 C_{p1} \partial_t \zeta_1^*(x, t) - k_1 \Delta \zeta_1^*(x, t) = 0 \quad \text{in } \Omega \times (0, t_f). \tag{5.69}$$

Varying ϕ in $\Omega \times \{t_f\}$ and $\Omega \times \{0\}$, we get

$$\zeta_1^*(x, t_f) = \frac{-2(T_1^*(x, t_f) - T_s)^+}{\rho_1 C_{p1}} \quad \text{in } \Omega \times \{t_f\} \tag{5.70}$$

and

$$\mu_1^*(x) = \rho_1 C_{p1} \zeta_1^*(x, 0) \quad \text{in } \Omega \tag{5.71}$$

respectively. Varying ϕ on $\partial \Omega \setminus (\partial \Omega \cap \partial D) \times (0, t_f)$ and $(\partial \Omega \cap \partial D) \times (0, t_f)$, with zero normal flux ($k_1 \frac{\partial \phi}{\partial n} = 0$), we get

$$\nu^*(x, t) = -k_1 \frac{\partial \zeta_1^*}{\partial n}(x, t) \quad \text{on } \partial \Omega \setminus (\partial \Omega \cap \partial D) \times (0, t_f) \tag{5.72}$$

and

$$k_1 \frac{\partial \zeta_1^*}{\partial n}(x, t) = h_{c-a} q_1^*(x, t) \quad \text{on } (\partial \Omega \cap \partial D) \times (0, t_f). \tag{5.73}$$

Varying the normal flux of ϕ on $\partial \Omega \setminus (\partial \Omega \cap \partial D) \times (0, t_f)$ and $(\partial \Omega \cap \partial D) \times (0, t_f)$, with $\phi = 0$, we get

$$\zeta_1^*(x, t) = \xi^*(x, t) \quad \text{on } \partial \Omega \setminus (\partial \Omega \cap \partial D) \times (0, t_f) \tag{5.74}$$

and

$$\zeta_1^*(x, t) = q_1^*(x, t) \quad \text{on } (\partial \Omega \cap \partial D) \times (0, t_f). \tag{5.75}$$

The same analysis as previously holds for the partial derivative of \mathcal{L} with respect to \hat{T}_0 and results in the following equalities:

$$- \rho_0 C_{p0} \partial_t \zeta_0^*(x, t) - k_0 \Delta \zeta_0^*(x, t) = 0 \quad \text{in } (D \setminus \Omega) \times (0, t_f), \tag{5.76}$$

$$\zeta_0^*(x, t_f) = 0 \quad \text{in } (D \setminus \Omega) \times \{t_f\}, \quad (5.77)$$

$$\mu_0^*(x) = \rho_0 C_{p0} \zeta_0^*(x, 0) \quad \text{in } D \setminus \Omega, \quad (5.78)$$

$$\nu^*(x, t) = -k_0 \frac{\partial \zeta_0^*}{\partial n}(x, t) \quad \text{on } \partial\Omega \setminus (\partial\Omega \cap \partial D) \times (0, t_f), \quad (5.79)$$

$$k_0 \frac{\partial \zeta_0^*}{\partial n}(x, t) = -h_{m-a} q_0^*(x, t) \quad \text{on } (\partial D \setminus \partial\Omega) \times (0, t_f), \quad (5.80)$$

$$\zeta_0^*(x, t) = \xi^*(x, t) \quad \text{on } \partial\Omega \setminus (\partial\Omega \cap \partial D) \times (0, t_f), \quad (5.81)$$

and

$$\zeta_0^*(x, t) = -q_0^*(x, t) \quad \text{on } (\partial D \setminus \partial\Omega) \times (0, t_f). \quad (5.82)$$

Equations (5.69)-(5.82) show that ζ_1^* and ζ_0^* solve the adjoint states (5.55) and (5.56) respectively. Before computing the shape derivative of $P_{th}(\Omega)$, we write again the Lagrangian function (5.57), after an intergration by parts, as

$$\begin{aligned} \mathcal{L}(\Omega, \widehat{T}_1, \widehat{T}_0, \widehat{\zeta}_1, \widehat{\zeta}_0, \widehat{\mu}_1, \widehat{\mu}_0, \widehat{\nu}, \widehat{\xi}, \widehat{q}_1, \widehat{q}_0) = & \\ & \int_{\Omega} \left[(\widehat{T}_1(x, t_f) - T_s)^+ \right]^2 dx + \int_0^{t_f} \int_{\Omega} (\rho_1 C_{p1} \partial_t \widehat{T}_1(x, t) \widehat{\zeta}_1(x, t) + k_1 \nabla \widehat{T}_1(x, t) \cdot \nabla \widehat{\zeta}_1(x, t)) dx dt \\ & + \int_0^{t_f} \int_{\Omega} (\rho_0 C_{p0} \partial_t \widehat{T}_0(x, t) \widehat{\zeta}_0(x, t) + k_0 \nabla \widehat{T}_0(x, t) \cdot \nabla \widehat{\zeta}_0(x, t)) dx dt \\ & - \int_0^{t_f} \int_{\partial\Omega} k_1 \frac{\partial \widehat{T}_1}{\partial n}(s, t) \widehat{\zeta}_1(s, t) ds dt + \int_0^{t_f} \int_{\partial\Omega} k_0 \frac{\partial \widehat{T}_0}{\partial n}(s, t) \widehat{\zeta}_0(s, t) ds dt \\ & + \int_{\Omega} (\widehat{T}_1(x, 0) - T_{in}(x)) \widehat{\mu}_1(x) dx + \int_{\Omega} (\widehat{T}_0(x, 0) - T_{in}(x)) \widehat{\mu}_0(x) dx \\ & + \int_0^{t_f} \int_{(\partial\Omega \setminus (\partial\Omega \cap \partial D))} (\widehat{T}_1(s, t) - \widehat{T}_0(s, t)) \widehat{\nu}(s, t) ds dt \\ & + \int_0^{t_f} \int_{(\partial\Omega \setminus (\partial\Omega \cap \partial D))} (k_1 \frac{\partial \widehat{T}_1}{\partial n} - k_0 \frac{\partial \widehat{T}_0}{\partial n}) \widehat{\xi}(s, t) ds dt \\ & + \int_0^{t_f} \int_{(\partial\Omega \cap \partial D)} (k_1 \frac{\partial \widehat{T}_1}{\partial n} - h_{c-a}(\widehat{T}_1 - T_{air})) \widehat{q}_1(s, t) ds dt \\ & + \int_0^{t_f} \int_{(\partial D \setminus \partial\Omega)} (k_0 \frac{\partial \widehat{T}_0}{\partial n} - h_{m-a}(\widehat{T}_0 - T_{air})) \widehat{q}_0(s, t) ds dt. \end{aligned} \quad (5.83)$$

The shape derivative of $P_{th}(\Omega)$ equals the shape derivative of \mathcal{L} at the optimal point:

$$\begin{aligned}
P'_{th}(\Omega)(\theta) = & \int_{\partial\Omega} \theta(s) \cdot n(s) [(T_1^*(s, t_f) - T_s)^+]^2 ds \\
& + \int_{\partial\Omega} \theta(s) \cdot n(s) \int_0^{t_f} (\rho_1 C_{p1} \partial_t T_1^*(s, t) \zeta_1^*(s, t) + k_1 \nabla T_1^*(s, t) \cdot \nabla \zeta_1^*(s, t)) dt ds \\
& + \int_{\partial\Omega} \theta(s) \cdot n(s) \int_0^{t_f} (\rho_0 C_{p0} \partial_t T_0^*(s, t) \zeta_0^*(s, t) + k_0 \nabla T_0^*(s, t) \cdot \nabla \zeta_0^*(s, t)) dt ds \\
& - \int_{\partial\Omega} \theta(s) \cdot n(s) \int_0^{t_f} \left[H(s) k_1 \frac{\partial T_1^*}{\partial n}(s, t) \zeta_1^*(s, t) + \frac{\partial}{\partial n} (k_1 \frac{\partial T_1^*}{\partial n}(s, t) \zeta_1^*(s, t)) \right] dt ds \\
& + \int_{\partial\Omega} \theta(s) \cdot n(s) \int_0^{t_f} \left[H(s) k_0 \frac{\partial T_0^*}{\partial n}(s, t) \zeta_0^*(s, t) + \frac{\partial}{\partial n} (k_0 \frac{\partial T_0^*}{\partial n}(s, t) \zeta_0^*(s, t)) \right] dt ds \\
& + \int_{\partial\Omega} \theta(s) \cdot n(s) [(T_1^*(s, 0) - T_{in}(s)) \mu_1^*(s)] ds \\
& - \int_{\partial\Omega} \theta(s) \cdot n(s) [(T_0^*(s, 0) - T_{in}(s)) \mu_0^*(s)] ds \\
& + \int_{\partial\Omega} \theta(s) \cdot n(s) \int_0^{t_f} \left[H(s) (T_1^*(s, t) - T_0^*(s, t)) \nu^*(s, t) + \frac{\partial}{\partial n} ((T_1^*(s, t) - T_0^*(s, t)) \nu^*(s, t)) \right] dt ds \\
& + \int_{\partial\Omega} \theta(s) \cdot n(s) \int_0^{t_f} [H(s) (k_1 \frac{\partial T_1^*}{\partial n}(s, t) - k_0 \frac{\partial T_0^*}{\partial n}(s, t)) \xi^*(s, t)] \\
& + \frac{\partial}{\partial n} (k_1 \frac{\partial T_1^*}{\partial n}(s, t) - k_0 \frac{\partial T_0^*}{\partial n}(s, t)) \xi^*(s, t)] dt ds \\
& = \int_{\partial\Omega} \theta(s) \cdot n(s) [(T_1^*(s, t_f) - T_s)^+]^2 ds \\
& + \int_{\partial\Omega} \theta(s) \cdot n(s) \int_0^{t_f} (\rho_1 C_{p1} \partial_t T_1^*(s, t) \zeta_1^*(s, t) - \rho_0 C_{p0} \partial_t T_0^*(s, t) \zeta_0^*(s, t)) dt ds \\
& + \int_{\partial\Omega} \theta(s) \cdot n(s) \int_0^{t_f} (k_1 \frac{\partial T_1^*}{\partial n}(s, t) \frac{\partial \zeta_1^*}{\partial n}(s, t) + k_1 \frac{\partial T_1^*}{\partial \tau}(s, t) \frac{\partial \zeta_1^*}{\partial \tau}(s, t) \\
& - k_0 \frac{\partial T_0^*}{\partial n}(s, t) \frac{\partial \zeta_0^*}{\partial n}(s, t) - k_0 \frac{\partial T_0^*}{\partial \tau}(s, t) \frac{\partial \zeta_0^*}{\partial \tau}(s, t)) dt ds \\
& - \int_{\partial\Omega} \theta(s) \cdot n(s) \int_0^{t_f} \left[+ \frac{\partial}{\partial n} (k_1 \frac{\partial T_1^*}{\partial n}(s, t) \zeta_1^*(s, t)) \right] dt ds \\
& + \int_{\partial\Omega} \theta(s) \cdot n(s) \int_0^{t_f} \left[+ \frac{\partial}{\partial n} (k_0 \frac{\partial T_0^*}{\partial n}(s, t) \zeta_0^*(s, t)) \right] dt ds \\
& + \int_{\partial\Omega} \theta(s) \cdot n(s) \int_0^{t_f} \left[+ \frac{\partial}{\partial n} ((T_1^*(s, t) - T_0^*(s, t)) \nu^*(s, t)) \right] dt ds \\
& + \int_{\partial\Omega} \theta(s) \cdot n(s) \int_0^{t_f} \left[+ \frac{\partial}{\partial n} (k_1 \frac{\partial T_1^*}{\partial n}(s, t) - k_0 \frac{\partial T_0^*}{\partial n}(s, t)) \xi^*(s, t) \right] dt ds \\
& = \int_{\partial\Omega} \theta(s) \cdot n(s) [(T_1^*(s, t_f) - T_s)^+]^2 ds \\
& + \int_{\partial\Omega} \theta(s) \cdot n(s) \int_0^{t_f} (\rho_1 C_{p1} \partial_t T_1^*(s, t) \zeta_1^*(s, t) - \rho_0 C_{p0} \partial_t T_0^*(s, t) \zeta_0^*(s, t)) dt ds \\
& + \int_{\partial\Omega} \theta(s) \cdot n(s) \int_0^{t_f} ((k_1 - k_0) \frac{\partial T_1^*}{\partial \tau}(s, t) \frac{\partial \zeta_1^*}{\partial \tau}(s, t) + (\frac{1}{k_1} - \frac{1}{k_0}) k_1 \frac{\partial T_1^*}{\partial n}(s, t) k_1 \frac{\partial \zeta_1^*}{\partial n}(s, t)) dt ds \\
& - \int_{\partial\Omega} \theta(s) \cdot n(s) \int_0^{t_f} \left[+ \frac{\partial}{\partial n} (k_1 \frac{\partial T_1^*}{\partial n}(s, t) \zeta_1^*(s, t) + \frac{\partial T_1^*}{\partial n}(s, t) k_1 \frac{\partial \zeta_1^*}{\partial n}(s, t)) \right] dt ds \\
& + \int_{\partial\Omega} \theta(s) \cdot n(s) \int_0^{t_f} \left[+ \frac{\partial}{\partial n} (k_0 \frac{\partial T_0^*}{\partial n}(s, t) \zeta_0^*(s, t) + \frac{\partial T_0^*}{\partial n}(s, t) k_0 \frac{\partial \zeta_0^*}{\partial n}(s, t)) \right] dt ds \\
& + \int_{\partial\Omega} \theta(s) \cdot n(s) \int_0^{t_f} \left[(+ \frac{\partial T_1^*}{\partial n}(s, t) - \frac{\partial T_0^*}{\partial n}(s, t)) (-k_1 \frac{\partial \zeta_1^*}{\partial n}(s, t)) \right] dt ds \\
& + \int_{\partial\Omega} \theta(s) \cdot n(s) \int_0^{t_f} \left[+ \frac{\partial}{\partial n} (k_1 \frac{\partial T_1^*}{\partial n}(s, t) - k_0 \frac{\partial T_0^*}{\partial n}(s, t)) \xi^*(s, t) \right] dt ds \\
& = \int_{\partial\Omega} \theta(s) \cdot n(s) [(T_1^*(s, t_f) - T_s)^+]^2 ds \\
& + \int_{\partial\Omega} \theta(s) \cdot n(s) \int_0^{t_f} (\rho_1 C_{p1} \partial_t T_1^*(s, t) \zeta_1^*(s, t) - \rho_0 C_{p0} \partial_t T_0^*(s, t) \zeta_0^*(s, t)) dt ds \\
& + \int_{\partial\Omega} \theta(s) \cdot n(s) \int_0^{t_f} ((k_1 - k_0) \frac{\partial T_1^*}{\partial \tau}(s, t) \frac{\partial \zeta_1^*}{\partial \tau}(s, t) + (\frac{1}{k_1} - \frac{1}{k_0}) k_1 \frac{\partial T_1^*}{\partial n}(s, t) k_1 \frac{\partial \zeta_1^*}{\partial n}(s, t)) dt ds \\
& - 2 \int_{\partial\Omega} \theta(s) \cdot n(s) \int_0^{t_f} k_1 \frac{\partial \zeta_1^*}{\partial n}(s, t) (+ \frac{\partial T_1^*}{\partial n}(s, t) - \frac{\partial T_0^*}{\partial n}(s, t)) dt ds,
\end{aligned}$$

and we deduce

$$\begin{aligned}
P'_{th}(\Omega)(\theta) = & \int_{\partial\Omega} \theta(s) \cdot n(s) [(T_1^*(s, t_f) - T_s)^+]^2 ds \\
& + \int_{\partial\Omega} \theta(s) \cdot n(s) \int_0^{t_f} (\rho_1 C_{p1} \partial_t T_1^*(s, t) \zeta_1^*(s, t) - \rho_0 C_{p0} \partial_t T_0^*(s, t) \zeta_0^*(s, t)) ds dt \\
& + \int_{\partial\Omega} \theta(s) \cdot n(s) \int_0^{t_f} ((k_1 - k_0) \frac{\partial T_1^*}{\partial \tau}(s, t) \frac{\partial \zeta_1^*}{\partial \tau}(s, t) + (\frac{1}{k_1} - \frac{1}{k_0}) k_1 \frac{\partial T_1^*}{\partial n}(s, t) k_1 \frac{\partial \zeta_1^*}{\partial n}(s, t)) ds dt \\
& - 2 \int_{\partial\Omega} \theta(s) \cdot n(s) \int_0^{t_f} (\frac{1}{k_1} - \frac{1}{k_0}) k_1 \frac{\partial T_1^*}{\partial n}(s, t) k_1 \frac{\partial \zeta_1^*}{\partial n}(s, t)) ds dt \\
= & \int_{\partial\Omega} \theta(s) \cdot n(s) [(T_1^*(s, t_f) - T_s)^+]^2 ds \\
& + \int_{\partial\Omega} \theta(s) \cdot n(s) \int_0^{t_f} (\rho_1 C_{p1} \partial_t T_1^*(s, t) \zeta_1^*(s, t) - \rho_0 C_{p0} \partial_t T_0^*(s, t) \zeta_0^*(s, t)) ds dt \\
& + \int_{\partial\Omega} \theta(s) \cdot n(s) \int_0^{t_f} ((k_1 - k_0) \frac{\partial T_1^*}{\partial \tau}(s, t) \frac{\partial \zeta_1^*}{\partial \tau}(s, t) - (\frac{1}{k_1} - \frac{1}{k_0}) k_1 \frac{\partial T_1^*}{\partial n}(s, t) k_1 \frac{\partial \zeta_1^*}{\partial n}(s, t)) ds dt,
\end{aligned} \tag{5.84}$$

which completes the proof. \square

5.3.5 Linear transient heat equation with piecewise discontinuous conductivity and heat flux across the moving boundary

Until now we have assumed that the temperature is continuous across the interface of the mold and the cast part. The two parts are assumed to be in contact and natural transmission conditions (continuity of the temperature and of the normal flux) are automatically imposed by the solution of the heat equation. However, this is not always the case for the simulation of the solidification process. According to Lewis et al. [85], the contraction of the metal during solidification can result in the creation of gaps along the interface of the mold and the metal. The gas occupying these holes has a different thermal conductivity (usually much lower) than the metal or the mold and therefore there is a discontinuity in the temperature field across the interface. To simulate this discontinuity, Fourier conditions are set on the interface using a heat transfer coefficient, that depends on the materials that take part in the casting process.

The coupled pdes that describe the above process read

$$\left\{ \begin{array}{ll} \rho_1 C_{p1} \partial_t T_1(x, t) - k_1 \Delta T_1(x, t) = 0 & \text{in } \Omega \times (0, t_f) \\ T_1(x, 0) = T_{in}(x) & \text{in } \Omega \times \{0\} \\ k_1 \frac{\partial T_1}{\partial n}(x, t) - h_{c-m}(T_0(x, t) - T_1(x, t)) = 0 & \text{on } \partial\Omega \setminus (\partial D \cap \partial\Omega) \times (0, t_f) \\ k_1 \frac{\partial T_1}{\partial n}(x, t) - h_{c-a}(T_1(x, t) - T_{air}) = 0 & \text{on } (\partial D \cap \partial\Omega) \times (0, t_f) \end{array} \right. \tag{5.85}$$

and

$$\left\{ \begin{array}{ll} \rho_0 C_{p0} \partial_t T_0(x, t) - k_0 \Delta T_0(x, t) = 0 & \text{in } (D \setminus \Omega) \times (0, t_f) \\ T_0(x, 0) = T_{in}(x) & \text{in } (D \setminus \Omega) \times \{0\} \\ k_0 \frac{\partial T_0}{\partial n}(x, t) - h_{c-m}(T_0(x, t) - T_1(x, t)) = 0 & \text{on } \partial\Omega \setminus (\partial D \cap \partial\Omega) \times (0, t_f) \\ k_0 \frac{\partial T_0}{\partial n}(x, t) - h_{m-a}(T_0(x, t) - T_{air}) = 0 & \text{on } (\partial D \setminus \partial\Omega) \times (0, t_f). \end{array} \right. \tag{5.86}$$

Proposition 5.3.8. *Let $T_1(x, t)$ and $T_0(x, t)$ be solutions of equations (5.85) and (5.86) respectively and $T(x, t)$ defined as in (5.52). Then, the shape derivative of (5.3) reads*

$$\begin{aligned}
P'_{th}(\Omega)(\theta) = & \int_{\partial\Omega} \theta(s) \cdot n(s) [(T_1(s, t_f) - T_s)^+]^2 ds \\
& - \int_{\partial\Omega} \int_0^{t_f} \theta(s) \cdot n(s) (H(s) h_{c-m}(T_0(s, t) - T_1(s, t)) (\zeta_1(s, t) - \zeta_0(s, t))) dt ds \\
& + \int_{\partial\Omega} \int_0^{t_f} \theta(s) \cdot n(s) (\rho_1 C_{p1} \partial_t T_1(s, t) \zeta_1(s, t) - \rho_0 C_{p0} \partial_t T_0(s, t) \zeta_0(s, t)) dt ds \\
& + \int_{\partial\Omega} \int_0^{t_f} \theta(s) \cdot n(s) (k_1 \frac{\partial T_1}{\partial \tau} \frac{\partial \zeta_1}{\partial \tau} - k_0 \frac{\partial T_0}{\partial \tau} \frac{\partial \zeta_0}{\partial \tau} - h_{c-m}(\zeta_1 - \zeta_0) (\frac{\partial T_0}{\partial n} - \frac{\partial T_1}{\partial n})) dt ds,
\end{aligned} \tag{5.87}$$

where H is the mean curvature, τ is the field of vectors orthogonal to n and ζ_1 and ζ_0 are solutions of the adjoint equations

$$\left\{ \begin{array}{ll} -\rho_1 C_{p1} \partial_t \zeta_1(x, t) - k_1 \Delta \zeta_1(x, t) = 0 & \text{in } \Omega \times (0, t_f) \\ \zeta_1(x, t_f) + \frac{2[T_1(x, t_f) - T_s]^+}{\rho_1 C_{p1}} = 0 & \text{in } \Omega \times \{t_f\} \\ k_1 \frac{\partial \zeta_1(x, t)}{\partial n} - h_{c-m}(\zeta_0(x, t) - \zeta_1(x, t)) = 0 & \text{on } \partial\Omega \setminus (\partial D \cap \partial\Omega) \times (0, t_f) \\ k_1 \frac{\partial \zeta_1(x, t)}{\partial n} - h_{c-a}(\zeta_1(x, t)) = 0 & \text{on } (\partial D \cap \partial\Omega) \times (0, t_f) \end{array} \right. \quad (5.88)$$

and

$$\left\{ \begin{array}{ll} -\rho_0 C_{p0} \partial_t \zeta_0(x, t) - k_0 \Delta \zeta_0(x, t) = 0 & \text{in } (D \setminus \Omega) \times (0, t_f) \\ \zeta_0(x, t_f) = 0 & \text{in } (D \setminus \Omega) \times \{t_f\} \\ k_0 \frac{\partial \zeta_0(x, t)}{\partial n} - h_{c-m}(\zeta_0(x, t) - \zeta_1(x, t)) = 0 & \text{on } \partial\Omega \setminus (\partial D \cap \partial\Omega) \times (0, t_f) \\ k_0 \frac{\partial \zeta_0(x, t)}{\partial n} - h_{m-a}(\zeta_0(x, t)) = 0 & \text{on } (\partial D \setminus \partial\Omega) \times (0, t_f). \end{array} \right. \quad (5.89)$$

Proof. We formulate the Lagrangian function

$$\begin{aligned} \mathcal{L}(\Omega, \hat{T}_1, \hat{T}_0, \hat{\zeta}_1, \hat{\zeta}_0, \hat{\mu}_1, \hat{\mu}_0, \hat{\nu}_1, \hat{\nu}_0, \hat{q}_1, \hat{q}_0) = & \\ & \int_{\Omega} [(\hat{T}_1(x, t_f) - T_s)^+]^2 dx + \int_0^{t_f} \int_{\Omega} (\rho_1 C_{p1} \partial_t \hat{T}_1(x, t) - k_1 \Delta \hat{T}_1(x, t)) \hat{\zeta}_1(x, t) dx dt \\ & + \int_0^{t_f} \int_{\Omega} (\rho_0 C_{p0} \partial_t \hat{T}_0(x, t) - k_0 \Delta \hat{T}_0(x, t)) \hat{\zeta}_0(x, t) dx dt + \int_{\Omega} (\hat{T}_1(x, 0) - T_{in}(x)) \hat{\mu}_1(x) dx \\ & + \int_{\Omega} (\hat{T}_0(x, 0) - T_{in}(x)) \hat{\mu}_0(x) dx \\ & + \int_0^{t_f} \int_{(\partial\Omega \setminus (\partial\Omega \cap \partial D))} (k_1 \frac{\partial \hat{T}_1}{\partial n}(s, t) - h_{c-m}(\hat{T}_0(s, t) - \hat{T}_1(s, t))) \hat{\nu}_1(s, t) ds dt \\ & + \int_0^{t_f} \int_{(\partial\Omega \setminus (\partial\Omega \cap \partial D))} (k_0 \frac{\partial \hat{T}_0}{\partial n}(s, t) - h_{c-m}(\hat{T}_0(s, t) - \hat{T}_1(s, t))) \hat{\nu}_0(s, t) ds dt \\ & + \int_0^{t_f} \int_{(\partial\Omega \cap \partial D)} (k_1 \frac{\partial \hat{T}_1}{\partial n} - h_{c-a}(\hat{T}_1 - T_{air})) \hat{q}_1(s, t) ds dt \\ & + \int_0^{t_f} \int_{(\partial D \setminus \partial\Omega)} (k_0 \frac{\partial \hat{T}_0}{\partial n} - h_{m-a}(\hat{T}_0 - T_{air})) \hat{q}_0(s, t) ds dt. \end{aligned} \quad (5.90)$$

Fixing the domain Ω , the first order optimality conditions for \mathcal{L} at the optimal point

$$w^* \equiv (\Omega, T_1^*, T_0^*, \zeta_1^*, \zeta_0^*, \mu_1^*, \mu_0^*, \nu_1^*, \nu_0^*, q_1^*, q_0^*)$$

read

$$\frac{\partial \mathcal{L}}{\partial \zeta_1}(w^*)(\phi) = 0 \Rightarrow \rho_1 C_{p1} \partial_t T_1^*(x, t) - k_1 \Delta T_1^*(x, t) = 0 \quad \text{in } \Omega \times (0, t_f), \quad (5.91)$$

$$\frac{\partial \mathcal{L}}{\partial \mu_1}(w^*)(\phi) = 0 \Rightarrow T_1^*(x, 0) = T_{in}(x) \quad \text{in } \Omega \times \{0\}, \quad (5.92)$$

$$\frac{\partial \mathcal{L}}{\partial \nu_1}(w^*)(\phi) = 0 \Rightarrow k_1 \frac{\partial T_1^*}{\partial n}(x, t) = h_{c-m}(T_0^*(x, t) - T_1^*(x, t)) \quad \text{on } \partial\Omega \setminus (\partial\Omega \cap \partial D) \times (0, t_f), \quad (5.93)$$

$$\frac{\partial \mathcal{L}}{\partial \nu_0}(w^*)(\phi) = 0 \Rightarrow k_0 \frac{\partial T_0^*}{\partial n}(x, t) = h_{c-m}(T_0^*(x, t) - T_1^*(x, t)) \quad \text{on } \partial\Omega \setminus (\partial\Omega \cap \partial D) \times (0, t_f), \quad (5.94)$$

$$\frac{\partial \mathcal{L}}{\partial q_1}(w^*)(\phi) = 0 \Rightarrow k_1 \frac{\partial T_1^*}{\partial n}(x, t) = h_{c-a}(T_1^*(x, t) - T_{air}) \quad \text{on } (\partial\Omega \cap \partial D) \times (0, t_f), \quad (5.95)$$

$$\frac{\partial \mathcal{L}}{\partial \zeta_0}(w^*)(\phi) = 0 \Rightarrow \rho_0 C_{p0} \partial_t T_0^*(x, t) - k_0 \Delta T_0^*(x, t) = 0 \quad \text{in } (D \setminus \Omega) \times (0, t_f) \quad (5.96)$$

$$\frac{\partial \mathcal{L}}{\partial \mu_0}(w^*)(\phi) = 0 \Rightarrow T_0^*(x, 0) = T_{in}(x) \quad \text{in } D \setminus \Omega \times \{0\}, \quad (5.97)$$

$$\frac{\partial \mathcal{L}}{\partial q_0}(w^*)(\phi) = 0 \Rightarrow k_0 \frac{\partial T_0^*}{\partial n}(x, t) = h_{m-a}(T_0^*(x, t) - T_{air}) \quad \text{on } (\partial D \setminus \partial\Omega) \times (0, t_f). \quad (5.98)$$

From equations (5.91),(5.92),(5.93), (5.95), we deduce that T_1^* solves equation (5.85), while equations (5.94),(5.96), (5.97),(5.98) show that T_0^* solves equation (5.86).

The partial derivative of \mathcal{L} with respect to \widehat{T}_1 in the direction of a test function ϕ reads

$$\begin{aligned} \frac{\partial \mathcal{L}}{\partial \widehat{T}_1}(w^*)(\phi) = & \int_{\Omega} 2(T_1^*(x, t_f) - T_s)^+ \phi(x, t_f) dx + \int_{\Omega} \phi(x, 0) \mu_1^*(x) dx \\ & + \int_0^{t_f} \int_{\Omega} (\rho_1 C_{p1} \partial_t \phi(x, t) - k_1 \Delta \phi(x, t)) \zeta_1^*(x, t) dx dt \\ & + \int_0^{t_f} \int_{(\partial\Omega \setminus (\partial\Omega \cap \partial D))} (k_1 \frac{\partial \phi}{\partial n}(s, t) \nu_1^*(s, t) + h_{c-m} \phi(s, t) \nu_1^*(s, t)) ds dt \\ & + \int_0^{t_f} \int_{(\partial\Omega \setminus (\partial\Omega \cap \partial D))} h_{c-m} \phi(s, t) \nu_0^*(s, t) ds dt \\ & + \int_0^{t_f} \int_{(\partial\Omega \cap \partial D)} (k_1 \frac{\partial \phi}{\partial n} - h_{c-a} \phi) q_1^*(s, t) ds dt. \end{aligned} \quad (5.99)$$

Replacing in (5.99) the equality (5.67) we get

$$\begin{aligned} \frac{\partial \mathcal{L}}{\partial \widehat{T}_1}(w^*)(\phi) = & \int_{\Omega} 2(T_1^*(x, t_f) - T_s)^+ \phi(x, t_f) dx \int_{\Omega} \rho_1 C_{p1} \zeta_1^*(x, t_f) \phi(x, t_f) dx \\ & - \int_{\Omega} \rho_1 C_{p1} \zeta_1^*(x, 0) \phi(x, 0) dx - \int_0^{t_f} \int_{\Omega} \rho_1 C_{p1} \partial_t \zeta^*(x, t) \phi(x, t) dx dt \\ & - \int_0^{t_f} \int_{\Omega} k_1 \Delta \zeta_1^*(x, t) \phi(x, t) dx dt + \int_{\Omega} \phi(x, 0) \mu_1^*(x) dx \\ & - \int_0^{t_f} \int_{\partial\Omega} k_1 \frac{\partial \phi}{\partial n}(s, t) \zeta_1^*(s, t) ds dt + \int_0^{t_f} \int_{\partial\Omega} k_1 \frac{\partial \zeta_1^*}{\partial n}(s, t) \phi(s, t) ds dt \\ & + \int_0^{t_f} \int_{(\partial\Omega \setminus (\partial\Omega \cap \partial D))} (k_1 \frac{\partial \phi}{\partial n}(s, t) \nu_1^*(s, t) + h_{c-m} \phi(s, t) \nu_1^*(s, t)) ds dt \\ & + \int_0^{t_f} \int_{(\partial\Omega \setminus (\partial\Omega \cap \partial D))} h_{c-m} \phi(s, t) \nu_0^*(s, t) ds dt \\ & + \int_0^{t_f} \int_{(\partial\Omega \cap \partial D)} (k_1 \frac{\partial \phi}{\partial n} - h_{c-a} \phi) q_1^*(s, t) ds dt. \end{aligned} \quad (5.100)$$

Taking ϕ with compact support in $\Omega \times (0, t_f)$, we get

$$- \rho_1 C_{p1} \partial_t \zeta_1^*(x, t) - k_1 \Delta \zeta_1^*(x, t) = 0 \quad \text{in } \Omega \times (0, t_f). \quad (5.101)$$

Varying ϕ in $\Omega \times \{t_f\}$ and $\Omega \times \{0\}$, we get

$$\zeta_1^*(x, t_f) = \frac{-2(T_1^*(x, t_f) - T_s)^+}{\rho_1 C_{p1}} \quad \text{in } \Omega \times \{t_f\} \quad (5.102)$$

and

$$\mu_1^*(x) = \rho_1 C_{p1} \zeta_1^*(x, 0) \quad \text{in } \Omega \quad (5.103)$$

respectively. Varying ϕ on $\partial\Omega \setminus (\partial\Omega \cap \partial D) \times (0, t_f)$ and $(\partial\Omega \cap \partial D) \times (0, t_f)$, with zero normal flux ($k_1 \frac{\partial \phi}{\partial n} = 0$), we get

$$(\nu_1^*(x, t) + \nu_0^*(x, t)) = -k_1 \frac{\partial \zeta_1^*}{\partial n}(x, t) \quad \text{on } \partial\Omega \setminus (\partial\Omega \cap \partial D) \times (0, t_f) \quad (5.104)$$

and

$$k_1 \frac{\partial \zeta_1^*}{\partial n}(x, t) = h_{c-a} q_1^*(x, t) \quad \text{on } (\partial\Omega \cap \partial D) \times (0, t_f). \quad (5.105)$$

Varying the normal flux of ϕ on $\partial\Omega \setminus (\partial\Omega \cap \partial D) \times (0, t_f)$ and $(\partial\Omega \cap \partial D) \times (0, t_f)$, with $\phi = 0$, we get

$$\zeta_1^*(x, t) = \nu_1^*(x, t) \quad \text{on } \partial\Omega \setminus (\partial\Omega \cap \partial D) \times (0, t_f) \quad (5.106)$$

and

$$\zeta_1^*(x, t) = q_1^*(x, t) \quad \text{on } (\partial\Omega \cap \partial D) \times (0, t_f). \quad (5.107)$$

The same analysis as previously holds for the partial derivative of \mathcal{L} with respect to \widehat{T}_0 and results in the following equalities:

$$-\rho_0 C_{p0} \partial_t \zeta_0^*(x, t) - k_0 \Delta \zeta_0^*(x, t) = 0 \quad \text{in } (D \setminus \Omega) \times (0, t_f), \quad (5.108)$$

$$\zeta_0^*(x, t_f) = 0 \quad \text{in } (D \setminus \Omega) \times \{t_f\}, \quad (5.109)$$

$$\mu_0^*(x) = \rho_0 C_{p0} \zeta_0^*(x, 0) \quad \text{in } D \setminus \Omega, \quad (5.110)$$

$$(\nu_1^*(x, t) + \nu_0^*(x, t)) = -k_0 \frac{\partial \zeta_0^*}{\partial n}(x, t) \quad \text{on } \partial\Omega \setminus (\partial\Omega \cap \partial D) \times (0, t_f), \quad (5.111)$$

$$k_0 \frac{\partial \zeta_0^*}{\partial n}(x, t) = -h_{m-a} q_0^*(x, t) \quad \text{on } (\partial D \setminus \partial\Omega) \times (0, t_f), \quad (5.112)$$

$$\zeta_0^*(x, t) = -\nu_0^*(x, t) \quad \text{on } \partial\Omega \setminus (\partial\Omega \cap \partial D) \times (0, t_f), \quad (5.113)$$

and

$$\zeta_0^*(x, t) = -q_0^*(x, t) \quad \text{on } (\partial D \setminus \partial\Omega) \times (0, t_f). \quad (5.114)$$

Equations (5.101)-(5.114) show that ζ_1^* and ζ_0^* solve the adjoint states (5.88) and (5.89) respectively. Before computing the shape derivative of $P_{th}(\Omega)$, we write again the Lagrangian function (5.90), after an intergration by parts, as

$$\begin{aligned} \mathcal{L}(\Omega, \widehat{T}_1, \widehat{T}_0, \widehat{\zeta}_1, \widehat{\zeta}_0, \widehat{\mu}_1, \widehat{\mu}_0, \widehat{\nu}_1, \widehat{\nu}_0, \widehat{q}_1, \widehat{q}_0) = & \\ & \int_{\Omega} \left[(\widehat{T}_1(x, t_f) - T_s)^+ \right]^2 dx + \int_0^{t_f} \int_{\Omega} (\rho_1 C_{p1} \partial_t \widehat{T}_1(x, t) \widehat{\zeta}_1(x, t) + k_1 \nabla \widehat{T}_1(x, t) \cdot \nabla \widehat{\zeta}_1(x, t)) dx dt \\ & + \int_0^{t_f} \int_{\Omega} (\rho_0 C_{p0} \partial_t \widehat{T}_0(x, t) \widehat{\zeta}_0(x, t) + k_0 \nabla \widehat{T}_0(x, t) \cdot \nabla \widehat{\zeta}_0(x, t)) dx dt \\ & - \int_0^{t_f} \int_{\partial\Omega} k_1 \frac{\partial \widehat{T}_1}{\partial n}(s, t) \widehat{\zeta}_1(s, t) ds dt + \int_0^{t_f} \int_{\partial\Omega} k_0 \frac{\partial \widehat{T}_0}{\partial n}(s, t) \widehat{\zeta}_0(s, t) ds dt \\ & + \int_{\Omega} (\widehat{T}_1(x, 0) - T_{in}(x)) \widehat{\mu}_1(x) dx + \int_{\Omega} (\widehat{T}_0(x, 0) - T_{in}(x)) \widehat{\mu}_0(x) dx \\ & + \int_0^{t_f} \int_{(\partial\Omega \setminus (\partial\Omega \cap \partial D))} (k_1 \frac{\partial \widehat{T}_1}{\partial n}(s, t) - h_{c-m}(\widehat{T}_0(s, t) - \widehat{T}_1(s, t))) \widehat{\nu}_1(s, t) ds dt \\ & + \int_0^{t_f} \int_{(\partial\Omega \setminus (\partial\Omega \cap \partial D))} (k_0 \frac{\partial \widehat{T}_0}{\partial n}(s, t) - h_{c-m}(\widehat{T}_0(s, t) - \widehat{T}_1(s, t))) \widehat{\nu}_0(s, t) ds dt \\ & + \int_0^{t_f} \int_{(\partial\Omega \cap \partial D)} (k_1 \frac{\partial \widehat{T}_1}{\partial n} - h_{c-a}(\widehat{T}_1 - T_{air})) \widehat{q}_1(s, t) ds dt \\ & + \int_0^{t_f} \int_{(\partial D \setminus \partial\Omega)} (k_0 \frac{\partial \widehat{T}_0}{\partial n} - h_{m-a}(\widehat{T}_0 - T_{air})) \widehat{q}_0(s, t) ds dt. \end{aligned} \quad (5.115)$$

The shape derivative of $P_{th}(\Omega)$ equals the shape derivative of \mathcal{L} at the optimal point:

$$\begin{aligned}
P'_{th}(\Omega)(\theta) = & \int_{\partial\Omega} \theta(s) \cdot n(s) [(T_1^*(s, t_f) - T_s)^+]^2 ds \\
& + \int_{\partial\Omega} \theta(s) \cdot n(s) \int_0^{t_f} (\rho_1 C_{p1} \partial_t T_1^*(s, t) \zeta_1^*(s, t) + k_1 \nabla T_1^*(s, t) \cdot \nabla \zeta_1^*(s, t)) dt ds \\
& + \int_{\partial\Omega} \theta(s) \cdot n(s) \int_0^{t_f} (\rho_0 C_{p0} \partial_t T_0^*(s, t) \zeta_0^*(s, t) + k_0 \nabla T_0^*(s, t) \cdot \nabla \zeta_0^*(s, t)) dt ds \\
& - \int_{\partial\Omega} \theta(s) \cdot n(s) \int_0^{t_f} \left[H(s) k_1 \frac{\partial T_1^*}{\partial n}(s, t) \zeta_1^*(s, t) + \frac{\partial}{\partial n} (k_1 \frac{\partial T_1^*}{\partial n}(s, t) \zeta_1^*(s, t)) \right] dt ds \\
& + \int_{\partial\Omega} \theta(s) \cdot n(s) \int_0^{t_f} \left[H(s) k_0 \frac{\partial T_0^*}{\partial n}(s, t) \zeta_0^*(s, t) + \frac{\partial}{\partial n} (k_0 \frac{\partial T_0^*}{\partial n}(s, t) \zeta_0^*(s, t)) \right] dt ds \\
& + \int_{\partial\Omega} \theta(s) \cdot n(s) [(T_1^*(s, 0) - T_{in}(s)) \mu_1^*(s)] ds \\
& - \int_{\partial\Omega} \theta(s) \cdot n(s) [(T_0^*(s, 0) - T_{in}(s)) \mu_0^*(s)] ds \\
& + \int_{\partial\Omega} \theta(s) \cdot n(s) \int_0^{t_f} [H(s) (k_1 \frac{\partial T_1^*}{\partial n}(s, t) - h_{c-m}(T_0^*(s, t) - T_1^*(s, t))) \nu_1^*(s, t) \\
& + \frac{\partial}{\partial n} (k_1 \frac{\partial T_1^*}{\partial n}(s, t) - h_{c-m}(T_0^*(s, t) - T_1^*(s, t))) \nu_1^*(s, t)] dt ds \\
& + \int_{\partial\Omega} \theta(s) \cdot n(s) \int_0^{t_f} [H(s) (k_0 \frac{\partial T_0^*}{\partial n}(s, t) - h_{c-m}(T_0^*(s, t) - T_1^*(s, t))) \nu_0^*(s, t) \\
& + \frac{\partial}{\partial n} (k_0 \frac{\partial T_0^*}{\partial n}(s, t) - h_{c-m}(T_0^*(s, t) - T_1^*(s, t))) \nu_0^*(s, t)] dt ds \\
& = \int_{\partial\Omega} \theta(s) \cdot n(s) [(T_1^*(s, t_f) - T_s)^+]^2 ds \\
& + \int_{\partial\Omega} \theta(s) \cdot n(s) \int_0^{t_f} (\rho_1 C_{p1} \partial_t T_1^*(s, t) \zeta_1^*(s, t) - \rho_0 C_{p0} \partial_t T_0^*(s, t) \zeta_0^*(s, t)) dt ds \\
& + \int_{\partial\Omega} \theta(s) \cdot n(s) \int_0^{t_f} (k_1 \frac{\partial T_1^*}{\partial n}(s, t) \frac{\partial \zeta_1^*}{\partial n}(s, t) + k_1 \frac{\partial T_1^*}{\partial \tau}(s, t) \frac{\partial \zeta_1^*}{\partial \tau}(s, t) \\
& - k_0 \frac{\partial T_0^*}{\partial n}(s, t) \frac{\partial \zeta_0^*}{\partial n}(s, t) - k_0 \frac{\partial T_0^*}{\partial \tau}(s, t) \frac{\partial \zeta_0^*}{\partial \tau}(s, t)) dt ds \\
& - \int_{\partial\Omega} \theta(s) \cdot n(s) \int_0^{t_f} \left[H(s) k_1 \frac{\partial T_1^*}{\partial n}(s, t) \zeta_1^*(s, t) + \frac{\partial}{\partial n} (k_1 \frac{\partial T_1^*}{\partial n}(s, t) \zeta_1^*(s, t)) \right] dt ds \\
& + \int_{\partial\Omega} \theta(s) \cdot n(s) \int_0^{t_f} \left[H(s) k_0 \frac{\partial T_0^*}{\partial n}(s, t) \zeta_0^*(s, t) + \frac{\partial}{\partial n} (k_0 \frac{\partial T_0^*}{\partial n}(s, t) \zeta_0^*(s, t)) \right] dt ds \\
& + \int_{\partial\Omega} \theta(s) \cdot n(s) \int_0^{t_f} [H(s) (k_1 \frac{\partial T_1^*}{\partial n}(s, t) - h_{c-m}(T_0^*(s, t) - T_1^*(s, t))) \zeta_1^*(s, t) \\
& + \frac{\partial}{\partial n} (k_1 \frac{\partial T_1^*}{\partial n}(s, t) - h_{c-m}(T_0^*(s, t) - T_1^*(s, t))) \zeta_1^*(s, t)] dt ds \\
& + \int_{\partial\Omega} \theta(s) \cdot n(s) \int_0^{t_f} [H(s) (k_0 \frac{\partial T_0^*}{\partial n}(s, t) - h_{c-m}(T_0^*(s, t) - T_1^*(s, t))) (-\zeta_0^*(s, t)) \\
& + \frac{\partial}{\partial n} (k_0 \frac{\partial T_0^*}{\partial n}(s, t) - h_{c-m}(T_0^*(s, t) - T_1^*(s, t))) (-\zeta_0^*(s, t))] dt ds \\
& = \int_{\partial\Omega} \theta(s) \cdot n(s) [(T_1^*(s, t_f) - T_s)^+]^2 ds \\
& + \int_{\partial\Omega} \theta(s) \cdot n(s) \int_0^{t_f} (\rho_1 C_{p1} \partial_t T_1^*(s, t) \zeta_1^*(s, t) - \rho_0 C_{p0} \partial_t T_0^*(s, t) \zeta_0^*(s, t)) dt ds \\
& + \int_{\partial\Omega} \theta(s) \cdot n(s) \int_0^{t_f} (k_1 \frac{\partial T_1^*}{\partial \tau}(s, t) \frac{\partial \zeta_1^*}{\partial \tau}(s, t) - k_0 \frac{\partial T_0^*}{\partial \tau}(s, t) \frac{\partial \zeta_0^*}{\partial \tau}(s, t) \\
& + \frac{\partial T_1^*}{\partial n}(s, t) h_{c-m}(\zeta_0^*(s, t) - \zeta_1^*(s, t)) - \frac{\partial T_0^*}{\partial n}(s, t) h_{c-m}(\zeta_0^*(s, t) - \zeta_1^*(s, t))) dt ds \\
& - \int_{\partial\Omega} \theta(s) \cdot n(s) \int_0^{t_f} [H(s) h_{c-m}(T_0^*(s, t) - T_1^*(s, t)) (\zeta_1^*(s, t) - \zeta_0^*(s, t)) \\
& - h_{c-m}(k_1 - k_0) (\frac{\partial T_0^*}{\partial n}(s, t) - \frac{\partial T_1^*}{\partial n}(s, t))] dt ds
\end{aligned}$$

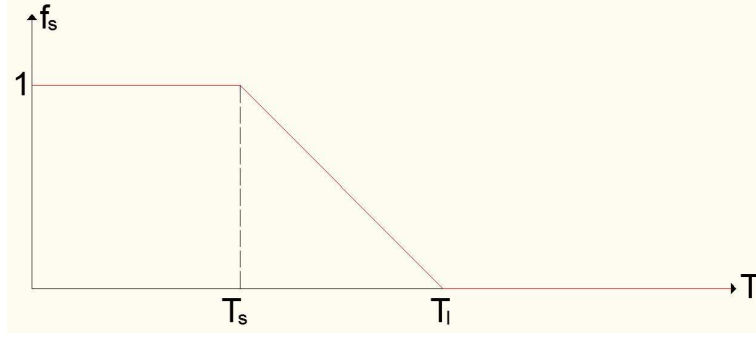


Figure 5.4: Solid fraction.

and we finally deduce

$$\begin{aligned}
P'_{th}(\Omega)(\theta) = & \int_{\partial\Omega} \theta(s) \cdot n(s) [(T_1^*(s, t_f) - T_s)^+]^2 ds \\
& - \int_{\partial\Omega} \int_0^{t_f} \theta(s) \cdot n(s) (H(s) h_{c-m} (T_0^*(s, t) - T_1^*(s, t)) (\zeta_1^*(s, t) - \zeta_0^*(s, t))) dt ds \\
& + \int_{\partial\Omega} \int_0^{t_f} \theta(s) \cdot n(s) (\rho_1 C_{p1} \partial_t T_1^*(s, t) \zeta_1^*(s, t) - \rho_0 C_{p0} \partial_t T_0^*(s, t) \zeta_0^*(s, t)) dt ds \\
& + \int_{\partial\Omega} \int_0^{t_f} \theta(s) \cdot n(s) (k_1 \frac{\partial T_1^*}{\partial \tau} \frac{\partial \zeta_1^*}{\partial \tau} - k_0 \frac{\partial T_0^*}{\partial \tau} \frac{\partial \zeta_0^*}{\partial \tau} - h_{c-m} (\zeta_1^* - \zeta_0^*) (\frac{\partial T_0^*}{\partial n} - \frac{\partial T_1^*}{\partial n})) dt ds,
\end{aligned} \tag{5.116}$$

which completes the proof. \square

The above state and adjoint equations are easy to solve when the mesh used for the finite element analysis is adapted to the interface between the mold and the cast part, i.e. to the zero level-set of the level-set function [9, 158]. However, this process is very delicate, especially in 3d and one may find preferable to use a fixed mesh. In this case, the discontinuity of the temperature cannot be captured using standard finite elements on a single mesh. However, a solution to the problem can be achieved by extending both problems (5.85) and (5.86) in the whole working domain D , using a classical "ersatz" material expansion

$$k_1(x) = \begin{cases} k_1 & \text{in } \Omega, \\ \varepsilon k_1 & \text{in } D \setminus \Omega \end{cases} \quad \text{and} \quad k_0(x) = \begin{cases} k_0 & \text{in } D \setminus \Omega, \\ \varepsilon k_0 & \text{in } D \setminus \Omega, \end{cases}$$

where $\varepsilon \ll 1$. Then, the variational equations of the two problems can be added and solved at the same time, i.e. we solve a problem of $2n$ unknowns, n being the size of the mesh and the total temperature field $T(x, t)$ is given by (5.52).

5.3.6 Non-linear transient heat equation with phase-change

At this point, we have all the ingredients in order to study the fully non-linear transient heat equation with phase-change that describes the solidification process. We are interested for the solidification of alloys, for which there is no clear solidification interface, as it is the case with pure metals and eutectics [85]. Between the liquid $T(x) \geq T_l$ and the solid zone $T(x) \leq T_s$, there is a region of mixture, called the mushy zone. The local solid fraction (f_s) is assumed to be a linear function of the temperature in this zone, i.e.

$$f_s(T) = \begin{cases} 0, & T > T_l, \\ \frac{T_l - T}{T_l - T_s}, & T_s \leq T \leq T_l, \\ 1, & T < T_s. \end{cases} \tag{5.117}$$

The latent heat term is modelled as a source term in the non-linear heat equation with temperature dependent coefficients. The equation reads

$$\rho(x, T) C_p(x, T) \partial_t T(x, t) - \nabla \cdot (k(x, T) \nabla T(x, t)) = \rho(x, T) L \partial_t f_s, \quad \forall (x, t) \in \Omega \times (0, t_f), \tag{5.118}$$

where L denotes the latent heat fusion. Substituting

$$\frac{\partial f_s}{\partial t} = \frac{\partial f_s}{\partial T} \frac{\partial T}{\partial t},$$

equation (5.118) is written

$$(\rho(x, T)C_p(x, T) - \rho(x, T)L\frac{\partial f_s}{\partial T})\partial_t T(x, t) - \nabla \cdot (k(x, T)\nabla T(x, t)) = 0, \quad \forall (x, t) \in \Omega \times (0, t_f). \quad (5.119)$$

Defining the equivalent heat capacity as

$$\widetilde{C}_p(x, T) = C_p(x, T) - L\frac{\partial f_s}{\partial T}(x, T), \quad (5.120)$$

equation (5.119) is also written in the form

$$\rho(x, T)\widetilde{C}_p(x, T)\partial_t T(x, t) - \nabla \cdot (k(x, T)\nabla T(x, t)) = 0, \quad \forall (x, t) \in \Omega \times (0, t_f). \quad (5.121)$$

In order to calculate the shape derivative of this new problem in an easy way, we shall transform it again into a transmission problem. The state equation of the solidification problem reads

$$\left\{ \begin{array}{ll} \rho_1(x, T_1)\widetilde{C}_{p1}(x, T_1)\partial_t T_1(x, t) - \nabla \cdot (k_1(x, T_1)\nabla T_1(x, t)) & = 0 \quad \text{in } \Omega \times (0, t_f) \\ T_1(x, 0) & = T_{in}(x) \quad \text{in } \Omega \times \{0\} \\ k_1(x, T_1)\frac{\partial T_1(x, t)}{\partial n} - h_{c-m}(T_0(x, t) - T_1(x, t)) & = 0 \quad \text{on } (\partial\Omega \setminus (\partial D \cap \partial\Omega)) \times (0, t_f) \\ k_1(x, T_1)\frac{\partial T_1(x, t)}{\partial n} - h_{c-a}(T_1(x, t) - T_{air}) & = 0 \quad \text{on } (\partial D \cap \partial\Omega) \times (0, t_f) \end{array} \right. \quad (5.122)$$

and

$$\left\{ \begin{array}{ll} \rho_0(x, T_0)\widetilde{C}_{p0}(x, T_0)\partial_t T_0(x, t) - \nabla \cdot (k_0(x, T_0)\nabla T_0(x, t)) & = 0 \quad \text{in } (D \setminus \Omega) \times (0, t_f) \\ T_0(x, 0) & = T_{in}(x) \quad \text{in } (D \setminus \Omega) \times \{0\} \\ k_0(x, T_0)\frac{\partial T_0(x, t)}{\partial n} - h_{c-m}(T_0(x, t) - T_1(x, t)) & = 0 \quad \text{on } (\partial\Omega \setminus (\partial D \cap \partial\Omega)) \times (0, t_f) \\ k_0(x, T_0)\frac{\partial T_0(x, t)}{\partial n} - h_{m-a}(T_0(x, t) - T_{air}) & = 0 \quad \text{on } (\partial D \setminus \partial\Omega) \times (0, t_f). \end{array} \right. \quad (5.123)$$

Proposition 5.3.9. *Let $T_1(x, t)$ and $T_0(x, t)$ be solutions of equations (5.122) and (5.123) respectively and $T(x, t)$ defined as in (5.52). Then, the shape derivative of (5.3) reads*

$$\begin{aligned} P'_{th}(\Omega)(\theta) = & \int_{\partial\Omega} \theta(s) \cdot n(s) [(T_1(s, t_f) - T_s)^+]^2 ds \\ & - \int_{\partial\Omega} \int_0^{t_f} \theta(s) \cdot n(s) (H(s)h_{c-m}(T_0(s, t) - T_1(s, t))(\zeta_1(s, t) - \zeta_0(s, t))) dt ds \\ & + \int_{\partial\Omega} \int_0^{t_f} \theta(s) \cdot n(s) (\rho_1(s, T_1)\widetilde{C}_{p1}(s, T_1)\partial_t T_1(s, t)\zeta_1(s, t) - \rho_0(s, T_0)\widetilde{C}_{p0}(s, T_0)\partial_t T_0(s, t)\zeta_0(s, t)) dt ds \\ & + \int_{\partial\Omega} \int_0^{t_f} \theta(s) \cdot n(s) (k_1(s, T_1)\frac{\partial T_1}{\partial \tau} \frac{\partial \zeta_1}{\partial \tau} - k_0(s, T_0)\frac{\partial T_0}{\partial \tau} \frac{\partial \zeta_0}{\partial \tau} - h_{c-m}(\zeta_1(s, t) - \zeta_0(s, t))(\frac{\partial T_0}{\partial n} - \frac{\partial T_1}{\partial n})) dt ds, \end{aligned} \quad (5.124)$$

where H is the mean curvature, τ is the field of vectors orthogonal to n and ζ_1 and ζ_0 are solutions of the linear adjoint equations

$$\left\{ \begin{array}{ll} -\rho_1(x, T_1)\widetilde{C}_{p1}(x, T_1)\partial_t \zeta_1(x, t) - k_1(x, T_1)\Delta \zeta_1(x, t) & = 0 \quad \text{in } \Omega \times (0, t_f) \\ \zeta_1(x, t_f) + \frac{2[T_1(x, t_f) - T_s]^+}{\rho_1(x, T_1(x, t_f))C_{p1}(x, T_1(x, t_f))} & = 0 \quad \text{in } \Omega \times \{t_f\} \\ k_1(x, T_1)\frac{\partial \zeta_1(x, t)}{\partial n} - h_{c-m}(\zeta_0(x, t) - \zeta_1(x, t)) & = 0 \quad \text{on } (\partial\Omega \setminus (\partial D \cap \partial\Omega)) \times (0, t_f) \\ k_1(x, T_1)\frac{\partial \zeta_1(x, t)}{\partial n} - h_{c-a}(\zeta_1(x, t)) & = 0 \quad \text{on } (\partial D \cap \partial\Omega) \times (0, t_f) \end{array} \right. \quad (5.125)$$

and

$$\left\{ \begin{array}{ll} -\rho_0(x, T_0) \widetilde{C}_{p0}(x, T_0) \partial_t \zeta_0(x, t) - k_0(x, T_0) \Delta \zeta_0(x, t) = 0 & \text{in } (D \setminus \Omega) \times (0, t_f) \\ \zeta_0(x, t_f) = 0 & \text{in } (D \setminus \Omega) \times \{t_f\} \\ k_0(x, T_0) \frac{\partial \zeta_0(x, t)}{\partial n} - h_{c-m}(\zeta_0(x, t) - \zeta_1(x, t)) = 0 & \text{on } (\partial \Omega \setminus (\partial D \cap \partial \Omega)) \times (0, t_f) \\ k_0(x, T_0) \frac{\partial \zeta_0(x, t)}{\partial n} - h_{m-a}(\zeta_0(x, t)) = 0 & \text{on } (\partial D \setminus \partial \Omega) \times (0, t_f). \end{array} \right. \quad (5.126)$$

Proof. The proof is almost identical to the one of Proposition 5.3.8 and is omitted here. \square

Remark 5.3.10. For the derivation of the adjoint state equation, the derivability of the thermal coefficients with respect to the temperature is needed. However, the equivalent heat capacity, as it has been defined in (5.120), is a step function, due to the term

$$\frac{\partial f_s(T)}{\partial T} = \begin{cases} 0, & T > T_l, \\ \frac{1}{T_s - T_l}, & T_s \leq T \leq T_l, \\ 0, & T < T_s. \end{cases}$$

For reasons of simplicity, we follow the approach proposed in [143] and we consider instead

$$\frac{\partial f_s(T)}{\partial T} = \frac{1}{T_s - T_l} (H_\varepsilon(T - T_s) - H_\varepsilon(T - T_l)), \quad (5.127)$$

where $H_\varepsilon(x)$ is a regularized Heaviside function, given by

$$H_\varepsilon(x) = \begin{cases} 0, & x < -\varepsilon, \\ \frac{1}{2} + \frac{x}{2\varepsilon} + \frac{1}{2\pi} \sin\left(\frac{\pi x}{\varepsilon}\right), & -\varepsilon \leq x \leq \varepsilon, \\ 1, & x > \varepsilon. \end{cases}$$

The regularization interval ε was chosen to be $\varepsilon = 0.1(T_l - T_s)$, as in [143].

5.3.7 Numerical results

In this section, we test the first three thermal models of section 5.3, i.e. the Poisson equation, the linear transient heat equation and the eigenvalue approximation. Our goal here is not to compare quantitatively the results obtained with each model. The reason is that the reference example, with respect to which any comparison should be made, is the one using the non-linear heat equation with phase change, which unfortunately we have not yet implemented. Therefore, we stay on some qualitative observations and remarks, as far as the use of simplified thermal models in casting is concerned.

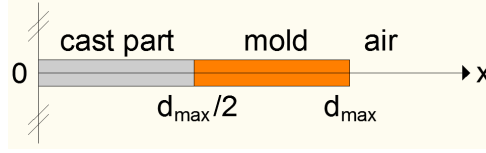
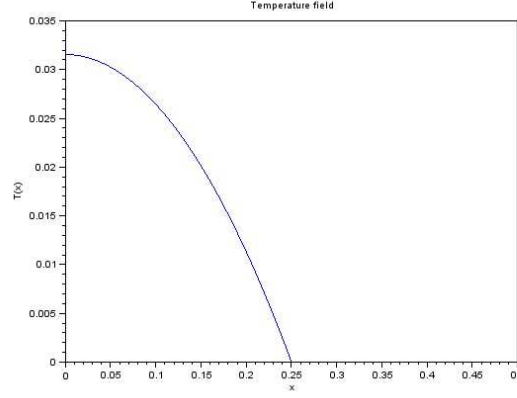
Of course, we have explained earlier how the temperature constraint can be connected with the thickness of the structure. Therefore, independent of casting, one can view the above thermal constraints as an implicit way to impose a maximum thickness specification. Then, some sort of comparison can be made, but the reader shall always take care that the results may depend strongly on the assumed model for the connection between the temperature field and the local thickness.

The 2d cantilever of Figure 3.27 is chosen as test-case for all models. Same as in Chapter 3, the working domain D is meshed using 160×80 $Q1$ finite elements for the elasticity analysis, the Young modulus E is set to 1 for the "strong" and to 10^{-3} for the "weak" material, while the Poisson ratio for both materials is set to 0.3. The same initialization as in Figure 3.28(a) is used for all examples in this section.

The Poisson equation and the linear transient heat equation model have been coded in SYSTUS [140], while for the eigenvalue approximation model a 2d Scilab [119] code has been used.

The optimization problem reads

$$\begin{aligned} \min_{\Omega} \quad & \int_{\Omega} dx \\ \text{s.t.} \quad & \int_{\partial \Omega} g \cdot u ds \leq g_{max}^1, \\ P_{th}(\Omega) = & \left(\frac{\int_{\Omega} f(T(x, t_f)) T(x, t_f)^2 dx}{\int_{\Omega} f(T(x, t_f)) dx} \right)^{\frac{1}{2}} \leq T_s, \end{aligned} \quad (5.128)$$

Figure 5.5: Casting system for the adjustment of T_s .Figure 5.6: Temperature field in the one-dimensional casting system of Figure 5.5, for $d_{max} = 0.50$, using the Poisson equation (5.4).

where $g_{max}^1 = 40$ is an upper bound for the compliance. The maximum solidification time, for time-dependent models, is set to $t_f = 20$. For each model, we adjust the upper bound on the temperature, T_s , so that it corresponds to the maximum temperature in the cast part for the one-dimensional casting system of Figure 5.1, for $d_{max} = 0.50$. Due to symmetry, only the half-domain is used (see Figure 5.5).

Poisson equation

We start with the Poisson equation as thermal model. Solving equation (5.4) for the casting system of Figure 5.5 and taking the thermal diffusivity equal to one ($\alpha = 1$), we obtain the temperature field of Figure 5.6. Its maximum value at $x = 0$ is 0.03156, thus we set $T_s = 0.03156$.

Remark 5.3.11. *The Poisson equation (5.4) can be solved analytically for the one-dimensional problem of Figure 5.6. The equation reads*

$$\begin{cases} -a \frac{dT^2(x)}{dx^2} = 1 & \text{in } (0, d_{max}/2), \\ T(x) = 0 & \text{in } [d_{max}/2, d_{max}], \\ \frac{dT(x)}{dx} = 0 & \text{on } \{0\}, \end{cases} \quad (5.129)$$

where the source term f has been set to unity all over the domain. At $x = 0$ the value of the temperature is $T(0) = \frac{(d_{max}/2)^2}{2a} = 0.03125$. However, for the sake of consistency we prefer to work with the value obtained by the numerical approximation of the equation.

Solving problem (5.128), we obtain the optimized shape of Figure 5.7(a). In Figure 5.7(b), we plot the thickness violation $(|d_\Omega(x) - d_{max}/2|)$.

Linear transient heat equation

We now pass to the linear transient heat equation model. We set the thermal diffusivity α equal to 10^{-3} and start from a uniform temperature field:

$$T_{in}(x) = \begin{cases} 700, & \text{if } x \in \Omega, \\ 0, & \text{if } x \in D \setminus \Omega. \end{cases} \quad (5.130)$$

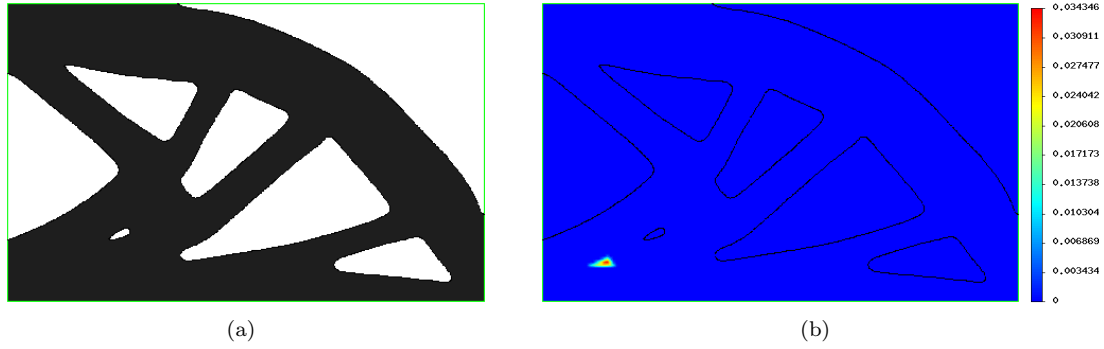


Figure 5.7: (a): optimized shape and (b): thickness violation $(|(d_{\Omega}(x) - d_{max}/2)^-|)$, using the Poisson thermal model.

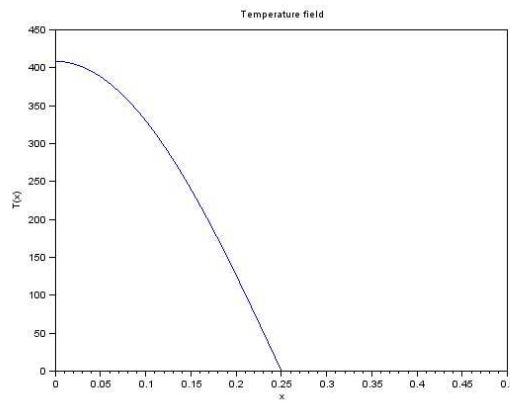


Figure 5.8: Temperature field in the one-dimensional casting system of Figure 5.5, for $d_{max} = 0.50$, using the linear transient heat equation (5.14).

In Figure 5.8, we show the solution of equation (5.14) at time t_f , for the casting system of Figure 5.5. The equation is solved using an implicit finite differences scheme and the time interval is discretized using 100 steps. The maximum value of the temperature field, at $x = 0$, is 408.75, thus we set $T_s = 408.75$. Solving problem (5.128), we obtain the optimized shape of Figure 5.9(a). The thickness violation $(|(d_{\Omega}(x) - d_{max}/2)^-|)$ is shown in Figure 5.9(b).

Eigenvalue approximation

Finally, the eigenvalue approximation is tested. The same parameters as for the linear transient heat equation model are used. The approximation of the actual temperature field at the final time, $T^f(x)$, defined in (5.33), is plotted in Figure 5.10 for the casting system of Figure 5.5. The maximum value of the temperature field, at $x = 0$, is 404.36, thus we set $T_s = 404.36$. Solving problem (5.128), we obtain the optimized shape of Figure 5.11(a). In 5.11(b), we plot the thickness violation $(|(d_{\Omega}(x) - d_{max}/2)^-|)$.

Preliminary conclusions

Let us start with a remark about the qualitative behaviour of all the three above models. We have observed, as expected, that the same type of instability due to small holes can appear, as with the maximum thickness constraint in Chapter 3. More specifically, the thermal functional (5.2) is not continuous with respect to topological changes, therefore the disappearance of small holes can increase significantly the value of the functional.

We shall expect, as usual, the existence of plenty of local minima and, thus, there is no reason to expect the optimized shaped to resemble. As far as the final results are concerned, we can see in Table 5.1 that the linear transient heat equation model resulted for this example in a lighter structure, which is

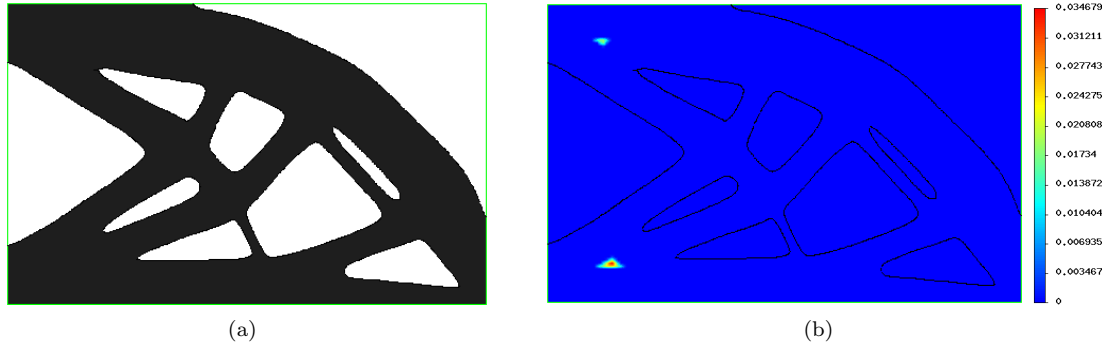


Figure 5.9: (a): optimized shape and (b): thickness violation $|(d_{\Omega}(x) - d_{max}/2)^{-}|$, using the linear heat equation thermal model.

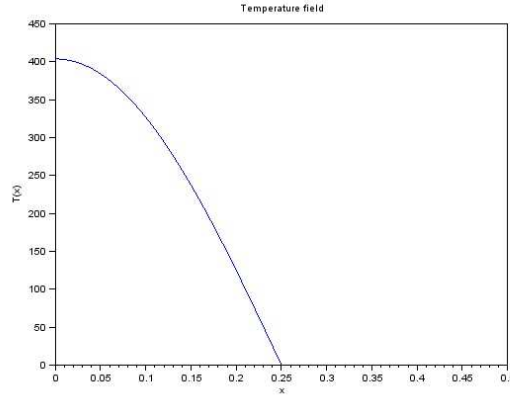


Figure 5.10: Temperature field in the one-dimensional casting system of Figure 5.5, for $d_{max} = 0.50$, using the first eigenvalue approximation (5.33).

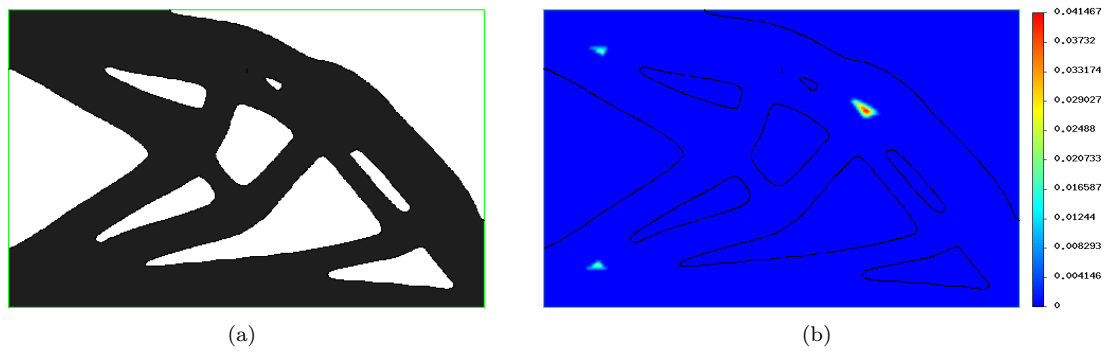


Figure 5.11: (a): optimized shape and (b): thickness violation $|(d_{\Omega}(x) - d_{max}/2)^{-}|$, using the eigenvalue approximation model.

Table 5.1: Results using different thermal models.

	Volume	Compliance	$P_{th}(\Omega)$	$P_{MaxT}(\Omega)$
Poisson equation	3.850	39.95	0.3161	0.262
Linear transient heat equation	3.775	39.98	408.93	0.256
Eigenvalue approximation	3.812	39.98	385.99	0.262

also closer to satisfy the maximum thickness functional $P_{MaxT}(\Omega)$. On the other hand, this model is far more costly than the other two. In case one wants to use such a model as an alternative for a geometric constraint on the maximum thickness, it seems that the Poisson equation model is the easiest to use and computationally the less expensive.

Part III

Multi-phase optimization

Chapter 6

Multi-phase structural optimization

Contents

6.1	Introduction	180
6.2	Sharp-interface formulation in a fixed mesh framework	181
6.2.1	Description of the problem	181
6.2.2	Shape-sensitivity analysis of the sharp-interface problem	182
6.3	Shape derivative in the smoothed-interface context	186
6.3.1	Description of the problem	186
6.3.2	Shape derivative of the compliance in the multi-materials setting	187
6.3.3	Approximate formulas for the shape derivative	188
6.3.4	Convergence of the smoothed-interface shape optimization problem to the sharp-interface problem	189
6.4	Discussion and comparison with previous formulae in the literature	191
6.5	Extension to more than 2 materials	192
6.6	Numerical results	194
6.6.1	Level-set representation	194
6.6.2	Two materials in the sharp interface context	194
6.6.3	Two materials in the smoothed-interface context	195
6.6.4	Four materials in the smoothed interface context	200
6.6.5	Multi-functional optimization example	214
6.7	Material design using inverse homogenization	217
6.7.1	Setting of the problem	217
6.7.2	Calculation of the homogenized properties	218
6.7.3	Shape derivative	220
6.7.4	Numerical results	221

The major part of this chapter is a joint work with G. Allaire, C. Dapogny and G. Delgado, which has been accepted for publication in ESAIM: Control, Optimisation and Calculus of Variations, under the title

G. Allaire, C. Dapogny, G. Delgado and G. Michailidis, *Multi-phase structural optimization via a level-set method*.

Compared to this article, the section concerning the derivation of the signed distance function has been already presented in Chapter 3 and is therefore omitted here, while the section containing the numerical results has been enriched with more examples on structural optimization and subsection 6.6.5 about multi-functional optimization. Finally, we consider additional tests for this method in the design of materials' microstructure using inverse homogenization, which is presented in section 6.7.

This work has been motivated by discussions with people from the SIMaP laboratory (the Materials and Processes Science and Engineering Laboratory) of Joseph Fourier University in Grenoble. We have collaborated in the study of the impact of the material interface properties in the optimal design of structures. Our work has been submitted for publication in SMO (Structural and Multi-disciplinary Optimization), under the title

N. Vermaak, G. Michailidis, G. Parry, R. Estevez, Y. Brechet, and G. Allaire, *Material interface effects on the topology optimization of multi-phase thermoelastic structures using a level set method* and has been added in the Appendix.

6.1 Introduction

In the previous sections we have supposed that the optimizable shape is composed by a single material with constant material properties. However, many industrial applications and problems in material science are concerned with finding the optimal distribution of several materials in a fixed working domain, in order to minimize a criterion related to the overall mechanical behavior or cost of the phases mixture. Intuition is usually very limited in such problems and shape and topology optimization can provide valuable help to the designers and researchers.

A crucial issue in the modeling of this problem is the parametrization of the phases mixture. While the exact formulation requires the material properties, or the global Hooke's tensor, to be discontinuous at the interfaces between two materials, it is often convenient, for numerical purposes, to devise an appropriate interpolation scheme to smoothen the coefficients or equivalently to replace sharp interfaces by diffuse ones using some monotonic interpolation scheme. This diffuse or smeared interface approach has its own interest when one is interested in the optimization of functionally graded materials, where more general interpolation functions can be used [31], [88], [137], [146], [150] (see also the Appendix).

There is already a vast literature about multiphase optimization with constant material properties and various methods have been proposed to address this problem. The Hadamard method of geometric shape optimization, as described in [49], [71], [130], [132] was used, for example, in [69] for optimal composite design. The homogenization method [3], [41], [142] was the main tool in the multiphase problem studied in [7] for the optimal reloading of nuclear reactors (sequential laminates were shown to be optimal composite materials). In the framework of the SIMP (Solid Isotropic Material with Penalization) method, several interpolation schemes have been proposed for the mathematical formulation of the Hooke's tensor of the mixture [28], [139], [163]. In general, material interpolation schemes can be quite involved [163] and one may design such a model in order to favor certain phases [139]. Applications range from the design of materials with extreme or unusual thermal expansion behavior [129] to multi-material actuators [126], through conductivity optimization for multi-phase microstructural materials [167]. In the framework of the phase-field method, a generalized Cahn-Hilliard model of multiphase transition was implemented in [166] to perform multimaterial structural optimization.

The first publications on multiphase optimization, using the level set method, are these of Mei et al. [94] and Wang et al. [153] (see also [93], [152], [154]). Following an idea of Vese and Chan [151], the authors in [94], [153] used m level set functions to represent up to $n = 2^m$ materials: we shall adhere to this setting (see section 6.5). The level set functions are advected through eikonal Hamilton-Jacobi equations in which the normal velocity is given by the shape derivative of the objective function. Unfortunately, the shape derivatives, derived in [94] and [153], are not correct in full mathematical rigor as we explain in section 6.4. Fortunately, these shape derivatives are approximations of the correct formula upon various assumptions. A first goal of the present paper is to clarify the issue of shape differentiability of a multiphase optimization problem. In section 6.2 we give the correct shape derivative in the setting of a sharp interface between phases (see Proposition 6.2.1). It was first obtained in [15] for a problem of damage and fracture propagation but, in a scalar setting, previous contributions can be found in [72], [29], [108]. Because the phase properties are discontinuous through the interfaces, the transmission conditions imply that only the elastic displacement and the normal stress are continuous at the interfaces, leaving the tangential stress and the normal strain discontinuous. These discontinuities yield obvious difficulties which must be handled carefully. The exact or continuous shape derivative turns out to be somehow inadequate for numerical purposes since it involves jumps of strains and stresses through the interfaces, quantities which are notably hard to evaluate with continuous finite elements. Therefore, Proposition 6.2.4 gives a discrete variant of this shape derivative which does not involve any jumps and is similar to the result of [94] and [153]. The idea is to consider a finite element approximation of the elasticity system, the solution of which has no derivative jumps through the interface, implying that the shape derivative is much easier to compute.

Another delicate issue in multiphase optimization using the level set method is that the interface is inevitably diffuse and its thickness may increase, thus deteriorating the performance of the analysis and eventually of the optimization. Note that, for most objective functions, it is always advantageous to introduce intermediate values of the material properties, so that the interface spreading is produced by the optimization process itself and not merely by the numerical diffusion. In [94] the authors introduced a penalization term to control the width of the interpolation zone between the materials. In [153] the level set functions are re-initialized to become signed distance functions, which permits a more explicit control of the interpolation width. A second goal of the present paper is to propose a smoothed interface setting which guarantees a fixed thickness of the interface without any increase in its width (as it is

already the case in the standard single material level set method for shape and topology optimization). In section 6.3 we describe a regularization of the interface which relies on the signed distance function to the interface. Note that the signed distance function has nothing to do with the level set function which is used in numerical simulations. Indeed, the solution of the advection Hamilton-Jacobi equation (with a velocity given by the shape derivative) is usually not the signed distance function (which explains why reinitialization is often used in practice). In such a smoothed interface setting our main result is Theorem 6.3.2 which gives the shape derivative of the objective function. It requires several intermediate technical results, notably finding the shape derivative of the distance function (first obtained in [48]) and using a coarea formula to reduce a volume integral to a product integral on the interface and along normal rays, which have been presented in Chapter 3. Once again, we show in section 6.3.3 that, when a regularised Heaviside function is used as interpolation function for the material properties and the regularization parameter (or the thickness of the diffuse interface) is vanishingly small, the exact shape derivative can be approximated by the formula already obtained in Proposition 6.2.4 which corresponds to the result of [94] and [153] too.

Section 6.3.4 explains how the smoothed interface model converges to the sharp interface problem as the regularization parameter goes to zero. Next, Section 6.4 is devoted to a comparison with [94] and [153]. Since, for simplicity, all the previous theoretical results were stated in the case of a single interface between two phases, we explain how to generalize our smoothed interface setting to more materials in section 6.5. In section 6.6 we show several 2-d results and make comparisons between the different settings and formulas for the shape derivatives. Some optimal designs obtained by our approach are compared to those previously computed in [153] and [154]: ours are more symmetric and sometimes slightly different. We believe it is due to our use of a correct shape derivative instead of an approximate one. Finally, in Section 6.7 we apply this method in the design of materials' microstructure using inverse homogenization.

6.2 Sharp-interface formulation in a fixed mesh framework

To simplify the exposition in the first sections we limit ourselves to the case of two materials. Of course, the proposed approach extends to more phases and the corresponding details are given in section 6.5.

6.2.1 Description of the problem

The general purpose of this paper is to optimize the position of the interface Γ between two linear elastic materials, hereafter labeled as 0 and 1, with respective Hooke's laws A_0, A_1 . These materials fill two respective subdomains Ω^0, Ω^1 of a (bounded) working domain D of \mathbb{R}^N , ($N = 2$ or 3) which accounts for the resulting structure of the optimal distribution of materials, i.e. $D = \Omega^0 \cup \Gamma \cup \Omega^1$. To avoid mathematical technicalities, we assume that Γ is a smooth surface without boundary and strictly included in D , that is, $\Gamma \cap \partial D = \emptyset$. We refer to Ω^1 as the *exterior* subdomain, so that $\partial\Omega^0 = \Gamma$ (see Figure 6.1). Thus, the shape of the interface Γ is altogether conditioned by that of Ω^0 , and conversely. In the sequel, the variable of shape optimization is denoted either by Γ or Ω^0 , without distinction.

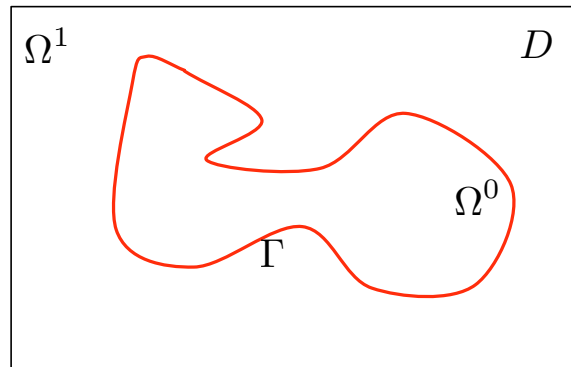


Figure 6.1: Fixed working domain D occupied by two distinct materials Ω^0 and Ω^1 separated by a smooth interface Γ .

The structure D is clamped on a part $\Gamma_D \subset \partial D$ of its boundary, and is submitted to *body forces* and *surface loads*, to be applied on a part $\Gamma_N \subset \partial D$, which are given as two vector-valued functions defined

on D , respectively $f \in L^2(D)^N$, and $g \in H^1(D)^N$.

Perhaps the most natural and physical way to model such a distribution of two materials among a fixed working domain is the so-called *sharp-interface formulation*. More specifically, the total Hooke's law on D is defined as $A_\chi := A_0\chi_0 + A_1\chi_1$, where χ_i stands for the characteristic function of the phase Ω^i . In this context, the *displacement field* u is the unique solution in $H^1(D)^N$ to the linearized elasticity system

$$\begin{cases} -\operatorname{div}(A_\chi e(u)) &= f & \text{in } D \\ u &= 0 & \text{on } \Gamma_D \\ (A_1 e(u)) \cdot n &= g & \text{on } \Gamma_N, \end{cases} \quad (6.1)$$

where $e(u) = \frac{\nabla u^T + \nabla u}{2}$ is the strain tensor, and n stands for the outer unit normal vector to ∂D .

Our purpose is to minimize an objective function of the interface Γ , which is rather expressed as a function $J(\Omega^0)$ of the interior subdomain,

$$J(\Omega^0) = \int_D j(x, u) dx + \int_{\Gamma_N} k(x, u) ds, \quad (6.2)$$

where $j(x, u)$ and $k(x, u)$ are smooth functions satisfying adequate growth conditions. A typical example is the *compliance* of the structure D , which reads

$$J(\Omega^0) = \int_D f \cdot u dx + \int_{\Gamma_N} g \cdot u ds = \int_D A_\chi(x) e(u) : e(u) dx. \quad (6.3)$$

6.2.2 Shape-sensitivity analysis of the sharp-interface problem

There exists a vast literature on the Hadamard method for computing derivatives with respect to the exterior boundary (see e.g. [4], [48], [71], [130] and references therein) but relatively few works on the derivation with respect to an interface between two regions. In the conductivity context (i.e. replacing (6.1) by a scalar equation), derivatives with respect to an interface have been obtained in [72], [29], [108]. These results were extended to the elasticity setting in [15]. Let us also mention the works [75], [103] where similar results are obtained for a stratified media (where the interfaces are flat and parametrized by a single scalar parameter).

As noticed in [15] and [108], the essential ingredients that must be considered in the calculation of the shape derivative of a problem such as (6.1) are the transmission conditions and the differentiability of the solution u with respect to the interface Γ . Furthermore, when a numerical implementation is sought, an additional element must be taken into account: the way in which the transmission conditions (continuity of the displacement and continuity of the normal stress across the interface) are interpreted by finite element methods in a fixed mesh framework. In general these methods either partially preserve the transmission conditions (e.g. classical Lagrange finite elements method) or exactly preserve the transmission conditions (e.g. extended finite elements XFEM [136], adapted interface meshing [44], etc.).

It is known [15], [108] that the solution $u \in H^1(D)$ of (6.1) is not shape differentiable with respect to the interface Γ . The reason is that some spatial derivatives of u are discontinuous across the interface because of the jump of the material elastic properties. Note however that the transported (or pull-back) function $u_\theta := u \circ (Id + \theta)$ is indeed differentiable with respect to θ (this is the difference between the material derivative in the latter case and the shape derivative in the former case, see [4], [71]). It is not necessary to use the concept of material derivative for computing the shape derivative of the objective function. One can stay in a Eulerian framework and use Céa's formal Lagrangian method [35] to find the correct formula for the shape derivative $J'(\Omega^0)(\theta)$. In order to circumvent the non-differentiability of u , the idea is to introduce the restrictions of u on Ω^0 and Ω^1 , denoted by $u^0 := u|_{\Omega^0}$ and $u^1 := u|_{\Omega^1}$.

We recall the result of [15] for the shape derivation of the objective function (6.2). We need to introduce some notations about jumps through the interface Γ . For any quantity s which is discontinuous across Γ , taking values s^0 (resp. s^1) on Ω^0 (resp. Ω^1), denote as $[s] = s^1 - s^0$ the *jump* of s . We also introduce at each point of Γ the local basis obtained by gathering the unit normal vector n (pointing outward Ω^0) and a collection of unit tangential vectors, denoted by τ , such that (τ, n) is an orthonormal frame. For a symmetric $N \times N$ matrix \mathcal{M} , written in this basis, we introduce the notation

$$\mathcal{M} = \begin{pmatrix} \mathcal{M}_{\tau\tau} & \mathcal{M}_{\tau n} \\ \mathcal{M}_{n\tau} & \mathcal{M}_{nn} \end{pmatrix}$$

where $\mathcal{M}_{\tau\tau}$ stands for the $(N-1) \times (N-1)$ minor of \mathcal{M} , $\mathcal{M}_{\tau n}$ is the vector of the $(n-1)$ first components of the n -th column of \mathcal{M} , $\mathcal{M}_{n\tau}$ is the row vector of the $(n-1)$ first components of the n -th row of \mathcal{M} , and \mathcal{M}_{nn} the (n, n) entry of \mathcal{M} . Finally, we define the adjoint problem

$$\begin{cases} -\operatorname{div}(A_\chi e(p)) &= -j'(x, u) & \text{in } D, \\ p &= 0 & \text{on } \Gamma_D, \\ (A_1 e(p)) \cdot n &= -k'(x, u) & \text{on } \Gamma_N, \end{cases} \quad (6.4)$$

where the symbol $'$ denotes differentiation with respect to u .

Proposition 6.2.1. *The shape derivative of the cost function J , defined in (6.2), reads*

$$J'(\Omega^0)(\theta) = - \int_{\Gamma} \mathcal{D}(u, p) \theta \cdot n \, ds, \quad (6.5)$$

$$\mathcal{D}(u, p) = -\sigma(p)_{nn} : [e(u)_{nn}] - 2\sigma(u)_{n\tau} : [e(p)_{n\tau}] + [\sigma(u)_{\tau\tau}] : e(p)_{\tau\tau}.$$

where $[\cdot] = \cdot^1 - \cdot^0$ denotes the jump through Γ , $n = n^0 = -n^1$ and $\sigma(v) = A_\chi e(v)$.

Remark 6.2.2. *To better appreciate the expression (6.5) where some terms have jumps and others not, we recall that the tangential strain tensors $e(u)_{\tau\tau}$ and $e(p)_{\tau\tau}$ are continuous through the interface Γ while the normal components $e(u)_{nn}$, $e(u)_{n\tau}$, $e(p)_{nn}$ and $e(p)_{n\tau}$ are discontinuous. On the contrary, the normal components of the stress tensors $\sigma(u)_{nn}$, $\sigma(u)_{n\tau}$, $\sigma(p)_{nn}$ and $\sigma(p)_{n\tau}$ are continuous through Γ while their tangential parts $\sigma(u)_{\tau\tau}$ and $\sigma(p)_{\tau\tau}$ are discontinuous.*

Proof. We merely sketch the proof that can be found in [15]. In order to apply C ea's Lagrangian method [35], we first introduce the restrictions of u on Ω^0 and Ω^1 , denoted by $u^0 := u|_{\Omega^0}$ and $u^1 := u|_{\Omega^1}$, which satisfy the transmission problem:

$$\begin{cases} -\operatorname{div}(A_1 e(u^1)) &= f & \text{in } \Omega^1 \\ u^1 &= 0 & \text{on } \Gamma_D \cap \partial\Omega^1 \\ (A_1 e(u^1)) \cdot n &= g & \text{on } \Gamma_N \cap \partial\Omega^1 \\ u^1 &= u^0 & \text{on } \Gamma \\ (A_0 e(u^0)) \cdot n^0 + (A_1 e(u^1)) \cdot n^1 &= 0 & \text{on } \Gamma, \end{cases} \quad (6.6)$$

and

$$\begin{cases} -\operatorname{div}(A_0 e(u^0)) &= f & \text{in } \Omega^0 \\ u^1 &= u^0 & \text{on } \Gamma \\ (A_0 e(u^0)) \cdot n^0 + (A_1 e(u^1)) \cdot n^1 &= 0 & \text{on } \Gamma. \end{cases} \quad (6.7)$$

Of course, (6.1) and (6.6)-(6.7) are equivalent. Note that, by standard regularity theory [92], u is smooth on each subdomain, namely $u^0 \in H^2(\Omega^0)$ and $u^1 \in H^2(\Omega^1)$. Then, we define the Lagrangian

$$\begin{aligned} \mathcal{L}(\theta, v^1, v^0, q^1, q^0) &= \sum_{i=0,1} \left(\int_{(Id+\theta)\Omega^i} j(x, v^i) dx + \int_{\Gamma_N} k(x, v^i) ds \right) \\ &+ \sum_{i=0,1} \left(\int_{(Id+\theta)\Omega^i} A_i e(v^i) : e(q^i) dx - \int_{(Id+\theta)\Omega^i} f \cdot q^i dx - \int_{\Gamma_N} g \cdot q^i ds \right) \\ &+ \frac{1}{2} \int_{(Id+\theta)\Gamma} (\sigma^1(v^1) + \sigma^0(v^0)) n \cdot (q^1 - q^0) ds \\ &+ \frac{1}{2} \int_{(Id+\theta)\Gamma} (\sigma^1(q^1) + \sigma^0(q^0)) n \cdot (v^1 - v^0) ds, \end{aligned} \quad (6.8)$$

where the last two surface integrals account for the transmission conditions. Differentiating \mathcal{L} with respect to q^1, q^0 yields the state equations (6.6)-(6.7), while differentiating with respect to v^1, v^0 leads to the adjoint equation (6.4). Then a standard, albeit nasty, computation (see [15] for full details) shows that

$$J'(\Omega^0)(\theta) = \frac{\partial \mathcal{L}}{\partial \theta}(0, u^1, u^0, p^1, p^0)(\theta),$$

which yields the result. \square

Remark 6.2.3. Proposition 6.2.1 can be extended in several ways. For example, if the integrand j depends on χ , namely if the objective function is

$$J(\Omega^0) = \int_D j_\chi(x, u) dx + \int_{\Gamma_N} k(x, u) ds := \sum_{i=0,1} \int_{\Omega^i} j_i(x, u) dx + \int_{\Gamma_N} k(x, u) dx,$$

we obtain a shape derivative which is

$$J'(\Omega^0)(\theta) = - \int_{\Gamma} \left([j_\chi(x, u)] + \mathcal{D}(u, p) \right) \theta \cdot n ds,$$

with the same expression (6.5) for $\mathcal{D}(u, p)$.

Although formula (6.5) for the shape derivative makes perfect sense in a continuous setting, its numerical discretization is not obvious. Indeed, (6.5) involves jumps through the interface which are difficult to evaluate from a numerical point of view if the interface is not exactly meshed. Let us explain the difficulty by making some specific discretization choices, keeping in mind that any other numerical method will feature similar drawbacks. Suppose D is equipped with a conformal simplicial mesh $D_h = \bigcup_{i=1}^N K_i$ with N elements K_i of maximal size h . Let $\Pi_1(D_h)$ and $\Pi_0(D_h)$ be the finite-dimensional spaces of Lagrange \mathbb{P}^1 , respectively \mathbb{P}^0 , finite element functions. Define $u_h, p_h \in \Pi_1(D_h)$ the internal approximations of u and p respectively, i.e.,

$$\int_D A_\chi e(u_h) : e(v_h) dx = \int_D f \cdot v_h dx + \int_{\Gamma_N} g \cdot v_h ds, \quad \forall v_h \in \Pi_1(D_h), \quad (6.9)$$

and

$$\int_D A_\chi e(p_h) : e(v_h) dx = - \int_D j'(x, u_h) \cdot v_h dx - \int_{\Gamma_N} k'(x, u_h) \cdot v_h ds, \quad \forall v_h \in \Pi_1(D_h). \quad (6.10)$$

Since the discrete strain tensors $e(v_h)$ are constant in each cell K_i , we can replace A_χ in the above internal approximate variational formulation by its \mathbb{P}^0 interpolate A^* defined by

$$A^*|_K = \rho A^0 + (1 - \rho) A^1, \quad \text{with } \rho = \int_K \chi dx.$$

Within this discretized framework the naive evaluation of the jumps in (6.5) has no meaning. Indeed, consider the generic case of an element K cut in its interior by the interface Γ (see Figure 6.2). For \mathbb{P}^1 Lagrange finite elements the strain tensors $e(v_h)$, for $v_h = u_h, p_h$, are constant in K , thus yielding a zero jump. Similarly, if the stress tensors are evaluated as $\sigma_h = A^* e(v_h)$, they are constant in K and their jump is again zero, leading to a vanishing shape derivative ! There is an alternative formula for the stress tensor which is $\sigma_h = A_\chi e(v_h)$: it yields a non-vanishing jump $[A]e(v_h)$ and the discretization of (6.5) would be

$$(\mathcal{D}(u, p))_h = ([A]e(u))_{\tau\tau} : e(p)_{\tau\tau}, \quad (6.11)$$

which is different from the discrete formula (6.13) by lack of any normal components. On the same token, note that the "exact" continuity of the normal stress through Γ does not hold for $\sigma_h = A_\chi e(v_h)$ with $v_h = u_h, p_h$ since

$$[\sigma_h \cdot n] = ([A]e(v_h)) \cdot n \neq 0.$$

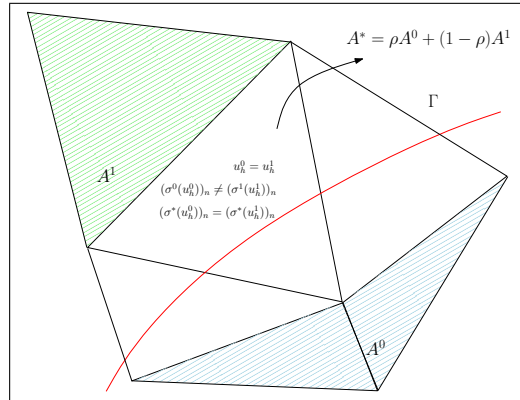


Figure 6.2: Transmission condition in a fixed mesh framework.

Therefore some special care is required for the numerical approximation of (6.5). A complicated process was proposed in [15] for computing the jump of a discontinuous quantity s_h , based on the diffuse interface approximation

$$[s_h] \approx \left((1 - \chi)s_h - \chi s_h \right). \quad (6.12)$$

Notwithstanding this approximation seems to work well when the contrast between the two elastic phases is very large (as is the case in damage or fracture models, see [15]), more general numerical experiences for comparable elastic moduli indicate a much worse behavior of this approximation, up to the point that (6.5) does not any longer provide a proper descent direction to minimize (6.2) (see section 6.6.2).

This difficulty in the numerical evaluation of the shape derivative (6.5) is just another example of the well-known paradigm "should we differentiate first and then discretize or *vice versa*?" as already studied in [104]. In order to get around this issue it is tempting, and we do so now, to investigate the case when we first discretize and then differentiate. In other words we consider the objective function

$$J_h(\Omega^0) = \int_D j(x, u_h) dx + \int_{\Gamma_N} k(x, u_h) ds,$$

where $u_h \in \Pi_1(D_h)$ is the discrete solution of (6.9).

Proposition 6.2.4. *Assume that the interface Γ generically cuts the mesh D_h , namely that it is never aligned with part of a face of any cell K_i . Then, the solution u_h of (6.9) is shape differentiable and the shape derivative of the cost function J_h is given by*

$$J'_h(\Omega^0)(\theta) = - \int_{\Gamma} [A_{\chi}]e(u_h) : e(p_h)\theta \cdot n ds, \quad (6.13)$$

where $[\cdot]$ denotes the jump through Γ and p_h is the solution of (6.10).

Remark 6.2.5. *Note that Proposition 6.2.4 holds true for most finite elements discretization and not merely \mathbb{P}^1 Lagrange finite elements. The assumption on the interface Γ is necessary in the sense that, if a face of an element K of the mesh is embedded in Γ , then neither u_h nor J_h are shape differentiable (in the most favorable case, there would be two directional derivatives corresponding to Γ moving on one side or on the other of this face of K). However, if instead of Lagrange finite elements, we use Hermite finite elements which ensure that $e(u_h)$ is continuous on D , then the results of Proposition 6.2.4 hold true without any assumption on Γ .*

Proof. Let us denote by $\phi_i(x)$ the basis functions of the finite element space $\Pi_1(D_h)$. The solution $u_h \in \Pi_1(D_h)$ is decomposed as

$$u_h(x) = \sum_i U_i^h \phi_i(x),$$

and the vector U^h of components U_i^h is the solution of the linear system

$$K^h U^h = F^h,$$

where the stiffness matrix K^h and the right hand side F^h are defined as

$$K_{i,j}^h = \int_D A_{\chi} e(\phi_i) : e(\phi_j) dx, \text{ and } F_i^h = \int_D f \cdot \phi_i dx + \int_{\Gamma_N} g \cdot \phi_i ds.$$

The basis functions ϕ_i are independent of Γ so the shape differentiability of the function u_h reduces to that of the vector U^h and thus of the rigidity matrix K^h . Since the quantity $e(\phi_i) : e(\phi_j)$ is piecewise constant on each element K , we need our assumption on Γ which does not overlap any face of K . In such a case we obtain

$$(K_{ij}^h)'(\Gamma)(\theta) = \int_{\Gamma} [A_{\chi}]e(\phi_i) : e(\phi_j)\theta \cdot n ds$$

and thus

$$u'_h(\Gamma)(\theta) = \sum_i (U_i^h)'(\Gamma)(\theta) \phi_i, \text{ where } (U^h)'(\Gamma)(\theta) = -(K^h)^{-1} (K^h)'(\Gamma)(\theta) U^h.$$

Once u_h is shape differentiable, it is not necessary anymore to consider a complicated Lagrangian like (6.8), taking into account the transmission conditions through Γ (which, by the way, do not hold true for u_h). Therefore we define a discrete Lagrangian as

$$\mathcal{L}_h(\theta, v_h, q_h) = \int_D j(x, v_h) dx + \int_{\Gamma_N} k(x, v_h) ds + \int_D A_{(Id+\theta)\chi} e(v_h) : e(q_h) dx - \int_D f \cdot q_h dx - \int_{\Gamma_N} g \cdot q_h ds,$$

to which it is easy to apply C  a's method. Note that the adjoint problem obtained by differentiating \mathcal{L}_h with respect to v_h is exactly (6.10) which was a discretization of the continuous adjoint. Therefore we deduce

$$J'_h(\Omega^0)(\theta) = \frac{\partial \mathcal{L}_h}{\partial \theta}(0, u_h, p_h)(\theta),$$

which yields the desired result. \square

There is a clear difference between the discrete derivative (6.13) and the continuous one (6.5). Even if the continuous derivative is further discretized as suggested in (6.11), there is still a difference between (6.13) and (6.11) which is that the latter one is restricted to the tangential components of the stress and strain tensors.

There is however one case where both formulas coincide which is when one of the phases is void. Indeed, assume that $A_0 = 0$ (and similarly that $f = 0$ and $j = 0$ in Ω^0 so that no loads are applied to the void region). Then, in the domain Ω^0 we have

$$\sigma(p)_{nn} = 0, \sigma(p)_{n\tau} = 0, \sigma(u)_{nn} = 0 \text{ and } \sigma(u)_{n\tau} = 0.$$

Thus, we deduce that the continuous derivative (6.5) becomes

$$J'(\Omega^0)(\theta) = - \int_{\Gamma} \sigma(u^1)_{\tau\tau} : e(p^1)_{\tau\tau} \theta \cdot n ds,$$

which, upon discretization, coincides with the discrete derivative (6.13)

$$J'_h(\Omega^0)(\theta) = - \int_{\Gamma} A^1 e(u_h) : e(p_h) \theta \cdot n ds,$$

since $\sigma(u^1)_{nn} = \sigma(u^1)_{n\tau} = 0$ on Γ .

The above study shows that the numerical discretization of the sharp-interface problem should be handled carefully when a standard finite element method is used for solving the state and adjoint systems (6.1) and (6.4) in a fixed mesh setting. The main reason of this difficulty lies in the difference of regularity of the exact and approximated solutions through the interface. The discrete derivative (6.13) is very efficient in numerical practice. Many examples are given in [50] in the context of optimal design of laminated composite panels.

6.3 Shape derivative in the smoothed-interface context

6.3.1 Description of the problem

We now present an alternative approach to that of section 6.2 which can be coined as smoothed or diffuse interface approach. It can be seen as a mathematically convenient approximation of the sharp-interface problem but, as explained in the introduction, it has its own merits for some problems in material science which feature physically thick transition zones [31], [137], [146], [150]. More precisely, either for a mathematical approximation or for physical reasons, it may be desirable to model the interface Γ between Ω^0 and Ω^1 as a thin layer of (small) width $2\varepsilon > 0$ rather than as a sharp interface. In this context, we rely on the notion of signed distance function (1.3.2).

The material properties in D are defined as a smooth interpolation between A_0 and A_1 in the layer of width 2ε around Γ , so that the resulting Hooke's tensor $A_{\Omega^0, \varepsilon}$ reads

$$A_{\Omega^0, \varepsilon}(x) = A_0 + h_\varepsilon(d_{\Omega^0}(x))(A_1 - A_0), \quad \forall x \in D, \quad (6.14)$$

where $h_\varepsilon : \mathbb{R} \rightarrow \mathbb{R}$ is a smooth approximation of the Heaviside function, that is, a smooth monotone function enjoying the properties : $h_\varepsilon(t) = 0$ for $t < -\varepsilon$, $h_\varepsilon(t) = 1$ for $t > \varepsilon$. In the sequel, we chose the \mathcal{C}^2 function

$$\forall t \in \mathbb{R}, \quad h_\varepsilon(t) = \begin{cases} 0 & \text{if } t < -\varepsilon \\ \frac{1}{2} \left(1 + \frac{t}{\varepsilon} + \frac{1}{\pi} \sin\left(\frac{\pi t}{\varepsilon}\right) \right) & \text{if } -\varepsilon \leq t \leq \varepsilon \\ 1 & \text{if } t > \varepsilon. \end{cases} \quad (6.15)$$

Remark 6.3.1. Formula (6.15) expresses a simple choice for the interpolation of the material properties between the two materials, and of course, one could think of different interpolation rules. Moreover, the interpolation function could also contain parameters that are themselves subject to optimization (e.g. the layer width ε) and both a geometric and parametric optimization could be combined using a method of alternating directions. Therefore, this method could be generalized to the shape and topology optimization of functionally graded materials in a straightforward way (see [150] for the use of non-monotone interpolation functions).

We modify (6.1) so that the elastic displacement now solves

$$\begin{cases} -\operatorname{div}(A_{\Omega^0, \varepsilon} e(u)) &= f & \text{in } D \\ u &= 0 & \text{on } \Gamma_D \\ (A_1 e(u)) \cdot n &= g & \text{on } \Gamma_N. \end{cases} \quad (6.16)$$

The objective function does not change and we still minimize (6.2) which depends on d_{Ω^0} through (6.14).

6.3.2 Shape derivative of the compliance in the multi-materials setting

We now differentiate the cost function (6.2) with respect to the domain, using the results of Section 3.3. We keep the geometrical assumptions of section 6.2, namely for a given bounded open set $D \subset \mathbb{R}^N$ which is partitioned in two subdomains $\Omega^0, \Omega^1 \subset D$, Ω^0 is a strict subset of D in the sense that its boundary Γ , as well as its thick approximation, does not touch ∂D (see Figure 6.1) and Γ is smooth.

We define the adjoint problem

$$\begin{cases} -\operatorname{div}(A_{\Omega^0, \varepsilon} e(p)) &= -j'(x, u) & \text{in } D, \\ p &= 0 & \text{on } \Gamma_D, \\ (A_1 e(p)) \cdot n &= -k'(x, u) & \text{on } \Gamma_N, \end{cases} \quad (6.17)$$

where the symbol $'$ denotes differentiation with respect to u .

Our main result is the following.

Theorem 6.3.2. *The objective function (6.2) is shape differentiable in the sense of Gâteaux, namely $\theta \mapsto J((Id + \theta)\Omega^0)$ admits a Gâteaux derivative at $\theta = 0$, which is*

$$J'(\Omega^0)(\theta) = - \int_{\Gamma} \theta(x) \cdot n(x) (f_0(x) + f_1(x)) dx, \quad \forall \theta \in W^{1, \infty}(D, \mathbb{R}^N), \quad (6.18)$$

where n is the outer unit normal to Ω^0 and f_0, f_1 are scalar functions defined by

$$\begin{aligned} f_0(x) &= \int_{\operatorname{ray}_{\Gamma}(x) \cap \Omega^0} h'_{\varepsilon}(d_{\Omega^0}(z)) (A_1 - A_0) e(u)(z) : e(p)(z) \prod_{i=1}^{N-1} (1 + d_{\Omega^0}(z) \kappa_i(x)) dz, \\ f_1(x) &= \int_{\operatorname{ray}_{\Gamma}(x) \cap \Omega^1} h'_{\varepsilon}(d_{\Omega^0}(z)) (A_1 - A_0) e(u)(z) : e(p)(z) \prod_{i=1}^{N-1} (1 + d_{\Omega^0}(z) \kappa_i(x)) dz, \end{aligned}$$

where z denotes a point in the ray emerging from $x \in \Gamma$.

Proof. The rigorous proof of existence of the shape derivative stems from classical arguments (typically the implicit function theorem) similar to those invoked in [130] or chapter 5 in [71]. We rather focus on the actual computation of the shape derivative and use once again the formal Lagrangian method of C  a [35]. As the computation unfolds very similarly to that in the proof of Theorem 3.6 in [16], we limit ourselves to the main arguments.

Define first the functional space $V := \{v \in H^1(D)^N \text{ such that } v = 0 \text{ on } \Gamma_D\}$, in which are sought the solution of the state equation (6.16) and of the adjoint equation (6.17). We introduce the Lagrangian $\mathcal{L} : W^{1, \infty}(D, \mathbb{R}^N) \times V \times V \rightarrow \mathbb{R}$, defined by

$$\mathcal{L}(\theta, v, q) = \int_D j(x, v) dx + \int_{\Gamma_N} k(x, v) ds + \int_D A_{(Id+\theta)\Omega^0, \varepsilon} e(v) : e(q) dx - \int_D f \cdot q dx - \int_{\Gamma_N} g \cdot q ds. \quad (6.19)$$

Here, q is intended as the Lagrange multiplier associated to the enforcement of the state equation. As usual, stationarity of the Lagrangian provides the optimality conditions for the minimization problem.

At $\theta = 0$, cancelling the partial derivative of \mathcal{L} with respect to q yields the variational formulation of the state u . In the same way, the nullity of the partial derivative of \mathcal{L} with respect to v leads to the variational formulation of the adjoint p .

Eventually, the shape derivative of the objective function is the partial derivative of \mathcal{L} with respect to θ , evaluated at u and p

$$J'(\Omega^0)(\theta) = \frac{\partial \mathcal{L}}{\partial \theta}(0, u, p)(\theta).$$

Some elementary algebra, using the shape differentiability of $d_{\Omega^0}(x)$ for almost every $x \in D$, yields

$$\begin{aligned} J'(\Omega^0)(\theta) &= \int_D (A_{(Id+\theta)\Omega^0, \varepsilon})'(\theta) e(u) : e(p) dx \\ &= - \int_D h'_\varepsilon(d_{\Omega^0}(x)) (\theta(p_\Gamma(x)) \cdot n(p_\Gamma(x))) (A_1 - A_0) e(u) : e(p) dx, \end{aligned} \quad (6.20)$$

where $(A_{(Id+\theta)\Omega^0, \varepsilon})'(\theta)$ is the directional shape derivative of $A_{(Id+\theta)\Omega^0, \varepsilon}$ while h'_ε is the standard derivative of the real function h_ε . It remains to transform this expression by the coarea formula in order to deduce a boundary integral. Using formula (3.11) for (6.20), we get

$$J'(\Omega^0)(\theta) = - \int_\Gamma \theta(x) \cdot n(x) \left(\int_{\text{ray}_\Gamma(x) \cap D} h'_\varepsilon(d_{\Omega^0}(z)) (A_1 - A_0) e(u)(z) : e(p)(z) \prod_{i=1}^{N-1} (1 + d_{\Omega^0}(z) \kappa_i(x)) dz \right) dx.$$

Now decomposing the above integral over Ω^0 and Ω^1 readily yields the desired result. \square

Remark 6.3.3. *Theorem 6.3.2 provides a simple way of choosing a descent direction for a shape gradient based algorithm. Indeed it is enough to perturb the interface Γ by choosing the vector field*

$$\theta(x) = (f_0(x) + f_1(x))n(x),$$

which ensures that the directional derivative (6.18) is negative and thus yields a decrease of the objective function (6.3). This is in sharp contrast with Corollary 3.3.6 which provided formula (3.7) for the shape derivative. However it was impossible to extract directly from (3.7) an explicit value of θ which was a guaranteed descent direction.

Remark 6.3.4. *In the case of compliance minimization, namely for the objective function (6.3), we have $j' = f$, $k' = g$ and thus $p = -u$. If we assume that material 1 is stronger than material 0, in the sense that $A^1 \geq A^0$ as positive definite tensors, we deduce from the formulas of Theorem 6.3.2 that both f_0 and f_1 are non-positive because $1 + \kappa_i(x)d_{\Omega^0}(z) \geq 0$ by virtue of Lemma 3.3.9. Thus, a descent direction is obtained by choosing θ such that $\theta(x) \cdot n(x) < 0$ on Γ , namely we expand Ω^1 . This is in accordance with the mechanical intuition that a more robust mixture of the two materials is achieved when A^1 prevails over A^0 . Of course, for the problem to be reasonable, a volume constraint is imposed on the phases.*

6.3.3 Approximate formulas for the shape derivative

Although formula (6.18) is satisfying from a mathematical point of view, its numerical evaluation is not completely straightforward. There are two delicate issues. First, one has to compute the principal curvatures $\kappa_i(x)$ for any point $x \in \Gamma$ on the interface. Second, one has to perform a 1-d integration along the rays of the energy-like quantity $[A]e(u) : e(p)$. This is a classical task in the level-set framework [120] but, still, it is of interest to devise a simpler approximate formula for the shape derivative.

A first approximate formula is to assume that the interface is roughly plane, namely to assume that the principal curvatures κ_i vanish. In such a case we obtain a "Jacobian-free" approximate shape derivative

$$\begin{aligned} J'(\Omega^0)(\theta) &= - \int_\Gamma \theta(x) \cdot n(x) (f_0(x) + f_1(x)) dx \\ f_i(x) &= \int_{\text{ray}_\Gamma(x) \cap \Omega^i} h'_\varepsilon(d_{\Omega^0}(z)) (A_1 - A_0) e(u)(z) : e(p)(z) dz. \end{aligned} \quad (6.21)$$

A second approximate formula is obtained when the smoothing parameter ε is small. Note that, since the support of the function h'_ε is of size 2ε , the integral in formula (6.18) is confined to a tubular neighborhood of Γ of width 2ε . Therefore, if ε is small, one may assume that the functions depending on z are constant along each ray, equal to their value at $x \in \Gamma$. In other words, for small ε we assume

$$e(u)(z) \approx e(u)(x), \quad e(p)(z) \approx e(p)(x) \quad \text{and} \quad d_{\Omega^0}(z) \approx d_{\Omega^0}(x) = 0,$$

which yields the approximate formulas, for $x \in \Gamma$,

$$\begin{aligned} f_0(x) &\approx (A_1 - A_0)e(u)(x) : e(p)(x) \int_{ray_\Gamma(x) \cap \Omega^0} h'_\varepsilon(d_{\Omega^0}(z)) dz, \\ f_1(x) &\approx (A_1 - A_0)e(u)(x) : e(p)(x) \int_{ray_\Gamma(x) \cap \Omega^1} h'_\varepsilon(d_{\Omega^0}(z)) dz. \end{aligned}$$

Furthermore, most rays have a length larger than 2ε so that

$$\int_{ray_\Gamma(x) \cap \Omega^0} h'_\varepsilon(d_{\Omega^0}(z)) dz + \int_{ray_\Gamma(x) \cap \Omega^1} h'_\varepsilon(d_{\Omega^0}(z)) dz = h_\varepsilon(\varepsilon) - h_\varepsilon(-\varepsilon) = 1.$$

In turn we obtain the following approximate formula for (6.18)

$$J'(\Omega^0)(\theta) \approx - \int_\Gamma (A_1 - A_0)e(u) : e(p) \theta \cdot n dx, \quad (6.22)$$

which is nothing but the discrete shape derivative (6.13) that we obtained in the sharp-interface case. This computation seems a bit miraculous but makes sense as a kind of commutation property between interface regularization and optimization.

Our numerical results show that the latter simplification (6.22), which we shall refer to as the *approximate shape derivative*, works very well in practice for problems of compliance minimization. Formula (6.22) is also used by other authors in their numerical simulations [153].

6.3.4 Convergence of the smoothed-interface shape optimization problem to the sharp-interface problem

When the smoothed-interface setting is used as an approximation of the sharp-interface case, it is a natural task to prove that this approximation is mathematically consistent. In this section, we present a result in this direction. More specifically, for a given regular interface Γ , we prove that the shape gradient obtained in Theorem 6.3.2 for a smoothed transition layer of width 2ε converges, as ε goes to 0, to the corresponding shape gradient in the sharp-interface context, recalled in Proposition 6.2.1.

To set ideas, let us limit ourselves to the case of compliance minimization, the case of a general objective function such as (6.2) being no different in principle. In order to make explicit the dependence on the half-thickness ε of the smoothed transmission area, the solution of the state system (6.16) is denoted u_ε in this section. Similarly the stress tensor is $\sigma(u_\varepsilon) = A_{\Omega^0, \varepsilon} e(u_\varepsilon)$ and the compliance is

$$J_\varepsilon(\Omega^0) = \int_D \sigma(u_\varepsilon) : e(u_\varepsilon) dx.$$

The solution of the state system (6.1) in the sharp-interface case is still denoted as u , and the associated compliance as $J(\Omega^0)$.

To find the limit of $J'_\varepsilon(\Omega_0)$, as $\varepsilon \rightarrow 0$, requires some knowledge of the asymptotic behavior of $e(u_\varepsilon)$ and $\sigma(u_\varepsilon)$ in the vicinity of the interface Γ . Unfortunately, one cannot expect all the components of $e(u_\varepsilon)$ and $\sigma(u_\varepsilon)$ to converge toward their counterpart in $e(u)$ and $\sigma(u)$ in any space of smooth enough functions. Indeed, for fixed ε , $e(u_\varepsilon)$ is smooth over D (because so is the associated Hooke's tensor), whereas we recalled in Remark 6.2.2 that $e(u)_{\tau n}$ and $e(u)_{nn}$ are discontinuous across Γ , as imposed by the transmission conditions. However, some of the components of $e(u_\varepsilon)$ and $\sigma(u_\varepsilon)$ do behave well as $\varepsilon \rightarrow 0$. This is the purpose of the following lemma, which is a consequence of rather classical results in elliptic regularity theory (see [44] for a proof).

Lemma 6.3.5. *Assuming Γ is a \mathcal{C}^2 interface, there exists a tubular neighborhood $V \subset\subset D$ of Γ such that one can define a smooth extension in V of the normal n and of a set of tangentials and orthonormal vectors τ . Then, the following strong convergences hold true*

$$\begin{aligned} e(u_\varepsilon)_{\tau\tau} &\xrightarrow{\varepsilon \rightarrow 0} e(u)_{\tau\tau} && \text{in } H^1(V)^{(N-1)^2} \text{ strong,} \\ \sigma(u_\varepsilon)_{\tau n} &\xrightarrow{\varepsilon \rightarrow 0} \sigma(u)_{\tau n} && \text{in } H^1(V)^N \text{ strong,} \\ \sigma(u_\varepsilon)_{nn} &\xrightarrow{\varepsilon \rightarrow 0} \sigma(u)_{nn} && \text{in } H^1(V) \text{ strong.} \end{aligned}$$

Remark 6.3.6. *The components of the strain and stress tensors which converge in Lemma 6.3.5 correspond exactly to those which are continuous through the interface Γ as explained in Remark 6.2.2.*

We are now in a position to state the main result of the present section which implies that the shape derivative of the smoothed-interface objective function is a consistent approximation of the corresponding shape derivative in the sharp-interface case.

Theorem 6.3.7. *Under the above assumptions, we have*

$$\lim_{\varepsilon \rightarrow 0} J'_\varepsilon(\Omega^0)(\theta) = J'(\Omega^0)(\theta) \quad \forall \theta \in W^{1,\infty}(D, \mathbb{R}^N).$$

Sketch of the proof. As the proof involves rather classical arguments, but tedious computations, we limit ourselves with an outline of the main steps, referring to [44] for details. The goal is to pass to the limit $\varepsilon \rightarrow 0$ in formula (6.18), for a fixed $\theta \in W^{1,\infty}(D, \mathbb{R}^N)$. To achieve this, the rays $\text{ray}_\Gamma(x) \cap \Omega^0$ and $\text{ray}_\Gamma(x) \cap \Omega^1$ are expressed as integrals over the segment $(0, 1)$. Therefore, (6.18) becomes

$$J'_\varepsilon(\Omega^0)(\theta) = - \int_\Gamma \theta(x) \cdot n(x) \left(f_0^\varepsilon(x) + f_1^\varepsilon(x) \right) dx,$$

where $f_0^\varepsilon, f_1^\varepsilon \in L^1(\Gamma)$ are defined as

$$f_0^\varepsilon(x) = \int_{-1}^0 h'_\varepsilon(s\varepsilon)(A_1 - A_0)e(u_\varepsilon)(x + s\varepsilon n(x)) : e(u_\varepsilon)(x + s\varepsilon n(x)) k_\varepsilon(x, s) ds, \quad (6.23)$$

$$f_1^\varepsilon(x) = \int_0^1 h'_\varepsilon(s\varepsilon)(A_1 - A_0)e(u_\varepsilon)(x + s\varepsilon n(x)) : e(u_\varepsilon)(x + s\varepsilon n(x)) k_\varepsilon(x, s) ds, \quad (6.24)$$

with

$$k_\varepsilon(x, s) = \prod_{i=1}^{N-1} (1 + s\varepsilon \kappa_i(x)).$$

Since $h'_\varepsilon(s\varepsilon)$ does not depend on ε , to pass to the limit in (6.23) and (6.24) requires merely the following simple technical convergence result (see [44] for a proof)

$$\int_0^1 v(s) f_\varepsilon(x + s\varepsilon n(x)) g_\varepsilon(x + s\varepsilon n(x)) ds \xrightarrow{\varepsilon \rightarrow 0} \left(\int_0^1 v(s) ds \right) f(x) g(x) \quad \text{in } L^1(\Gamma) \quad (6.25)$$

for a smooth function $v(s)$ and any sequences $f_\varepsilon, g_\varepsilon \in H^1(D)$, which converge strongly in $H^1(D)$ to f, g respectively. In order to apply (6.25) we rewrite expressions (6.23) and (6.24) in terms of the components $e(u_\varepsilon)_{\tau\tau}$ and $\sigma(u_\varepsilon)_{\tau n}$, $\sigma(u_\varepsilon)_{nn}$ of the strain and stress tensors, which have a fine behavior at the limit $\varepsilon \rightarrow 0$ as guaranteed by Lemma 6.3.5. After some algebra, we obtain the following rearrangement for the integrand in f_0^ε and f_1^ε :

$$\begin{aligned} (A_1 - A_0)e(u_\varepsilon) : e(u_\varepsilon)(x + s\varepsilon n(x)) &= \mu'(s) (e(u_\varepsilon)_{\tau\tau} : e(u_\varepsilon)_{\tau\tau})(x + s\varepsilon n(x)) \\ &+ \frac{\mu'(s)}{\mu(s)^2} (\sigma^\varepsilon(u_\varepsilon)_{\tau n} \cdot \sigma^\varepsilon(u_\varepsilon)_{\tau n})(x + s\varepsilon n(x)) \\ &+ \frac{4\mu^2(s)\lambda'(s) + 2\mu'(s)\lambda^2(s)}{(2\mu(s) + \lambda(s))^2} \text{tr}(e(u_\varepsilon)_{\tau\tau})^2(x + s\varepsilon n(x)) \\ &+ \frac{2\mu'(s) + \lambda'(s)}{(2\mu(s) + \lambda(s))^2} \sigma^\varepsilon(u_\varepsilon)_{nn}^2(x + s\varepsilon n(x)) \\ &+ \frac{4\mu(s)\lambda'(s) - 4\mu'(s)\lambda(s)}{(2\mu(s) + \lambda(s))^2} (\sigma^\varepsilon(u_\varepsilon)_{nn} \text{tr}(e(u_\varepsilon)_{\tau\tau}))(x + s\varepsilon n(x)) \end{aligned},$$

with

$$\lambda(s) = \lambda_0 + h_\varepsilon(s\varepsilon)(\lambda_1 - \lambda_0), \quad \mu(s) = \mu_0 + h_\varepsilon(s\varepsilon)(\mu_1 - \mu_0),$$

where λ_0, μ_0 and λ_1, μ_1 are the Lamé coefficients of materials 0, 1 respectively. Note that all the functions of s involving $\lambda(s)$ and $\mu(s)$ appearing in the above expression arise as exact derivatives of functions of $\lambda(s)$ and $\mu(s)$. Passing to the limit in the above expression using (6.25) leads to

$$(f_0^\varepsilon + f_1^\varepsilon) \rightarrow \mathcal{D}(u, u) \quad \text{in } L^1(\Gamma),$$

where $\mathcal{D}(u, u)$ is defined as

$$\begin{aligned} \mathcal{D}(u, u)(x) &= 2[\mu] e(u)_{\tau\tau}(x) : e(u)_{\tau\tau}(x) - \left[\frac{1}{\mu} \right] \sigma(u)_{\tau n}(x) \cdot \sigma(u)_{\tau n}(x) \\ &+ \left[\frac{2\lambda\mu}{(2\mu + \lambda)} \right] \text{tr}(e(u)_{\tau\tau}(x))^2 - \left[\frac{1}{2\mu + \lambda} \right] \sigma(u)(x)_{nn}^2 \\ &+ \left[\frac{2\lambda}{2\mu + \lambda} \right] \sigma(u)_{nn}(x) \text{tr}(e(u)_{\tau\tau}(x)) \end{aligned},$$

which after some algebra rewrites as (6.5). This completes the proof. \square

6.4 Discussion and comparison with previous formulae in the literature

To our knowledge, the first works on multi-phase optimization using a level-set method are [94] and [153]. Further references include [93], [152], [154]. In all these works the computation of the shape derivative is not mathematically rigorous and the obtained formulas are not strictly correct. Indeed, either the shape differentiation is performed in the sharp-interface case and then the non-differentiable character of the solution of (6.1) is ignored (as explained in section 6.2.2), or the shape derivative is evaluated in the smoothed-interface case and then the derivative of the signed distance function is not taken into account. Fortunately, the shape derivative formulas in [94] and [153] coincide with what we called our approximate shape derivatives obtained in Proposition 6.2.4 for a discretization of the sharp-interface case and in (6.22) for a very thin smoothed interface. A third possibility for interpreting these works is to consider that the regularization of the interface is made with the help of the level set function ψ (used in numerical practice for representing and advecting the shape, see section 6.6 below) rather than with the signed distance function d_Ω . Then the differentiation is performed with respect to ψ rather than with respect to the shape Ω . It alleviates all the technical details of section 6.3 but it has one major flaw that we now describe.

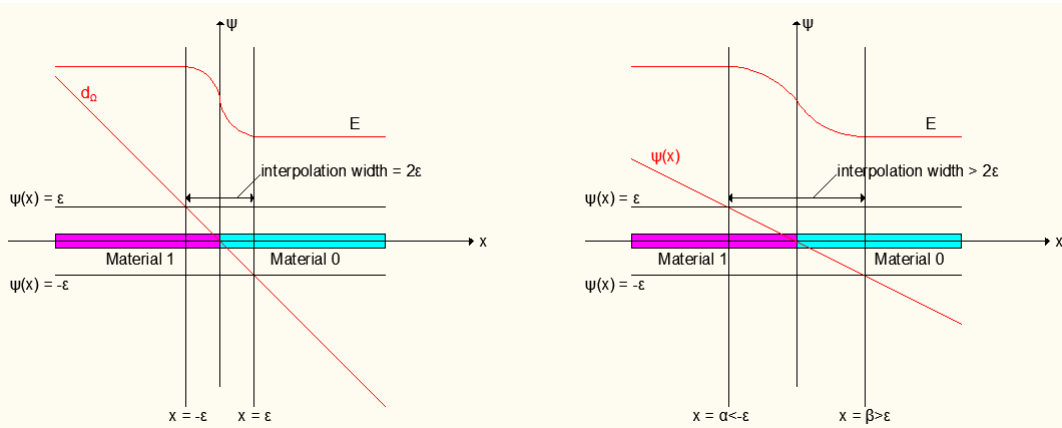


Figure 6.3: Intermediate zone for regularization with the signed distance function (left) or with a level set function (right).

Indeed, in the context of section 6.3 on the smoothed interface approach, one may replace the regularization formula (6.14) by a similar one

$$A_{\Omega^0, \varepsilon}(x) = A_0 + h_\varepsilon(\psi(x))(A_1 - A_0), \quad \forall x \in D, \quad (6.26)$$

where the signed distance function d_Ω has simply been replaced by the level set function ψ . Then, as is done in [94] and [93], one may differentiate the objective function with respect to ψ . A serious problem that rises directly from this choice, is that the interpolation zone, where $A_{\Omega^0, \varepsilon}$ takes intermediate values between A_0 and A_1 , can thicken during the optimization process, especially if the level set function ψ is not frequently reinitialized towards the signed distance function to the boundary (see Figure 6.3). The reason is that the interpolation zone corresponds to some kind of homogenized material made of A_0 and A_1 , which is known to be more advantageous than pure phases in most problems [4]. The optimization process therefore does not only move the interface location but also flatten the level set function ψ so that the interpolation zone gets thicker. Even when the level set function is reinitialized, there remains a difficulty in the sense that the value of the objective function may change before and after reinitialization. A partial remedy to this inconvenient, as suggested in [94], is to add to the objective function a penalization term to control the enlargement.

The computation of the shape derivative is slightly different in [153]: the authors carry out the derivation with the level set function ψ but in the resulting formula they assume that ψ coincides with the signed distance function to the interface d_Ω . More precisely, following the notations of Corollary 3.3.6, they consider a functional

$$J(\Omega) = \int_D m(x, \psi(x)) dx, \quad (6.27)$$

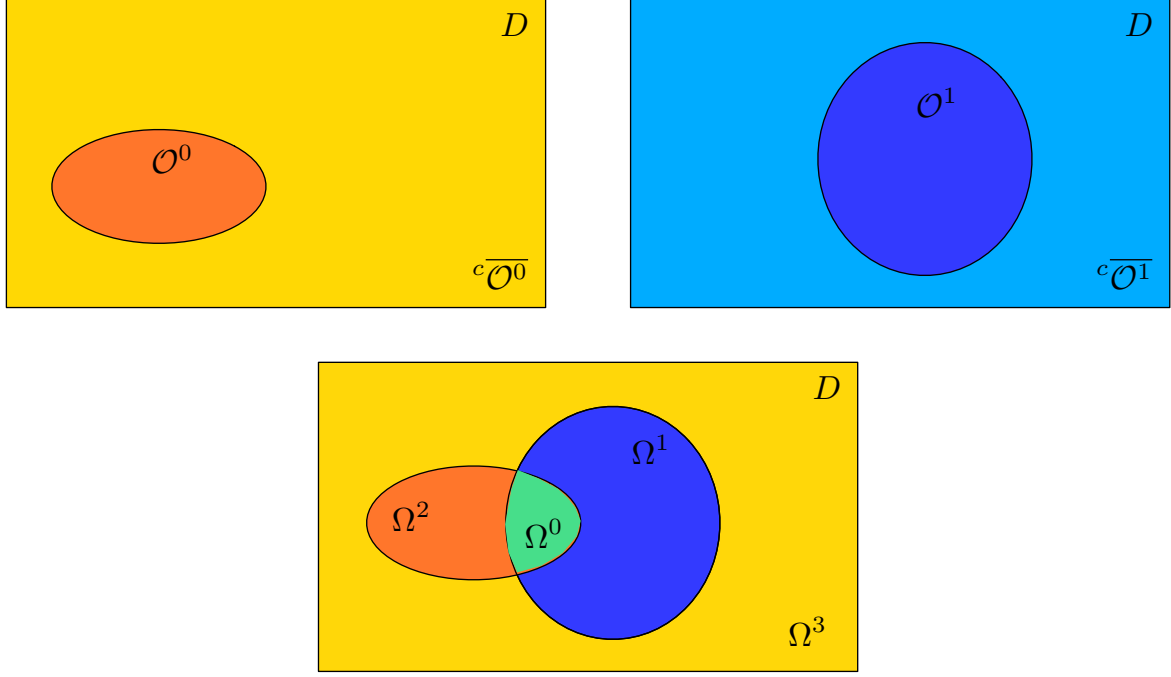


Figure 6.4: Two subdomains of D (top) and the four phase domains derived by combining them together (down).

where ψ is a solution of the Hamilton-Jacobi equation

$$\frac{\partial \psi}{\partial t} + \theta \cdot n |\nabla \psi| = 0.$$

Then, the authors claim that the shape derivative is

$$J'(\Omega)(\theta) = - \int_D \frac{\partial m}{\partial \psi}(x, \psi(x)) \theta(x) \cdot n(x) dx. \quad (6.28)$$

Note the difference with our formula (3.7), which involves the projection $p_\Gamma(x)$ of x on the boundary $\Gamma = \partial\Omega$, and that we recall as

$$J'(\Omega)(\theta) = - \int_D \frac{\partial m}{\partial \psi}(x, d_\Omega(x)) \theta(p_\Gamma(x)) \cdot n(p_\Gamma(x)) dx.$$

Unfortunately, there is no a priori guarantee that the transported signed distance function to the boundary $\partial\Omega$ remains the signed distance function to the transported boundary $(Id + \theta)\partial\Omega$. Therefore, the shape derivative $d'_\Omega(\theta)(x)$ cannot be replaced by the expression $\frac{\partial \psi}{\partial t} = -\theta \cdot n |\nabla \psi|$ coming from the Hamilton-Jacobi equation, as it is done in [94] and [153], without making any further assumptions. For example, in [59] it is shown that the transported level set function remains the signed distance function (at least for a small time) if the advection velocity remains constant along the normal, namely $(\theta \cdot n)(x) = (\theta \cdot n)(p_\Gamma(x))$.

A difficulty with (6.28) is that it does not satisfy the Hadamard structure theorem (see e.g. [4], [49], [71], [130] and references therein) since it does not depend solely on the normal trace $\theta \cdot n$ on the interface $\Gamma = \partial\Omega$. In fact, assuming that the support of $\frac{\partial m}{\partial \psi}$ is concentrated around Γ , formula (6.28) would be similar to what we called earlier approximate shape derivative, obtained in Proposition 6.2.4 for a discretization of the sharp-interface case and in (6.22) for the smoothed-interface case when the regularization parameter ε is small. In any case, (6.28) does not guarantee a descent direction in general, unless $\frac{\partial m}{\partial \psi}$ keeps a constant sign along the normal, at least for the width of the intermediate zone.

6.5 Extension to more than 2 materials

The methods presented in sections 6.2 and 6.3 for two phases can be extended to the case of several materials to be optimally placed in the domain D , following a classical idea in the level-set framework [151], [153].

Hitherto, we considered a single subdomain $\Omega^0 \subset D$, which allows to account for two separate phases within D , occupying respectively the domains Ω^0 and $\Omega^1 := {}^c\Omega^0$ (where c denotes the complementary part in D). To consider more phases, we introduce m subdomains $\mathcal{O}^0, \dots, \mathcal{O}^{m-1} \subset D$ which are not subject to any geometrical constraints (they can intersect, or not, and they don't need to cover D). These m subdomains allows us to treat up to 2^m distinct phases, filling respectively the phase domains $\Omega^0, \dots, \Omega^{2^m-1} \subset D$, defined as (see Figure 6.5)

$$\begin{cases} \Omega^0 &= \mathcal{O}^0 \cap \mathcal{O}^1 \cap \dots \cap \mathcal{O}^{m-1}, \\ \Omega^1 &= {}^c\mathcal{O}^0 \cap \mathcal{O}^1 \cap \dots \cap \mathcal{O}^{m-1}, \\ &\vdots \\ \Omega^{2^m-1} &= {}^c\mathcal{O}^0 \cap {}^c\mathcal{O}^1 \cap \dots \cap {}^c\mathcal{O}^{m-1}. \end{cases} \quad (6.29)$$

Note that $\Omega^0, \dots, \Omega^{2^m-1}$ is a partition of D . To simplify the exposition, from now on we take $m = 2$, meaning that we consider four different materials, with respective Hooke's law A_0, A_1, A_2, A_3 . Two subdomains $\mathcal{O}^0, \mathcal{O}^1$ of D are then introduced, and each material A_i fills an area $\Omega^i \subset D$, defined through formula (6.29).

For the sharp-interface problem, the definition of the mixture Hooke's tensor A_χ is standard. Introducing χ_0 and χ_1 the characteristic functions of \mathcal{O}^0 and \mathcal{O}^1 , respectively, we define

$$A_\chi(x) := \chi_0(x)\chi_1(x)A_0 + (1 - \chi_0(x))\chi_1(x)A_1 + \chi_0(x)(1 - \chi_1(x))A_2 + (1 - \chi_0(x))(1 - \chi_1(x))A_3. \quad (6.30)$$

For the smoothed-interface problem, we propose a formula inspired from (6.30)

$$\begin{aligned} A_{\mathcal{O}^0, \mathcal{O}^1, \varepsilon}(x) &= (1 - h_\varepsilon(d_{\mathcal{O}^0}(x)))(1 - h_\varepsilon(d_{\mathcal{O}^1}(x)))A_0 + h_\varepsilon(d_{\mathcal{O}^0}(x))(1 - h_\varepsilon(d_{\mathcal{O}^1}(x)))A_1 \\ &+ (1 - h_\varepsilon(d_{\mathcal{O}^0}(x)))h_\varepsilon(d_{\mathcal{O}^1}(x))A_2 + h_\varepsilon(d_{\mathcal{O}^0}(x))h_\varepsilon(d_{\mathcal{O}^1}(x))A_3, \end{aligned} \quad (6.31)$$

where h_ε is the smooth approximation (6.15) of the Heaviside function and $d_{\mathcal{O}^0}, d_{\mathcal{O}^1}$ are the signed distance functions to \mathcal{O}^0 and \mathcal{O}^1 respectively. Of course, there are other interpolation formulas and any alternative choice which, as (6.31), satisfies the following consistency

$$A_{\mathcal{O}^0, \mathcal{O}^1, \varepsilon}(x) = \begin{cases} A_0 & \text{if } d_{\mathcal{O}^0}(x) < -\varepsilon \text{ and } d_{\mathcal{O}^1}(x) < -\varepsilon, \\ A_1 & \text{if } d_{\mathcal{O}^0}(x) > +\varepsilon \text{ and } d_{\mathcal{O}^1}(x) < -\varepsilon, \\ A_2 & \text{if } d_{\mathcal{O}^0}(x) < -\varepsilon \text{ and } d_{\mathcal{O}^1}(x) > +\varepsilon, \\ A_3 & \text{if } d_{\mathcal{O}^0}(x) > +\varepsilon \text{ and } d_{\mathcal{O}^1}(x) > +\varepsilon, \\ \text{a smooth interpolation between } A_0, A_1, A_2, A_3 & \text{otherwise,} \end{cases} \quad (6.32)$$

will do. In particular, for applications in material science where the thick interface has a clear physical interpretation, one could choose a physically relevant choice of the interpolant Hooke's law for the mixture of A_0, A_1, A_2, A_3 in the intermediate areas, like a sequential laminate or another microstructure achieving Hashin and Shtrikman bounds [95]. On the other hand, if the smoothed-interface problem is merely a mathematical approximation of the sharp-interface case, then it is a consistent approximation since, as the regularizing parameter ε goes to 0, the smooth tensor $A_{\mathcal{O}^0, \mathcal{O}^1, \varepsilon}$ converges to the discontinuous one A_χ .

In the multiphase case, the definition of the objective function (6.2) does not change

$$J(\mathcal{O}^0, \mathcal{O}^1) = \int_D j(x, u) dx + \int_{\Gamma_N} k(x, u) ds, \quad (6.33)$$

and the state or adjoint equations are the same, up to changing the previous Hooke's tensor by $A_{\mathcal{O}^0, \mathcal{O}^1, \varepsilon}$. There are now two variable subdomains, $\mathcal{O}^0, \mathcal{O}^1$, as design variables for the optimization problem. Accordingly, we introduce two separate vector fields $\theta_0, \theta_1 \in W^{1, \infty}(D, \mathbb{R}^N)$ in order to vary the subdomains $\mathcal{O}^0, \mathcal{O}^1$.

According to Corollary 3.3.6, the partial shape derivative of the objective function (6.33) with respect to \mathcal{O}^0 and \mathcal{O}^1 , which we shall denote as $\frac{\partial J}{\partial \mathcal{O}^0}$ and $\frac{\partial J}{\partial \mathcal{O}^1}$ respectively, in the direction of θ^0 and θ^1 , respectively, are

$$\frac{\partial J}{\partial \mathcal{O}^0}(\mathcal{O}^0, \mathcal{O}^1)(\theta_0) = \int_D \theta_0(p_{\partial \mathcal{O}^0}(x)) \cdot n_0(p_{\partial \mathcal{O}^0}(x)) \frac{\partial A}{\partial d_{\mathcal{O}^0}}(d_{\mathcal{O}^0}, d_{\mathcal{O}^1})e(u) : e(p) dx, \quad (6.34)$$

$$\frac{\partial J}{\partial \mathcal{O}^1}(\mathcal{O}^0, \mathcal{O}^1)(\theta_1) = \int_D \theta_1(p_{\partial \mathcal{O}^1}(x)) \cdot n_1(p_{\partial \mathcal{O}^1}(x)) \frac{\partial A}{\partial d_{\mathcal{O}^1}}(d_{\mathcal{O}^0}, d_{\mathcal{O}^1})e(u) : e(p) dx, \quad (6.35)$$

where $A(d_{\mathcal{O}^0}, d_{\mathcal{O}^1}) = A_{\mathcal{O}^0, \mathcal{O}^1, \varepsilon}$, defined in (6.32). Of course, one can apply Theorem 6.3.2 to simplify (6.34) and (6.35) and transform them in surface integrals on $\partial \mathcal{O}^0$ and $\partial \mathcal{O}^1$.

Remark 6.5.1. In the sharp interface context one could compute shape derivatives of the objective function J with respect to \mathcal{O}^0 and \mathcal{O}^1 too, thus recovering formulas similar to (6.34) and (6.35). However, it is possible only if we assume that the boundary of \mathcal{O}^0 and \mathcal{O}^1 do not superpose. Indeed if, for example, $\partial\mathcal{O}^0 = \partial\mathcal{O}^1$, then moving \mathcal{O}^0 inside \mathcal{O}^1 , or vice versa, implies that one phase or another one appears. This means that a topology change is occurring which cannot be handled by Hadamard's method. At most, one can expect to compute two different directional derivatives (inward and outward) which clearly shows that there is no differentiability in this case. Note that there is no such difficulty in the smoothed interface setting: formulas (6.34) and (6.35) hold true for any geometrical situation of \mathcal{O}^0 and \mathcal{O}^1 since $A_{\mathcal{O}^0, \mathcal{O}^1, \varepsilon}$ is a smooth function of x in D .

6.6 Numerical results

6.6.1 Level-set representation

Following the lead of [14], [16], we represent the moving and optimizable interfaces by level set functions [106] defined on a fixed mesh in an Eulerian framework. According to Section 6.5, using m level-set functions we can represent up to 2^m separate phases.

When there are only two phases to optimize, it suffices to use one level-set function to represent the interface Γ between two complementary sub-domains Ω^0 and Ω^1 of the working domain D . The level set function ψ (see Figure 6.5) is defined by

$$\begin{cases} \psi(x) = 0 & \text{for } x \in \Gamma = \partial\Omega_0, \\ \psi(x) < 0 & \text{for } x \in \Omega^0, \\ \psi(x) > 0 & \text{for } x \in \Omega^1. \end{cases}$$

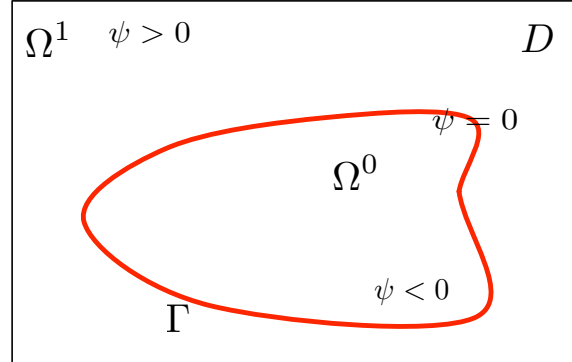


Figure 6.5: Level-set representation of the domains Ω^0 and Ω^1 .

In order to describe up to four distinct phases, two level-set functions ψ_0 and ψ_1 are defined such that

$$\begin{cases} \psi_0(x) = 0 & \text{for } x \in \partial\mathcal{O}^0, \\ \psi_0(x) < 0 & \text{for } x \in \mathcal{O}^0, \\ \psi_0(x) > 0 & \text{for } x \in \overline{\mathcal{O}^0}, \end{cases} \quad \text{and} \quad \begin{cases} \psi_1(x) = 0 & \text{for } x \in \partial\mathcal{O}^1, \\ \psi_1(x) < 0 & \text{for } x \in \mathcal{O}^1, \\ \psi_1(x) > 0 & \text{for } x \in \overline{\mathcal{O}^1}, \end{cases}$$

following the notations of Figure 6.5. Then, each level-set function ψ_i , $i = 0, 1$, is transported independently solving (1.29), where V_i , $i = 0, 1$ results from the formulas (6.34) and (6.35).

6.6.2 Two materials in the sharp interface context

We work in the context of Section 6.2, namely in a sharp interface framework. We compare the two shape derivatives: the continuous formula furnished by Proposition 6.2.1 and the discrete formula given in Proposition 6.2.4. The numerical implementation of the continuous formula of the shape derivative in Proposition 6.2.1 is achieved according to the scheme proposed in [16] for computing the jump approximation (6.12). We consider a long cantilever of dimensions 2×1 , discretized by 100×50 $P1$ elements, clamped at its left side and submitted to a unit vertical load at the middle of its right side (see Figure

6.8). The domain is filled by two isotropic materials 0 and 1, with different Young's moduli, respectively $E^0 = 0.5$ and $E^1 = 1$ (material 1 is stiffer than material 0) but with the same Poisson ratio $\nu = 0.3$. We minimize the compliance (6.3) with a constraint of fixed volume for the two phases. The computations are done with the FreeFem++ package [114].

For all the numerical examples in this paper, an augmented Lagrangian method is applied to handle the constraints. Following the approach in [101], supposing that our problem contains m equality constraints of the type $c_i(\Omega^0) = 0$ ($i = 1, \dots, m$), an augmented Lagrangian function is constructed as

$$L(\Omega^0, \ell, \mu) = J(\Omega^0) - \sum_{i=1}^m \ell_i c_i(\Omega^0) + \sum_{i=1}^m \frac{\mu_i}{2} c_i^2(\Omega^0),$$

where $\ell = (\ell_i)_{i=1, \dots, m}$ and $\mu = (\mu_i)_{i=1, \dots, m}$ are Lagrange multipliers and penalty parameters for the constraints. The Lagrange multipliers are updated at each iteration n according to the optimality condition $\ell_i^{n+1} = \ell_i^n - \mu_i c_i(\Omega_n^0)$. The penalty parameters are augmented every 5 iterations. With such an algorithm the constraints are enforced only at convergence (see for example Figure 6.7). Of course, other (and possibly more efficient) optimization algorithms could be used instead.

The results are displayed on Figure 6.6. As usual the strong phase 1 is black and the weak phase 0 is white. The design obtained with the discrete formula is quite similar to the one exposed in Figure 6.9 (c). However the continuous formula gives a different optimal shape which is worse in terms of the objective function than the one obtained with the discrete formula (see Figure 6.7). This is completely natural, since the discrete shape gradient is exactly the gradient of the (discrete) indeed computed objective function.

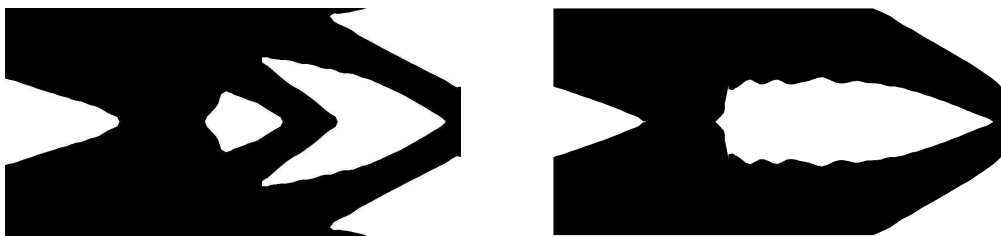


Figure 6.6: Optimal shapes for the long cantilever using the discrete shape gradient (left) and the continuous formula (right).

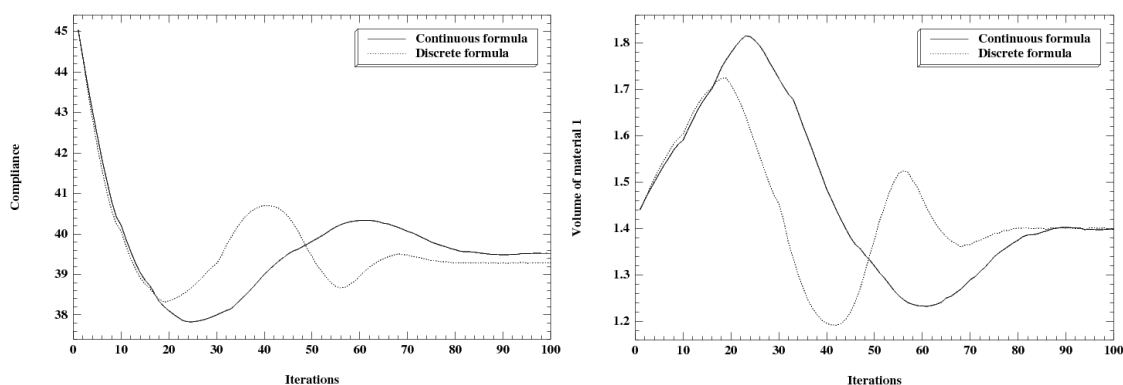


Figure 6.7: Convergence history of the compliance (left) and the volume (right) for the sharp interface results displayed on Figure 6.6.

6.6.3 Two materials in the smoothed-interface context

We now switch to the smoothed-interface setting as described in Section 6.3. All examples using a smoothed-interface are coded in Scilab [119]. We perform the same test case, with the same parameter values, as in Section 6.6.2. A mesh composed of 160×80 elements is used. A first goal is to compare

the smoothed-interface approach to the sharp-interface one. A second goal is to compare the various formulas for the shape derivative obtained in Section 6.3.

We minimize again the compliance (6.3) with a constraint of fixed volume for the two phases which is written

$$\int_D h_\varepsilon(d_{\Omega^0}(x))dx = V_T,$$

where V_T is the target volume of the strong phase occupying Ω^1 .

We test three different formulas for the shape gradient. The first one is the "true" formula given by (6.18) (see also (6.34) and (6.35) in the case of more than two phases). The second one, called "Jacobian-free", is (6.21) which is obtained from (6.18) by neglecting the part of the integrand corresponding to the Jacobian of the projection application $p_{\partial\Omega}$ (see Remark 3.3.8). The reason for this choice is that the curvature is not precisely calculated using a fixed mesh and therefore we may introduce a significant approximation error. In any case, it amounts to neglecting a positive factor (because of Lemma 3.3.9). The third one is the "approximate" formula (6.22) obtained for a very thin smoothing zone around the interface.

First, we consider the case of a "thin" interface. The interpolation width is chosen as $\varepsilon = 2\Delta x$, where Δx is the uniform mesh size. The results for $V_T = 0.7|D|$ and $V_T = 0.2|D|$ are shown in Figure 6.9 and 6.10. We plot the Young modulus distribution (black being the strong material A_1 and white the weak material A_0). The convergence histories are almost identical for the "true" and "Jacobian-free" formulas of the shape derivative. It is slightly more oscillating for the "approximate" formula although it converges to almost the same value of the objective function. The resulting optimal designs are very similar.

For a larger interpolation width $\varepsilon = 8\Delta x$ ("thick" interface), the results are shown in Figure 6.11. We clearly see a difference for the optimal shape obtained using the "true" formula of the shape derivative: in this case, the algorithm produces a very long and oscillating interface in such a way that the overall structure is almost like a composite structure. This is due to the fact that the intermediate zone inside the interface is very favorable compared to the pure phases. Nevertheless, despite the differences in the final shapes, the values of the compliance are almost the same for the "true" and "Jacobian-free" formulas, slightly worse for the "approximate" formula of the shape gradient.

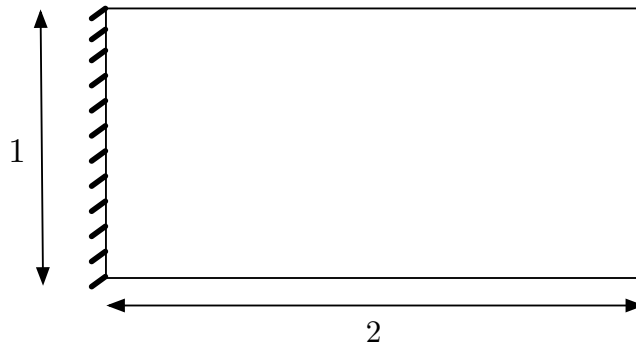


Figure 6.8: Boundary conditions for the 2×1 cantilever.

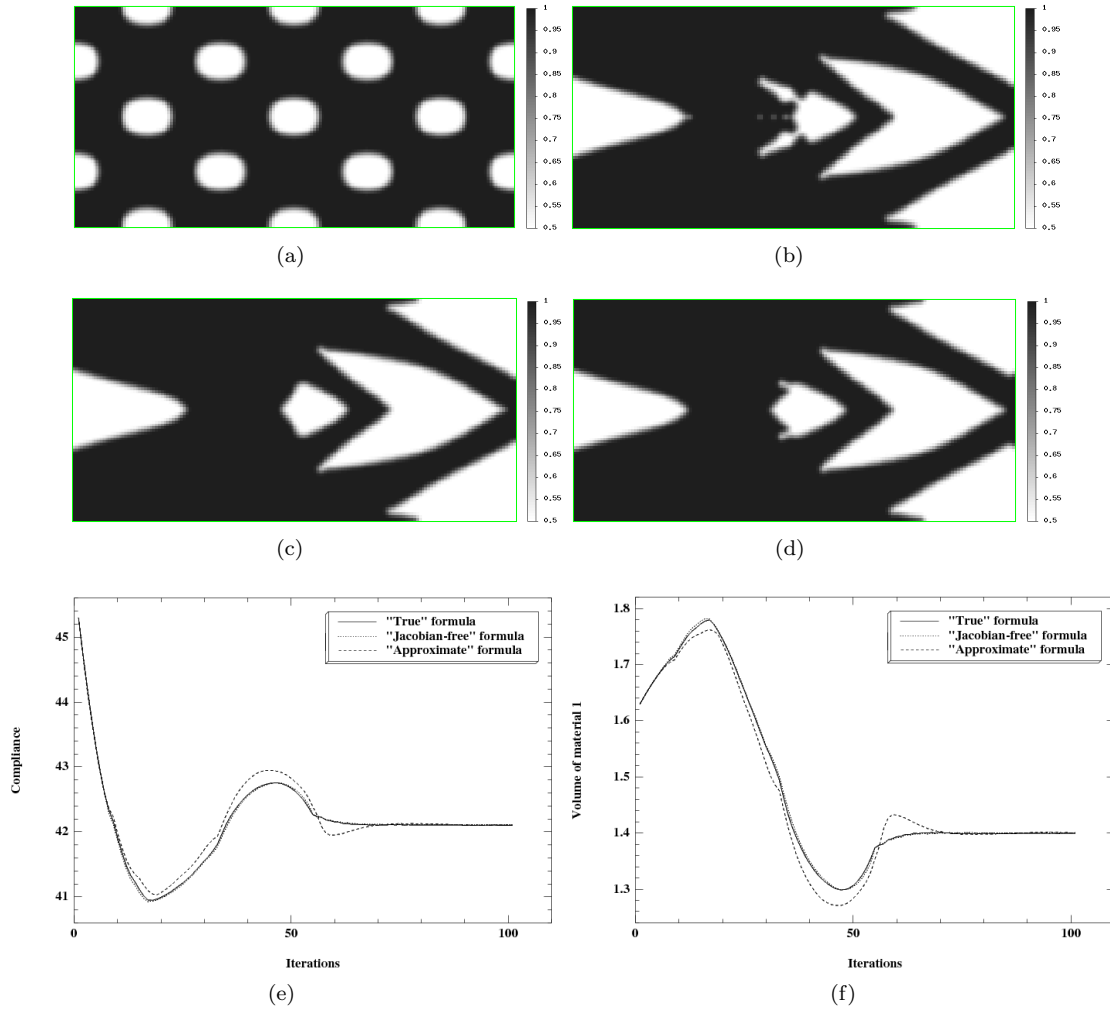


Figure 6.9: "Long cantilever" using two phases with $V_T = 0.7|D|$ and a small smoothing parameter $\varepsilon = 2\Delta x$; (a): initialization; (b): optimized shape using the "true" formula; (c): optimized shape using the "Jacobian-free" formula; (d): optimized shape using the "approximate" formula; (e): convergence of the compliance; (f): convergence of the volume.

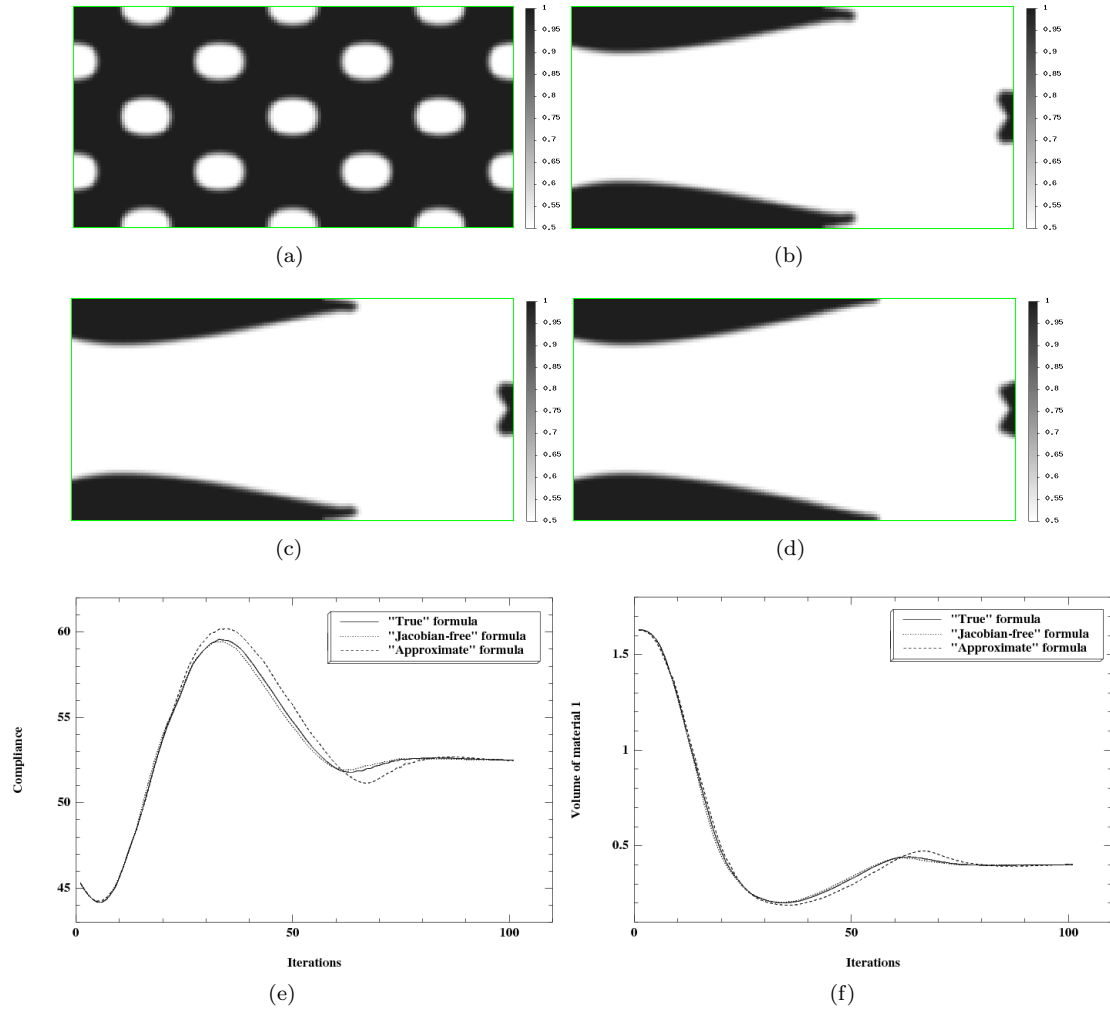


Figure 6.10: "Long cantilever" using two phases with $V_T = 0.2|D|$ and a small smoothing parameter $\varepsilon = 2\Delta x$; (a): initialization; (b): optimized shape using the "true" formula; (c): optimized shape using the "Jacobian-free" formula; (d): optimized shape using the "approximate" formula; (e): convergence of the compliance; (f): convergence of the volume.

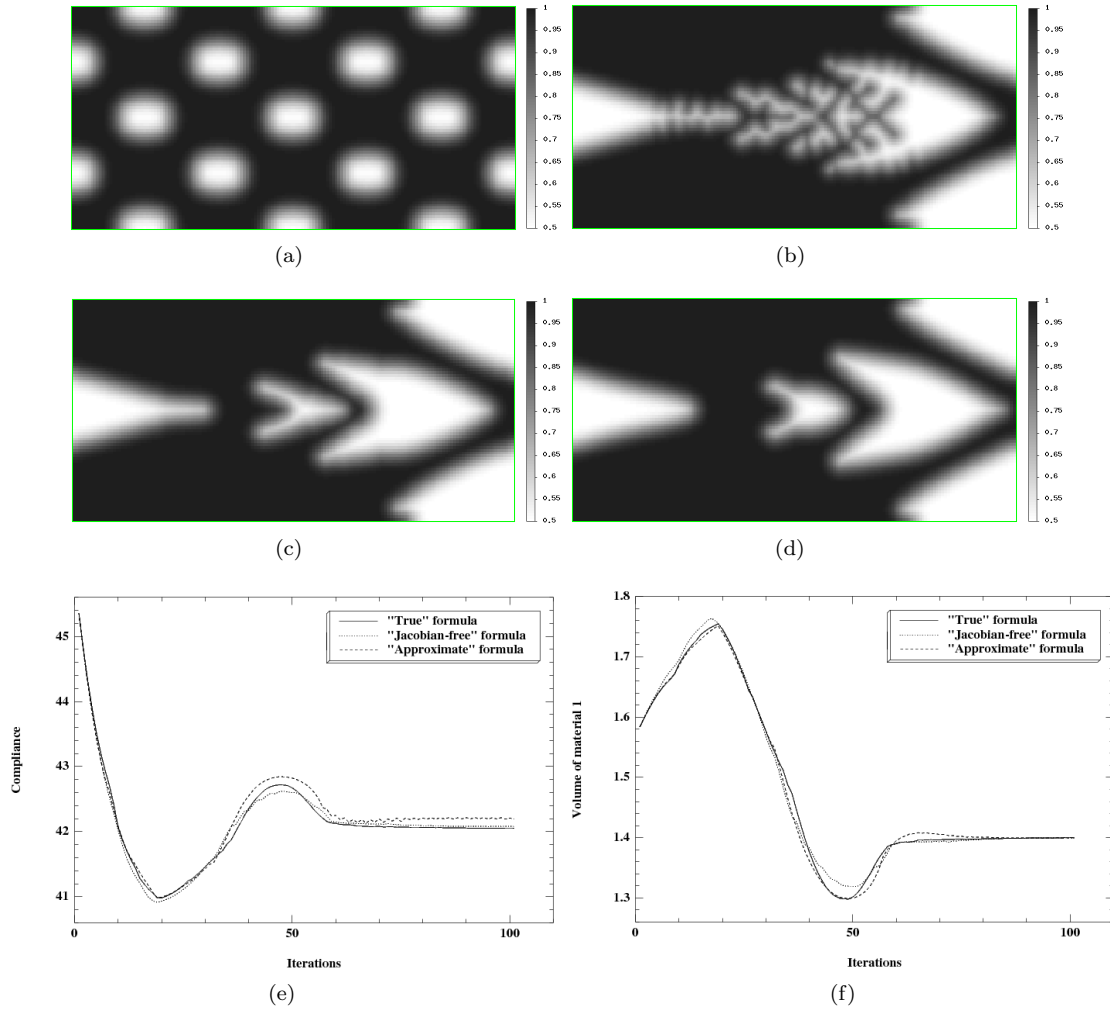


Figure 6.11: "Long cantilever" using two phases with $V_T = 0.7|D|$ and a large smoothing parameter $\varepsilon = 8\Delta x$; (a): initialization; (b): optimized shape using the "true" formula; (c): optimized shape using the "Jacobian-free" formula; (d): optimized shape using the "approximate" formula; (e): convergence of the compliance; (f): convergence of the volume.

Mesh-dependency study

In order to examine the mesh-dependency of the smoothed-interface method, the same example as in Section 6.6.3 is considered and two different tests are performed. First, the grid size " Δx " varies and the interface half-width " ε " is chosen as $\varepsilon = 2\Delta x$. In the second case, ε has the constant value 0.025 (the same as in Figure 6.9) independently of the grid size variation. For all tests, the "Jacobian-free" formula and the initialization of Figure 6.9 (a) has been used. The results are shown in Figure 6.12 and 6.13. Comparing qualitatively the results, we can say that they look quite similar, as soon as the grid resolution allows for a satisfying enough description of the geometry and an accurate enough approximation of the geometric quantities in play.

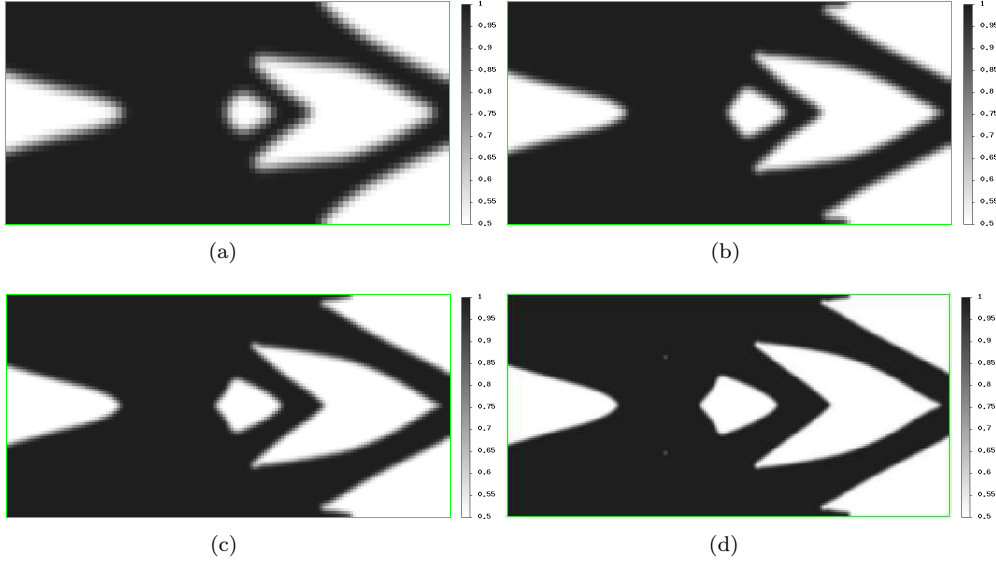


Figure 6.12: *Long cantilever using two phases with $V_T = 0.7|D|$, $\varepsilon = 2\Delta x$ and a grid of; (a): 80×40 ; (b): 120×60 ; (c): 160×80 ; (d): 240×120 elements.*

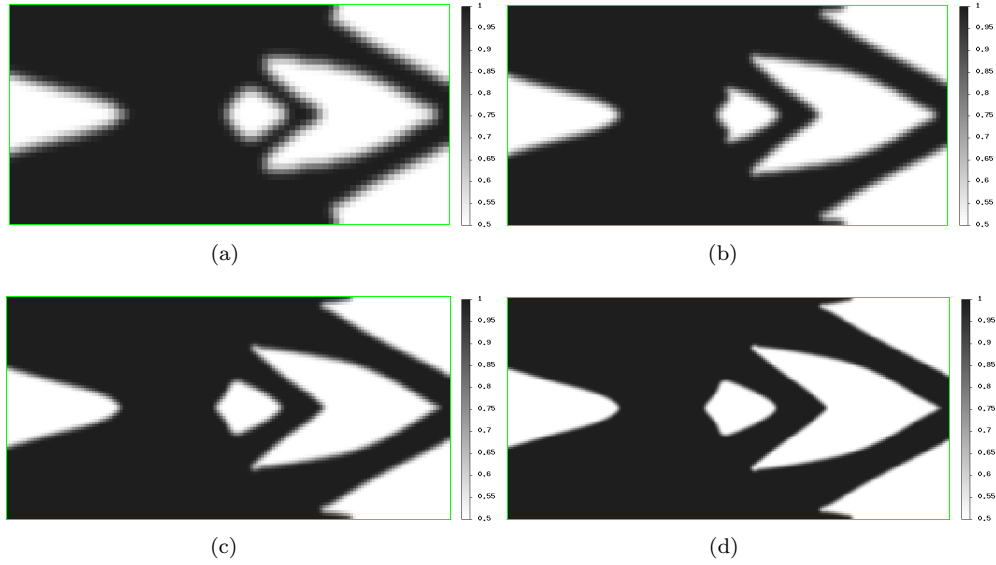


Figure 6.13: *Long cantilever using two phases with $V_T = 0.7|D|$, $\varepsilon = 0.025$ and a grid of; (a): 80×40 ; (b): 120×60 ; (c): 160×80 ; (d): 240×120 elements.*

6.6.4 Four materials in the smoothed interface context

We consider now the case of using up to four phases and consequently two level-set functions. A smoothed approximation of the characteristic function of each phase can be constructed using combinations of the functions h_ε , defined in equation (6.15), as follows

$$\begin{cases} \chi_0 = (1 - h_\varepsilon(d_{\mathcal{O}^0}))(1 - h_\varepsilon(d_{\mathcal{O}^1})), \\ \chi_1 = h_\varepsilon(d_{\mathcal{O}^0})(1 - h_\varepsilon(d_{\mathcal{O}^1})), \\ \chi_2 = (1 - h_\varepsilon(d_{\mathcal{O}^0}))h_\varepsilon(d_{\mathcal{O}^1}), \\ \chi_3 = h_\varepsilon(d_{\mathcal{O}^0})h_\varepsilon(d_{\mathcal{O}^1}), \end{cases} \quad (6.36)$$

and the global Hooke's tensor is given by (6.31). The optimization problem now reads

$$\begin{aligned} \min_{\mathcal{O}^0, \mathcal{O}^1 \in \mathcal{U}_{ad}} J(\mathcal{O}^0, \mathcal{O}^1) &= \int_D A_{\mathcal{O}^0, \mathcal{O}^1, \varepsilon}(x) e(u) : e(u) \, dx \\ \text{s.t.} \quad \int_D \chi_i \, dx &= V_T^i, \, i = 0, \dots, 3, \end{aligned} \quad (6.37)$$

where V_T^i is the target volume for the phase i (they sum up to the volume of D). As previously, an augmented Lagrangian algorithm is applied to enforce the constraints. In this section we work with a "thin" interface, namely $\varepsilon = 2\Delta x$.

We test our method with several benchmark examples presented in [153] and [154]. Since the initial designs are different, as well as the numerical methods, it is hard to make a quantitative comparison and we satisfy ourselves with a qualitative comparison.

Short-cantilever using two materials and void

In this paragraph we consider only three phases, made of two materials and void. The first structure to be optimized is a two-dimensional short cantilever, of dimensions 1×2 , discretized using 80×160 $Q1$ elements. The left part of the structure is clamped and a unitary vertical force is applied at the mid point of its right part (see Figure 6.14). The Young moduli of the four phases are defined as $E^0 = 0.5, E^1 = 10^{-3}, E^2 = 1$ and $E^3 = 10^{-3}$, where both phases 1 and 3 represent void. The target volumes for phases 0 and 2 are set to $V_T^0 = 0.2|D|$ and $V_T^2 = 0.1|D|$. The results are shown in Figure 6.15. We plot the Young modulus with a grey scale: dark stands for the stronger phase, white for void and grey for the intermediate phase.

This test case was previously studied in [153] (see figures 7 and 8 therein for two different initializations). Our results are roughly similar to those in [153] and even slightly better since the designs of Figure 6.15 are symmetric (as expected), contrary to the results in [153].

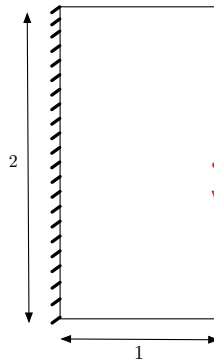


Figure 6.14: Boundary conditions and initialization for the 2d short-cantilever.

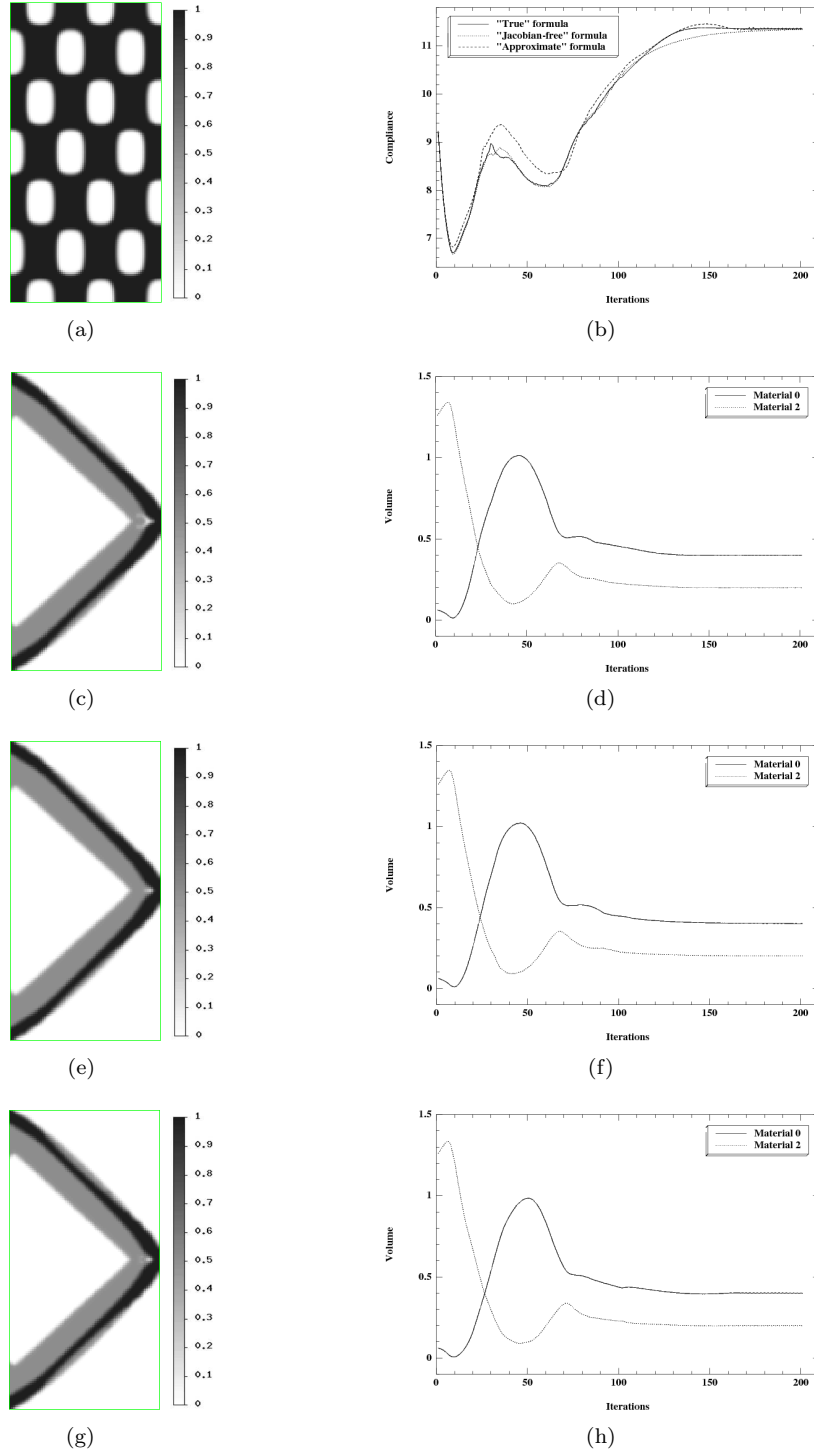


Figure 6.15: "Short cantilever" using two phases and void; (a): initialization; (b): convergence diagram for the compliance; (c): optimized shape using the "true" formula; (d): convergence of the volume for the "true" formula; (e): optimized shape using the "Jacobian-free" formula; (f): convergence of the volume for the "Jacobian-free" formula; (g): optimized shape using the "approximate" formula; (h): convergence of the volume for the "approximate" formula.

Short-cantilever using three materials and void

The same example as previously is considered here, but half of the volume of phase 0 is replaced by a weaker phase. The Young moduli of the four phases are defined as $E^0 = 0.5$, $E^1 = 0.25$, $E^2 = 1$ and $E^3 = 10^{-3}$ and the target volumes for phases 0, 1 and 2 are set to $V_T^0 = V_T^1 = V_T^2 = 0.1|D|$. The results are shown in Figure 6.16.

This test case was also studied in [153] (see figures 11 and 12 therein for two different initializations). Our result differs notably from these previous ones. Indeed, in [153] the strong material 2 always forms a two-bar truss which is further reinforced by the other materials. On the contrary, in Figure 6.16 the strong phase is disconnected and the intermediate material 0 plays a more active role in the transfer of the load to the fixed wall.

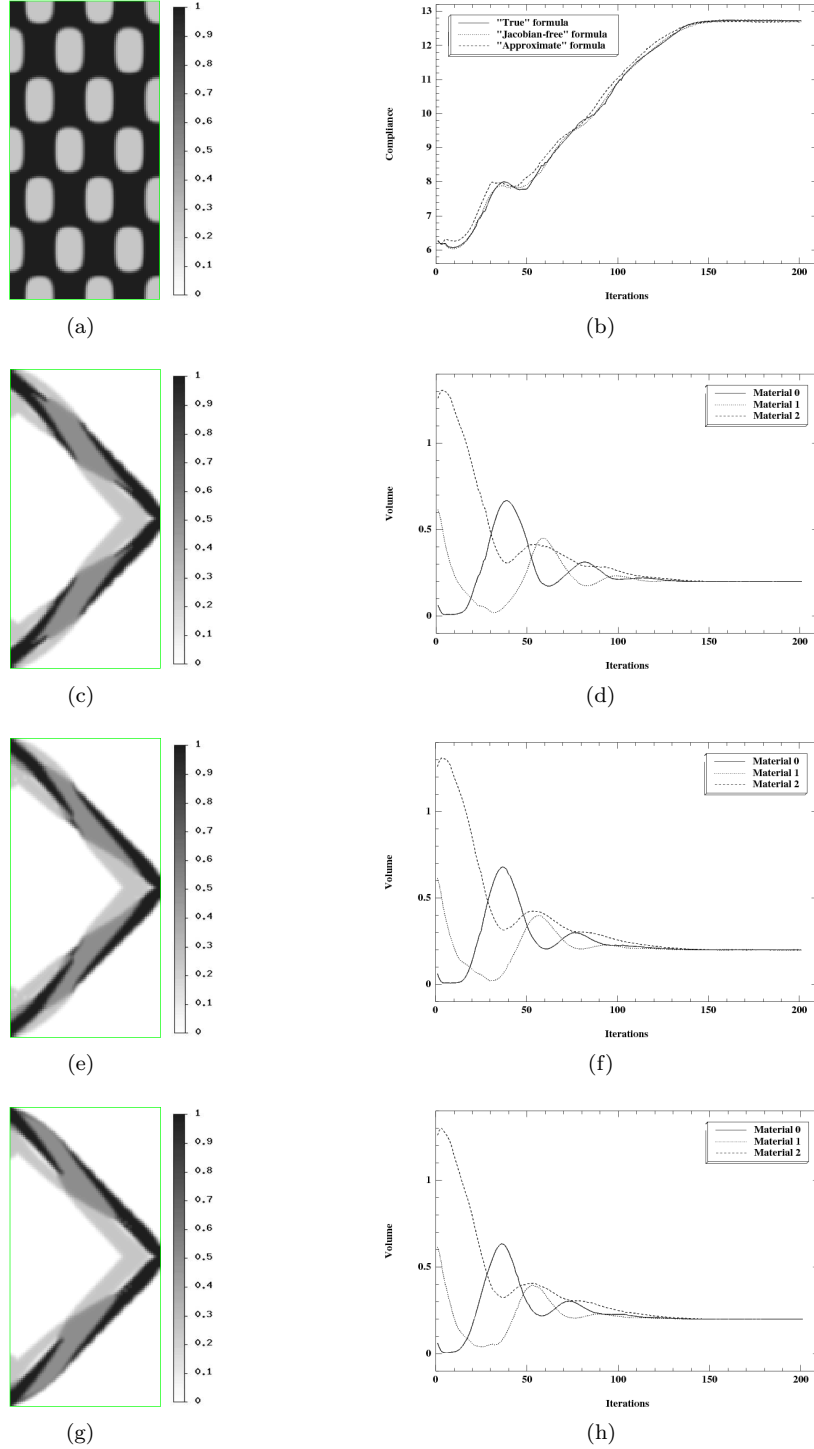


Figure 6.16: "Short cantilever" using three phases and void; (a): initialization; (b): convergence diagram for the compliance; (c): optimized shape using the "true" formula; (d): convergence of the volume for the shape gradient formula; (e): optimized shape using the "Jacobian-free" formula; (f): convergence of the volume for the "Jacobian-free" formula; (g): optimized shape using the "approximate" formula; (h): convergence of the volume for the "approximate" formula.

3-force bridge using two materials and void

A bridge-type structure of dimensions 2×1 is studied, discretized by 160×80 $Q1$ elements. Both the horizontal and vertical displacement are fixed at the lower left part as well as the vertical displacement of the lower right part. Three equally distributed forces are applied at the lower part (see Figure 6.17). The value of F is set to 1. The Young moduli of the four phases are set to $E^0 = 0.5$, $E^1 = 10^{-3}$, $E^2 = 1$ and $E^3 = 10^{-3}$ and the target volumes for phases 0 and 2 are set to $V_T^0 = 0.2|D|$ and $V_T^2 = 0.1|D|$. The results are shown in Figure 6.18.

Once again this test case was performed in [153] (see Figure 13 therein). Our results are quite different. First, our designs in Figure 6.18 are symmetric, as they should be, except of a slight non-symmetry when the "approximate" formula is used. Second, a major difference occurs in the use of the strong phase. In our design, the strong material is used in the lower part of the "radial" bars whereas it was absent in figure 13 of [153] (and rather used in the upper "arch").

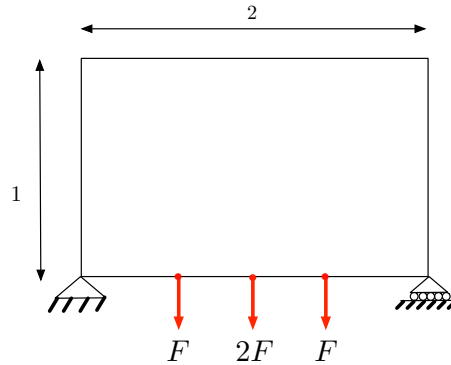


Figure 6.17: Boundary conditions and initialization for the 3-force bridge.

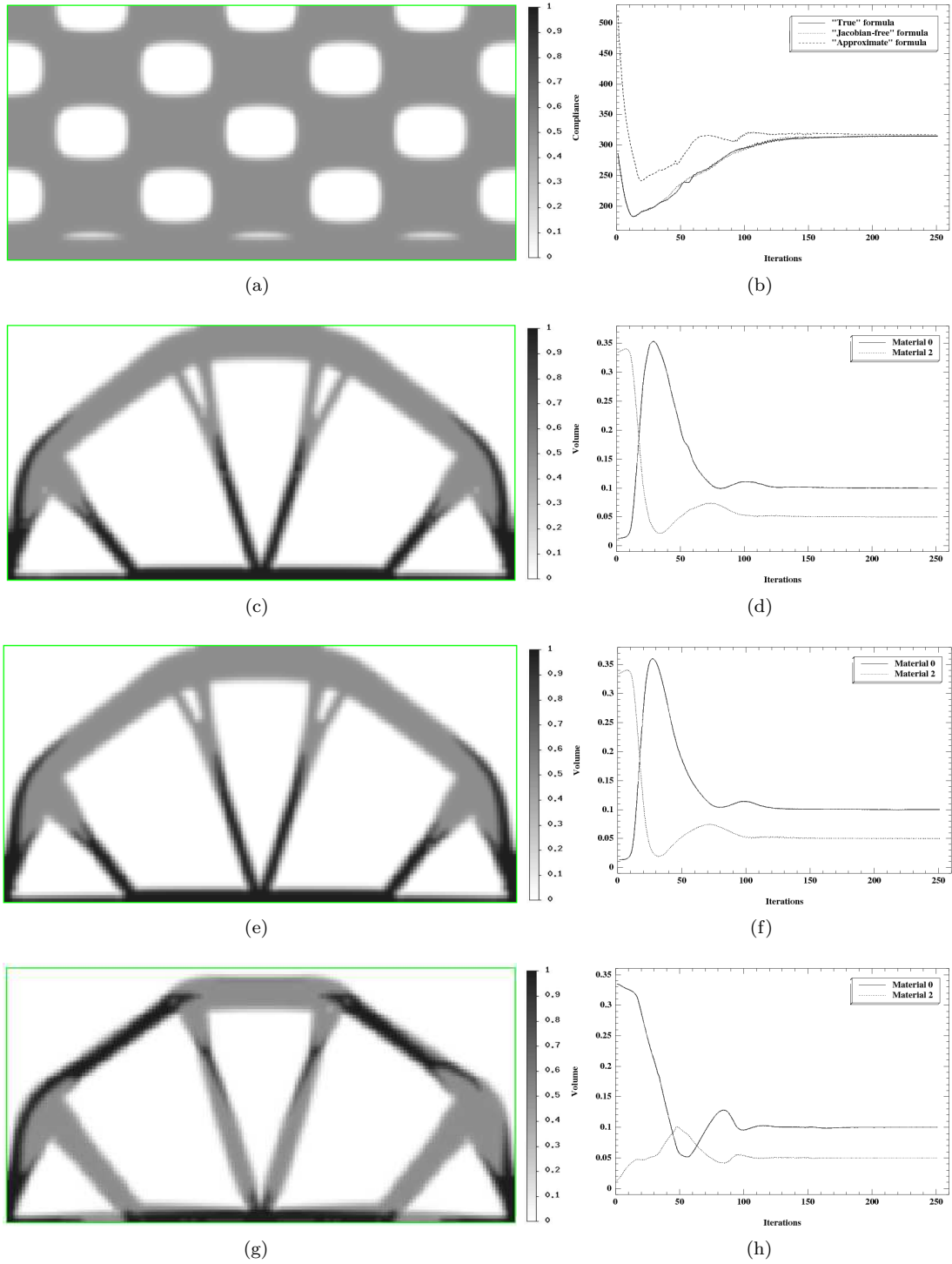


Figure 6.18: "3-force bridge" using two phases and void; (a): initialization; (b): convergence diagram for the compliance; (c): optimized shape using the "true" formula; (d): convergence of the volume for the "true" formula; (e): optimized shape using the "Jacobian-free" formula; (f): convergence of the volume for the "Jacobian-free" formula; (g): optimized shape using the "approximate" formula; (h): convergence of the volume for the "approximate" formula.

3-force bridge using three materials and void

The same example as previously is considered here, but half of the volume of phase 0 is replaced by a weaker phase. The Young moduli of the four phases are defined as $E^0 = 0.5$, $E^1 = 0.25$, $E^2 = 1$ and $E^3 = 10^{-3}$ and the target volumes for phases 0, 1 and 2 are set to $V_T^0 = V_T^1 = V_T^2 = 0.1|D|$. The results are shown in Figure 6.19.

This test case can be found in [153] (Figure 14) too, and again our results are quite different.

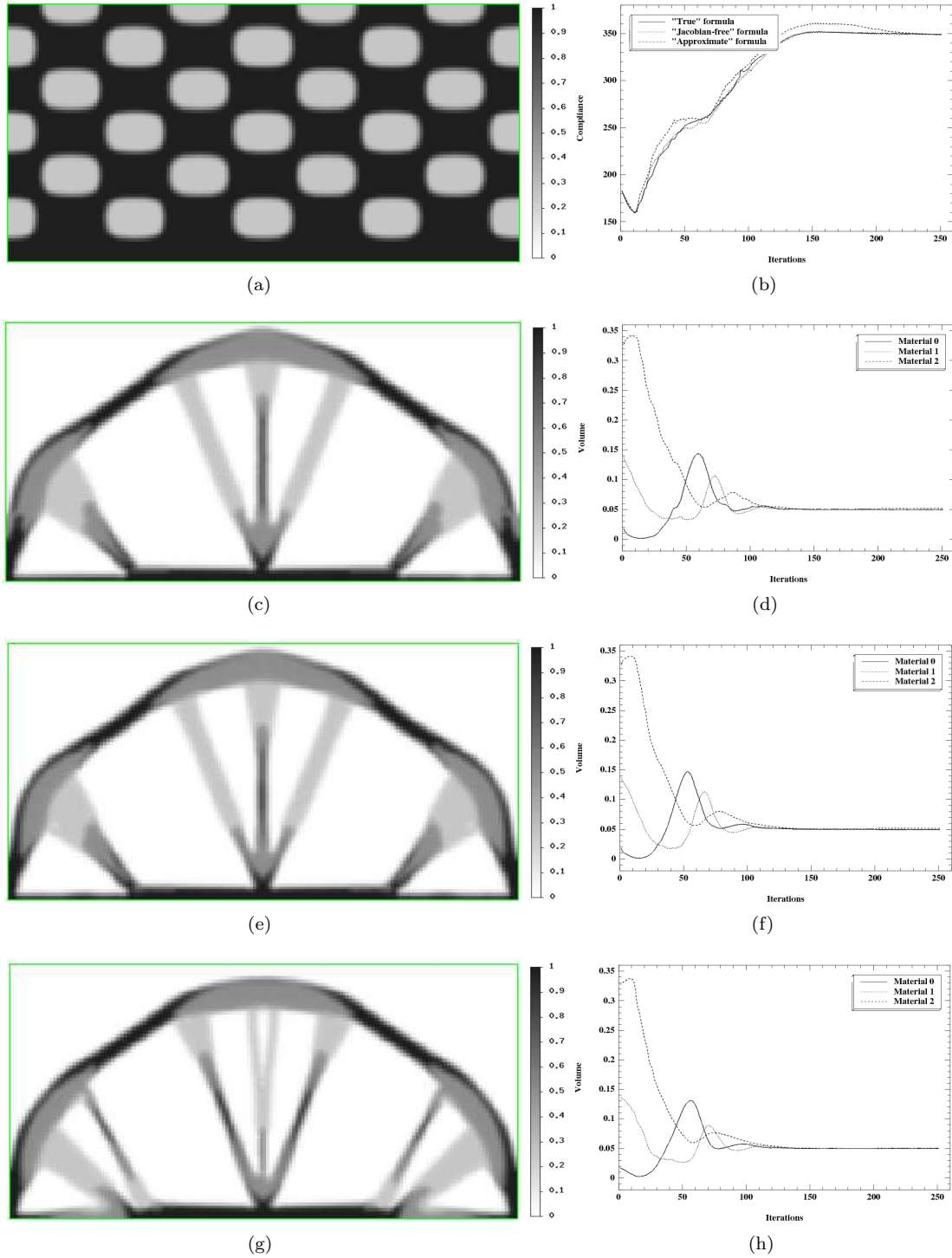


Figure 6.19: "3-force bridge" using three phases and void; (a): initialization; (b): convergence diagram for the compliance; (c): optimized shape using the "true" formula; (d): convergence of the volume for the "true" formula; (e): optimized shape using the "Jacobian-free" formula; (f): convergence of the volume for the "Jacobian-free" formula; (g): optimized shape using the "approximate" formula; (h): convergence of the volume for the "approximate" formula.

Medium cantilever using three materials and void

The next structure is a medium cantilever, of dimensions 3.2×2 , discretized using 120×75 $Q1$ elements. The left part of the structure is clamped and a unitary vertical force is applied at the bottom of its

right part (see Figure 6.20). The Young moduli of the four phases are defined again as $E^0 = 0.5$, $E^1 = 0.25$, $E^2 = 1$ and $E^3 = 10^{-3}$ and the target volumes for phases 0, 1 and 2 are set to $V_T^0 = V_T^1 = V_T^2 = 0.1|D|$. The results are shown in Figure 6.21.

This test case was also performed in [154] (see Figure 7 therein). Our optimal designs have a more complex topology and a different layout of the three materials. However, the final volumes of the three materials in [154] are not the same as ours and thus a comparison is not easy to establish.

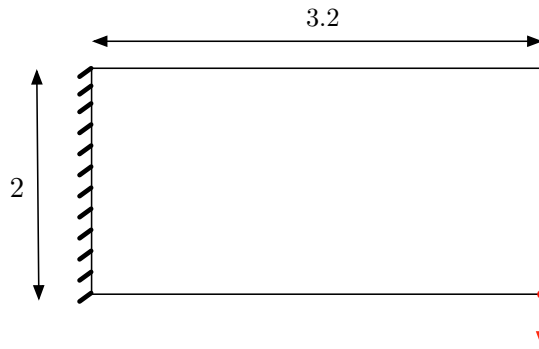


Figure 6.20: Boundary conditions and initialization for the 2D medium-cantilever.

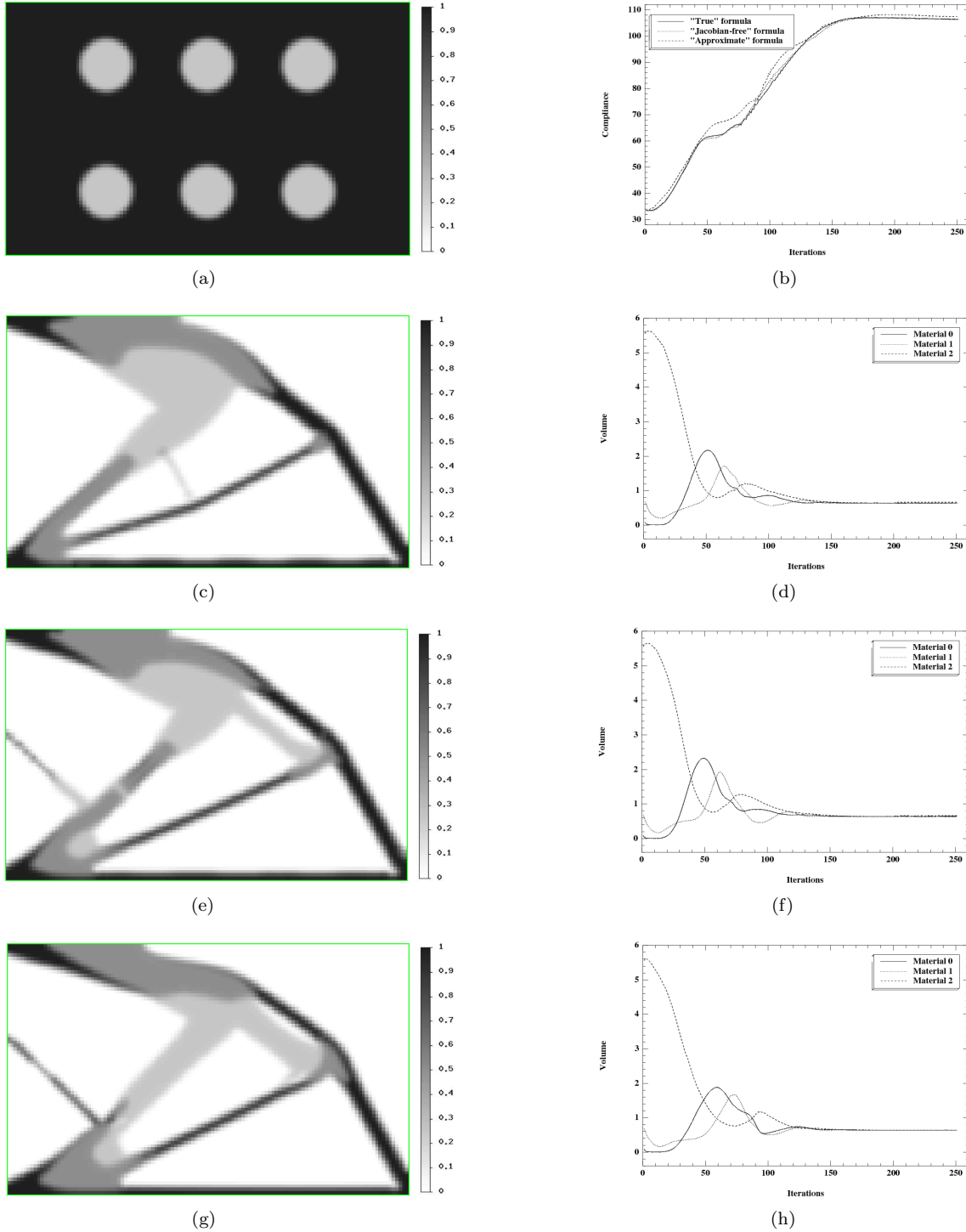


Figure 6.21: "Medium cantilever" using three phases and void; (a): initialization; (b): convergence diagram for the compliance; (c): optimized shape using the "true" formula; (d): convergence of the volume for the "true" formula; (e): optimized shape using the "Jacobian-free" formula; (f): convergence of the volume for the "Jacobian-free" formula; (g): optimized shape using the "approximate" formula; (h): convergence of the volume for the "approximate" formula.

L-shaped structure

The example of an L-shaped structure of dimensions 1×1 is borrowed from Chapter 2.9 in [28]. The domain is discretized using 120×120 $Q1$ elements and a non-optimizable area of dimensions 0.6×0.6 is imposed on its upper-right part. The structure is clamped on its upper side and a unitary vertical force

is applied on the middle of its right side (see Figure 6.22).

Figures 6.23 (a), (b), (c) present the results of using two phases with ratio of Young moduli equal to 0.2, 0.5 and 0.8. The two materials are represented by phases 0 and 2. The Young modulus of phase 0 is set to $E^0 = 1.0$. Phases 1 and 3 represent void and their Young moduli are set to $E^1 = E^3 = 10^{-4}$. The target volumes for phases 0 and 2 are $V_T^0 = V_T^2 = 0.25|D|$. The results are slightly different than those in [28], but they follow the same logic in the placement of materials.

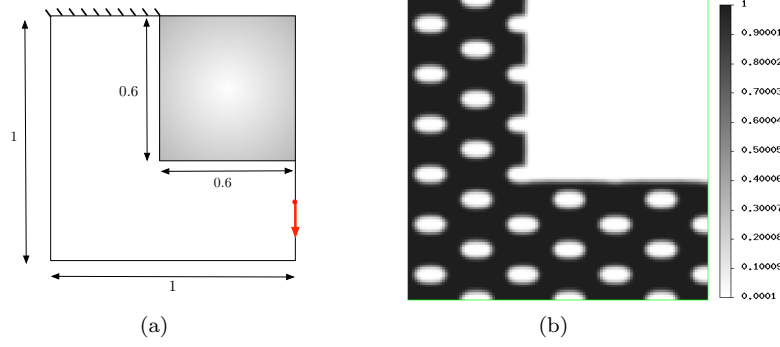


Figure 6.22: (a): Boundary conditions and (b): initialization for the L-shaped structure.

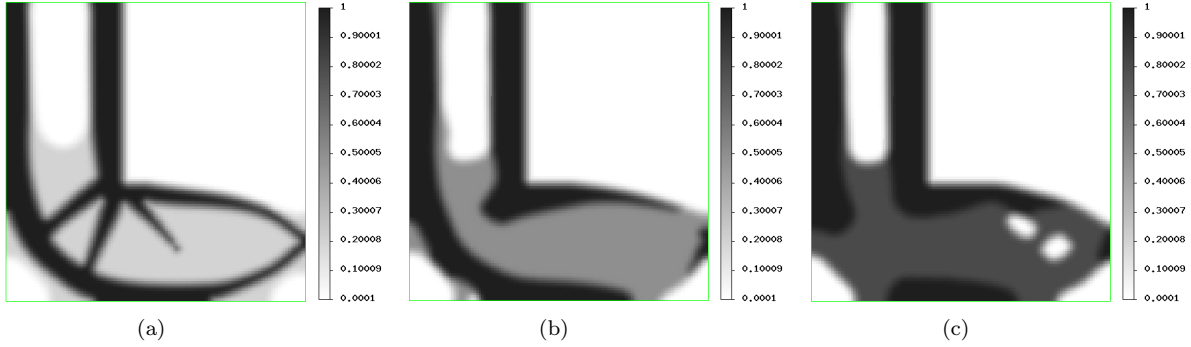


Figure 6.23: Results for the L-shaped structure.

Instead of considering an equality constraint for the volume of each phase, we can adequately constrain it by fixing the Lagrange multipliers. In this case an unconstrained multi-objective optimization problem is built for the minimization of the objective function $J(\mathcal{O}^0, \mathcal{O}^1)$, which reads

$$J(\mathcal{O}^0, \mathcal{O}^1) = \int_D A(d_{\mathcal{O}^0}, d_{\mathcal{O}^1}) e(u) : e(u) dx + \sum_{i=0}^3 \ell^i \int_D \chi_i(x) dx. \quad (6.38)$$

We then carry out a standard constraint-free steepest descent algorithm in order to minimize J . For the rest of the numerical examples we have used only the "Jacobian-free" formula.

In most of the examples below, a small tolerance parameter $tol > 0$ (in our examples, we have used $tol = 0.02$) over acceptance of the produced shapes is introduced so as to ease the occurrence of topological changes and is then turned off after some iterations. More accurately, in the course of the optimization process, a step $\mathcal{O}_n^0 \rightarrow \mathcal{O}_{n+1}^0$ and $\mathcal{O}_n^1 \rightarrow \mathcal{O}_{n+1}^1$ is accepted provided:

$$J(\mathcal{O}_{n+1}^0, \mathcal{O}_{n+1}^1) < (1 + tol)J(\mathcal{O}_n^0, \mathcal{O}_n^1).$$

Long-cantilever

The structure of Figure 6.8 is considered once more here. The Young moduli are set to $E^0 = 0.5$, $E^1 = 10^{-3}$, $E^2 = 1$ and $E^3 = 10^{-3}$. For the results shown in Figure 6.24, we have set the fixed Lagrange multipliers in (6.38) to $\ell^0 = 100$, $\ell^1 = 0$, $\ell^2 = 200$, $\ell^3 = 0$. We see that the strongest material is distributed at the areas of high stress, while the weak material completes the shape of an optimized cantilever. Figure

6.25 shows the final domains \mathcal{O}^0 and \mathcal{O}^1 , whose combinations give the final shape of Figure 6.24.

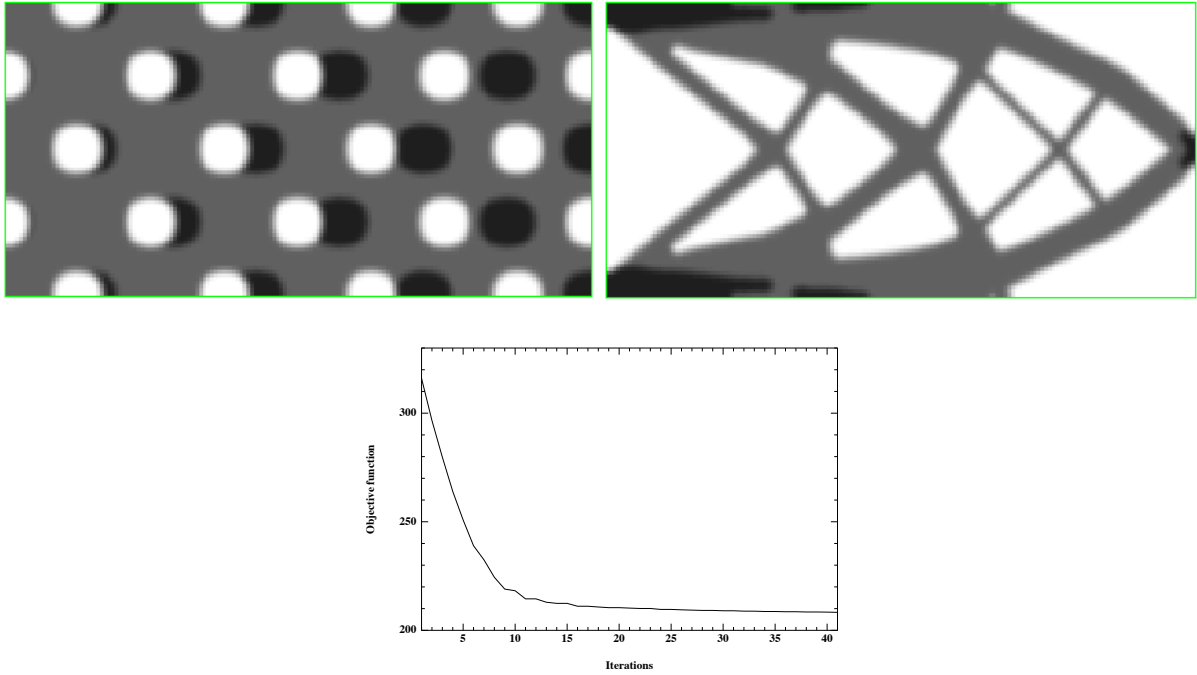


Figure 6.24: Initialization with 4 materials (top), optimized shape and convergence diagram (bottom) for $\ell^0 = 100, \ell^1 = 0, \ell^2 = 200, \ell^3 = 0$.

Figure 6.25: Final shapes for ψ_0 (left) and ψ_1 (right).

Then, we distribute again four materials, with only one of them representing void. The parameters of the computation are: $E^0 = 0.7, E^1 = 0.5, E^2 = 1$ and $E^3 = 10^{-3}$, while the different Lagrange multipliers are set to $\ell^0 = 100, \ell^1 = 50, \ell^2 = 200$. Doing so, the volume of the strongest material is more severely penalized than that of the others. In the results of Figure 6.26, one can see that material 2 has completely disappeared, while material 0, which is strongest than materials 1 and 3, has been placed at regions of high stress values.

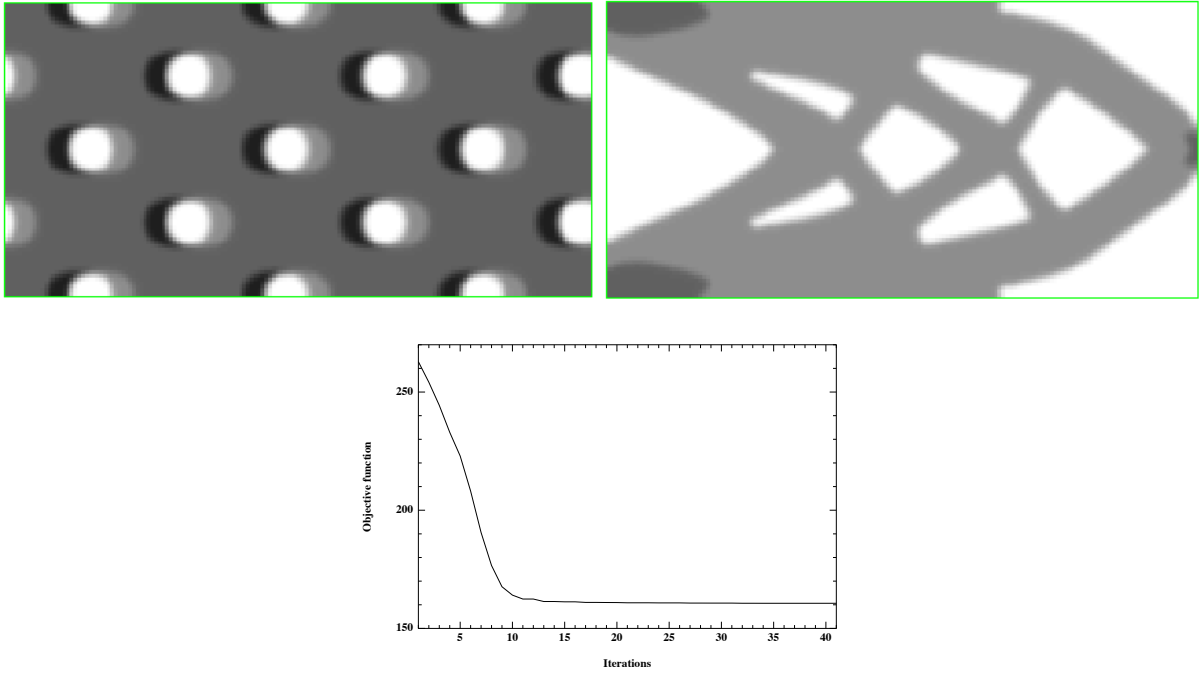


Figure 6.26: Initialization with four materials (top), optimized shape and convergence diagram (bottom) for $\ell^0 = 100, \ell^1 = 50, \ell^2 = 200$.

Changing the value of ℓ^2 to 100, we witness the apparition of all materials (see Figure 6.27).

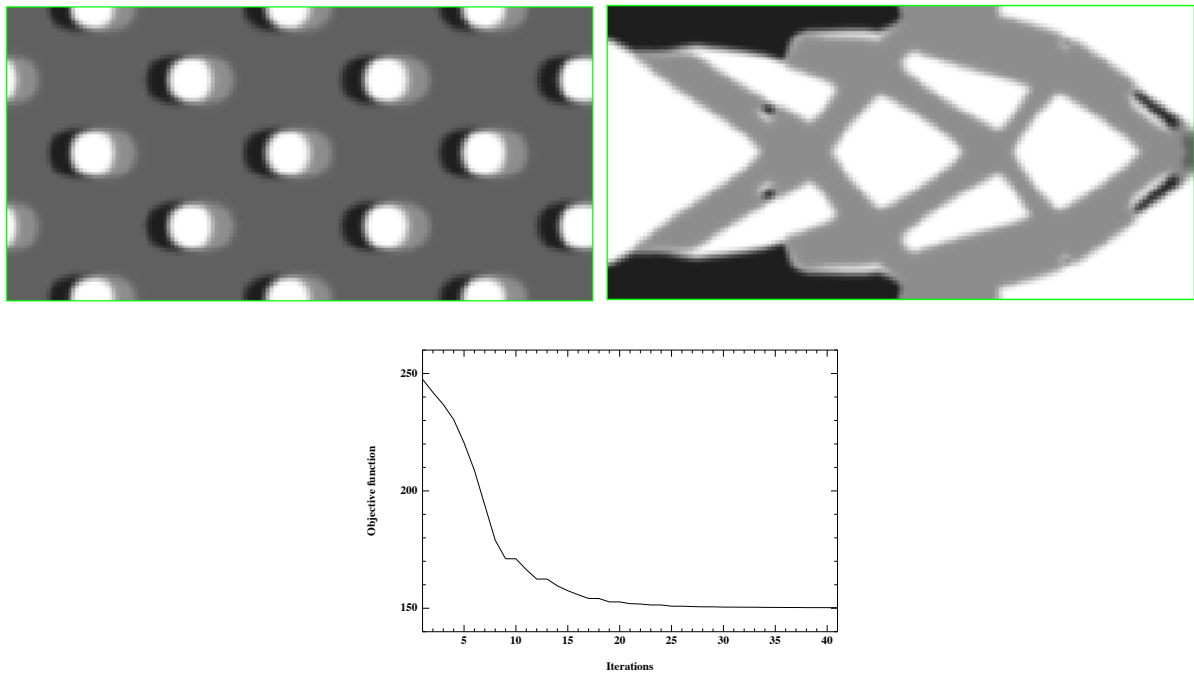


Figure 6.27: Initialization with four materials (top), optimized shape and convergence diagram (bottom) for $\ell^0 = 100, \ell^1 = 50, \ell^2 = 100$.

2d bridge

The second structure to be optimized is a two-dimensional bridge of dimensions 2×1.2 , discretized by means of 160×96 $Q1$ elements. The boundary conditions are displayed in Figure 6.28. The same

materials as in the previous example are used and the Lagrange multipliers for the volumes are set to $\ell^0 = 11$, $\ell^1 = 9$, $\ell^2 = 17$.

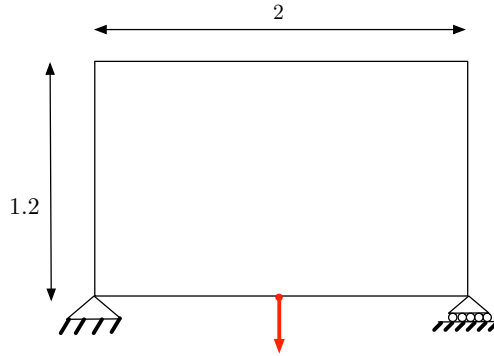


Figure 6.28: Boundary conditions and initialization for the 2D bridge.

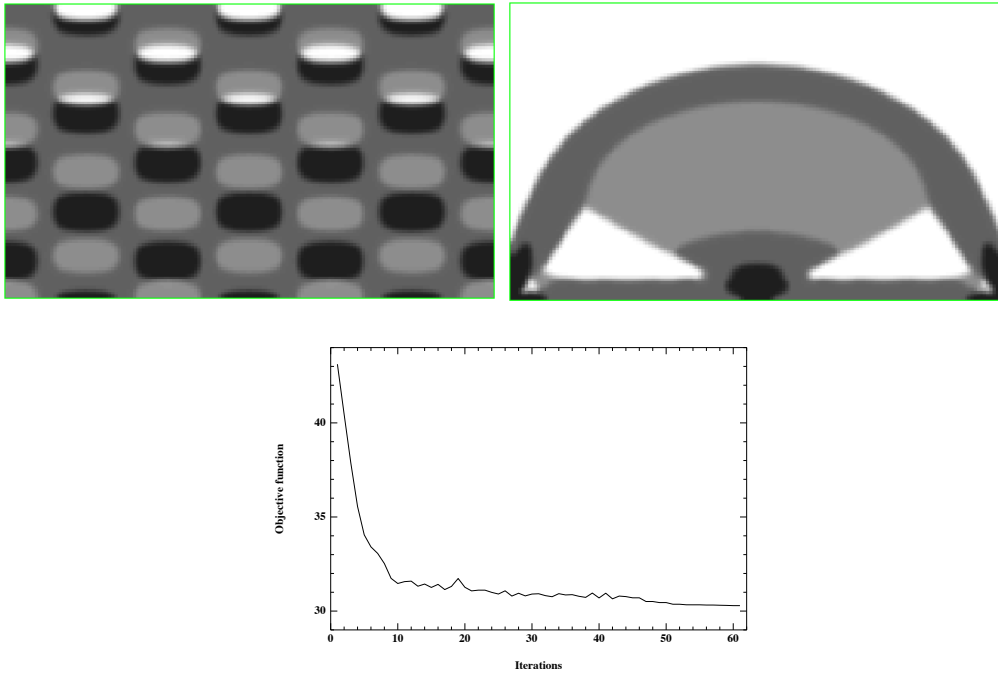


Figure 6.29: Initialization, optimized shape and convergence diagram for $\ell^1 = 11$, $\ell^2 = 9$, $\ell^3 = 17$.

The optimized shape and the convergence diagram are shown on Figure 6.29. Once again the strong material is placed at the regions of high stress, while the rest of the structure is dominated by material 2.

L-beam

The next structure to be optimized is an L-shape structure. Its dimensions are 1×1 , discretized by 120×120 $Q1$ elements. The boundary conditions are shown in Figure 6.30. The upper-left quarter of the domain is considered non-optimizable, filled with the material 3, representing void. The same materials as in the previous example are used and the Lagrange multipliers for the volumes are set to $\ell^0 = 170$, $\ell^1 = 130$, $\ell^2 = 240$. The optimized shape and the corresponding convergence diagram are shown in Figure 6.31.

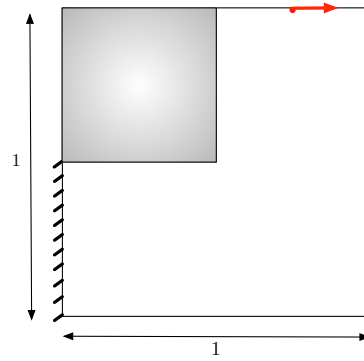


Figure 6.30: Boundary conditions and initialization for the L-shape structure.

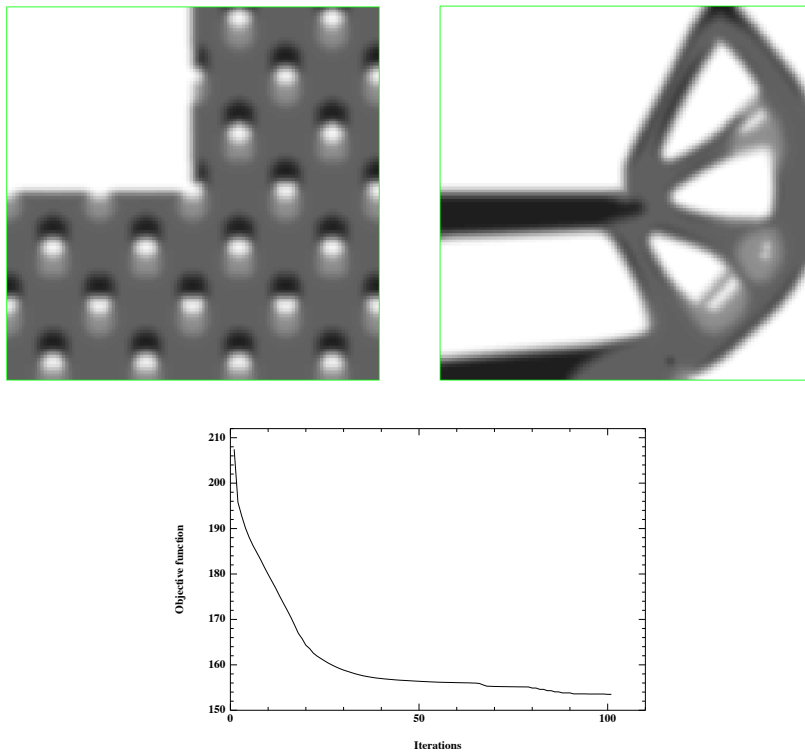


Figure 6.31: Initialization, optimized shape and convergence diagram for the L-shape test case.

Multi-load case

The final example to be presented is a multi-load case. A cantilever of dimensions 1×1 , discretized by means is 120×120 $Q1$ elements, is subjected to two independent load cases, shown in Figure 6.32 (i.e. the loads are not applied simultaneously). The objective function to be minimized is an aggregated sum of the total compliance in each case and the volumes of the materials. The same materials as previously are used and the Lagrange multipliers for the volumes are set to $\ell^0 = 90$, $\ell^1 = 70$, $\ell^2 = 120$.

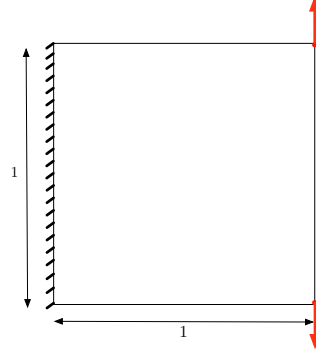


Figure 6.32: Boundary conditions and initialization for the multi-load case.

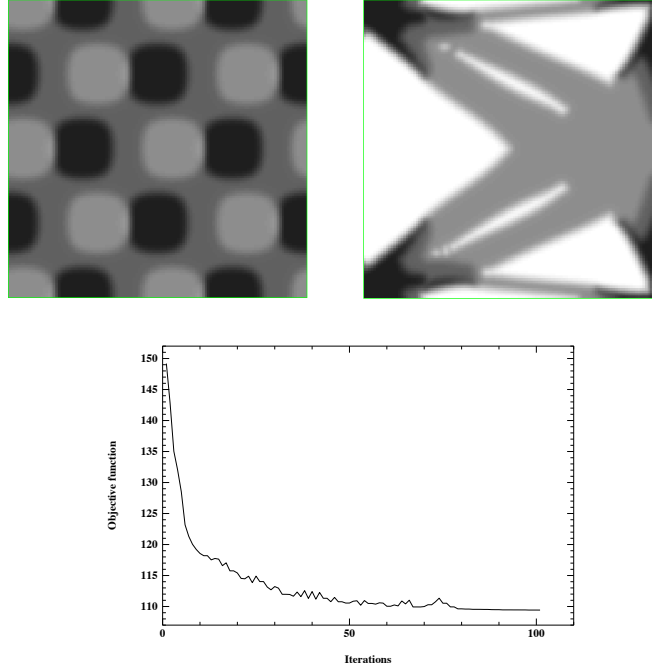


Figure 6.33: Initialization, optimized shape and convergence diagram for the multi-load case.

6.6.5 Multi-functional optimization example

This example couples a structural and a thermal problem. A 6×1 structure is considered (see Figure 6.34), having two non-optimizable areas (in blue) at the upper and lower part, occupied by material 1. The structure is subjected to two uncoupled mechanical problems. For the structural load case, the shape is considered clamped at its right and left boundary and a load is applied at the middle of the lower part. For the thermal load case, homogeneous Dirichlet conditions are considered for the lower part and the structure is subjected to a thermal flux. We distinguish between the "out-of-plane" case, where the flux Φ_1 comes from the upper side of the structure and the "in-plane" case, in which the flux Φ_2 is set to its left and right side. The PDE describing the thermal problem reads

$$\left\{ \begin{array}{ll} -\operatorname{div}(k(d_\Omega(x)) \nabla T) &= 0 \quad \text{in } D, \\ T &= 0 \quad \text{on } \Gamma_D, \\ k(d_\Omega(x)) \frac{\partial T}{\partial n} &= \Phi_i \quad \text{on } \Gamma_N, \\ \frac{\partial T}{\partial n} &= 0 \quad \text{on } \Gamma_0, \end{array} \right. \quad (6.39)$$

where $i = 1$ or 2 . Our goal is to distribute in an optimal way two materials with different properties, so as to create a structure that is stiff and thermally isolating at the same time. Material 1 has normalized

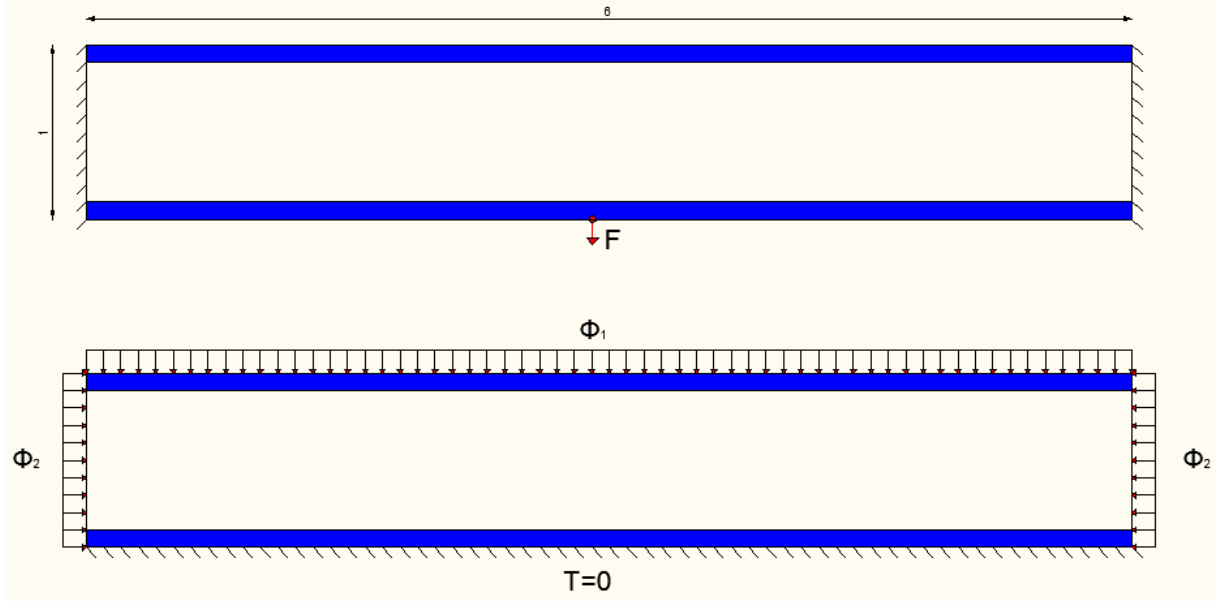


Figure 6.34: Boundary conditions. "Out-of-plane" flux corresponds to $\Phi_1 \neq 0, \Phi_2 = 0$, while "in-plane" flux corresponds to $\Phi_2 \neq 0, \Phi_1 = 0$.

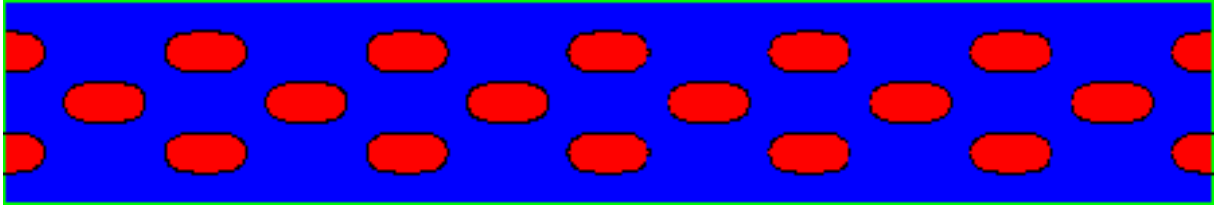


Figure 6.35: Initialization.

Young modulus and thermal conductivity $E^1 = k^1 = 1$, while material 2 has $E^2 = k^2 = 0.1$, i.e. material 1 is stiffer but thermally more conductive than material 2. The sharp interface between the two materials is approximated using a smooth interpolation of half-width $\varepsilon = 2\Delta x$.

As objective function to minimize, we have adopted the following choice presented in [81]:

$$J(\Omega) = \frac{\left(\int_D A(d_\Omega(x)) e(u) : e(u) dx \right)^{1-a}}{\left(\int_D k(d_\Omega(x)) \nabla T \cdot \nabla T dx \right)^a}, \quad a \in [0, 1]. \quad (6.40)$$

The term in the numerator is the mechanical compliance, while the term in the denominator is the thermal compliance. The parameter "a" is chosen so as to highlight the importance of one or the other load case. For $a = 0$ the problems turns to the minimization of the mechanical compliance and thus all the optimisable area will be covered with the stiff material 1, while for $a = 1$ the problem is to maximize the thermal compliance, i.e. maximize the thermal isolation, and therefore the material 2 will be chosen. For intermediate values of "a", the algorithm will search for an optimal mixture of the two materials. We have chosen not to impose a volume constraint. The derivation of functional (6.40) is done according to Theorem 6.3.2.

We consider both the case of "out-of-plane" and "in-plane" flux. The initialization for both cases is shown in Figure 6.35. The optimized shape and the convergence diagram for "out-of-plane" flux and $a = 0.3$ is depicted in figures 6.36 and 6.37. In this figure we can see clearly that material 1 (in blue) is placed so as to bear the structural load, whereas material 2 (in red) tries to prevent the thermal flux.

The case of "in-plane" flux is shown in figures 6.38 and 6.39 for $a = 0.5$. In this case, material 2 tries to isolate thermally the structure by being concentrated around the place that the flux is applied.

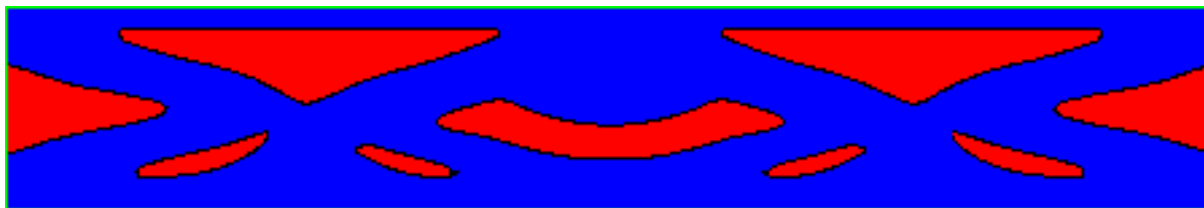


Figure 6.36: Optimized shape for "out-of-plane" flux and $a = 0.3$.

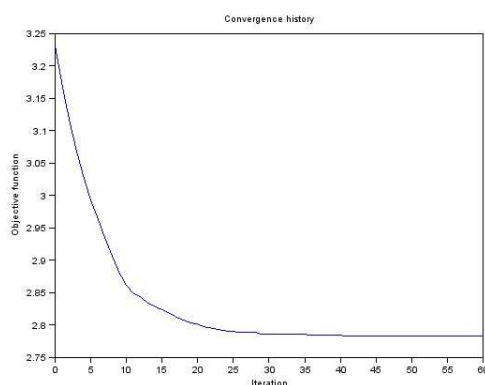


Figure 6.37: Convergence diagram for the result of Figure 6.36.



Figure 6.38: Optimized shape for "in-plane" flux and $a = 0.5$.

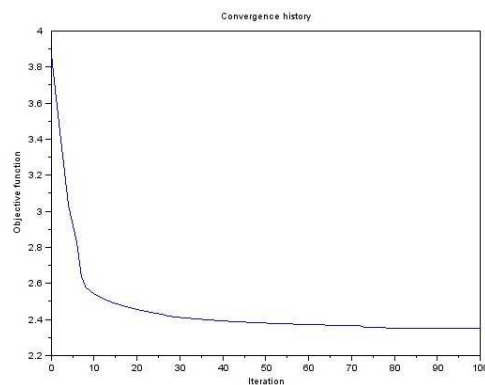


Figure 6.39: Convergence diagram for the result of Figure 6.38.

6.7 Material design using inverse homogenization

The topic of materials design with extreme or prescribed properties using shape and topology optimization is well known in the literature [166, 129, 69, 22, 124, 125, 57, 156, 147, 32]. In this Section, we would like to apply the method presented in this Chapter for a problem of microstructure optimization in periodic media. The same study has been conducted in [156], but the shape derivative therein was not calculated correctly as will be explained in the sequel.

6.7.1 Setting of the problem

Let $D \subset \mathbb{R}^N$ be a bounded domain, occupied by a linear elastic periodic medium with period ε . The period is assumed to be very small compared to the size of the domain D . We will call $Y = (0, 1)^N$ the rescaled unit periodicity cell. The material properties in D are described by a periodic fourth order Hooke's tensor $A(y)$ and a periodic second order thermal stress tensor $A^{th}(y)$, with $y = x/\varepsilon \in Y$ and $x \in D$. The thermal stress tensor is given as $A^{th}(y) = A(y)\alpha^{th}(y)$, where $\alpha^{th}(y)$ is the thermal strain tensor.

Denoting $f(x)$ the external force and imposing Dirichlet boundary conditions (for simplicity), the linearized elasticity model reads

$$\begin{cases} -\operatorname{div} \left(A\left(\frac{x}{\varepsilon}\right) e(u_\varepsilon) - A^{th}\left(\frac{x}{\varepsilon}\right) \delta T(x) \right) &= f & \text{in } D, \\ u_\varepsilon &= 0 & \text{on } \partial D, \end{cases} \quad (6.41)$$

where u_ε is the displacement vector field, $e(u_\varepsilon) = \frac{1}{2}(\nabla u_\varepsilon + \nabla u_\varepsilon^T)$ is the strain tensor, equal to the symmetrized gradient of u_ε and $\delta T(x)$ is a temperature field.

The homogenized or averaged properties of the heterogeneous domain D are found using an asymptotic analysis [4, 6]. We are searching to distribute one or multiple phases in the unit cell Y , such that the coefficients of the homogenized tensors attain some prescribed values.

For the sake of simplicity, we will describe the case of two phases, called phase 0 and 1. Phase 0 occupies the domain Ω and phase 1 occupies the domain $Y \setminus \Omega$. The optimizable interface between the two phases, denoted Γ is defined implicitly using a periodic level-set function ψ such that (see Figure 6.7.1)

$$\begin{cases} \psi(x) = 0 & \text{for } x \in \Gamma = \partial\Omega, \\ \psi(x) < 0 & \text{for } x \in \Omega, \\ \psi(x) > 0 & \text{for } x \in Y \setminus \Omega. \end{cases}$$

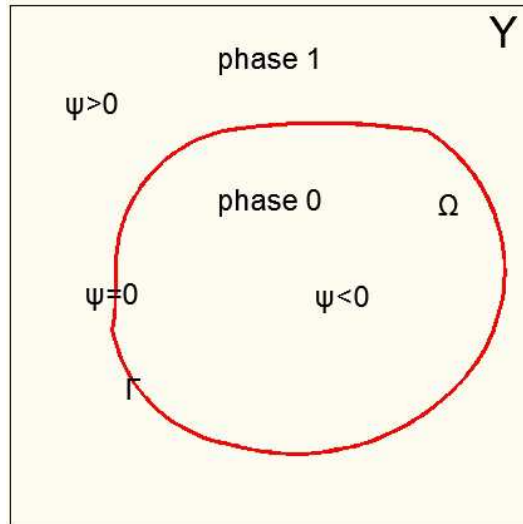


Figure 6.40: Level-set description of two materials occupying the periodic unit cell Y .

Moreover, both the elasticity and the thermal stress tensors are assumed to be smooth in the unit cell Y . The smooth interpolation between the material properties of the distinct phases is done using the signed-distance function to the boundary of the domain Ω , as described in Section 6.3. We define an

objective function that is a weighted sum of the square deviation of the homogenized coefficients to the target ones

$$J(\Omega) = \frac{1}{2} \sum_{i,j,k,l} \eta_{ijkl} (A_{ijkl}^*(d_\Omega) - A_{ijkl}^T)^2 + \frac{1}{2} \sum_{i,j} \mu_{ij} (A_{ij}^{th*}(d_\Omega) - A_{ij}^{thT})^2, \quad (6.42)$$

where $(\cdot)^*$ and $(\cdot)^T$ denote an homogenized and a target quantity respectively and η_{ijkl} and μ_{ij} are weight coefficients with the same symmetries as the elasticity and the thermal stress tensors respectively.

6.7.2 Calculation of the homogenized properties

In order to find the homogenized properties of the heterogeneous domain D , an asymptotic analysis of equation (6.41) is performed as the period ε goes to zero. The displacement u_ε is written as a series of powers in ε

$$u_\varepsilon(x) = \sum_{i=0}^{+\infty} \varepsilon^i u_i(x, \frac{x}{\varepsilon}), \quad (6.43)$$

where each term $u_i(x, y)$ is a Y -periodic function of y .

The first term u_0 of this series will be identified as the solution of the equation, said *homogenized*, whose elasticity tensor A_{ijkl}^* will describe the macroscopic properties of an equivalent homogenized medium.

The following derivation rule is applied

$$\nabla \left(u_i(x, \frac{x}{\varepsilon}) \right) = (\varepsilon^{-1} \nabla_y u_i + \nabla_x u_i) \left(x, \frac{x}{\varepsilon} \right),$$

thus,

$$\nabla u_\varepsilon(x) = \varepsilon^{-1} \nabla_y u_0(x, \frac{x}{\varepsilon}) + \sum_{i=0}^{+\infty} \varepsilon^i (\nabla_y u_{i+1} + \nabla_x u_i) \left(x, \frac{x}{\varepsilon} \right).$$

The above series is inserted in equation (6.41), which becomes a series of ε :

$$\begin{aligned} & -\varepsilon^{-2} \left(\text{div}_y \left(A(\frac{x}{\varepsilon}) e_y(u_0) \right) \right) \left(x, \frac{x}{\varepsilon} \right) \\ & -\varepsilon^{-1} \left(\text{div}_y \left(A(\frac{x}{\varepsilon}) (e_x(u_0) + e_y(u_1)) \right) + \text{div}_x \left(A(\frac{x}{\varepsilon}) e_y(u_0) \right) - \text{div}_y \left(A^{th}(\frac{x}{\varepsilon}) \Delta T \right) \right) \left(x, \frac{x}{\varepsilon} \right) \\ & - \sum_{i=0}^{+\infty} \varepsilon^i \left(\text{div}_x \left(A(\frac{x}{\varepsilon}) (e_x(u_i) + e_y(u_{i+1})) \right) + \text{div}_y \left(A(\frac{x}{\varepsilon}) (e_x(u_{i+1}) + e_y(u_{i+2})) \right) \right) \left(x, \frac{x}{\varepsilon} \right) \\ & + \text{div}_x \left(A^{th}(\frac{x}{\varepsilon}) \Delta T \right) = f(x), \end{aligned} \quad (6.44)$$

where we have denoted $e_x(\cdot) = \frac{1}{2}(\nabla_x(\cdot) + \nabla_x(\cdot)^T)$ and $e_y(\cdot) = \frac{1}{2}(\nabla_y(\cdot) + \nabla_y(\cdot)^T)$.

The equation in ε^{-2} gives:

$$- \text{div}_y (A(y) e_y(u_0)) = 0, \quad (6.45)$$

which is interpreted as an equation in the unit cell Y with periodic boundary conditions. Therefore

$$u_0(x, y) \equiv u(x). \quad (6.46)$$

Since $e_y(u_0) = 0$, the equation in ε^{-1} becomes:

$$- \text{div}_y (A(y) e_y(u_1)) = \text{div}_y (A(y) e_x(u_0)) - \text{div}_y (A^{th}(y) \Delta T), \quad (6.47)$$

which has as unknown u_1 in the periodic cell Y .

By superposition, we can split the problem into a mechanical and a thermal problem:

$$u_1(x, y) = u_1^m(x, y) + u_1^\theta(x, y), \quad (6.48)$$

where u_1^m is the solution of equation

$$- \text{div}_y (A(y) e_y(u_1^m)) = \text{div}_y (A(y) e_x(u_0)) \quad (6.49)$$

and

$$u_1^\theta(x, y) = w^\theta(y) \delta T(x),$$

$w^\theta(y)$ being the solution of equation

$$- \text{div}_y (A(y) e_y(w^\theta)) = - \text{div}_y (A^{th}(y)). \quad (6.50)$$

We denote $e_{ij} = (e_i \otimes e_j + e_j \otimes e_i)/2$, $1 \leq i, j \leq N$. Then, $\forall e_{ij}$, we call the *cell problem* the equation

$$\begin{cases} -\operatorname{div}_y (A(y) (e_{ij} + e_y(w_{ij}(y)))) &= 0 & \text{in } Y \\ y \rightarrow w_{ij}(y) & & Y - \text{periodic.} \end{cases} \quad (6.51)$$

By linearity, we obtain

$$u_1^m(x, y) = \frac{1}{2} \sum_{i=1}^N \sum_{j=1}^N \left(\frac{\partial(u_0)_i}{\partial x_j}(x) + \frac{\partial(u_0)_j}{\partial x_i}(x) \right) w_{ij}(y).$$

Finally, the equation in ε^0 is:

$$\begin{aligned} & -\operatorname{div}_x (A(y) (e_x(u_0) + e_y(u_1))) - \operatorname{div}_y (A(y) (e_x(u_1) + e_y(u_2))) \\ & + \operatorname{div}_x (A^{th}(y) \delta T(x)) = f(x) \Rightarrow \\ & -\operatorname{div}_y (A(y) e_y(u_2)) = \operatorname{div}_y (A(y) e_x(u_1)) \\ & + \operatorname{div}_x (A(y) (e_x(u_0) + e_y(u_1))) - \operatorname{div}_x (A^{th}(y) \delta T(x)) + f(x) \end{aligned} \quad (6.52)$$

Equation (6.52) admits a unique solution (up to a constant) if the average of the right-hand side in equation (6.52) vanishes, i.e. if

$$\int_Y [\operatorname{div}_y (A(y) e_x(u_1)) + \operatorname{div}_x (A(y) (e_x(u_0) + e_y(u_1))) - \operatorname{div}_x (A^{th}(y) \delta T(x)) + f(x)] dy = 0. \quad (6.53)$$

After integration by parts, the first term disappears and equation (6.53) finally results in

$$-\operatorname{div}_x \left(\int_Y [A(y) (e_x(u_0) + e_y(u_1)) - A^{th}(y) \delta T(x)] dy \right) = f(x). \quad (6.54)$$

Because of equation (6.48), (6.54) becomes

$$\begin{aligned} & -\operatorname{div}_x \left(\int_Y [A(y) (e_x(u_0) + e_y(u_1^m)) + A(y) e_y(w^\theta) \delta T(x) - A^{th}(y) \delta T(x)] dy \right) = f(x) \Rightarrow \\ & -\operatorname{div}_x \left(\int_Y [A(y) (e_x(u_0) + e_y(u_1^m))] dy + \int_Y [A(y) e_y(w^\theta) \delta T(x) - A^{th}(y) \delta T(x)] dy \right) = f(x) \Rightarrow \\ & -\operatorname{div}_x (A^* e_x(u_0) - A^{th*} \delta T(x)) = f(x), \end{aligned} \quad (6.55)$$

where

$$A^* e_x(u_0) = \frac{1}{2} \sum_{i=1}^N \sum_{j=1}^N \left(\frac{\partial(u_0)_i}{\partial x_j}(x) + \frac{\partial(u_0)_j}{\partial x_i}(x) \right) \int_Y A(y) (e_{ij} + e_y(w_{ij})) dy$$

and

$$A^{th*} = \int_Y (A^{th}(y) - A(y) e_y(w^\theta)) dy = \int_Y A(y) (\alpha^{th}(y) - e_y(w^\theta)) dy.$$

Therefore

$$A_{ijkl}^* = \int_Y A(y) (e_{ij} + e_y(w_{ij})) e_{kl} dy,$$

or, in symmetric form,

$$A_{ijkl}^* = \int_Y A(y) (e_{ij} + e_y(w_{ij})) (e_{kl} + e_y(w_{kl})) dy \quad (6.56)$$

and

$$A_{ij}^{th*} = \int_Y A(y) (\alpha(y) - e_y(w^\theta)) e_{ij} dy,$$

or

$$A_{ij}^{th*} = \int_Y A(y) (e_{ij} - e_y(w_{ij})) (\alpha(y) - e_y(w^\theta)) dy. \quad (6.57)$$

6.7.3 Shape derivative

The method of C  a is used for the calculation of the shape derivative of the objective function (6.42). We define the Lagrangian function

$$\begin{aligned} \mathcal{L}(\Omega, \widehat{w}_{pq}, \widehat{\xi}_{pq}, \widehat{w}^\theta, \widehat{\zeta}) &= \frac{1}{2} \sum_{i,j,k,l} \eta_{ijkl} (A_{ijkl}^* (\widehat{w}_{pq}) - A_{ijkl}^T)^2 \\ &+ \frac{1}{2} \sum_{i,j} \mu_{ij} (A_{ij}^{th*} (\widehat{w}_{pq}, \widehat{\xi}_{pq}) - A_{ij}^{thT})^2 \\ &+ \sum_{p=1}^N \sum_{q=1}^N \int_Y [A(y) (e_{pq} + e_y(\widehat{w}_{pq}(y))) : e_y(\widehat{\xi}_{pq}(y))] dy \\ &+ \int_Y (A(y) e_y(\widehat{w}^\theta) - A^{th}(y)) : e_y(\widehat{\zeta}(y)) dy, \end{aligned} \quad (6.58)$$

where the functions $\widehat{w}_{pq}, \widehat{\xi}_{pq}, \widehat{w}^\theta$ and $\widehat{\zeta}$ are assumed to be vector-valued functions defined in Y and independent of Ω .

Taking the partial derivative of \mathcal{L} with respect to $\widehat{\xi}_{pq} \forall p = 1, \dots, N, \forall q = 1, \dots, N$, in the direction of a given vector ϕ and setting it to be zero at the optimal point $w_{pq}^*, \xi_{pq}^*, w^{\theta*}, \zeta^*$ we get

$$\frac{\partial \mathcal{L}}{\partial \widehat{\xi}_{pq}}(\phi) = \int_Y [A(y) (e_{pq} + e_y(w_{pq}^*(y))) : e_y(\phi(y))] dy = 0 \quad \forall p = 1, \dots, N, \forall q = 1, \dots, N. \quad (6.59)$$

Therefore, w_{pq}^* is the solution of the *cell problem* $\forall p = 1, \dots, N, \forall q = 1, \dots, N$.

The partial derivative of \mathcal{L} with respect to $\widehat{\zeta}$ in the direction of ϕ results in

$$\frac{\partial \mathcal{L}}{\partial \widehat{\zeta}}(\phi) = \int_Y (A(y) e_y(w^{\theta*}) - A^{th}(y)) e_y(\phi(y)) dy = 0, \quad (6.60)$$

thus $w^{\theta*}$ is the solution of the *thermal cell problem* described by equation (6.50).

The partial derivative of \mathcal{L} with respect to \widehat{w}_{pq} , in the direction of $\phi, \forall p = 1, \dots, N, \forall q = 1, \dots, N$ gives

$$\begin{aligned} \frac{\partial \mathcal{L}}{\partial \widehat{w}_{pq}}(\phi) &= \sum_{k,l} 2\eta_{pqkl} (A_{pqkl}^* - A_{pqkl}^T) \left(\int_Y [A(y) (e_{kl} + e_y(w_{kl}^*)) e_y(\phi)] dy \right) \\ &- \mu_{pq} (A_{pq}^{th*} - A_{pq}^{thT}) \left(\int_Y [A(y) (\alpha(y) - e_y(w^{\theta*})) e_y(\phi)] dy \right) \\ &+ \int_Y [A(y) (e_y(\xi_{pq}^*)) e_y(\phi)] dy \\ &= \sum_{k,l} 2\eta_{pqkl} (A_{pqkl}^* - A_{pqkl}^T) \left(\int_Y [A(y) (e_{kl} + e_y(w_{kl}^*)) e_y(\phi)] dy \right) \\ &+ \int_Y [A(y) (e_y(\xi_{pq}^*)) e_y(\phi)] dy = 0 \quad \forall p = 1, \dots, N, \forall q = 1, \dots, N. \end{aligned} \quad (6.61)$$

Finally, the partial derivative of \mathcal{L} with respect to \widehat{w}^θ , in the direction of ϕ results in

$$\begin{aligned} \frac{\partial \mathcal{L}}{\partial u_1^\theta}(\phi) &= 0 \Rightarrow \\ \int_Y [A(y) (e_y(\zeta^*)) e_y(\phi)] dy - \sum_{p,q} \mu_{pq} (A_{pq}^{th*} - A_{pq}^{thT}) \int_Y [A(y) (e_{pq} - e_y(w_{pq}^*)) e_y(\phi)] dy &= 0. \end{aligned} \quad (6.62)$$

Deforming the interface Γ in the direction of a smooth vector field θ (see section 1.3.1 for details), the shape derivative of the objective function is found to be the shape derivative of the Lagrangian at the optimal point

$$J'(\Omega)(\theta) = \mathcal{L}'(\Omega, w_{pq}^*, \xi_{pq}^*, u_1^{\theta*}, \zeta^*)(\theta),$$

thus

$$\begin{aligned} J'(\Omega)(\theta) &= \sum_{i,j,k,l} \eta_{ijkl} (A_{ijkl}^* - A_{ijkl}^T) \int_Y [d'_\Omega(\theta) A'(d_\Omega) (e_{ij} + e_y(w_{ij}^*)) : (e_{kl} + e_y(w_{kl}^*))] dy \\ &+ \sum_{i,j} \mu_{ij} (A_{ij}^{th*} - A_{ij}^{thT}) \int_Y [d'_\Omega(\theta) A'(d_\Omega) (e_{ij} - e_y(w_{ij}^*)) : (\alpha(d_\Omega) - e_y(u_1^{\theta*}))] dy \\ &+ \sum_{i,j} \mu_{ij} (A_{ij}^{th*} - A_{ij}^{thT}) \int_Y [A(d_\Omega) (e_{ij} - e_y(w_{ij}^*)) : (d'_\Omega(\theta) \alpha'(d_\Omega))] dy \\ &+ \sum_{p=1}^N \sum_{q=1}^N \int_Y [d'_\Omega(\theta) A'(d_\Omega) (e_{pq} + e_y(w_{pq}^*)) : (e_y(\xi_{pq}^*))] dy \\ &+ \int_Y [d'_\Omega(\theta) A'(d_\Omega) (e_y(u_1^{\theta*}) - \alpha(y)) : (e_y(\zeta^*))] dy \\ &- \int_Y [A(y) (d'_\Omega(\theta) \alpha'(d_\Omega)) : (e_y(\zeta^*))] dy, \end{aligned} \quad (6.63)$$

Table 6.1: Homogenized coefficients for the optimized microstructure of Figure 6.41.

ijkl	A_{ijkl}^*	A_{ijkl}^T
1111	0.1465	0.200
1122	-0.0716	-0.100
2222	0.1461	0.200

where $A'(d_\Omega)$ and $\alpha'(d_\Omega)$ denote derivation with respect to d_Ω . The coarea formula (see 3.3.7) is then used in order to obtain an expression of the shape derivative in the form of equation (6.18).

Remark 6.7.1. *As we have foresaid, the same problem has been studied in [156]. The authors have claimed that the problem is self-adjoint, which is not true as we have shown in this section. Thus, the shape derivative in [156] is not correctly calculated.*

6.7.4 Numerical results

In all examples of this section, (6.42) has been chosen as objective function. In contrast with [156], inequality constraints have been imposed for the volume of each phase. A smooth interpolation of the material properties of half-width $\varepsilon = 2\Delta x$ has been used between the different phases. The values of the material properties, the target coefficients and most of the weight factors are the same as in [156].

In the first three examples, one strong phase with Young modulus $E = 0.91$ is used and only structural coefficients are included in the formulation of the problem (namely, $A^{th} \equiv 0$). Void is represented by a weak phase with Young modulus equal to 10^{-3} and thermal strain coefficients equal to 0. The rest of the examples contain two strong phases, with different structural and thermal properties, and void. An optimal mixture that minimizes the deviation from some prescribed structural and thermal homogenized coefficients is sought. For all examples, a mesh of 100×100 Q1 elements has been used.

Example 1

For the first example, the optimization problem reads

$$\begin{aligned} \min_{\Omega} \quad & J(\Omega) = \frac{1}{2}\eta_{1111}(A_{1111}^* - A_{1111}^T)^2 + \frac{1}{2}\eta_{1122}(A_{1122}^* - A_{1122}^T)^2 + \frac{1}{2}\eta_{2222}(A_{2222}^* - A_{2222}^T)^2, \\ \text{s.t.} \quad & V_T \leq 0.5|D|, \end{aligned}$$

where $\eta_{1111} = \eta_{2222} = 1$, $\eta_{1122} = 10$, $A_{1111}^T = A_{2222}^T = 0.2$ and $A_{1122}^T = -0.1$, i.e. we are searching for a material that contracts in one direction when expands in the other. In case the material is isotropic, the above target coefficients would correspond to a material with Poisson ratio equal to -0.5 . The results are shown in figures 6.41 and 6.42. The value of the homogenized coefficients for the optimized shape are shown in Table 6.1. The volume constraint is active at convergence, i.e. $V_T = 0.5|D|$.

Example 2

The second optimization problem reads

$$\begin{aligned} \min_{\Omega} \quad & J(\Omega) = \frac{1}{2}\eta_{1111}(A_{1111}^* - A_{1111}^T)^2 + \frac{1}{2}\eta_{1122}(A_{1122}^* - A_{1122}^T)^2 \\ & + \frac{1}{2}\eta_{2222}(A_{2222}^* - A_{2222}^T)^2 + \frac{1}{2}\eta_{1212}(A_{1212}^* - A_{1212}^T)^2, \\ \text{s.t.} \quad & V_T \leq 0.4|D|, \end{aligned}$$

where $\eta_{1111} = \eta_{1122} = \eta_{2222} = \eta_{1212} = 1$, $A_{1111}^T = A_{2222}^T = A_{1122}^T = 0.1$ and $A_{1212}^T = 0$. The values of the coefficients are chosen so that the algorithm tries to create an isotropic material with Poisson ratio equal to 1. The optimization results are shown in figures 6.43 and 6.44 and the value of the homogenized coefficients in Table 6.2. The final volume is $V_T = 0.4|D|$.

Example 3

In the final one-phase example, a microstructure is searched as solution of the problem

$$\begin{aligned} \min_{\Omega} \quad & J(\Omega) = \frac{1}{2}\eta_{1111}(A_{1111}^* - A_{1111}^T)^2 + \frac{1}{2}\eta_{1122}(A_{1122}^* - A_{1122}^T)^2 + \frac{1}{2}\eta_{2222}(A_{2222}^* - A_{2222}^T)^2, \\ \text{s.t.} \quad & V_T \leq 0.47|D|, \end{aligned}$$

where $\eta_{1111} = \eta_{1122} = \eta_{2222} = 1$, $A_{1111}^T = A_{2222}^T = 0.2$ and $A_{1122}^T = 0$, we want that the material does not deform in one direction when it expands or contracts in the other. The optimization results and the

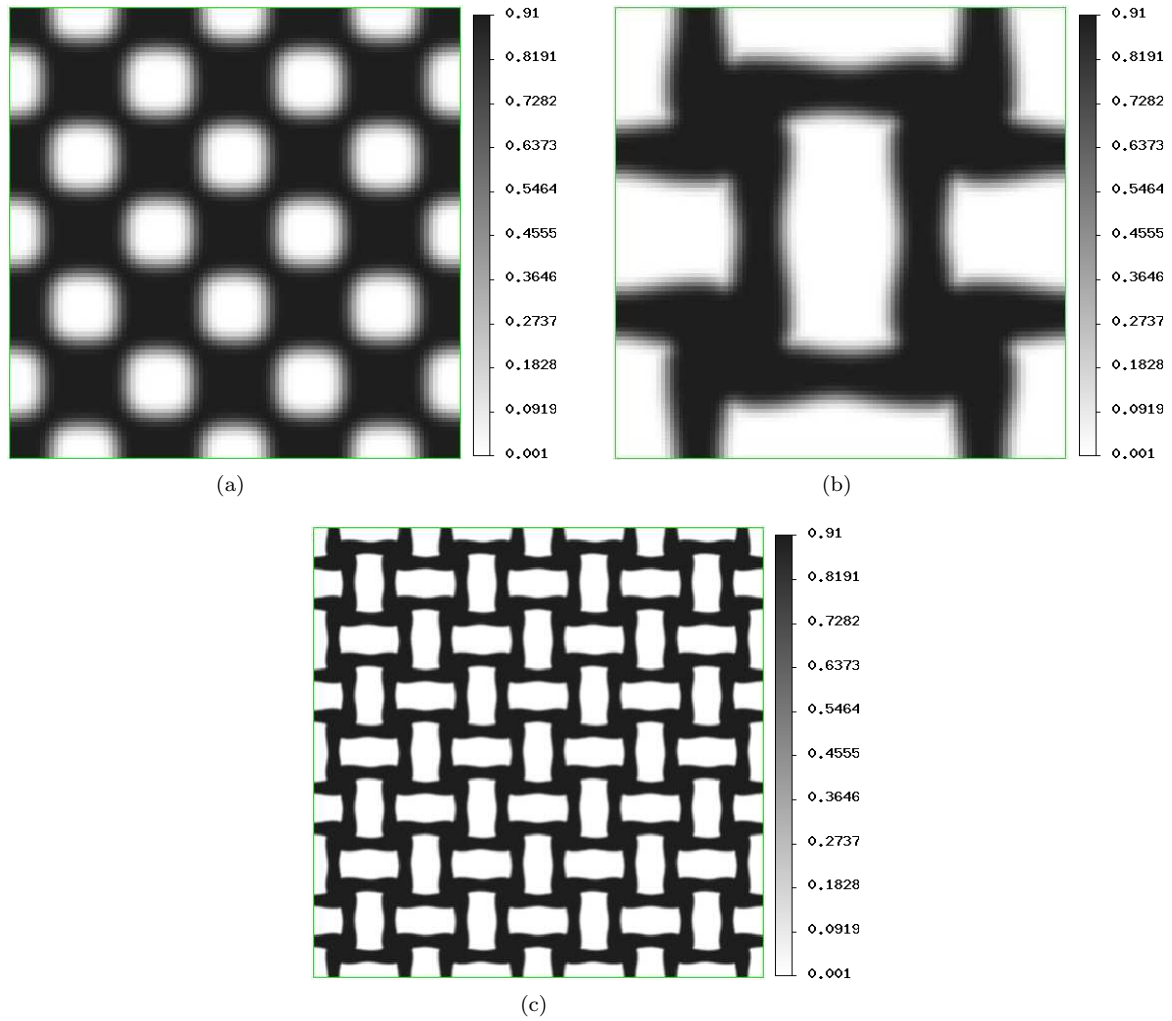


Figure 6.41: Optimized microstructure for Example 1; (a): initialization and (b): optimized unit cell; (c): optimized microstructure (16 unit cells).

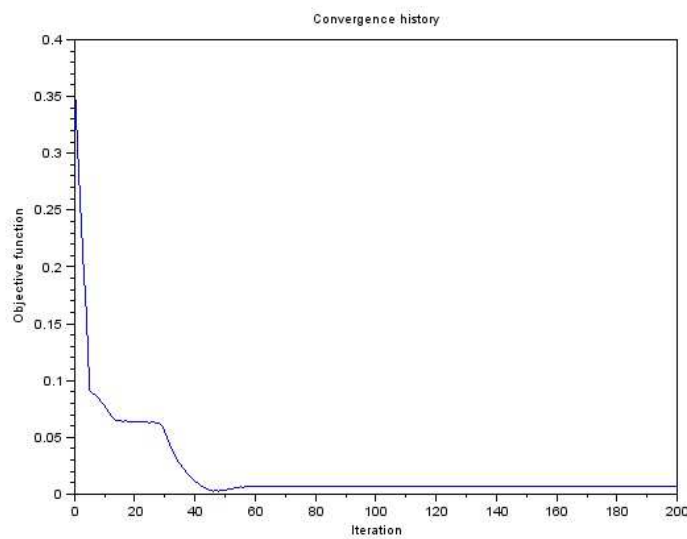


Figure 6.42: Convergence diagram for the results of Figure 6.41.

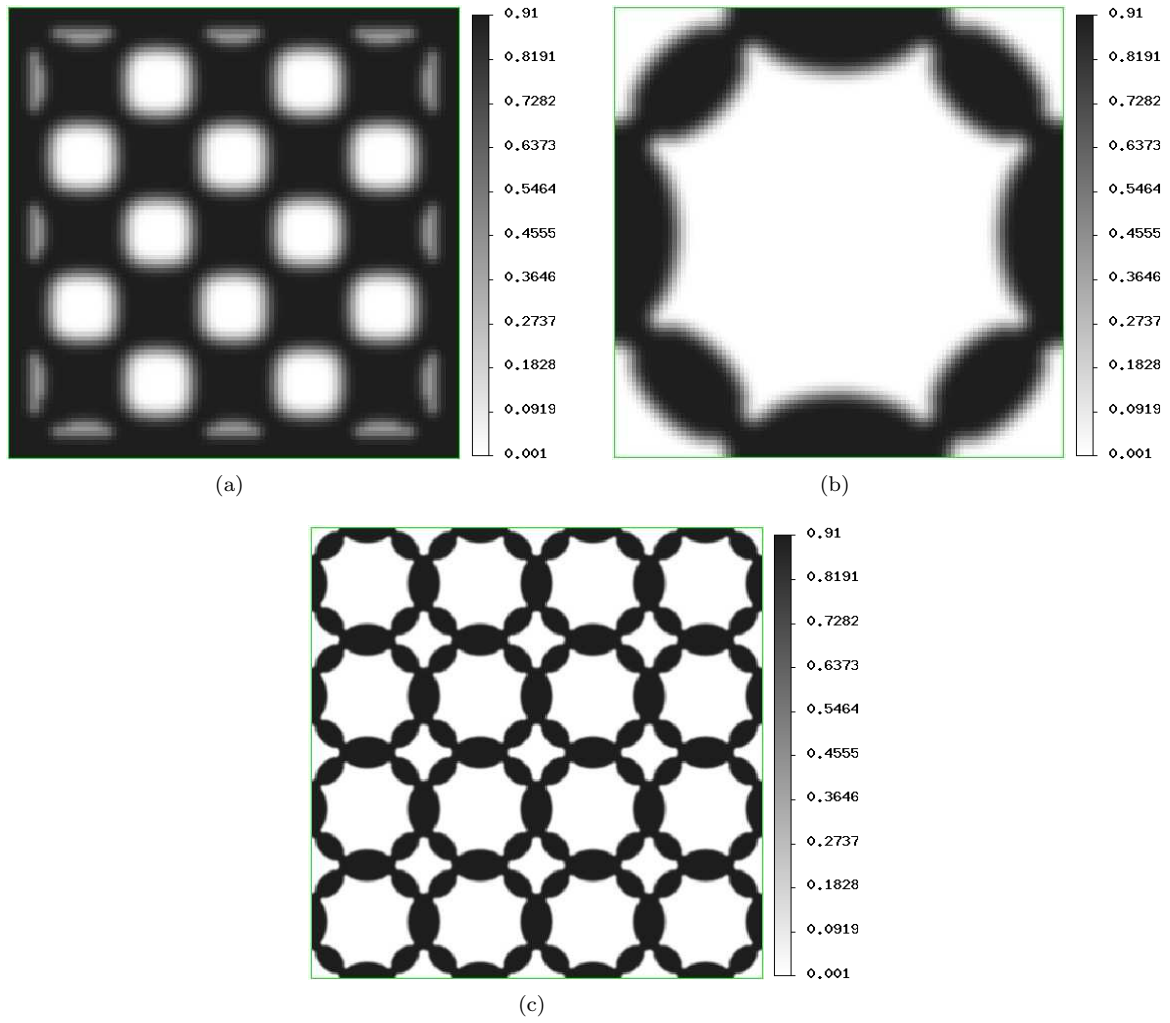


Figure 6.43: Optimized microstructure for Example 2; (a): initialization and (b): optimized unit cell; (c): optimized microstructure (16 unit cells).

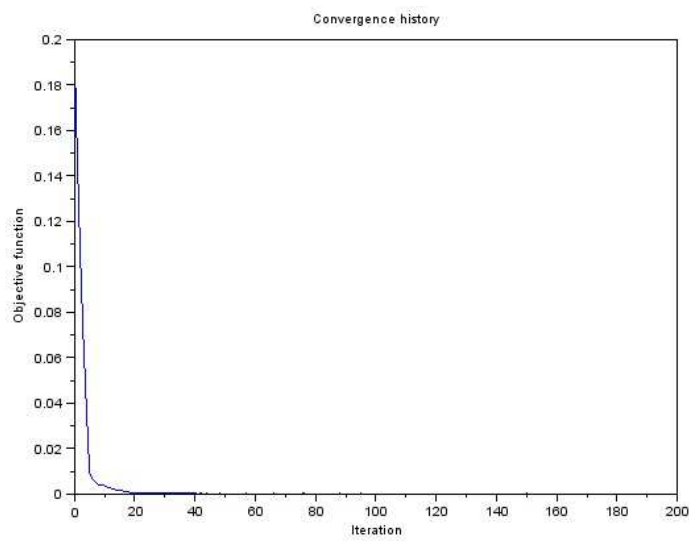


Figure 6.44: Convergence diagram for the results of Figure 6.43.

Table 6.2: Homogenized coefficients for the optimized microstructure of Figure 6.43.

ijkl	A_{ijkl}^*	A_{ijkl}^T
1111	0.1029	0.100
1122	0.0865	0.100
2222	0.1029	0.100
1212	0.0102	0

Table 6.3: Homogenized coefficients for the optimized microstructure of Figure 6.45.

ijkl	A_{ijkl}^*	A_{ijkl}^T
1111	0.2045	0.200
1122	0.0145	0
2222	0.2045	0.200

value of the homogenized coefficients are shown in figures 6.45, 6.46 and Table 6.3. The final volume is $V_T = 0.42|D|$.

Example 4

In this example, two isotropic materials are used (materials 0 and 1). The Young moduli are set to $E^0 = 0.91$ and $E^1 = 0.455$, while the thermal strain coefficients take the values $\alpha_{11}^{th0} = \alpha_{22}^{th0} = 1.0$, $\alpha_{11}^{th1} = \alpha_{22}^{th1} = 5.0$ and $\alpha_{12}^{th1} = \alpha_{12}^{th2} = 0$. The optimization problem reads

$$\begin{aligned}
\min_{\Omega} \quad & J(\Omega) = \frac{1}{2}\eta_{1111}(A_{1111}^* - A_{1111}^T)^2 + \frac{1}{2}\eta_{2222}(A_{2222}^* - A_{2222}^T)^2 \\
& + \frac{1}{2}\mu_{11}(A_{11}^{th*} - A_{11}^{thT})^2 + \frac{1}{2}\mu_{22}(A_{22}^{th*} - A_{22}^{thT})^2, \\
\text{s.t.} \quad & V_T^0 \leq 0.20|D|, \\
& V_T^1 \leq 0.24|D|, \\
& A_{1212}^* \geq 0.05,
\end{aligned}$$

where $\eta_{1111} = \eta_{2222} = 10$, $\mu_{11} = \mu_{22} = 1$, $A_{1111}^T = A_{2222}^T = 0.05$ and $A_{11}^{thT} = A_{22}^{thT} = 0.1$. In this Example, the principal goal is to create a material with equal thermal expansion coefficients, while the structural coefficients are imposed to ensure sufficient rigidity of the microstructure. The optimization results and the value of the homogenized coefficients are shown in figures 6.47, 6.48 and Table 6.4. The final volume of each phase is $V_T^0 = 0.20|D|$ and $V_T^1 = 0.06|D|$.

Example 5

Here, again two isotropic materials are used with Young moduli $E^0 = 0.91$ and $E^1 = 0.455$ and thermal strain coefficients $\alpha_{11}^{th0} = \alpha_{22}^{th0} = 1.0$, $\alpha_{11}^{th1} = \alpha_{22}^{th1} = 10.0$ and $\alpha_{12}^{th1} = \alpha_{12}^{th2} = 0$. The optimization problem reads

$$\begin{aligned}
\min_{\Omega} \quad & J(\Omega) = \frac{1}{2}\eta_{1212}(A_{1212}^* - A_{1212}^T)^2 + \frac{1}{2}\mu_{11}(A_{11}^{th*} - A_{11}^{thT})^2 + \frac{1}{2}\mu_{22}(A_{22}^{th*} - A_{22}^{thT})^2, \\
\text{s.t.} \quad & V_T^0 \leq 0.25|D|, \\
& V_T^1 \leq 0.34|D|,
\end{aligned}$$

where $\mu_{11} = \mu_{22} = 1$, $A_{1212}^T = 0.04$, $A_{11}^{thT} = 0.4$ and $A_{11}^{thT} = -0.4$. Here we search for a material with opposite thermal expansion coefficients, while the coefficient A_{1212}^* is added in order to ensure sufficient stiffness of the material. Starting from the initial shape of Figure(6.41(a)) and setting the value of the

Table 6.4: Homogenized coefficients for the optimized microstructure of Figure 6.47.

ijkl	A_{ijkl}^*	A_{ijkl}^T	ij	A_{ij}^{th*}	A_{ij}^{thT}
1111	0.0525	0.050	11	0.1208	0.100
2222	0.0525	0.050	22	0.1208	0.100
1212	0.0536	≥ 0.050			

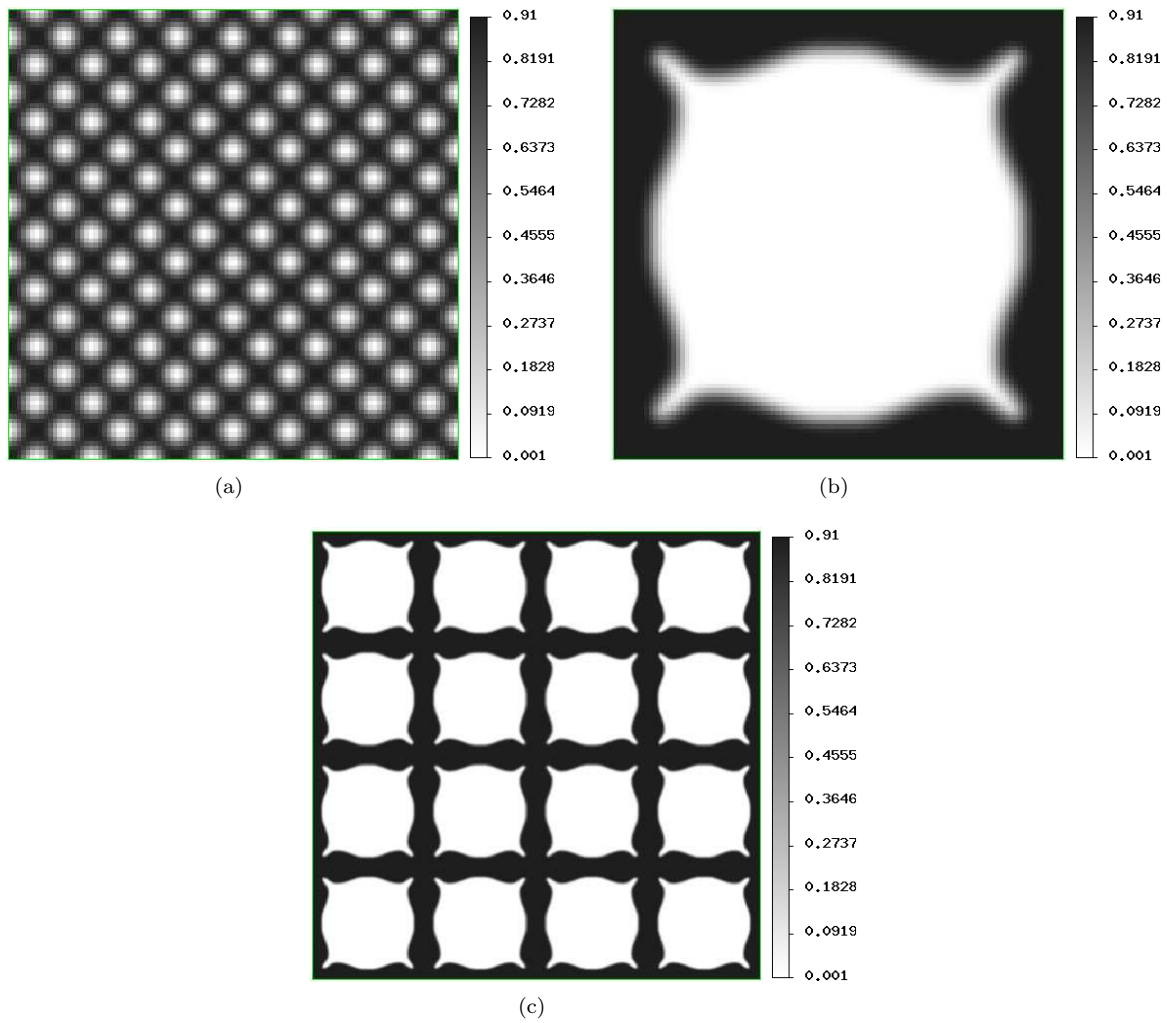


Figure 6.45: Optimized microstructure for Example 3; (a): initialization and (b): optimized unit cell; (c): optimized microstructure (16 unit cells).

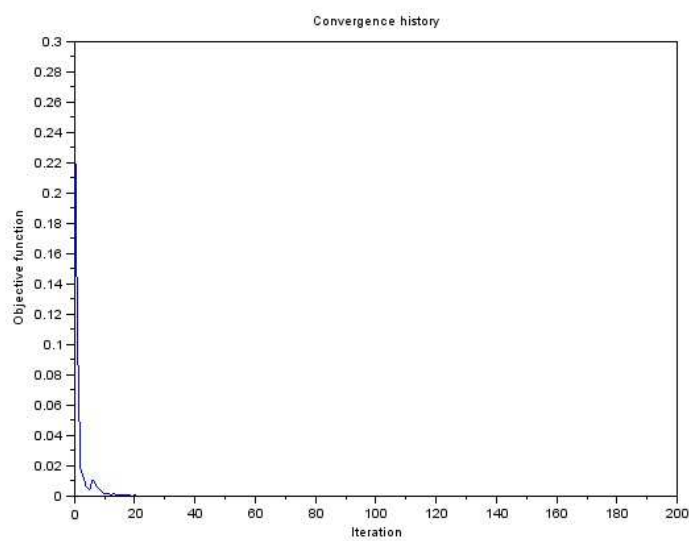


Figure 6.46: Convergence diagram for the results of Figure 6.45.

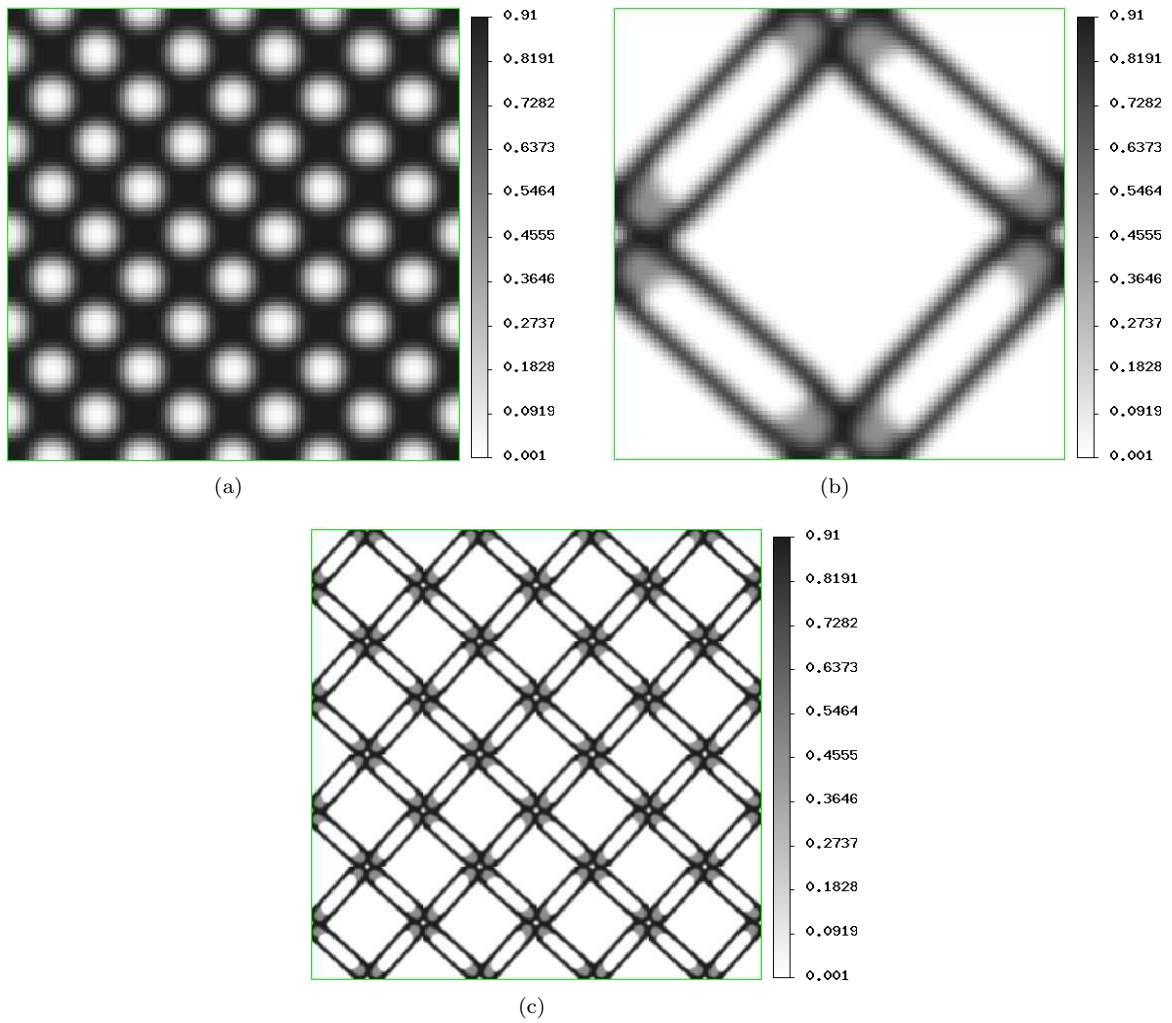


Figure 6.47: Optimized microstructure for Example 4; (a): initialization and (b): optimized unit cell; (c): optimized microstructure (16 unit cells).

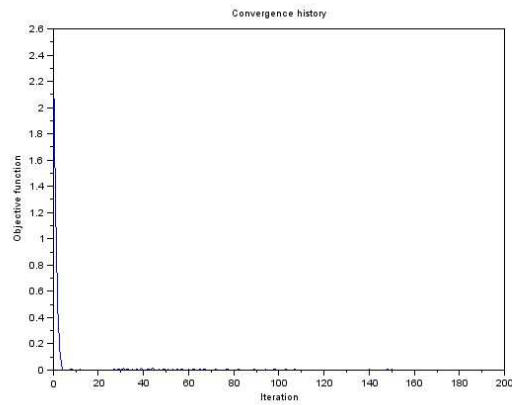


Figure 6.48: Convergence diagram for the results of Figure 6.47.

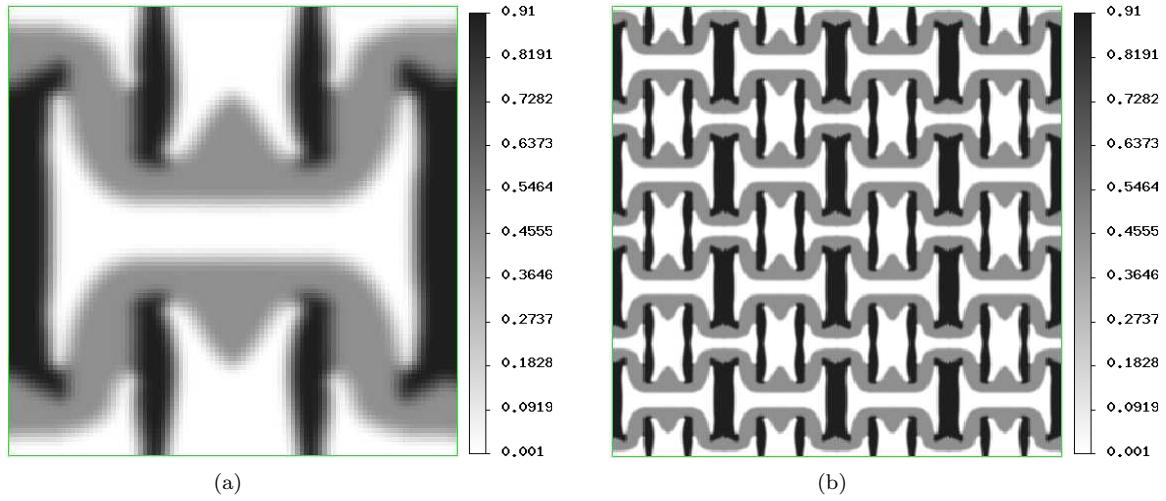


Figure 6.49: (a): Optimized unit cell and (b): optimized microstructure (16 unit cells), for Example 5 and $\eta_{1212} = 10$.

Table 6.5: Homogenized coefficients for the optimized microstructure of Figure 6.49.

ijkl	A_{ijkl}^*	A_{ijkl}^T	ij	A_{ij}^{th*}	A_{ij}^{thT}
1212	0.0061	0.040	11	0.4429	0.400
			22	-0.3370	-0.400

weight coefficient η_{1212} equal to 10, we obtain the shapes of Figure 6.49 , while for $\eta_{1212} = 50$ we get a stiffer structure, shown in Figure 6.50. For both cases the volume constraints are active at convergence.

Table 6.6: Homogenized coefficients for the optimized microstructure of Figure 6.50.

ijkl	A_{ijkl}^*	A_{ijkl}^T	ij	A_{ij}^{th*}	A_{ij}^{thT}
1212	0.0337	0.040	11	0.4413	0.400
			22	-0.2713	-0.400

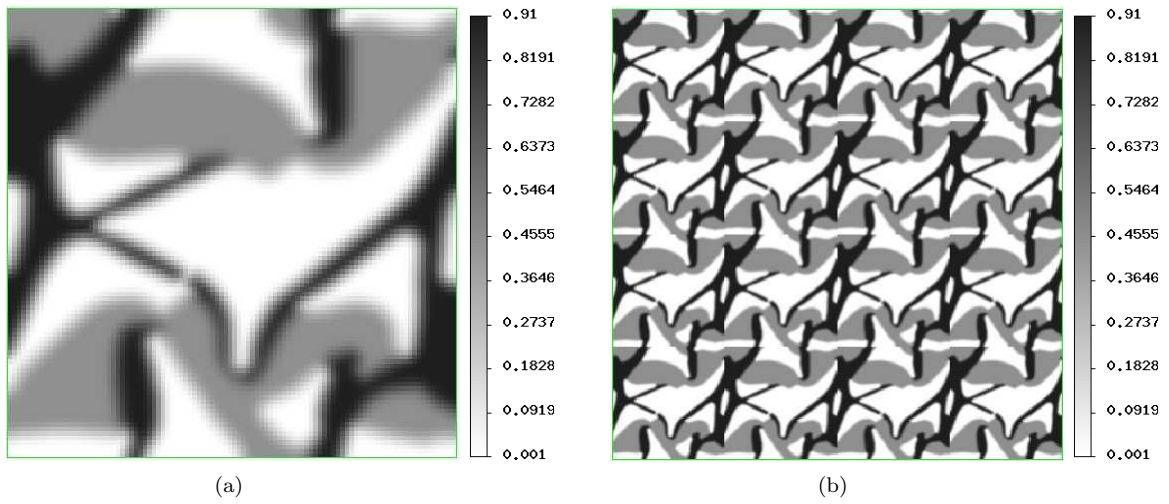


Figure 6.50: (a): Optimized unit cell and (b): optimized microstructure (16 unit cells), for Example 5 and $\eta_{1212} = 50$.

Conclusions and future work

Manufacturing constraints

The main conclusions from our work on manufacturing constraints, i.e. Chapter 3, 4 and 5 are presented in the sequel:

- We have proposed some novel formulations for the control of the thickness in the design domain, using the signed distance function to the shape. A simple augmented Lagrangian method has been implemented to enforce the constraints, which proved to be sufficient in most cases when few constraints are handled, albeit very slow to convergence in the majority of the examples tested.
- For the Maximum Thickness constraint, we have explained the inherent problem of distortions close to joints and to the design domain boundary and proposed a "volumetric" formula to reduce their effect. We have also discussed the discontinuity of the constraint with respect to topological changes and explained its possible impact on the optimization algorithm. Finally, we have proposed to apply this constraint since the beginning of the shape optimization problem.
- On the contrary, the Minimum Thickness constraint and the Minimum Members' Distance constraint are suggested to be applied at a second step, after the optimization problem has been solved without them. The computation of these constraints and of their shape derivative is quite difficult and we propose alternatively the use of several energy functionals.
- The results obtained for the thickness control are quite encouraging, especially when compared to those from existing commercial software.
- We have proposed a strategy to take into consideration constraints on the molding direction of cast parts. When no thickness constraints (or just the Maximum Thickness constraint) are applied, we believe that the method proposed by Xia et al. [159] is sufficient and very simple to implement. In case we also need to impose limitations on the minimum thickness or the minimal distance between members of the structure, we have proposed a two-step strategy. First, the optimization problem is solved without these two constraints and the method of Xia et al. is applied. Then, we add the constraints in the optimization problem and use some of the proposed generalized casting constraint.
- Alternatively to the Maximum Thickness constraint, we have proposed to treat the feedability specification via a thermal constraint. The complete casting system is neglected during the optimization part and much simpler thermal models, than the actual one simulating the solidification process, are tested at a first step. Despite the possible interest of this work in different mechanical frameworks, we believe that the results follow the same logic and present similar difficulties as the Maximum Thickness constraint, while they add on an extra difficulty due to the computation of the thermal problem. However, some of the simplified models we have presented, like the Poisson model, could possibly be interesting for other topology optimization methods.

Some future work on the above topics is proposed here:

- Since the number of constraints involved in industrial applications is quite large and the problems are computationally much more expensive compared to those presented in this work, more efficient optimization methods shall be tested and the global formulation of the constraints shall be adjusted accordingly. In the framework of the RODIN project, different methods of sequential linear programming are already being tested and the results are quite encouraging.
- The constraints shall be coded and tested for the case of an adapted mesh, which is expected to alleviate several numerical problems regarding the calculation of surface integrals, but also be more sensitive during the shape variations.

- Although several formulations have been proposed for the generalized casting constraint, only those based on the signed distance function have been tested, mainly due to their resemblance with the thickness constraints. However, they are very costly. We propose to test in the future the formulation using the normal vector, which is expected to be computationally more efficient and easier to be adjusted to other optimization methods.

Multi-phase optimization

Our analysis of multi-phase shape and topology optimization problems has led to the following remarks:

- The exact formula of the shape derivative for sharp-interface, multi-phase shape optimization problems is usually not properly approximated on a fixed mesh using continuous finite elements, since the jump in some components of the stress and strain tensor is not detected. In this case, derivating the discretized problem seems to give more accurate results.
- The sharp-interface problem can be approximated using a smooth-interface formulation, where the material properties are interpolated in a finite zone using smoothed Heaviside functions. The correct shape derivative for this formulation, based on the signed distance function, has been computed and it has been shown to converge to the original sharp-interface formula when the interpolation width tends to zero.
- The use of the exact shape derivative formula seems to have an impact on the optimized shapes when the width of the transmission zone augments, compared to the results obtained with the "approximate" formula, which is met in the previous literature. A good compromise between the two seems to be achieved by the "Jacobian-free" formula.
- The validity of the proposed method is proved by a variety of optimization problems on rigidity maximization, multi-functional design and material design using inverse homogenization.

As future work on the topic, we would suggest the following:

- It would be interesting to use the adapted-mesh technique, described in [44], for more than two phases and to compare the results using the exact shape derivative formula with those presented in Chapter 6.
- The topic of material design using inverse homogenization shall be further explored, since the accurate position of the phases in play using the level-set description seems to be very tempting for people from material science and industry.
- The correct shape derivative formula allows to work on the optimization of general functionally graded structures. In this case, some further ideas about optimizing the gradation type between different phases shall be developed.

Appendices

Appendix A

Material interface effects on the topology optimization of multi-phase structures

This appendix contains an article that we submitted for publication in the SMO (Structural and Multi-disciplinary Optimization) journal. It is a joint work with a team from the SIMaP laboratory (the Materials and Processes Science and Engineering Laboratory) of Joseph Fourier University in Grenoble, who were interested to apply the techniques described in Chapter 6 in order to study the effect of material interface properties on the optimal shape of structures composed by multiple phases.

Material Interface Effects on the Topology Optimization of Multi-Phase Structures Using A Level Set Method

Natasha Vermaak · Georgios Michailidis · Guillaume Parry · Rafael Estevez ·
Grégoire Allaire · Yves Bréchet

the date of receipt and acceptance should be inserted later

Abstract A level set method is used as a framework to study the effects of including material interface properties in the optimization of multi-phase elastic and thermoelastic structures. In contrast to previous approaches, the material properties do not have a discontinuous change across the interface that is often represented by a sharp geometric boundary between material regions. Instead, finite material interfaces with monotonic and non-monotonic property variations over a physically motivated interface zone are investigated. Numerical results are provided for several 2D problems including compliance and displacement minimization of structures

composed of two and three materials. The results highlight the design performance changes attributed to the presence of the continuously graded material interface properties.

Keywords shape optimization · graded interface · thermoelastic · elasticity · level set method · multi-material · multi-phase · topology

1 Introduction

Recent advances in the development of the level set method for topology optimization (Allaire et al 2013a) have enhanced the treatment of material interfaces, a key feature introduced in multi-phase models that is nevertheless typically ignored. The interfaces of interest are those of dissimilar materials (bi-material) or heterophase boundaries within the classification of solid or bulk interfaces. For this class of interfaces, lattice-parameter changes in the interfacial region, induced by interfacial stresses, may have a pronounced effect on the physical properties and chemical composition at or near the interface (Wolf 1992). The present work seeks to capitalize on these potential property differences. In a variety of fields material interfaces play a pivotal role in the performance of structures, often dictating tolerances and processing choices, lifetime and failure characteristics. Explicitly accounting for interfacial properties beyond a simple interpolation between bulk properties is necessary if one is to take full advantage of incorporating materials science input into optimal shape design methodologies.

The benefits of integrated engineering paradigms that allow simultaneous and cooperative feedback among advanced manufacturing methods and computational modeling – including optimization – have been recently recognized and broadly advised (Committee on Integrated Computational Materials Engineering 2008). Advances in precision and control of additive manufacturing now allow for consideration

Natasha Vermaak
SIMaP-Université de Grenoble, INPG, 1130 rue de la Piscine B.P. 75,
38402 St. Martin d'Hères Cedex, France
Tel.: +33-4-76826647
Fax: +33-4-76826644
E-mail: Natasha.Vermaak@simap.grenoble-inp.fr
Present address: of N. Vermaak: Lehigh University, Mechanical Engineering & Mechanics, 19 Memorial Drive West, Bethlehem, PA 18015-3085 USA
Tel.: +011-610-758-5693
Fax: +011-610-758-6224
E-mail: vermaak@lehigh.edu

Georgios Michailidis
Centre de Mathématiques appliquées (UMR 7641), École Polytechnique, 91128 Palaiseau, France

Guillaume Parry
SIMaP-Université de Grenoble, INPG, 1130 rue de la Piscine B.P. 75,
38402 St. Martin d'Hères Cedex, France

Rafael Estevez
SIMaP-Université de Grenoble, UMR 5266 CNRS / INPG / UJF, 1130 rue de la Piscine B.P. 75, 38402 St. Martin d'Hères Cedex, France

Grégoire Allaire
Centre de Mathématiques appliquées (UMR 7641), École Polytechnique, 91128 Palaiseau, France

Yves Bréchet
SIMaP-Université de Grenoble, INPG, 1130 rue de la Piscine B.P. 75,
38402 St. Martin d'Hères Cedex, France

of interface characteristics in structure and material design optimization. These advances include techniques such as: 3D printing, laser stereo-lithography and electron beam melting (Pasko et al 2011; Lipson and Pollack 2000; Ikuta and Hirowatari 1993; Harrysson et al 2008), along with characterization techniques at the interfacial level such as blister, wedge, and essential work of fracture tests (Braccini and Dupeux 2012). In the present work, only elastic and thermoelastic structural optimization will be considered but the application to material design is forthcoming.

Multi-phase topology optimization for problems of elastic and thermoelastic structures and materials design has been widely studied within the framework of the homogenization method (Allaire et al 1997; Bendsoe and Kikuchi 1988) and its variants, such as the Solid Isotropic Material Penalization (SIMP) method (Bendsoe and Sigmund 1999, 2004). This topic has also been explored (Wang et al 2004) using the level set method for shape and topology optimization (Allaire et al 2004; Wang et al 2003). The level set method was originally developed by Osher and Sethian (1988) for numerically tracking fronts and free boundaries. The level set method is extremely versatile, used in many fields including fluid mechanics and image processing, and is computationally very efficient. Previously, multi-phase or multi-material topology optimization of structures using the level set method has been performed for problems of compliance only (Allaire et al 2013a; Wang and Wang 2004) and thermoelastic structural problems have utilized only one material (and voids) (Xia and Wang 2008b; Laszcyk 2011).

The level set method has also been applied for optimization problems that incorporate concepts of functionally-graded materials and heterogeneous structures (Wang and Wang 2005; Xia and Wang 2008a). In Wang and Wang (2005), the interface between the different phases in a heterogeneous structure was considered to be a geometrically sharp boundary, but each of the phases was allowed to have graded properties. In contrast, the present work focuses on graded interfaces between isotropic bulk materials. In Wang and Wang (2005), polynomials were used to describe the gradation in properties within a material region and a sensitivity analysis was performed that considered the polynomial coefficients as parameters of the optimization problem. However, numerical results were presented only for piecewise constant materials. In Xia and Wang (2008a), the authors presented a method for the simultaneous optimization of the shape and of the material properties of a structure. They used the level set method for shape and topology optimization. Additionally, a density field was defined in the domain, to account for variation in the material properties, and its distribution was optimized solving the classic “variable thickness sheet” problem.

The enabling theory for the account of material interface effects in the level set methodology of topology opti-

mization has already been presented in a rigorous mathematical framework in Allaire et al (2013a) and will be summarized below. This theory allows the designer to replace the ideal and mathematically sharp material interface with a finite and physically meaningful interface transition zone. Previously, including Allaire et al (2013a), this transition zone has employed smoothly-monotonic Heaviside-type interpolation within the transition function. The present work, inspired by a similar choice in thermodynamic modeling presented by the ideal Gibbs interface and the Guggenheim model (Guggenheim 1959) (see Figure 1), seeks to take advantage of new design possibilities enabled by the interfacial transition zone. In particular, we investigate thermoelastic models and non-monotonic interpolations of the material properties within the transition zone, which were not considered in Allaire et al (2013a).

Interfaces between materials are not neutral: they result often from interdiffusion and reactions between two parent phases. For instance, the interface between two polymers may be the locus for chain reptation and entanglement. The interface between two different steels may lead to carbon diffusion and the creation, after quenching, of a martensitic layer or, conversely, a decarburized layer. The interface between copper and nickel (two elements with full miscibility) will lead to a solid solution. These examples show the variety of situations encompassed by the term “interface.” They also indicate that the properties of interest may not be an average of the bulk properties: in general, a martensitic layer has a yield stress higher than the yield stress of the bulk materials, and a decarburized layer has a lower yield stress. Additionally, the electrical and thermal conductivity of a solid solution is lower than that of the pure metals (such as copper and nickel). Therefore, using the interfacial properties as an input in the design of optimal structures requires the consideration of non-monotonic transition functions within the interface that exhibit maxima or minima with respect to the bulk material values.

Depending on processing and manufacturing conditions, finite interface zones with smooth monotonic and non-monotonic interface property transitions can be promoted. The engineering of these transition zones profits from the mature studies of functionally graded materials (Miyamoto et al 1999; Xia and Wang 2008a; Mello and Silva 2013) and advances in polymer science (Creton et al 2002) among many others. Non-smooth (not C-1 continuous) non-monotonic interface properties are also possible (Simar et al 2012), but the non-smoothness of such transitions poses an additional difficulty for the numerical fixed-mesh approximation and are thus not addressed herein. Nevertheless, the introduction of smooth non-monotonic transition functions over a finite interface zone allows for properties that differ, sometimes markedly, from that of the bulk materials alone.

The article is organized in the following way. First, the background and use of the level set approach for topological optimization is described. The description and influence of additional parameters related to interface properties are also introduced. In the second section, the optimization protocol is used on some benchmark problems in 2D under plane stress conditions. These problems involve the compliance minimization of multi-material elastic structures and also displacement minimization in thermoelastic structures. The restriction to 2D is without loss of generality as the ease of extension to 3D is one of the benefits of the level set method (Allaire et al 2004).

2 Topological optimization

There are many topology optimization methods that address the optimal distribution of materials in a fixed working domain in order to minimize an objective related to overall mechanical behavior or cost (Eschenauer and Olhoff 2001; Bendsoe and Sigmund 2004). For example, density approaches are based on a fixed mesh of the design domain, D (Figure 2), wherein a density field is defined. The objective function is evaluated by solving the physical equations with material properties that depend on the density field by following an interpolation scheme that specifies how, for example, the elastic modulus tensor varies from that of the constitutive material when the density value is 1, to zero when the density is 0. This material interpolation scheme may be fictitious, such as a power law used in SIMP method (Bendsoe and Sigmund 1999, 2004), or based on Hashin-Strickman bounds derived by the homogenization method (Bendsoe and Sigmund 1999). The optimization is then reduced to a functional optimization with respect to the density function, based on an analytical derivative. At the end of the optimization procedure, a composite solution is obtained with a density between 0 and 1. When composites are not desired, a penalization step is added in order to progressively eliminate the non-physical intermediate values of density. The main disadvantage of these density approaches is that the obtained optimized shape is strongly sensitive to the density interpolation scheme as well as the penalization method.

The level set method is a way to implicitly define the domain, Ω , on a fixed mesh of the design domain, D (Figure 2). The iterative optimization of the shape is done by advecting the level set function with a velocity field that is found through shape derivation (Allaire et al 2004; Wang et al 2003). The transport equation is usually a Hamilton-Jacobi equation (Sethian 1999). Physical equations are solved on the full design domain and voids or pores are mimicked with extremely weak material properties. Sometimes, a smoothed fictitious interface is introduced such as is done in phase field simulations (Wang and Zhou 2004; Zhou and Wang 2007). In 2D, when Hamilton-Jacobi equations are solved

using a Courant-Friedrichs-Lewy (CFL) time step restriction, only partial topological changes are allowed. The CFL condition or maximum principle asserts that the numerical waves should propagate at least as fast as the physical waves which ensures that the propagating front crosses no more than one element in one time step (Sethian 1999; Osher and Fedkiw 2002). Indeed, the maximum principle satisfied by this transport equation makes the nucleation of new material during advection impossible. Nevertheless, coarsening of existing inclusions and features can occur, enabling at least partial topological changes. Consequently, initialization of the domain is usually done so that there are a large number of material inclusions or voids. A remedy to this problem is the use of a topological derivative (Sokolowski and Zochowski 1999; Allaire et al 2005), but it is not included in this work. In the following, the level set method using a Hamilton-Jacobi transport equation is used for the optimization.

The feature common to these methods in their treatment of multiple materials is in their numerical approach to interface modeling. While an exact formulation of the optimization problem would require that disparate material properties be discontinuous at the interface between two materials, it is numerically challenging to incorporate this discontinuity. As an alternative to including this interface discontinuity, it is general practice to devise an appropriate numerical interpolation scheme to “smooth out” the problem. These material density interpolation schemes can be quite involved (Yin and Ananthasuresh 2002) and much work has been done in exploring their effects from a numerical standpoint (see (Allaire et al 2013a) for further discussion). Previously, to the best of the authors’ knowledge, only smooth and monotonic interpolation schemes have been employed at the interface. Furthermore, these schemes have been used with an emphasis on numerical application and the ability to penalize (when composites were not desired) fictitious “intermediate” properties or densities that had no physical meaning. The focus of the present work is the reinterpretation of the numerical short-cut of the “smoothed out” interface from a materials perspective that allows new functionality to be derived and exploited in topological optimization and design.

The new generalized level set topology optimization formulation developed in Allaire et al (2013a) extends the applicability of the method to account for the influence of finite interfaces. The focus of Allaire et al (2013a) is to explain why the shape derivatives used in the literature so far for multi-material problems are not correct in full mathematical rigor. They also provide the appropriate theorems for exact shape derivatives with finite interface zones between materials. Furthermore, they demonstrate how these converge to the shape derivatives for mathematically sharp interfaces when a regularized Heaviside function is used for the interpolation

scheme and when the interface zone thickness approaches zero. In the following, the application of the generalized finite material interface formulation will be presented in order to study the effects of including physically-motivated interface characteristics under both elastic and thermoelastic conditions.

2.1 Shape optimization of multi-phase structures in thermoelasticity

2.1.1 Setting of the problem

Without loss of generality, the case of two isotropic materials will be described with and without void. A typical case study is defined in which the objective is to optimize the distribution of two materials in a fixed working domain, D , in order to minimize a cost function related to the displacement field. In this work, we consider the maximization of the structure's stiffness by minimizing its total compliance (work done by the loads), as well as the minimization of a target displacement. The structure deforms under a load g applied to a part of its boundary and also due to thermal strain mismatch. The boundary of D is typically comprised of three disjoint parts such that $\partial D = \partial D_0 \cup \Gamma_D \cup \Gamma_N$, where Dirichlet boundary conditions are applied at Γ_D , homogeneous Neumann conditions at ∂D_0 and non-homogeneous Neumann conditions at Γ_N . Instead of a sharp interface between the two materials, an intermediate zone in which the material properties are interpolated is considered (Figure 3). The width of this zone and the interpolation functions for the material properties are described using the signed-distance function to the intermediate surface $\partial\Omega$ of the two materials. This surface is implicitly defined as the zero level set of a one dimension higher level set function ϕ and separates the domain into two subdomains Ω and $D \setminus \Omega$; where $D \setminus \Omega$ is the remaining subdomain defined by the absence of Ω from the full domain (Figure 2). The displacement u is the unique solution of the thermo-elasticity system

$$\begin{cases} -\operatorname{div}(A(d_\Omega)(e(u) - \alpha(d_\Omega)\Delta T)) = 0 & \text{in } D, \\ u = 0 & \text{on } \partial\Gamma_D, \\ (A(d_\Omega)(e(u) - \alpha(d_\Omega)\Delta T))n = 0 & \text{on } \partial D_0, \\ (A(d_\Omega)(e(u) - \alpha(d_\Omega)\Delta T))n = g & \text{on } \Gamma_N, \end{cases} \quad (1)$$

where ΔT is the fixed and constant change in temperature, A is the Hooke's tensor, α is the coefficient of thermal expansion (CTE) tensor and d_Ω is the signed-distance function to $\partial\Omega$. The explicit dependence of the coefficients A and α on the distance function d_Ω will be specified in sections 3.1 and 3.2.

The optimization problem reads

$$\begin{aligned} & \min_{\Omega \in \mathcal{U}_{ad}} J(u(\Omega)) \\ & \text{s.t.} \quad \int_{\Omega} dx = V_{tar}, \end{aligned} \quad (2)$$

where $u(\Omega)$ is the unique solution of eq. (1), \mathcal{U}_{ad} is a set of admissible shapes (requiring some smoothness), $J(u(\Omega))$ is the objective function and V_{tar} is the target volume for one of the materials occupying the domain Ω .

2.1.2 Shape derivative

In order to implement the above equality constraint, an augmented Lagrangian method, suitable for inequality constraints as well, was applied. Inequality constraints were also explored but are not presented herein; see (Rao 2009) for details regarding the augmented Lagrangian formulation for inequality constraints. The method of C  a (1986) is used for the formal calculation of the shape derivative. The Lagrangian reads

$$\begin{aligned} L(v, q, \mu) = & J(v) \\ & + \int_D -\operatorname{div}(A(d_\Omega)(e(v) - \alpha(d_\Omega)\Delta T)) \cdot q \, dx \\ & + \int_{\Gamma_D} \mu \cdot v \, ds \\ & + \int_{\partial D_0} A(d_\Omega)(e(v) - \alpha(d_\Omega)\Delta T)n \cdot q \, ds \\ & + \int_{\Gamma_N} (A(d_\Omega)(e(v) - \alpha(d_\Omega)\Delta T)n - g) \cdot q \, ds \\ & + \lambda a(\Omega) + \frac{r}{2} a(\Omega)^2, \end{aligned} \quad (3)$$

where λ, r are scalars to be updated at each iteration so that the volume constraint is satisfied at convergence; v, q, μ are vector-valued functions defined in D (independent of Ω) and

$$a(\Omega) = \int_{\Omega} dx - V_{tar}. \quad (4)$$

Taking the partial derivative of L with respect to q , in the direction ϕ , a given vector-valued function defined in D and equating it with zero at the optimal point u, p, μ^* , results in

$$\int_D -\operatorname{div}(A(d_\Omega)(e(u) - \alpha(d_\Omega)\Delta T)) \cdot \phi \, dx = 0, \quad (5)$$

$$\int_{\partial D_0} A(d_\Omega)(e(u) - \alpha(d_\Omega)\Delta T)n \cdot \phi \, ds = 0, \quad (6)$$

and

$$\int_{\Gamma_N} (A(d_\Omega)(e(u) - \alpha(d_\Omega)\Delta T)n - g) \cdot \phi \, ds = 0, \quad (7)$$

and thus

$$-\operatorname{div}(A(d_\Omega)(e(u) - \alpha(d_\Omega)\Delta T)) = 0 \quad \text{in } D, \quad (8)$$

$$A(d_\Omega)(e(u) - \alpha(d_\Omega)\Delta T)n = 0 \quad \text{on } \partial D_0, \quad (9)$$

and

$$A(d_\Omega)(e(u) - \alpha(d_\Omega)\Delta T)n = g \quad \text{on } \Gamma_N. \quad (10)$$

In the same way, the partial derivative of L with respect to μ results in

$$u = 0 \quad \text{on } \Gamma_D. \quad (11)$$

Eq. (8) - (11) show that u is indeed the unique solution of eq.(1). In order to calculate the adjoint state, the Lagrangian is written in the following form

$$\begin{aligned} L(v, q, \mu) = & J(v) \\ & + \int_D A(d_\Omega) e(v) e(q) dx \\ & - \int_D A(d_\Omega) \alpha(d_\Omega) \Delta T e(q) dx \\ & - \int_{\Gamma_D} A(d_\Omega) e(v) n q ds \\ & + \int_{\Gamma_D} A(d_\Omega) \alpha(d_\Omega) n \Delta T q ds \\ & - \int_{\Gamma_N} g \cdot q ds \\ & + \int_{\Gamma_D} \mu \cdot v ds + \lambda a(\Omega) \\ & + \frac{r}{2} a(\Omega)^2. \end{aligned} \quad (12)$$

Setting the partial derivative of L with respect to v in the direction ϕ equal to zero, at the optimal point

$$\begin{aligned} & J'(u(\Omega))(\phi) \\ & + \int_D A(d_\Omega) e(\phi) e(p) dx - \int_{\Gamma_D} A(d_\Omega) e(\phi) n \cdot p ds \\ & + \int_{\Gamma_D} \mu^* \cdot \phi ds = 0 \\ \Rightarrow & J'(u(\Omega))(\phi) \\ & + \int_D -\text{div}(A(d_\Omega) e(p)) \cdot \phi dx + \int_{\partial D_0} A(d_\Omega) e(p) n \cdot \phi ds \\ & + \int_{\Gamma_N} A(d_\Omega) e(p) n \cdot \phi ds \\ & + \int_{\Gamma_D} A(d_\Omega) e(p) n \cdot \phi ds - \int_{\Gamma_D} A(d_\Omega) e(\phi) n \cdot p ds + \int_{\Gamma_D} \mu^* \cdot \phi ds = 0. \end{aligned} \quad (13)$$

In the case of the compliance, $J(v)$ has the form

$$J(v) = \int_{\Gamma_N} g \cdot v ds + \int_D A(d_\Omega) \alpha(d_\Omega) \Delta T e(v) dx. \quad (14)$$

Therefore,

$$J'(v)(\phi) = \int_{\Gamma_N} g \cdot \phi ds + \int_D A(d_\Omega) \alpha(d_\Omega) \Delta T e(\phi) dx, \quad (15)$$

and the following equations are derived

$$\mu^* = -A(d_\Omega) e(p) n, \quad (16)$$

$$p = 0 \quad \text{on } \Gamma_D, \quad (17)$$

$$A(d_\Omega)(e(p) - \alpha(d_\Omega)\Delta T)n = -g \quad \text{on } \partial\Gamma_N, \quad (18)$$

$$A(d_\Omega)(e(p) - \alpha(d_\Omega)\Delta T)n = 0 \quad \text{on } \partial D_0, \quad (19)$$

$$-\text{div}(A(d_\Omega)(e(p) + \alpha(d_\Omega)\Delta T)) = 0 \quad \text{in } D. \quad (20)$$

Thus $p = -u$ and the problem is said to be self-adjoint.

In the case of minimizing the displacement at a target point x_{tar} , we can consider an objective function of the type

$$J(v) = \int_D \delta(x_{tar}) v^2 dx, \quad (21)$$

where $\delta(x_{tar})$ is a Dirac mass function concentrated at point x_{tar} . In this case,

$$J'(v)(\phi) = \int_D \delta(x_{tar}) 2v\phi dx \quad (22)$$

and the eq. (17 - 20) defining the adjoint state, now take the form

$$p = 0 \quad \text{on } \Gamma_D, \quad (23)$$

$$A(d_\Omega)(e(p) - \alpha(d_\Omega)\Delta T)n = 0 \quad \text{on } \Gamma_N \cup \partial D_0, \quad (24)$$

$$-\text{div}(A(d_\Omega)(e(p) + \alpha(d_\Omega)\Delta T)) = -\delta(x_{tar}) 2u \quad \text{in } D. \quad (25)$$

Finally, deforming the structure in the direction of a smooth vector field θ (see Allaire et al 2004 for details), the shape derivative of the objective function is found to be the shape derivative of the Lagrangian at the optimal point

$$J'(u(\Omega))(\theta) = L'(u, p, \mu^*)(\theta), \quad (26)$$

which, after some algebra, for the compliance case results in

$$J'(u(\Omega))(\theta) = \begin{cases} \int_D \frac{\partial d_\Omega}{\partial \Omega}(\theta) [2A'(d_\Omega) \alpha(d_\Omega) \Delta T e(u) \\ + 2A(d_\Omega) \alpha'(d_\Omega) \Delta T e(u) \\ - A'(d_\Omega) e(u) e(u)] dx \\ + \lambda \int_{\partial \Omega} \theta \cdot n ds \\ + r \left(\int_{\Omega} dx - V_{tar} \right) \int_{\partial \Omega} \theta \cdot n ds, \end{cases} \quad (27)$$

while for the displacement case, it takes the form

$$J'(u(\Omega))(\theta) = \begin{cases} \int_D \frac{\partial d_\Omega}{\partial \Omega}(\theta) [A'(d_\Omega)(e(u) - \alpha(d_\Omega)\Delta T)e(p) \\ - A(d_\Omega)\alpha'(d_\Omega)\Delta T e(p)] dx \\ + \lambda \int_{\partial\Omega} \theta \cdot n ds \\ + r \left(\int_\Omega dx - V_{tar} \right) \int_{\partial\Omega} \theta \cdot n ds. \end{cases} \quad (28)$$

The shape derivative of the signed-distance function has been discussed in detail in Allaire et al (2013a). The Eulerian derivative of d_Ω was found to be

$$\frac{\partial d_\Omega}{\partial \Omega}(\theta)(x) = -\theta(p_{\partial\Omega}(x)) \cdot n(p_{\partial\Omega}(x)) \quad \text{for any point } x \in D, \quad (29)$$

where $p_{\partial\Omega}(x)$ denotes the orthogonal projection of x on the boundary of Ω .

Substituting (29) in (27) and (28) does not directly provide an explicit descent direction, i.e., a vector field, θ , along which the interface $\partial\Omega$ should be moved. Instead, a coarea formula is used to obtain the standard form of the shape derivative (Allaire et al 2013a):

$$J'(u(\Omega))(\theta) = \int_{\partial\Omega} \theta(s) \cdot n(s) j'(\Omega)(s) ds, \quad (30)$$

which gives a descent direction using $\theta(s) = -j'(\Omega)(s)n(s)$.

This form of the shape derivative provides a descent direction only on the interface $\partial\Omega$, which is limiting from a numerical point of view. Therefore, an additional step is added to extend and regularize the shape derivative to the whole working domain D (see (Allaire et al 2004, 2013a)). The shape transformation occurs through the transport of a level set function via a Hamilton-Jacobi equation (Allaire et al 2004).

A corresponding optimization algorithm has been implemented in Scilab (Version 5.3.3) (Scilab Enterprises 2012), a software for numerical computation, and is as follows:

Algorithm for 2D shape optimization under an area equality constraint.

1. Initialize the level set function to obtain a starting geometry and area fraction.
2. While the maximum number of iterations is not reached:
 - (a) Evaluate the objective function and shape derivative.
 - (b) Deform the shape by transporting the level set function with the Hamilton-Jacobi equation. The equation is solved on a time step dt and for a normal velocity $V = -j'(\Omega)$.
 - (c) Update the Lagrange coefficient based on its previous value and the previous constraint errors.

- (d) Reinitialize the level set function to the signed distance function. This improves the conditioning for the Hamilton-Jacobi equation while keeping the same zero contour or level line.

3 Results of Numerical Examples

In this section, several examples of topology optimization with two isotropic materials A , B (Figure 3) or two materials and void are presented. They illustrate the benefits of optimization schemes that account for features at the interfacial level that are either by design or unavoidable and are derived from the fabrication and manufacturing processes when multiple materials are involved. The objective or cost functional is, in the first examples, the minimization of the compliance or work done by the loads. Elastic structures comprised of two materials are presented, followed by elastic structures with two materials and void. Finally, a two-material thermoelastic case is also discussed.

In order to better visualize trends for the bi-material cases, equality constraints on the lower modulus or higher CTE bulk material are imposed (50% of the domain). Note that this constraint is not necessarily arbitrary. It can, for example, be beneficial when use of a less expensive material with inferior properties is desired. Additional constraints that are specific to individual manufacturing processes are not included in this initial 2D study. Further work in 3D could include for example, constraints based on thermal stress induced warping that occurs in some types of 3D printing processes.

In all of the strictly two material cases, unless otherwise noted, the following parameters were used in obtaining the results. Poisson's ratio was kept constant at 0.3. The applied point-load force was normalized to unity ($g = 1$) and a normalized Young's modulus $E_A = 1$ was used. These normalized parameters were used without loss of generality because the problem is within the domain of linear elasticity. Moreover, these non-dimensional properties remain representative for a variety of engineering applications. The inelastic strain ($\alpha\Delta T$), resulted from a distributed load provided by a uniform thermal excursion (ΔT). Although the inelastic strain is presented as originating from thermal expansion, it is also analogous to swelling in problems of soft materials like some polymers or biological materials. Thus interpretation of the thermoelastic results below is not restricted to thermal effects.

Two loading conditions were considered. The first kind of problem was purely mechanical with a point-load force (no thermal excursion) (Figures 5 and 10). The second kind of problem involved only distributed or bulk force loading via a uniform thermal excursion (Figure 14, $\Delta T = 1$). These numerical tests with point loads or uniform bulk force loading were chosen in order to comply with the usual bench-

mark problems. However considering more realistic distributed loads is no more difficult than point loads, but will be the topic of future work for more specialized applications.

Typically, at least 400 optimization iterations were performed to ensure convergence in the optimization process. For the cases shown in Figures 5 and 14, symmetry was employed such that only one-half of the numerical domain was needed. A variety of mesh densities were investigated for the finite element analysis and results are presented with a fine mesh (150 elements in the x_1 -direction and 150 elements in the x_2 -direction, Figure 5). This mesh choice is also informed by mesh sensitivity studies performed elsewhere (Allaire et al 2013a). The magnitude of the interface zone thickness has been kept constant by setting $\varepsilon = 4dx$, where ε is half of the total interface zone thickness and dx is the element size (Figure 3).

Most cases in the following sections were initialized with inclusions of material B distributed within a matrix of material A. This choice of initialization is typical for topology optimization by the level set method because there is usually no independent material nucleation mechanism included in the algorithm (section 2.1.2). Nevertheless, the present algorithm is still capable of topology optimization: inclusions may still pinch off, merge, or morph, to create topological changes in 2D (Allaire et al 2004).

3.1 Using monotonically graded interfaces

The Young's modulus, E , and CTE, α , were smoothly interpolated (C-1 continuous) between bulk values: E_A and E_B ; α_A and α_B . For example, in the case of the Young's Modulus, the variation of E across an interface was prescribed by:

$$E = E_A + h_{int}^{mono}(E_B - E_A). \quad (31)$$

The monotonic interpolation scheme, h_{int}^{mono} , used was that proposed by Osher and Fedkiw (2002):

$$h_{int}^{mono} = \begin{cases} 0, & \text{if } d_\Omega < -\varepsilon \\ \frac{1}{2} + \frac{d_\Omega}{2\varepsilon} + \frac{1}{2\pi} \sin \frac{\pi d_\Omega}{\varepsilon}, & \text{if } |d_\Omega| < \varepsilon \\ 1, & \text{if } d_\Omega > \varepsilon, \end{cases} \quad (32)$$

where the signed-distance function, d_Ω , instead of the level set function, ϕ , was used for the advection of the shape.

3.2 Using non-monotonically graded interfaces

For non-monotonic interface interpolation, a 6th-order polynomial was employed whose coefficients were determined by imposed constraints. At the borders of the interface zone

($d_\Omega = \pm\varepsilon$), the bulk material properties must be recovered, i.e. E_A or E_B , α_A or α_B . Moreover, the material property distributions must be C-1 continuous, so that the first derivatives at the interface zone boundaries ($d_\Omega = \pm\varepsilon$, Figure 3), were also required to be zero. Two coefficients and two boundary conditions remain. As the interpolation is non-monotonic, the presence of an intermediate maximum or minimum in the interpolation function is assumed. Presently, the location of this maximum or minimum is fixed to be at $d_\Omega = 0$, Figure 3. It is worth noting that this non-monotonically graded interface interpolation scheme would not be tractable using previous formulations of the shape derivative because those previous formulations depend only on the value of the interpolation derivative at $d_\Omega = 0$, which is zero in this case.

For an intermediate maximum at $d_\Omega = 0$, the property value, P , is $P_{d_\Omega=0} = mval * (\max(P_A, P_B))$ and similarly for an intermediate minimum at $d_\Omega = 0$, the property value, P , is $P_{d_\Omega=0} = mval * (\min(P_A, P_B))$. Where $mval$ is the multiplying factor that determines the nature of the interface zone transition between the bulk properties P_A and P_B (Figure 3). The final coefficient is solved for by requiring that the first derivative at the location of the intermediate maximum or minimum is also zero. For example, in the case of the Young's Modulus ($P = E$), the variation of E across the interfacial interpolation zone, between the bulk values of E_A, E_B , was:

$$E = h_0 + E_A h_1 + E_B h_2, \quad (33)$$

where

$$h_0 = \begin{cases} 0, & \text{if } d_\Omega < -\varepsilon \\ mval - d_\Omega^2 \left(\frac{2mval}{\varepsilon^2} - \frac{mval d_\Omega^2}{\varepsilon^4} \right), & \text{if } |d_\Omega| < \varepsilon \\ 0, & \text{if } d_\Omega > \varepsilon. \end{cases} \quad (34)$$

and

$$h_1 = \begin{cases} 1, & \text{if } d_\Omega < -\varepsilon \\ -d_\Omega^2 \left(d_\Omega \left(\frac{5}{4\varepsilon^3} - d_\Omega \left(\frac{3d_\Omega}{4\varepsilon^3} - \frac{1}{2\varepsilon^4} \right) \right) - \frac{1}{\varepsilon^2} \right), & \text{if } |d_\Omega| < \varepsilon \\ 0, & \text{if } d_\Omega > \varepsilon. \end{cases} \quad (35)$$

and

$$h_2 = \begin{cases} 0, & \text{if } d_\Omega < -\varepsilon \\ d_\Omega^2 \left(d_\Omega \left(\frac{5}{4\varepsilon^3} - d_\Omega \left(\frac{3d_\Omega}{4\varepsilon^3} + \frac{1}{2\varepsilon^4} \right) \right) + \frac{1}{\varepsilon^2} \right), & \text{if } |d_\Omega| < \varepsilon \\ 1, & \text{if } d_\Omega > \varepsilon. \end{cases} \quad (36)$$

By taking account of material interface characteristics, the number of potential design parameters has significantly

increased to include the thickness of the interfacial zone and six possible profiles for each of the properties E and CTE . These include: monotonically decreasing or increasing cases, and non-monotonically decreasing or increasing with an intermediate global maximum or minimum in the property values. In purely mechanical analyses, some of these aforementioned cases are redundant, but for thermoelastic analyses they remain relevant. Intermediate maximums or minimums that fall within the bounding values of the bulk properties are not of interest in this study.

However, not all of the possible combinations of monotonic and non-monotonic transition functions are physical, nor are they strictly independent. For example, typically, natural and man-made materials follow an anti-correlated relationship between Young's modulus and CTE due to interatomic energy considerations. Consequently, a material with high Young's modulus usually has lower values of CTE (Figure 4 and see also for example, CES EduPack (Limited 2010)). Positively correlated relationships do exist, but are much more restrictive and are not considered herein. The thickness of the interfacial zone is also not strictly independent of the material choices, but it is treated as such for the purposes of this study due to the highly tunable nature of this parameter using heat treatments and innovative processing techniques.

3.2.1 Two-material elastic structure

The first example is a structure with a domain ratio of 2:1 that is fully clamped at both the right and left edges while being loaded vertically ($g = -1$) at the mid-point of the bottom edge (Figure 5). The normalized domain size parameters are thus $h = 1$ and $w = 2$. This structure remains uniformly at its reference temperature, such that the thermoelastic formulation simplifies to the classic mechanical-only compliance problem. Two materials (A-blue, B-yellow) are assumed with a ratio of 10:1 for the Young's modulus (material A has a higher E). The problem includes an equality volume constraint ($V_{tar} = 0.5|D|$) on the lower modulus material-B using an augmented Lagrangian formulation. The half-domain is discretized on a fixed Eulerian grid with 150×150 quadrilateral elements (employing symmetry).

Analyses with two different property profiles were conducted. In the first case Figures 6, 6(a), a monotonic transition across the graded material interface is used. This case was initialized with inclusions of material B distributed within a matrix of material A as shown in Figure 6(c), "Iteration 1." Figure 6(c) also displays some intermediate results during the optimization iterations and the final design on the full domain is shown in Figure 6(b).

In the second case, a non-monotonic transition was used that included an intermediate maximum such that the interface Young's modulus at $d_\Omega = 0$ (Figures 3, 7(a)) was

two times greater than the larger bulk material modulus). This case was initialized (see Figure 7(c), "Iteration 1") using the solution from the previous monotonic result (Figure 6(b)). Initializing from the previous final design, the properties within the interface width are reinterpreted using the non-monotonic scheme and the level set based optimization is able to improve upon the design, lowering the objective function (Table 1, see equation 14).

Initializing the optimization with the previous solution allows direct comparison of the results, but can also be a restriction on the optimization as currently, the topological derivative is not included in the analysis. Without the topological derivative, nucleation of material A or B, is not possible. Nevertheless, significant topological changes can be made through the possibility of merging. As such, a third example (Figure 8) with the same non-monotonic transition scheme is presented (Figure 8(a)). The third example returns to the initialization scheme used in Figure 6(c) and follows the same approach. The final design (Figure 8(b)) is significantly different from the previous result in Figure 7(b).

To illustrate the design's further dependence on the interface property profile choice, a non-monotonic transition with a larger magnitude in its variation is introduced in Figure 9. In this case, the non-monotonic transition includes an intermediate maximum such that the interface Young's modulus at $d_\Omega = 0$ is five times greater than the larger bulk material modulus, Figure 9(a). All four results are compared in Table 1. Table 1 also shows the objective and volume constraint convergence histories for each case. These histories illustrate the reductions in compliance attributed to the changing shape and topology while showing how closely the volume constraint is respected. All of the non-monotonic schemes improve on the objective function defined as the minimization of the compliance of the structure. The more non-monotone the interface is, the more complex is the optimal topology since the interface zone has a higher Young's modulus than either of the bulk materials. Initializing from the monotonic solution yields a 29% reduction and initializing with same inclusion scheme as the monotonic-transition case yields a 35% reduction in the structural compliance. Enhancing the interface property disparity even further ($5 \times \max(E_A, E_B)$) yields a 69% reduction in the objective compliance.

3.2.2 Elastic structure with two materials and void

Next, the classic short-cantilever problem (Wang and Wang 2004) of compliance minimization that yields a two-bar frame is considered (Figure 10). The design domain consists of a rectangular area with the normalized size parameters $h = 1$ and $w = 2$. A normalized vertical load of value $g = -1$ is applied at the middle of the right edge and the boundary is fixed ($u_1 = u_2 = 0$) on the left edge. There is no thermal load applied to this structure so that comparison with the classic

analytical optimum-topology solution of two beams at an angle of 45° that supports the applied load can be made. The two materials assumed have a ratio of 2:1 for the Young's modulus and the same Poisson's ratio ($\nu = 0.3$). The problem includes equality constraints on the volume of each of the materials using an augmented Lagrangian formulation. The volume constraints are 10% and 20% of the domain for the higher and lower modulus materials, respectively, as was done in Wang and Wang (2004). The full design domain is discretized on a fixed Eulerian grid with 80×160 quadrilateral elements.

Two level set functions are employed. Their combination can describe up to four distinct phases. In this case, the level sets represent two material phases: material A (higher E_A) and material B (lower E_B), and two phases of void. The external interfaces between material and void are treated with a fixed width; the same width is enforced between the internal material interfaces ($\varepsilon = 2dx$). This width is considered "thin" or "sharp" in comparison with the thicker material interface results presented in section 3.2.1, in order to correspond more closely with the work presented in Wang and Wang (2004). The phases representing void are modeled using the traditional ersatz material approach with an extremely weak normalized Young's modulus ($E_{void} = 0.001$).

Analyses with two different property profiles were conducted (Figures 11 - 13). In all cases contours of the Young's modulus are shown in greyscale in the results. In the first case, a monotonic transition across the "sharp" material interface is employed, Figure 11(a). This case was initialized with distributed voids or pores in the initial design as shown in Figure 11(c) "Iteration 1", with the rest of the domain consisting of the first and second materials. Figure 11(c) also displays some intermediate results during the optimization and the final design is shown in Figure 11(b).

In the second case (Figure 12), a non-monotonic transition was used that included an intermediate maximum such that the interface Young's modulus at $d_\Omega = 0$ was two times greater than the larger bulk material modulus, Figure 12(a). This case was initialized (Figure 12(c), "Iteration 1") using the solution from the previous monotonic result (Figure 11(b)). Using this initialization, the properties within the interface width are reinterpreted using the non-monotonic scheme and the level set based optimization is able to improve upon the design, lowering the objective compliance function (Table 2, see equation 14).

As before, initializing the optimization with the previous solution can be a restriction on the optimization and a third example (Figure 13) is presented. This example has the same non-monotonic transition scheme, Figure 13(a), as Figure 12(a). The example in Figure 13, returns to the initialization scheme used in Figure 11(c) and follows the same approach. All three results are compared in Table 2 where it is seen that both of the non-monotonic schemes improve on

the objective function: initializing from the monotonic solution yields a 24% reduction and initializing with the same shape as the monotonic design yields a 28% reduction in the objective compliance function. Table 2 also presents the objective function and volume constraint on material-A convergence histories for each case. The volume constraint on material-B has similar convergence and is not shown.

3.2.3 Two materials in a thermoelastic structure

As previously in section 3.2.1, the built-in beam with two materials and without void is chosen as the configuration for study. This problem is related to that studied in Xia and Wang (2008b). A normalized and uniform Young's modulus $E_A = E_B = 1$ is used. The contrast in CTE is $\alpha_A / \alpha_B = 2/3$, where α_A and α_B are proportional to the identity tensor. A uniform thermal excursion of $\Delta T = 1$ is imposed (Figure 14) and the objective function is altered to minimize the vertical (x_2 -direction) displacement at the point of interest in Figure 14 (see eq.21). The normalized domain size parameters are again $h = 1$ and $w = 2$. The volume constraint on the larger CTE material-B is 50% of the domain. The other parameters are unchanged and the optimization results are shown in Figures 15 - 18.

In the first case (Figure 15), a monotonic interface transition is considered. The final design in Figure 15(c) resembles a checkerboard pattern which may be intuitive as an arrangement of the materials that minimizes vertical displacement in Figure 14. To check this intuition, a second case with monotonic property transition was also conducted and is shown in Figure 16. This case was initialized with an idealized checkerboard pattern and it is seen that both the initialization from the regular array of inclusions and this case evolve towards a biased checkerboard final design (Figures 15(c), 16(c)).

In Figure 17, the non-monotonic transition included an intermediate maximum in the CTE such that the interface CTE at $d_\Omega = 0$ was two times greater than the smaller bulk CTE and the Young's modulus remained uniform across the bi-material interface (Figures 17(a), 17(b)). This case was initialized (see "Iteration 1" in Figure 16(d)) using the solution from the previous monotonic result (Figure 15(c)).

In the last case, Figure 18, the non-monotonic transition scheme from Figures 17(a), 17(b) is utilized. Figure 18 returns to the initialization scheme used in Figure 15(d) and follows the same approach. All four results are compared in Table 3 where it is seen that only one of the non-monotonic results (rows 3 and 4) is able to improve on the final objective function values compared to the monotonic transition results (rows 1 and 2). When initializing from the monotonic solution, the monotonic final design is reinterpreted with the non-monotonic material properties and the resulting *initial* objective function value: the value at "Iteration 1", in row 3

of Table 3 is higher than the final objective value in row 1 of Table 3. As a result, although further iterations allow the objective function value to slightly decrease, the converged final design objective function value (last column in row 3 of Table 3) remains larger than the monotonic case's final objective function value (last column in row 1 of Table 3) by 6 %. When the non-monotonic initialization scheme uses the array of inclusions ("Iteration 1" in Figure 18(d)), more topological changes are allowed and the non-monotonic solution is able to provide a 17% decrease in the final objective function value, comparing rows 1 and 4.

4 Discussion

The interface between bulk materials is explicitly accounted for in the shape optimization problem outlined above via the level set method. In these first examples, isotropic bulk materials are considered, but extension to anisotropic properties or graded material regions as was done in Wang and Wang (2005) is also of interest. Several features related to the influence of the graded properties across the interface zone alone (Figure 3) are highlighted below.

4.1 Sensitivity to interface interpolation scheme

As evidenced in the results above (Tables 1 - 3), the material interface zone interpolation scheme can significantly impact the efficacy of the design. Certainly for the elastic compliance and thermoelastic displacement problems investigated herein, the results are highly sensitive to initialization – as is commonly the case in optimization methods (Allaire et al 2004). Sometimes, as in the case of one material and void problems of elastic compliance, a global optimum seems to be more easily established. Nevertheless, significant gains can be attained by taking more detailed account of interface characteristics in the optimization protocol. Alternatively, more conservative or realistic designs could also be found if the interface properties were considered deleterious in the design.

In the purely elastic compliance problems of Figures 6, 11, the monotonic treatment strongly resembles the classic one material and void result (Allaire et al 2004; Wang and Wang 2004). This is to be expected because the lower modulus material simply replaces the void in the design. When non-monotonic transitions are employed that favor the interface (as the Young's modulus within the interfacial zone is twice that of the higher modulus material A), the optimal designs feature curved and sometimes tortuous interface trajectories that increase the interface perimeter while respecting the volume constraint. It should be noted that, in cases where the interface is clearly preferred (higher modulus in

this problem), optimizing without the volume constraint produces designs in which the interface practically replaces the formerly strongest "bulk" material. As the interface thickness is fixed, designs in which one element of material A and material B are present only by definition, produce a worm-wood type structure that is neither physical nor illuminating, and are not presented herein.

In Figure 7, the final design differs very little from the initialization. Recall this is the restrictive case as nucleation of material is not accounted for in the formulation of the problem. When initializing from the monotonic solution, small changes in the design (note the scale of the volume convergence diagrams in Table 1) cause significant reductions in the objective function and slightly curving the features compared to the monotonic design suffices to allow the optimization to converge to a local optimum and a 29% compliance reduction (Table 1).

Initializing from the less restrictive array of inclusions in Figure 8 allows a greater reduction in compliance with a significantly different final design. Cuboidal features with curved edges predominate. A slight resemblance to the monotonic final design (Figure 6(b)) can still be found in that the higher modulus material is present along the 45° line of force with a secondary support emanating from the bottom left corner at an angle of 45°. The smallest features are present at the point of loading which means that the interface is favored at this location.

By enhancing the favorable interfacial properties (Figure 9), the propensity to promote curving trajectories that maximize the presence of the interface is revealed. Recall that the volume of the lower modulus material-B is always constrained to be 50 % of the design domain. In this case, a dog-bone-like structure is present, reminiscent of the theory of the equilibrium shape of crystals detailed by Wulff (Wulff 1901). Wulff's theory showed that the distance from a common center of a small crystallite to any given surface facet is proportional to the surface free energy of the facet. Here, surface free energy is not explicitly included, but the interface stiffness properties are significantly higher than either of the bulk material modulus in a compliance minimization problem; a situation analogous to a theoretical crystallite transforming with low surface free energy. The optimal design follows a single orientation along the 45° line of force and the features comprised of material B (the lower modulus bulk material) remain of relatively uniform size, increasing the perimeter of the interface. Again the smallest features are found at the point of application of the load.

Similar trends are found in the case of the short-cantilever (Figures 10–13). For ease of presentation, all results in these figures utilizing two materials and void show the distribution of Young's modulus in greyscale instead of the distribution of materials in color. The monotonic case, Figure 11, results in the classic two-bar Michell-like structure (Michell

1904). The higher modulus material is more prevalent in the area where the load is applied (medium grey in Figure 11(b)). When initializing from the monotonic solution, Figure 12(c) “Iteration 1”, minor changes in the design result in substantial decreases in the objective function value (Table 2), promoting little difference in the shape of the final design (Figures 12(b), 12(c)). The orientation of the beams is preserved and the interface with its favorable properties is promoted towards the outer edges of the beams. In this final design (Figure 12(b)), regions of the higher modulus material align such that sections of the interface line up along the 45° line of force and the interface perimeter is in general increased within the beams. The non-uniform beam thickness is promoted by the unequal volume constraints applied on the higher and lower modulus materials. By initializing from the array of voids (Figure 13(c)) and enabling greater flexibility in favoring the interface, a more distributed design results that lowers the objective by 28% (Table 2).

Finally, introducing the volumetric thermal loads in Figures 14 – 18, introduces the opportunity for more complex conditions that are less intuitive. In order to start simply, the Young’s modulus was assumed to be uniform for both materials and across the bi-material interface. A uniform thermal excursion $\Delta T = 1$ was imposed and the vertical (x_2) displacement at the point of interest, displayed in Figure 14, was minimized.

For the monotonic case, material A (blue) with the lowest *CTE* is clearly preferred at the point of interest where vertical displacement (in the x_2 -direction in Figure 14) is not desired. The final design, Figure 15(c), resembles a checkerboard arrangement of the two materials. The checkerboard pattern is an intuitive measure against vertical global displacement. However, the idealized checkerboard (“Iteration 1” in Figure 16(d)), results in horizontal isocontours of displacement in the x_2 -direction (Figure 14). When the checkerboard pattern is slightly biased, as is seen in the final designs in Figures 15(c) and 16(c), the displacement at the point of interest is decreased.

The most effective design is found using the non-monotonic interface transition profile. When initializing from the monotonic solution (Figure 17(d) “Iteration 1”, see also Figure 15(c)), no topological changes are made and very little benefit in decreasing the objective function value is derived (Table 3). However, when initializing from the array of inclusions (Figure 18(d) “Iteration 1”), many topological changes occur that enable a 17% reduction in the objective function value (comparing the last columns in rows 1 and 4 of Table 3). This is not intuitive as the interface has the largest *CTE* in the design domain. Instead of limited use of interfaces in the domain, the design features many oriented “fibers” of the interface at the corners and opposite the point of interest in Figure 18(c). While these interface “fibers” seemingly violate the assumption of the disparity of scales between the

interface and the bulk materials, the results demonstrate the trend and more discussion on this point follows.

4.2 On the interface parameters

In contrast to previous level set topology optimization formulations, the interface zone width, ϵ (Figure 3), is physically motivated and is not restricted to a convenient numerical approximation. Thus, the interface zone width introduces a length scale into the optimization problem. Nevertheless, final designs may be considered size-independent, provided everything, including the interface, is scaled uniformly.

However, changing only the interface zone width in the optimization formulation can affect the final optimized designs. Its influence is generally negligible when the dimensions of the optimized structure are much larger than *epsilon* (see Figures 6(b), 15(c), 16(c), 17(c)). Its influence becomes more important when the interface zone width approaches the same magnitude as the “bulk” material features in the design (see Figures 7(b), 8(b), 9(b), 12(b), and 13(b) near the application of the point load or see the corners in Figure 18(c)). The magnitude of the interface zone thickness (Figure 3) has been kept constant: the length of 8 elements ($\epsilon = 4dx$) for Figures 6 – 9 and 15 – 18, and the length of 4 elements ($\epsilon = 2dx$) for Figures 11 – 13.

The fact that the interface zone thickness is fixed is a numerical restriction. It is not yet possible to continuously vary the width of the interface zone within the same design for the level set optimization framework. This restriction can be partially circumvented by parametrically varying the thickness value to explore its effects.

Nevertheless, the interface thickness must also be sufficiently large compared to element size in order to adequately capture the non-monotonic nature of the property variations. Recall that a polynomial dictates the values at the elemental nodes within the interface region; this provides an estimate on the lower bound. At the other extreme, the interface region is typically energetically limited to approximately 10% of the smallest feature of a design. As such, the interface does not saturate the design or become sandwiched between material features of comparable thickness to, or smaller thickness than, the interface zone. This final point, that all design features must remain at least 10 times greater in dimension than the fixed interface thickness, is a geometric constraint that is numerically difficult to directly implement. Indirectly, the requirement can be approximated by including interface perimeter penalization within the objective function. For the present work, neither approach is utilized and the unencumbered designs are presented to better illustrate the trends in interface effects. These trends may also be used to inspire more manufacturable manual interpretations of the final design as was done in Sigmund (2000).

Accounting for *epsilon* as a length scale determines how refined the discretization needs to be and is likely to prevent mesh-dependencies in the optimization results. Moreover, we propose that future work decouples the definition of the interface interpolation zone width, ϵ , from the definition of the uniform grid mesh size. Instead, adaptive (non-uniform) mesh methods such as those found in Allaire et al (2013b) could be employed that would also allow a more detailed study of the influence of the interface zone thickness. Regardless of the meshing techniques, the fixed interface thickness distinguishes the effects of including interface characteristics from simply adding another bulk material. The interface is, by definition, sandwiched between materials A and B, whereas an additional bulk material, C, could be isolated within material A or B without contact to the remaining bulk material.

5 Conclusions

The influence of the interface between disparate bulk materials on the optimal design of elastic and thermoelastic structures has been investigated. The methodology employs a recent formulation that accounts for a finite interface zone in a shape optimization framework (Allaire et al 2004). The description is extended to include a physically-motivated interface thickness with graded properties that can be monotonically varying between bulk materials but also non-monotonically varying with local properties that are larger or smaller than either of the bulk properties alone. Examples of these types of interface transitions, commonly found in materials science and biological materials, are given. The motivation of the present study is to highlight the importance of interface properties in optimal design and to direct the development of design tools that capitalize on advanced manufacturing capabilities. Two cases are presented: an elastic problem in which the compliance is minimized for a given point load and a thermoelastic case in which the displacement at a point of interest is minimized. An additional reference case, consisting in the minimization of the compliance of a short-cantilever beam, is also reported for comparison with similar shape optimization formulations found in Wang and Wang (2004). The main results are:

- Interface properties can be explicitly accounted for in shape optimization formulations. The interface thickness incorporates a physically motivated length scale into the problem formulation.
- The effect of interface properties depends both on the type of loading and boundary conditions of the problem considered, and on the transition profile relative to the bulk properties. The interface transition profiles identified are not restricted to an interval bounded by the sur-

rounding bulk values but can be larger or smaller in magnitude.

- Accounting for interface properties can significantly improve the optimization results.
- The present formulation can be used to probe the influence of the interface characteristics in structures, but also to direct the development and processing of new materials, and in particular, bio-inspired materials. This is the aim of forthcoming studies.

Acknowledgements This work was supported by The Centre of Excellence of Multifunctional Architected Materials sponsored by the French National Research Agency (LABEX CEMAM) and the French Ministry of Higher Education through the French University Institute (IUF) program. G. A. is a member of the Détermination de Formes et Identification (DEFI) project at INRIA Saclay Ile-de-France.

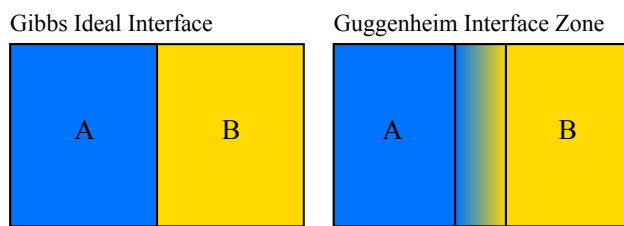


Fig. 1: Classic models for material interfaces: Gibbs ideal sharp interface (left) and Guggenheim smooth or graded interface zone (right).

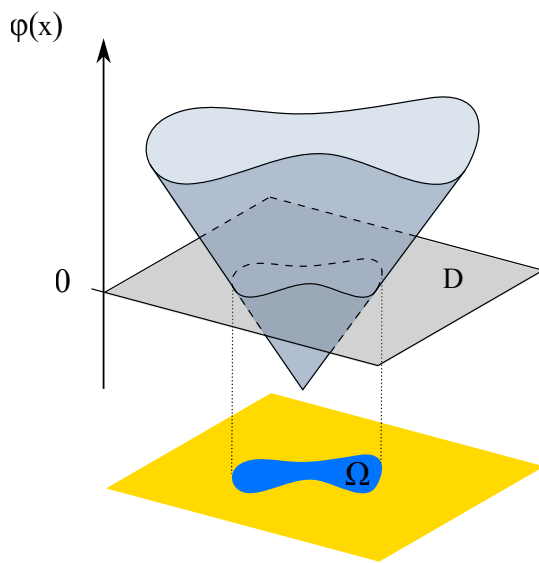


Fig. 2: Schematic level set function, $\phi(x)$, and the corresponding domain, Ω .

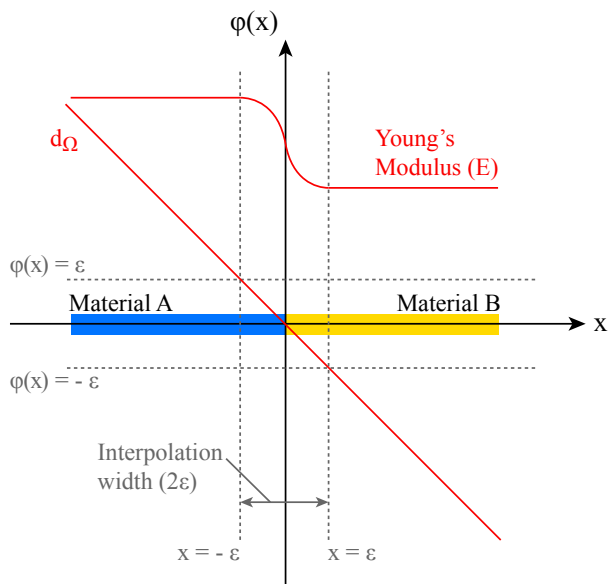


Fig. 3: Numerical approach to model material interfaces with varying properties across the interface.

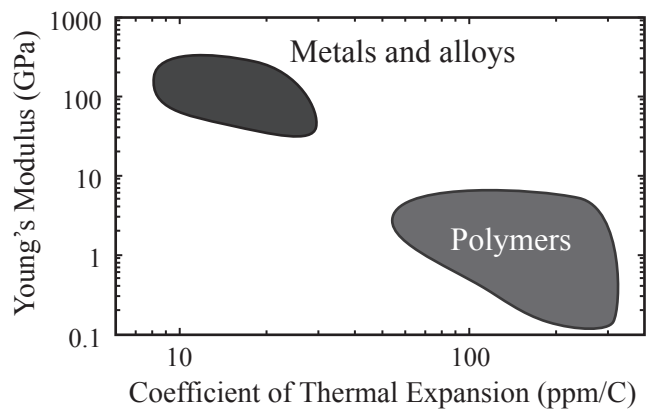


Fig. 4: Schematic plot of families of materials in the space of thermal expansion and stiffness.

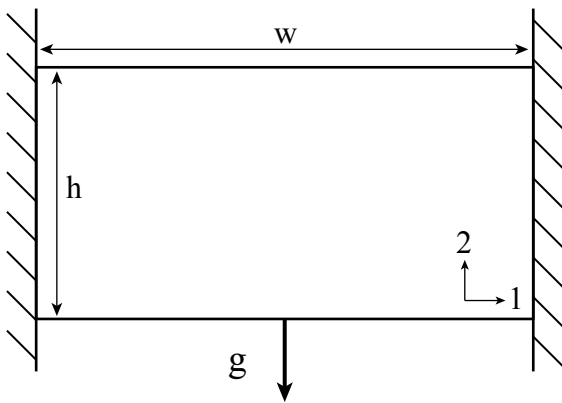


Fig. 5: The design problem for the built-in-beam with loading and boundary conditions.

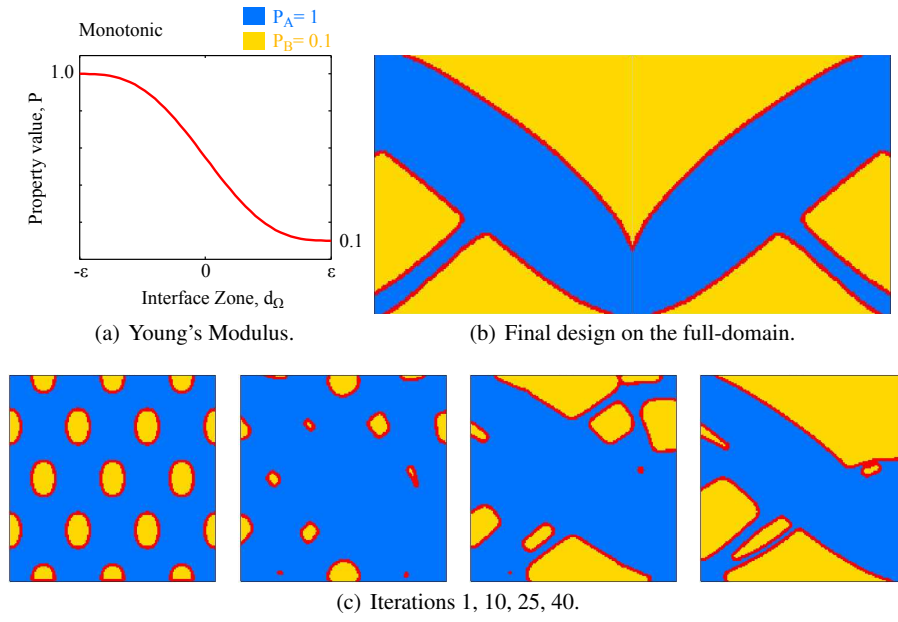


Fig. 6: Case for monotonic interface interpolation applied in the built-in-beam subjected to a point load (Figure 5). Results shown on the half-domain unless otherwise noted. The design images show the distribution of materials A (blue) and B (yellow) in the domain, with the interface zone highlighted in red.

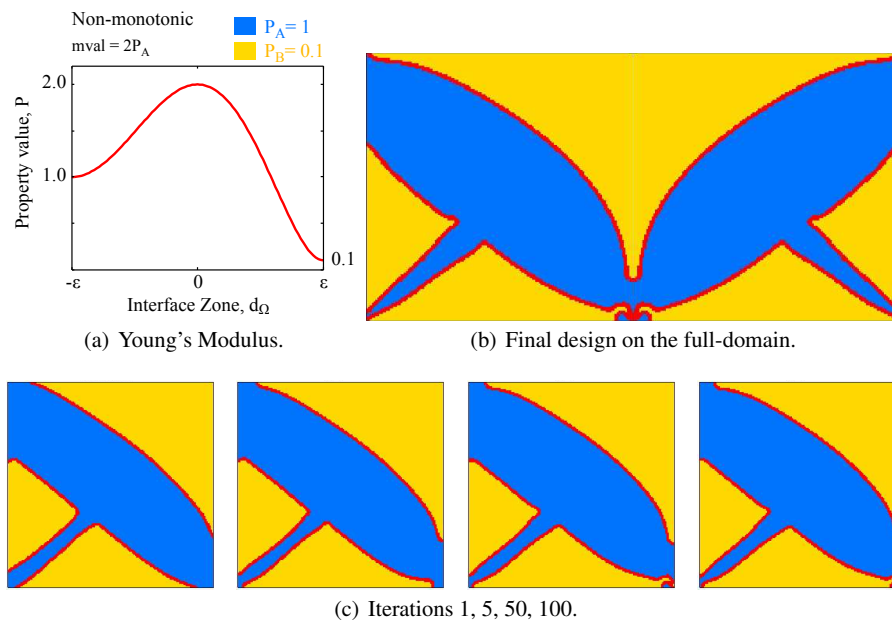


Fig. 7: Case for non-monotonic interface interpolation applied in the built-in-beam problem (Figure 5). Results were initialized ("Iteration 1" in (c)) with the final design from the monotonic interface interpolation scheme (see Figure 6(b)).

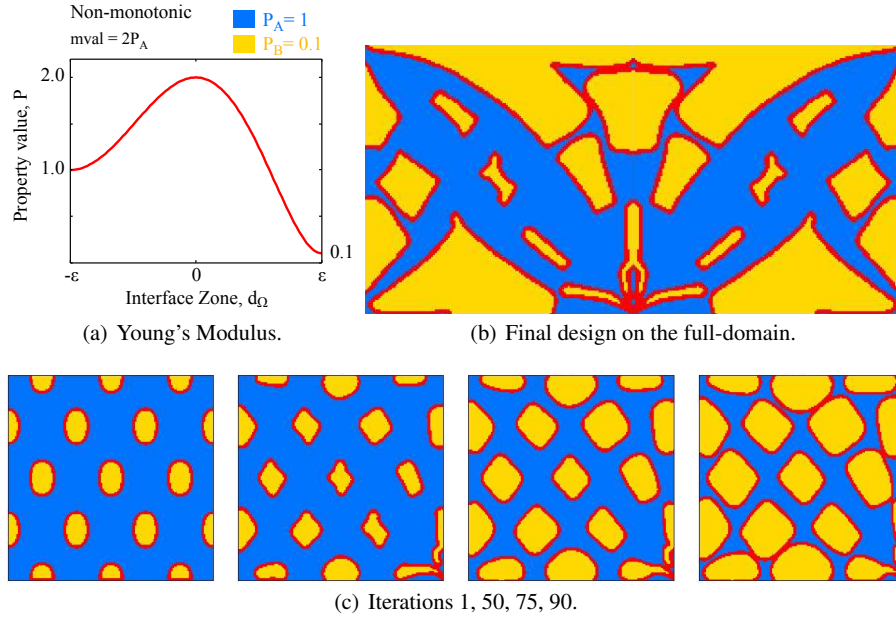


Fig. 8: Case for non-monotonic interface interpolation applied in the built-in-beam problem (Figure 5). Results were initialized from a regular array of inclusions ("Iteration 1" in (c)) and are shown on the half-domain unless otherwise noted.

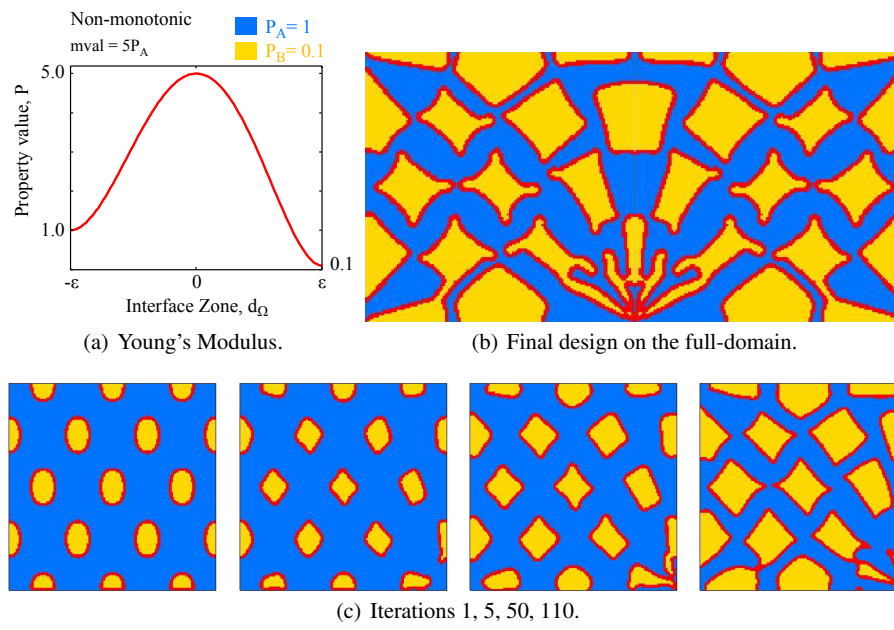
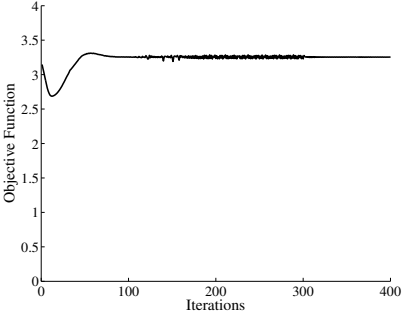
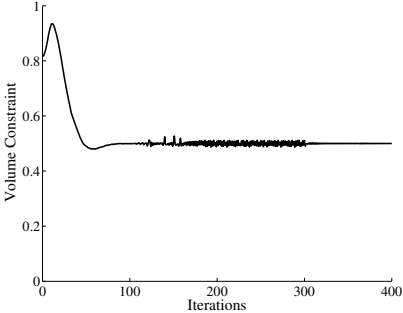
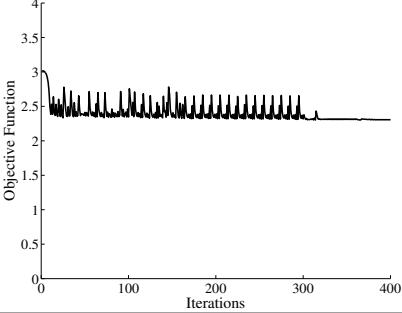
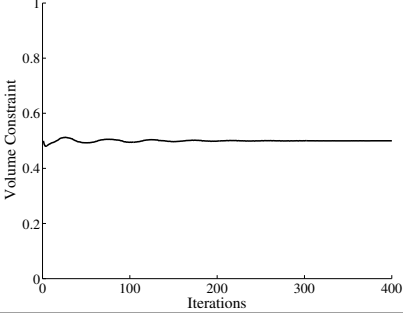
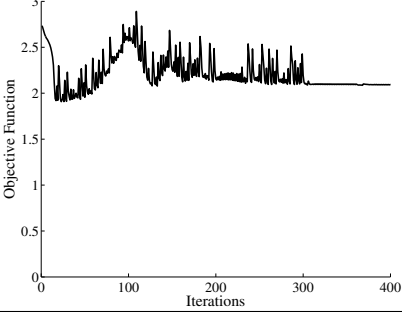
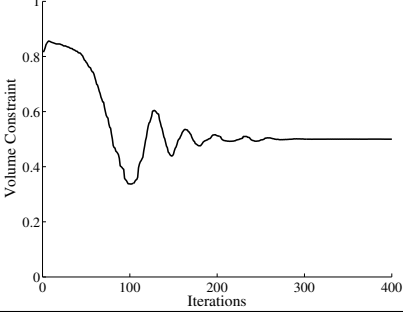
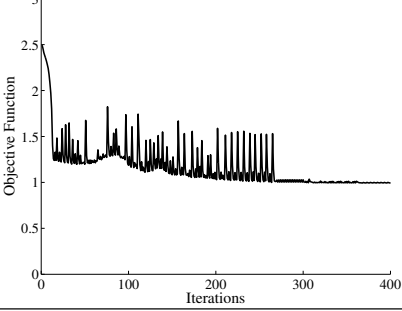
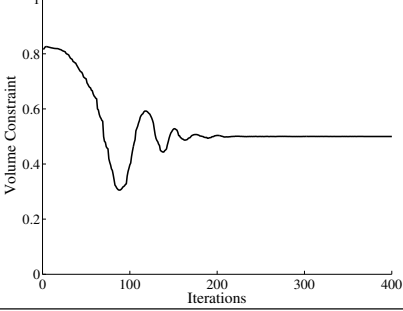


Fig. 9: Case for another non-monotonic interface interpolation scheme applied in the built-in-beam problem. Results were initialized from a regular array of inclusions ("Iteration 1" in (c)) and are shown on the half-domain unless otherwise noted.

Table 1: A table of final objective function values for the minimization of the compliance of the built-in beam problem (Figure 5) for different property transition profiles. All results used $\varepsilon = 4dx$ (Figure 3) and a 150×150 element mesh on the half-domain.

Case	Objective Convergence	Volume Convergence	Final Objective
Figure 6			3.25
Figure 7			2.30
Figure 8			2.10
Figure 9			1.00

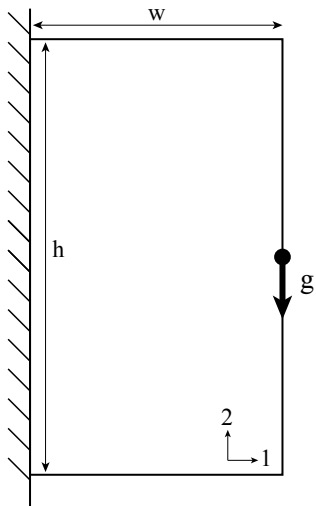


Fig. 10: The mechanical design problem for the short-cantilever with loading and boundary conditions.

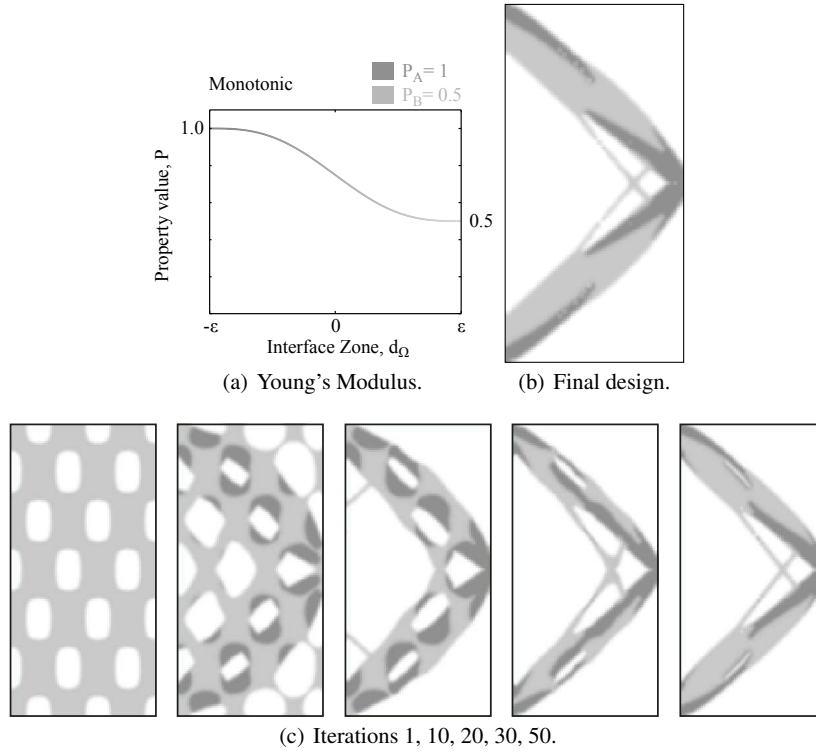


Fig. 11: Short-cantilever problem with two materials and void using monotonic interface interpolation. Results were initialized from a regular array of voids in the bulk materials. The design images show the distribution of Young's modulus in the domain: the higher modulus material (medium grey), lower modulus material (light grey) and void (white). With this scheme, the monotonic interface is not highlighted between the higher and lower modulus materials.

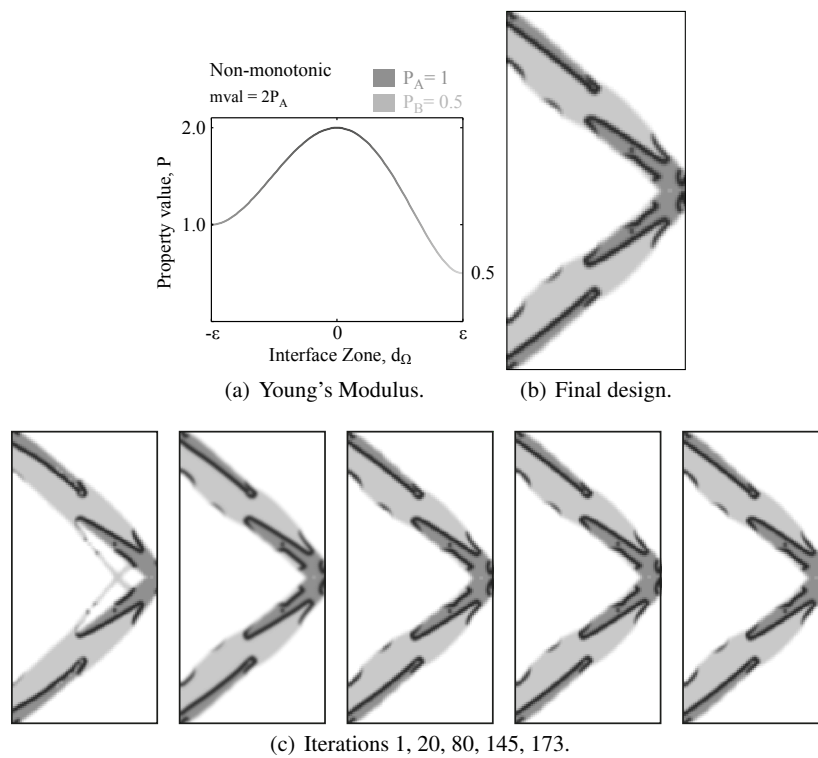


Fig. 12: Short-cantilever problem with two materials and void using non-monotonic interface interpolation. Results were initialized with the final design from the monotonic interface interpolation scheme (Figure 11(b)). The design images show the distribution of Young's modulus in the domain: the higher modulus material (medium grey), lower modulus material (light grey) and void (white). With this scheme, the non-monotonic interface is highlighted in dark grey as it has the largest Young's modulus.

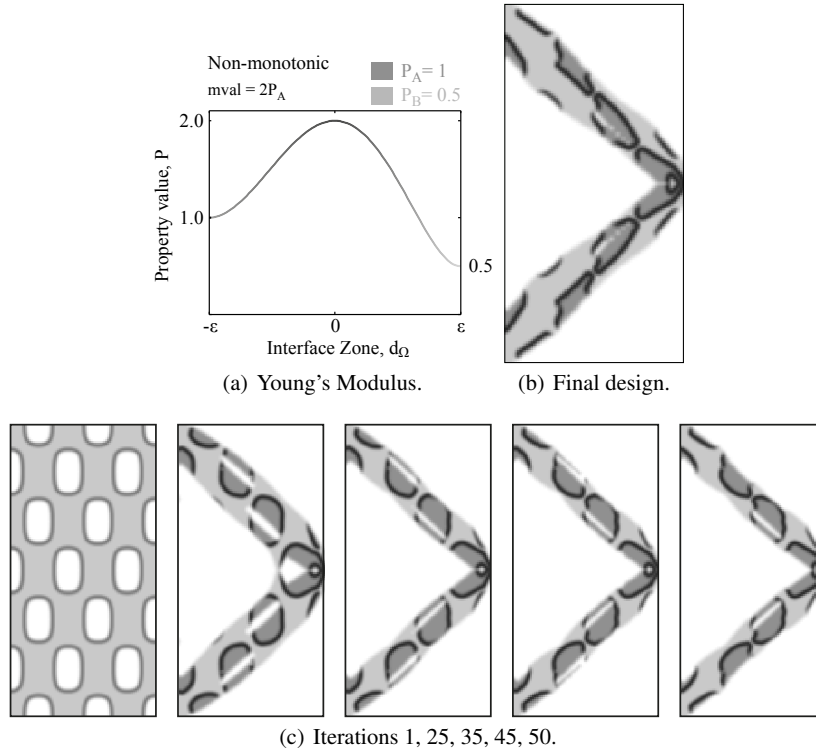
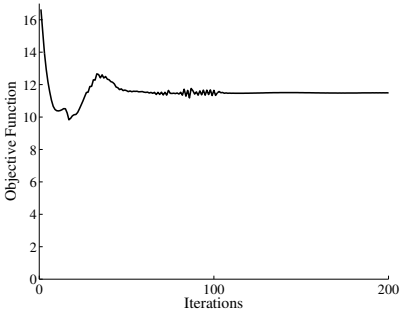
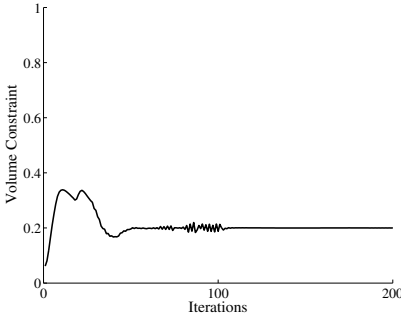
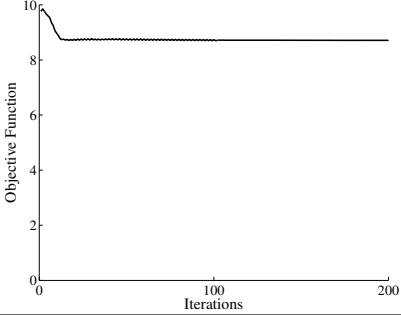
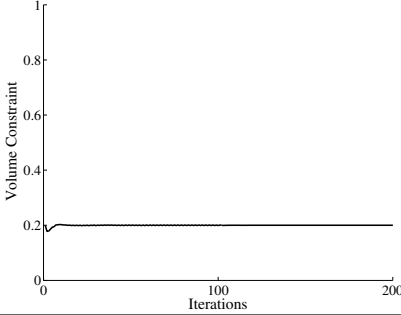
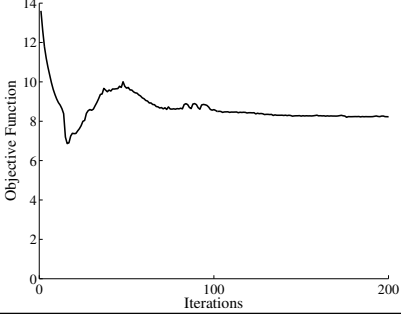
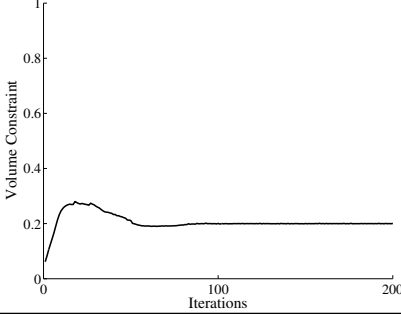


Fig. 13: Short-cantilever problem with two materials and void using non-monotonic interface interpolation. Results were initialized from a regular array of voids in the bulk materials. The design images show the distribution of Young's modulus in the domain: the higher modulus material (medium grey), lower modulus material (light grey) and void (white). With this scheme, the non-monotonic interface is highlighted in dark grey as it has the largest Young's modulus.

Table 2: A table of final objective function values for the minimization of the compliance of the short-cantilever problem (Figure 10) for different property transition profiles. All results used $\varepsilon = 2dx$ (Figure 3) and a 80×160 element mesh.

Case	Objective Convergence	Material A Volume Convergence	Final Objective
Figure 11			11.50
Figure 12			8.71
Figure 13			8.23

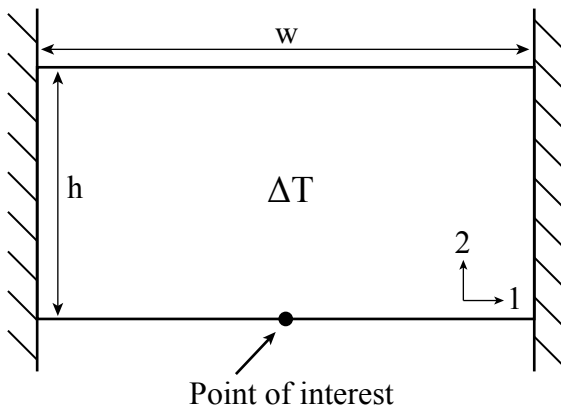


Fig. 14: The design problem for the built-in-beam with loading and boundary conditions. The analysis is thermoelastic with $\Delta T=1$.

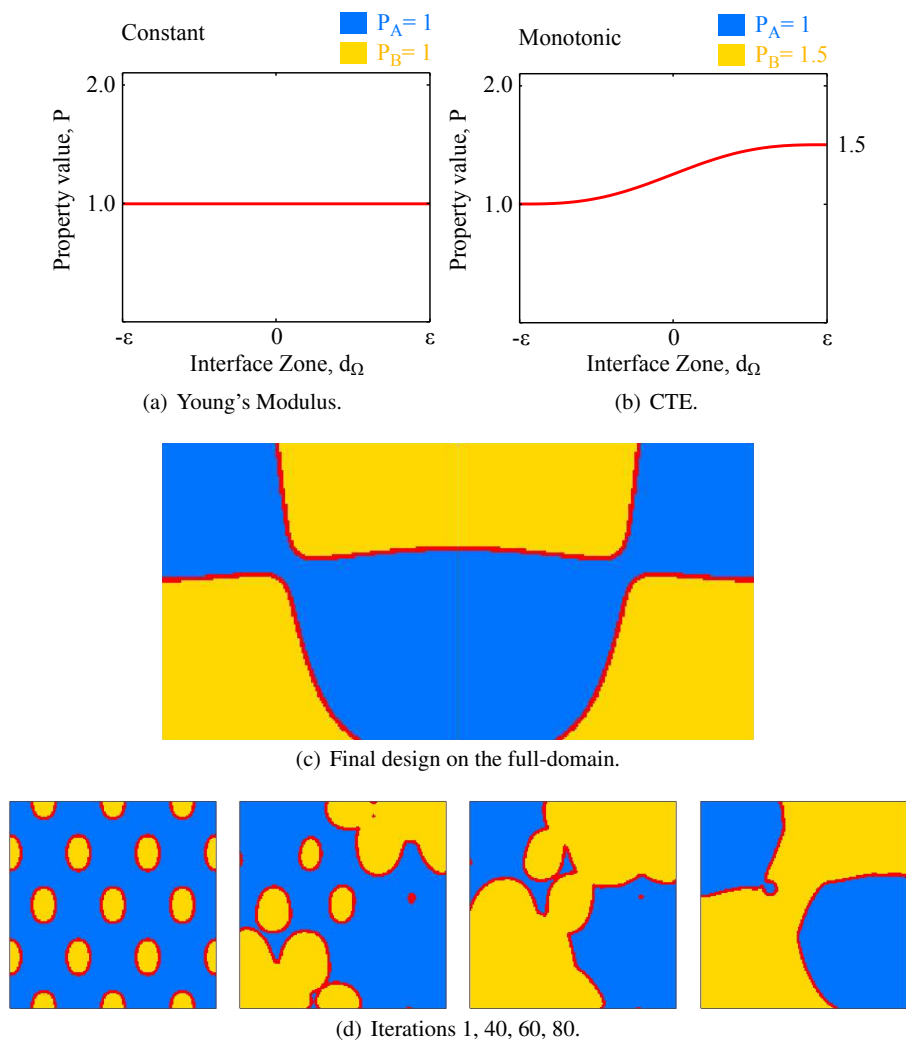


Fig. 15: Case for monotonic interface interpolation applied in the built-in-beam problem under a thermal excursion ($\Delta T=1$), Figure 14. Results shown on the half-domain unless otherwise noted. The design images show the distribution of materials A (blue) and B (yellow) in the domain, with the interface zone highlighted in red.

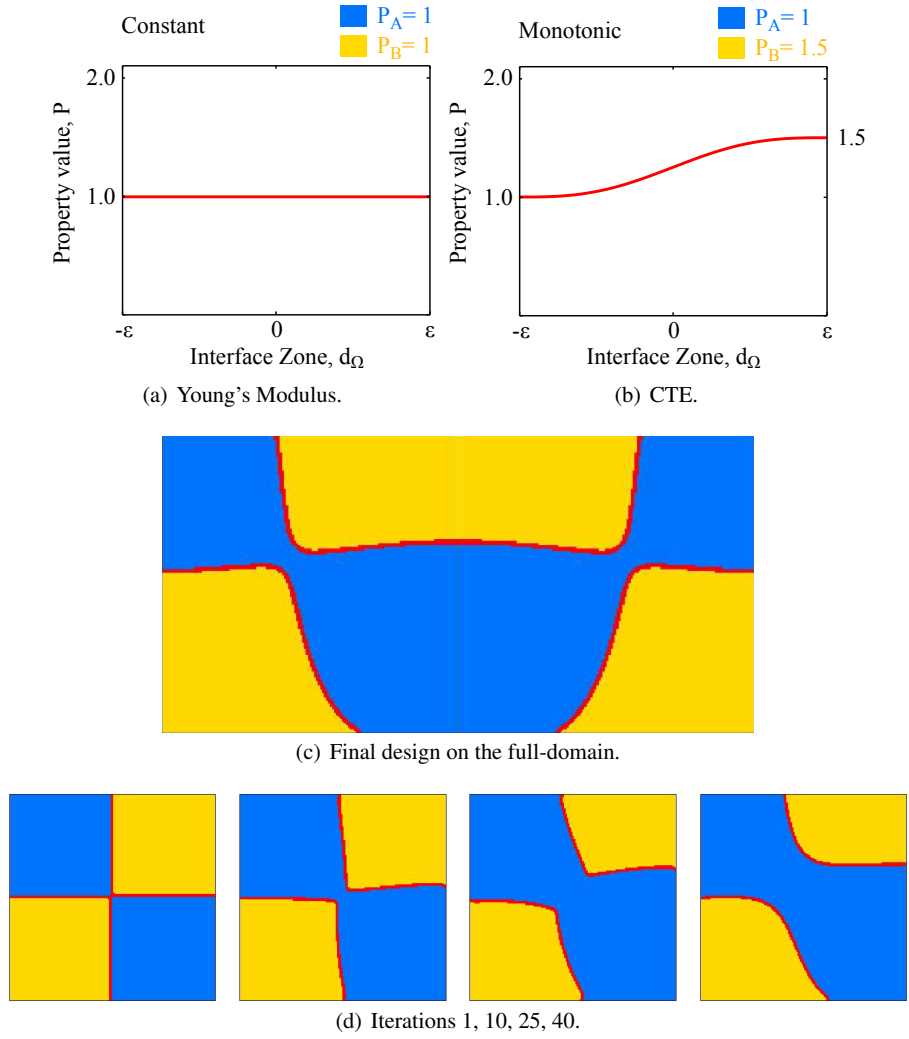


Fig. 16: Case for monotonic interface interpolation applied in the built-in-beam problem under a thermal excursion ($\Delta T=1$), Figure 14. Results shown on the half-domain unless otherwise noted. Results were initialized with the a checkerboard pattern ("Iteration 1" in (d)) inspired by the final design of the monotonic interface interpolation scheme (see Figure 15(c)).

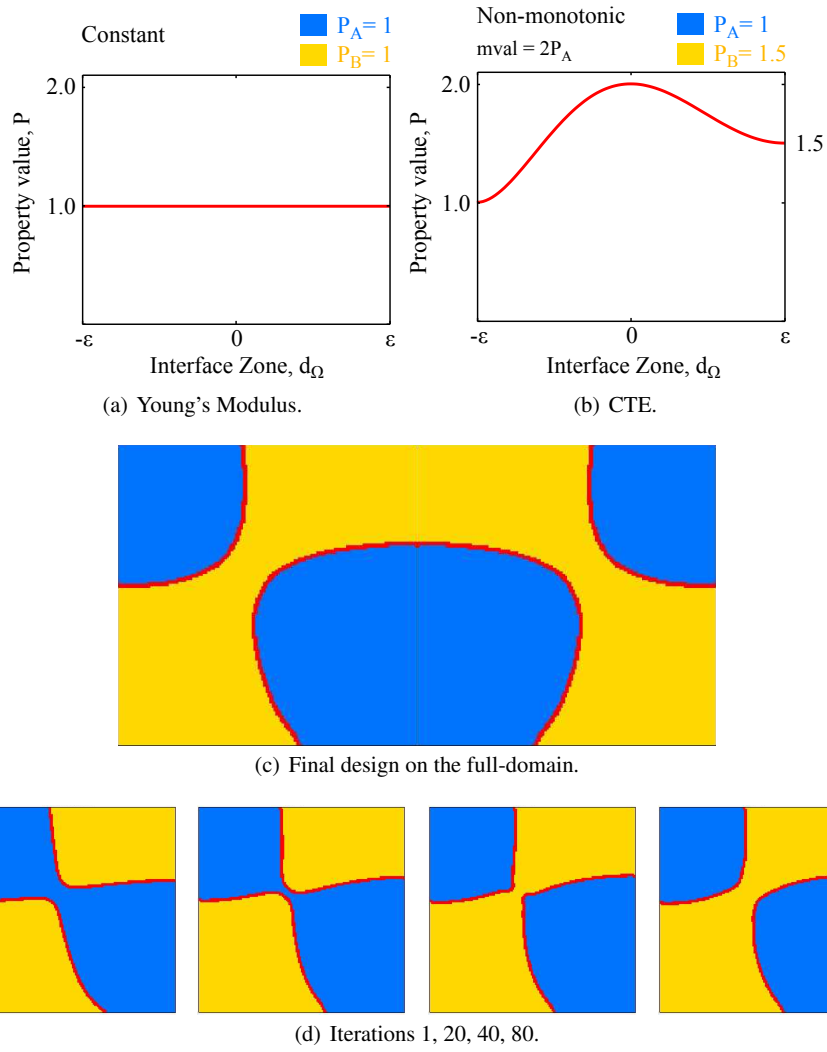


Fig. 17: Case for non-monotonic interface interpolation applied in the built-in-beam problem under a thermal excursion ($\Delta T=1$), Figure 14. Results shown on the half-domain unless otherwise noted. Results were initialized ("Iteration 1" in (d)) with the final design of the monotonic interface interpolation scheme (see Figure 15(c)).

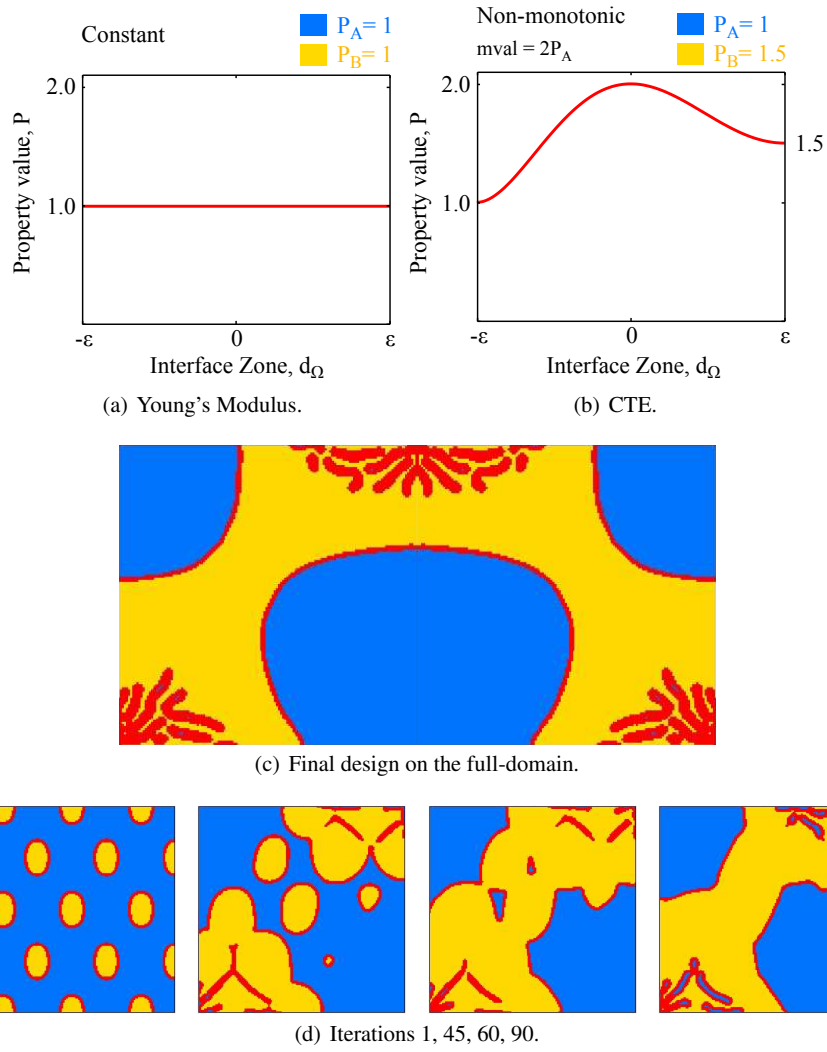
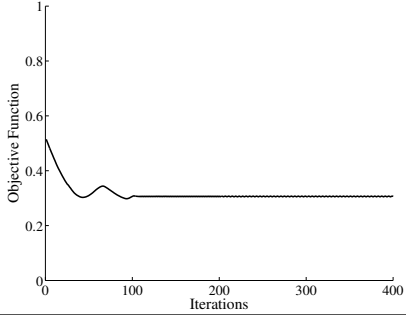
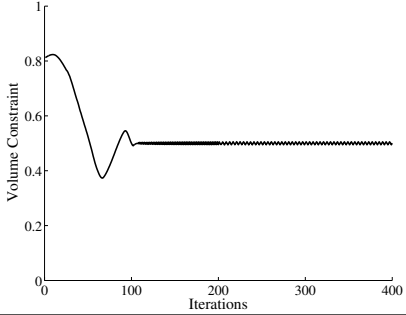
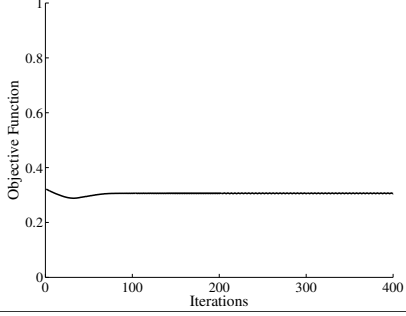
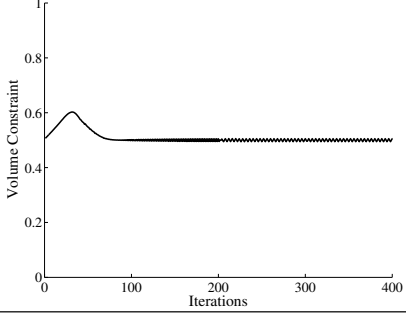
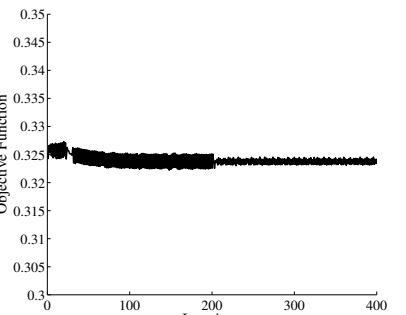
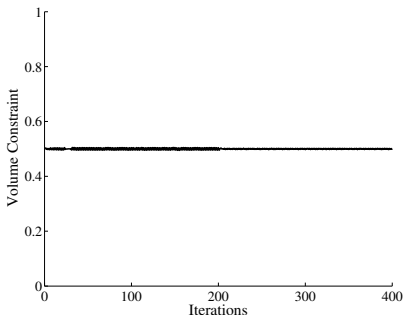
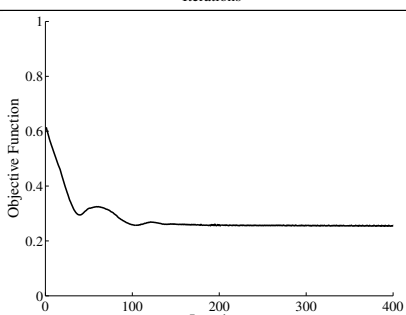
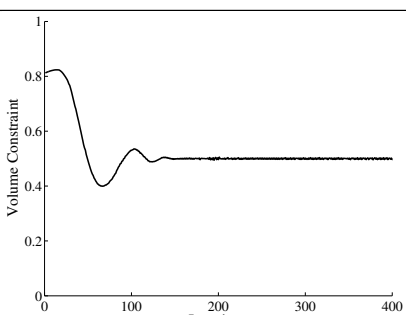


Fig. 18: Case for non-monotonic interface interpolation applied in the built-in-beam problem under a thermal excursion ($\Delta T=1$), Figure 14. Results were initialized from a regular array of inclusions (“Iteration 1” in (d)) and are shown on the half-domain unless otherwise noted.

Table 3: A table of final objective function values for the minimization of the vertical (u_2) displacement at the point of interest indicated in the built-in beam problem (Figure 14) for different property transition profiles. All results used a uniform normalized Young's modulus distribution ($E_A = E_B = E_{interface} = 1.0$), $\varepsilon = 4dx$, and a 150×150 element mesh on the half-domain.

Case	Objective Convergence	Volume Convergence	Final Obj. $(u_2)^2$
Figure 15			0.305
Figure 16			0.306
Figure 17			0.323
Figure 18			0.254

References

- Allaire G, Bonnetier E, Francfort G, Jouve F (1997) Shape optimization by the homogenization method. *Numerische Mathematik* 76:27–68
- Allaire G, Jouve F, Toader AM (2004) Structural optimization using sensitivity analysis and a level-set method. *Journal of Computational Physics* 194:363–393
- Allaire G, De Gournay F, Jouve F, Toader A (2005) Structural optimization using topological and shape sensitivity via a level set method. *Control and cybernetics* 34(1):59
- Allaire G, Dapogny C, Delgado G, Michailidis G (2013a) Multi-phase structural optimization via a level-set method, accepted to ESAIM: Control, Optimisation and Calculus of Variations. Preprint available at: <http://hal.upmc.fr/docs/00/83/94/64/PDF/multiphasepreprint.pdf>
- Allaire G, Dapogny C, Frey P (2013b) A mesh evolution algorithm based on the level set method for geometry optimization. *Structural and Multidisciplinary Optimization* 48(4):711–715
- Bendsoe M, Kikuchi N (1988) Generating optimal topologies in structural design using a homogenization method. *Computer methods in applied mechanics and engineering* 71:197–224
- Bendsoe M, Sigmund O (1999) Material interpolation schemes in topology optimization. *Archive of Applied Mechanics* 69:635–654
- Bendsoe M, Sigmund O (2004) *Topology optimization: theory, methods and applications*. Springer
- Braccini M, Dupeux M (2012) *Mechanics of Solid Interfaces*. Wiley Online Library
- Céa J (1986) Conception optimale ou identification de formes: calcul rapide de la dérivée directionnelle de la fonction cout. *Modélisation mathématique et analyse numérique* 20:371–402
- Creton C, Kramer EJ, Brown HR, and Hui CY (2002) Adhesion and fracture of interfaces between immiscible polymers: From the molecular to the continuum scale. *Molecular Simulation Fracture Gel Theory. Advances in Polymer Science* 156:53–136
- Eschenauer H, Olhoff N (2001) Topology optimization of continuum structures: A review. *Appl Mech Rev* 54, no 4
- Guggenheim E (1959) *Thermodynamics*. North Holland Publishing Company
- Harrysson OL, Cansizoglu O, Marcellin-Little DJ, Cormier DR, West II HA (2008) Direct metal fabrication of titanium implants with tailored materials and mechanical properties using electron beam melting technology. *Materials Science and Engineering: C* 28(3):366–373
- Ikuta K, Hirowatari K (1993) Real three dimensional micro fabrication using stereo lithography and metal molding. In: *Micro Electro Mechanical Systems, 1993, MEMS'93, Proceedings An Investigation of Micro Structures, Sensors, Actuators, Machines and Systems*. IEEE., IEEE, pp 42–47
- Committee on Integrated Computational Materials Engineering NRC (2008) *Integrated Computational Materials Engineering: A Transformational Discipline for Improved Competitiveness and National Security*. The National Academies Press, URL http://www.nap.edu/openbook.php?record_id=12199
- Laszczyk L (2011) Homogenization and topological optimization of architected panels. PhD thesis, Université de Grenoble
- Limited GD (2010) *CES EduPack 2010*, Copyright Granta Design Limited.
- Lipson H, Pollack JB (2000) Automatic design and manufacture of robotic lifeforms. *Nature* 406(6799):974–978
- Mello LAM, Silva ECN (2013) Conceptual design of electrothermo-mechanical microactuators with functionally graded metallic materials using topology optimization for response time reduction. In: *10th World Congress on Structural and Multidisciplinary Optimization*, May19-24, Orlando, Florida, USA
- Michell AGM (1904) The limits of economy of material in frame-structures. *Philosophical Magazine* 8:589–597
- Miyamoto Y, Kaysser W, Rabin B, Kawasaki A, Ford R (1999) *Functionally graded materials: design, processing and applications*
- Osher S, Fedkiw R (2002) *Level set methods and dynamic implicit surfaces*, vol 153. Springer
- Osher S, Sethian J (1988) Fronts propagating with curvature dependent speed: algorithms based on hamilton-jacobi formulations. *Journal of Computational Physics* 79:12–49
- Pasko A, Fryazinov O, Vilbrandt T, Fayolle PA, Adzhiev V (2011) Procedural function-based modelling of volumetric microstructures. *Graphical Models* 73(5):165–181
- Rao S (2009) *Engineering optimization: theory and practice*. Wiley
- Scilab Enterprises (2012) *Scilab: Free and Open Source software for numerical computation*. Scilab Enterprises, Orsay, France, URL <http://www.scilab.org>
- Sethian J (1999) *Level set methods and fast marching methods: evolving interfaces in computational geometry, fluid mechanics, computer vision, and materials science*, vol 3. Cambridge university press
- Sigmund O (2000) A new class of extremal composites. *Journal of the Mechanics and Physics of Solids* 48(2):397–428
- Simar A, Brechet Y, De Meester B, Denquin A, Gallais C, Pardoën T (2012) Integrated modeling of friction stir welding of 6xxx series Al alloys: Process, microstructure and properties. *Progress in Materials Science* 57(1):95–183
- Sokolowski J, Zochowski A (1999) On the topological derivative in shape optimization. *SIAM journal on control and optimization* 37(4):1251–1272
- Wang MY, Wang X (2004) "color" level sets: a multi-phase method for structural topology optimization with multiple materials. *Computer Methods in Applied Mechanics and Engineering* 193:469–496
- Wang MY, Wang X (2005) A level-set based variational method for design and optimization of heterogeneous objects. *Computer-Aided Design* 37(3):321–337
- Wang MY, Zhou S (2004) Phase field: a variational method for structural topology optimization. *Comput Model Eng Sci* 6(6):547–566
- Wang MY, Wang X, Guo D (2003) A level set method for structural topology optimization. *Computer methods in applied mechanics and engineering* 192(1):227–246
- Wang X, Mei Y, Wang MY (2004) Level-set method for design of multi-phase elastic and thermoelastic materials. *International Journal of Mechanics and Materials in Design* 1:213–239
- Wolf D (1992) *Materials interfaces: atomic-level structure and properties*. Chapman & Hall
- Wulff G (1901) Zur frage der geschwindigkeit des wachstums und der aufoesung der krystallflächen. *Z Kryst* 34:449–530
- Xia Q, Wang MY (2008a) Simultaneous optimization of the material properties and the topology of functionally graded structures. *Computer-Aided Design* 40(6):660–675
- Xia Q, Wang MY (2008b) Topology optimization of thermoelastic structures using level set method. *Comput Mech* 42:837–857
- Yin L, Ananthasuresh G (2002) A novel topology design scheme for the multi-physics problems of electro-thermally actuated compliant micromechanisms. *Sensors and Actuators, A: Physical* 97:599–609
- Zhou S, Wang M (2007) Multimaterial structural topology optimization with a generalized cahn–hilliard model of multiphase transition. *Structural and Multidisciplinary Optimization* 33(2):89–111

Bibliography

- [1] H.K. Ahn, M. De Berg, P. Bose, S.W. Cheng, D. Halperin, J. Matoušek, and O. Schwarzkopf. Separating an object from its cast. *Computer-Aided Design*, 34(8):547–559, 2002.
- [2] O. Alexandrov and F. Santosa. A topology-preserving level set method for shape optimization. *Journal of Computational Physics*, 204(1):121–130, 2005.
- [3] G. Allaire. *Shape optimization by the homogenization method*, volume 146. Springer, 2002.
- [4] G. Allaire. *Conception optimale de structures*, volume 58. Springer, 2006.
- [5] G. Allaire. *Numerical analysis and optimization: an introduction to mathematical modelling and numerical simulation*. Oxford University Press, 2007.
- [6] G. Allaire, E. Bonnetier, G. Francfort, and F. Jouve. Shape optimization by the homogenization method. *Numerische Mathematik*, 76(1):27–68, 1997.
- [7] G. Allaire and C. Castro. A new approach for the optimal distribution of assemblies in a nuclear reactor. *Numerische Mathematik*, 89(1):1–29, 2001.
- [8] G. Allaire, C. Dapogny, G. Delgado, and G. Michailidis. Mutli-phase structural optimization via a level-set method. (*to appear in ESAIM: Control, Optimisation and Calculus of Variations*), 2013.
- [9] G. Allaire, C. Dapogny, and P. Frey. Topology and geometry optimization of elastic structures by exact deformation of simplicial mesh. *Comptes Rendus Mathématique*, 349(17):999–1003, 2011.
- [10] G. Allaire and F. Jouve. A level-set method for vibration and multiple loads structural optimization. *Computer methods in applied mechanics and engineering*, 194(30):3269–3290, 2005.
- [11] G. Allaire and F. Jouve. Minimum stress optimal design with the level set method. *Engineering analysis with boundary elements*, 32(11):909–918, 2008.
- [12] G. Allaire, F. Jouve, and G. Michailidis. Thickness constraints in structural optimization via a level-set method. (*In preparation*), 2013.
- [13] G. Allaire, F. Jouve, and A.M. Toader. A level-set method for shape optimization. *Comptes Rendus Mathématique*, 334(12):1125–1130, 2002.
- [14] G. Allaire, F. Jouve, and A.M. Toader. Structural optimization using sensitivity analysis and a level-set method. *Journal of computational physics*, 194(1):363–393, 2004.
- [15] G. Allaire, F. Jouve, and N. Van Goethem. Damage evolution in brittle materials by shape and topological sensitivity analysis. Technical report, Technical Report 676, Ecole Polytechnique, 2010.
- [16] G. Allaire, F. Jouve, and N. Van Goethem. Damage and fracture evolution in brittle materials by shape optimization methods. *Journal of Computational Physics*, 230(12):5010–5044, 2011.
- [17] G. Allaire and R.V. Kohn. Optimal design for minimum weight and compliance in plane stress using extremal microstructures. *European journal of mechanics. A. Solids*, 12(6):839–878, 1993.
- [18] G. Allaire and O. Pantz. Structural optimization with \ tt {FreeFem++}. *Structural and Multidisciplinary Optimization*, 32(3):173–181, 2006.
- [19] G. Allaire, D. Silva, and O. Pantz. Sur un problème inverse de détermination de coefficients de diffusion. Rapport interne, n. 560, CMAP, Ecole Polytechnique, Novembre 2004.

- [20] L. Ambrosio. Lecture notes on geometric evolution problems, distance function and viscosity solutions. *Calculus of variations and partial differential equations. Topics on geometrical evolution problems and degree theory*, pages 5–94, 1997.
- [21] L. Ambrosio and G. Buttazzo. An optimal design problem with perimeter penalization. *Calculus of Variations and Partial Differential Equations*, 1(1):55–69, 1993.
- [22] C. Barbarosie. Numerical approach to the inverse homogenization problem. In *Proceedings of the International Conference on Differential Equations*, volume 1, page 7. World Scientific, 1999.
- [23] A. Baumgartner, L. Harzheim, and C. Mattheck. Sko (soft kill option): the biological way to find an optimum structure topology. *International Journal of Fatigue*, 14(6):387–393, 1992.
- [24] M.P. Bendsøe. Optimal shape design as a material distribution problem. *Structural and Multidisciplinary Optimization*, 1(4):193–202, 1989.
- [25] M.P. Bendsøe and A.R. Díaz. Optimization of material properties for mindlin plate design. *Structural Optimization*, 6(4):268–270, 1993.
- [26] M.P. Bendsøe and A.R. Díaz. Optimization of material properties for improved frequency response. *Structural optimization*, 7(1-2):138–140, 1994.
- [27] M.P. Bendsøe and N. Kikuchi. Generating optimal topologies in structural design using a homogenization method. *Computer methods in applied mechanics and engineering*, 71(2):197–224, 1988.
- [28] M.P. Bendsoe and O. Sigmund. *Topology optimization: theory, methods and applications*. Springer, 2004.
- [29] C. Bernardi and O. Pironneau. Sensitivity of darcy’s law to discontinuities. *Chinese Annals of Mathematics*, 24(02):205–214, 2003.
- [30] Blaise Bourdin. Filters in topology optimization. *International Journal for Numerical Methods in Engineering*, 50(9):2143–2158, 2001.
- [31] H.-J. Butt, K. Graf, and M. Kappl. Introduction. *Physics and Chemistry of Interfaces*, pages 1–3, 2004.
- [32] J. E. Cadman, S. Zhou, Y. Chen, and Q. Li. On design of multi-functional microstructural materials. *Journal of Materials Science*, 48(1):51–66, 2013.
- [33] J. Campbell. *Castings, 1991*. Butterworth Heinemann, Great Britain, 1964.
- [34] P. Cannarsa and P. Cardaliaguet. Representation of equilibrium solutions to the table problem of growing sandpiles. *Interfaces and free boundaries*, 6(4):435, 2004.
- [35] J. Céa. Conception optimale ou identification de formes: calcul rapide de la dérivée directionnelle de la fonction coût. *Modélisation mathématique et analyse numérique*, 20(3):371–402, 1986.
- [36] I. Chavel. *Riemannian geometry: a modern introduction*. Cambridge university press, 2006.
- [37] S. Chen and W. Chen. A new level-set based approach to shape and topology optimization under geometric uncertainty. *Structural and Multidisciplinary Optimization*, 44(1):1–18, 2011.
- [38] S. Chen, M.Y. Wang, and A.Q. Liu. Shape feature control in structural topology optimization. *Computer-Aided Design*, 40(9):951–962, 2008.
- [39] D. Chenais. On the existence of a solution in a domain identification problem. *Journal of Mathematical Analysis and Applications*, 52(2):189–219, 1975.
- [40] G. Cheng, Y. Mei, and X. Wang. A feature-based structural topology optimization method. In *IUTAM Symposium on Topological Design Optimization of Structures, Machines and Materials*, pages 505–514. Springer, 2006.
- [41] A. Cherkaev. *Variational methods for structural optimization*, volume 140. Springer, 2000.

- [42] P.W. Christensen and A. Klarbring. *An introduction to structural optimization*, volume 153. Springer, 2009.
- [43] A.N. Christiansen, M. Nobel-Jørgensen, N. Aage, O. Sigmund, and J.A. Bærentzen. Topology optimization using an explicit interface representation. *Structural and Multidisciplinary Optimization*, pages 1–13, 2013.
- [44] C. Dapogny. *Ph.D. Thesis*. PhD thesis, Université Pierre et Marie Curie, In preparation.
- [45] C. Dapogny, C. Dobrzynski, and P. Frey. Three-dimensional adaptive domain remeshing, implicit domain meshing, and applications to free and moving boundary problems. 2013.
- [46] C. Dapogny and P. Frey. Computation of the signed distance function to a discrete contour on adapted triangulation. *Calcolo*, 49(3):193–219, 2012.
- [47] F. de Gournay. Velocity extension for the level-set method and multiple eigenvalues in shape optimization. *SIAM journal on control and optimization*, 45(1):343–367, 2006.
- [48] M.C. Delfour and J. Zolesio. Shape identification via metrics constructed from the oriented distance function. *Control and Cybernetics*, 34(1):137, 2005.
- [49] M.C. Delfour and J.P. Zolésio. *Shape and geometries*, volume 19. 2001.
- [50] G. Delgado. *Ph.D. Thes*. PhD thesis, In preparation.
- [51] X.L. Deng and L. Proslier. Optimization of structures under technological casting constraints. *Structural and Multidisciplinary Optimization*, 10(3):180–190, 1995.
- [52] P. Duysinx and M.P. Bendsøe. Topology optimization of continuum structures with local stress constraints. *International Journal for Numerical Methods in Engineering*, 43(8):1453–1478, 1998.
- [53] P. Duysinx, L. Van Miegroet, E. Lemaire, O. Brüls, and M. Bruyneel. Topology and generalized shape optimization: why stress constraints are so important? *International Journal for Simulation and Multidisciplinary Design Optimization*, 2(4):253–258, 2008.
- [54] SA Ebrahimi, DA Tortorelli, and JA Dantzig. Sensitivity analysis and nonlinear programming applied to investment casting design. *Applied Mathematical Modelling*, 21(2):113–123, 1997.
- [55] L.C. Evans and R.F. Gariepy. *Measure theory and fine properties of functions*. CRC, 1991.
- [56] M.W. Fu, A.Y.C. Nee, and J.Y.H. Fuh. The application of surface visibility and moldability to parting line generation. *Computer-Aided Design*, 34(6):469–480, 2002.
- [57] D. Fujii, B.C. Chen, and N. Kikuchi. Composite material design of two-dimensional structures using the homogenization design method. *International Journal for Numerical Methods in Engineering*, 50(9):2031–2051, 2001.
- [58] S. Garreau, P. Guillaume, and M. Masmoudi. The topological asymptotic for pde systems: the elasticity case. *SIAM Journal on Control and Optimization*, 39(6):1756–1778, 2001.
- [59] J. Gomes and O. Faugeras. Reconciling distance functions and level sets. *Journal of Visual Communication and Image Representation*, 11(2):209–223, 2000.
- [60] J.E. Gordon. *Structures: or why things don't fall down*. Da Capo Press, 2009.
- [61] J.K. Guest. Imposing maximum length scale in topology optimization. *Structural and Multidisciplinary Optimization*, 37(5):463–473, 2009.
- [62] J.K. Guest, A. Asadpoure, and S.-H. Ha. Eliminating beta-continuation from heaviside projection and density filter algorithms. *Structural and Multidisciplinary Optimization*, 44(4):443–453, 2011.
- [63] J.K. Guest, J.H. Prévost, and T. Belytschko. Achieving minimum length scale in topology optimization using nodal design variables and projection functions. *International Journal for Numerical Methods in Engineering*, 61(2):238–254, 2004.

- [64] S.-H. Ha and S. Cho. Topological shape optimization of heat conduction problems using level set approach. *Numerical Heat Transfer, Part B: Fundamentals*, 48(1):67–88, 2005.
- [65] O.L.A. Harrysson, O. Cansizoglu, D.J. Marcellin-Little, D.R. Cormier, and H.A. West II. Direct metal fabrication of titanium implants with tailored materials and mechanical properties using electron beam melting technology. *Materials Science and Engineering: C*, 28(3):366–373, 2008.
- [66] L. Harzheim and G. Graf. Topshape: An attempt to create design proposals including manufacturing constraints. *International journal of vehicle design*, 28(4):389–409, 2002.
- [67] L. Harzheim and G. Graf. A review of optimization of cast parts using topology optimization: II - topology optimization without manufacturing constraints. *Structural and multidisciplinary optimization*, 30(5):491–497, 2005.
- [68] L. Harzheim and G. Graf. A review of optimization of cast parts using topology optimization: I - topology optimization with manufacturing constraints. *Structural and multidisciplinary optimization*, 31(5):388–399, 2006.
- [69] J. Haslinger and J. Dvorak. Optimum composite material design. *RAIRO-M2AN Modelisation Math et Analyse Numerique-Mathem Modell Numerical Analysis*, 29(6):657–686, 1995.
- [70] J. Haslinger, A. Hillebrand, T. Kärkkäinen, and M. Miettinen. Optimization of conducting structures by using the homogenization method. *Structural and multidisciplinary optimization*, 24(2):125–140, 2002.
- [71] A. Henrot and M. Pierre. *Variation et optimisation de formes: une analyse géométrique*, volume 48. Springer, 2005.
- [72] F. Hettlich and W. Rundell. The determination of a discontinuity in a conductivity from a single boundary measurement. *Inverse Problems*, 14(1):67, 1998.
- [73] K. Ikuta and K. Hirowatari. Real three dimensional micro fabrication using stereo lithography and metal molding. In *Micro Electro Mechanical Systems, 1993, MEMS'93, Proceedings An Investigation of Micro Structures, Sensors, Actuators, Machines and Systems. IEEE.*, pages 42–47. IEEE, 1993.
- [74] W. Kapturkiewicz, E. Fraś, and A.A. Burbelko. Dlaczego modelowanie komputerowe jest w odlewnictwie potrzebne? why is the computer modelling needed in casting?
- [75] A.L. Karchevsky. Reconstruction of pressure velocities and boundaries of thin layers in thinly-stratified layers. *Journal of Inverse and Ill-Posed Problems*, 18(4):371–388, 2010.
- [76] R. Kimmel and A.M. Bruckstein. Shape offsets via level sets. *Computer-Aided Design*, 25(3):154–162, 1993.
- [77] R. Kimmel, D. Shaked, N. Kiryati, and A.M. Bruckstein. Skeletonization via distance maps and level sets. In *Photonics for Industrial Applications*, pages 137–148. International Society for Optics and Photonics, 1995.
- [78] M. Kocvara and M. Stingl. Free material optimization for stress constraints. *Structural and Multidisciplinary Optimization*, 33(4):323–336, 2007.
- [79] A. Laadhari, C. Misbah, and P. Saramito. On the equilibrium equation for a generalized biological membrane energy by using a shape optimization approach. *Physica D: Nonlinear Phenomena*, 239(16):1567–1572, 2010.
- [80] N.D. Lagaros, L.D. Psarras, M. Papadrakakis, and G. Panagiotou. Optimum design of steel structures with web openings. *Engineering Structures*, 30(9):2528–2537, 2008.
- [81] L. Laszczyk. *Homogénéisation et optimisation topologique de panneaux architecturés*. PhD thesis, Université de Grenoble, 2011.
- [82] J.P. Leiva, B.C. Watson, and I. Kosaka. An analytical bi-directional growth parameterization to obtain optimal castable topology designs. In *10 th AIAA/ISSMO Multidisciplinary Analysis and Optimization Conference*, 2004.

- [83] J.P. Leiva, B.C. Watson, and I. Kosaka. An analytical directional growth topology parameterization to enforce manufacturing requirements. In *Proc. of 45th AIAA/ASME/ASCE/AHS/ASC Structures, Structural Dynamics, and Material Conference, Palm Springs, CA*, 2004.
- [84] RW Lewis, MT Manzari, and DT Gethin. Thermal optimisation in the sand casting process. *Engineering Computations*, 18(3/4):392–417, 2001.
- [85] R.W. Lewis and K. Ravindran. Finite element simulation of metal casting. *International journal for numerical methods in engineering*, 47(1-3):29–59, 2000.
- [86] Q. Li, G.P. Steven, O.M. Querin, and Y.M. Xie. Shape and topology design for heat conduction by evolutionary structural optimization. *International Journal of Heat and Mass Transfer*, 42(17):3361–3371, 1999.
- [87] H. Lipson and J.B. Pollack. Automatic design and manufacture of robotic lifeforms. *Nature*, 406(6799):974–978, 2000.
- [88] R. Lipton. Design of functionally graded composite structures in the presence of stress constraints. *International journal of solids and structures*, 39(9):2575–2586, 2002.
- [89] J. Luo, Z. Luo, S. Chen, L. Tong, and M.Y. Wang. A new level set method for systematic design of hinge-free compliant mechanisms. *Computer Methods in Applied Mechanics and Engineering*, 198(2):318–331, 2008.
- [90] C. Mantegazza and A.C. Mennucci. Hamilton-jacobi equations and distance functions on riemannian manifolds. *Applied Mathematics and Optimization*, 47(1):1–26, 2003.
- [91] C. Mattheck. Design and growth rules for biological structures and their application to engineering. *Fatigue & Fracture of Engineering Materials & Structures*, 13(5):535–550, 1990.
- [92] W.C.H. McLean. *Strongly elliptic systems and boundary integral equations*. Cambridge university press, 2000.
- [93] Y. Mei and X. Wang. A level set method for structural topology optimization and its applications. *Advances in Engineering Software*, 35(7):415–441, 2004.
- [94] Y. Mei and X. Wang. A level set method for structural topology optimization with multi-constraints and multi-materials. *Acta Mechanica Sinica*, 20(5):507–518, 2004.
- [95] G.W. Milton. *The theory of composites*, volume 6. Cambridge University Press, 2002.
- [96] B. Mohammadi and O. Pironneau. *Applied shape optimization for fluids*, volume 28. Oxford University Press Oxford, 2001.
- [97] U. Montanari. A method for obtaining skeletons using a quasi-euclidean distance. *Journal of the ACM (JACM)*, 15(4):600–624, 1968.
- [98] T.E. Morthland, P.E. Byrne, D.A. Tortorelli, and J.A. Dantzig. Optimal riser design for metal castings. *Metallurgical and Materials Transactions B*, 26(4):871–885, 1995.
- [99] F. Murat and J. Simon. Etude de problèmes d’optimal design. *Optimization Techniques Modeling and Optimization in the Service of Man Part 2*, pages 54–62, 1976.
- [100] F. Murat and L. Tartar. Calcul des variations et homogénéisation. *Les méthodes de l’homogénéisation: théorie et applications en physique*, (57):319–369, 1985.
- [101] J. Nocedal and S.J. Wright. *Numerical optimization*. Springer Science+ Business Media, 2006.
- [102] A.A. Novotny and J. Sokołowski. *Topological Derivatives in Shape Optimization*. Springer, 2013.
- [103] Zh.O. Oralbekova, K.T. Iskakov, and A.L. Karchevsky. Existence of the residual functional derivative with respect to a coordinate of gap point of medium. *APPLIED AND COMPUTATIONAL MATHEMATICS*, 12(2):222–233, 2013.
- [104] J.M. Ortega and W.C. Rheinboldt. On discretization and differentiation of operators with application to newton’s method. *SIAM journal on numerical analysis*, 3(1):143–156, 1966.

- [105] S. Osher and R. Fedkiw. *Level set methods and dynamic implicit surfaces*, volume 153. Springer Verlag, 2003.
- [106] S. Osher and J.A. Sethian. Fronts propagating with curvature-dependent speed: algorithms based on hamilton-jacobi formulations. *Journal of computational physics*, 79(1):12–49, 1988.
- [107] S.J. Osher and F. Santosa. Level set methods for optimization problems involving geometry and constraints: I. frequencies of a two-density inhomogeneous drum. *Journal of Computational Physics*, 171(1):272–288, 2001.
- [108] O. Pantz. Sensibilité de l’équation de la chaleur aux sauts de conductivité. *Comptes Rendus Mathématique*, 341(5):333–337, 2005.
- [109] W.K.S. Pao, R.S. Ransing, R.W. Lewis, and C. Lin. A medial-axes-based interpolation method for solidification simulation. *Finite elements in analysis and design*, 40(5):577–593, 2004.
- [110] M. Papadrakakis and N.D. Lagaros. Reliability-based structural optimization using neural networks and monte carlo simulation. *Computer methods in applied mechanics and engineering*, 191(32):3491–3507, 2002.
- [111] A. Pasko, O. Fryazinov, T. Vilbrandt, P.-A. Fayolle, and V. Adzhiev. Procedural function-based modelling of volumetric microstructures. *Graphical Models*, 73(5):165–181, 2011.
- [112] J. Petersson and O. Sigmund. Slope constrained topology optimization. *International Journal for Numerical Methods in Engineering*, 41(8):1417–1434, 1998.
- [113] O. Pironneau. *Optimal shape design for elliptic systems*. Springer, 1982.
- [114] O. Pironneau, F. Hecht, and A. Le Hyaric. Freefem++ version 2.15-1.
- [115] T.A. Poulsen. A new scheme for imposing a minimum length scale in topology optimization. *International Journal for Numerical Methods in Engineering*, 57(6):741–760, 2003.
- [116] P.N. Rao et al. *Manufacturing technology: Foundry, forming and welding*. Tata McGraw-Hill, 1999.
- [117] H. Rodrigues, J.M. Guedes, and M.P. Bendsoe. Hierarchical optimization of material and structure. *Structural and Multidisciplinary Optimization*, 24(1):1–10, 2002.
- [118] B. Rousselet and D. Chenais. Continuité et différentiabilité d’éléments propres: application à l’optimisation de structures. *Applied Mathematics and Optimization*, 22(1):27–59, 1990.
- [119] Scilab. A scientific software developed by inria and enpc, freely downloadable at <http://www.scilab.org>.
- [120] J.A. Sethian. *Level set methods and fast marching methods: evolving interfaces in computational geometry, fluid mechanics, computer vision, and materials science*, volume 3. Cambridge university press, 1999.
- [121] J.A. Sethian and A. Wiegmann. Structural boundary design via level set and immersed interface methods. *Journal of computational physics*, 163(2):489–528, 2000.
- [122] A.P. Seyranian, E. Lund, and N. Olhoff. Multiple eigenvalues in structural optimization problems. *Structural Optimization*, 8(4):207–227, 1994.
- [123] S. Shamasundar and T.M. Manjunatha. Computer simulation and analysis of investmentcasting process, 2004.
- [124] O. Sigmund. Materials with prescribed constitutive parameters: an inverse homogenization problem. *International Journal of Solids and Structures*, 31(17):2313–2329, 1994.
- [125] O. Sigmund. Tailoring materials with prescribed elastic properties. *Mechanics of Materials*, 20(4):351–368, 1995.
- [126] O. Sigmund. Design of multiphysics actuators using topology optimization—part ii: Two-material structures. *Computer methods in applied mechanics and engineering*, 190(49):6605–6627, 2001.

- [127] O. Sigmund. Manufacturing tolerant topology optimization. *Acta Mechanica Sinica*, 25(2):227–239, 2009.
- [128] O. Sigmund. On the usefulness of non-gradient approaches in topology optimization. *Structural and Multidisciplinary Optimization*, 43(5):589–596, 2011.
- [129] O. Sigmund and S. Torquato. Design of materials with extreme thermal expansion using a three-phase topology optimization method. *Journal of the Mechanics and Physics of Solids*, 45(6):1037–1067, 1997.
- [130] J. Simon and F. Murat. Sur le contrôle par un domaine géométrique. *Preprint*, (76015):725–734, 1976.
- [131] J. Sokolowski, A. Zochowski, et al. On topological derivative in shape optimization. 1997.
- [132] J. Sokolowski and J.-P. Zolesio. *Introduction to shape optimization*. Springer, 1992.
- [133] D.M. Stefanescu. *Science and engineering of casting solidification*. Springer, 2008.
- [134] M. Stolpe and K. Svanberg. An alternative interpolation scheme for minimum compliance topology optimization. *Structural and Multidisciplinary Optimization*, 22(2):116–124, 2001.
- [135] J. Strain. Semi-lagrangian methods for level set equations. *Journal of Computational Physics*, 151(2):498–533, 1999.
- [136] N. Sukumar, D.L. Chopp, N. Moës, and T. Belytschko. Modeling holes and inclusions by level sets in the extended finite-element method. *Computer methods in applied mechanics and engineering*, 190(46):6183–6200, 2001.
- [137] S. Suresh, A. Mortensen, and S. Suresh. *Fundamentals of functionally graded materials*. Institute of Materials London, 1998.
- [138] K. Svanberg. The method of moving asymptotes a new method for structural optimization. *International journal for numerical methods in engineering*, 24(2):359–373, 1987.
- [139] C.C. Swan and I. Kosaka. Voigt-reuss topology optimization for structures with linear elastic material behaviours. *International Journal for Numerical Methods in Engineering*, 40(16):3033–3057, 1997.
- [140] SYSTUS. A finite element software of esi-group.
- [141] A. Takezawa, S. Nishiwaki, and M. Kitamura. Shape and topology optimization based on the phase field method and sensitivity analysis. *Journal of Computational Physics*, 229(7):2697–2718, 2010.
- [142] L. Tartar. *The general theory of homogenization: a personalized introduction*, volume 7. Springer, 2009.
- [143] R. Tavakoli. Minimum weight topology optimization subject to unsteady heat equation and space-time pointwise constraints—toward automatic optimal riser design in the shape casting process. 2011.
- [144] R. Tavakoli and P. Davami. Optimal riser design in sand casting process by topology optimization with simp method i: Poisson approximation of nonlinear heat transfer equation. *Structural and Multidisciplinary Optimization*, 36(2):193–202, 2008.
- [145] R. Tavakoli and P. Davami. Optimal riser design in sand casting process with evolutionary topology optimization. *Structural and Multidisciplinary Optimization*, 38(2):205–214, 2009.
- [146] R.J.D. Tilley. *Understanding solids: the science of materials*. John Wiley & Sons, 2004.
- [147] S. Torquato. Optimal design of heterogeneous materials. *Annual Review of Materials Research*, 40:101–129, 2010.
- [148] D.A. Tortorelli, M.M. Tiller, and J.A. Dantzig. Optimal design of nonlinear parabolic systems. part i: Fixed spatial domain with applications to process optimization. *Computer methods in applied mechanics and engineering*, 113(1):141–155, 1994.

- [149] D.A. Tortorelli, J.A. Tomasko, T.E. Morthland, and J.A. Dantzig. Optimal design of nonlinear parabolic systems. part ii: Variable spatial domain with applications to casting optimization. *Computer methods in applied mechanics and engineering*, 113(1):157–172, 1994.
- [150] N. Vermaak, G. Michailidis, G. Parry, R. Estevez, Y. Brechet, and G. Allaire. Material interface effects on the topology optimization of multi-phase thermoelastic structures using a level set method. (*submitted in SMO: Structural and Multi-disciplinary Optimization*), 2013.
- [151] L.A. Vese and T.F. Chan. A multiphase level set framework for image segmentation using the mumford and shah model. *International journal of computer vision*, 50(3):271–293, 2002.
- [152] M.Y. Wang, S. Chen, X. Wang, and Y. Mei. Design of multimaterial compliant mechanisms using level-set methods. *Journal of Mechanical Design*, 127:941, 2005.
- [153] M.Y. Wang and X. Wang. Color level sets: a multi-phase method for structural topology optimization with multiple materials. *Computer Methods in Applied Mechanics and Engineering*, 193(6):469–496, 2004.
- [154] M.Y. Wang and X. Wang. A level-set based variational method for design and optimization of heterogeneous objects. *Computer-Aided Design*, 37(3):321–337, 2005.
- [155] M.Y. Wang, X. Wang, and D. Guo. A level set method for structural topology optimization. *Computer methods in applied mechanics and engineering*, 192(1):227–246, 2003.
- [156] X. Wang, Y. Mei, and M.Y. Wang. Level-set method for design of multi-phase elastic and thermoelastic materials. *International Journal of Mechanics and Materials in Design*, 1(3):213–239, 2004.
- [157] X. Wang, M.Y. Wang, and D. Guo. Structural shape and topology optimization in a level-set-based framework of region representation. *Structural and Multidisciplinary Optimization*, 27(1):1–19, 2004.
- [158] Q. Xia, T. Shi, S. Liu, and M.Y. Wang. A level set solution to the stress-based structural shape and topology optimization. *Computers and Structures*, 9091(0):55 – 64, 2012.
- [159] Q. Xia, T. Shi, M.Y. Wang, and S. Liu. A level set based method for the optimization of cast part. *Structural and Multidisciplinary Optimization*, 41(5):735–747, 2010.
- [160] Q. Xia, T. Shi, M.Y. Wang, and S. Liu. Simultaneous optimization of cast part and parting direction using level set method. *Structural and Multidisciplinary Optimization*, 44(6):751–759, 2011.
- [161] T. Yamada. *A Level Set-Based Topology Optimization incorporating concept of the phase-field method*. PhD thesis, 2010.
- [162] T. Yamada, K. Izui, S. Nishiwaki, and A. Takezawa. A topology optimization method based on the level set method incorporating a fictitious interface energy. *Computer Methods in Applied Mechanics and Engineering*, 199(45):2876–2891, 2010.
- [163] L. Yin and G.K. Ananthasuresh. Topology optimization of compliant mechanisms with multiple materials using a peak function material interpolation scheme. *Structural and Multidisciplinary Optimization*, 23(1):49–62, 2001.
- [164] M. Zhou and G.I.N. Rozvany. The coc algorithm, part ii: topological, geometrical and generalized shape optimization. *Computer Methods in Applied Mechanics and Engineering*, 89(1):309–336, 1991.
- [165] M. Zhou, Y.K. Shyy, and H.L. Thomas. Topology optimization with manufacturing constraints. In *Proceedings of the 4th World Congress of Structural and Multidisciplinary Optimization*, 2001.
- [166] S. Zhou and Q. Li. Computational design of multi-phase microstructural materials for extremal conductivity. *Computational Materials Science*, 43(3):549–564, 2008.
- [167] S. Zhou and M.Y. Wang. Multimaterial structural topology optimization with a generalized cahn–hilliard model of multiphase transition. *Structural and Multidisciplinary Optimization*, 33(2):89–111, 2007.

- [168] C.G. Zhuang, Z.H. Xiong, and H. Ding. A level set method for topology optimization of heat conduction problem under multiple load cases. *Computer methods in applied mechanics and engineering*, 196(4):1074–1084, 2007.
- [169] G. Zoutendijk. Methods of feasible directions: a study in linear and non-linear programming. 1960.